BALTICA VI

Life Management and Maintenance for Power Plants Vol. 2

Fortum Helsinki Energy

VTT SYMPOSIUM 234

Keywords:
power plant, maintenance, boiler, machinery, equipment, inspection, monitoring, condition, life, performance, risk, reliability

BALTICA VI

Life Management and Maintenance for Power Plants

Vol. 2

Helsinki – Stockholm – Helsinki
8–10 June, 2004

Edited by

Juha Veivo & Pertti Auerkari

Organised by

VTT Industrial Systems

ISBN 951–38–6293–3 (soft back ed.)
ISSN 0357–9387 (soft back ed.)

ISBN 951–38–6294–1 (URL:http://www.vtt.fi/inf/pdf/)
ISSN 1455–0873 (URL: http://www.vtt.fi/inf/pdf/)

JULKAISIJA – UTGIVARE – PUBLISHER

VTT, Vuorimiehentie 5, PL 2000, 02044 VTT
puh. vaihde (09) 4561, faksi 456 4374

VTT, Bergsmansvägen 5, PB 2000, 02044 VTT
tel. växel (09) 4561, fax 456 4374

VTT Technical Research Centre of Finland
Vuorimiehentie 5, P.O.Box 2000, FIN–02044 VTT, Finland
phone internat. + 358 9 4561, fax + 358 9 456 4374

VTT Tuotteet ja tuotanto, Kemistintie 3, PL 1704, 02044 VTT
puh. vaihde (09) 4561, faksi (09) 456 7002, (09) 456 7010, (09) 456 5875

VTT Industriella System, Kemistvägen 3, PB 1704, 02044 VTT
tel. växel (09) 4561, fax (09) 456 7002, (09) 456 7010, (09) 456 5875

VTT Industrial Systems, Kemistintie 3, P.O.Box 1704, FIN–02044 VTT, Finland
phone internat. + 358 9 4561, fax + 358 9 456 7002, + 358 9 456 7010, + 358 9 456 5875

Otamedia Oy, Espoo 2004

Preface

Market liberalisation and requirements of environmentally benign production continue to shape the framework for successfully managing the condition and life of power plants. Operational demands for fast response and flexibility to benefit from market pricing or from cheap low grade fuels can impose considerable challenge, because the foreseen benefit must also cover for the additional loading and damage to equipment. At the same time, there is an underlying and unchanged need for driving down cost, and continuous technical development in processes, equipment design, manufacturing, materials and maintenance systems (including services) will introduce new solutions to both old and new challenges in the plant.

As the power market, production equipment and technology remain under a continuing transition, the tri-annual BALTICA Conference aims to provide a review on the current status and future expectations on the essential issues on life management and maintenance for power plants. Much of this review is contained in the conference presentations and therefore in the two volumes of this publication. However, to fully benefit from the extensive knowledge and experience of the colleagues and experts, the participants are also strongly encouraged to take the opportunity for personal discussion on further details or particular areas of interest during the conference.

The editors wish to express their sincere gratitude to the authors for providing the excellent state-of-the-art papers and presentations for the conference. The kind effort by the referees, many of them in the Board of the Conference, is very much appreciated for helping to maintain the required quality of the publication. Special thanks are due to Ms Karin Waltari, the Conference Secretary at VTT, for her most valuable contribution in taking good care of the conference arrangements. We would also like to thank Ms Åsa Åvall and Ms Sanni Mustala at VTT for helping to edit the proceedings. Finally, financial and other support by the sponsoring organisations is most gratefully acknowledged.

Espoo, June 2004

Juha Veivo Pertti Auerkari

BALTICA VI Editors

Contents

Contents of Volume 2

3 B. Life and damage in high temperature materials and components

Creep and creep damage

Session 4. Developments in monitoring and inspection

Plant life management applications

W. Däuwel
Framatome ANP
Erlangen, Germany

Abstract

The deregulation of the power generation industry has resulted in increased competitive pressure and is forcing operators to improve plant operating economy while maintaining high levels of plant safety. A key factor to meeting this challenge is to apply a comprehensive plant life management (PLIM) approach which addresses all relevant ageing and degradation mechanisms regarding the safety concept, plant components and documentation, plant personnel, consumables, operations management system and administrative controls. For this reason, Framatome ANP has developed an integrated PLIM concept focussing on the safety concept, plant components and documentation.

Representative examples of customer tailored Framatome ANP PLIM applications from plant wide analysis to cost optimized LM strategies associated with specific component types are described. The Framatome ANP PLIM concept supports the plant owner for taking the strategic decisions involved in plant life extension (PLEX).

1. Introduction: Framatome ANP concept of plant life management

In view of the deregulation of the power generation industry with its increased competitive pressure, nuclear power plants must today provide for and maintain a high level of plant safety and availability at low power generating costs. An overall approach to plant life management (PLIM) is a key factor in maintaining plant safety, improving performance characteristics and optimizing economic plant operation.

Framatome ANP has developed an integrated PLIM concept [1] addressing all ageing phenomena regarding plant safety concept, mechanical, electrical and I&C components as well as civil structures, plant documentation, plant personnel, operations management system (OMS),consumables and administrative controls. The focus of the Framatome ANP PLIM concept is on the safety concept, all components and the plant documentation.

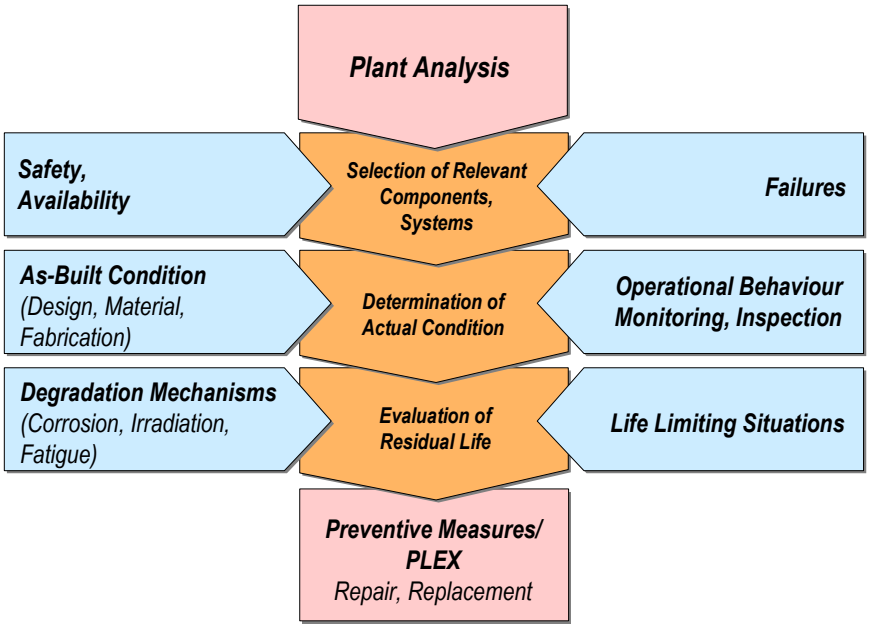

Figure 1. Strategic approach for plant analysis.

Using above mentioned PLIM concept, the respective strategic approach for the plant wide analysis is shown in Fig. 1.

The analysis starts regarding the safety concept. System functions and associated components/structures important to safety are identified on the basis of stipulations in the licensing procedure or using the results of a periodic safety review. If possible, a categorization depending on importance to safety can be performed. (For example, the PSR as described in Section 2 will provide the pertinent information.)

In addition system functions and components/structures important for economic reasons (particularly for plant availability or due to high costs for replacement) are identified on the basis of operating experience and expert judgement or using the results of reliability analyses. If possible, a categorization depending on the importance to availability and component/structure costs can also be performed.

In the next step an evaluation is performed for safety and availability relevant plant components in order to identify potential degradation mechanisms, which may affect the function or integrity of components concerned. An example of "interesting news" is given in Section 3.

When the selection of the components and structures, for which specific life management (LM) measures or strategies have to be applied, has been performed, subsequently the determination of the as-is condition of these components and structures has to be done. The knowledge of the as-is condition consists of the knowledge gained during erection of the plant and during

operation. Sections 4 and 5 are dealing with applications regarding efficient documentation with IT-tools (COMSY) and on-line monitoring (SIPLUG).

The final stage of the assessment is the determination of the residual life of the components and structures, which serve as the basis for PLEX planning or for planning of preventive or repair respectively replacement measures. Section 6 describes corresponding Framatome ANP applications (e.g. FAMOS, FLUES).

2. Plant life management of safety concept

To use the term “ageing” in connection with a safety concept is not as common as in connection with materials and components. Nevertheless, there are ageing aspects to be considered in safety concepts such as changes in the state of the art regarding:

- Incidents and accidents to be postulated for a specific NPP design
- The degree of uncertainties in transient and accident analysis models and codes
- Larger required design margins, or other design aspects of systems or components.

Judging the strengths and weaknesses of a safety concept, i.e. judging whether new insights as described above will be covered or compensated within the safety concept, is, in general, a complex matter. Sometimes, experience with incidents or comparison with other NPPs or with requirements set by rules and regulations may reveal a clear deficit. However, in a well kept NPP, weaknesses on the one hand or overdesign on the other are usually not so easy to find and will not show up in the routine of normal operation.

Because of this, it has become common practice worldwide to conduct a review of the safety concept about every 10 years using more elaborate analyses than are possible on a routine basis (Periodic Safety Review, PSR).

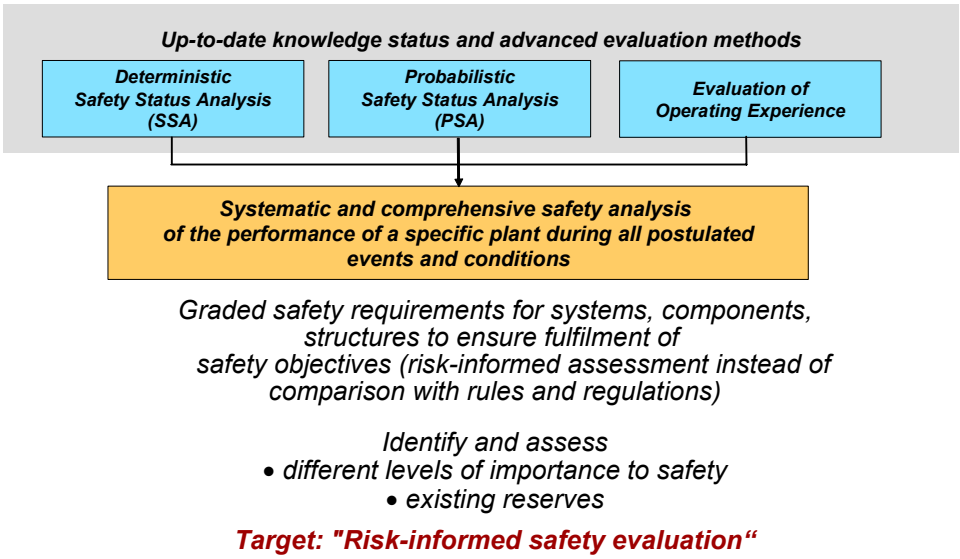

Figure 2. Integrated safety objective based periodic safety review.

In Germany the PSR consists of three main elements (Fig. 2):

- An evaluation of operating experience
- A (deterministic) safety status analysis (SSA)
- A probabilistic safety analysis (PSA).

The **evaluation of operating experience** will give valuable information on the quality of the measures on the first two safety levels (normal operation and upset conditions) of the defence-in-depth concept, which is an important part of the safety concept. These evaluations will show in an integral way whether the risk of occurrence of accidents is high or low and is decreasing or increasing with operating experience, and whether there are problems with the reliability of safety systems. Experience gained in operation including results of in-service inspections can reveal weaknesses in operational systems, in which faults may lead to events that can be precursors of accidents, and in systems and components important to safety.

Information in this respect can not only be gained from the operational experience of the NPP under investigation but also by using national and international reporting systems for incidents.

The **PSA** methods used worldwide are basically similar, so a description is not necessary. A PSA provides information about the frequencies of initiating events, the unavailability of safety related systems and components and the balance of the safety concept.

Regarding the **SSA**, there is greater variance in methods; in most cases procedures similar to those applied in the licensing process are used (comparing

systems, structures and components with the requirements of current rules and standards in the country of the operator and/or the designer).

To avoid problems that are inherent when comparing an older NPP (designed to rules and standards in effect during construction) to more recent rules and standards (aimed at a new generation of NPPs) Siemens/KWU (now Framatome ANP GmbH) joined forces with the operator of Neckar NPP to develop an SSA methodology for a safety objective based safety assessment /2/. The advantages of this methodology are:

a. integral assessment of accident resistance taking into account plant specific aspects which are not always covered by current rules and standards, thereby giving a possibility to compensate deficiencies and over-design to some extent
b. derivation of different degrees of importance to safety for system functions (depending on the necessity for accident control and the grace period available)
c. compatibility with results of the PSA (SSA supplementing and supporting results of the PSA and vice versa).

The safety objective based Safety Status Analysis derives the requirements applicable to safety functions or to system and structure functions from a systematic accident analysis in a step by step approach.

Since 1994 this safety status analysis methodology has been applied to eight nuclear power plants in Germany and abroad. In those cases in which licensing review has been completed analyses a positive assessment has been given by the authorities. It is worth mentioning that this methodology conforms to the US NRC definition of “risk informed regulation or safety evaluation”.

All in all, in combination with the PSA and the evaluation of operating experience, this methodology allows a precise judgement of the completeness and reliability of the measures for accident prevention and accident control, and of the defence-in-depth and safety concepts.

Furthermore, the combination of SSA, PSA and evaluation of operating experience can be used as a powerful tool to define a safety ranking of components and thereby select components for different life management strategies.

3. Failures

In general the relevant degradation mechanisms to be expected for specific components or structures are known. Nevertheless, with increasing operational experience the knowledge of degradation mechanisms does also increase. In case

a failure or defect has been identified, the most important question to be clarified by subsequent root cause analyses is, whether the investigated failure is a single failure or a generic one and whether the failure is comparable to already known failures.

In the following a recent example is given for a failure, which is quite new in relation to the used material. In Germany type X1CrNiMoCu25 20 5 (German designation 1.4539) material, which is a high alloyed material with approx. 5 wt-% molybdenum, has been used without problems for components in contact with river water. Recently it has bee recognized that river water causes pitting in this material in stagnant areas under crevice conditions. The reason for that is, that due to the improved environmental conditions the variety of microbiological organisms in the rivers has been increased, which leads to enhanced microbiologically influenced corrosion (MIC) resulting in local changes of the water chemistry and hence in pitting.

4. IT support for life management

IT support in the context of plant life management is becoming more and more important as PLIM methods require the systematic processing of large amounts of data which has to be continuously updated. The most important requirements for life management software tools are the following:

- Simplified access to plant data, to mitigate loss of competence in connection with staff fluctuations,
- Retrospective plant documentation, indicating the service history and NDE results for components
- Storage, updating and management functions for all LM relevant data,
- Computational functionality for quantification of degradation mechanisms and maintenance scheduling.

As an example, for mechanical components the COMSY (Condition Oriented ageing and plant life Monitoring SYstem) program (see /3–5/), provides the following features:

- Component data sheets compiling specific PLIM relevant data over the plants service history
- As-built data of components in comparison to specified values,
- A material library as a knowledge base for details on material properties
- A number of engineering tools for data processing to compute stresses, water chemistry and flow conditions,

- Numerical models to predict a variety of damage mechanisms and the residual life expectancy of components,
- Tools to store, manage and evaluate a wide variety of NDE, inspection or monitoring data.

A trending function supports the comparison of the as-measured condition with the predicted progress of degradation while making allowance for measurement tolerances. The results of this comparison are used in order to improve the accuracy of future life expectancy predictions. During the ageing control process the COMSY database is continuously kept up to date. Information resulting from surveillance activities, e.g. NDE results, is thus consistently used to provide the capability to systematically trace the current condition of LM components.

5. Operational behavior, monitoring and inspection

As already mentioned PLIM serves for optimizing economic plant operation. More and more on-line monitoring tools are used, which help to better identify weak points during operation resulting in a better focus or planning of maintenance or inspections to be performed. In the following the SIPLUG / ADAM tool for valve diagnosis and analysis is described.

For motor-operated valves, the SIPLUG® technique of measuring active power at the motor control center ensures that all parameters relevant to valve and actuator performance are reliably monitored.

The software module ADAM® automatically compares the measured data against nominal ratings and allowable limits. Specified values and limits are defined on the basis of functional and load models, taking accuracy of measurement and analysis into account. A database that runs under the program MS-ACCESS® manages the component data and the analytical results. It permits trending of valve performance as well as statistical analysis of evaluation criteria for valves of the same design (i.e. same type, nominal diameter and actuator).

Evaluation is either menu-driven or automatic using type-specific algorithms. An immediately available results listing shows the active power converted to mechanical data (e.g. torque and thrust) and gives a comparison with nominal ratings and allowable limits.

This method of measurement at the motor control center as well as the associated equipment is in use at numerous Framatome ANP -built plants. Calibration measurements as well as special measurements carried out directly at the valve (e.g. of stem thrust) can be incorporated as and where necessary. A complete on-

line monitoring system for MOVs using the SIPLUG®/ADAM® technology is also already in operation in NPPs.

6. Evaluation of residual life time and measure planning

This section describes several applications aiming at optimized planning in order to prevent unplanned outages.

Nowadays steam generator or reactor pressure vessel head replacement due to alloy 600 primary water stress corrosion cracking is a big issue. Utilities would like to know in this respect the degradation rate of the SG-tubes. With the help of Weibull statistics a correlation of percentage of cracked tubes versus operating time could be established for French 900 MW plants. On basis of this correlation optimized replacement planning was possible for these utilities.

As already mentioned in Section 4 with the help of the COMSY tool besides efficient documentation of component data and NDE results also trending functions for the determination of residual life time are included. In Fig. 3 the in-service inspection optimization process for the damage mechanism erosion corrosion based on COMSY-support is depicted.

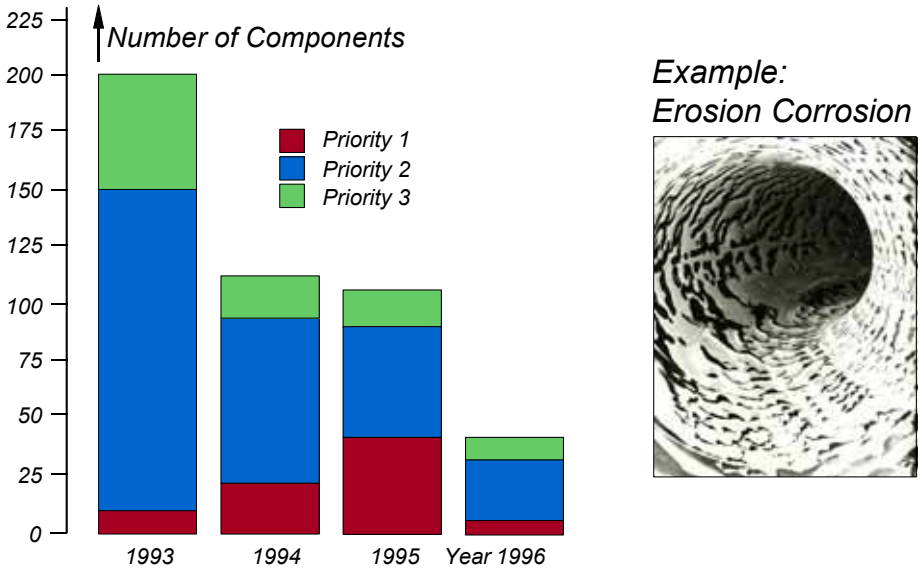

Figure 3. Optimization process for in-service inspections using COMSY.

It can be seen that the amount of the inspections has been reduced by more than 75% from 1993 until 1996. Furthermore it should be mentioned that replacement planning was included. In the Year 1995 several priority 1 components, which were near to their end of life situation, were replaced.

Fig. 3 shows the optimization by "only" using the knowledge on the degradation mechanism itself. A further reduction of in-service inspections is possible when applying risk-informed techniques, e.g. in combination with periodic safety reviews mentioned in Section 2 or availability analyses.

Another application related to alloy 600 PWSCC can be the moisture and leak detection system FLUES, which can be attached to the RPV head or bottom and which is able to detect leak rates with high sensitivity (< 1 kg/h). With the help of FLUES leaks can be detected at an early stage resulting in minimization of secondary damage. If necessary, leak trend plotting can also be performed.

With the fatigue monitoring system FAMOS the residual life time of components can be determined with higher accuracy. Fig. 4 shows the FAMOS application.

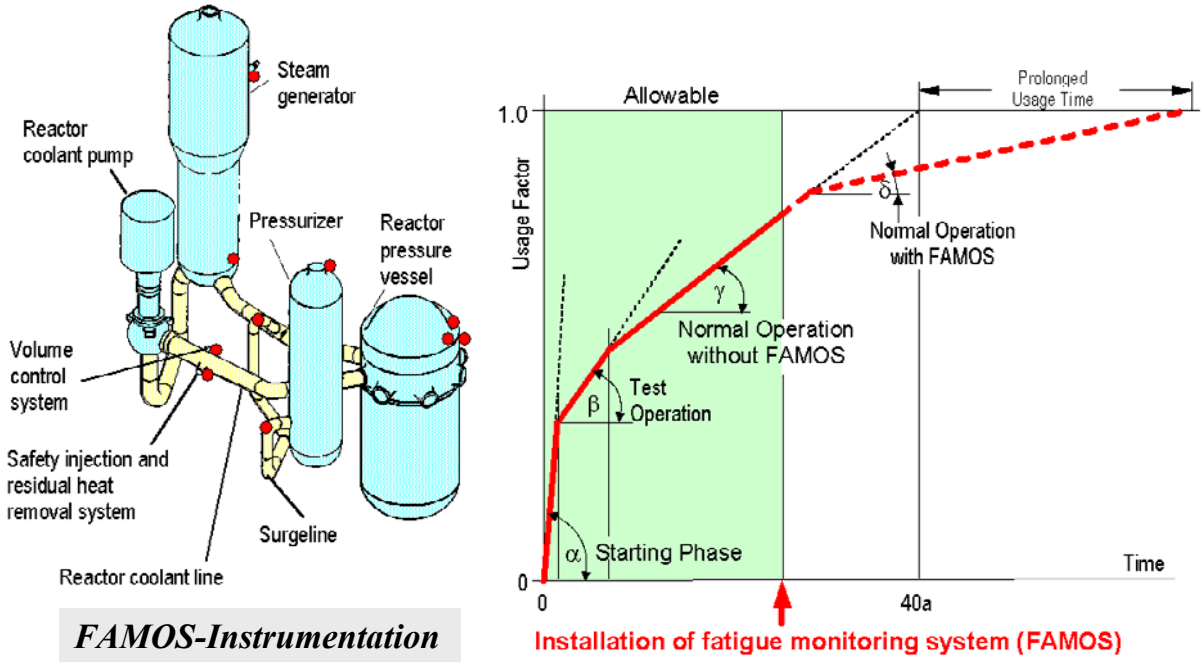

Figure 4. Fatigue monitoring system FAMOS.

From Fig. 4 it can be seen that the increase of the usage factor can be monitored. This can lead to a prolongation of component life time, because during the design phase usage factors are determined in a conservative way. On the other hand side monitoring can also lead to recognize a reduced component life time, in case when e.g. specific transients were not predicted during the design phase (e.g. thermal stratifications in spray lines). However, in this case the knowledge of reduced lifetime enables the operator to start replacement planning at an early stage instead of facing an unplanned outage.

Finally it should be mentioned that the Framatome ANP PLIM concept has been applied as a plant wide analysis for Kozloduy units 3 and 4 in the so called “rest life time evaluation project”. For the most critical safety components of the plant (primary circuit, secondary side, spent fuel pool, electrical equipment, hoisting equipment and civil structures) the residual life time has been determined. This was the basis for subsequent planning of preventive measures. Furthermore an ageing management database has been established to support PLIM with efficient IT-documentation.

References

1. W. Däuwel, W. Biemann, R. Danisch, B. Kastner, W. Meyer, H. Nopper, U. Waas & L. Warnken. Framatome ANP GmbH Concept of Plant Life Management (PLIM), Kerntechnik, Vol. 67, No. 4, August 2002.

2. W. Schwarz, U. Waas & B. Kühne. Überprüfung der Störfallsicherheit, Schutzzielorientierte Sicherheitsstatusanalyse am Beispiel von Neckar-1, atw 42, S. 23, Januar 1997.

3. H. Nopper, M. Erve, W. Kastner & L. Scharf. COMSY – A Program System for Aging and Plant Life Management. Plim&Plex Meeting on Plant Life Management and Plant Life Extension in Nuclear Facilities, 3–5 November 1999, Madrid, Spain.

4. H. Nopper & B. Kastner. Cost effective plant life management, Nuclear Engineering International, P36–37, November 2000.

5. H. Nopper, W. Daeuwel & W. Kastner. Ageing and Plant Life Management Software COMSY, Ninth International Conference on Nuclear Engineering, Nice Acropolis – France, April 8–12, 2001.

Effective information systems enabling high availability – CMMS renewal project

Kari Kotirinta & Jukka Saarinen
Fortum Service Oy
Espoo, Finland

Abstract

The peak load demand for electric power in Finland varies from about 6 GW in summertime to about 11 GW in winter. The four nuclear units (two 840 MWe BWR units in Olkiluoto and two 510 MWe PWR units in Loviisa) generate about one third of the electric energy in Finland. The optimisation of the generation of the Loviisa NPP includes, firstly, to minimise the disturbances during the operation period (wintertime) and, secondly, to minimise the duration of the annual outages. As the latter should not be achieved at the expense of the former, the main principle of the maintenance should be versatile and efficient utilisation of condition monitoring and a detailed long-term modification program for the components. In order to meet the minimised outage times and, vice versa, maximised availability factor the outage should be based on detailed and accurate outage planning, utilisation of condition-based maintenance programs and on effective and high quality maintenance work. These tasks can not be reached without effective IT tools that enable both accurate outage planning and real time outage project management. In Loviisa NPP it was seen that the current IT tools are reaching their lifetime and they need to be updated. For that reason it was established a LOKE4 project in 2002 which main goal was to renew the current maintenance management system and its support systems.

1. Introduction

Fortum is a leading energy company in the Nordic countries and the other parts of the Baltic Rim. Fortum's activities cover the generation, distribution and sale of electricity and heat; the production, refining and marketing of oil; the operation and maintenance of power plants as well as energy-related services.

Fortum's power generating capacity is approximately 11,300 MW (in 2002), of which 11,091 MW is in the Nordic countries. Power generation in Fortum's wholly and partly owned power plants was 50.6 TWh. In the Nordic countries Fortum generated 46.5 TWh of electricity of which the nuclear power accounted

some 22.0 TWh, or 47% of Fortum's own power generation. The rest was hydropower, about 18.1 TWh (39%), and thermal power 6.5 TWh (14%).

Fortum's Loviisa NPP has two 510 MWe PWR units, Loviisa 1 and Loviisa 2 that were completed in 1977 and 1980 in respectively. The annual power generation was about 7.7 TWh in 2003. The plant efficiency and operational reliability translated into load factors of the two units have been remarkably above the international average. This has been reached by following the maintenance strategy that is based on the periodicity of the inservice inspection, preventive maintenance and surveillance test programs as well as developing of the maintenance and the annual outage procedures in which the computerised maintenance management system (CMMS) plays an important role, e.g. in minimising the duration of outages.

The first generation of Loviisa NPP's CMMS system was developed at the beginning of the eighties. The current, second generation system, LOTI/HAMA, was developed at the mid/late eighties. The system was designed by Loviisa experts and it handles the equipments, spare parts, materials, purchases, as well as preventive maintenance and other works, work tasks and safety procedures and project management.

The renewal of the LOTI/HAMA system has been under development for a long time. It was seen that the system hardware and software environment had become obsolete, and e.g. the hardware support and availability of the spare parts are limited. This was the main reason to start the renewal project, as the basic functions of the LOTI/HAMA system are state of art; those functions have helped Loviisa NPP to reach remarkably high load factors.

2. Project description

2.1 Definition project

The LOKE4 renewal project of Loviisa NPP's LOTI/HAMA system was started in the beginning of the 2002 by establishing a definition sub-project which target was to define the general strategy for the project. One of the first practical tasks of the project was to prepare facility for the project personnel. In Loviisa it was used barracks to build temporary work rooms with computers, data projectors and other equipment.

One key task of the sub-project was to make descriptions of the present state of the systems and also to define the target and demand state of the future systems. The target state was defined for both the existing systems that were to be

renewed and completely new systems that were to be implemented during the project.

The following Figure 1 illustrates the defined operation environment of the LOKE4 project. The main systems are Maintenance management system and Laboratory system. Other systems, Project management system, Material inspection system, Graphical navigation and Operation diary are supporting systems that supplement the functions of the main systems. The Operational diary and Graphical navigation are new systems that are implemented in the LOKE4 project.

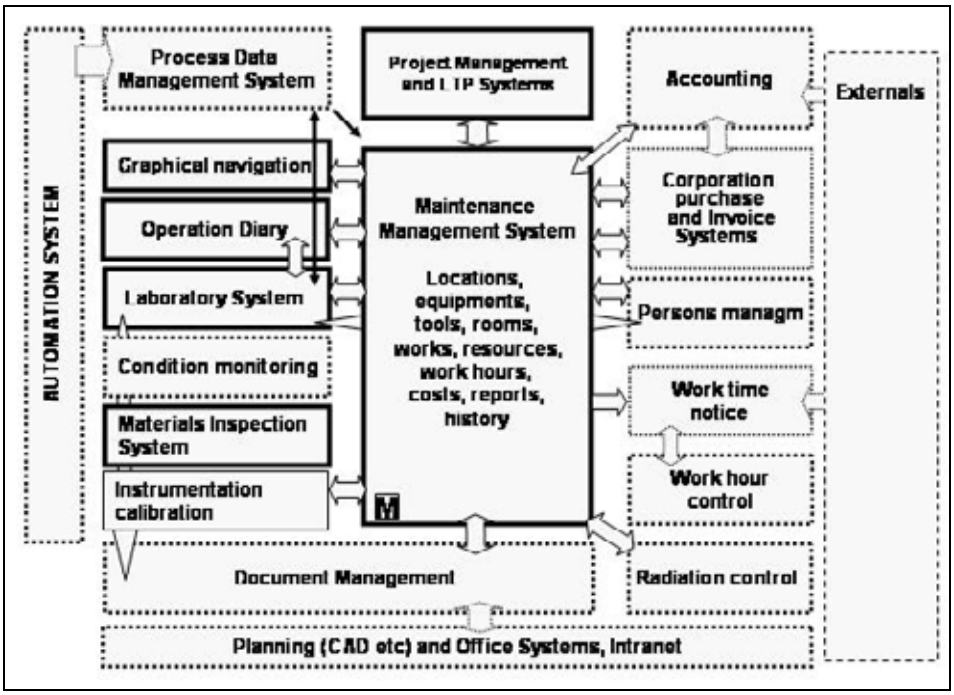

Figure 1. The LOKE4 project operation environment. Bold borders indicate the systems that are implemented during LOKE4 project.

The main functions of the Maintenance management system are analogous with standard CMMS requirements, with management of equipments, spare parts, materials, purchases, as well as preventive maintenance and other works. Some special functions e.g. strict work permit and safety (EHS) procedures differ from conventional CMMS products. The Laboratory system's main functions are to manage sample collection, provide various calculations (including radio chemistry) and manage other laboratory functions.

Project management system is a system integrated with CMMS and it enables the management of e.g. outage projects and works, tasks and resources. Material inspection system is a tool for NDT and corrosion data management. Graphical

navigation is a module that utilises PI diagrams and it brings a visual view for many planning tasks. Operation diary will replace Loviisa's current, approximately 20 manual diaries and log books.

2.2 Implementation project

After the definition sub-project the invitations to tender were sent out and the present and target state descriptions were used as a part of the tender invitation material. After the tendering period and tender evaluation period the selected software products were evaluated in order to find out how the Loviisa NPP's requirements were attainable. The final task before the implementation project was to select the software module suppliers, sign the contracts and establish the organisation of the implementation project. Number of Loviisa's personnel in the project organisation is approximately 50. The following Figure 2 shows the organisation chart of the LOKE4 project.

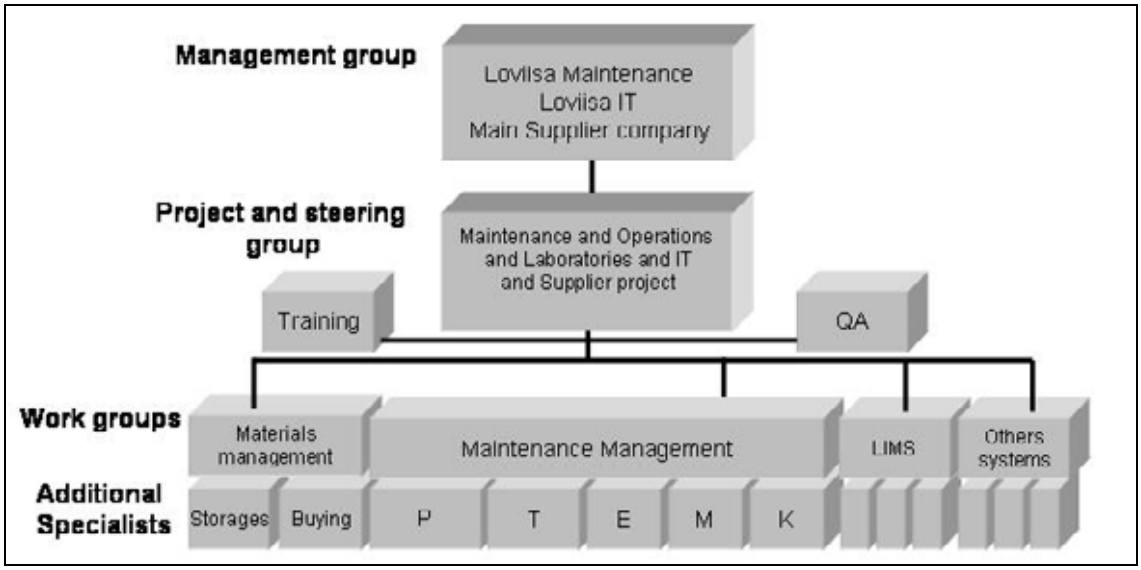

Figure 2. The organisation chart of the LOKE4 project.

The implementation project of all the software modules began with the detailed definition period. The period included definition workshops together with Loviisa NPP's and product vendor's experts. In these workshops the technical requirements of the each module was defined, bearing in mind the target state definitions as well as the basic functions of the each software product. Reason for the detailed definition workshops was to minimise the gap between the supplier's tender documents and Loviisa NPP's requirements and to give detailed instructions for the programmers who execute the adaptation and modifications.

Currently, early 2004, the implementation project is midway and the sub-projects are in different phases.

The project management module was implemented early 2003, in the beginning of the project, as it is used for the scheduling the LOKE4 implementation project itself. The implementation of the Maintenance management system was split into two, materials management and maintenance management. The detailed definition of the materials management has been done and the implementation is on going. For the maintenance management the finalisation of the detailed definition is on going. The 1st FAT of Laboratory system has been completed and the commissioning is on going.

The supporting systems; Material inspection system, Graphical navigation and Operation diary are in the different phases of definition and commissioning. All system modules, both main and support, are planned to be ready for testing and production at the end of 2004.

The following Figure 3 illustrates the general work process of the LOKE4 project with some major mile stones.

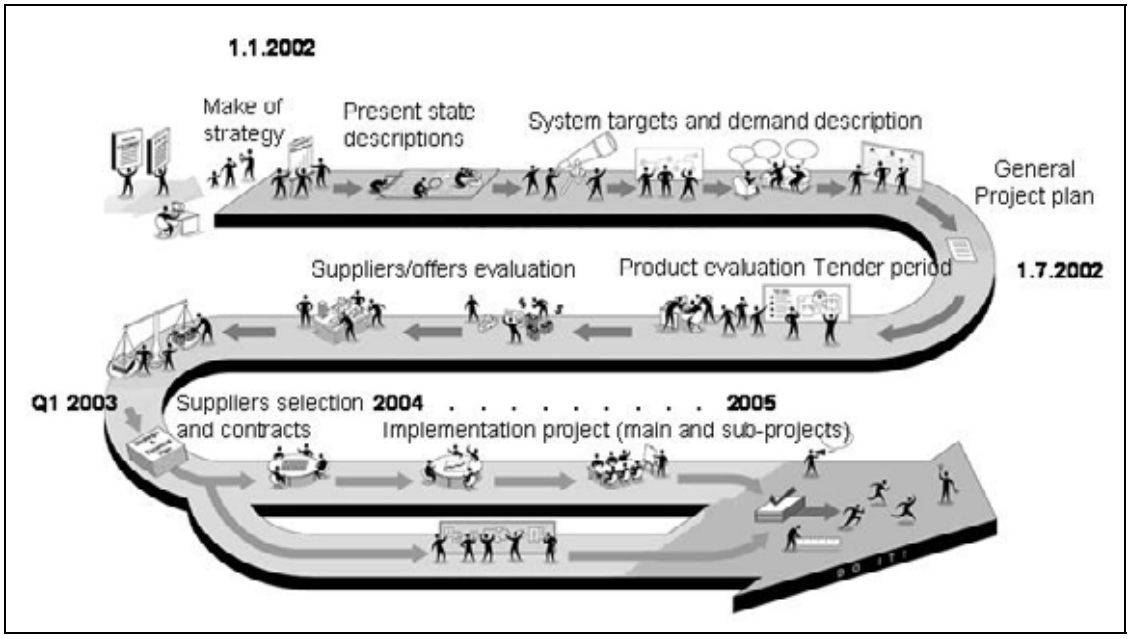

Figure 3. The general LOKE4 project work process.

After the implementation project the post project will be established. The main tasks will be finalising the documentation and archiving as well as disassemble the project facility like barracks and equipment.

3. Discussion

Large IT projects, like LOKE4, are remarkably challenging, and high quality project management, both in the supplier's and customer's side, will facilitate the success of the project. Also, the support of the O&M organisation is needed. In Loviisa NPP the demands of the project were foreseen and the implementation project was grounded by careful planning and strategy development.

The main strategy and targets that were set to the project and the final result incorporated the requirement that in spite of the fact that Loviisa NPP is ageing, the load factors of the plant should remain on the high level. The detailed key targets contain e.g. Ensuring the development of IT architecture; Improvement of the safety and plant life time management and maintenance and costs analyses.

During the implementation project there have been project management issues that have emerged, like the management of the work procedures e.g. document management and the test procedures. Here the document management include management of the modifications and document versions, as well as management of the freezing procedure of modifications and document approval. One key issue that one has to bear in mind and that reflects to the whole documenting procedure is the agreement of the common terminology between the vendor and purchaser.

Also, as LOKE4 project consists of several sub-projects and contracts, the multi-project management and interface management between the software modules proved to be issue that should be planned carefully. As well, the authorities have been one party and this has added still one view for the project.

4. Conclusions

A renewal project of a computerised maintenance management system is a remarkably challenging task, and when the project is done in the nuclear power plant additional requirements, like requirements for the safety procedures and directions of the authorities, are set to the project.

The ground of the successful project is a high quality project management and documentation. Also, a special care should be focused to the quality of the tender invitation material and supply contract. In view of the project management some key areas that need attention, are the management of the time schedule, and when the project consist of several suppliers and contracts, management of the project as a whole.

The misconception(s) of ASTM E399, plane-strain fracture toughness K_{IC}

Kim Wallin
VTT Industrial Systems
Espoo, Finland

Abstract

The plane-strain fracture toughness, is assumed to represent a size insensitive lower bound value. The materials used for the development of ASTM E 399 were all aluminum and titanium alloys or extra high strength steels. The materials had in common that their fracture micro-mechanism was ductile fracture. The fracture toughness did not show the expected decreasing trend with increasing specimen size, but generally the opposite trend. The specimen thickness was assumed to be the limiting dimension, even though the experimental data indicated that the specimen ligament size controlled the fracture toughness. This lead to several misconceptions regarding the significance of K_{IC}.

1. Introduction

Integrity assessment of structures containing planar flaws (real or postulated) necessitates the use of fracture mechanics. Fracture mechanics compares in principle two different crack growth parameters: the driving force and the material resistance. The driving force is a combination of the flaw size (geometry) and the loading conditions, whereas the material resistance describes the materials capability to resist a crack from propagating. Up to date, there exist several different testing standards (and non-standardized procedures) by which it is possible to determine some parameter describing the materials fracture resistance (ASTM E 399, ASTM E 1820, BS 7448, ESIS P2 etc.). Unfortunately, this has lead to a myriad of different parameter definitions and their proper use in fracture assessment may be unclear.

Historically, fracture mechanics evolved from a continuum mechanics understanding of the fracture problem. It was assumed that there existed a single fracture toughness value controlling the materials fracture. If the driving force was less than this fracture toughness, the crack would not propagate and if it exceeded the fracture toughness the crack would propagate. Thus, crack initiation and growth were assumed to occur at a constant driving force value. The only

thing assumed to affect this critical value was the constraint of the specimen (or structure). Since at that time there were no means to quantitatively assess the effect of constraint on the fracture toughness, the fracture toughness had to be determined with a specimen showing as high a constraint as possible. This lead to the use of, deeply cracked, bend specimens for the fracture toughness determination.

Historically, the micro-mechanisms of fracture were not considered. It was assumed that the stress state assumption of the continuum mechanics analysis were valid for fracture toughness as well, regardless of fracture micro-mechanism. This allegation has later been proven to be wrong. Different fracture micro-mechanisms exhibit different physical features that affect the properness of a specific fracture toughness parameter to describe that fracture micro-mechanism.

The common interpretation of the plane-strain fracture toughness K_{IC}, defined by ASTM E 399, is a specimen size insensitive lower bound fracture toughness corresponding to plane-strain stress state. The interpretation is due to the original work by George Irwin where he postulated the expected effect of specimen thickness on fracture toughness (Fig. 1). George Irwin based his conclusions on maximum load toughness behavior of center cracked tension (CC(T)) specimens and 3-point bend (SE(B)) specimens of two aluminum alloys, combined with the specimens macroscopic fracture surface appearance [1]. Even though the experiments did not really correspond to any proper fracture toughness description, nor fracture event, the postulated thickness effect was soon adopted as representing the physical "truth" of fracture behavior. This constituted also the expectations for the development of the ASTM E 399 testing standard.

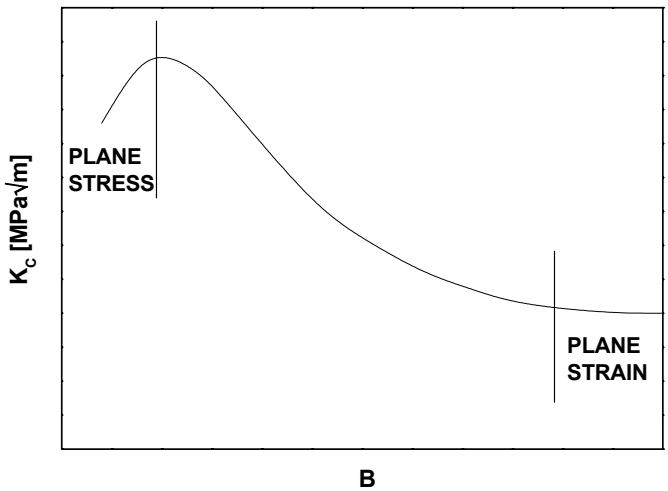

Figure 1. Schematic presentation of the assumption of thickness effect on fracture toughness.

The original Irwin data did not, however, reflect the effect of specimen size on fracture toughness. The original data is shown in Fig. 2 [2]. In reality, the data shows the difference in maximum load toughness between low constraint specimens with a large slim ligament and high constraint specimens with a short nearly square ligament. The aluminum alloy in question failed by a typical ductile fracture mechanism. Today it is commonly known that the ductile fracture process is connected with a rising tearing resistance curve. The steepness of the curve is related to, besides material, loading geometry and ligament slimness (Fig. 3).

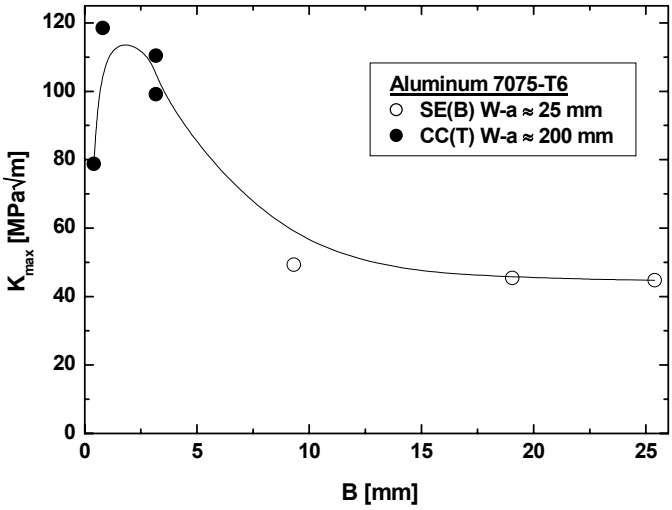

Figure 2. Original Irwin data used to postulate classical thickness effect [2].

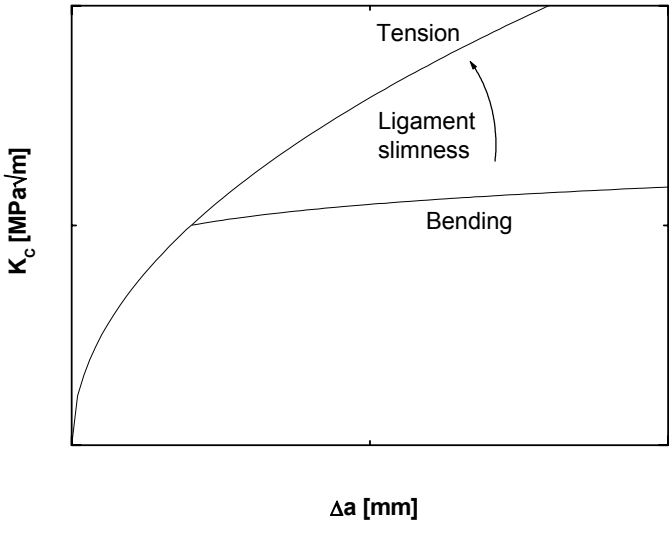

Figure 3. Schematic presentation of the geometry effect on tearing resistance.

The CC(T) specimens with a slim ligament, or a large W-a, in relation to B, show a steeper tearing resistance curve than the bend specimens. This explains part of the fracture toughness difference observed by Irwin [2]. Additionally, the amount of ductile crack growth that corresponds to maximum load is roughly proportional to the original ligament size. The CC(T) specimens, used by Irwin, had a 200 mm long ligament compared to the 25 mm ligament of the bend specimens he used. This means that the crack growth of the CC(T) specimens was nearly 10 times larger than for the bend specimens. This is the main reason for the fracture toughness difference observed by Irwin [2]. Actually, in the original test report [2] it is mentioned that the CC(T) specimens experienced large crack growth before load maximum. The amount of crack growth was even monitored during the test by making ink markings on the specimens. This large crack growth was, however, ignored as it occurred during the rising load part of the test. This erroneous interpretation was made, because the existence of rising tearing resistance curves was not recognized. Even though the experiments in no way reflected the effect of specimen thickness, the thickness effect was still taken as the postulate for the development of ASTM E 399. The assumption was that a valid K_{IC} value must represent a minimum toughness value of the material.

2. Experimental trends

The materials used for the development of ASTM E 399 were generally aluminum and titanium alloys or extra high strength and maraging steels. The materials had in common that their fracture micro-mechanism was ductile fracture, i.e. the materials showed a rising tearing resistance curve. Unfortunately, this was not understood at that time, when the continuum mechanics type fracture behavior was assumed. The standard developers confronted therefore a new problem, when it was observed that the fracture toughness did not generally show the expected decreasing trend with increasing specimen size, but the opposite trend as shown by Fig. 4 [3]. This increasing toughness led to the introduction of the additional demand that $P_{max}/P_Q < 1.1$.

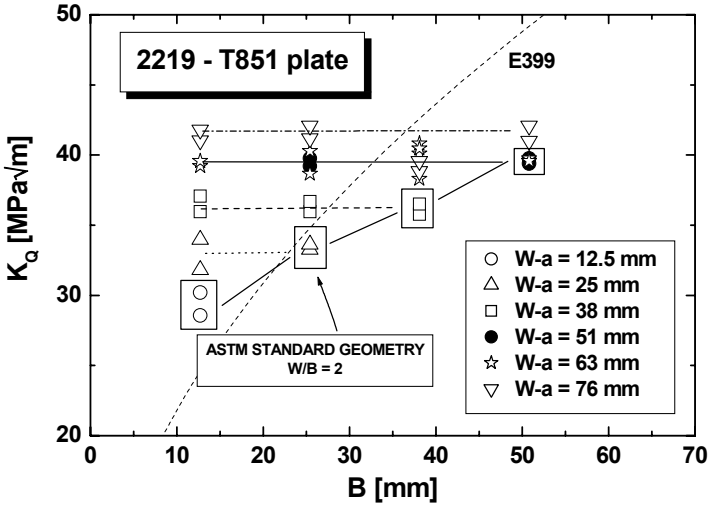

Figure 4. Old K_Q data used to develop ASTM E 399 showing increasing toughness with increasing specimen size [3].

The specimen thickness was still assumed to control the materials fracture toughness, as postulated by Irwin. The assumption prevailed, even though the experimental data indicated that it is the specimen ligament size, not thickness, that controls the fracture toughness value (Fig. 5) [3]. The belief in the plane-strain, plane-stress postulate was so strong that this evidence was disregarded. Also, the plane-strain fracture toughness was assumed to be a lower bound specimen size insensitive material parameter, even though the results indicated the reverse, i.e. that K_{IC} increases with specimen size. Evidently, because it was tried to explain the results solely based on the constraint effect, the real reason for this increase in toughness was never understood correctly. Based on the present physical understanding of ductile fracture, the increase in fracture toughness is easy to explain.

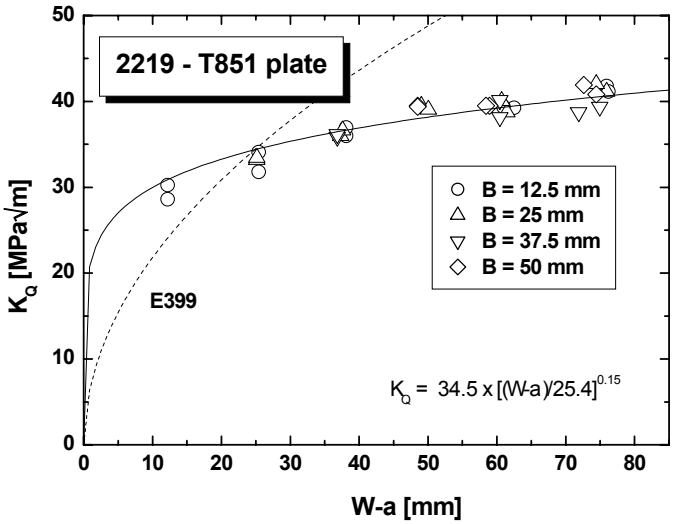

Figure 5. Same data as in Fig. 4 showing that ligament size controls the increasing toughness [3].

At the time of the development of the K_{IC} standard, there were no reliable means of monitoring crack growth during the test and also, crack growth was assumed to occur at a constant value of K_{IC}. This led to using the 95% secant method for the determination of K_Q. If all non-linearity in a load-displacement curve of a K_{IC} test specimen were due to crack growth, a 95% secant would correspond to approximately a 2% crack growth with respect to the ligament. With increasing ligament size, also the absolute crack growth, defined by the 95% secant, increases. Knowing that materials in the case of ductile crack growth exhibit rising tearing resistance curves, the increasing toughness with increasing specimen size is quite understandable.

3. Discussion

All examined data sets show identifiably consistent trends. The absolute specimen thickness is not relevant for the fracture toughness value determined according to ASTM E 399. If the material has a rising tearing resistance curve, the fracture toughness will be simply a function of the specimen's ligament size. Only if the ligament becomes so slim that the steepness of the tearing resistance curve is affected, thinner specimens begin to show increasing fracture toughness. Since the standard does not allow slim ligaments, even this phenomena will not affect the results. For standard geometries, only the ligament size affects the fracture toughness. This size dependence is a direct consequence of the 95% secant procedure used in ASTM E 399 to define K_{IC}. The only way to remove the ligament size dependence would be to determine K_{IC} at some absolute amount of crack growth, like in the case of J_{IC} as defined in ASTM E1820. The problem was partly recognized in the development of ASTM E 399, but since the rise in fracture toughness was connected to thickness and not ligament size, only a partly functional remedy to the problem was pursued. The solution was thought to be the $P_{max}/P_Q \leq 1.1$ criterion that was introduced as a consequence of the data presented in Fig. 4 [3]. It was assumed that the P_{max}/P_Q ratio was a function of constraint, since the rising tearing resistance curve was thought to be the result of insufficient constraint. In reality, P_{max}/P_Q is mainly connected to the tearing resistance of the material. A simplified analysis of the significance of the criterion is given next.

3.1 Significance of the $P_{max}/P_Q \leq 1.1$ criteria

In a linear-elastic situation, the crack driving force K_I is a function of load and crack length (eq. 1).

$$K_I = P \cdot g(geometry) \cdot f(a/W) \tag{1}$$

The ductile tearing resistance of the material can usually be approximated by a power law expression (Eq. 2).

$$K_I = A \cdot \Delta a^m \tag{2}$$

Combination of Eqs 1 and 2 enables the load to be written as a function of crack growth. Maximum load occurs when the derivative of the function equals zero. Thus, the amount of crack growth at maximum load is for linear-elastic loading described by Eq. 3.

$$\Delta a_{\max} = \frac{m \cdot f}{f'} \tag{3}$$

The amount of crack growth is governed by the power of the tearing resistance curve. It is equally easy to estimate the amount of ductile crack growth at the load P_Q, using the specimen compliance equation. The crack growth at P_{max} and P_Q is presented graphically for C(T) and SE(B) specimens in Fig. 6. P_Q corresponds quite closely to a 2% crack growth of the ligament.

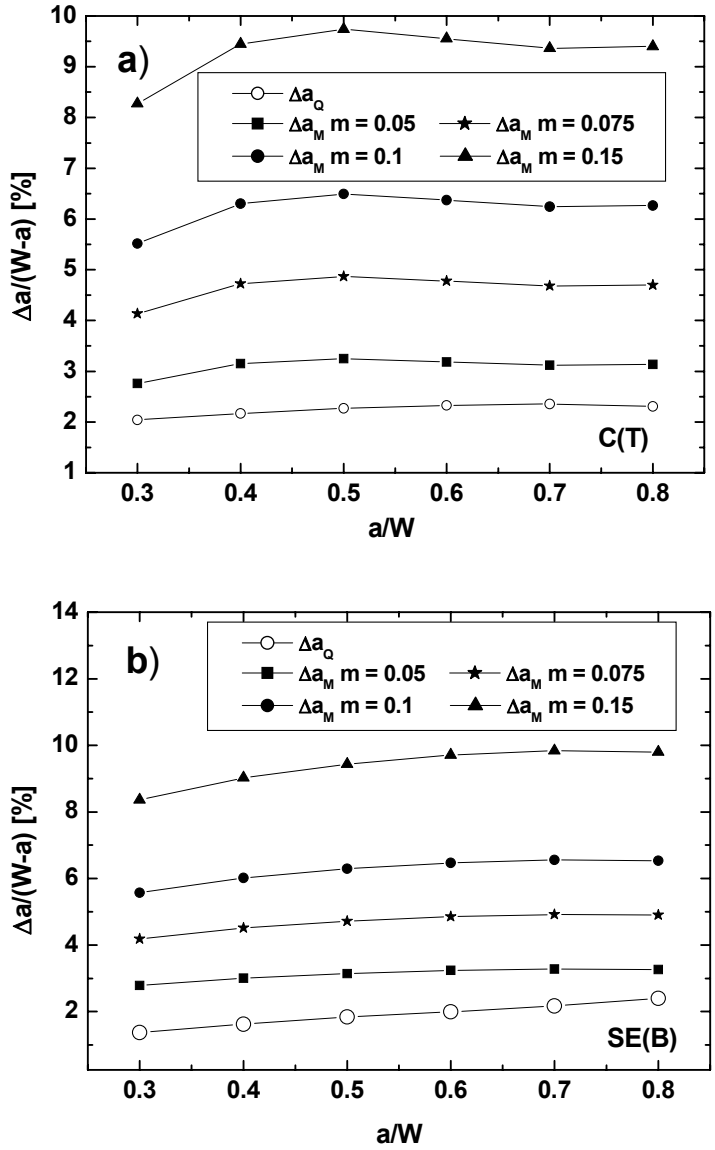

Figure 6. Theoretical estimation of crack growth at maximum load in a linear-elastic test. a) C(T) specimen, b) SE(B) specimen.

The knowledge of crack growth both at P_{max} and P_Q enables also an estimation of the P_{max}/P_Q ratio as a function of crack length and tearing resistance curve steepness. The result is presented in Fig. 7.

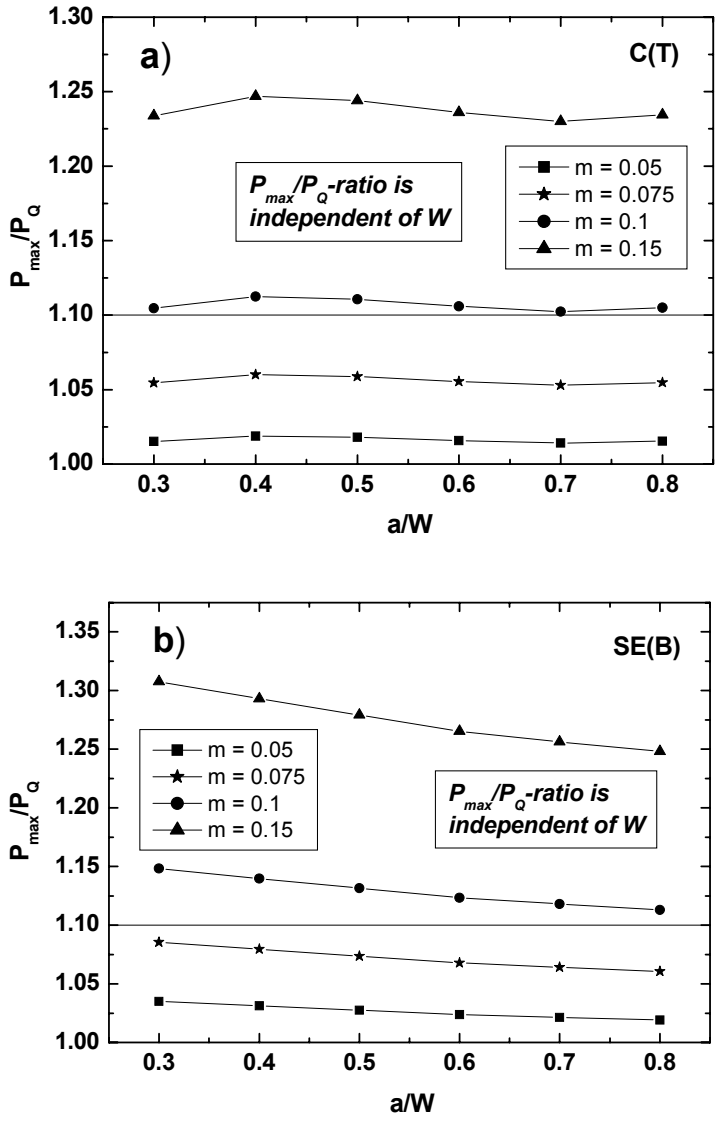

Figure 7. Theoretical estimation of the P_{max}/P_Q ratio as a function of crack length and tearing resistance curve steepness. a) C(T) specimen, b) SE(B) specimen.

Fig. 7 reveals some interesting details. Regardless of specimen type, the tearing resistance curve must be quite flat (m < 0.1) to fulfill the P_{max}/P_Q criterion. It is slightly easier to fulfill the criteria with C(T) specimens than with SE(B) specimens. The crack length has a negligible effect on the P_{max}/P_Q ratio. The above derivation is of course highly simplified and it should not be regarded as the absolute truth. Qualitatively the outcome of the derivation is valid. An example of the predictive capability of the above derivation is presented in Fig. 8. Here, the K_Q data from Fig. 5 were used to predict the maximum load K_{max} values for the same specimens [3]. On the average, the prediction is quite good, but the K_{max} values show trends that are not described by the simplified derivation. The prediction overestimates the toughness of the large specimens and underestimates that of the smallest specimens. The trend is due to crack

tunneling, which is also connected to the specimen slimness effect. For a specific specimen thickness, the ligament slimness increases with increasing ligament size. This causes the tearing resistance curves to become steeper and the K_{max} values to become higher. Ductile crack growth in a plane sided specimen occurs mainly in the center of the specimen. The crack growth at the side surface of the specimen is suppressed, causing the crack to form a tunnel shape. Ligament slimness enhances the tunneling effect and this is the main reason for the steepening of the tearing resistance curve. At relatively small crack growths, like at K_Q, the tunneling effect is still quite small and quite slim ligaments are needed to see a significant enhancement of the fracture toughness. At load maximum, the crack growth is significantly larger and thus is also the ligament slimness effect enhanced. An example of this is seen in Fig. 8, where the different thickness specimens lead to different K_{max} values, contrary to the K_Q results in Fig. 5.

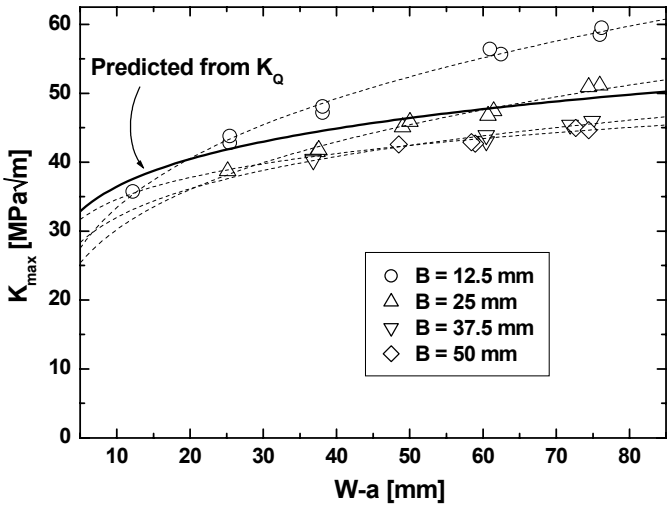

Figure 8. Effect of ligament size and thickness on load maximum values [3], compared to simple prediction based on K_Q behavior.

Fig. 9 shows the P_{max}/P_Q ratio as a function of ligament slimness. A clear rising trend is visible with increasing slimness. This is a direct result of the crack tunneling. Noteworthy is that the ligament size dependence of K_Q predicts an average P_{max}/P_Q ratio of approximately 1.24, but the actual data indicates a saturated average value of 1.12. This shows something about the qualitative nature of the simplified analysis.

The one thing that is clear, based on the simple analysis, is that the P_{max}/P_Q criteria has no significance whatsoever, concerning the matter of plane-strain. First, it describes only events occurring after K_Q has already been reached and second, it only gives information regarding the steepness of the materials tearing resistance curve. There is no theoretical justification for the criteria to be used as a measure of plane-strain. Use of side-grooved specimens removes the tunneling

and thus also the slimness effect. For some materials, side-grooving may lower the tearing resistance curve, thus lowering the P_{max}/P_Q ratio. However, since there is no need for this ratio in the first place, discussions regarding side-grooved specimens are not needed. Side-grooving is not expected to affect the K_Q value, only the K_{max} value. Since K_Q is considered the critical value, there is no reason not to allow the use of side-grooved specimens.

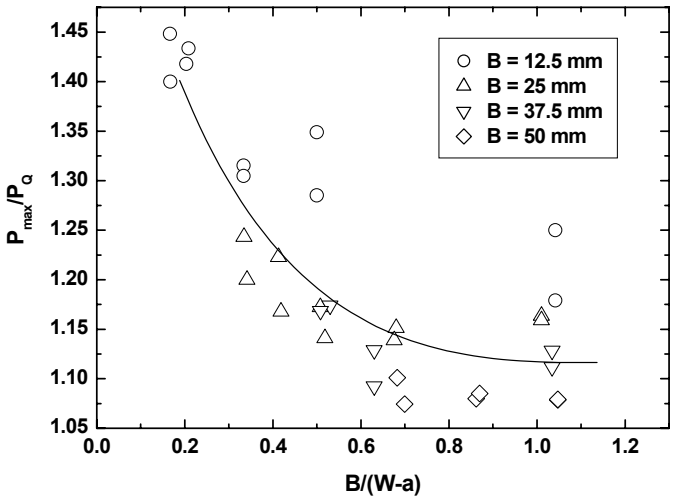

Figure 9. P_{max}/P_Q ratio as a function of ligament slimness [3].

3.2 Significance of the size criterion

The size criterion in ASTM E 399 is really not needed to ensure plane-strain conditions at the crack tip. Elastic-plastic standards like ASTM E 1820 allow a magnitude smaller specimens and even these have a plane-strain condition at the crack tip. Globally, the specimens are closer to plane-stress, but locally at the crack tip, where fracture takes place, the stress state is plane-strain. The real need for a size criterion in the K_{IC} standard comes from the need to be able to describe the fracture toughness based only on load. This requires that the specimen is globally in the linear-elastic regime. If excess plasticity occurs, the fracture toughness estimated based on load only underestimates the true fracture toughness. Since linear-elasticity, not the stress state, is the controlling requirement, the size criterion should be given in terms of the ligament, not thickness. A simple analysis of the possible error in fracture toughness as a function of loading can be performed i.e. using the Irwin plasticity correction [4]. This way it is possible to express the ratio between the plasticity corrected K_{ep} and the linear part K_I as a function of the linear loading K_I. An example of this is presented in Fig. 10. Based on the Irwin plasticity correction, the present size criteria produces at maximum approximately a 4% underestimate of the true fracture toughness. If a 10% error could be tolerated, the criteria could be relaxed from 2.5 to 1.1. Since the plasticity correction does not account for strain

hardening, it will usually overestimate the true fracture toughness to some extent. An example of a real material is given in Fig. 11. Here data from a cold formed stainless steel is compared with the Irwin plasticity correction. The data, from a 25 mm thick C(T) specimen, is presented in the form of normalized elastic plastic K_J and the linear part of loading from load only. For this real material, it is seen that the error in using a criterion of 1.1 (instead of 2.5) still leads to a negligible error in the fracture toughness estimate.

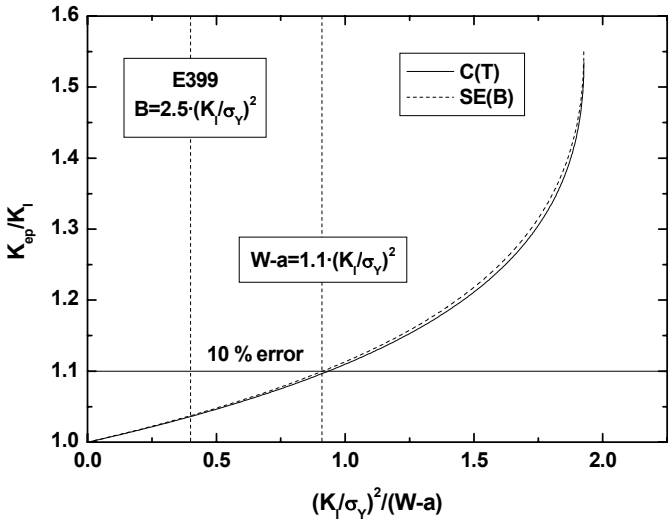

Figure 10. Simple estimate of plasticity induced error in K_I, based on the Irwin plasticity correction [4].

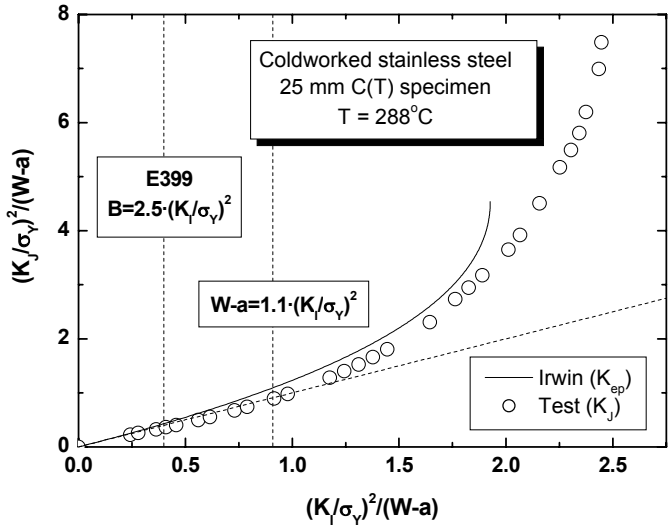

Figure 11. Comparison of the Irwin plasticity correction with behavior of real strain hardening material.

If the present ASTM E 399 size criterion is compared to the specimens limit loads, one can see that the reserve, with respect to general yielding, is approximately a factor of 2 (Fig. 12). If the criterion would be relaxed to 1.1, the reserve would still be approximately 1.5. In most cases, a criterion of 1.1 would result only in a slight underestimation of the true fracture toughness.

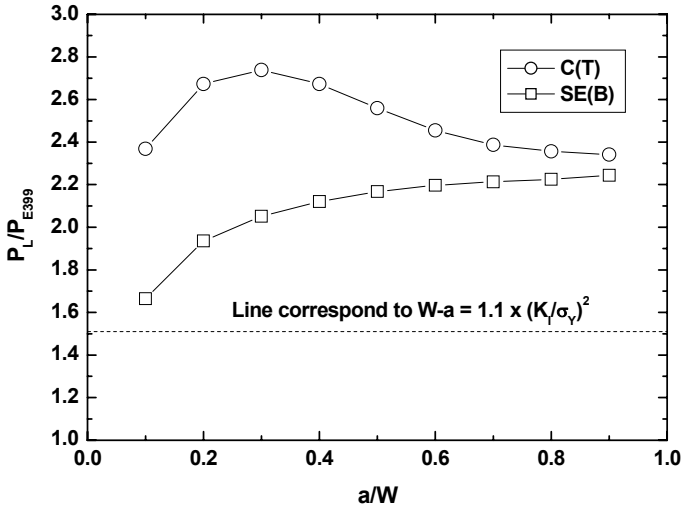

Figure 12. Examination of distance between load corresponding to ASTM E 399 size criterion and limit load.

4. Summary and conclusions

Data sets containing data revealing the effect of specimen size on the K_{IC} defined by ASTM E 399 have been analyzed based on present knowledge regarding the fracture mechanisms. The data sets show consistent trends. The absolute specimen thickness is not relevant for the fracture toughness value determined according to ASTM E 399. If the material has a rising tearing resistance curve, the fracture toughness will be simply a function of the specimen's ligament size. Only if the ligament becomes so slim that the steepness of the tearing resistance curve is affected, thinner specimens begin to show increasing fracture toughness. Since the standard does not allow slim ligaments, this phenomena will not affect the results. For standard geometries, only the ligament size affects the fracture toughness. This size dependence is a direct consequence of the 95% secant procedure used in ASTM E 399 to define K_{IC}. The only way to remove the ligament size dependence is to determine K_{IC} at some constant amount of crack growth. Based on the analysis, the following can be concluded:

- The specimen thickness is not the controlling dimension in a K_{IC} test.

- The controlling dimension is the ligament size, which, due to the 95% secant definition of P_Q, leads to specimen size dependent fracture toughness values.
- The ligament size dependence can only be removed by introducing a ligament size dependent P_Q-secant definition.
- The P_{max}/P_Q criterion should be removed.
- The specimen size criteria can be somewhat relaxed and should be based on ligament size, not thickness.
- Moderate side-grooving should be allowed.

5. Acknowledgements

This work is a part of the Integrity and Life Time of Reactor Circuits project (INTELI) belonging to the Safety of Nuclear Power Plants – Finnish national research programme 2003–2006 (SAFIR), financed by the Ministry of Trade and Industry, the Technical Research Centre of Finland (VTT) and the Radiation and Nuclear Safety Authority (STUK).

References

Irwin, G.R. Fracture Mode Transition for a Crack Traversing a Plate. Journal of Basic Engineering, 1960, pp. 417–425.

Irwin, G.R., Kies, J.A. & Smith, H.L. Fracture Strengths Relative to Onset and Arrest of Crack Propagation. ASTM Proceedings, Vol. 58, 1958, pp. 640–660.

Kaufman, J.G. & Nelson, F.G. More on Specimen Size Effects in Fracture Toughness Testing. Fracture Toughness and Slow-Stable Cracking, ASTM STP 559, American Society for Testing and Materials, Philadelphia, 1973, pp. 74–98.

Anderson, T.L. Fracture Mechanics – Fundamentals and Applications. Second Edition, CRC Press, Boca Raton, 1995.

Evaluation of weld metal hydrogen cracking risk in a 2.25Cr-1Mo-0.25V-TiB (T24) boiler steel

Pekka Nevasmaa, Anssi Laukkanen & Juha Häkkilä*
VTT Industrial Systems, Espoo, Finland
*Foster Wheeler Energia Oy, Varkaus, Finland

Abstract

Standardised methods for the assessment of hydrogen cracking risk are mostly developed for HAZ cracking cases, where cracking often occurs as root cracking. The applied experiments are therefore usually single-pass cracking tests. For multiple-pass welding, and when the cracking sensitivity of weld metal dictates the required preheat, European standards do not give reliable guidance on how to assess the need of preheat. Standard EN 1011-2 considers the possibility of weld metal cracking, however, it does not provide the user with a validated methodology for the calculation of the actual level of 'safe' preheat temperature. The suitability of a given standard procedure, or calculation method, for multipass welds therefore has to be investigated on case by case basis. This paper is concerned with the assessment of required preheat/interpass temperature for the avoidance of hydrogen cracking in matching type multipass weld metal in a 2.25%Cr-1.0%Mo-0.25%V boiler steel using experimental and numerical methods. The applied methods were: (i) EN 1011-2 Method, (ii) Crack – no crack diagram method developed by VTT, and (iii) deep-notch Implant test based analytical method developed by Osaka University and VTT. Necessary pre-cautions for safe welding are given. Recent developments in numerical modelling of hydrogen diffusion in multipass welding are discussed.

1. Introduction

Weldability of the low alloy creep-resisting steels is mainly governed by their hydrogen cold cracking tendency. Owing to the relatively high contents of Cr, Mo and V, rapid cooling cycles easily lead to hard bainitic-martensitic microstructures in the heat-affected zone (HAZ) and in the weld metal. Welding procedures must therefore contain the necessary safeguards against cracking, which calls for appropriate preheating and the use of low-hydrogen filler metals.

Current environmental policy sets greater demands for higher efficiencies and the increase of operating pressure and temperature in thermal power stations, with

the aim at making use of the fossil fuels more efficiently. The high maximum temperatures of power plants requires the development of advanced steels with better creep rupture strength at elevated steam temperatures and pressures. As a result, new grades of 2.25%Cr-1%Mo (T22) steel have been developed especially for the tubes in water-walls of the modern boilers. Compared to conventional 10CrMo9-10 (T22) steel, in the new grade T24 (2.25%Cr-1%Mo-0.25%V-TiB, i.e., 7CrMoVTiB10-10) additions of vanadium (V), titanium (Ti) and boron (B) result in an improvement in creep rupture strength, whilst reduction of carbon (max. 0.07%) reduces HAZ hardness thereby improving weldability. Thus, the use of T24 leads to remarkable reduction in wall thickness of tubes and pipes or, alternatively, higher operating pressures, compared to traditional T22 grades. Weight savings of 30–60% for different components have been reported [1]. These new grades provide enhanced creep properties at 550°C, as well as low hardness in the as-welded condition and hence lower risk to hydrogen cracking in the HAZ.

The required preheat temperature to prevent hydrogen cracking in ferritic steel weldments depends on steel/weld metal chemical composition, section thickness, heat input and weld diffusible hydrogen content [2]. For the 2.25%Cr-1%Mo (T22) steels, preheat temperatures of 75–300°C are generally required [1,2], with the subsequent post-weld heat treatment (PWHT). As regards to the T24 grade, welding procedure tests carried out by the manufacturer (Vallourec & Mannesmann Tubes) have demonstrated that thin wall pipes (≈ 6 mm) can be welded either without preheating, or with preheating of 200°C, as well as without PWHT [1]. Owing to the low C content, the steel has a bainitic-martensitic structure over a large range of cooling rates. This manifests itself as a HAZ hardness of about 350 HV in the as-welded condition [1]. In fact, tendency for hydrogen cracking of these V modified steels appeared quite similar to the corresponding Cr-Mo steels without V [1].

In modern steels, improved resistance of the HAZ to hydrogen cold cracking may be accompanied by an undesired effect of having cracks in the weld metal, instead. Consequently, with increasing strength required preheat may be dictated by cracking sensitivity of the weld metal [3]. Many of the standard methods for the assessment of hydrogen cracking risk and necessary precautions for safe welding are developed for HAZ cracking cases, where cracking occurs as root, under-bead or toe cracking. The applied experiments are therefore usually single-pass cracking tests. For multiple pass welding situations, and provided cracking sensitivity of weld metal dictates the required preheat, European standards do not give reliable guidance on how to assess the need of preheat. Standard EN 1011-2 [2] does consider the possibility of weld metal cracking under certain conditions, however, it does not provide the user with any unified, well validated methodology for the calculation of the actual level of ‘safe’ preheat temperature. Of the calculation formulae predicting necessary preheat for weld metals, only

few are systematically based on experiments that actually involve multipass welding. The others are usually either modifications of previously existing formulae intended originally for HAZ cracking cases, or are solely based on results of single-pass cracking tests, such as Tekken, CTS, G-BOP or Implant test. These are of little assistance in the provision of procedural guidance for multipass welds, because one cannot know whether the results are really descriptive of the multipass welded structure. Testing full-scale products, on the other hand, only indicates cracking susceptibility of the particular structure under given welding conditions, but the results do not necessarily have general relevance to other cases. The suitability of a given standard procedure, or calculation method, for the assessment of weld metal cracking risk in multipass welding of boiler steels therefore has to be investigated on case by case basis.

This paper is concerned with the assessment of required preheat/interpass temperature for the avoidance of weld metal cracking in 7CrMoVTiB10-10 type multipass weld metal.

2. Materials and experiments

In order to produce multipass weld metal for cracking tests, weldments were made using Böhler-Thyssen 7CrMoVTiB10-10 type filler metal (CrMoVTiB) and welding parameters [10] corresponding to actual production welding. A 20 mm thick plate with 60° V groove preparation, root gap and backing bar was adopted to minimise any dilution from parent plate. The chemical composition of the 7CrMoVTiB10-10 weld metal is given in Table 1.

Table 1. Chemical composition of the 7CrMoVTiB10-10 type weld metal.

Electrode / w-%	**C**	**Si**	**Mn**	**S**	**P**	**Cr**	**Mo**	**V**
	0.045	0.31	0.45	0.003	0.012	2.16	0.87	0.23
Electrode / w-%	**Ni**	**Cu**	**Al**	**Ti**	**B**	**W**	**Co**	CE(IIW)
	0.14	0.12	0.05	0.020	0.0023	< 0.01	0.024	0.79

Implant test specimens of 8 mm in diameter were machined from the filling layers of the multipass weldment. Implant tests were carried out using deep-½V notched specimens of 2 mm notch depth; the neck diameter in the bottom of the notch thereby became 4 mm. Specimens were inserted into a hole drilled through the support plate. To introduce hydrogen into the specimen, bead-on-plate weld was deposited onto the support plate with its penetration adjusted to melt the bottom of the specimen notch. Matching 7CrMoVTiB10-10 grade electrodes were used. Three weld hydrogen levels: low, medium and high, were obtained using re-dried, as-received and moistured SMAW electrodes, respectively, according to a procedure described elsewhere [10]. The intention of applying

deep-½V notch was that the tri-axial stress state created in the bottom of the notch during axial loading of the specimen promotes hydrogen diffusion into the desired microstructure along the notch. Also microstructures with a strength level beyond that of the specimen material can be tested without plastic deformation of the specimen [6–8].

Weld diffusible hydrogen content H_0 ($\equiv H_D$) was measured using the Osaka University mercury method that was shown [6–9] to have a linear correlation to the IIW mercury method c.f. ISO/IIW 3690. Chemical composition of the weld metal was determined using optical emission spectroscopy. Weld hardness profiles were determined as Vickers hardness HV_5. The heat input used for bead-on-plate welds was 2.0 kJ/mm. Complete data are reported elsewhere [10].

3. Results and Discussion

Required preheat/interpass temperature T_0/T_i for 7CrMoVTiB10-10 weld metal was estimated applying: (i) EN 1011-2 Method [2], (ii) Crack – No Crack Diagram Method [3–5] and (iii) deep-notch Implant test based analytical method [6–9].

3.1 Assessment according to standard EN 1011-2:2001

Standard EN 1011-2:2001 Annex C [2] provides two alternative methods for estimating T_0/T_i for creep resisting steels: recommendations according to Table C.5 and analytical *Method B*.

Table C.5 is designed especially for creep-resisting steels and gives the minimum T_0/T_i as a function of steel grade, section thickness and hydrogen scale (A-D). These recommendations are applicable to butt welds in plates and pipes; it is stated that fillet welds may sometimes require higher temperatures than those given in Table C.5. The standard does not, however, clearly indicate whether Table C.5 is applicable also to the cases where cracking tendency of the weld metal dominates the need of the required preheat. Moreover, Table C.5 does not contain a V-mod. 2.25%Cr-1%Mo-0.25%V grade, but only the 2.25%Cr-1%Mo grade without V. Assuming that hydrogen cracking sensitivity of V-mod. Cr-Mo steels does not differ essentially from those without V, as was claimed elsewhere [1], the following T_0/T_i temperatures are obtained for the 2.25%Cr-1.0%Mo grade and low hydrogen Scale D, i.e., $H_D \leq 5$ ml/100g deposited metal (IIW):

- for section thickness ≤ 15 mm: the minimum T_0/T_i is 75°C
- for section thickness > 15 mm: the minimum T_0/T_i is 100°C
- maximum T_i : 350°C.

It is noteworthy that the data in Table C.5 does not fully comply with the view [1] that tendency for hydrogen cracking of V-mod. steels would appear similar to those without V. In fact, Table C.5 implies that somewhat higher T_0/T_i may be needed for V containing Cr-Mo steels.

Method B gives the following formula for calculating estimates of safe T_0/T_i :

$$T_0 = 697CET + 160\tanh(d/35) + 62H_D^{0.35} + (53CET - 32)Q - 328 \ (°C) \quad (1)$$

$$CET = C + (Mn + Mo)/10 + (Cr + Cu)/20 + Ni/40 \ (\%) \quad (2)$$

where CET is a German carbon equivalent c.f. Eq. (2), d is section thickness (mm), H_D is weld diffusible hydrogen content (ml/100g) and Q is heat input (kJ/mm). *Method B* is stated [2] to be valid also to weld metal cracking cases with the following condition: if the CET of the parent metal does not exceed that of the weld metal by 0.03%, then the calculation of the required preheat has to be based on the CET of the weld metal increased by 0.03%. With respect to Cr (max. 1.5%), Mo (max. 0.75%) and V (max. 0.18%), however, the V-mod. 2.25%Cr-1%Mo-0.25%V weld metal is beyond the validity limits of Eqs (1) and (2), which weakens the reliability of preheat assessment in the present case. Further note that Eq. (2) does not contain any terms for V, Ti or B, for example.

Nevertheless, adopting the following values [10] for weld metal CET, d, H_D and Q, the required minimum T_0/T_i temperature was estimated as follows:

- CET = 0.2945 (%) + 0.03 (%) = 0.3245 (%)
- d = 10 mm
- H_D = 5.0 ml/100g deposited weld metal (IIW)
- Q = 0.6 kJ/mm.

Applying Eqs (1) and (2) for the 7CrMoVTiB10-10 weld metal gives a minimum T_0/T_i of 43°C. Compared with Table C.5, the T_0/T_i according to Method B is suspiciously low and should therefore be treated with caution. It is, however, in line with the finding [1] that T24 tubes of 6 mm max. section thickness should be weldable even without preheat, as far as HAZ hydrogen cracking is concerned.

3.2 Assessment according to Crack – No Crack Diagram Method

VTT has recently developed a procedure [3–5] for the assessment of hydrogen cracking risk in multipass weld metal. The procedure has its basis on experiments employing rigidly bolted specimens subjected to forced cooling. This was shown [3–5] to prevent distortion and deformations during welding, thereby maximising the build-up of residual welding stresses and enabling low interpass temperature

T_i and short interpass time t_i to be obtained simultaneously. According to diffusion theory, the combination of low T_i and short t_i should minimise the effusion of hydrogen during multipass welding, thereby accentuating the accumulation of hydrogen and hence the elevation of the local final hydrogen concentration towards the filling runs. Thus, the procedure describes weld metal cracking risk in a thick plate under the most stringent thermal and structural conditions producing lower-bound estimates of critical hydrogen and required preheat. The procedure has been validated for ferritic weld metals in the 455–900 MPa yield strength range [3–5], but not for creep resisting weld metals.

The procedure comprises two steps: *Step 1* provides a worst-case estimate of the weld critical hydrogen H_{cr} as a function of either the actual chemical composition in terms of P_{cm} weldability index, or the individual maximum hardness HV_{5max} of the weld metal, and under conditions involving T_0/T_i = 70–100°C. Crack free welding conditions are met if the H_{cr} is higher than the weld diffusible hydrogen content H_D according to single-pass hydrogen test conforming to ISO/IIW 3690.

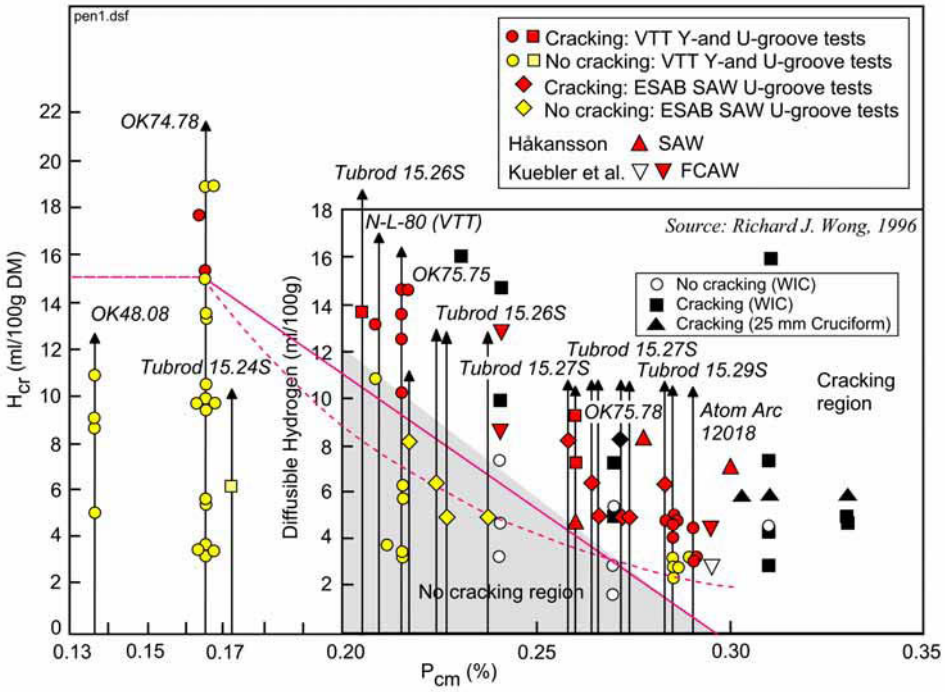

Figure 1. Weld critical hydrogen content H_{cr} as a function of weld metal P_{cm} [3].

The Crack – No Crack Diagrams are shown in Figures 1 and 2. The lower-bound safe lines of the diagrams have been shown [3–5] to obey Eqs (3) and (4) as:

$$H_{cr} = 116\,(0.295 - P_{cm}) \quad \text{(ml/100g deposited metal, IIW)} \qquad (3)$$

$$H_{cr} = 280 * 10^{(-0.00585\,HV_{max})} \quad \text{(ml/100g deposited metal, IIW)} \qquad (4)$$

$$P_{cm} = C + Si/30 + (Mn + Cu + Cr)/20 + Ni/60 + Mo/15 + V/10 + 5B\ (\%) \qquad (5)$$

Using weld metal chemical composition given in Table 1 and the measured [10] Vickers hardness of the 7CrMoVTiB10-10 weld metal, gives the following:

- P_{cm} = 0.286%
- HV_{max} = 383 HV

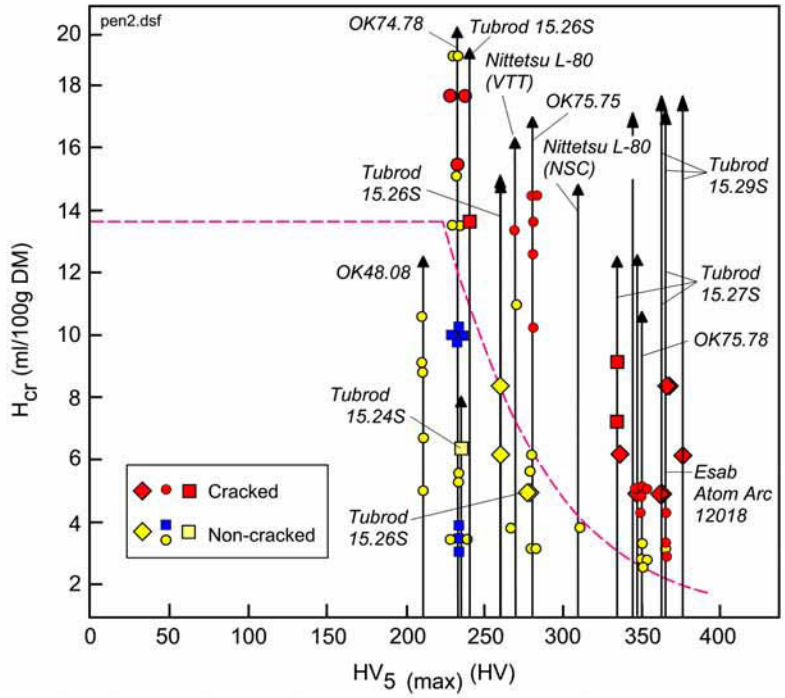

Figure 2. Weld critical hydrogen content H_{cr} as a function of weld metal maximum hardness $HV_{5(max)}$ (T_i = 70–100°C) [3].

Placing the above P_{cm} and HV_{max} values into Eqs (3) and (4), respectively, gives the following lower bound values for weld critical hydrogen H_{cr} according to the Step 1 estimation scheme:

- According to Fig. 1 and Eq. (3): $H_{cr} \approx$ 1.0 ml/100g deposited metal (IIW).
- According to Fig. 2 and Eq. (4): $H_{cr} \approx$ 1.6 ml/100g deposited metal (IIW).

The results show that the measured HV_{max} of 383 HV is somewhat higher than the 350 HV stated [1] as being typical for T24 pipe material. This is presumably due to the low applied heat input of 0.6 kJ/mm. Further note that unlike EN 1011-2 Method, the P_{cm} index c.f. Eq. (5) accounts for effects of both V and B on hardenability. As a result, the weld H_{cr} from the weld metal cracking standpoint becomes so low that the need of preheat appears evident in the present case. Consequently, Step 2 analysis was performed.

Step 2 provides two equations for predicting safe estimates of the required T_0/T_i as a function of weld H_D, weld build-up thickness a_w and either the actual weld

metal CET, or weld metal hardness in terms of HV_{5max}. The two formulae for the assessment of T_0/T_i are given as follows [4, 5]:

$$T_0/T_i = 2195CET + 367\tanh(a_w/60) + \{[2310\ln(H_D)]/[12H_D^{0.15}]\} - 1074\ (°C) \quad (6)$$

$$T_0/T_i = 1.62HV_{max} + 367\tanh(a_w/60) + \{[2310\ln(H_D)]/[12H_D^{0.15}]\} - 776\ (°C) \quad (7)$$

The principal difference between Eqs (6) and (7) is that the CET c.f. Eq. (2) does not contain B nor V, whereas the HV_{max} measured from weld metal incorporates the effect of weld metal alloying in full and the weld thermal cycle. Thus, in the present case, Eq. (7) is expected to yield higher T_0/T_i estimates than Eq. (6).

The following input data was taken for the analysis according to Step 2 estimation scheme and the results of the analysis are presented in Table 2:

- HV_{max} = 383 HV
- d = 10 mm
- H_D = 2.0; 3.0 and 5.0 ml/100g deposited metal (IIW).

Table 2. Required minimum T_0/T_i according to the Step 2 estimation scheme.

Weld H_D / T_0/T_i (°C)	T_0/T_i : c.f. Eq. (6)	T_0/T_i : c.f. Eq. (7)
2.0 ml/100g DM	20	20
3.0 ml/100g DM	20	85
5.0 ml/100g DM	20	148

Table 2 shows that Eq. (6) based on the CET yields very low values of T_0/T_i that, considering the absence of V and B, are presumably unrealistically low, except for weld H_D < 3 ml/100g DM(IIW). Contrary to this, Eq. (7) that is based on measured weld hardness data results in the T_0/T_i estimates that are very close to those in EN 1011-2 Annex C [2]. Consistently, they both demonstrate that with section thickness < 10 mm and weld H_D < 3.0 ml/100g DM(IIW), T_0/T_i temperatures of no more than 75–85°C are necessary. This applies typically to TIG and GMAW processes with solid wires. With re-dried SMAW electrodes associated with weld $H_D \approx$ 3.0–5.0 ml/100g, somewhat higher T_0/T_i of 150°C might be necessary to prevent weld metal hydrogen cracking, even though the 7CrMoVTiB10-10 steel itself would be weldable without preheating.

3.3 Assessment according to the VTT–Osaka method

Since the preheat assessment according to EN 1011-2 Annex C [2] is essentially based on self-restraint type cracking tests, structural rigidity of a component is built-in to the assessment in terms of specimen thickness. For single-pass cracking tests intended for HAZ cracking cases and longitudinal cracks, the

governing stress component is the transverse net stress across the weld throat, σ_{net}. As there is no external loading, the net stress build-up occurs due to welding residual stresses. The level of σ_{net} depends on material strength and specimen rigidity, i.e., structural restraint against transverse shrinkage R_F that is expressed via specimen thickness: thicker specimens allow greater increase in σ_{net} until it finally reaches the level of true weld metal yield strength, $\sigma_{y(WM)}$. Thin sections and under-matching weld metals therefore have lesser risk of HAZ hydrogen cracks, hence requiring lower preheating temperatures. The effects of specimen's rigidity and developing stresses on hydrogen cracking as defined in EN 1011-2 Annex C [2] are thereby included in 'section thickness', d.

The above holds true as long as component's rigidity is determined essentially by its thickness. If shaping of a structural detail is such that essential part of its structural rigidity comes from geometry-related details like e.g. sudden variations in section thickness, flanges, etc., structural rigidity can locally be much higher than that indicated by the R_F calculated from thickness of a plate-shape panel. In this case, the need of preheat should be estimated assuming $\sigma_{net} \approx \sigma_{y(WM)}$, as shown in the VTT-Osaka assessment [6–9].

VTT and Osaka University jointly developed a preheat assessment method based on the deep-notch Implant cold cracking test suited to HAZ cracking cases and single-pass welds, i.e., root cracking. The VTT-OU method is based on the comparison of two values of the stress field parameter ΣI at the crack initiation area. The required value of ΣI is assessed by the restraint of the structure and the welded joint/groove geometry. The attainable level of ΣI is determined by the steel composition, weld thermal cycle and diffusible hydrogen content. The details of the method are described elsewhere [6–9, 13]. Being originally developed for butt welds and correlated to the Restraint cracking tests [6–8], the method was later shown [9] to apply also to fillet welds and agree e.g. with the outcome of the CTS cracking tests. Recently, the VTT-OU method was applied also to weld metal using specimens machined from actual multipass welds [11, 12]; the method predicted correctly that in order to avoid weld metal cracking in a thick 690 MPa yield strength DQT steel, a preheat temperature higher than that required for the prevention of HAZ cracking, was necessary.

The results of Implant tests on the 7CrMoVTiB10-10 weld metal are reported in full elsewhere [10]. Figure 3 summarises the critical Implant fracture stress σ_{cr} and its scatter bands as a function of weld initial diffusible hydrogen content H_0. Table 3 presents the measured and estimated values of σ_{cr} at a given weld diffusible hydrogen content H_0.

Earlier work [6] on deep-V notch specimens has shown that the σ_{cr} in the case of HAZ hydrogen cracking obeys Eq. (8):

$$\sigma_{cr} = 1350 - 2.0HV_{max} - 430\log(H_{R100(FM)}) \quad (8)$$

Table 3 shows that the scatter in the experimental results is comparatively large. Figure 3 reveals that the dependency of σ_{cr} on weld hydrogen content H_0 is less steep than Eq. (8) suggests, i.e., the weld metal appears less sensitive to hydrogen addition than according to Eq. (8). On the other hand the absolute levels of σ_{cr} are comparatively low, indicating that the weld metal microstructure would be quite sensitive to hydrogen cracking.

Table 3. Results of the Implant cold cracking tests (at room temperature).

Weld H_0 (ml/100g DM IIW)	Electrode condition	Measured σ_{cr} (N/mm^2)	Estimated σ_{cr} (N/mm^2)	Measured HV_{max} (HV)	Calculated $H_{R100(DM)}$ (ml/100g)	Calculated $H_{R100(FM)}$ (ml/100g)
4.9	re-dried	350	438	383	3.74	2.25
6.6	as-rec.	332	383	383	5.04	3.03
9.9	moistur.	325	308	383	7.56	4.54

σ_{cr} :measured critical Implant fracture stress (mean values); estimated Implant fracture stress calculated according to Eq. (8).

H_{R100} :the remaining weld diffusible hydrogen content at the temperature of 100°C, calculated from the weld cooling time t_{100} (c.f. Table 3) in accordance with [6, 7]; DM: deposited metal, FM: fused metal c.f. Eq. (8).

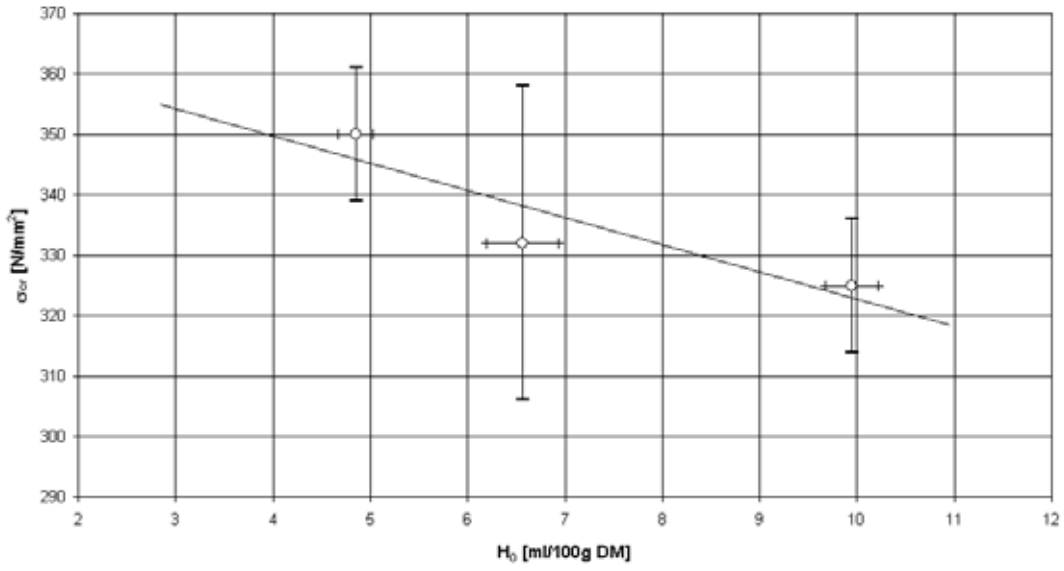

Figure 3. Critical Implant fracture stress σ_{cr} (N/mm^2) as a function of weld initial diffusible hydrogen H_0 (ml/100g DM IIW).

Table 4 summarises the measured weld cooling time data and the influence of weld thermal cycle on weld hydrogen content. It can be seen that the increase in

preheat temperature T_p above 100°C prolongs considerably the cooling time t_{100}, thereby enhancing hydrogen effusion (an increase in the diffusion factor $\Sigma D\Delta t$). The gradually increasing hydrogen removal from the weld during cooling manifests itself as a progressively decreasing values in the remaining diffusible hydrogen H_{R100}, at a given initial diffusible hydrogen, H_0. This, in turn, elevates the Implant fracture stress σ_{cr} in accordance with Eq. (8), see Table 3.

Table 4. The dependence of weld H_{R100} on welding thermal cycle.

T_p (°C)	Measured t_{100} (sec)	Calculated $\Sigma D\Delta t$ (cm^2)	Weld H_0 (ml/100g DM IIW)	H_{R100} / H_0 -ratio	Calculated weld H_{R100} (ml/100g) $H_{R100(DM)}$ $H_{R100(FM)}$	
20	148	0.003842	4.9	0.764	3.74	2.25
100	700	0.014472	4.9	0.363	1.78	1.07
150	1500	0.031813	4.9	0.108	0.529	0.318
200	2000	0.043845	4.9	0.0465	0.228	0.137

t_{100} :measured weld cooling time from the peak temperature down to 100°C.

$\Sigma D\Delta t$:calculated [6–8] thermal factor of hydrogen diffusion (cm^2).

H_{R100}/H_0 :ratio between the remaining weld diffusible hydrogen content at the incident of cracking and the initial weld diffusible hydrogen content immediately after welding.

Determining the actual level of the σ_{cr} of a given weld metal as a function of weld H_0 c.f. Figure 3 by carrying out Implant tests at room temperature, and using Table 4 that establishes the effect of elevated T_p on lowering weld H_{R100} , one can calculate the reduction in the "430 log($H_{R100(FM)}$)" hydrogen term resulting from the decrease in weld $H_{R100(FM)}$ as the T_p is raised. Assuming the dependence of σ_{cr} on weld $H_{R100(FM)}$ to obey Eq. (8), allows one to calculate the corresponding change in the σ_{cr} at any given preheat temperature T_p, even though measured Implant results at that particular temperature were not available.

At a given notch stress severity parameter F_I, the attainable stress field parameter $\Sigma I_{cr\text{-}att}$ has been shown [7, 8] to depend on the Implant fracture stress σ_{cr}. For the applied deep-V notch specimen, $F_I \approx 0.58$ [7, 8]. Consequently, Eq. (8) can be re-written into the form:

$$\Sigma I_{cr\text{-}att} = 785 - 1.2HV_{max} - 250\log(H_{R100(FM)}) \quad (9)$$

The other factors remaining unchanged, the change in the hydrogen factor in Eq. (8) can be transferred into Eq. (9). Thus, the reduction in the "250 log($H_{R100(FM)}$)"

hydrogen term resulting from the decrease in weld $H_{R100(FM)}$, provides a means of using Eq. (9) in calculating the elevation in the $\Sigma I_{cr\text{-}att}$ corresponding to the reduction in weld $H_{R100(FM)}$ as the preheat temperature T_p is raised. To determine safe preheat temperature, the value of attainable $\Sigma I_{cr\text{-}att}$ is then compared against the value of the required $\Sigma I_{cr\text{-}req}$. Provided that $\Sigma I_{cr\text{-}att} > \Sigma I_{cr\text{-}req}$, there should be no hydrogen cracking at a corresponding level of preheat.

Table 5. Assessment of weld metal hydrogen cracking risk and the required T_0/T_i using the Implant method.

T_p (°C)	Weld H_0 (ml/100g DM IIW)	$H_{R100(FM)}$ (ml/100g FM IIW)	Determined $\Sigma I_{cr\text{-}att}$	Calculated $\Sigma I_{cr\text{-}req}$ (a) moderate restraint	Calculated $\Sigma I_{cr\text{-}req}$ (b) high restraint V groove	½-V groove
20	4.9	2.25	203	143	375	445
100	4.9	1.07	283	143	375	445
150	4.9	0.318	415	143	375	445
200	4.9	0.137	506	143	375	445

$\Sigma I_{cr\text{-}att}$: attainable value of stress field parameter c.f. Eq. (9).

$\Sigma I_{cr\text{-}req}$: (a) required value of stress field parameter in moderate restraint case c.f. Eq. (10a); input values: d = 10 mm ; m = 0.040 ; F_I = 0.89 (mean value for ½-V groove [7]).

$\Sigma I_{cr\text{-}req}$: (b) required value of stress field parameter in high restraint case c.f. Eq. (10b); input values: $\sigma_{net} = \sigma_{y(WM)}$ = 500 N/mm^2 ; F_I = 0.89 (mean value for ½-V groove), or, F_I = 0.75 (mean value for V groove [7]).

In this paper, two structural cases were chosen into the assessment:

(a) Moderate restraint structure where the σ_{net} remains considerably less than the level of weld metal yield strength $\sigma_{y(WM)}$. These are typically thin plate structures, in which case the R_F depends nearly linearly from the thickness d. In this case, $\Sigma I_{cr\text{-}req}$ can be calculated according to [7, 8]:

$$\Sigma I_{cr\text{-}req} = F_I * m * R_F = F_I * m * (400\, d) \qquad (10a)$$

where m is a constant shown to be about 0.040 [6–8].

(b) High restraint structure where the σ_{net} reaches the level of weld $\sigma_{y(WM)}$. This is a case for thick plate structures, or when shaping of a structural detail is such that essential part of its rigidity comes from geometry-related details. In these cases, $\Sigma I_{cr\text{-}req}$ can be calculated without knowing the actual R_F value, by setting $\sigma_{net} = \sigma_{y(WM)}$ and using an equation [7, 8] of the form:

$$\Sigma I_{cr\text{-}req} = F_I * \sigma_{net} = F_I * \sigma_{y(WM)} \quad (10b)$$

The preheat temperature assessment based on comparison between the $\Sigma I_{cr\text{-}att}$ determined and calculated from the Implant test results and the $\Sigma I_{cr\text{-}req}$ calculated from structural rigidity is given in Table 5.

It can be seen that in moderate restraint structures whose R_F is essentially determined by small section thickness of less than 10 mm, welding of the 7CrMoVTiB10-10 grade should be safe even without preheating, provided low hydrogen filler metals of weld $H_{D(IIW)} \leq 5$ ml/100g DM(IIW) are used.

In high restraint structures and welded details whose structural rigidity, due to local variations in section thickness, flanges, etc., can be much higher than indicated by the R_F value calculated from section thickness of a plate-shape panel, welding of the 7CrMoVTiB10-10 grade should be made applying a preheat temperature of around 150–180°C and with low hydrogen filler metals of weld $H_{D(IIW)} \leq 5$ ml/100g DM(IIW).

4. Numerical analysis of hydrogen diffusion

Advanced numerical calculation methods for modelling hydrogen diffusion in multiple-pass welding provide sophisticated means of evaluating the effects of (i) long inter-pass time, thin plate welding and small weld thickness coupled with open free surfaces both in the root and top side of the weldment, in promoting hydrogen effusion during welding. These phenomena are expected to reduce the true cracking risk, in relation to multipass welds in a thick plate. Consequently, applying the assessment based on VTT Crack – No Crack Diagrams in conjunction with numerical modelling is expected to provide more realistic estimates for the cases where factors such as long interpass time and thin plate enhance removal of hydrogen, thereby reducing the cracking risk from that estimated according to the worst-case assessment.

5. Summary and conclusions

The following main conclusions can be drawn regarding safe welding conditions for the creep-resisting 7CrMoVTiB10-10 grade to prevent weld metal hydrogen cracking:

- All the three assessment methods: EN 1011-2 Method, Crack – No Crack Diagram Method by VTT, and Deep-notch Implant test method by Osaka University and VTT, had certain limitations with respect to their

unconditional applicability to T24 (2.25%Cr-1%Mo-0.25%V-TiB) grade steel.

- For small section thickness less than 10 mm and moderate restraint conditions, no preheating is needed to prevent HAZ hydrogen cracking. This is in agreement with the other recent work [1] on modern creep resisting steels.
- Even for small section thickness < 10 mm and moderate restraint conditions, slight preheating of 75–85°C might become necessary to prevent hydrogen cracking in multipass weld metal with hardness of 380 HV and above. The use of low hydrogen filler materials should be preferred.
- In high restraint structures/welded details whose rigidity can, due to local variations in section thickness, flanges, etc., become much higher than indicated by the intensity of restraint calculated from section thickness of a plate-shape panel, welding should be made applying preheat temperatures of around 150–180°C and with low hydrogen consumables of weld $H_{D(IIW)} \leq 3.0$ ml/100g DM(IIW).
- Numerical modelling, in conjunction with the VTT Crack – No Crack Diagram Method is expected to provide more realistic estimates than the worst-case scenario, for the cases where factors such as long interpass time and thin plate welds with large open surface area will enhance removal of hydrogen, thereby reducing the cracking risk.

References

1. Lukkari, J. Creep Resisting Steels and Welding. ESAB Group Ltd. (to be published in 2004).
2. EN 1011-2:2001. CEN/TC 121, CEN 2001. 113 p.
3. Nevasmaa, P. Acta Universitatis Ouluensis: C Technica 191. University of Oulu: Department of Mechanical Engineering, Oulu 2003. 212 p.
4. Nevasmaa, P. Hitsaustekniikka 54(2004)1, pp. 8–24 (in Finnnish).
5. Nevasmaa, P. Welding in the World 48(2004) (to be released in 2004).
6. Karppi, R. Publication No. 1/1976. Espoo: Helsinki University of Technology, Laboratory of Materials Technology, 1976. 422 p.
7. Karppi, R. A stress field parameter for weld hydrogen cracking. VTT Publications 9. Espoo: Technical Research Centre of Finland, 1982. 119 p.

8. Karppi, R., Ruusila, J., Toyoda, M., Satoh, K. & Vartiainen, K. Scandinavian Journal of Metallurgy 13(1984), pp. 66–74.

9. Karppi, R. & Nevasmaa, P. Contribution to comparison of methods for determining welding procedures for the avoidance of hydrogen cracking. IIW-Doc. IX-1673-92/VTT Publications 107. Espoo: Technical Research Centre of Finland, 1992. 38 p. + app. 12 p.

10. VTT Tutkimusselostus TUO74-033322. Espoo: VTT Industrial Systems, 2003 (in Finnish).

11. Nevasmaa, P., Cederberg M. & Vilpas, M. Weldability of direct-quenched and tempered (DQT) high strength steel HT80. VTT Research Notes 1406. Espoo: Technical Research Centre of Finland, 1992. 32 p. + app. 12 p.

12. Nevasmaa P., Cederberg, M. & Vilpas, M. Weldability of new HT-50 and HT-80 class thermomechanically rolled high strength steels. Proceedings of the 5th Conference on Joining of Materials – JOM-5. Helsingör, 10–12 May 1991. Eds. R.L. Apps & O. Al-Erhayem. The European Institute for Joining of Materials, Denmark 1991. Pp. 387–394.

13. Terasaki, T., Karppi, R. & Satoh, K. Transactions of the Japan Welding Society 10(1979)1, pp. 53–57.

Observations of component and specimen behaviour in fatigue

Klaus Rahka
VTT-Industrial Systems
POB 1704, 02044 VTT
Finland

Abstract

Trends in structural integrity analysis for design show increased use of e.g. numerical FEM-analysis. FEM analysis produces pointwise strain or stress throughout a component. The distribution through the thickness is nonlinear and the meaning of these numbers compared to traditional stress by formulae call for new, realistic and reliable interpretation.

This paper presents a set of observations of component behaviour in fatigue when data is plotted as local strain fluctuation versus cycles to failure. Part of the paper shows the differences in raw data between standard uniaxial test data and component data, when both data are represented by the uniaxial equivalent value for the local maximum peak strain range or amplitude using octahedral shear strain equivalence theory (vMises) for simplicity.

The rest of the paper presents rules developed for bringing component data to coincide with standard uniaxial test data – thus providing a way to predict component behaviour based on material uniaxial data – and a new rule to estimate local yielding (plasticity correction) for structural analyses based on elasticity. The development work was done in a European Commission sponsored project "Fatigue Design" (BE 97-4658), which was practically completed in 2002.

1. Introduction

The writer's interest towards component behaviour in comparison to specimen behaviour in low-cycle fatigue bears a long term span of more than three decades, but it was not until the early 1990s that a dramatic demonstration of the reducing effect of product shape on local strain carrying capacity became evident through research on the cause of a structural failure – a "close call" for a colleague. In this case material had been stored from the tested and failed

pressure vessel and it could be experimentally demonstrated that the critical fracture strain at the notch tip was only 10% of the necking fracture strain in a tensile specimen. A true shape effect had been uncovered. The material was a casting of 17-7Ph with high strength (YS = 930, UTS = 1030 MPa) moderate tensile ductility (RA = 15%, hence e_f = 15%) but rather low impact toughness (KV = 6 Nm). For integrity engineering of larger significance this example was judged to indicate several items of concern when endeavouring usefull reliability for the interpretation of calculated numbers obtained for components through structual analysis by FEM and comparison to tensile data. FEM could be performed either fully elastically ignoring material yielding effects or using "true to material behaviour" assuming nonlinear material employing e.g. the true stress-true strain curve for the material. Strain would in nonliear analysis become larger than by elastic analysis. This paper presents several observations of interest for such interpretation including suggestions for quantitative assessment based on experiment.

2. Observation 1

Strain life material data for design of pressure vessels can be obtained by testing according to ASTM E 606. In the ASME Boiler and Pressure Vessel Code data is given for design with the most common structural materials of carbon, low alloy and stainless steels. These curves are based on such standard uniaxial material tests. Components - in this case full size test vessels - behave worse, Figure 1.

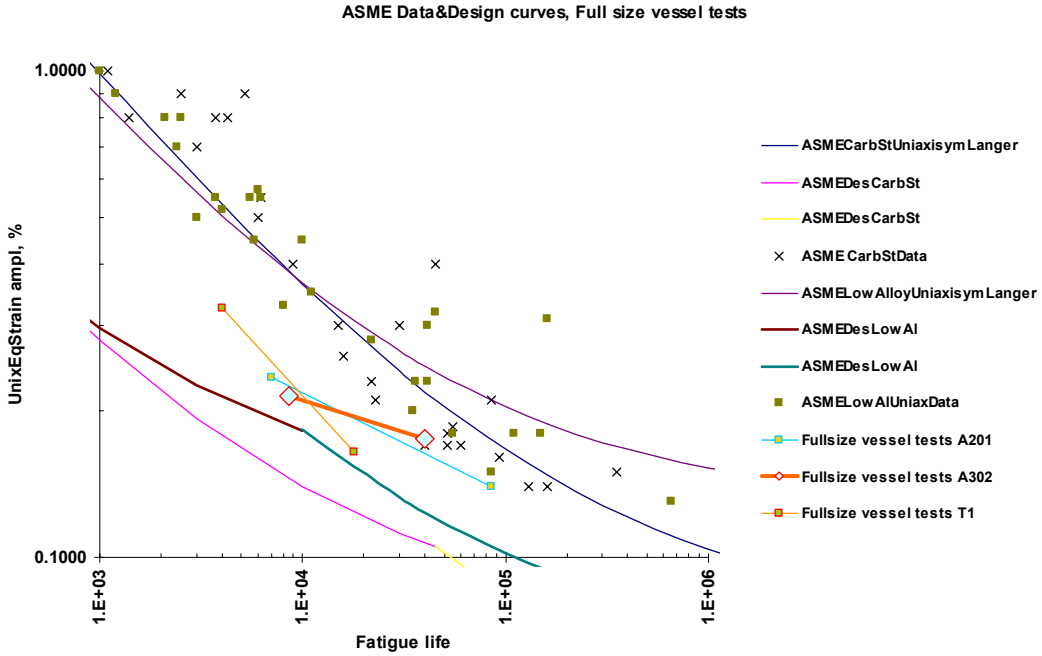

Figure 1. Strain life data comparing uniaxial specimen performance with full size vessel data.

The Code design margins of 2 on strain or 20 on cycles applied for obtaining the design curves are cited to not justify expectation of actual component performance for longer than their design life. The code committee thus recommends that effects not accounted by the uniaxial tests could affect component behaviour.

The writer withdraws from speculation of possible reasons (which may not be the most frequently speculated size effect related to material defects) for the inferior component behaviour compared to uniaxial specimen behaviour, but hypothesises that obvious differences are in the local states of strain and the through thickness strain gradients in the respective tested component geometries. Miniature test vessels seem to perform better than their full size companions, the size difference being in the through thickness strain gradient, which is steeper in the miniature vessel.

3. Observation 2

Material tests in strain controlled fatigue have originally been performed in the uniaxial, i.e. axisymmetric mode. More recently other states of strain have earned interest using e.g. thin tube testing, which allows the application of any strain states without introduction of a strain gradient through loading by internal pressure (hoop strain), torque (shear) and axial strain applied to the tubular specimen. Data in Figure 2 show that when surface strains move towards the equibiaxial (surface strains $e2/e1 > -\nu$ and up to 1) forcing shear to dominate out of the thin tube wall, fatigue life decreses for the same equivalent value of alternating strain or the equivalent strain capacity tends to diminish for the same fatigue life.

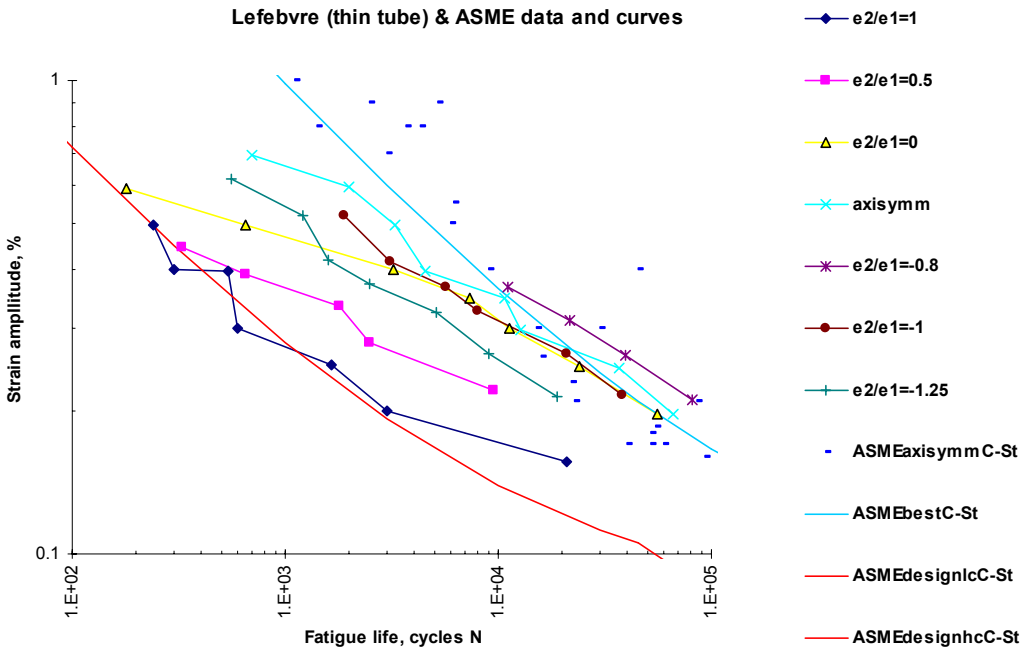

Figure 2. Strain-life data comparing thin tube data with uniaxial data.

Strain tolerance increases if the shear strain is forced to act along the thin tube wall - implying a deep-drawing effect moving towards pure in-plane shear of applied strain (surface strains e2/e1 < -ν down to pure in-plane shear =-1). These experiments clearly support the hypothesis that strain state moving towards equibiaxial (out of plane shear) is harmfull for component strength compared to tensile axisymmetric data. Plane strain with e2 = 0 and e3 < -ν would thus also be more damaging than uniaxial (or standard ASTM E606). Equibiaxial or plane strain would thus be "worst cases" for stress states with nonrotating principal stress axes.

4. Observation 3

Component geometries invariably introduce through thickness strain gradients at the surface of notches where local strains are largest. Figure 3 shows test results for fatigue specimens with various strain gradients at their notches. This was obtained using different notch tip radii and varying net thicknesses for the specimens loaded by bending.

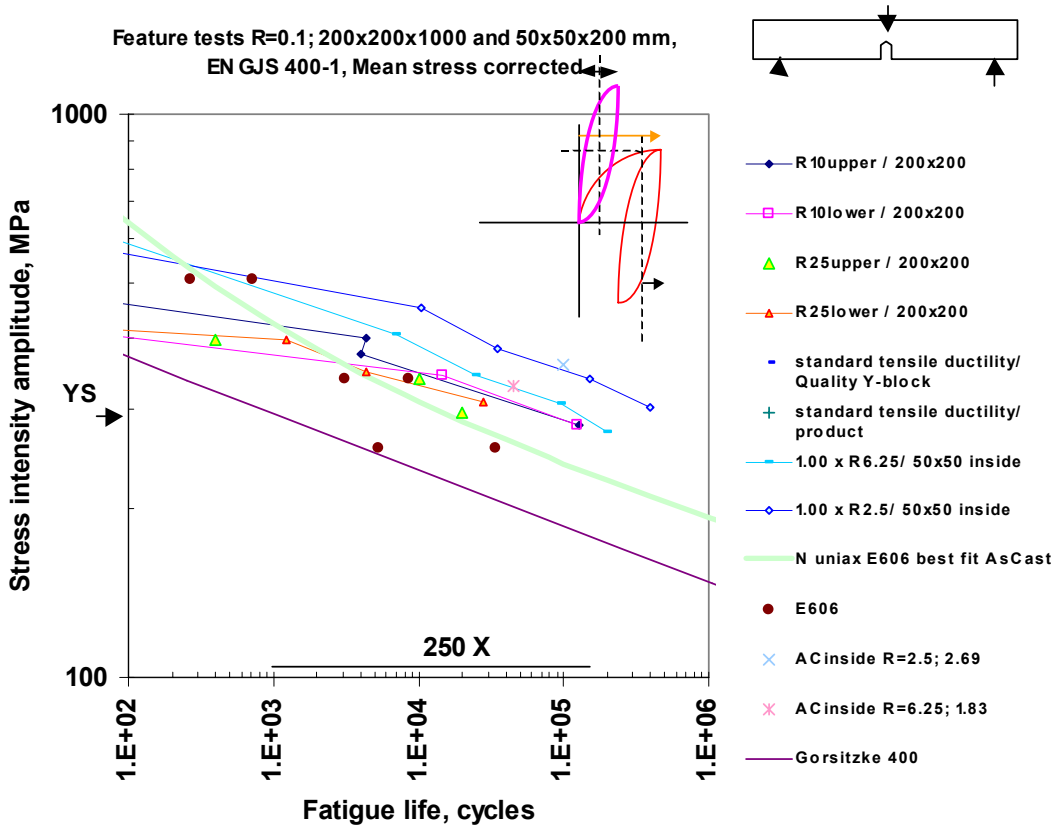

Figure 3. Fatigue data for notched specimens plotted using max local strain amplitude and comparison with uniaxial data. Fatigue life is directly proportional to the steepness of the local strain gradient with specimens with radius 2.5 mm and thickness 25 mm having the longest fatigue lives and radius 25 mm and thickness 100 mm having the shortest lives.

Notch tips are the most potential sites for fatigue damage. Such locations in loaded components are uniquely described by the largest local surface strain, and specimen fatigue lives in Figure 3 were plotted as a function of that strain fluctuation. Results show that fatigue strain capacity depends on the steepness of the gradient, the sharper the notch and the thinner the section, the longer is fatigue life for the same surface strain amplitude, Figure 3.

Notch surface strain may be measured or calculated. FEM calculation mostly gives conveniently the uniaxial equivalent plastic strain as output.

The strain gradient effect is geometric in nature and related to the dimension of expectable damage. Damage would be infinitesimally small for the local maximum strain which only acts at a point having no dimension. Local maximum strain is thus not a workable "unique" number for practical fatigue strength/damage characterisation.

5. A way out for designers

Component designers wish to come to as accurate estimates and use as simple material data as possible. It would be natural to suggest that ASTM E606 standard material data is that to be used for fatigue design. Observations 1, 2 and 3 presented above should thus be formulated in a way to allow direct quantification of their effect for the determination of the effect of strains calculated with e.g. FEM. To begin with we shall present a procedure that makes it possible to estimate the effects of the local strain gradient such that the gradient effect disappears to allow use of a single material strain-life curve. After that a way to care for material yielding is given when stress analysis is elastic.

Three correction factors for application to the maximum local strain ampltitude are needed to bring all different specimen geometries down to a common strain-life plot. The factors (all are < 1) are:

f_m = the microsupport factor emerging from the concept of explaining K_f that quantifies the fatigue limit of a notched specimen compared to its elastic stress concentration factor (for practical materials $K_f < K_t$ which translates to a larger local effective radius than the real acuity of the component).

$$f_m = (1+(K_t-1)/(\mathrm{sqrt}(1+3\rho/R)))/K_t \quad (1)$$

where for the rather coarse grained cast spheroidal iron $\rho = 2$ mm. In the equation the value 3 is variable according to material and strain state, but usually 3 applies over practical cases. Thus only ρ needs quantification. For steels it is on the order of tenths of a mm.

For the strain gradient effect the multiplication factor is

$$f_g = (f_{gp}+\Delta e_{peq}*E/2YS)/(1+\Delta e_{peq}*E/2YS) \quad (2)$$

for strains exceeding the fatigue limit, $f_{gp}= 0.5$ for plastic strain amplitudes $0.00015 < \Delta e_{peq}/2e_f < 0.03$. If strain is lower then $f_{gp} > 0.5$ and for larger strain $f_{gp} < 0.5$.

For the section thickness and loading boundary factor fe is additionally applied.

$$f_e = 1/\{1+[4/(3+e(1+P_m/P_b))]0.8\} \quad (3)$$

where e is the component net section thickness in millimetres and P_m and P_b are the linearised stress maxima across that section. They describe the global stress-strain gradient in the component and the loading boundary condition. For simplicity, shear across that section is ignored at this point

The above three factors considered bring test data into a band with minimum scatter of all data, Figure 4.

It may be observed that the minimum scatter band data do not end up on the E 606 curve. This is taken as an indication that the strain state of plane strain influences fatigue life as observation 2 would suggest.

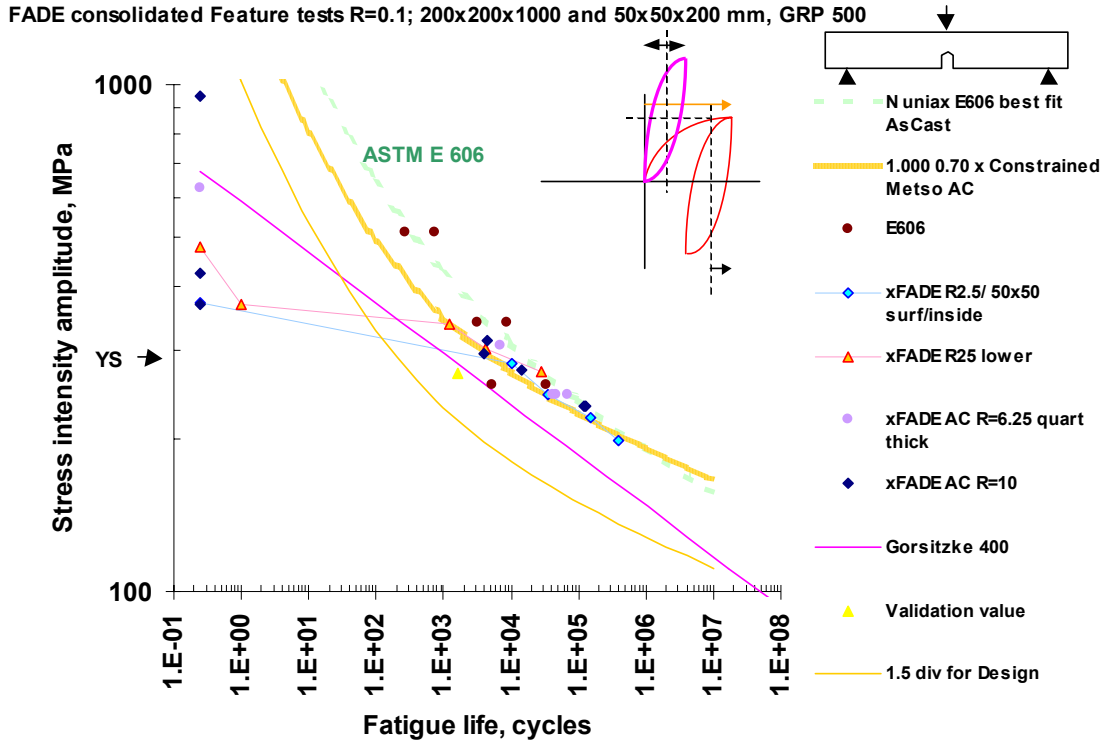

Figure 4. Raw strain-life data of figure 3 collapsed to minimum scatter using factors f_m, f_g and f_e.

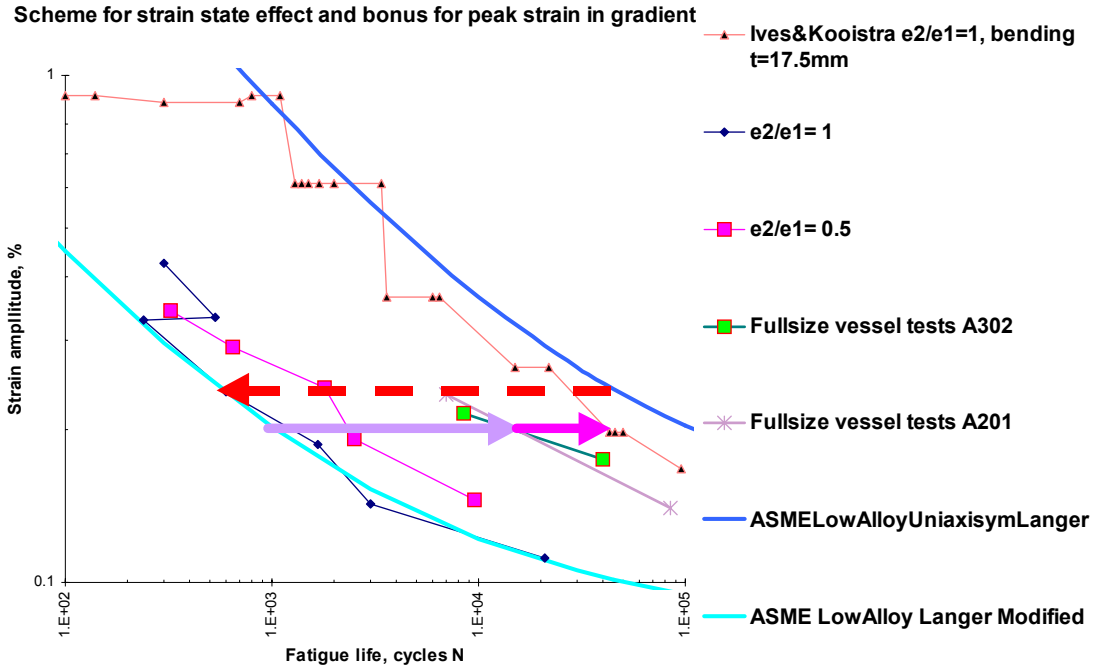

Figure 5. Schematic presentation of component behavioural features compared to uniaxial fatigue data that can fortuitiously bring component data close to uniaxial strain-life data.

In summary of component feature effects Figure 5 depicts the occasionally and potentially fortuitious proximity of biaxial bending data (bending introduces a through the thickness gradient) and uniaxial data and that the underlying systematical effects are more likely the "counteracting" effects of strain states and gradients. Strain states towards biaxial tension are "more damaging" than uniaxial and the local strain gradient seem to be apparenly "benign" effects when data is plotted using the unmodified "raw" value of local peak strain fluctuation.

6. Estimation of yielding for postprocessing of elastic stress analysis

FEM is not allways feasible using real material stress strain data because of cost reasons and therefore e.g. yielding effects need assessment methods for application to elastic strain analysis. It has been found that the strain energy density calculation favoured by e.g. Glinka [5] leads to a simple and straight forward formulation for the strain concentration factor K_e for strain hardening or even softening material assuming linear hardening:

$$K_e = 1/(1+S_m/S_E)(K_tP/S_E+S_m/(K_tP)) \quad (4)$$

here K_e is the yielding effect, i.e. local uniaxial equivalent strain $e_{local} = K_e*K_tP/E$, when stress analysis produces local max uniaxial equivalent stress as K_tP, P being the maximum principal linearised component of stresses in the actual component location. Comparison to strains calculated by FEM assuming an exponential hardening indicates that a good approximation for S_E is the material elastic limit estimated for e_p on the order or $0.5*10^{-4}$, assuming for the material e.g. the Ramberg-Osgood stress strain interdependence $e_{mat} = S_m/E + 2YS(e_p/0.002)^n$ (n = strain hardening exponent). Calculation of local strain range demands an iterative solution, because S_m and the calculated local strain range must match, i.e. $e_{mat} = e_{local}$. The factor 2 (in 2YS) is used because cyclic plastic strain range obeys the 2YS material curve (the hysteresis loop). Thus $S_E = 2YS*(10^{-4}/0.004)^n$.

Plasticity correction according to the above needs to be done as soon as $K_tP/2S_E$ exceeds 1, up to 1 shake-down will cause material to behave elastically. If the linearised section stress range $P = P_m+P_b$ stays below $2S_E$, only the above correction for local plasticity at the notch needs to be accounted for. If $P = P_m+P_b$ exceeds $2S_E$ (which is allowed only when ratchetting can be demonstrated not to occur) then section yielding occurs and some additional plasticity correction is needed.

7. Summary and conclusions

Calculated local maximum strain fluctuation in a component has been demonstrated not to predict component fatigue life from ASTM E606 standard strain-life fatigue data unless data is adjusted for strain state , local gradient and section thickness-loading boundary effects using related correction factors on maximum peak strain amplitude at notch as follows:

- strain state effect by adjustment of strain life curve, or appropriate test
- strain gradient effect by using factors f_m for Neuber microsupport and factor f_g for gradient damage accumulation effect
- far field stress gradient effect by using factor f_e for section thickness and degree of bending.

8. Acknowledgements

The findings reported in this paper were obtained in the EU-partly financed project Fatigue Design (BE 97-4658), with a consortium from Germany (2 partners), Great Britain (2 partners), Portugal (2 partners), Finland (3 partners) and Spain (1 partner). The considaretion of strain state effect, local strain corrections for gradient and section thickness were primarily contributed by VTT and the fatigue limit related correction by Siempelkamp, Germany.

References

1. Kooistra, L.F., Lange, E.A. & Pickett, A.G. Full-Size Pressure Vessel Testing and its Application to Design. In: "Pressure Vessels and Piping: Design and Analysis, A Decade of Progress", Vol. One, ASME, 1972, pp. 121–130.

2. Criteria of the ASME Boiler and Pressure Vessel Code for Design by Analysis in Sections III and VIII Division 2. In "Pressure Vessels and Piping: Design and Analysis, A Decade of Progress", Vol. One ASME 1972, pp. 61–83.

3. Burns, D.J., Karl, E. & Liljeblad, J. 1985. Methods for Predicting the Fatigue Performance of Vessels Intended for Operation in the Pressure Range 70 to 1400 MPa. In: Proceedings of the 1985 Pressure Vessels and Piping Conference, PVP-Vol. 98-8, American Society of Mechanical Engineers (ASME). Pp. 213–223.

4. Lefebvre, D.F. 1989. Hydrostatic Pressure Effect on Life Prediction in Biaxial Low-Cycle Fatigue, *Biaxial and Multiaxial Fatigue*, EGF 3 (Edited by M.W. Brown & K.J. Miller), 1989, Mechanical Engineering Publications, London. Pp. 511–533.

5. Glinka, G. 1988. Report on Elasto-Plastic Strain and Stress Calculation Methods for Notched Components, December 1998. University College London. 30 p. + figures.

6. Ives, K.D., Kooistra, L.F. & Tucker, J.T. Euibiaxial Low. Cycle fatigue properties of typical pressure vessel steels. In: "Pressure Vessels and Piping: Design and Analysis, A Decade of Progress", Vol. One, ASME, 1972. Pp 199–208.

7. Unpublished data from the Fatigue Design Project BE 974658.

Constitutive modeling of hydrogen cracking

A. Laukkanen & P. Nevasmaa
VTT Industrial Systems
Espoo, Finland

Abstract

Hydrogen cracking in multiple-pass weld metals occurs when accumulating hydrogen concentration exceeds a certain critical level. This accumulation via diffusion is a thermally activated, continuing process taking place throughout welding, driven also by the emerging residual stresses. The results of diffusion analyses are difficult to quantify in terms of cracking risk since no reliable coupling between the local hydrogen concentration and material damage has been available.

Numerical analyses enabling solution of hydrogen diffusion and local concentration in welds having complex geometries are performed. A predefined temperature solution is used as an input to a finite element transient diffusion analysis. In the mass diffusion problem, a three-dimensional residual stress field is input to describe the pressure stress dependency of the transient diffusion process. The resulting concentration profiles are considered by use of a novel damage mechanics material model in a finite element analysis (FEA) with a cohesive zone modeling framework, which links the local concentration to a continuum mechanics damage description. By use of the damage mechanics constitutive material model, conditions for hydrogen cracking are evaluated for a multipass butt weld. The results of the mass diffusion analysis are in agreement with experimental findings and measured hydrogen concentrations, while the damage mechanics analysis is illustrated to provide means for evaluating the rupture process by use of continuum mechanics.

1. Introduction

Weld hydrogen cold cracking is attributable to three main factors: crack-sensitive microstructure, sufficiently high hydrogen concentration in terms of weld diffusible hydrogen and elevated stress caused by high structural restraint. Cracking is of delayed nature: crack initiation and especially propagation may take several hours, or sometimes even days or weeks, after welding has been completed. The risk of cracking becomes apparent and increases as strength of

parent steel and/or weld metal increases, and when welding thick plate sections that often employ multipass welding techniques [1, 2]. Generally, higher strength and greater contents of alloying elements tend to favor cracking in weld metal (WM), at the expense of heat-affected zone (HAZ) cracking [1, 2].

Fabricators are still experiencing cases of hydrogen cold cracking in welding of high strength steels and in the weld metal. Small hydrogen cracks easily escape detection by normal non-destructive testing (NDT) methods. In the case of extra-high strength steels and weld metals, microcracks of the size of a few tenths of a mm to a few mm:s may already become critical from the standpoint of structural integrity of a component. Hydrogen cracks in weldments can also act as potential nuclei for later failures in manufacturing or service, e.g. by lamellar tearing, brittle fracture or fatigue. The most challenging problem from a practical point of view is to predict when WM cracking might occur and to define quantitatively the minimum precautions to avoid it. Currently, the few calculation formulae [3, 4, 5] that do exist for the cracking risk assessment for multipass welds can give greatly varying predictions, the differences sometimes becoming confusingly large.

2. Hydrogen cracking in multipass weld metals

Hydrogen cracking in weld metal occurs either transverse or longitudinal to the weld direction, the orientation of cracks depending on the presence of gaps and notches and the direction of the controlling stress [4]. Consideration needs to be given, whenever making relatively thick restrained multipass butt welds with the yield strength exceeding 550 MPa.

In single-pass welds, the root gap or root bevel/face preparation provides a stress concentration with respect to stresses transverse to the weld. This leads to longitudinal hydrogen cracks in the weld metal, which is often the predominant form in high-strength pipelines where cracks can be encountered in single-pass welds, as well as in the root run of multipass welds. In the case of high-strength multipass welds and relatively thick restrained plates, hydrogen cracking will generally occur in the transverse direction, either normal to the weld surface or at an angle orientation of about 45° in the weld thickness direction. In this chevron cracking, high longitudinal tensile stress causes slip bands to form at 45° angle and the concentration of plastic strain in the intergranular proeutectoid grain-boundary ferrite coupled with the transport of hydrogen into these regions leads to crack initiation.

According to microplasticity theory, hydrogen in the lattice ahead of the crack tip assists and promotes whatever microscopic deformation and crack growth process the particular microstructure will allow. Cracking can occur by various modes, i.e. cleavage, quasi-cleavage, microvoid coalescence or in an intergranular

manner along prior-austenite grain boundaries, depending on weld microstructure, crack tip stress intensity level and concentration of hydrogen. The crack propagation phase usually includes both transgranular and intergranular fracture morphologies [4]. With increasing stress intensity, a transition from intergranular to cleavage/quasi-cleavage to microvoid coalescence occurs in the early stages of fracture, i.e. a transition from failure mechanisms where negligible plasticity is involved to failure mechanisms associated with high levels of plastic deformation. The amount of crystalline area resembling brittle cleavage fracture has been recognised to increase with weld metal alloying and hence strength. Findings of hydrogen cracks in the 800 MPa tensile strength weld metals have shown that cracking had occurred in regions of intense plastic strain in isolated locations of the weld and then linked up with existing cracks. Cracking was observed along slip bands parallel to laths of martensite and also partly along slip bands across laths. The fracture surface was described as quasi-cleavage mode with many tiny shallow dimples [8].

The initiation and propagation events of hydrogen cracking can be elucidated via observations on microscale processes that emerge at the crack tip and fracture process zone under the presence of hydrogen. Focusing on surface effects and hydrogen-dislocation interactions, three mechanisms are defined: hydrogen enhanced decohesion (HEDE), hydrogen enhanced localised plasticity (HELP) and adsorption induced dislocation emission (AIDE). All these processes involve a complex combination of a number of events: hydrogen dissosiation, adsorption and transport to the crack tip, dislocation emission and egress, hydrogen diffusion and movement of vacancies, transport of hydrogen to dislocations, hydrogen effects on dislocation mobility and hydrogen trapping at particle-matrix interfaces. Usually, AIDE and HEDE mechanisms operate at lower temperatures, whereas HELP occurs at higher temperatures.

Effects of residual stress on the cracking risk of multipass weld metals has traditionally been encountered using comparatively "global", causal parameters, i.e. critical "threshold" level of stress and applying regression analyses, instead of sophisticated local approach-based numerical modelling capable of determining local stresses and distributions at and near a crack tip, providing means in theory even capable of predicting the initial crack nucleation. Whilst the principal causal factors contributing to hydrogen cracking in multipass weld metals are comparatively well understood, investigation of intrinsict factors as it comes to local conditions at the crack tip under the presence of hydrogen and stress have received much less attention. The assessment of the hydrogen - crack tip interactions applying local approach treatise of damage-based parameters according to continuum based mechanics, coupled with local stresses, actual hydrogen concentration, microstructure and actual failure mechanism, are yet relatively poorly understood, but provide the latitude for performance of analyses utilizing the micromechanical descriptions of hydrogen cracking.

3. Hydrogen diffusion analyses

FEAs were performed to determine the hydrogen concentration as a function of time during welding and also in conjunction with local approach treatment of the concentration results. The diffusion problem is governed by the law of mass conservation, i.e.

$$\int_{\Omega} \dot{c} d\Omega + \int_{\partial\Omega} \underline{n} \cdot \underline{J}\, d\partial\Omega = 0\,, \tag{1}$$

where Ω is any volume with an outward normal $\underline{n}$ to $\partial\Omega$, $\dot{c}$ is the rate of concentration and $\underline{J}$ is the concentration flux. The applied constitutive equation is given by

$$J = -sD\left\{\frac{\partial}{\partial \underline{x}}\left(\frac{c}{s}\right) + \kappa_s \frac{\partial}{\partial \underline{x}}\left(\ln\left[T - T^K\right]\right) + \kappa_p \frac{\partial p}{\partial \underline{x}}\right\}, \tag{2}$$

where s is the solubility, D the diffusivity, κ_s the Soret factor, T the temperature, T^K the temperature scale reference temperature, κ_p the pressure stress factor and $p = -1/3 \cdot \sigma_{ij}\delta_{ij}$, where σ_{ij} is the Cauchy stress tensor and δ_{ij} the Kronecker's delta operator. The FE diffusion analyses were performed for a test specimen presented in Figure 1. The transient diffusion history was solved over welding of the final pass utilizing the respective temperature and stress field conditions. The concentration distributions were extracted and input to a local approach analysis.

4. Local approach analyses

Local approach analyses applying interface cohesive elements were performed using the WARP3D research code [7] and a constitutive damage mechanics model outlined below. The analyses were performed for 10-10-55 mm^3 size single-edge notched bend fracture mechanics specimens, i.e. essentially the diffusion analysis results were extracted from the domains considered succeptible for hydrogen cracking and input to the local approach analysis. This permitted one to evaluate the associated decrease of fracture toughness, which in the current investigation focuses on crack initiation.

The foundation of the material model is a notion that the relationship between critical hydrogen concentration and critical applied stress has been noted to be of the form

$$\sigma_{critical} = A - B \cdot HV_{\max} - C \cdot \log\left(c^H\right), \tag{3}$$

where A, B, C are constants, $HV_{\max}$ is the maximum hardness and c^H is a parameter identified with hydrogen concentration. In a cohesive zone framework the cohesive energy of a unit cell can be identified with

$$\Gamma = \int_0^\infty t d\delta, \tag{4}$$

where t is the cohesive traction and δ the associated displacement. Using an exponential cohesive law to define the traction one typically has

$$t = \frac{\partial \varphi}{\partial \delta} = \ln(e)\sigma^c \frac{\delta}{\delta^c} \exp\left(-\frac{\delta}{\delta^c}\right), \tag{5}$$

where the superscript c refers to characteristic values. By taking the variation of Equation with respect to time and postulating that the relationship between the cohesive stress and critical stress for hydrogen cracking is retained, a time and concentration dependent cohesive law results:

$$t = \frac{\partial \varphi}{\partial \delta} = \ln(e)\left\{\sigma^c\big|_{t=0} - \int_0^t \frac{F}{\ln(10)} \frac{\dot{c}}{c} dt\right\} \frac{\delta}{\delta^c} \exp\left(-\frac{\delta}{\delta^c}\right), \tag{6}$$

where F can be identified from Equation and results presented in [8]. This expression was applied to simulate effects to initiation fracture toughness as implied by the transient hydrogen analysis. The principle is presented in Figure 2 to illustrate the dependency of cohesive energy on the concentration parameter.

5. Results and discussion

The results for the diffusion analysis at different times between transient and steady-state responses of the analysis from a section near the beginning of welding of the final pass are presented in Figure 3. The Figure 3c corresponds in practise to steady-state conditions while Figure 3a is extracted from a period of time where the heat source has just passed through the section. Two distinct behavior patterns are noted. First, the thermal field drives the hydrogen to form a concentration peak within approximately 45° axis from the corner of the displayed section, where the corner corresponds to the final deposited weld metal. Second, it is noted that a local maximum concentration appears near the weld metal to parent metal fusion line, whilst near the parent material hydrogen escape from the weld to the parent metal is observed. The first peak is attributed to the temperature field, the second having to do with the larger transverse residual stresses near the parent material.

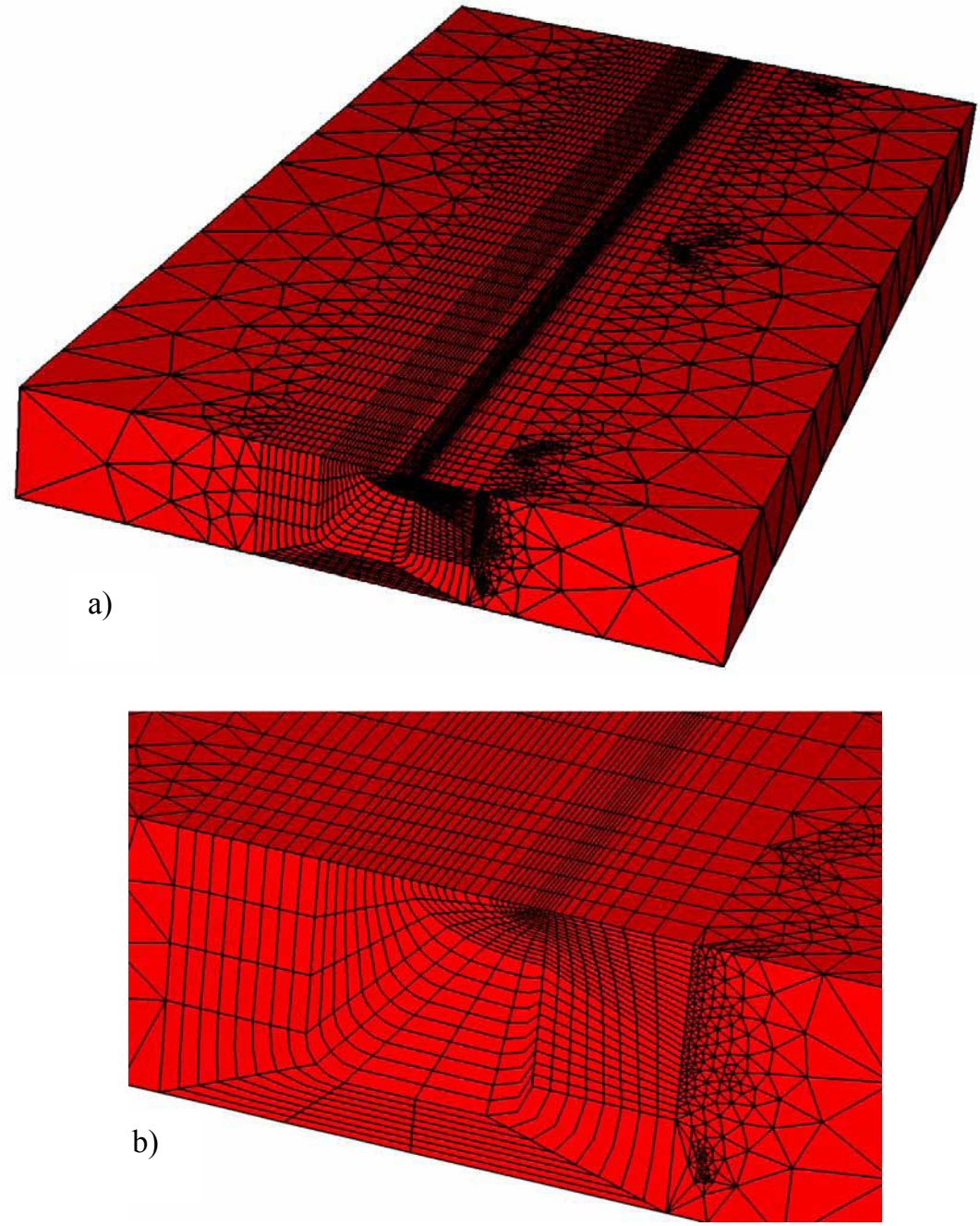

Figure. 1. Finite element mesh for the transient diffusion problem. Weld located at center of the model. a) global mesh of the specimen and b) detail of mesh design where the final pass region is modeled using a denser mesh.

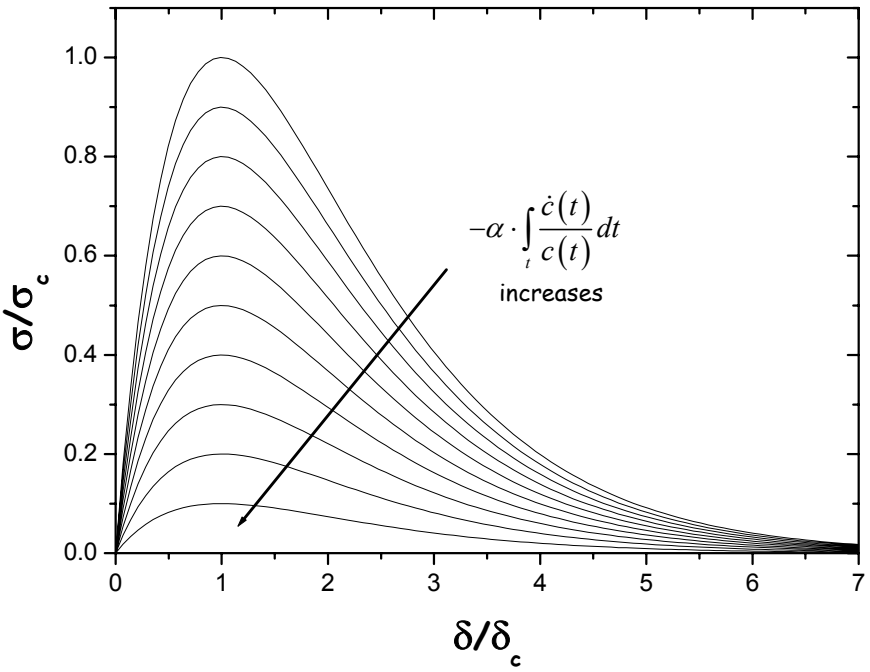

Figure 2. Dependency of normalized cohesive traction on the concentration dependent parameter as a function of normalized cohesive displacement.

The results of the cohesive zone analyses in terms of crack initiation fracture toughness are presented in Figure 4. The used fracture parameter is the J-integral. The results display that with the current best estimate values for the cohesive parameters, $\sigma_c/\sigma_0 = 1.3$, where σ_0 is the parent metal yield strength, under steady-state conditions fracture toughness decreases of the order of 50% are expected, which is in harmony with expectations from experimental basis. The transient diffusion history effects to the Master Curve, as defined in standard ASTM E1921, are presented in Figure 5 for the cohesive zone simulation having the greatest cohesive stress. The steady state results for all analyzed cases are given in Figure 6. The results illustrate that once a cohesive zone model is calibrated for a certain material, the described analysis enables one to attain quantified values of fracture toughness and risk of hydrogen cracking.

a)

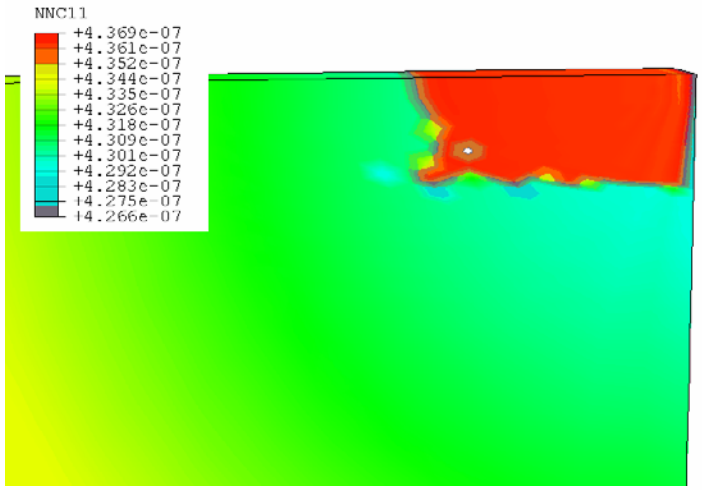

b)

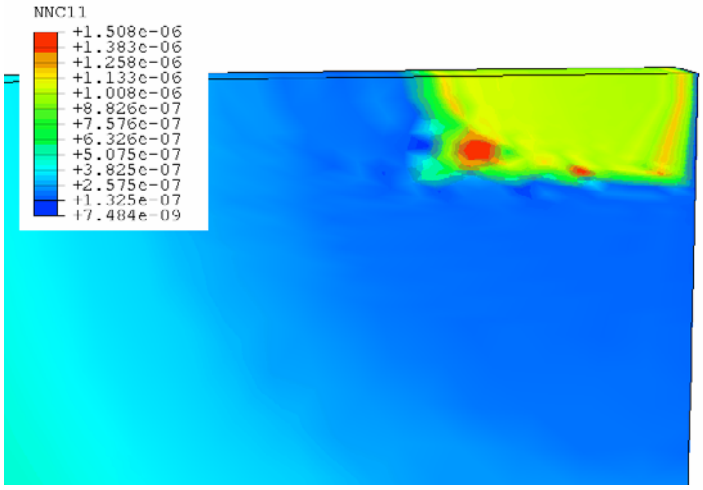

c)

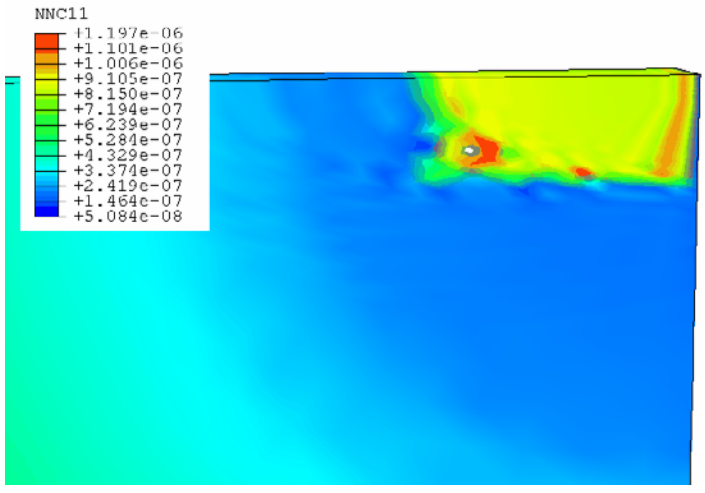

Figure 3. Contours of normalized concentration, c/s, at a) beginning of transient loading, b) during stabilization of the transient response and c) near steady-state.

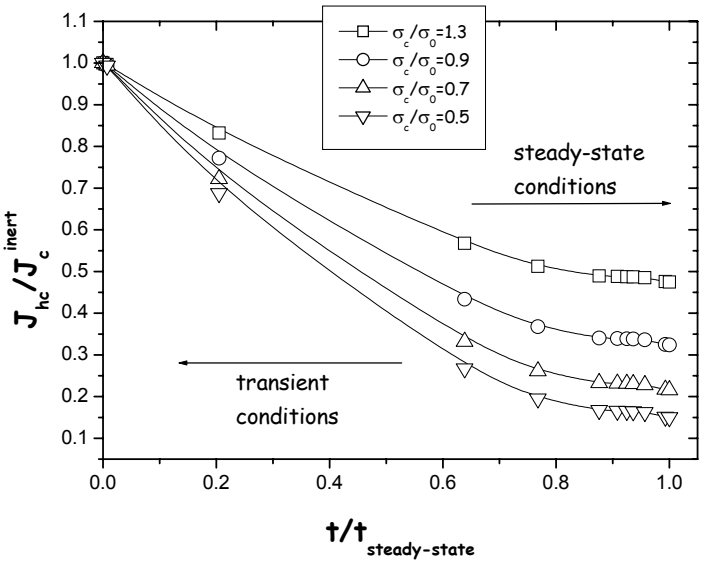

Figure 4. Ratio of initiation fracture toughness under hydrogen loading to that of inert conditions with different values of the cohesive strength to parent metal yield strength.

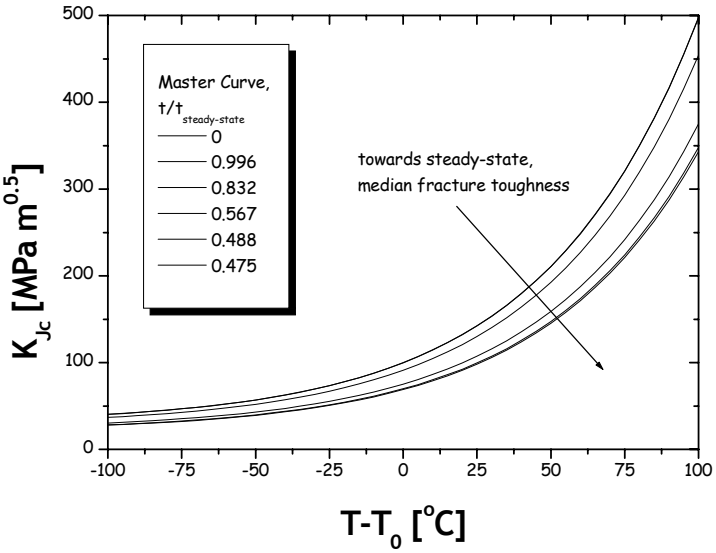

Figure 5. The fracture toughness Master Curve representation for $\sigma_c/\sigma_0 = 1.3$ *as a function of temperature minus the reference temperature, T_0, for different stages of the welding process.*

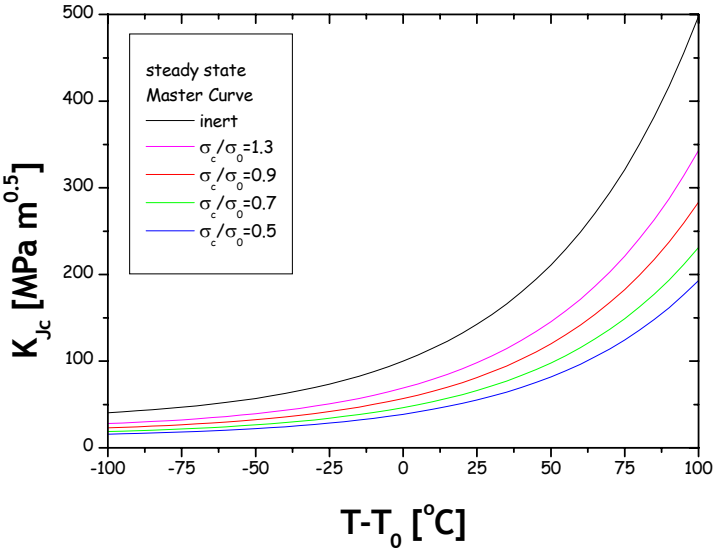

Figure 6. The fracture toughness Master Curves for different cohesive zone parameter values at steady state conditions.

6. Summary and conclusions

Numerical analyses were performed to investigate the mass diffusion and failure processes in a multipass weldment. The results of the work can be concluded as follows:

- Two types of hydrogen concentration maxima were observed, one focusing near the weld metal to parent metal interface and other to the furthermost point of the final pass. The latter was identified to be related to characteristics of the temperature field and extraction of hydrogen from the final weld pool, while the foremost to the residual stress gradient near the specimen surface.
- The levels of residual stresses were in agreement with experimental results referenced in [8], whilst the significance of transverse residual stress gradient near specimen surface is in agreement with findings implying low risk of hydrogen cracking in thin plates, along with more favorable temperature histories due to primarily two-dimensional thermal conduction.
- The hydrogen concentration results were in agreement with results reported elsewhere (see e.g. [1,9]), i.e. the peak values ranged from 1.5–2.5 times the nominal initial hydrogen concentration.
- The cohesive zone constitutive model with parameters identified from experimental results was able to produce decreases of fracture toughness that can be considered reasonable when assessing the effect of locally concentrated hydrogen to macroscopic fracture properties, the mechanism being that of ductile void growth and coalescence. The results were connected to the Master Curve fracture toughness representation.

References

[1] Nevasmaa, P. & Laukkanen, A. ’Procedure for the prevention of hydrogen cracking in multipass weld metal with emphasis on the assessment of cracking risk in 2.25Cr-1Mo-0.25V-TiB (T24) boiler steel’. IIW-Doc IX-2131-04. Japan, 2004. 38 p.

[2] Coe, F.R. ‘Welding steels without hydrogen cracking’. The Welding Institute, Cambridge, United Kingdom, 1973. 68 p.

[3] Okuda, N., Ogata, Y., Nishikawa, Y., Aoki, T., Goto, A. & Abe, T. ‘Hydrogen-induced cracking susceptibility in high-strength weld metal’. Welding Journal 66 (1987) May, pp. 141–146.

[4] Suzuki, H. & Yurioka, N. ‘Prevention against cold cracking in welding steels’. Australian Welding Journal 27 (1982) 1, Autumn 1982, pp. 9–27.

[5] Thier, H., Eisenbeis, C. & Winkler, R. ‘Untersuchungen zur Absicherung der Berechnung der Mindestvor- wärmtemperatur beim Mehrlagen-schweissen’. Schweissen und Schneiden 49 (1997) 7, pp. 426–430.

[6] Pargeter, R.J. ‘Effects of arc energy, plate thickness and preheat on C-Mn steel weld metal hydrogen cracking’. TWI Research Report (CRP) No. 461/1992. The Welding Institute, UK, November 1992.

[7] Warp3d 13.9, users manual.

[8] Nevasmaa, P. 'Predictive model for prevention of weld metal hydrogen cracking in high strength multipass welds'. Acta Universitatis Ouluensis: C Technica 191. University of Oulu: Department of Mechanical Engineering, Oulu 2003. 212 p.

[9] Yurioka, N. et al. 'An analysis of microstructure, strain and stress on the hydrogen accumulation in the weld heat-affected zone'. IIW-Doc IX-1161-80. Japan, 1980. 18 p.

Simulation of development of creep damage in welds of X 20 CrMoV 12 1 by use of the finite element method

Jan Storesund, Det Norske Veritas AB,
Weilin Zang, Det Norske Veritas AB, www.dnv.com &
Kjeld Borggreen, SydTek AB, www.sydtek.se, Sweden

Abstract

Welds are frequently subjected to creep damage in high temperature operation. The formation of creep damage in the welds is influenced by a number of parameters. In the present work the influence of (i) the creep rate in the heat affected zone, (ii) the material constant α, which is related to the multiaxial rupture criterion, and (iii) axial system stresses on creep life has been studied by finite element simulations of a circumferential X 20 CrMoV 12 1 steel pipe weld. By use of a modified Kachanov-Rabotnov constitutive equation implemented in the ABAQUS code the damage and life time are predicted for a number of cases. The results show, for example, that an increase of (i) the constant α, (ii) axial stress and (iii) creep rate in the heat affected zone all result in a reduction of creep life. Especially a combination of two of these factors has a large effect in the life time reduction. The variation of the cross section distribution of damage is also demonstrated in a couple of cases.

1. Introduction

Pipe lines and other constructions operating in the creep range will sooner or later develop creep damage that in the worst case may lead to rupture. The welded joints constitute "components" that in most cases show relatively early damage, often before the design life time has been reached. Examples of experiences of early creep damage development are given in [1]–[7] where also the reasons to the damages are discussed.

Depending on the extent and the severity of the creep damage, that has been mapped by replica testing, actions are recommended e.g. according to Nordtest [8]. The recommendations are to the greatest part based on the experience of low alloy steels. For X 20 CrMoV 12 1, the experience of components that have received higher damage ratings, is still scarce. Nevertheless, this material is investigated and assessed in the same way as the low alloy steels.

As a complement to experience of plant operation and accelerated creep testing simulations by use of the finite element method (FEM) successfully have been carried out on low alloy steels to improve the understanding of the creep behaviour that, for example in a welded joint is extremely complicated. A number of the parameters that control the creep process can be studied clearest in a FE-analysis.

In the present work some of the parameters that can be estimated to have a large influence on the creep life of welded joints of X 20 CrMoV 12 1 have been studied.

2. Aim of the study

As mentioned above the life time of a welded joint depends on a number of parameters. These may vary widely and lead to reduction of the creep life. This influence may in some cases be shown clearest by use of numerical simulation.

In the present study the creep process in a welded joint is simulated in order to study the effect of (i) the material properties in the weld metal and the heat affected zone (HAZ) as well as (ii) the load, on creep life. In addition a parametric study of the material constant that controls the rupture criterion is performed. This constant can be determined experimentally but data is scarce, particularly for the X 20 CrMoV 12 steel: no data at all was found in a literature survey dealing with creep in this steel [9].

The creep properties of the HAZ are varied widely in the simulations as creep testing of the HAZ indicates that large variations may occur [10]–[12]. Concerning the load a plain service internal pressure in a girth pipe weld and also two levels of system stresses added to the hoop have been studied.

The results aim to increase the understanding of the creep damage development in welds of the X 20 -steel and in which degree the mentioned parameters influences the creep life. An important possibility with the simulations is to be able to control the welding parameters such as the damage first will appear at the outer surface of the pipe, making Non-Destructive Examination methods of the surface most useful.

3. Theoretical background

In design of pressure vessels with respect to creep a strongly simplified methodology is used (Design By Formulae – DBF) as the material properties and 3-D stress conditions lead to extremely complicated relationships. This involves

that the results of the design work are not so precise and a large effort must be put on the follow – up of the creep damage development in operation, not least in welds. With the development of codes and powerful computers is it now possible to study complicated creep processes. This gives opportunities to by calculations (Design By Analysis – DBA) better predict the life time of the structure etc. The theoretical model used in the present study is given as follows:

A typical creep curve for a steel of current type is shown in Figure 1. Characteristic values for the material constitutes of minimum creep rate $\dot{\varepsilon}_{\min}$ and creep rupture life t_r as well as the creep rupture elongation ε_f. Available data for the designer is given by the design values for 10 000 and 100 000 h life time and the stress which gives the creep elongation 1% after 10 000 and 100 000 h. The meaning of these values is illustrated in Figure 1. To describe the entire creep process it is required to take to account the "decrease in stiffness" that results in the accelerating creep rate in the tertiary stage of the creep life. A simple model for uni-axial creep is according to Kachanov – Rabotnov:

$$\dot{\varepsilon} = \frac{B\sigma^n}{(1-\omega)^\nu} \tag{1}$$

$$\dot{\omega} = \frac{B\sigma^\chi}{(1-\omega)^\phi} \tag{2}$$

The rupture takes place when ω approaches the value 1.

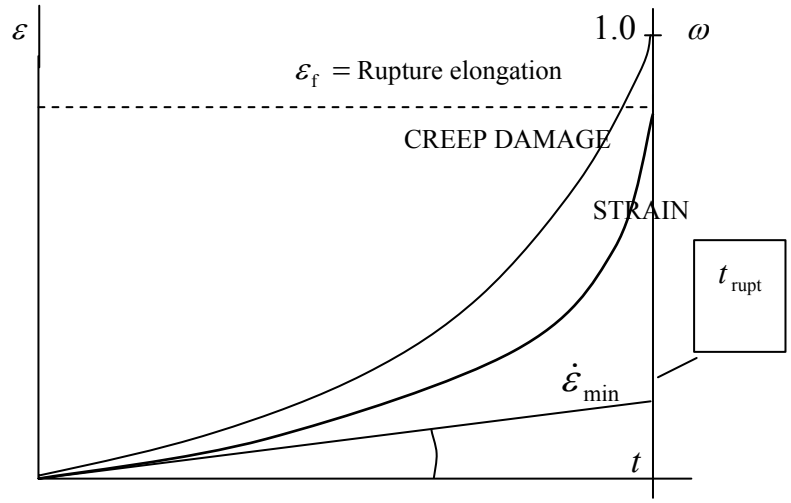

Figure 1. Typical result of long term creep test on metallic materials.

The model is adapted to the uni-axial creep curve and gives possibility to carefully calculate the life time of the material. To calculate the life time in 3-D structures a more general description of the material is needed.

A modified Kachanov-Rabotnov constitutive equation which accounts for inhomogenity in creep damage is used [13, 14]. Neglecting plasticity and primary creep the total strain rate is

$$\frac{d\varepsilon_{ij}^{tot}}{dt} = \frac{d\varepsilon_{ij}^{el}}{dt} + \frac{d\varepsilon_{ij}^{cr}}{dt}, \tag{3}$$

where

$$\frac{d\varepsilon_{ij}^{el}}{dt} = \frac{1+\nu}{E}\left[\left(\frac{d\sigma_{ij}}{dt}\right) - \frac{\nu}{1+\nu}\left(\frac{d\sigma_{kk}}{dt}\right)\delta_{ij}\right], \tag{4}$$

$$\frac{d\varepsilon_{ij}^{cr}}{dt} = \frac{3}{2}B\sigma_e^{n-1}s_{ij}\left[(1-\rho)+\rho(1-D)^{-n}\right], \tag{5}$$

and

$$\frac{dD}{dt} = g\frac{A}{\phi+1}\frac{\left[\alpha\sigma_I + (1-\alpha)\sigma_e\right]^{\upsilon}}{(1-D)^{\phi}}, \tag{6}$$

$$D_{crit} = 1-(1-g)^{1/(\phi+1)}. \tag{7}$$

In the equations given above ε_{ij}^{tot}, ε_{ij}^{el}, ε_{ij}^{cr}, σ_{ij} and s_{ij} are the total strain, elastic strain, creep strain, stress and stress deviator tensor, respectively. σ_I and σ_e are the maximum principal stress and von Mises stress, E and ν the modulus of elasticity and Poisson's ratio, D and D_{crit} the damage variable and critical damage. The material creep life is assumed to be fully utilised when D/D_{crit} reaches the value one. α is the material constant relating to the multiaxial rupture criterion which ranges from zero to unity, B, n, A and υ are the material constants relating to the minimum creep strain rate and rupture behaviour, g, ϕ and ρ the constants accounting for the inhomogenity of the damage where ρ represents the volumetric ratio of the damaged phase.

4. Material properties and data

Creep data of Bürgel et al. [15] on parent metal and weld metal of X 20 CrMoV 12 1 have been used for the simulations. The creep properties and material constants in Table 1 were determined by analysing creep curves from testing at 160 MPa and 550°C.

Table 1. Creep properties and material constants of the analysed material.

	Parent metal	**Weld metal**	**HAZ**
B **(MPa^{-1}h^{-1})**	2.8E-17	5.266E-16/ f_w	2.8E-17*f
n	4,866	4	4,866
A **(MPa^{-m}h^{-1})**	2.06583E-19	2.9883E-20/ f_w	2.06583E-19*f
m	6.5	6.8	6.5
g	0.965	0.97	0.965
ϕ	1.561	1.0253	1.561
ρ	0.13	0.2	0.13
α	*variable*	*variable*	*variable*
E **(GPa)**	160.0	160.0	160.0
ν	0.3	0.3	0.3

In Figures 2 and 3 the agreement between the experimental creep data and the curve fitting at 160 MPa and 100 MPa by use of data (Table 1) is shown for parent metal and weld metal, respectively (when $f_w = 1$).

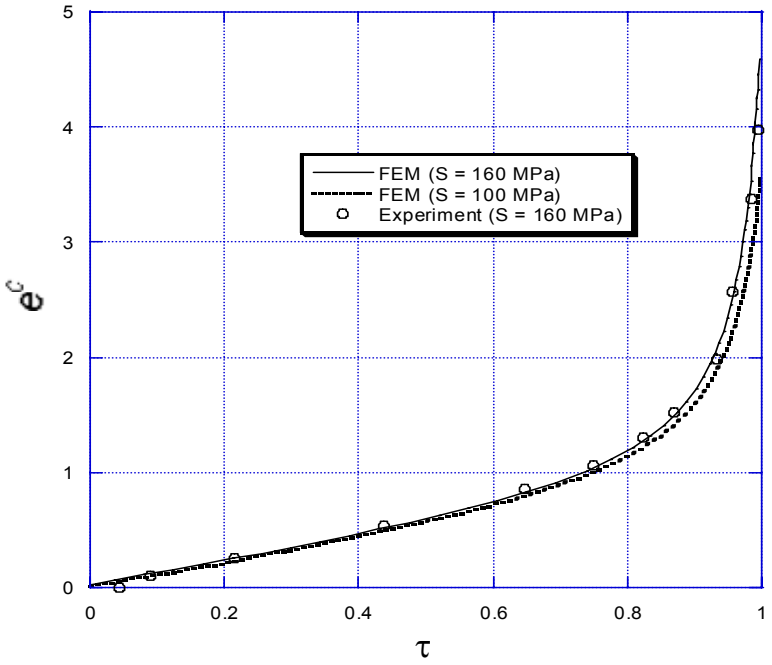

Figure 2. Creep behaviour of the parent metal under the uni-axial loading.

The parameters τ and e^c in Figures 2 and 3 are defined as,

$$\begin{cases} \tau = t / t_f & (8) \\ e^c = \dfrac{\varepsilon^{cr}}{\left[d\left(\varepsilon^{cr}\right)/dt\right]_{\min} \cdot t_f} & (9) \end{cases}$$

where t_f is the time to rupture.

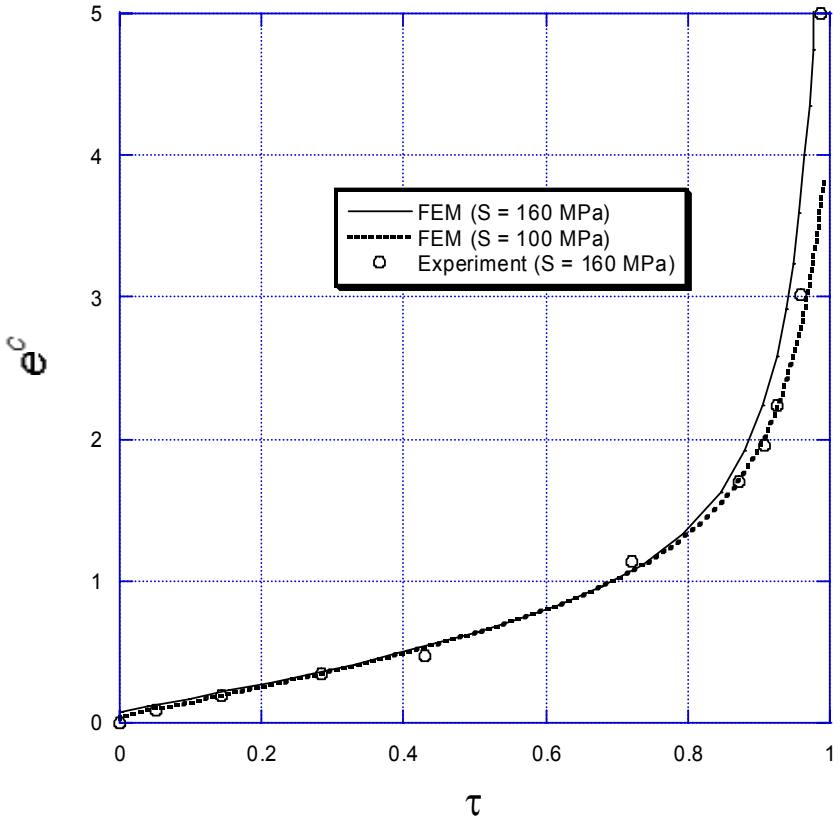

Figure 3. Creep behaviour of the weld metal under the uni-axial loading.

4.1 Creep properties in the HAZ

As the HAZ in common is too small for creep testing, it is possible to conduct heat treatments of a larger amount of parent metal resulting in similar micro-structures to the different parts of the heat affected zone as a result of the weld thermal cycle. The heat treated material is then creep tested. Results from such simulated HAZ have been used as a basis for the FE-analyses of the HAZ.

Few results of simulated HAZ creep test results were found for the X 20 steel [12] but some more could be found for the related steel P91 [10, 11]. These results indicate creep strengths in the simulated HAZs that are between 10–60 times lower than the ones in the parent metal.

In the present study two sets of HAZ creep properties were chosen:

1. A minimum creep rate 10 times faster than the parent metal with a corresponding lower creep strength, $f = 10$ in Table 1.
2. A minimum creep rate 100 times faster than the parent metal with a corresponding lower creep strength, $f = 100$ in Table 1.

A model of equal creep behaviour in the entire HAZ is a simplification of the reality. HAZ consists basically of three parts: a coarse grained, a fine grained and an intercritical part. The creep properties in these parts vary considerably. Coarse grained microstructure has in general essentially higher creep strength and lower creep ductility than a fine grained one. The creep strength in the intercritical microstructure is even lower than in the fine grained. The model of one HAZ property is most relevant in cases where the coarse grained HAZ to large amounts has been refined during multi-pass welding. In other cases it may be possible keep the model of one HAZ property if the coarse HAZ is counted into the weld metal which can have quite similar creep properties.

4.2 System stresses

The influence of system stresses on creep life is studied by introduction of an extra axial load. In reality system stresses also may consist of bending stresses but this is too demanding to calculate. Two cases of extra axial stresses have been studied:

i) 1.25 x axial stress at internal pressure
ii) 1.5 x axial stress at internal pressure.

As the axial stress is about half the hoop stress the stress enhancements are relatively small: axial stress components of 0.625 and 0.75 x the hoop stress, respectively.

4.3 Multiaxiality

In the equations above the material constant α can be found. It takes a value between 0 and 1 and determine the fraction of von Mises stress and maximum principal stress in the rupture criterion. With a large and a small α, the rupture criterion is dominated by the maximum principal and the von Mises stress, respectively. Some experimental values of α in low alloy steels can be found in the literature [16, 17]. In earlier work, e.g. [18, 19], the value 0.42 was used. However, α may vary between different materials, batches of the same material, weld constituents as well as degree of service exposure [17].

5. Geometry of the finite element model

The geometry of the FE model in a through thickness cross section of a girth pipe weld in is shown in Figure 4. The sizes of the pipe and the weld correspond to actual dimensions of a retired live steam line pipe weld of the current steel. It can be seen in the figure that the width of the HAZ is 2.5 mm which correspond to measures on metallographically prepared samples of the retired weld.

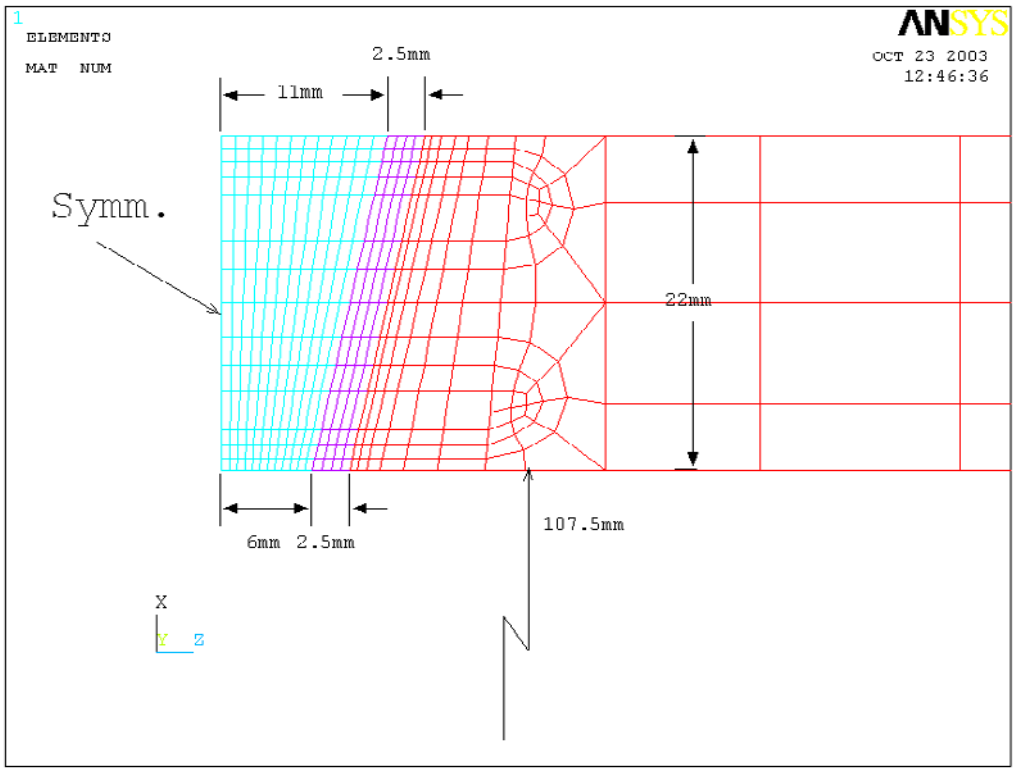

Figure 4. Geometry of the FE model.

The simulations were carried out at 550°C with the following loads:

Internal pressure, $P_0 =$ 22 MPa

Axial force, $F_z = f_{zz} * P_0 r_{in}^2 \pi$ (10)

and f_{zz} is an axial load parameter.

6. Results of the simulations

The different load cases are summarised in Table 2 where also the resulting times to rupture are given.

Table 2. Simulated cases and the resulting rupture times.

Case	f (HAZ)	f_w	f_{zz}	α	t_f (hours)
1	10	1	1.00	0.4	315 260
2	10	1	1.25	0.4	290 100
3	10	1	1.50	0.4	245 500
4	10	1	1.00	0.2	340 000
5	10	1	1.00	0.6	300 000
6	10	1	1.00	0.8	292 000
7	10	1	1.50	0.6	189 100
8	100	1	1.00	0.4	285 800
9	100	1	1.25	0.4	141 300
10	100	1	1.50	0.4	30 000
11	100	1	1.00	0.2	347 700
12	100	1	1.00	0.6	175 350
13	100	1	1.00	0.8	95 280
14	100	1	1.50	0.6	20 600

6.1 Time to rupture

In the table it can be seen that large variations in rupture times exist between the different cases. In figure 5 the rupture time vs. α is plotted at:

- two creep strain rates in the HAZ, f(haz) = 10 * parent metal minimum creep strain rate and f(haz) = 100 * parent metal minimum creep strain rate.
- enhanced axial stress, f_{zz} = 1.5 when f(haz) = 10 and f(haz) = 100.

The curve in the figure with f(haz) = 100 show a strong decrease in rupture time with increasing α whereas at f(haz) = 10 the decrease is rather small. In the case with an extra axial stress of f_{zz} = 1.5 the decrease seems to be quite strong for both f(haz) = 10 and f(haz) = 100. High f(haz) and extra axial stress in addition result in a large reduction of creep rupture life. The rupture times for f(haz) = 100 and f_{zz} = 1.5 is shorter by a factor of 10 than for f(haz) = 10 and f_{zz} = 1.

It can be observed that when the minimum creep rate in the HAZ is relatively low the influence of α on rupture time is low but becomes large when the extra axial load is introduced.

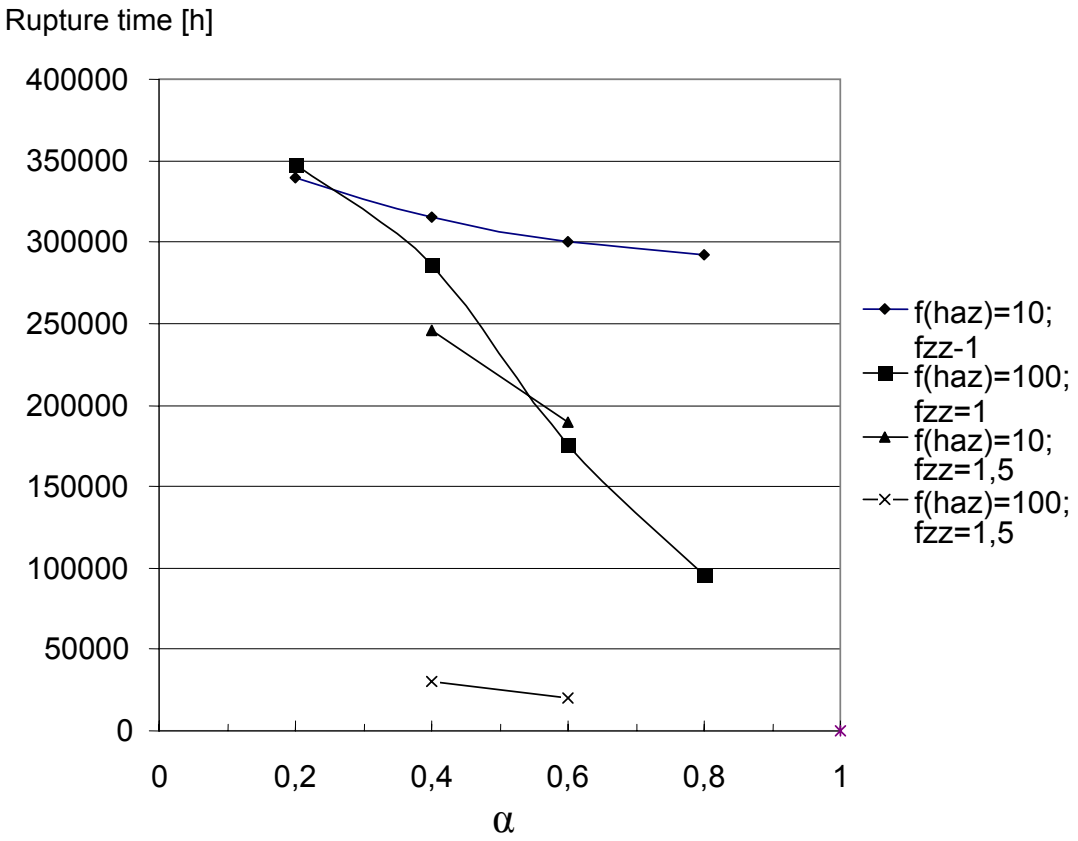

Figure 5. Effect of the material constant α on time to rupture with 10 and 100 times higher creep rate in the HAZ than in the parent metal, without extra axial stress and with an axial stress 1.5 times the axial stress of the internal pressure.

When the minimum creep rate in the HAZ is relatively high the influence of α on rupture time is large. At the lowest value of α the rupture time is even somewhat longer than in the case with the lower HAZ strain rate before it falls. The extra axial load reduces the life time strongly in this case.

In Figure 6 the influence of extra axial load on rupture time for α = 0.4 is shown. From the figure, it can be seen that the pipe weld with the lower creep strength in the HAZ is much more affected by extra axial load than the one with the higher HAZ creep strength.

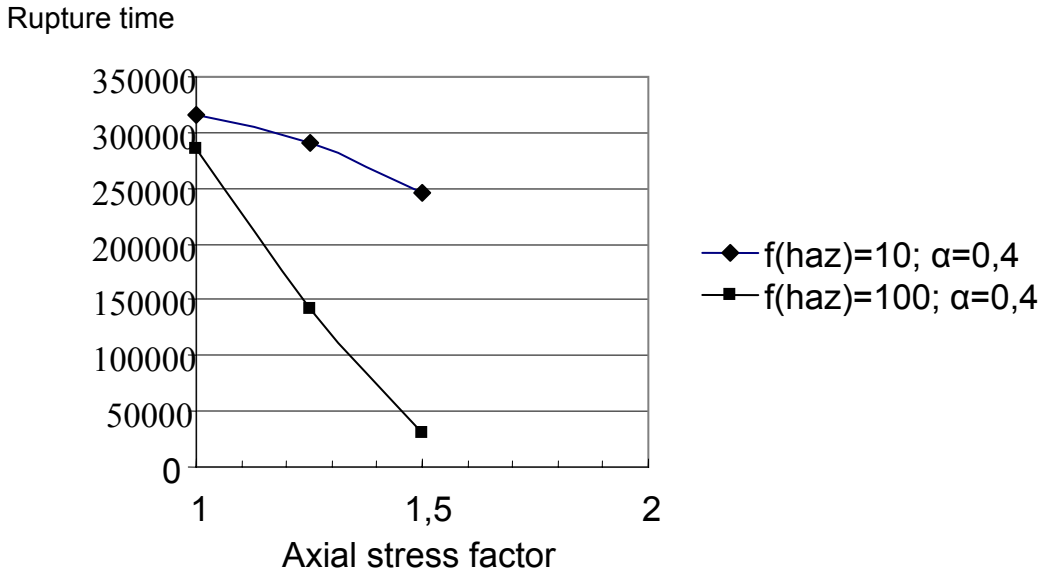

Figure 6. Effect of extra axial stress on rupture time at α=0,4 and creep strain rates in the HAZ being 10 and 100 times faster than in the parent metal.

6.2 Development and distribution of creep damage

An example of the development and the distribution of creep damage from the simulations, Case 1 in Table 2 (f(haz) =10, α = 0.4 and fzz = 1) is given in Figure 7. The figure shows the damage distribution from about half the creep life and then stepwise to the partial damage D/D_{cr} = 1 i.e. when local creep cracks or micro-cracks in a more spread manner have been developed. The figure, which in original is in colour, is somewhat troublesome to interpret in a greyscale. The earliest stage is dark and the greyscale becomes lighter for each step up to a partial damage D/D_{crit} = 0.66 (this occur up to 250 000 h and 275 000 h for the weld metal and the parent metal + HAZ, respectively). Then the steps in the greyscale become darker until the last one which is light again. In the last plot at 315 260 h, however, there is no visible area corresponding to this last light step. This is because the entire weld metal receives almost critical damage at the end of the simulation.

Another example, Case 5 (f(haz) =10, α = 0.6 and fzz = 1) is shown in Figure 8. In this case the damage is concentrated also to the HAZ just below the outer surface and through about half the wall. From the other cases it can be seen that this behaviour, which can be described as move of the most critical damage from the weld metal to the HAZ, is evident as α increases, when extra axial stress increase and when the creep strength in the HAZ decreases.

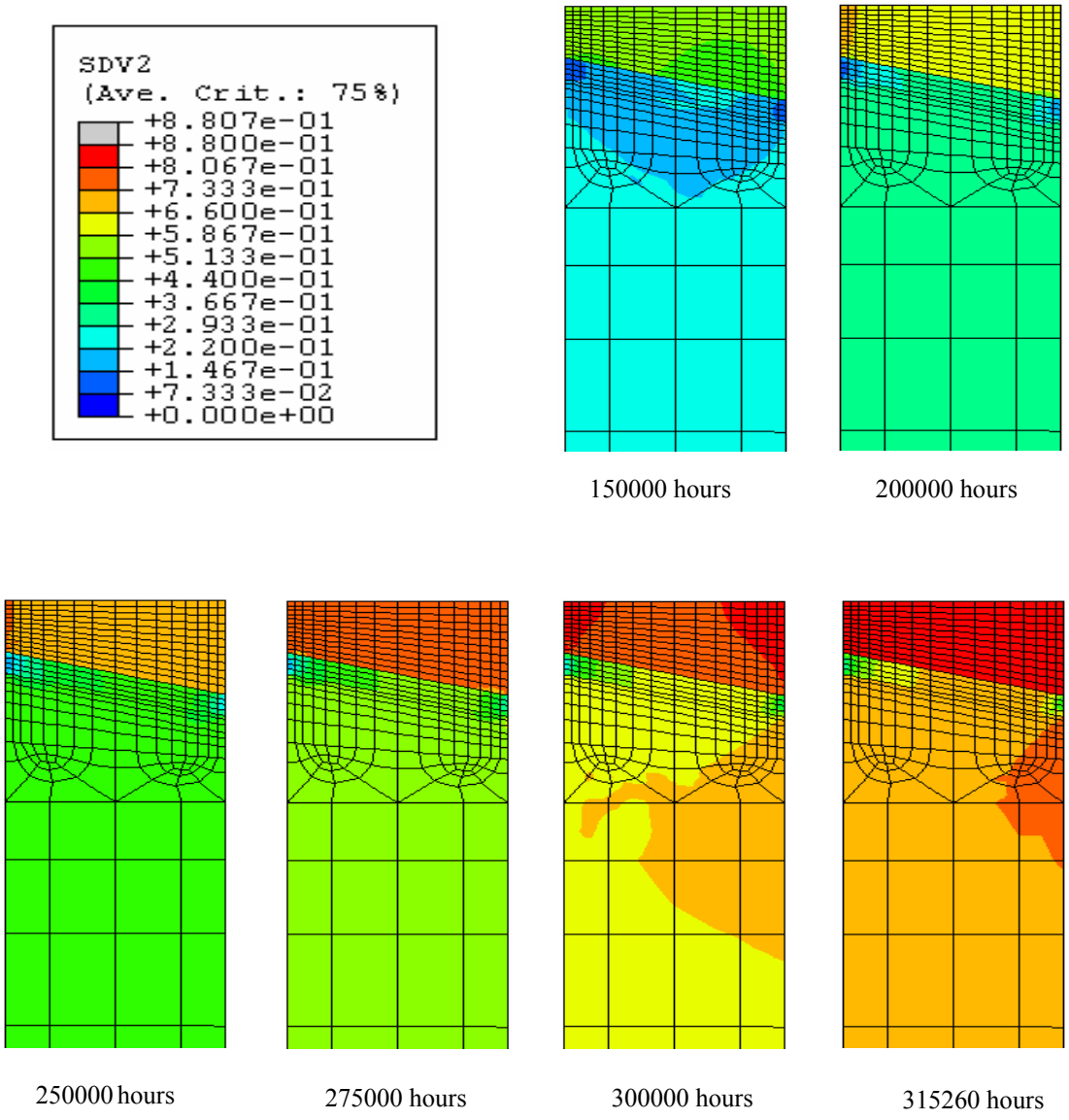

Figure 7. Case 1, f(haz) = 10; f_w = 1; f_{zz} = 1; α = 0.4.

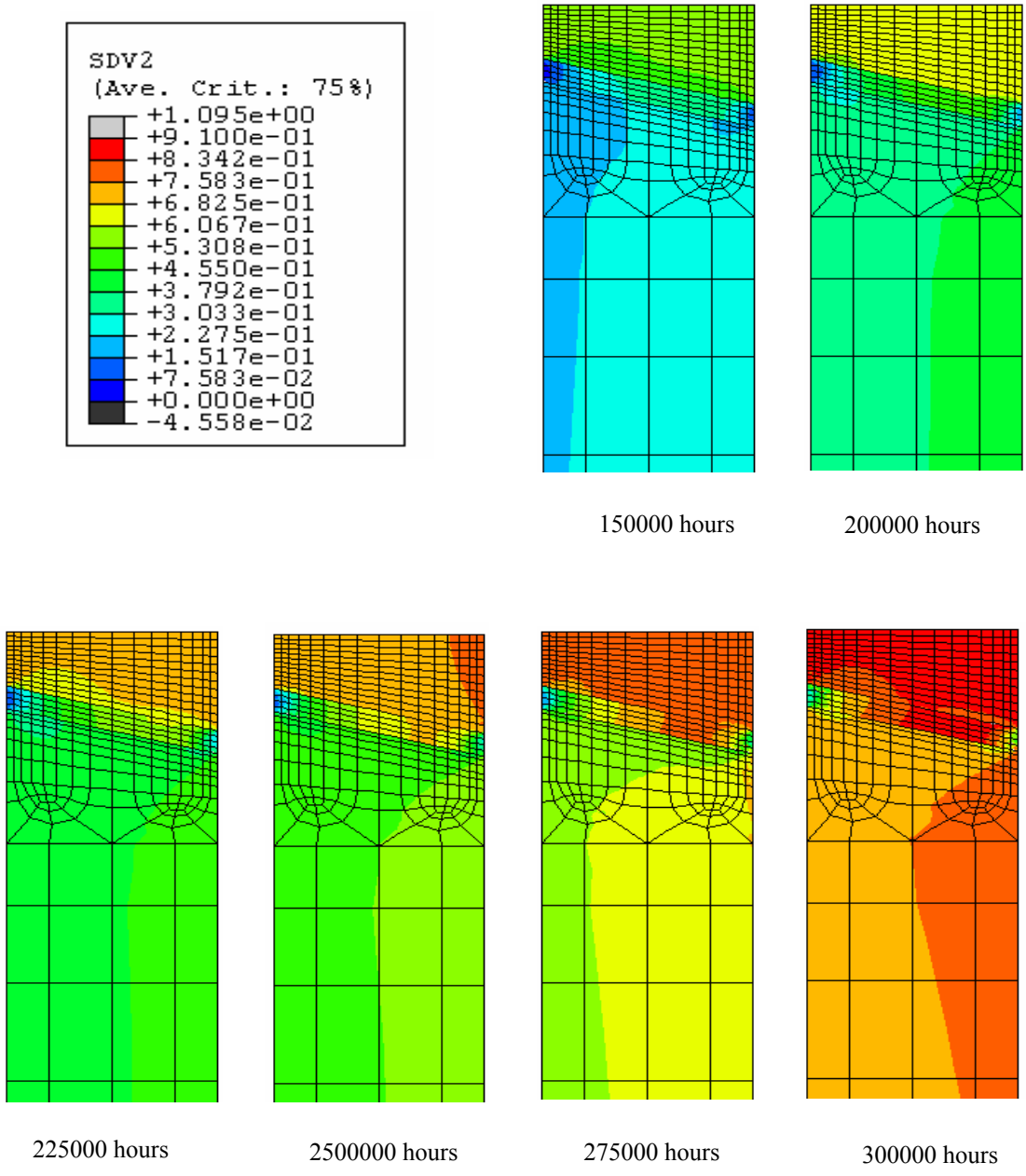

Figure 8. Case 5, f(haz) = 10; f_w = 1; f_{zz} = 1; α = 0.6.

7. Discussion

Also in simulations of low alloy steel welds it has been found that system stresses – in the form of extra axial stresses - have a strong influence on creep life [20]. The decrease in life time as an effect of increasing axial stress is seen in Figure 6. These curves can be assumed to look about the same for low alloy steels. An important difference is, however, that the creep strength of the X 20 steel is much higher than for low alloy steels. An extra axial stress of 50% is in

the order of 30 MPa and 15 MPa for X 20 and low alloy steels, respectively. This means that an axial system stress of, for example, 15 MPa, will have quite small affect on a X 20 steel whereas the creep life in low alloy steels will be drastically reduced.

Principally, the cases without system stress and f(haz) = 10 agree with plant experience of X 20 steel welds where creep cavitation up to date, with service times up to approximately 200 000 h, is quite rare [21].

From Figure 5 it is obvious that materials with high α should be avoided, especially in positions where system stresses may occur as well as extra axial stress as a result of the component geometry such as branches etc.

Although α may vary to some extent in for example, the different constituents of the welded joint [17], it was kept constant in the present study in order to obtain interpretable results. Effects of α on creep life have been studied previously on cross-weld creep test specimens [17]. In this study α had a relatively small influence on creep life in waisted specimens. With strong triaxiality, obtained by a circular notch in the specimen at the position where the interface between intercritical HAZ and parent metal appeared, the creep life was more than a decade longer at α = 0 than at α = 1. There is also a linear log (t_f) – α relationship in this case. Although the effect of α on creep life in the present simulations all fall within the range represented by the two type of creep test specimens in [17] it is obviously not straight forward to make closer predictions of pipe weld behaviour in different cases from results of cross weld creep tests and cross weld analysis. Therefore, FE-analysis of welded components is a useful complement.

The effect of *f*(haz) is strong, at least as long as α not is small. In real welds f(haz) has a minimum in the intercritical HAZ which may go up to a value of about 100. This zone is very thin and will be strongly constrained in a weld. In studies where the HAZ creep rate has been calculated backwards in creep tests of parent metal weld metal and cross weld specimens an average f(haz) which approximately equals 10 is indicated [22]. Therefore, the cases of f(haz) = 10 may better illustrate the behaviour of real welds than the cases where f(haz) = 100. However, it would be useful in future work to determine more exact representative HAZ creep properties and relate them to the welding parameters such as heat input etc.

8. Conclusions

Finite elements simulations of a girth pipe weld of X 20 steel has been performed with aim to study the influence of system stresses, HAZ creep properties and the properties of the rupture criterion, controlled by the material constant α. The creep properties in the parent and the weld metals were quite similar in this weld.

1. The creep strength in the HAZ has a considerable effect on the creep strength of the pipe weld.

2. The creep damage is mainly distributed to the weld metal when the HAZ creep strength is 10 times lower than in the parent metal but strongly concentrated to the HAZ when the HAZ creep strength is 100 times lower.

3. Influence of system stress and α is rather small as long as the HAZ creep strength is relatively high but gets the higher as the HAZ creep strength decreases.

4. At a low value of α the HAZ creep strength is of small importance but at intermediate and high values of α the HAZ creep strength is very important for the pipe weld life time.

5. The creep damage was concentrated to the weld metal and the HAZ some distance below the outer surface of the pipe. The HAZ damage became more severe on expense of the weld metal damage with decreasing HAZ creep strength as well as increasing axial stress and value of α.

6. Weld materials with high values of α are not appropriate at positions where high system stresses may occur.

9. Acknowledgement

The authors acknowledge the financial support from Värmeforsk (www.varmeforsk.se) for this project and for the permission to publish the results.

References

1. NUTEK Dnr 9 181 951, AMF Nr 90-0428: Utformning av dimensioneringsprinciper för moderna högtemperaturanläggningar som arbetar inom krypområdet. Dec. 1994.

2. J. Storesund. Life assessment from weld microstructures at high temperatures. Doctoral Thesis KTH/AMT-179, Sweden, May 1998.

3. R. Wu, J. Storesund & R. Sandström. Influence of post weld heat treatment on creep properties of 1Cr0.5Mo welded joints. Materials Science and Technology, Sept.1993, Vol. 9, pp. 773–780.

4. J. Storesund. Reparationssvetsning av kryppåkända komponenter i hög-temperaturanläggningar med rekommendationer. Värmeforsk rapport 657, 1999.

5. T.H. Hyde, W. Sun & A.A. Becker. Creep crack growth in welds: a damage mechanics approach to predicting initiation and growth of circumferential cracks. Advances in Defect assessment in High Temperature Plant", MPA Stuttgart, Germany, 4–6 October 2000.

6. D.R. Hayhurst. The Use of Continuum Damage Mechanics in Creep Analysis for Design. Journal of Strain Analysis Vol. 29, No. 3, 1994, pp. 233–241.

7. L.Å. Samuelson, P. Segle & J. Storesund. Life assessment of repaired welds in high temperature applications. Welding & Repair Technology for Fossil Power Plants, EPRI Int. Conf., Williamsburg, Va, USA 1994.

8. Nordtest Method NT NDT 010: High temperature components in power in power plants: remnant lifetime inspection, replica inspection, 1991.

9. J. Storesund & K. Borggreen. Krypskador i svetsar av X 20 CrMoV 12 1 Etapp 1. Värmeforskrapport 809, Stockholm, maj 2003.

10. G. Eggeler et al. Analysis of creep in welded P91 pressure vessel. Int. J. Pres. Ves. & Piping 60, 1994, pp. 237–257.

11. C.J. Middleton & E. Metcalf. A review of laboratory Type IV cracking data in high chromium ferritic steels. Int. conf. Steam Plant for the 1990s, 4–6 April 1990, IMechE, London, 1990.

12. K. Borggreen. Some effects of the solution heat treatment temperature on the properties of P 91. In: VTT Symposium 150. Edited by S. Hietanen & P. Auerkari. Espoo: Technical Research Centre of Finland, 1995.

13. Y. Liu, X.F. Sun & Q. Gao. A micro-composite model of localisation in creep damage 1991. Proceedings of Sixth Int. Conf. Material Mechanical Behaviour (ICM-6), Kyoto, Japan (eds. M. Jono and T. Ihone). Pergamon Press, Oxford, Vol. 3. Pp. 859–864.

14. F. Moberg. Implementation of constitutive equations for creep damage mechanics into the ABAQUS finite element code, SAQ/R&D-Report No. 95/05 (Subroutine UMAT) 1995.

15. R. Bürgel, B. Trück & K. Schneider. Schädigungsenwicklung an X 20 CrMoV 12 1 nach Langzeitbeanspruchung unt Zuordnung von Restlebens-dauer von Komponenten in Kriechbereich, Langzeitverhalten warmfäster Stähle und Hochtemeperaturwerkstoffe am 30. November 1990 in Düsseldorf, Verein Deutcher Eisenhütteleute.

16. R.J. Browne, D. Lonsdale & Flewitt P.E.J. Multiaxial stress rupture testing and compendium of data for creep resisting steels. Trans. ASME. 1982. J. Eng. Mat. Technol., Vol. 104, pp. 291–296.

17. T.H. Hyde, A. Tang & W. Sun. Analytical and computational stress analyses of welded components under creep conditions, Proc. Int. Conf. Integrity of High-Temperature Welds, Professional Engineering Publishing Limited, UK, 1998. Pp. 285–306.

18. L.Å Samuelson, S.-T. Tu & J. Storesund. Life Reduction in High Temperature Structures Due to Mis-Match of Weld and Parent Material Creep Properties, Mis-Matching of Welds. Mechanical Engineering Publications, London, 1994. Pp. 845–860.

19. J. Storesund, P. Andersson, L.Å. Samuelson & P. Segle. Prediction of creep cracks in low alloy steel pipe welds by use of the continuum damage mechanics approach. In: CAPE'97, Penny (Ed.), Balkema, Rotterdam, 1997.

20. J. Storesund & L.Å Samuelson. Creep life assessment of pipe girth weld repairs with recommendations. OMMI Journal, Vol. 1, Issue 3, December 2002, www.ommi.co.uk

21. K. Borggreen & J. Storesund. Creep Behaviour if Welds in X 20 CrMoV 12 1 Evaluated from Replica Inspection Results. Baltica VI – Int. Conf. on Life Management and Maintenance for Power Plants, VTT, Finland, 8–10 June, 2004.

22. J. Storesund & S.-T. Tu. Geometrical effect on creep in cross weld specimens. Int. J. Pres. Ves. & Piping, 62, 1995, pp.179–193.

Creep behaviour of welds in X 20 CrMoV 12 1 evaluated from replica inspection results

Kjeld Borggreen
SydTek AB, Malmö, Sweden
www.sydtek.se

Jan Storesund
Det Norske Veritas AB, Stockholm, Sweden
www.dnv.com

Abstract

Ordinary welds in eleven Danish main steam lines and hot reheat lines made of X 20 CrMoV 12 1 have been routinely inspected for creep damage by means of replication for more than 20 years. The results comprising more than 7000 individual replicas have been analysed. On this basis it can be concluded that X 20 CrMoV 12 1 performs exceptionally well over very long times. The steel is very unlikely to develop detectable creep damage in the base materials and weld zones within 200.000 hours of service and is in this respect more reliable than any comparable type of steel. Reasons for this can be found in the much higher time safety margin in combination with better creep and physical properties of X 20 CrMoV 12 1 compared to many competing types of steel.

1. Introduction

1.1 X20 in high pressure pipings in Denmark

The German developed martensitic creep resistant 12% Cr-steel X 20 CrMoV 12 1 (X20) has been popular in Denmark, and the first main steam pipe of this steel was installed already in 1963. X20 had its golden age in the years 1980–94 where 20 new steam pipe systems of this steel were commissioned. After 1996 all new high pressure steam pipe systems have been made of the 50% stronger martensitic 9% Cr-steel X 10 CrMoVNb 9 1 (P91). In Figure 1 is shown the number of live steam pipe systems of X20 and P91 in service in Danish main power plants during the period 1963–2004 [1]. Both main steam lines and hot reheat lines are included in the figure.

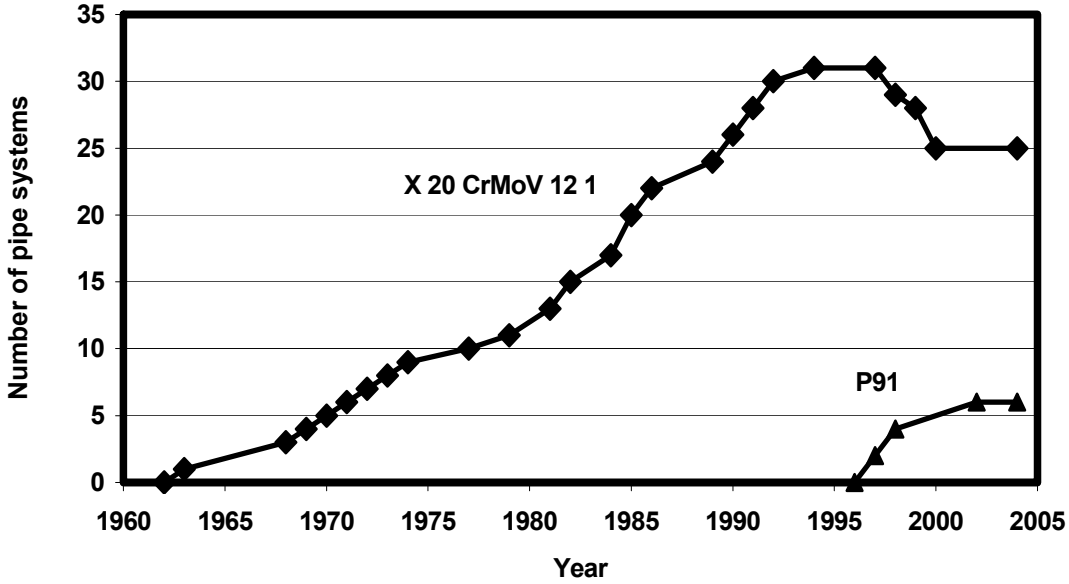

Figure 1. Number of live steam pipe systems of X 20 CrMoV 12 1 and P91 in service in Danish main power plants during the period 1963–2004 [1].

Beside its lower cost and some advantages in manufacturing, P91 has the advantage that the pipe systems become more slender and flexible compared to pipe systems made of X20. With this new steel and its stronger successors, large reductions in the system stresses are obtainable. As will be demonstrated in the following this may lead to a considerable increase in useful lifetime for these new steels.

1.2 Changes in design principles

According to TRD, high pressure steam pipe systems may be designed using either 100.000 hours or 200.000 hours mean creep rupture strength. In the first case, the safety factor on the stress is 1,5 and in the second case 1,25 (corresponding to a safety factor of 1,0 on the minimum creep rupture strength). The use of design rules based on 200.000 hours creep rupture strength was caused by the appearance of such values, which happened around 1980–85. Pipe systems made according to the new rules have slightly less wall thickness than previous pipe systems. This has no significance compared to the large tolerances allowed in manufacturing.

More important may be that the philosophy for designing hanger systems was changed around 1975. Before this time, the pipe systems were floating and had in principle unlimited possibilities for moving in any direction. The new philosophy dictated so-called z-stops, which probably have resulted in much lower system stresses in the terminal points of the system (junctions, connections to headers, and turbine etc.). Better design models, software, and calculating power have also been used after 1975. All this has probably had an important impact on the useful lifetime of many of the pipe systems made of X20 in Denmark.

1.3 Changes in manufacturing

Since the introduction of X20, the procedures for manufacturing and welding have been changed. Most important for the present project is the change in welding procedure, which took place around 1980 based on recommendations from Mannesmann Anlagenbau [2, 3]. From start, X20 was welded in the so-called "austenitic mode" using an interpass temperature of 400–450°C. The new approach was that the steel might also be welded in the so-called "martensitic mode", which nowadays is the most common. Martensitic welding requires an interpass temperature of only 250–300°C, which is advantageous for the welder.

Comprehension among the manufacturers of the delicate relationship between creep strength, microstructure, heat treatment temperature, and chemical composition for X20 came relatively late. In 1988, it was recommended by Mannesmann Röhrenwerke to decrease the maximum Ni-content from 0,8% to 0,6% to increase the A_{C1}-temperature and by VGB to decrease the upper tempering temperature from 780°C to 760°C not to reach the critical transformation temperature. Together with the more focus on the importance of correct hardening and tempering procedures for X20, the recommendations have probably since 1988 resulted in more reliable products with optimised creep strength and longer useful lifetime.

2. Background data and data bases

2.1 European data base for most common steels

In a common project shared between RWTÜV and EPRI, a data base of replica inspection results was compiled. The results were published by EPRI in 1993 [4, 5]. This data base consisted of the results of eight years of on-site inspection made by RWTÜV on European high pressure steam lines. Totally 10.000 data sets (replica evaluations) were included. Materials included were 14 MoV 6 3, 13 CrMo 4 4, 10 CrMo 9 10, and X 20 CrMoV 12 1. Of the last mentioned steel, only a small number of data were available, and only from plants with short expired lifetime.

The replica inspection and the classification of creep damage had been made according to the guidelines of Neubauer [6]. These guidelines use a scale with a simple verbal description of the five main damage classes (1 to 5) and a division of each class into three subclasses (.1 to .3). In the European data base this scale of discrete steps was made linear by multiplying with 10 giving a continuous scale from 10 to 50, which is more suitable for data analysis and graphic presentation.

The European data base is characteristic by containing data from many different plants with a large span in time of commissioning and in accumulated service life. Both main steam lines and hot reheat lines are included, and from these both welds and bends. The data base is very systematic structured so that every replica position is traceable. Information of pipe dimension, type of component, steam data, and service life (history) are kept.

2.2 Nordtest data base for X 20 CrMoV 12 1

For use in a Nordtest project the European data base was extended with inspection results from Danish high pressure lines of X20 [7]. This was possible as most replica inspections in Denmark had been made according to the German guidelines [8, 9]. By the end of the project in 1995, the X20 part of the data base had 1200 entries each consisting of 1 or 5 data sets.

An analysis of the data revealed that creep damage is only slowly developing in X20 (weld zones and base materials), and that only a slight difference in damage rate exists between base material, heat affected zone, and weld metal [7]. The reliability of the analysis was hampered by the relative small number of data for this steel and the relative short expired lifetime for the pipe systems. Furthermore, so-called ”falls calls” originating from inadequate etching procedures were supposed to add bias to the data population (it was expected that Class 2 Damage: ”Single cavities” was exaggerated on behalf of Class 1 Damage: ”No visible cavities”).

2.3 Värmeforsk data base for ordinary welds in X 20 CrMoV 12 1

The Danish experience with the long term behaviour of X20 is of general interest to the other Nordic countries. A project funded by Värmeforsk was consequently launched in 2002 [10, 11].

The premises of the Värmeforsk project were to evaluate the development of creep damage in ordinary welds in high pressure steam piping of X20. For this reason, it was decided to extend the Nordtest data base with the most recent inspection results from Danish plants obtained in the period 1995–2003. It was also decided only to consider welds of the same diameter as the main pipe system i.e. to exclude small welded-on branch pieces where particular stress conditions prevail. Finally, it was decided to exclude dissimilar metal welds, as these often fail prematurely for completely other reasons than ordinary welds do.

To study the effect of system stresses – in particular axial stresses – on the welds it was in the Värmeforsk data base distinguished between welds at terminal points and at non-terminal points. Terminal points exist where the different parts of the piping system are connected to each other or connected to the outlet

headers or turbine valves etc. It is known from other studies that the system stresses are often much higher in terminal points than elsewhere [5, 12]. For similar reasons it was decided to distinguish between main steam lines and hot reheat lines because the diameter to wall thickness ratio for low alloy steels is know to govern the extend of creep damage both within time and length along the circumference of the (butt) weld [5, 12, 13].

The version of the Värmeforsk data base used for the present analysis consists of data from 8 main steam lines and 3 hot reheat lines with an accumulated service time spanning from 92.000 hours to 191.000 hours. Years of commissioning span from 1978 to 1987. The number of entries in the data base is 1471 giving 7260 data sets. 55% of these data sets are from welds at terminal points, and 17% are from welds in hot reheat lines.

3. Data analysis and graphical presentations

3.1 Damage scales

For the interpretation and classification of creep damage in general two different scales have been used in the Nordic countries: the classical RWTÜV-scale invented by Neubauer and the new Nordtest-scale [8, 9]. The new Nordtest-scale is very similar to the VGB-scale nowadays used in Germany [14].

It is outside the scope of this paper to discuss the consistency of the different types of scales and the fact that these scales are made of discrete steps. Neither will the interesting question of using the same scales for both ferritic-bainitic low alloy steels and martensitic high alloy steels be dealt with here. For interpretation of the Värmeforsk data base results, the same formal linearization of the step-wise damage scales as used in the European data base is also adapted here. This makes the interpretation of the results easy and does not have a decisive affect on the conclusions of the analysis. Comparisons between the different damage scales are shown in Table 1.

Table 1. Correspondence between the classical RWTÜV-scale, the new Nordtest-scale, and the linear scale used for interpreting the data base results for X 20 CrMoV 12 1.

New Nordtest	**RWTÜV**	Linear
1	1	10
2a	2.1	20
	2.2	23
2b		25
	2.3	27
3a	3.1	30
	3.2	33
3b		35
	3.3	37
4a	4.1	40
	4.2	43
4b		45
	4.3	47
5	5	50

3.2 Data filtering and data analysis

To discriminate between defects coming from manufacturing and from service exposure the data were filtered for damages of the type: hot cracking (not to confuse with reheat cracking) and related defects. The excluded data were not dominating by number, but by their position on the damage scale. Data sets entirely from parent materials, entirely from HAZ's, and entirely from weld metals were analysed as separate and independent data populations.

The data sets describing the development of creep damage in the weld zones are shown in Figures 2–4 for parent material (PM), heat affected zone (HAZ), and weld metal (WM), respectively. The figures illustrate the behaviour of the welds on a linear damage scale for nearly 200.000 hours of service, which is also the design lifetime. In each figure, an upper boundary line is shown indicating a linear development in creep damage from Class 10: "No visual creep damage" at zero hours to Class 50: "Macro creep cracks" at the end of design life. This upper boundary line assumes that the visual damage in the microstructure starts to develop at zero hour which is not at all the case for low alloy steels and probably neither for X20.

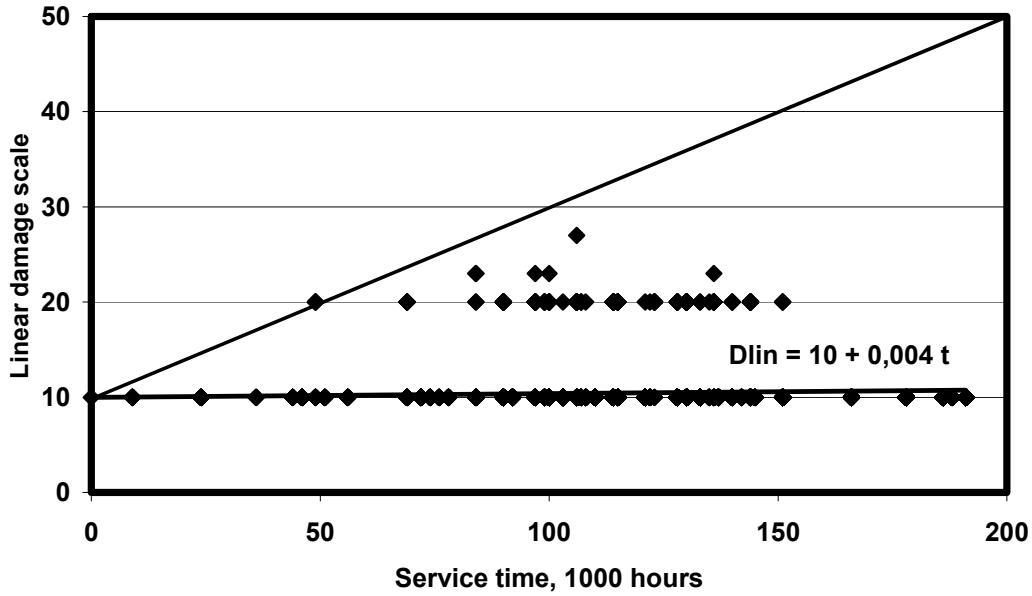

Figure 2. Creep damages observed in the parent material (PM) as function of the accumulated service time. The upper boundary line and the mean value line $D_{lin} = 10 + 0{,}004\ t$ *(kh) are shown.*

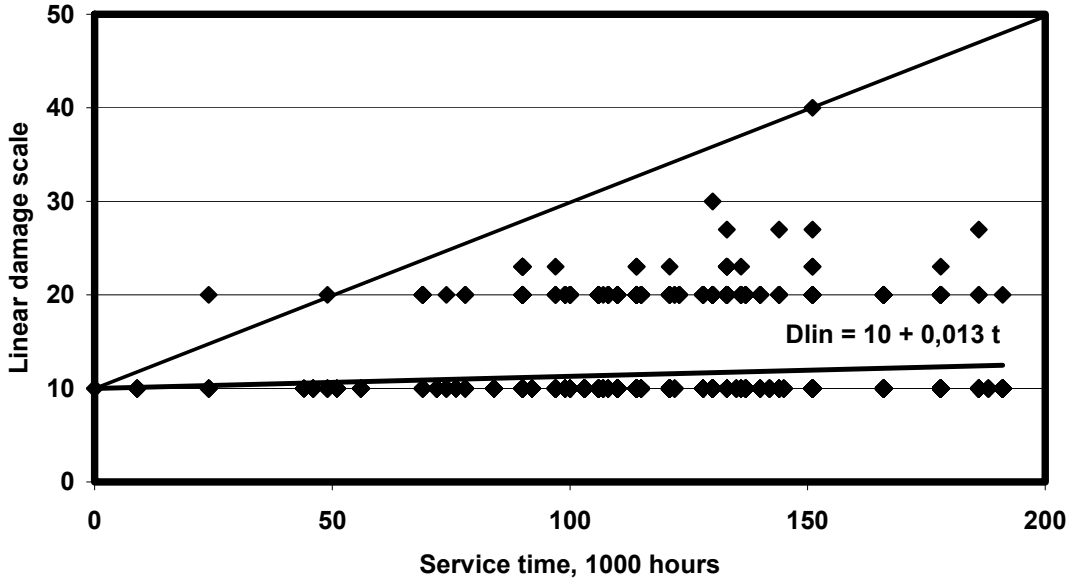

Figure 3. Creep damages observed in the heat affected zone (HAZ) as function of the accumulated service time. The upper boundary line and the mean value line $D_{lin} = 10 + 0{,}013\ t$ *(kh) are shown.*

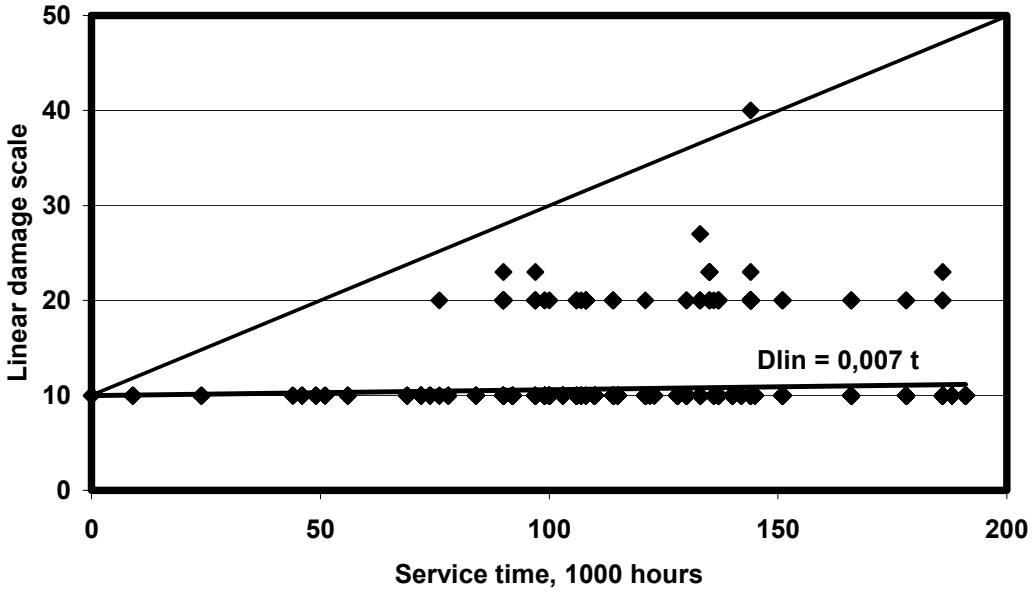

Figure 4. Creep damages observed in the weld metal (WM) as function of the accumulated service time (cases of hot cracking are excluded from the data). The upper boundary line and the mean value line D_{lin} = 10 + 0,007 t (kh) are shown.

Damage Class 10: ”No visual creep damage” has been observed in 94%, 87%, and 92% of all cases, and Damage Class 20: ”Isolated cavities in small amount” was observed in 5%, 11%, and 7% of all cases for PM, HAZ, and WM, respectively. Damage Class 23: ”Isolated cavities in medium amount” was only observed in 1%, 2%, and 2% of all cases for PM, HAZ, and WM, respectively. Including cases of hot cracking does not change these figures. Indeed these figures indicate a very low damage profile for X20 compared to other steels. For comparison, in earlier investigations of the base material of low alloy steels Damage Class 10 and Damage Class 20 were found in 58% and 28%, respectively of all cases [5].

3.3 Analysis of mean damage values

The creep damage data were further analysed by plotting the mean damage line extending from Class 10 at zero hours. The slope of this line gives a sort of indication of the susceptibility of the particular weld zone to develop visual creep damage. The slope values are given in Table 2. In this table, the number of extreme points have also been indicated. Extreme points are data points presenting damage values larger than 80% of the upper boundary value. As can be observed from the table almost all cases of hot cracking are extreme points.

It is observed that the mean value of damage is in all cases and at all time within the design life extremely small. This is regardless of the weld zone considered. The slope of the mean value line compared to the upper boundary line is merely

2%, 4%, and 7% for PM, HAZ, and WM, respectively. In mean, a damage class of only 13 on the linear scale from 10 to 50 will be reached in the weld metal after 200.000 hours of service. Such low damage rates has until now not been observed for other steels used for high pressure steam piping.

Table 2. Slope of the mean value lines and number of extreme data points for the different weld zones in ordinary welds in live steam pipes made of X 20 CrMoV 12 1. Results for welds at terminal points and welds in hot reheat lines are also presented.

Zone	Slope in units/10^3 h (linear scale)	Slope in per cent of upper boundary	Number of extreme points
Welds in main steam lines and hot reheat lines			
BM	0,004	2	0
HAZ	0,013	7	1
WM	0,007	4	1
WM + hot cracking	0,008	4	12
Welds in terminal points			
BM	0,005	3	0
HAZ	0,013	7	0
WM	0,006	3	1
Welds in hot reheat lines			
BM	0,004	2	0
HAZ	0,015	8	0
WM	0,006	3	0

3.4 Terminal points and hot reheat lines

If only the highly stressed terminal points are considered in the analysis it is observed from Table 2 that the creep damage in these welds does not develop earlier or at a faster rate than elsewhere in the pipe system. This strongly suggests that both base materials and welds in X20 are safe against local high stresses.

Earlier studies at CEGB have demonstrated that creep damage develops significantly faster in hot reheat lines than in main steam lines of 14 MoV 6 3 [12].

Analysis of data from the European data base has likewise shown that first sign of creep damage appears at an earlier time in hot reheat lines than in main steam lines. This is valid for base materials in pipe systems made of 13 CrMo 4 4 and 10 CrMo 9 10, and partly valid for systems of 14 MoV 6 3 [5].

From the slope data in Table 2, it becomes clear that for pipe systems made of X20 there is no difference between hot reheat lines and main steam lines. This observation also indicates that the higher axial stresses supposed often to prevail in hot reheat lines because of their much larger diameter to thickness ratio do not result in premature creep damage for this steel.

4. Lifetime safety aspects

4.1 Design rules and safety factors

According to TRD 301 pressurised pipe systems under surveillance are designed for a safe lifetime of 200.000 hours. Differences in design data and actual service conditions result in large differences between design lifetime and actual useful lifetime. Figure 5 illustrates for X20 the use of either mean and minimum creep rupture strength data in design principles based on either 100.000 hours or 200.000 hours creep rupture values at 540°C and with different stress safety factors.

During service with varying stresses the stress level in a pipe system affects the consumption of creep lifetime to a greater extend than under stationary conditions [15]. The stress level is also difficult to predict and to measure. For this reason, the actual stress level should be given more attention than predicted by the creep models. From creep strength data like those in Figure 5, the time safety margin for a particular design and material may be calculated. It can be shown that at high time safety margins, the useful lifetime varies very much with the variation in stress. Therefore, the maximum possible lifetime of a pipe system can only be fully exploited if the stress safety margin is sufficiently large [16].

4.2 Stress and time safety margins for X 20 CrMoV 12 1

Based on ISO creep rupture data for X20 and 10 CrMo 9 10 the design stresses and safety margins have been calculated for a typical service temperature of 540°C ± 10°C [17]. Two different design principles have been studied. The results are shown in Table 3, where the time safety margins and the exploitable lifetimes for pipe systems made of either X20 or 10 CrMo 9 10 can be compared.

In general, the time safety margin is much higher for pipe systems made of X20 than of 10 CrMo 9 10 (or any other low alloy steel). This is in particular the case

when the design temperature is decreased or the old design principle has been used. At 540°C the time safety margin is approximately 5 for 10 CrMo 9 10 but varies for X20 between 6 and 11 depending on the design conditions. In exploitable service time, this gives a bonus of extra 100.000–600.000 hours to pipe systems made of X20. The larger time safety margin generally found for X20 compared to the low alloy steels is believed to be the main – but not the only – premise for its good behaviour at long term in service.

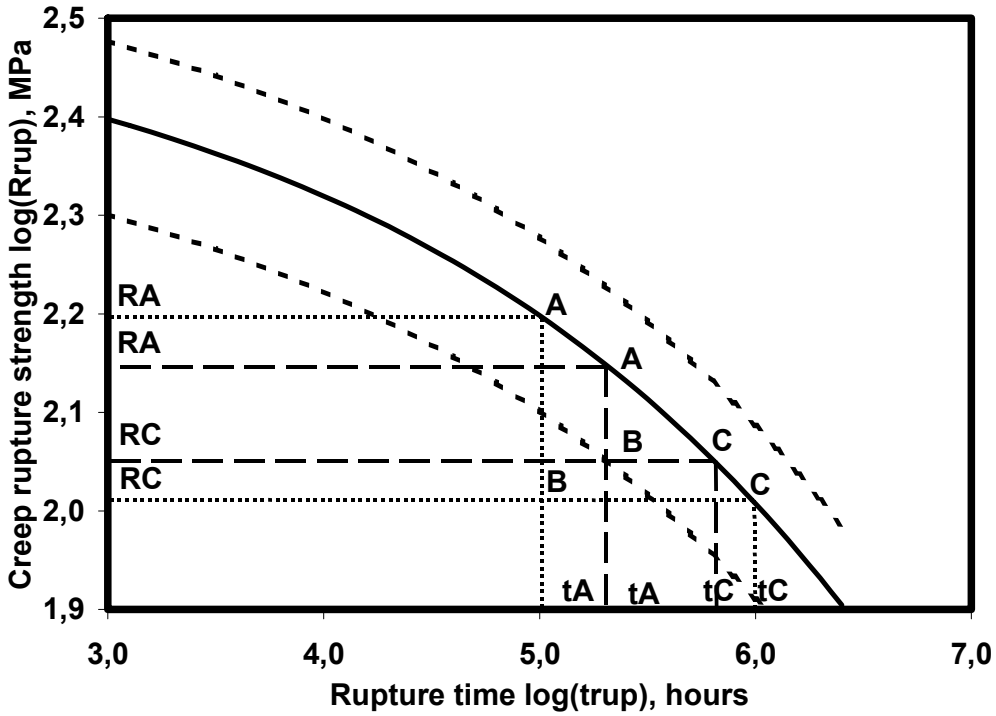

Figure 5. The creep rupture strength as function of the rupture time (log-log-diagram) for X 20 CrMoV 12 1 at 540°C. The mean value curve and the ± 20% boundary lines are shown. With a design lifetime of t_A and a design stress R_C the stress safety margin is AB and the time safety margin is BC.

4.3 Effects of system stresses and service temperatures

The large time safety margin for X20 may explain why welds at highly stressed terminal points do not suffer from premature creep damage. It may also explain why differences in creep damage between main steam lines and hot reheat lines are not observed.

As observed from Table 3, the time safety margin increases considerable with a minor decrease in temperature. In practice, the actual steam temperature in a pipe system is most of the time significantly less than the design temperature and never above this temperature. For this reason, the actual effective time safety margin may be much higher than foreseen from design calculations i.e. much higher than the values shown in Table 3.

Table 3. Creep rupture strength, design stress, relative time safety margin, absolute time safety margin, and the slope of the mean rupture strength curve at the design temperature ± 10°C for X 20 CrMoV 12 1 and 10 CrMo 9 10. Results for the two most often design principles are shown. Based on ISO creep rupture data [17].

Parameter	Unit	530°C			540°C			550°C		
		X20	10CrMo910	Ratio	X20	10CrMo910	Ratio	X20	10CrMo910	Ratio
					100.000 hours rupture time					
dRrup/dT	MPa/°C				-2,15	-1,12	1,9			
dRrup/dtrup	MPa/kh				-0,121	-0,176	0,7			
		Design based on 100.000 hours creep rupture strength								
Rrup,100.000h	MPa	180	91	2,0	158	79	2,0	137	69	2,0
Rdesign = Rrup/1,5	MPa	120	61	2,0	105	53	2,0	91	46	2,0
Rel. time safety margin *		11,2	5,3	2,1	8,9	5,0	1,8	7,1	4,7	1,5
Abs. time safety margin **	h	1.020.000	430.000	2,4	790.000	400.000	2,0	610.000	370.000	1,6
dRrup/dtrup	MPa/kh	-0,0229	-0,0306	0,7	-0,0270	-0,0289	0,9	-0,0314	-0,0273	1,2
		Design based on 200.000 hours creep rupture strength								
Rrup,200.000h	MPa	163	78	2,1	141	67	2,1	121	58	2,1
Rdesign = 0,8Rrup	MPa	130	62	2,1	113	54	2,1	97	47	2,1
Rel. time safety margin *		7,1	5,0	1,4	6,3	4,7	1,3	5,6	4,5	1,2
Abs. time safety margin **	h	610.000	400.000	1,5	530.000	370.000	1,4	460.000	350.000	1,3
dRrup/dtrup	MPa/kh	-0,0363	-0,0327	1,1	-0,0386	-0,0309	1,2	-0,0402	-0,0302	1,3

*) Relative to 100.00 hours rupture time.

**) 100.000 hours excluded.

5. Conclusions

Based on 20 years of systematic replica inspection of ordinary welds in Danish high pressure steam pipe systems made of X20 the following can be concluded:

1. The creep damage observed over long time is much smaller in systems made of X20 than in systems made of low alloyed steels.

2. After 200.000 hours in service the welds have in mean reached a damage class of only 13 on the linear scale from 10 to 50.

3. Within 200.000 hours of service neither of the welds has reached nor will reach the Linear Damage Class 50, which necessitates repair actions.

4. The development of creep damage in welds at terminal points is no larger than in welds at any other position.

5. The development of creep damage in welds in hot reheat lines is no larger than in welds in main steam lines.

6. The extend of creep damage in welds in high pressure steam pipes is apparently independent of the year of commissioning, principles of design, welding procedure, and service history.

7. The relative time safety margin at 540°C is 1.8 times larger for X20 compared to 10 CrMo 9 10 when the old design principle is used and 1.3 times larger when the new design principle is used.

8. The time safety margin increases considerably when the design temperature is decreased.

9. The high time safety margin of X20 can explain much of the good service experience obtained for this steel.

6. Acknowledgement

The authors acknowledge the financial support from Värmeforsk (www.varmeforsk.se) for this project and for the permission to publish the results. The Danish power stations are acknowledged for making the inspection results available for the project.

References

1. Primærværkernes Maskintekniske Materialeudvalg: Kraftværkernes Bestykningslister, Maskinanlæg, Store Anlæg, Januar 2002.

2. F. Brühl & H. Münsch. Welding of Alloyed Ferritic and Martensitic Steels in Piping Systems for High Temperature Service. Proc. of Conference on Ferritic Alloys for use in Nuclear Energy Technologies, Snowbird, 1983.

3. G.P. Kalwa, K. Haarmann & K.J. Janssen. Experience with Ferritic and Martensitic Steel Tubes and Piping in Nuclear and Non-nuclear Applications. Proc. of Conference on Ferritic Alloys for use in Nuclear Energy Technologies, Snowbird, 1983.

4. Life Assessment of Boiler Pressure Parts, Vol. 5: European Replica Data Base Evaluation. EPRI TR-103377-V5, Nov. 1993.

5. H. Fuhlrott, H.-R. Kaufmann, D. Loog, B. Neubauer, H. Heinrich & H.-D. Schulze. Zusammenfassung der Ergebnisse der Auswertungen der Replica. Datenbank der Technischen Überwachungs-Vereine RWTÜV, Essen, und TÜV Rheinland Köln, VGB Conference: Materials and Welding Technology in Power Plants 1994, VGB, Essen, 15.–16. März 1994. Pp 12.1–12.25.

6. B. Neubauer & U. Wedel. Restlife Estimation of Creeping Components by Means of Replicas. Advances in Life Prediction Methods, ASME, New York, 1983, pp. 307–314.

7. P. Auerkari, S. Holmström, J. Salonen, K. Borggreen, J. Storesund & R. Wu. Evaluation of Creep Damage from Replica Inspection Results. Nordtest Project Nr. 1306-96, VTT Report VALB 211, 1997.

8. High Temperature Components in Power Plants: Remnant Lifetime Assessment, Replica Inspection. Nordtest NT NDT 010, 1991.

9. P. Auerkari, J. Salonen & K. Borggreen. Guidelines for Evaluating In-service Creep Damage. NT Techn. Report 302, 1995.

10. J. Storesund & K. Borggreen. Krypskador i svetsar av X 20 CrMoV 12 1 – Etapp 1, Värmeforsk rapport nr. 809, maj 2003.

11. J. Storesund, K. Borggreen, W. Zang & H. Nilsson. Krypskador i svetsar av X 20 CrMoV 12 1 – Etapp 2, Värmeforsk rapport. In preparation.

12. S.J. Brett. Cracking Experience in Steam Pipework Welds in National Power. VGB Conference: Materials and Welding Technology in Power Plants 1994, VGM, Essen, 15.–16. März 1994. Pp. 8.1–8.17.

13. Private communication with S.J. Brett, 2000.

14. VGB-TW 507. Guidelines for the Assessment of Microstructure and Damage Development of Creep Exposed Materials for Pipes and Boiler Components, VGB, Essen 1992. 83 p.

15. M. Sander. Zum Zeitstandverhalten warmfester Stähle unter veränderlicher Belastning und Temperatur, thesis D17, Darmstadt 1974.

16. H. Weber. V. Internationales Symposium über warmfeste Werkstoffe, Vsetin, CSSR, 13.–16. September 1976.

17. ISO Technical Report 7488, 1981.

Influence of inhomogeneous recovery on creep strength and rupture ductility of ferritic creep resistant steels

Kazuhiro Kimura, Kota Sawada, Kiyoshi Kubo & Hideaki Kushima
Creep Group, National Institute for Materials Science
Tokyo, Japan

Abstract

Degradation behaviour during long-term creep exposure has been investigated on 9Cr-1Mo-V-Nb and 2.25Cr-1Mo steels. Inhomogeneous recovery has been considered to be a degradation mechanism of 9Cr-1Mo-V-Nb steel in the long-term, in contrast to homogeneous one in the short-term. Corresponding to inhomogeneous recovery, significant decreases in creep rupture strength and rupture ductility was observed. Creep rupture ductility of the 2.25Cr-1Mo steel tempered at the lower temperatures decreased with increase in creep exposure time, corresponding to inhomogeneous recovery. However, it increased in the long-term, as a result of overageing. On the other hand, no drop of rupture ductility was observed on the 2.25Cr-1Mo steel tempered at the higher temperatures. Decrease in not only creep strength, but also rupture ductility is caused by inhomogeneous recovery in the vicinity of prior austenite grain boundaries.

1. Introduction

Thermal power plant is a main source of electric power supply and it has been discharging considerable amounts of CO_2 by combustion of fossil fuels. Reducing environmental load due to wasting energy resources of oil, coal and natural gas, and exhausting CO_2 gas is an important problem assigned to power plant. Improvement in energy efficiency of thermal power plant by increasing the temperature and pressure of the steam is requested. Research and development have been widely conducted on ferritic creep resistant steels and many high strength materials, such as 9Cr-1Mo-V-Nb steel [1], NF616 [2], HCM12A [3] and E911 [4], have been developed. Enhanced creep strength of those materials has contributed to raise the efficiency of power plant through the higher operating steam temperature. However, accurate assessment of long-term creep strength of those ferritic creep resistant steels is difficult, since stress vs. time to rupture curve shows inflection in the long-term [5]. Inhomogeneous recovery preferentially takes place in the vicinity of prior austenite grain boundary is a

degradation mechanism of those steels in the long-term, in contrast to homogeneous recovery in the short-term [6]. Not only decrease in creep strength, but also decrease in rupture ductility has been observed in the long-term, corresponding to the inhomogeneous recovery [7]. Improvement in creep strength contributes to increase in energy efficiency of power plant and maintaining sufficient ductility of high temperature structural components is also important to secure safety and reliability of power plant. The aim of the present study is to investigate a correlation between rupture ductility and inhomogeneous recovery in the vicinity of prior austenite grain boundary. Creep rupture strength property, especially on rupture ductility, has been examined on multi heats of quenched and tempered 2.25Cr-1Mo steels, in conjunction with microstructural evolution during creep exposure.

2. Experimental procedure

Normalized and tempered 9Cr-1Mo-V-Nb steel (ASME SA-213 T91) [8] and quenched and tempered 2.25Cr-1Mo steels (ASTM A542) [9] were used in this study. The chemical compositions (mass%) and heat treatment conditions are shown in Table 1 and Table 2, respectively. Steel designated as MGC is 9Cr-1Mo-V-Nb steel and the other steels of MnA to MnJ are 2.25Cr-1Mo steels. Creep rupture data over the range of temperatures from 500 to 725^{o}C and those from 450 to 650^{o}C were investigated for 9Cr-1Mo-V-Nb steel and 2.25Cr-1Mo steels, respectively. Microstructure of the creep exposed specimen was examined under transmission electron microscope. Vickers hardness was measured on the 2.25Cr-1Mo steels in the as tempered condition and creep exposed specimen under load of 0.98N. Creep deformation behaviour of MnB and MnH heats of the 2.25Cr-1Mo steels at 600^{o}C and 98MPa was investigated.

Table 1. Chemical compositions (mass%) of the steels studied.

Steel	C	Si	Mn	Ni	Cr	Mo	V	Nb	Al	N
MGC	0.09	0.29	0.35	0.28	8.70	0.90	0.22	0.072	0.001	0.044
MnA	0.15	0.39	0.44	0.095	2.27	1.00	-	-	0.017	0.006
MnB	0.156	0.31	0.70	0.20	2.27	0.99	-	-	tr	0.0096
MnE	0.13	0.25	0.49	0.03	2.31	1.01	-	-	0.039	0.0115
MnF	0.14	0.21	0.53	0.14	2.40	1.01	-	-	0.018	0.0108
MnG	0.14	0.25	0.55	0.18	2.44	1.03	-	-	0.018	0.0102
MnH	0.14	0.31	0.52	0.19	2.40	1.04	-	-	0.017	0.0112
MnJ	0.08	0.42	0.54	0.03	2.28	0.96	-	-	0.001	0.0069

MGC: 9Cr-1Mo-V-Nb steel, MnA-MnJ: 2.25Cr-1Mo steels

Table 2. Heat treatment conditions of the steels studied.

Steel	Normalizing / Quenching	Tempering	
MGC	1,050°C/10min AC	765°C/30min AC	
MnA	920°C/2h FC, 930°C/2h WQ	640°C/4h WQ	620°C/2h FC
MnB	930°C/3.4h WQ	665°C/30h FC	
MnE	930°C/3h WQ	600°C/3h AC	625°C/4h FC
MnF	930°C/6h WQ	635°C/6h AC	600°C/2h AC
MnG	930°C/6h WQ	635°C/6h AC	600°C/2h AC
MnH	930°C/6h WQ	635°C/6h AC	600°C/2h AC
MnJ	900°C/70min WQ	630°C/75min AC	650°C/90min FC

AC: air cooling, WQ: water quenching, FC: furnace cooling

3. Results and discussion

3.1 Inhomogeneous recovery in 9Cr-1Mo-V-Nb steel

The stress vs. time to rupture curves of 9Cr-1Mo-V-Nb steel tested over the range of temperatures from 500 to 725°C are shown in Figure 1. In the long-term, the slope of the stress vs. time to rupture curve is steeper than that in the short-term. Remarkable change in slope of the curve, especially at 600 and 650°C, results in considerable overestimation for a prediction of long-term creep strength.

Rupture elongation (○) and reduction of area (●) of 9Cr-1Mo-V-Nb steel tested over the range of temperatures from 500 to 725°C are plotted against time to rupture and shown in Figure 2. Sufficient rupture ductility which is higher than 20% of elongation and 70% of reduction of area is observed in the short-term up to about 10,000h. However, it tends to decrease abruptly with exceeding 10,000h of creep exposure. Significant decrease in rupture ductility takes place corresponding to inflection of the stress vs. time to rupture curves observed at about 10,000h.

Bright field TEM images of 9Cr-1Mo-V-Nb steel (a) in the as tempered condition and the specimens creep ruptured at 600°C after (b) 971.2h at 160MPa, (c) 12,858.6h at 120MPa and (d) 34,141.0h at 100MPa are shown in Figure 3. Tempered martensitic microstructure with fine lath structure and high dislocation density is observed in the as tempered condition (Fig. 3(a)). Slightly recovered microstructure with increase in lath width and subgrain size and decrease in dislocation density is found in the specimen creep ruptured after 971.2h at 600°C-160MPa (Fig. 3(b)). Significant progress in recovery and collapsing of

lath martensite structure is observed in the specimen creep ruptured after 12,858.6h at 600°C-120MPa (Fig. 3(c)). On the other hand, different feature of the microstructural evolution is observed in the specimen creep ruptured after 34,141.0h at 600°C-100MPa (Fig. 3(d)). Markedly coarsened subgrain is observed along the prior austenite grain boundary, however, the microstructure within grain is still fine in comparison with that in the vicinity of grain boundary. Inhomogeneous recovery preferentially takes place in the vicinity of prior austenite grain boundary is a degradation mechanism in the long-term, in contrast to homogeneous recovery in the short-term [6]. It has been considered that decrease in rupture ductility in the long-term is caused by localized deformation due to inhomogeneous recovery.

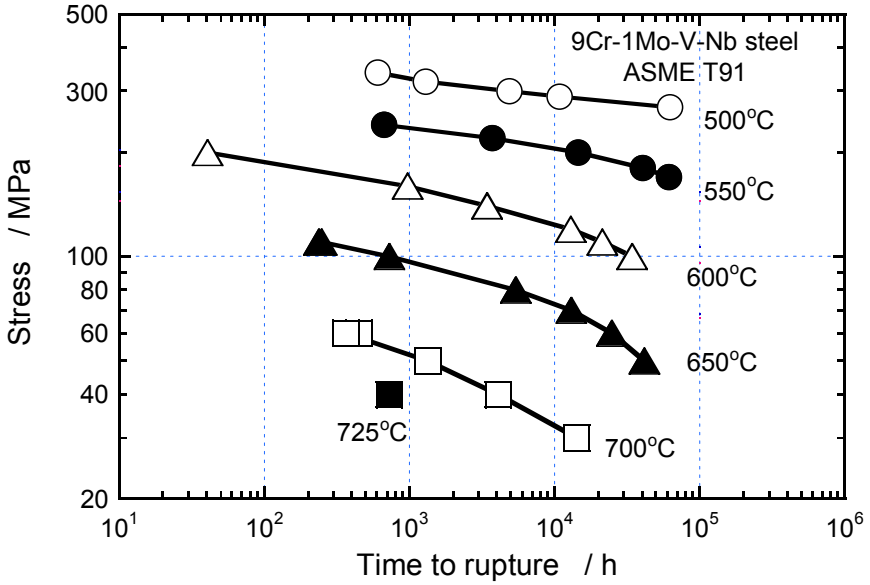

Figure 1. Stress vs. time to rupture curves of 9Cr-1Mo-V-Nb steel.

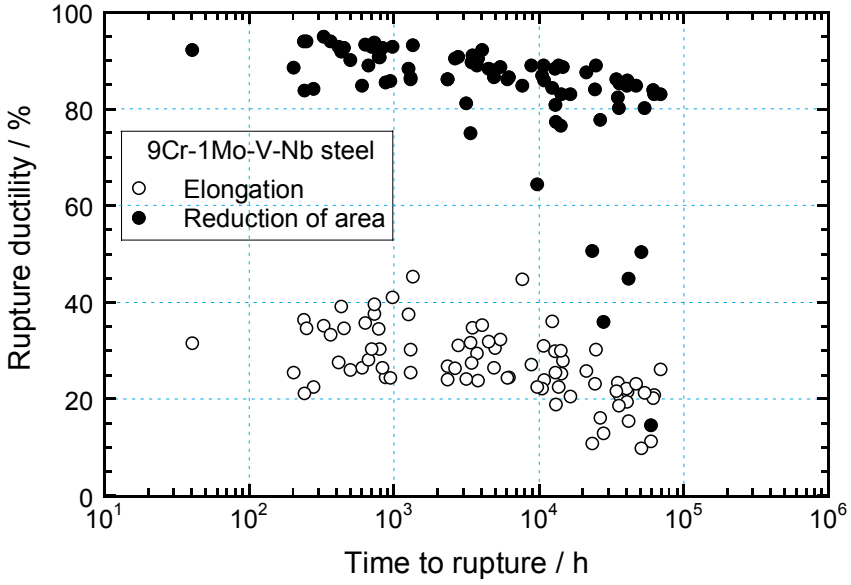

Figure 2. Rupture elongation and reduction of area of 9Cr-1Mo-V-Nb steel.

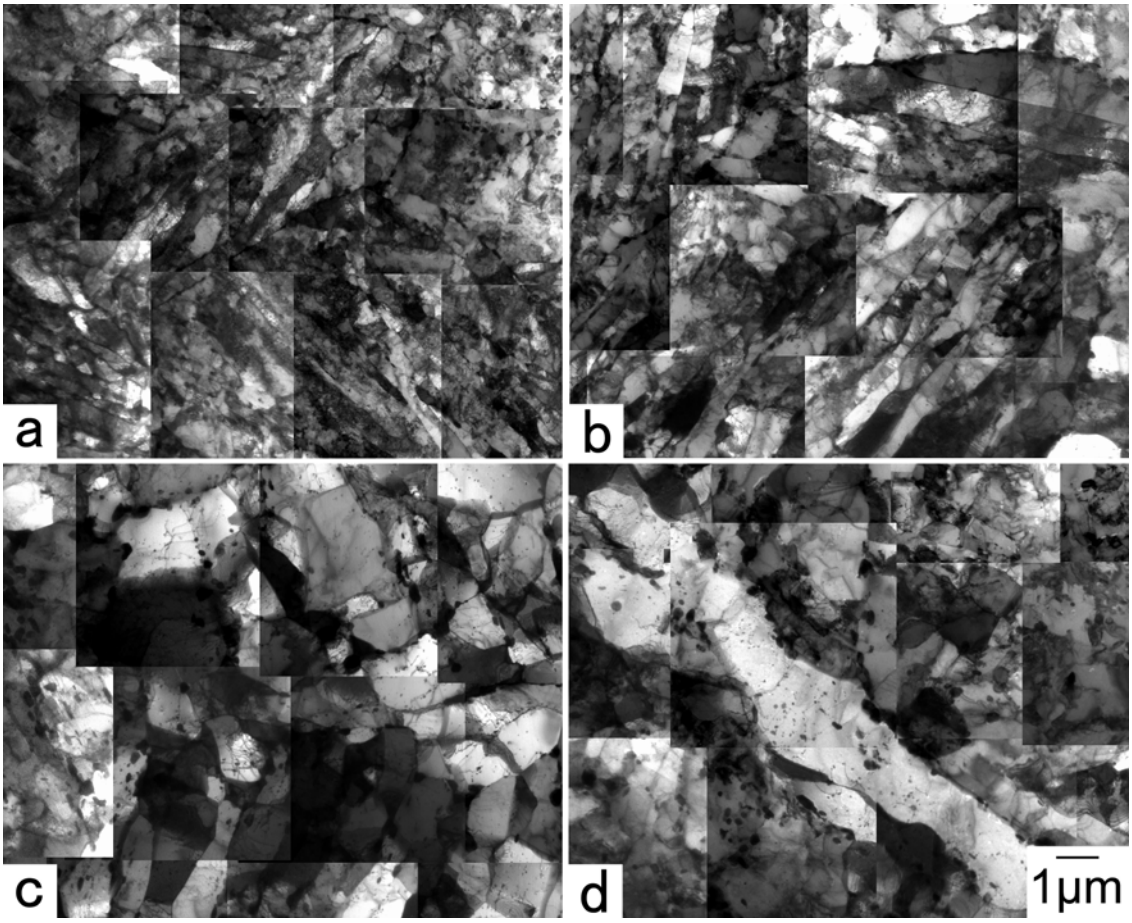

a) as tempered *b) t_r=971.2h*
c) t_r=12,858.6h *d) t_r=34,141.0h*

Figure 3. Bright field TEM images of 9Cr-1Mo-V-Nb steel (a) in the as tempered condition and specimen creep ruptured at 600°C after (b) 971.2h at 160MPa, (c) 12,858.6h at 120MPa and (d) 34,141.0h at 100MPa.

3.2 Creep rupture ductility of 2.25Cr-1Mo steels

The rupture elongation and the reduction of area of the 2.25Cr-1Mo steels tested over the range of temperatures from 450 to 650°C are plotted against a Larson–Miller parameter (C=20) and shown in Figure 4 and Figure 5, respectively. Behaviour of changes in rupture ductility with increase in creep exposure is clearly divided into first group consists of MnB and MnJ heats (solid symbol) and second one consists of the other heats (open symbol). Two heats of the first group indicate higher ductility than the other heats, which is higher than 20% of rupture elongation and higher than 80% of reduction of area, throughout the tested condition. Ductility of those two heats tends to increase slightly with increase in creep exposure. On the other hand, the other heats indicate significantly large change in rupture ductility, that is large drop and increase with increase in creep exposure. Although the ductility of the second group heats is

large in the short-term where a Larson–Miller parameter (LMP) is smaller than 17,000, similar to MnB and MnJ heats, it decreases abruptly in the range of LMP from 18,000 to 20,000. The ductility of the second group heats increases after long-term creep exposure. Remarkable change in ductility of the second group heats should be caused by microstructural evolution during creep exposure. The origin of the difference in rupture ductility between first group heats and second one should correspond to difference in evolution of microstructure during creep exposure.

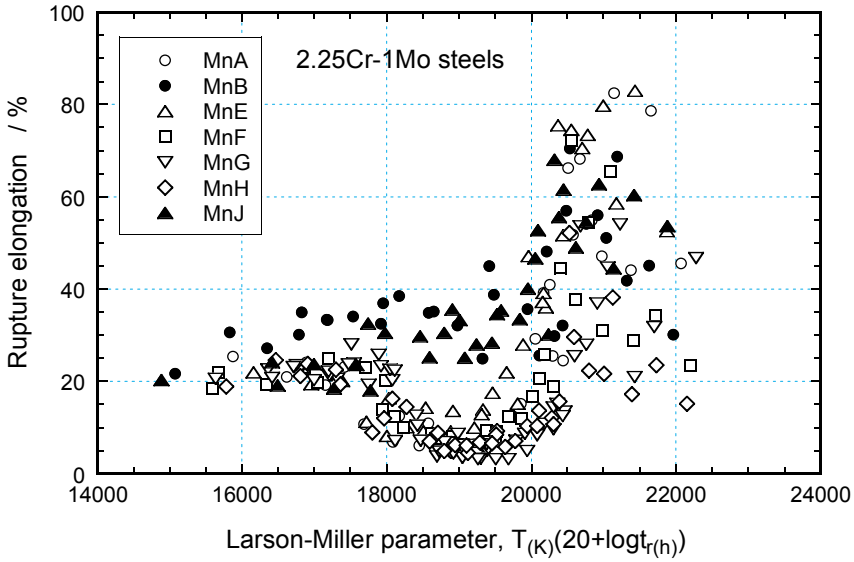

Figure 4. Rupture elongation of the 2.25Cr-1Mo steels plotted against a Larson–Miller parameter.

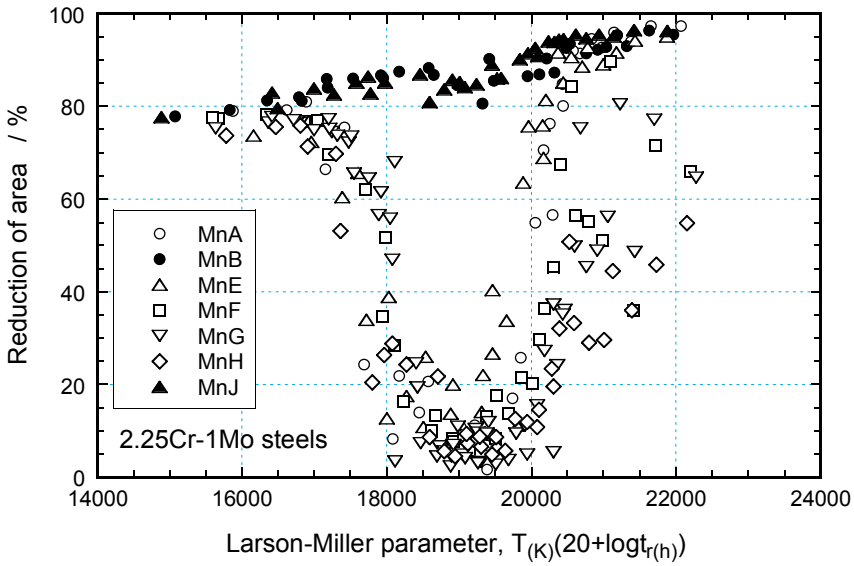

Figure 5. Reduction of area of the 2.25Cr-1Mo steels plotted against a Larson–Miller parameter.

3.3 Influence of tempering on ductility

Changes in reduction of area with increase in creep exposure time at 550°C of MnB and MnG heats of the 2.25Cr-1Mo steels are shown in Figure 6. The MnB heat has high value of reduction of area that is higher than 80%, independent of creep exposure time. On the other hand, the reduction of area of the MnG heat decreases from about 70% to less than 10% with increase in creep exposure time from 100 to 1,000h and increases with increasing creep exposure time beyond 10,000h. The rupture ductility of the MnG heat is significantly small in the time range from about 1,000 to 10,000h at 550°C.

Changes in Vickers hardness of the creep ruptured specimen of MnB and MnG heats with increase in creep exposure time at 550°C are shown in Figure 7. In the as tempered condition, the Vickers hardness of MnG heat is HV239 and it is higher than that of MnB heat of HV214. This difference in hardness should be caused by difference in tempering temperature, 635°C of MnG heat and 665°C of MnB heat. Vickers hardness decreased after creep exposure in both heats, and that of MnB heat was smaller than that of MnG heat even after short-term creep exposure. On the other hand, Vickers hardness of MnG heat was almost constant in the range of creep exposure time from 100 to 10,000h, and decreased remarkably after long-term creep exposure beyond 10,000h. After long-term creep exposure of 40,000 to 50,000h at 550°C, difference in hardness of both heats disappeared and Vickers hardness of both heats converged at about HV150. The difference in hardness of the creep ruptured specimen of two heats indicates difference in microstructural evolution during creep exposure, and it should correspond to marked difference in rupture ductility.

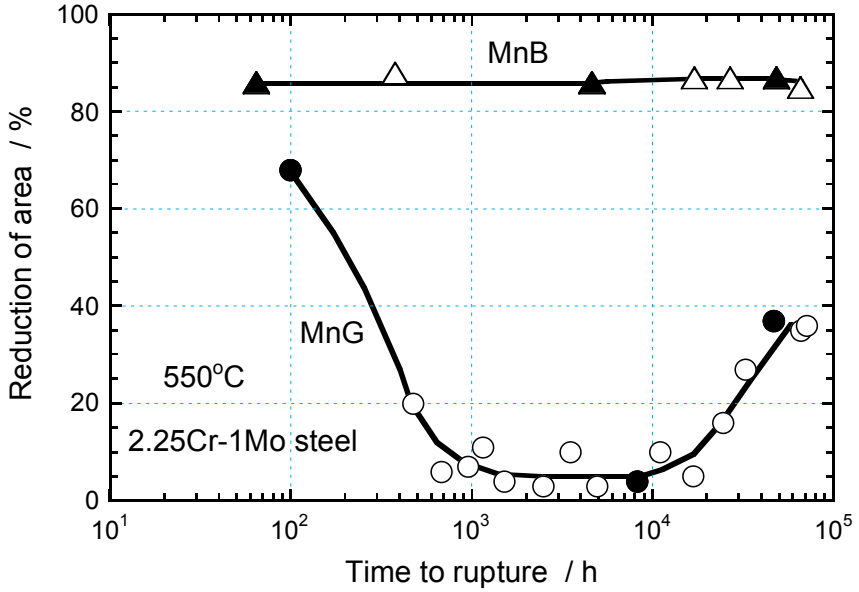

Figure 6. Changes in reduction of area with increase in creep exposure time at 550°C of MnB and MnG heats of 2.25Cr-1Mo steels.

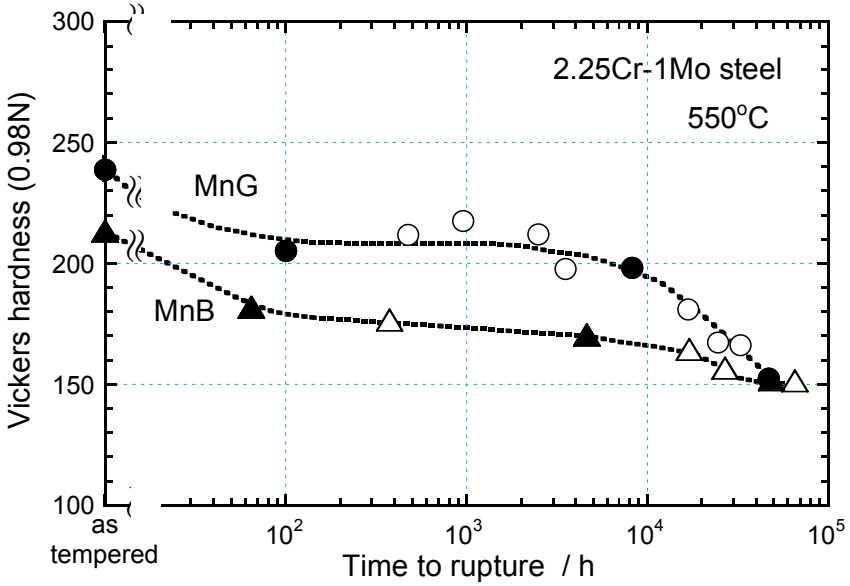

Figure 7. Changes in Vickers hardness with increase in creep exposure time at 550°C of MnB and MnG heats of 2.25Cr-1Mo steels.

In order to investigate a correlation between rupture ductility and microstructural evolution during creep exposure, microstructure of the creep ruptured specimen of MnG and MnB heats indicated by solid symbols in Figs. 6 and 7 were examined. Bright field TEM images of the MnG heat of 2.25Cr-1Mo steel (a) in the as tempered condition and specimen creep ruptured at 550°C after (b) 99.8h at 265MPa, (c) 8,203.0h at 137MPa and (d) 46,816.8h at 88MPa are shown in Figure 8. Tempered martensitic microstructure with fine lath and high dislocation density was observed in the as tempered condition (Fig. 8(a)). Homogeneously recovered microstructure consists of increased lath width and decreased dislocation density has been observed in the specimen creep ruptured after 99.8h (Fig. 8(b)). On the other hand, inhomogeneous progress in recovery was found in the specimen creep ruptured after 8,203.0h (Fig. 8(c)). In the specimen creep ruptured after 46,816.8h (Fig. 8(d)), martensitic lath structure has completely disappeared and dislocation density has significantly decreased.

Bright field TEM images of MnB heat of 2.25Cr-1Mo steel (a) in the as tempered condition and specimen creep ruptured at 550°C after (b) 64.3h at 216MPa, (c) 4,614.5h at 137MPa and (d) 48,458.3h at 88MPa are shown in Figure 9. In the as tempered condition, dislocation density of MnB heat was lower than that of MnG heat, corresponding to higher tempering temperature and lower hardness of MnB heat. In contrast to MnG heat, increase in lath width and decrease in dislocation density has proceeded homogeneously with increase in creep exposure time in MnB heat. Progress in recovery during creep exposure was not inhomogeneous, but homogeneous in MnB heat. Inhomogeneous progress in recovery was observed only in the specimen of MnG heat creep ruptured after 8,203.0h at 137MPa whose rupture ductility was significantly low (Fig. 8 (c)).

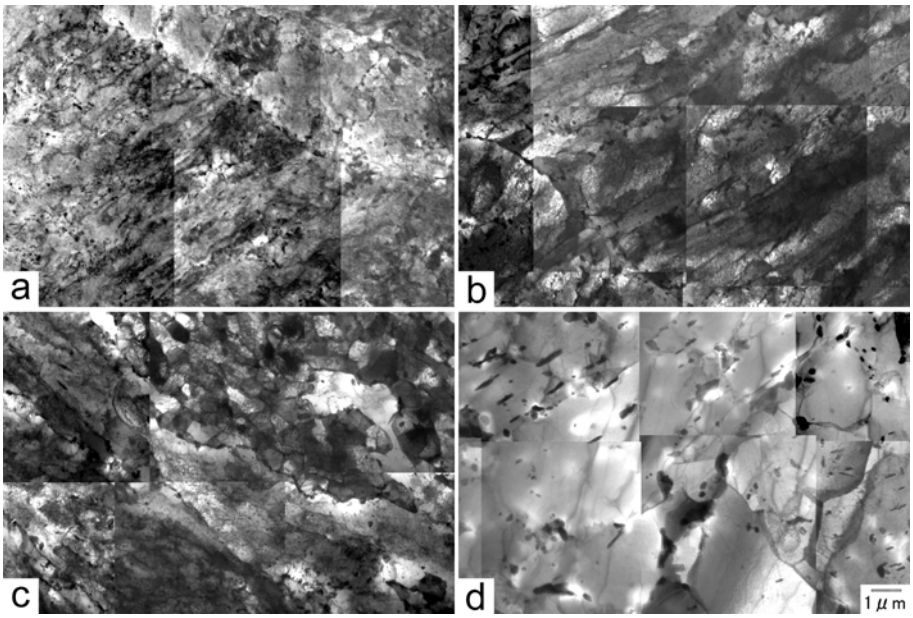

a) as tempered *b) t_r=99.8h, El=22%, RA=68%*
c) t_r=8,203.0h, El=3%, RA=4% *d) t_r=46,816.8h, El=14%, RA=37%*

Figure 8. Bright field TEM images of MnG heat of 2.25Cr-1Mo steel (a) in the as tempered condition and specimen creep ruptured at 550°C after (b) 99.8h at 265MPa, (c) 8,203.0h at 137MPa and (d) 46,816.8h at 88MPa. El: rupture elongation, RA: reduction of area.

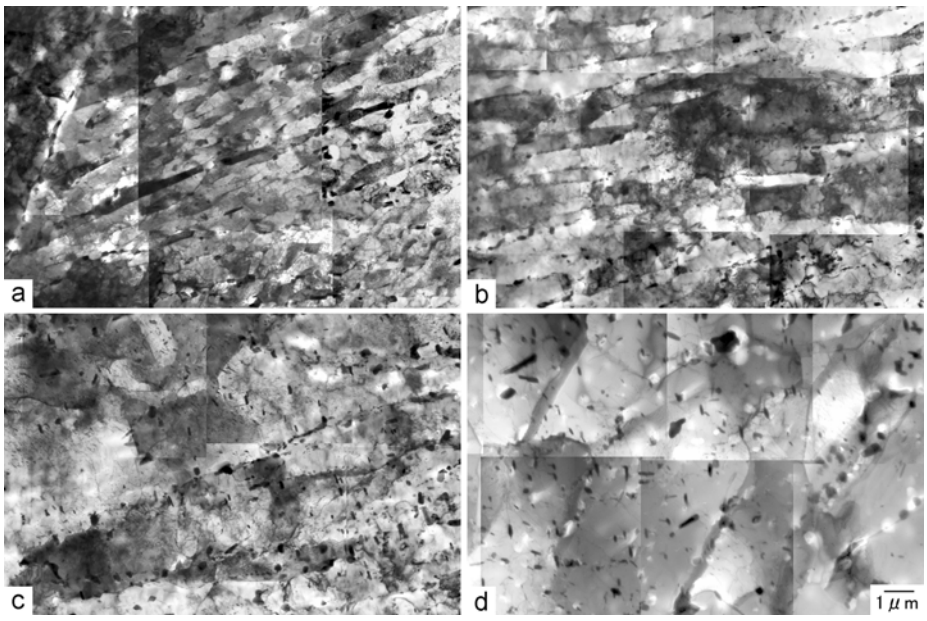

a) as tempered *b) t_r=64.3h, El=37%, RA=86%*
c) t_r=4,614.5h, El=39%, RA=86% *d) t_r=48,458.3h, El=30%, RA=87%*

Figure 9. Bright field TEM images of MnB heat of 2.25Cr-1Mo steel (a) in the as tempered condition and specimen creep ruptured at 550°C after (b) 64.3h at 216MPa, (c) 4,614.5h at 137MPa and (d) 48,458.3h at 88MPa.

The Vickers hardness of the 2.25Cr-1Mo steels in the as tempered condition was plotted against the tempering temperature and shown in Figure 10. Higher tempering temperature was used for the double tempered heats. The Vickers hardness decreases with increase in tempering temperature. Tempering temperature of MnB and MnJ heats which possess high ductility throughout the tested condition is higher than those of the other heats, and hardness of former two heats is lower than the others. Inhomogeneous progress in recovery was observed in the creep ruptured specimen of MnG heat, corresponding to significant low ductility. It has been supposed that ductility drop does not take place in MnB and MnJ heat as a result of homogeneous progress in recovery due to higher tempering temperature and softened microstructure in the as tempered condition. A role of low aluminum content on higher ductility should be also investigated in the future, since aluminum contents of MnB and MnJ heats are lower than those of the others.

Creep rate vs. time and strain curves of MnB and MnH heats at 600^{o}C and 98MPa are compared and shown in Figure 11. Creep deformation consisted of transient and accelerating creep stages and no obvious steady state region was observed on both heats. Although minimum creep rate of MnH heat was smaller than that of MnB heat, accelerating creep stage of MnH heat started at earlier and smaller strain than those of MnB heat. The onset of accelerating creep stage of MnH heat should be promoted by inhomogeneous recovery and, therefore, the rupture ductility of MnH heat is smaller than that of MnB heat. It has been concluded that significant decrease in rupture ductility is caused by inhomogeneous progress in recovery of tempered martensitic microstructure during creep exposure, and higher rupture ductility should be maintained by retarding inhomogeneous progress in recovery.

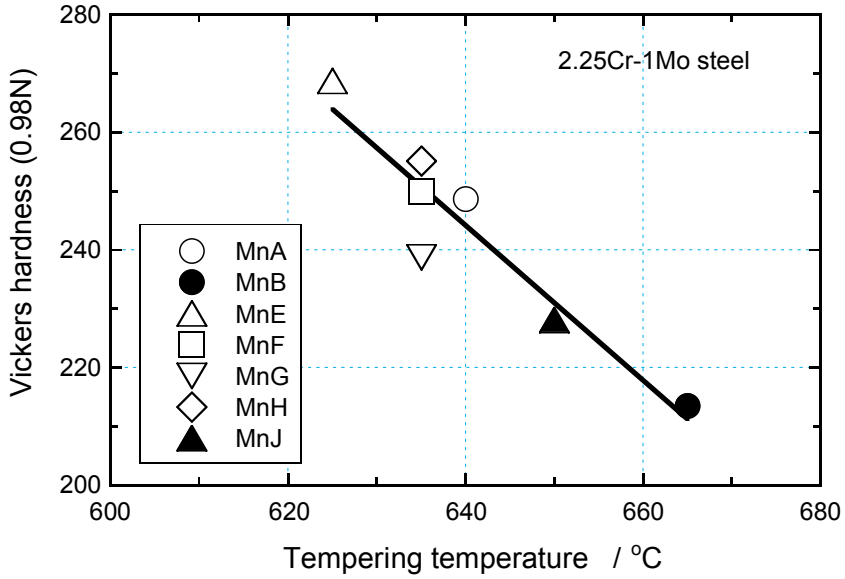

Figure 10. Relation between tempering temperature and Vickers hardness of 2.25Cr-1Mo steels in the as tempered condition.

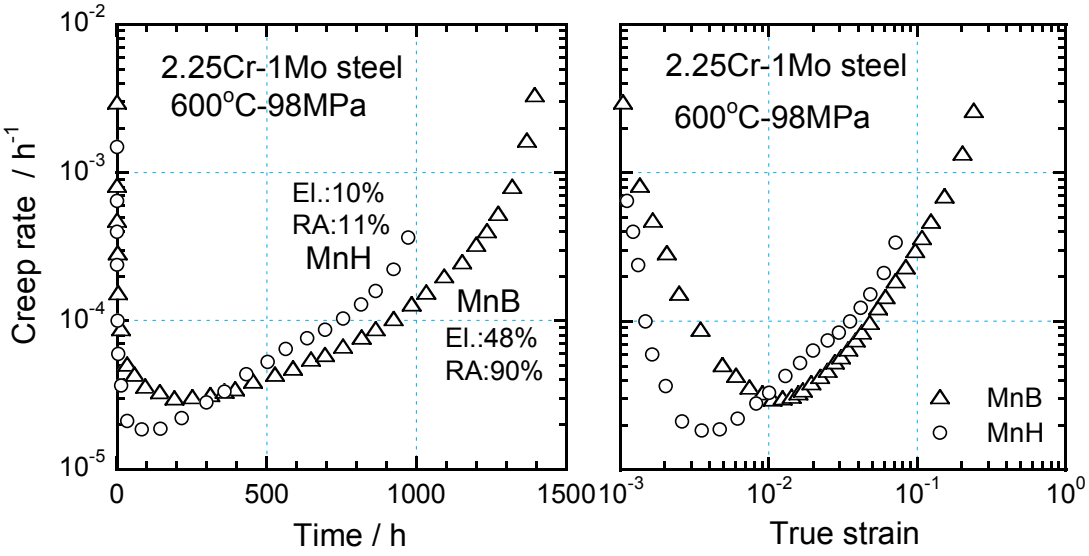

Figure 11. Creep rate vs. time and strain curves of MnB and MnH heats of 2.25Cr-1Mo steels at 600°C and 98MPa.

4. Conclusions

In order to investigate a correlation between rupture ductility and inhomogeneous recovery in the vicinity of prior austenite grain boundary, creep rupture ductility has been examined on multi heats of quenched and tempered 2.25Cr-1Mo steels. The following results are obtained.

1. Inhomogeneous recovery preferentially takes place in the vicinity of prior austenite grain boundary was observed in the creep exposed 9Cr-1Mo-V-Nb steel, corresponding to marked decrease in creep strength and rupture ductility in the long-term.

2. The 2.25Cr-1Mo steels tempered at higher temperatures had high rupture ductility throughout the tested condition, and ductility of those tempered at lower temperatures decreased with increasing creep exposure time and increased after long-term creep exposure.

3. Inhomogeneous progress in recovery was observed in the creep ruptured specimen whose rupture ductility was significantly low. In the specimen creep ruptured with increased rupture ductility after long-term creep exposure, martensitic lath structure was completely disappeared and dislocation density was significantly decreased.

4. It has been considered that ductility does not decrease if tempering temperature is high enough and recovery of microstructure progress homogeneously.

5. It has been concluded that significant decrease in rupture ductility is caused by inhomogeneous progress in recovery and higher rupture ductility should be maintained by retarding inhomogeneous progress in recovery.

References

[1] V.K. Sikka. 'Development of Modified 9Cr-1Mo Steel for Elevated-temperature Service'. *Proc. of Topical Conf. on Ferritic Alloys for Use in Nuclear Energy Technologies,* J.W. Davis & D.J. Michel eds., TMS-AIME, Warrendale, Pennsylvania, USA, (1984). Pp. 317–327.

[2] M. Sakakibara, H. Masumoto, T. Ogawa, T. Takahashi & T. Fujita. 'High Strength 9Cr-0.5Mo-1.8W Steel (NF616) Tube for Boilers'. *Thermal Nuclear Power*, 38(1987), pp. 841–850.

[3] A. Iseda, A. Natori, Y. Sawaragi, K. Ogawa, F. Masuyama & T. Yokoyama. 'Development of High Strength and High Corrosion Resistance 12%Cr Steel Tubes and Pipe (HCM12A) for Boilers'. *Thermal Nuclear Power*, 45(1994), pp. 900–909.

[4] M. Staubli, W. Bendick, J. Orr, F. Deshayes & Ch. Henry. 'European Collaborative Evaluation of Advanced Boiler Materials'. *Proc. of 6th Liege Conference on Materials for Advanced Power Engineering 1998*, J. Lecomte-Beckers et al. eds. Forschungszentrum Jülich GmbH, Liege, Belgium, October 1998, 5(1998). Pp. 87–103.

[5] V. Foldyna, Z. Kuboň, A. Jakobová & V. Vodárek. 'Development of Advanced High Chromium Ferritic Steels'. *Microstructural Development and Stability in High Chromium Ferritic Power Plant Steels,* A. Strang & D.J. Gooch eds., The Institute of Materials, 1997. Pp. 73–92.

[6] K. Kimura, H. Kushima & F. Abe. 'Heterogeneous changes in Microstructure and Degradation Behaviour of 9Cr-1Mo-V-Nb Steel During Long Term Creep'. *Key Engineering Materials*, 171–174(2000), pp. 483–490.

[7] K. Kimura, H. Kushima & F. Abe. 'Degradation and Assessment of Long-term Creep Strength of High Cr Ferritic Creep Resistant Steels'. *Proc. of EPRI Inter. Conf. on Advances in Life Assessment and Optimization of Fossil Power Plants*, EPRI, 2002.

[8] NRIM Creep Data Sheet, National Research Institute for Metals, No. 43(1996).

[9] NIMS Creep Data Sheet, National Institute for Materials Science, No. 36B(2003).

Assessment of long-term creep properties, creep failure and strength reduction factor of boiler tube and pipe weldments

Z. Kuboň & J. Sobotka
VÍTKOVICE Research and Development Ltd.
Ostrava, Czech Republic

Abstract

The paper summarises and analyses the results of long-term creep tests on both base material as well as welded joints made of steels 13 CrMo 4 4, 10 CrMo 9 10 (superheater tubes) and P 91 (steam pipe). The weakest locality controlling the creep rupture strength of all weldments is the intercritical part of the heat affected zone and in all cases the decline in creep strength of the weldment compared to the base material increases with increasing creep testing temperature and time. To quantify this, a strength reduction factor (SRF) is calculated for all weldments and microstructural analysis used to determine the failure locality exactly.

1. Introduction

Low-alloy CrMo creep resistant steels of the 1%Cr-0.5%Mo or 2.25%Cr-1%Mo types (Grade 11 or 12 and Grade 22, respectively) are broadly used in piping systems of power plant operating at temperatures up to 600°C. In the last decade great efforts have been made to increase steam temperatures as the way of thermal efficiency improvement and/or the restriction of CO_2 emissions. A new generation of creep resistant steels based on martensitic 9%Cr-1%Mo modified steel (Grade 91) has been developed, as low-alloy steel grades do not achieve sufficient long-term creep strength and high-temperature oxidation resistance for these applications. Despite the acceptable level of creep rupture strength of these steels, welded joints of boiler tubes are typically inferior to those base metals even, in numerous cases, to the applied weld metals.

This problem appears in consequence to type IV damage and cracking, i.e. preferential fracture locality in the intercritical part of heat affected zone (IC HAZ) near the transition to unaffected base metal. This phenomenon has been identified in most types of ferritic steels during,

- long-term operating service at high temperatures and pressures, and
- cross weld creep rupture testing.

Low-alloy creep resistant Cr-Mo steels of 0.3 to 0.5%Mo, 1%Cr-0.5%Mo and 2.25%Cr-1%Mo type were developed in the middle of the last century and widely used in power generation industry. Their compositions were based on the well-known solid solution strengthening mechanism with molybdenum atom in solid solution as well as precipitation strengthening by dispersed particles of Mo_2C and $M_{23}C_6$ carbides, the latter being especially found in steels with higher chromium contents. Carbon contents from 0.1 to 0.2% are typical in these steels to achieve sufficient short-term mechanical properties. Nevertheless, the long-term creep strength is relatively low in these steels, especially in comparison with low alloy CrMoV steels of 0.5%Cr-0.5%Mo%0.3%V and 0.8%Cr-0.5%Mo-0.6%V types. This shortness in long-term creep strength was overcome by using martensitic 12%Cr steels with a mean carbon content about 0.2% modified by additions of Mo, V, W and Nb. However the improved creep resistance of the modified 12%Cr steels was accompanied by poorer weldability owing to their higher carbon equivalent content and susceptibility to cold and annealing cracking as well as formation of regions in heat affected zone of weldments with high strength and low toughness. In order to solve these problems, the maximum carbon content was restricted to 0.10% and alloying with Mo, V, Nb and N was adopted. The typical representative of this trend is the martensitic steel P 91, which has a balanced chemical composition and up to about 50% higher creep rupture strength compared to earlier 12%Cr modified steels.

The intercritical region of heat affected zone seems to be the critical locality where creep fracture appears in tubes and pipes made from all of the mentioned low-alloy and modified chromium steels. The creep strength of welded joints is lower compared to that of the base material due to type IV cracking and, as a result, creep life of weldments is also shorter than that of the adjacent base material. Type IV cracking is a fracture appearing in the heat affected zone close to the base metal during long-term creep exposure or during cross weld creep rupture tests.

The declination of the slope of the stress-time to rupture curves observed in welded joints compared to the same dependency of the base material is a typical feature of type IV cracking being a dominant failure process. This is particularly evident in low stress regions and times to rupture exceeding 10^4 h [1–10].

Regardless the same mechanism and features, the drop of creep strength and creep life seems to be more pronounced in the advanced steels than in common grades of low alloy ferritic steels, because the creep rupture strength of base metal was increased but the same is not true for the creep rupture strength of welded joints

The aim of this paper is to quantify the drop of creep rupture strength of weld joints of the above-mentioned creep resistant steels.

2. Experiments and methods

2.1 Experimental material

For the present work, welded joints of superheater tubes ø38x4.5 mm made of 1%Cr-0.5%Mo (Grade 11 or 12) and 2.25%Cr-1%Mo (Grade 22) steel were prepared by using automated TIG orbital welding with controlled heat input about 0.6 kJ/mm. The wire OK Autrod 13.12 (GCrMo1Si according to EN 12070) was used as welding consumable in 1%Cr-0.5%Mo steel and SG CrMo2 in 2.25%Cr-1%Mo steel, in both case with the diameter 0.8 mm. No preheating was used in both cases. Mechanical as well as creep properties were tested in as-welded state (1%Cr-0.5%Mo steel) and after post-weld heat treatment performed at 720°C/2 h in 2.25%Cr-1%Mo steel. The chemical composition and mechanical properties of both steels are stated in Table 1.

Table 1. Chemical composition and mechanical properties of the base materials.

Steel	C	Mn	Si	P	S	Cr	Mo	V	Nb	N	R_e	R_m
	mass.%										MPa	
Grade 11	0.14	0.56	0.26	0.011	0.006	0.89	0.49	0.01	-	-	377	514
Grade 22	0.10	0.49	0.28	0.009	0.010	2.17	0.92	0.01	-	-	400	572
P 91	0.10	0.40	0.43	0.015	0.006	8.5	0.88	0.23	0.10	0.045	535	698

Pipe ø324x28 mm made from the 9% chromium modified P91 steel was used as the third material in which the long-term properties of weldments were tested. The circumferential weldment was prepared by a manual metal arc technique using FOX C9MV electrodes. Preheating and interpass temperature was kept in the interval 250 to 300°C. After welding the pipe was post-weld heat treated at 750°C for 5 hours. The electrodes used were of the Cr-Mo-V type so that there was a good chance to keep the high level of precipitation strengthening by vanadium-rich MX phase, even in the weld metal. The chemical compositions and ambient temperature mechanical properties of the base metal is stated in Table 1.

2.2 Methods of processing of the results

The creep properties of both base metals and welded joints were tested by uniaxial tensile cross-weld creep tests. Test bars of circular cross section were oriented perpendicularly to the weld axis. Testing temperatures and stresses typical for service applications of the respective steels were used, i. e. in case of 1%Cr-0.5%Mo steel 525 and 550°C, 550 and 575°C in steel 2.25%Cr-1%Mo and from 575 to 650°C in case of steel P91.

The creep rupture test results were processed using the Seifert parametric equation that correlates the applied stress and parameter $P = [T(C+\log t_r) \cdot 10^{-4}]$ in the form [11]:

$$\log R_{mT} = A_0 + A_1 P + A_2 P^2 \tag{1}$$

where R_{mT} is creep rupture strength (MPa), T is the test temperature in Kelvin, t_r is time to rupture in hours and C, A_0, A_1,A_2 are optimised constants.

The effect of welded joints in boiler pipes/tubes can be expressed by using the restriction coefficient W_r showing the extent of lowering of the creep strength and lifetime of the respective component. This coefficient should be used in the calculation of wall thickness S_v [12]:

$$S_v = \frac{p \cdot D_i}{(2\sigma_D - p) \cdot W_r} \tag{2}$$

where p represents the steam pressure, D_i is the inside diameter of tube/pipe and σ_D is the maximum allowable stress at temperature T_v in the tube wall

At the same time, the following relation is valid

$$W_r \le W_r^{\max} = f(T_v, t_r) \le 1 \tag{3}$$

here t_r is time to rupture and W_r^{max} represents the maximum value of W_r valid for the maximum loading of the weldment by the applied stress σ, oriented perpendicularly to the weld axis.

The optimum method of determining realistic restriction coefficient W_r^{max} values seems to be using uniaxial creep tests with the loading direction perpendicular to the welded joint. Such a test enables evaluation of both the stress-temperature dependence of the creep rupture strength as well as the failure locality in the weldment. However, the common practice of assessment of the maximum value of the restriction coefficient W_r^{max} is to compare the evaluated creep rupture strength of welded joints $R_{mT}(W)$ with the respective standard mean value of creep rupture strength for the same material - R_{mT} (AP):

$$W_r^{\max} = \frac{R_{mT}(W)}{R_{mT}(AP)} \le 1 \tag{4}$$

However, this approach is problematic because of the fluctuation of creep rupture strength that is acceptable for the individual heats and products of the same material [13, 14].

One of the possible methods to solve this problem is to replace the standardised value $R_{mT}(AP)$ in equation (4) by estimation of the creep rupture strength of the used boiler tube [15]. Such an estimation is only possible when the correlation between the creep properties (R_{mT} or t_r) and yield stress, tensile strength, microstructural parameters or creep rate is available [14, 16–18].

The best way to cope with the problem of the welded joint restriction parameter is to determine the maximum value of W_r^{max} by analysis of results of parallel long-term creep tests of both welded joints and base metal, i.e. the tube/pipe used for the preparation of weld joint [2]. In that case, the strength reduction factor SRF can be expressed in the form:

$$W_r^{\max} = SRF = \frac{R_{mT}(W)}{R_{mT}(BT)} = f(t_r, T) \leq 1 \tag{5}$$

where $R_{mT}(BT)$ is the creep rupture strength of base material (boiler tube).

Similarly to the conception of SRF there is a possibility to assess the shortening of the creep lifetime of the welded joint by using the lifetime reduction factor LFR [2]:

$$LRF = \frac{t_r(W)}{t_r(BT)} = f(\sigma, T) \leq 1 \tag{6}$$

here $t_r(W)$ is time to rupture of the welded joint and $t_r(BT)$ is time to rupture of base material (boiler tube), both evaluated at the same applied stress or lifetime of the base material.

3. Results

The results of creep rupture strength for creep life from 10^4 to 10^5 hours are summarized for all of the evaluated materials in Table 2. In parenthesis there are stated creep rupture strength values that are outside of the accepted extrapolation limit as specified in standard ISO 6303 [19]. Comparison of long-term creep strength of both base materials and weld joint is shown for all materials in Figs. 1, 3 and 4. The data are presented there in the form of temperature and stress dependence of time to rupture and temperature-time dependence of SRF.

Table 2. Creep rupture strength of weld joints (W) and base materials (BT) of the evaluated steels.

Material	T (°C)	t_r (h)	R_{mT}(W)	R_{mT}(BT)	R_{mT}(AP)	SRF	$\frac{R_{mT}(W)}{R_{mT}(AP)}$
			(MPa)				
Grade 11	525	10^4	140	141	165	0.99	0.85
		10^5	(63)	73	89	0.86	0.71
	550	10^4	86	88	110	0.98	0.78
		10^5	(36)	45	53	0.80	0.68
Grade 22	550	10^4	100	99	108	1	0.93
		10^5	62	67	69	0.92	0.90
	575	10^4	74	77	80	0.96	0.93
		10^5	(43)	48	47	0.90	0.91
Grade 91	575	10^4	113	138	159	0.82	0.71
		10^5	(81)	(108)	127	0.75	0.64
	600	10^4	83	108	123	0.77	0.67
		10^5	(58)	(82)	94	0.70	0.62
	625	10^4	60	82	94	0.73	0.64
		10^5	(40)	(61)	69	0.66	0.58

3.1 Grade 11

The results of creep rupture tests on both the base metal and welded joints together with the time dependence of strength reducing factor SRF are shown in Fig. 1. The curves describing the creep rupture strength of welded joint for times up to about $5 \cdot 10^3$ hours lie above those of base metal. Therefore, the strength reduction factor SRF in these cases equals 1. At longer times however, the decline of time dependence of the creep rupture strength of the welded joint is steeper and the SRF falls down as can be seen in the upper part of Fig. 1. It is expected that the higher the testing temperature the more pronounced is the difference between time to rupture and creep rupture strength of the welded joint and base material especially at higher temperatures and longer times to rupture.

The value of the strength reduction factor in 10^5 hours, SRF=0.86 and 0.80 for 525°C and 550°C, respectively seems to be fully acceptable for circumferential weld joints loaded primarily by the internal steam pressure. In most applications such high values could enable the designer to avoid the need to apply the restriction coefficient in the calculation of the allowable stress for respective components.

Creep tests confirmed the intercritical region of heat affected zone with tempered and partially reaustenized microstructure as a prevailing rupture locality in these joints [4, 7, 10, 20–23]. Type IV cracking of the specimen crept at 550°C and 80 MPa for 34229 hours is demonstrated in Fig. 2 also with a detail of a massive

cavitation in the fine-grained microstructure of the weakest locality on the opposite side to the rupture point of the weld joint.

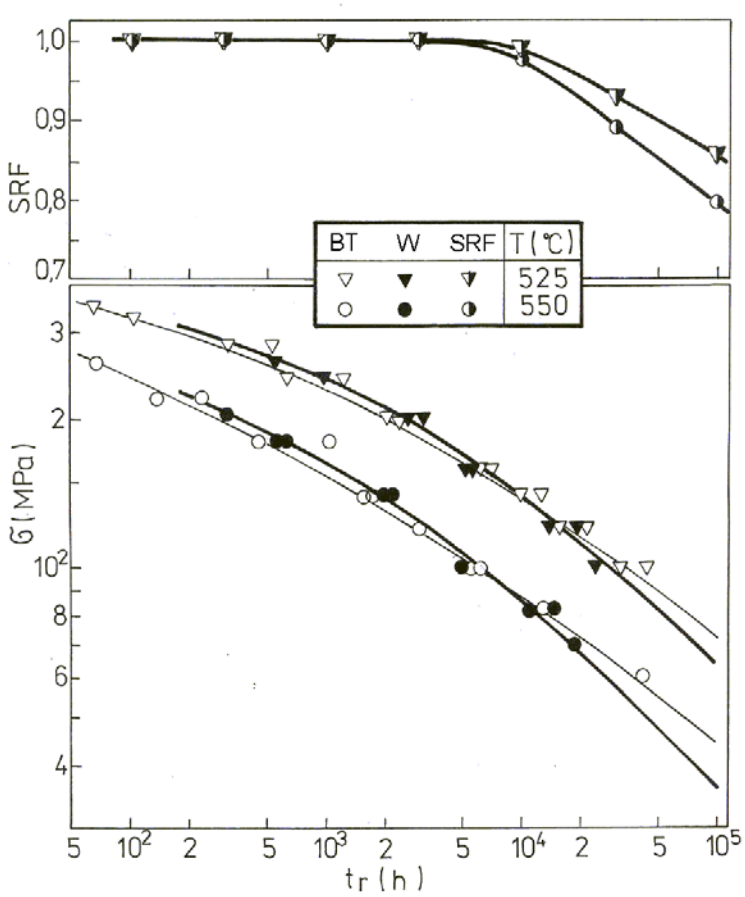

Figure 1. Stress—time-to-rupture dependence and SRF of Grade 11 steel.

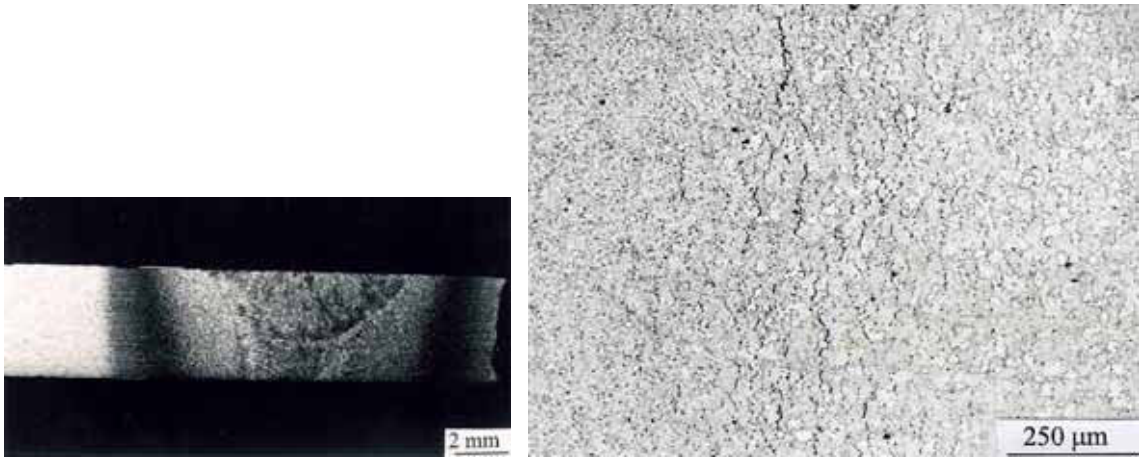

Figure 2. Macrostructure and cavitation in the fractured part of creep specimen after exposure 550°C/80 MPa/ 34229 h.

3.2 Grade 22

The results of creep rupture tests of base metal and weld joint are shown together with SRF in Fig. 3.

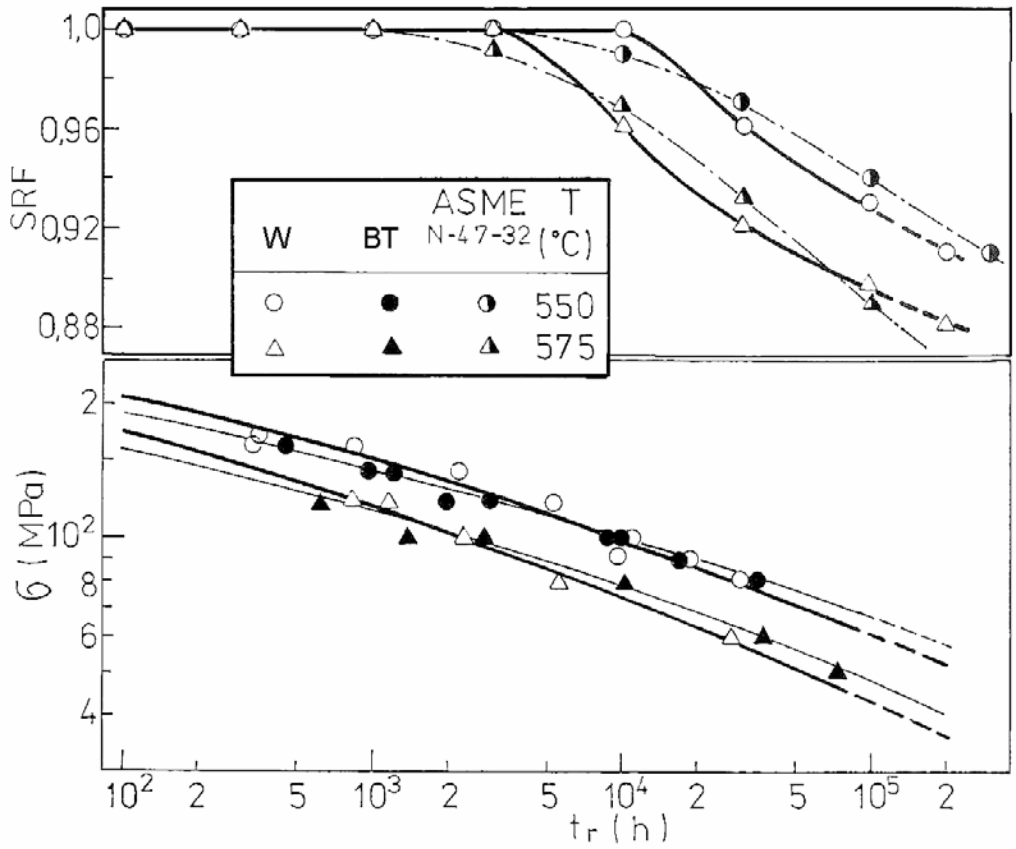

Figure 3. Stress—time-to-rupture dependence and SRF of Grade 22 steel.

Despite the fact that intercritical region of the HAZ acts as the preferential critical weld locality as far as the long-term creep rupture strength is concerned, the curves describing the creep rupture strength of the welded joint are very close to those for the base metal, even at longer times to rupture. It can be expected that the strength reduction factor SRF in this material will be higher and close to 1 even at relatively long-term creep exposures. SRF in the upper part of Fig. 3 is compared with the recommended values stated in the ASME Code Case N 47-32 [24]. In comparison to the Grade 11 steel, the deviation of the SRF from unity starts at longer times and the drop of creep rupture strength is much smaller in the Grade 22 steel than in the previous material. It is not surprising that high values of the strength reduction factor in 10^5 hours are fully acceptable for circumferential welded joints loaded primarily by internal steam pressure and means that there is no need to use the restriction coefficient in the calculation of the allowable stress for the design of respective components.

3.3 Grade 91

Similarly as in the previous cases, the results of the creep rupture tests on the welded joint are shown together with SRF in Fig. 4. This weldment shows a very pronounced drop of SRF with increasing temperature and/or time to rupture.

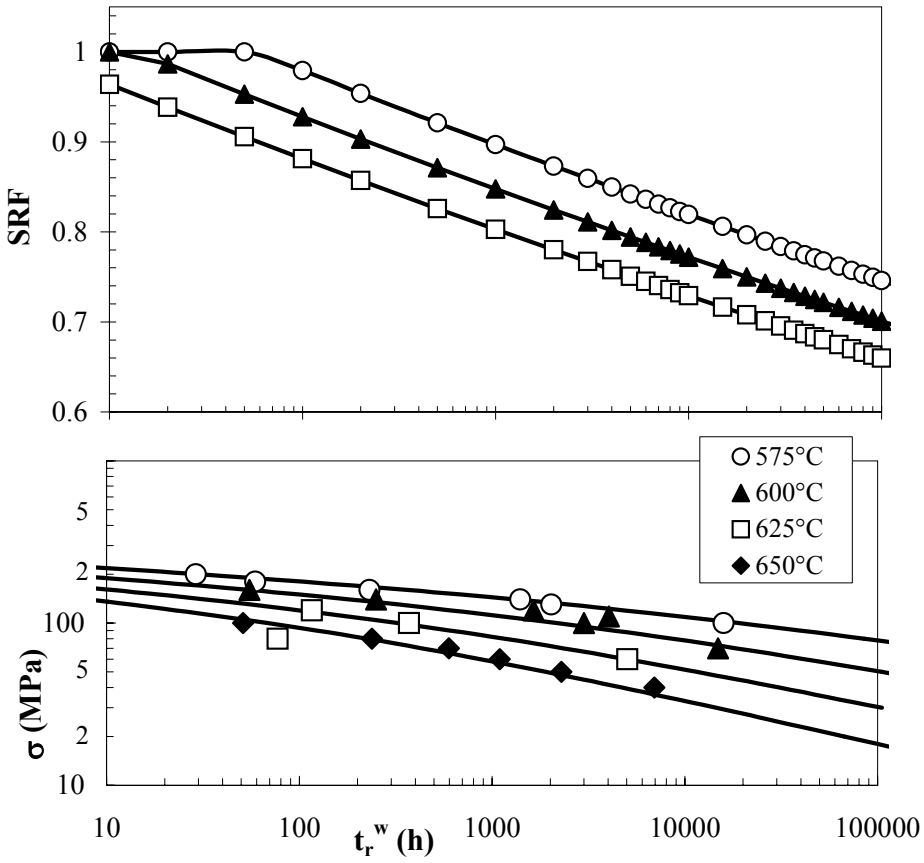

Figure 4. Results of creep tests of weld joint and SRF of Grade 91 steel.

Such behaviour can be expected especially in precipitation strengthened materials where degradation processes due to high temperature tempering and partial reaustenizing in the IC HAZ have a harmful effect on small precipitates and hence to the creep strength of the weldments. In the present welded joint the deviation of the SRF from unity starts at very short times to rupture except at the lowest temperature 575°C, but even there the drop starts at about 100 hours. Low values of the strength reduction factor in 10^5 hours being only 0.7 at 600°C indicate the necessity of using the restriction coefficient in the calculation of the allowable design stress of the respective component.

The time-temperature dependence of the life reduction factor LRF for the Grade 91 steel welded joint is shown in Fig. 5. From this it can be seen that the LRF factor markedly drops down with increasing temperature and/or time to rupture

and its value is as low as 0.10 at 600°C and 10^5 hours. It is evident that special attention should be paid to the maximum allowable stress in weldments of parts working in the pressurised system especially at temperatures close to 600°C.

Creep tests confirmed that the intercritical region of the heat affected zone is entirely the preferential rupture locality in this material. This is demonstrated in Fig. 6 showing the macrograph of the specimen crept at 650°C and 40 MPa for 16775 hours.

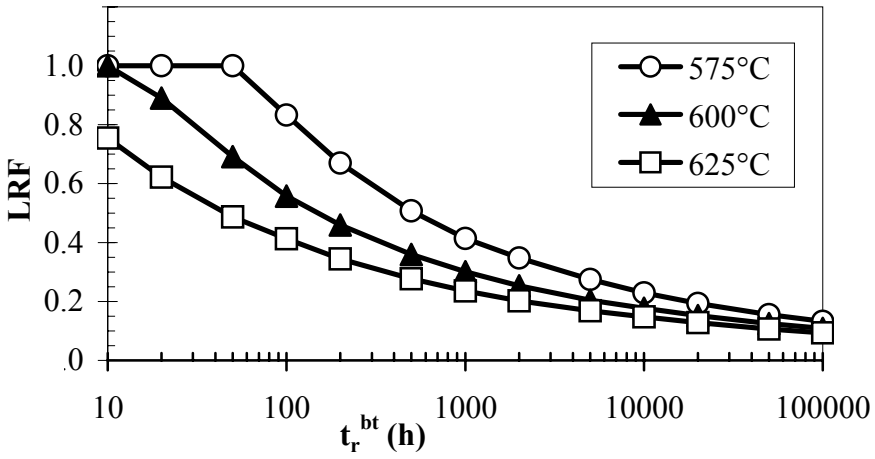

Figure 5. Life reduction factor of weld joint of Grade 91 steel.

Figure 6. Type IV cracking of steel 91 after creep exposure 650°C/40 MPa/16775 h.

4. Discussion and concluding remarks

In order to ensure the maximum reliability and credibility of the creep test results, the extent and parameters of testing of the welded joint as well as the base metal should:

- correspond to the behaviour and failure of the circumferential weld joints during exposure in the tube/piping system of steam boilers

- enable reproducibility and extrapolation to the typical lifetime of boiler tubes and/or pipes
- assure generalization to the various working conditions and corresponding changes of stress state of the weldment during exposure
- enable estimation of the restriction coefficient of the allowable stress.

In comparison to the base material, the weakest locality of the welded joint represents a narrow zone typically with the lowest creep resistance that is

- surrounded by zones with higher creep resistance
- characterized by preferential creep fracture
- limiting the lifetime of the tube/piping system of the steam boiler.

The results presented in this paper confirmed the previous ideas about the behaviour of welded joints prepared from either CrMo or CrMoV steel tubes [1–10]. Precipitation strengthening in CrMoV steels enhances the creep rupture strength of the base material as well as that of the welded joint. On the other hand, the creep strength of the typically weakest part of the welded joint – IC HAZ – is not improved to the same extent as the base material. Therefore, the difference between the creep strength of IC HAZ of CrMo and CrMoV steels is not so significant as in the base metals. That is why the value of the strength reduction factor in CrMoV steels is usually lower than that in CrMo steels, in which the role of precipitation strengthening is clearly less important, especially at long times to rupture.

The IC HAZ is a typical failure location for all commercially used low alloy and chromium modified steels. Type IV cracking is a quite common damage mode in creep test specimens of these steels and well corresponds to the mechanism of operation lifetime exhaustion of the real components. The difference between the creep strength of the base metal and welded joints increases with increasing temperature and time [2, 3]

The thermal history and microstructure of the intercritical part of HAZ provides the explanation for the lowering of SRF in CrMoV steels compared to CrMo steels. As to precipitation strengthened CrMoV steels, in this part of HAZ the temperature during welding rises up to A_{C1} and/or even more, i.e. in this region a partial reaustenization takes place. At temperatures close to A_{C1} vanadium carbide and/or carbonitride loses its stability and coarsen. Moreover, fine-grained microstructure facilitates creep deformation by grain boundary sliding and also provides more nucleation sites for cavity nucleation [25].

The multiaxial stress state introduced due to heterogeneity of the properties in the welded joints during creep exposure appears to be also a very important factor influencing the creep strength of welded joints. Redistribution of stress during creep exposure changes the stress state in the critical locality of the welded joint – IC HAZ, which results in shorter times to rupture [26].

The results of temperature and time dependence of the life reduction factor are in close connection with those of SRF. The fact that the value LRF=0.108 valid for 600°C and 10^5 hours means that for the safe exposure of a fully loaded welded joint (i.e. the applied stress oriented perpendicularly to the weld axis), the design stress of the component should respect time to rupture of base metal as long as 1,000.000 hours. The quantitative estimate of creep life shortening in tube weld locality (Fig. 5) seems to be in good agreement with LRF values calculated for thick plate weldments corresponding to modified Cr steel of 10Cr-2W-0.2V-0.06Nb-0.07N type [27]. This welded joint was performed by GTAW welding technology and creep tested at 650°C with times to rupture of up to 10^4 hours. The results confirmed that:

- SRF/650°C/10^4h was about 0.55
- for lifetimes longer than 10^5 hours, the estimated LRF value seemed to be lower than 0.1
- type IV cracking was the exclusive mechanism of creep failure of the welded joint studied.

There was also performed a comparison of two attitudes to the problem of restriction coefficient W_r^{max}. The first, according to Eq. 4, where measured and standardized values of creep rupture strength are compared, and the second, taking into account SRF concept (acc. to Eq. 5). As is evident, the comparison of the weld strength $R_{mT}(W)$ with the average creep rupture strength of the base metal according to the material standard (as is unfortunately commonly used) represents quite non-adequate overestimation of welding influence on the decrease in the creep strength of the boiler piping system in its welded joint localities (Fig. 7).

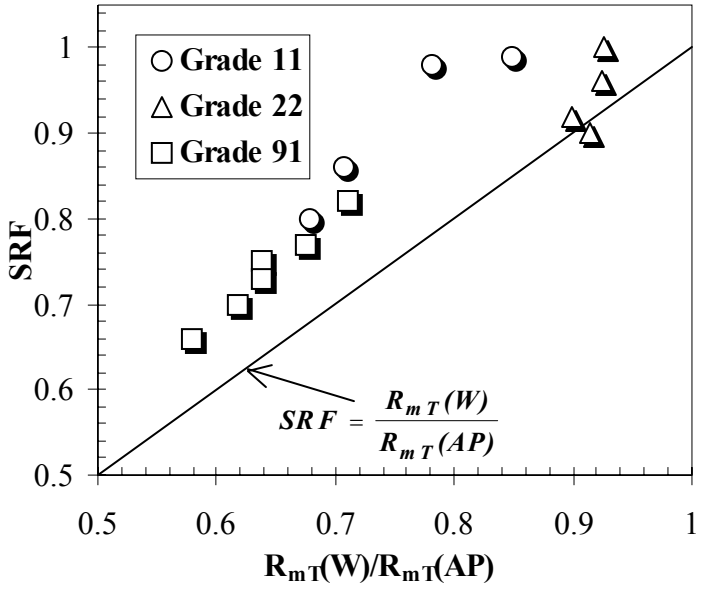

Figure 7. Comparison of experimental values of SRF and calculated ratio $\frac{R_{mT}(W)}{R_{mT}(AP)}$ *of the studied steels.*

5. Acknowledgement

The presented results were achieved under the sponsorship of the Grant Agency of Czech Republic (Grant project. No. 106/03/1353).

The authors are also much obliged to the Ministry of Industry and Trade of Czech republic for the support of this work (Project No. FD-K2/22).

References

1. Price, A.T. & Williams, J.A. In: Recent Advances in Creep and Fracture of Engineering Materials and Structures. Pineridge Press, ed. B. Wilshire, 1982, p. 265.
2. Etienne, C.F. & Heerings, J.H. Steel Research, 65, 1994, p. 187.
3. Kimmins, S.T., Coleman, M.C. & Smith, D.J. In: Creep and Fracture of Engineering. Materials and Structures, The Institute of Metals (Eds. B. Wilshire & R.W. Evans), 1993, p. 681–694.
4. Maile, K. et al. Steel Research, 62, 1991, p. 325.
5. Sobotka, J., Sojka, J. & Bobek, J. Zváranie, 42, 1993, p.73 (in Czech).
6. Sobotka, J. Zváranie-Svařování, 46, 1997, p. 97 (in Czech).

7. Sobotka, J., Theimel, K. & Bobek, J. Zváranie-Svařování, 48, 1999, p. 173. (in Czech).
8. Sobotka, J. et al. Zváranie, 33, 1984, p. 322 (in Czech).
9. Sobotka, J., Trejtnar, J. & Plíhal, A. Zváranie-Svařování, 47, 1998, p. 285 (in Czech).
10. Laha, K. et al. Metall. Mater. Trans., 32A, 2001, p. 115.
11. Seifert, W. Statistische Kenngrössen aus der Ausvertung von Zeitstandversuchen. In: Warmfeste metallische Werkstoffe, Zittau, Kammer der Technik, 1987, p. 129.
12. Nickel, H. et al. Int. J. Pres. Ves. & Piping, 47, 1991, p. 167.
13. Horton, C.A.P. & Lai, J.K. Metal Sci., 14, 1980, p. 502.
14. Sobotka, J. & Foldyna, V. Hutnické listy, 37, 1982, p. 484 (in Czech).
15. Sobotka, J. & Prnka, T. K otázce rozptylu vlastností žárupevných ocelí, Hutnické aktuality VÚHŽ, Vol. 13, 1972, No. 11 (in Czech).
16. Bína, V., Bielak, O. & Sobotka, J. Engineering Mechanics, 10, 2003, p. 83.
17. Prnka, T., Foldyna, V. & Sobotka, J. Archiv Eisenhüttenwesen, 44, 1973, p. 321.
18. Sobotka, J., Foldyna, V. & Prnka, T. Informationen ORGREB – Institut für Kraftwerke, 105, 1980, p. 61.
19. International Standard ISO 6303 – Derivation of Long Time Stress Rupture Properties, 1979.
20. Samuelson, L. A., Segle, P. & Andersson, P. In: Creep and Fatigue Crack Growth in High-temperature Plants, ed. J.C. Gautier, Saclay/Paris, 1998, ref. W9.
21. Wu, R., Storesund, J. & Sondström, R. Mater. Sci. Technology, 9, 1993, p. 773.
22. Storesund, J. & Tu, S.T. Int. J. Pres.Ves. and Piping, 62, 1995, p. 179.
23. Sobotka, J., Koman, P. & Thiemel, K. Zváranie-Svařování, 50, 2001, p. 151 (in Czech).
24. ASME Boiler and Pressure Vessel Code, Code Case N-47-32: Class 1 Components in Elevated Temperature Service, 1998.
25. Fujibayashi, S. & Endo, T. ISIJ International, 42, 2002, p. 1309.
26. Storesund, J. & Tu, S.T. Int. J. Pres. Ves. & Piping, 62, 1995, p. 179.
27. Tabuchi, M. et al. Int. J. Pres. Ves. & Piping, 78, 2001, p. 779.

Importance of the loading history in creep of 9% Cr steel

Luboš Kloc & Václav Sklenička
Institute of Physics of Materials, Academy of Sciences of the Czech Republic,
Brno, Czech Republic

Abstract

Stress change creep experiments were done on the P-91 type creep resistant steel at loading conditions corresponding to the low stress creep regime. The experiment was interrupted several times. The effect of both stress changes and temperature cycles on creep properties was analyzed. While the temperature cycle introduce some additional creep strain, the stress changes reduce the creep rate considerably. The creep life assessment is currently based on the phenomenological models mostly derived from the constant stress or constant load creep experiments. Since the loading history of the parts in industry used to be complicated and frequently unknown, the model data can be invalid.

1. Introduction

Vast majority of the creep data used in current phenomenological models was obtained from laboratory experiments under conditions rather different from that in industrial applications of the material. First of all, the higher stress and/or higher temperature is applied to get results in acceptable time. This introduces the necessary, but rather uncertain process of extrapolation.

Another difference is in the loading history. While the laboratory experiments are carried out mostly at constant load or constant stress and constant tempera- ture, the loading history of parts of industrial equipment used to be much more complicated.

It is practically impossible to carry out creep tests under conditions correspond- ing to the practical use of the materials due to the time factor. On the other hand, it is worth to study initial parts of creep curves at such conditions using the testing techniques with high strain sensitivity. It has been shown that the creep damage nuclei are generated during the initial stages of the creep, so the initial stages can provide important information on the overall creep strength of the material. Recent studies [1, 2] proved that the creep behavior is changing at 873 K below 100 MPa in the P-91 type creep resistant steel. The effect of stress changes and test interrupts (i.e. cooling down and heating up under load) is analyzed in this work.

2. Experiments

A 9% Cr ferritic-martensitic creep resistant steel of P-91 type was supplied by the Vitkovice Steel in the form of pipes in "ready to use" condition. Chemical composition of the material is shown in the Table 1.

Table 1. Chemical composition of the P-91 type steel (mass %).

C	Mo	Si	Mn	V	Ni	Nb	C	N	Al	P	S	Fe
8.5	0.88	0.43	0.40	0.23	0.10	0.10	0.10	0.045	0.018	0.015	0.006	bal.

Helicoid spring specimen technique [3] was used for the creep testing, together with conventional constant stress tensile experiment for comparison. The technique was modified to allow stress changes within the protective atmosphere of purified argon. Coil spacing was measured optically. Helicoid spring specimens were made by machining from the pipe to preserve original microstructure. Specimens have been aged by long term annealing at 923 K for 10 000 h before the creep test. The resulting microstructure is described elsewhere [4]. All creep tests were carried out at the temperature of 873 K (600 C) and stresses in the range 34–44 MPa. Since the stress and strain in the helicoid spring are essentially shear ones, they were transformed to the equivalent tensile quantities using a well known relations resulting from the von Mises criterion: $\sigma = \sqrt{3}\,\tau$ and $\varepsilon = \gamma/\sqrt{3}$, where σ is tensile stress, τ is shear stress, ε is tensile strain and γ is shear strain.

3. Results

The creep curves recorded in the experiment are shown in the Figures 1 and 2. The stress change experiment was interrupted, that is cooled down and after some time heated up again under constant load. The interrupts were done in quasi-steady state at various stress levels and are marked by the arrows in the figure. The relatively short term test at 34.5 MPa by helicoid spring specimen technique is included only to show the compatibility of results obtained by different testing techniques.

It is clear from the figures that both creep rate and overall creep strain are higher in the constant stress experiments than in stress change experiment.

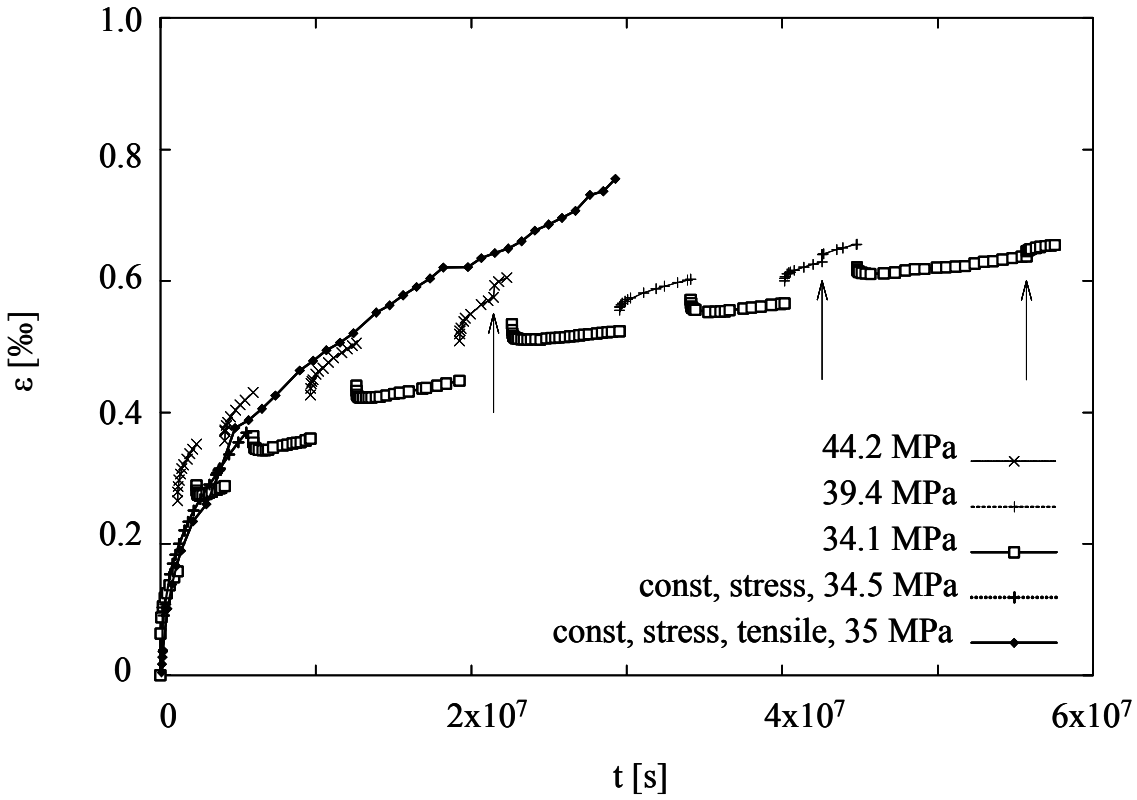

Figure 1. Creep curves for the stress change experiment and constant stress experiments. Interruptions of the experiment are marked by arrows.

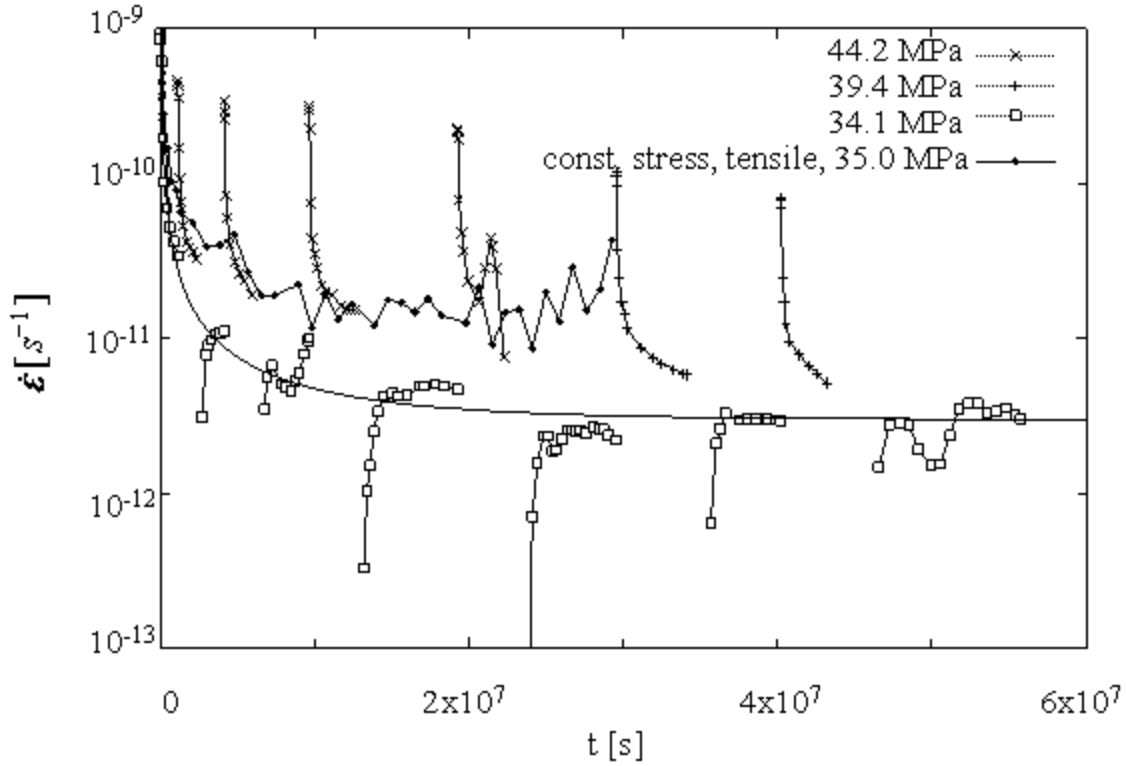

Figure 2. Creep curves of stress change experiment and constant stress experiment plotted as creep rate against time.

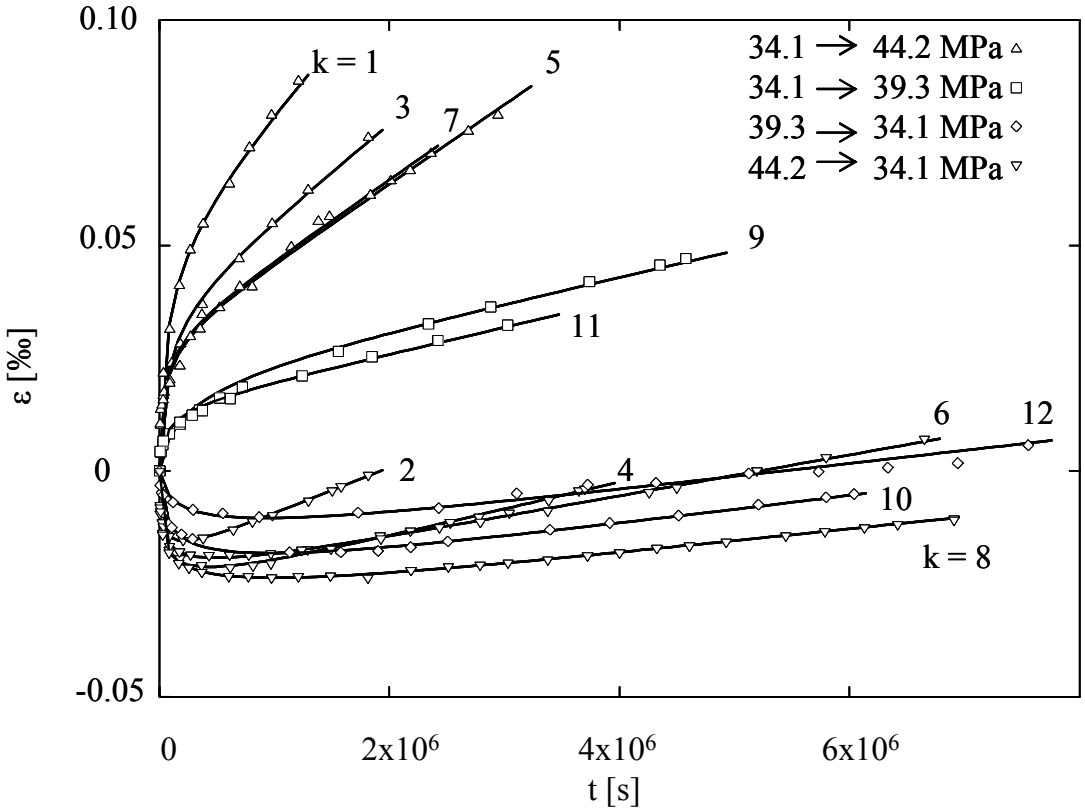

Figure 3. Individual segments of the creep curve after each stress change. k is a sequential number of the corresponding stress change.

Individual segments of the creep curve after stress changes are shown in detail in the Figure 3. Each stress change is followed by pronounced transient effect resembling primary stage of the constant stress creep curve. The creep curves of individual segments are fitted by the equation derived by Li [5]:

$$\varepsilon = \dot{\varepsilon}_s t \pm \dot{\varepsilon}_s t_p \ln\left(1 + \left(\exp\left(\frac{\varepsilon_t}{\dot{\varepsilon}_s t_p}\right) - 1\right)\left(1 - \exp\left(-\frac{t}{t_p}\right)\right)\right) \quad (1)$$

where ε is the strain, $\dot{\varepsilon}_i$ is the initial strain rate, $\dot{\varepsilon}_s$ is the steady state strain rate, t_p is the primary stage relaxation period and t is the time. The fit is generally good. The "quasi-steady state" or pseudo-secondary creep is described by the parameter $\dot{\varepsilon}_s$ while the transient creep can be characterized by the transient strain ε_t and the transient relaxation period t_p. Since the t_p is in the order of 10^6 s, it takes typically about one month before the quasi-steady state is reached. There is a relatively long stage of negative strain after each stress decrease.

The details of creep curve around the temperature cycle are depicted in the Figure 4. There is also a transient effect, but much shorter than that with the stress change. The strain rate returns to its original value within approximately one day. Nevertheless, there is an additional strain after the interruption which is not negligible.

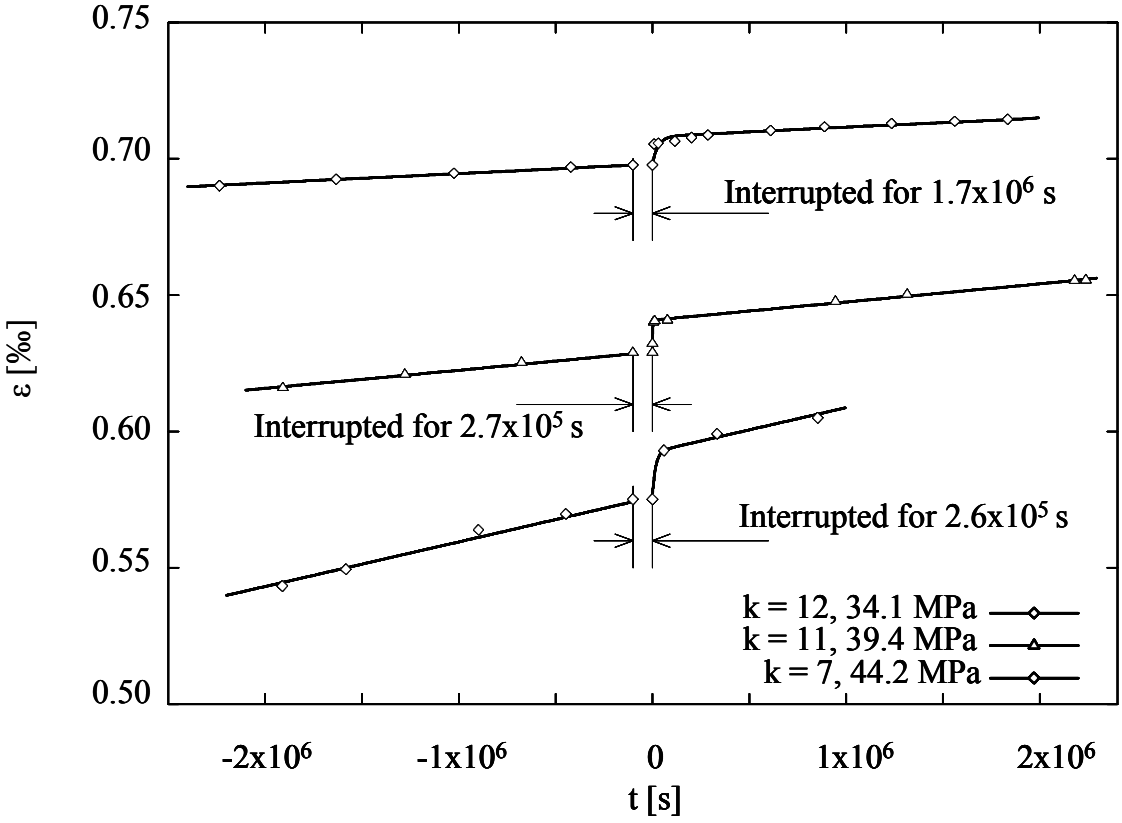

Figure 4. Details of the creep curve around the test interruptions, the curve for 34.1 MPa is slightly shifted upwards to prevent overlapping.

4. Discussion

The rigorous physical description of the creep phenomenon is still missing. It should be based on the state of the material, containing internal distribution of all microstructural elements, stress and strain. Since all the state parameters may have its own kinetics depending on all other parameters, the solution of the problem is very difficult. It is important to realize that there is no physical reason for conclusion, that every state of the material can be reached by simple integration path (loading history), like the constant stress constant temperature test. Since the creep rate after several stress changes is considerably lower than that after test under steady state conditions, it is clear that the state of the material is also considerably different.

4.1 Stress changes

Every stress change is followed by the transient stage resembling the primary stage of constant stress creep test, but the transient strain is negative after each stress decrease. This fact is fully consistent with the results of Milička and Dobeš [6] indicating that the internal back stress is equivalent to the applied stress at stresses

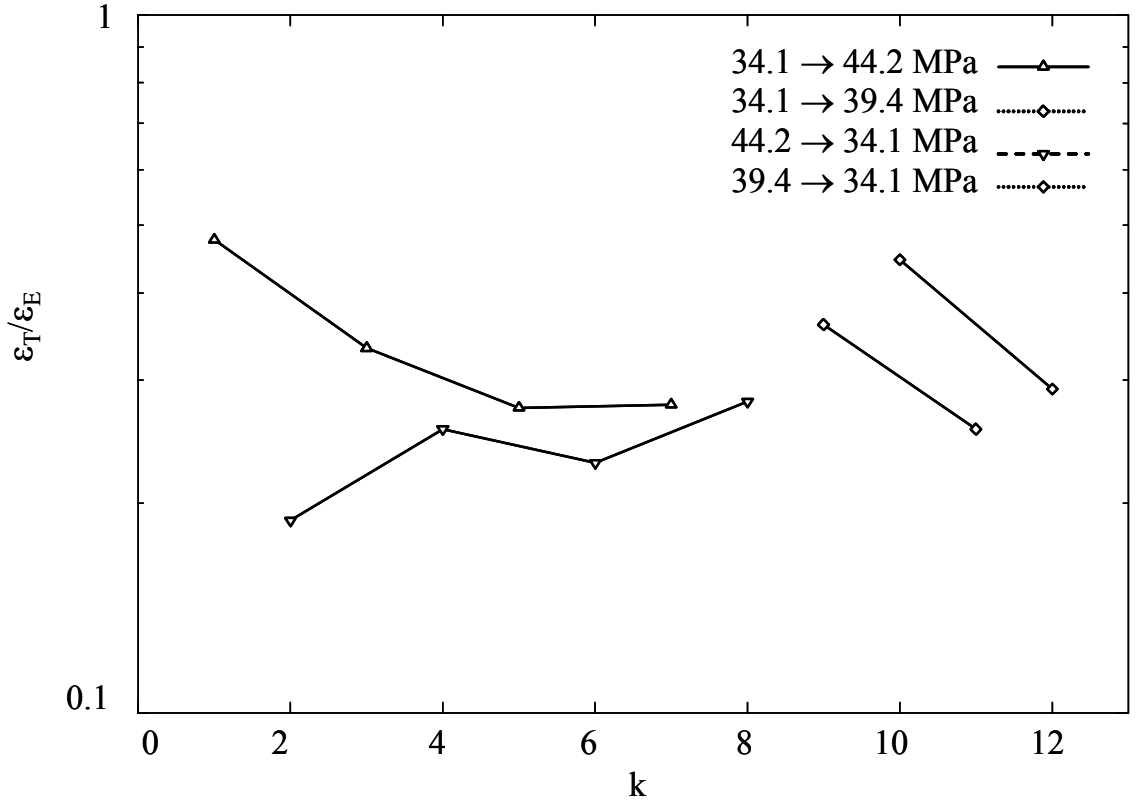

Figure 5. Transient strain ε_t *normalized by the corresponding elastic strain* ε_e *and plotted against the stress change sequential number* k.

below about 140 MPa. The creep rate after the stress increase and decrease back to original value tends to reach considerably lower level than that obtained by the constant stress test. It can bee seen in the Figure 2. This indicates that some kind of strengthening occurs during the period of the higher stress. On the other hand, it is not possible to find any changes in the microstructure before and after creep test by the standard methods of the optical and electron metallography. This is not surprising, because the total strain reached in this type of experiments is too low to cause visible changes. In this situation, any conclusions concerning the strengthening mechanism could be only speculative. The creep rate starts accelerate at the end of the constant stress creep test, while for stress change experiment remains more or less constant within longer time. This can be caused by some healing of the creep damage nuclei during the periods of negative creep flow. On the other hand, the structural development causing the decrease of the creep rate remains unclear. The positive influence of stress changes to the creep strength is consistent with the results of Kunz and Lukáš [7]. They investigated the fatigue-creep interactions and found, that the small vibrations superposed on the creep test improve the creep strength of the steel when compared to the pure creep test. The transient effect is caused probably by the stress redistribution [8] in the specimen. The $\varepsilon_t / \varepsilon_e \approx 0{:}3$ ratio remains more or less constant during the experiment – see the Figure 5.

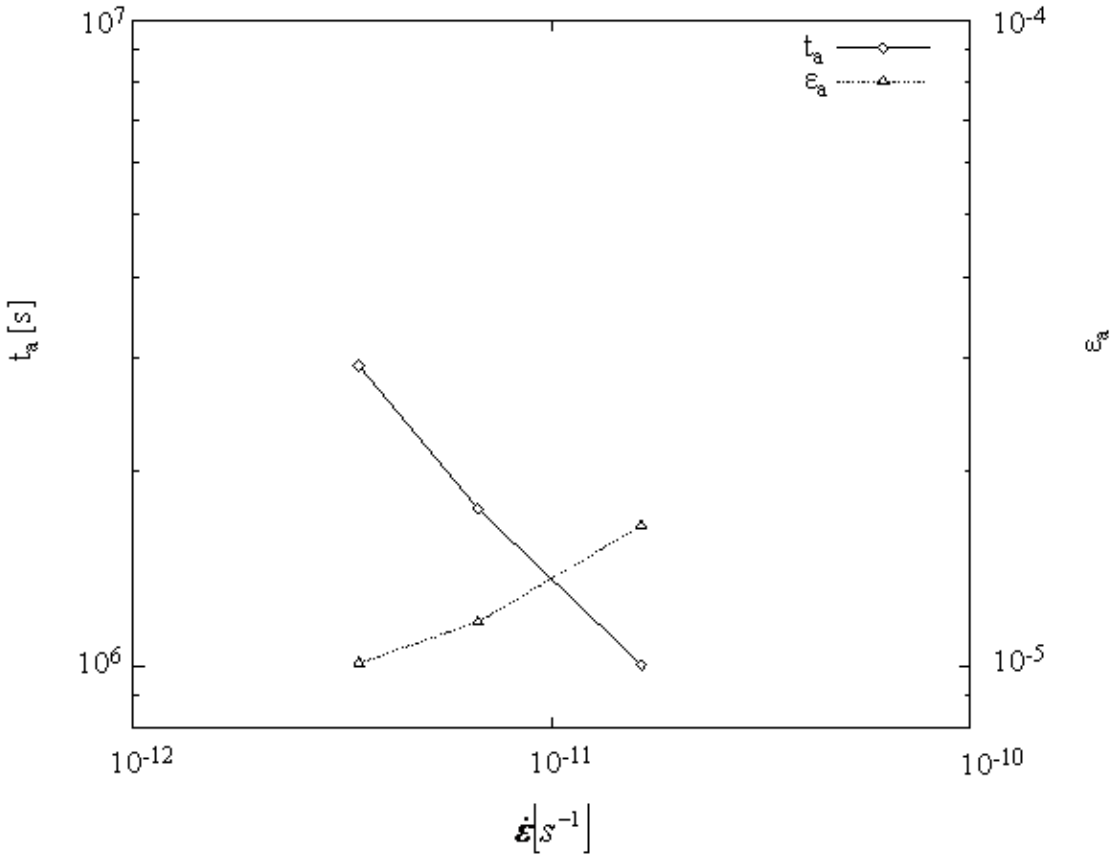

*Figure 6. Additional stress "*a *and additional time* ta *after test interruption plotted against the quasi-steady state creep rate _"s of the corresponding segment of the creep curve.*

4.2 Creep test interrupts

The quasi-steady state creep rate returns to its original value after creep test interrupt. Unlike the stress changes, there are no permanent effects on the microstructural state of the material. The thermal stresses generated during temperature changes leads to some additional strain "a when the specimen is heated up again to the nominal testing value. The additional time ta = "a= _"s gives an image of the effect of the additional strain. Both values are plotted in the Figure 6. It is clear from the figure, that the additional time can easy reach the value of 10^7 s. This means, that the interruption for a few hours can produce the additional strain corresponding to the several months of the steady state creep. The additional strain can nucleate some additional damage which can influence the later creep behavior, but there is no direct evidence for it.

5. Conclusion

The large effect of the stress changes was observed in creep of the P-91 type creep resistant steels at 873 K and stresses between 34 and 44 MPa. The stress changes lead to lower creep rate and lower creep strain in comparison to the constant stress creep test. That is, the stress changes cause notable creep strengthening of the material. On the other hand, the temperature changes consisting of cooling the material down to the laboratory temperature and heating it up again to nominal testing temperature causes some additional strain, but had no visible effect on the creep rate.

The physically based multiparametric description of the creep phenomenon and continuous monitoring of the critical parts of the industrial plants are needed to make the creep life assessment more accurate and reliable, taking into account the loading history of the parts.

6. Acknowledgement

This work was supported by the Grant Agency of the Academy of Sciences of the Czech Republic under Contract no. IAA2041101.

References

[1] L. Kloc & V. Sklenička. Mater. Sci. Eng. A234–236 (1997) 962.

[2] L.Kloc, V. Sklenička & J. Ventruba. Mater. Sci. Eng. A319–321 (2001) 774.

[3] J. Fiala & J. Čadek. Metal. Mater. 20 (1982) 277.

[4] V. Sklenička, K. Kuchařová, L. Kloc, M. Svoboda & M. Staubli. In: J. Lecomte-Beckers, M. Carton, F. Schubert & P.J. Ennis (Eds.). Materials for Advanced Power Engineering 2002, part II, Forschugszentrum Jülich, Jülich, Germany, 2002. P. 1189.

[5] J.C.M. Li. Acta Metall. 11 (1963) 1269.

[6] K. Milička and F. Dobeš, Engineering Mechanics 5 (1998) 165.

[7] L. Kunz & P. Lukáš. To be published in: Proc. of the Fifth International Conference on Low Cycle Fatigue LCF 5, Berlin, September 2003.

[8] G.S. Daehn. Mater. Sci. Eng. A319–321 (2001) 765.

Influence of welding on creep strength reduction of 2.25Cr-1Mo steel tubes

Tomáš Vlasák[1], Jan Hakl[1] & Jaromír Sobotka[2]
[1]SVÚM a.s., Prague, Czech Republic
[2]Vítkovice Research and Development Ltd., Ostrava, Czech Republic

Abstract

Due to a microstructural variability, welded joints represent weak locations in boiler tube systems. Strength and time reduction factors are often used for quantitative expression of this effect. These factors represent a ratio between creep strength and/or life-time of welded joint and base material. Aim of this contribution is to evaluate the dependence of strength and time factors on creep conditions by an adequate model based on data from long term creep tests of 2.25Cr-1Mo steel base material and weldments.

1. Introduction

Welds are typical examples of microstructural and strength inhomogeneities in the construction elements which affect, positively or negatively, the resistance to damage mechanisms. Welded joints in boiler tubing systems operating under creep conditions represent an example significant from the engineering view-point, where this effect is a negative one. Generally, this effect is more intensive towards higher temperatures of operation and longer times of exposure.

In view of that, dimensioning must be modified adequately. Therefore, a designer needs quantitative data taking into account the negative effect of the weld. The closer to reality is this quantification, the more safe, economic and reliable is the resulting structure. Experimentally feasible method to determine weld deterioration consists of comparing the creep resistance of the weld and base material, depending on the expected service conditions. Based on long-term creep test results for the 2.25Cr-1Mo steel, this paper presents a phenomenological model designed for this purpose.

2. Formulation of the problem

According to the ECCC methodology [1], the deterioration of the creep resistance of welded joints can be described using strength and time factors giving the ratio of the creep resistance properties of the weld joint against those of the base material. The following factors are used:

a) Strength factors

The **Weld Strength Factor** calculated at temperature T and time to rupture t

$$WSF(t/T) = \frac{R_{u(w)/t/T}}{R_{u/t/T}} \tag{1}$$

and the **Weld Strength Reduction Factor** calculated at temperature T and time to rupture t

$$SRF(t/T) = \frac{R_{u/t/T} - R_{u(w)/t/T}}{R_{u/t/T}}, \tag{2}$$

where

$R_{u(w)/t/T}$ is the weld creep rupture strength at temperature T and time to rupture t,

$R_{u/t/T}$ is the base material creep rupture strength at temperature T and time to rupture t.

b) Time factors

The **Weld Time Factor** calculated at stress σ and temperature T

$$WTF(\sigma/T) = \frac{t_{u(w)/\sigma/T}}{t_{u/\sigma/T}} \tag{3}$$

and the **Weld Time Reduction Factor** calculated at stress σ and temperature T

$$TRF(\sigma/T) = \frac{t_{u/\sigma/T} - t_{u(w)/\sigma/T}}{t_{u/\sigma/T}} \tag{4}$$

where

$t_{u(w)/t/T}$ is the time to rupture of weldment at temperature T and stress σ,

$t_{u/t/T}$ is the time to rupture of base material at temperature T and stress σ.

This paper aims to formulate an adequate mathematical model showing the dependence of the strength factor on temperature and time to rupture and of the time factor on temperature and stress.

3. Experiment

For the study of the base material and production of welded joints, one heat of boiler tubes made of VITKOVICE steel 15 313.5 of size ø324/20 mm was used. By a chemical analysis (see Table 1) and evaluation of the basic mechanical properties at room temperature (see Table 2), the full conformity with standards ČSN 41 5313 [2] and EN 10216 for grades 10 CrMo 9 10 [3], 11 CrMo 9–10 according to ISO 9329 [4] or SA 335, P 22 according to the ASME Code [5] was established. Moreover, the tube material was observed to have a very good metallurgical purity, as seen from the fairly low impurity contents given in Table 1.

Table 1. Chemical composition of base material 15 313.5.

	Content of element (wt.%)		
	Analysis of heat	Requirement of standard	
		min	max
C	**0.14**	0.08	0.15
Mn	**0.49**	0.40	0.80
Si	**0.27**	0.15	0.40
Cr	**2.14**	2.00	2.50
Mo	**0.90**	0.90	1.10
P	**0.011**		0.035
S	**0.015**		0.035
V	**0.006**		
Ni	**0.06**		
Cu	**0.06**		

	Content of element (wt.%)		
	Analysis of heat	Requirement of standard	
		min	max
Al	**0.004**		
Ti	**<0.005**		
As	**0.009**		
Sb	**0.003**		
Sn	**0.004**		
N	**0.011**		
O	**0.0068**		

To produce the experimental welds, the GTAW method using the Fox CM2Kb wire was used for the production of the weld root, and SMAW method by the electrode E Cr2Mo1-33B (OK 76.28, E-B 329) of diameters ø3.15 and ø4 mm was used for finishing of the weld. Post weld heat treatment consisted in procedure 730 to 740°C for 1.5 h.

Table 2. Results of tensile tests of base and weld material of 15 313.5 steel.

	Base material				Weldment		
	R_e	R_m	A_5	Z	Post weld heat treatment	R_e^*	R_m
	(MPa)		(%)			(MPa)	
Tube ø 324/20	370	527	34,8	79.0	730°C/1.5 h	350	531$^+$
Czech standard	min. 265	480–630	min. 20				

*) informative, +) rupture in base material

To characterize the weld quality, the usual range of testing was carried out. The results of the mechanical tests (see Table II) clearly show conformity to the standard requirements [2]. The test bars fracture occurred outside the weld in the base material. Cross sectional hardness measurements manifested the maximum (240–250 HV) in the weld metal and minimum (approx. 170 HV) in the intercritical area of the heat effected zone. During bend testing up to an angle of 120° no defects were observed. For the creep tests, bars with a gauge diameter and length of ø5x50mm were produced. To determine weldment properties the welds were located in middle of the test bar length.

The base material tests included a total of 524 485 test hours, with the longest test to rupture taking 94 584 h. The weldment testing included a total of 342 518 test hours with the longest test ending in rupture after 48 847 h. Six tests were interrupted after 52 500 h. In both cases, the creep tests were carried out in the temperature interval of 550 to 600°C. All findings are described in the research report [6].

4. Evaluation of weldments creep properties degradation

Before assessment the strength and time reduction factors, the creep tests of base material and weldments must be evaluated using a suitable regression relationship. Of the many available formulas, the one traditionally used was chosen [7]:

$$\log(\sigma) = A_{1i} + A_{2i} \cdot P + A_{3i} \cdot P^2,$$
$$P = T \cdot [\log(t_r) + A_{4i}], \quad (5)$$

where; T is temperature,
t_r is the time to rupture,
σ is stress,
A_{1i}, A_{2i}, A_{3i}, A_{4i} are material constants,
and i = 1 and 2 stands for the base material and the welds, respectively.

The material constants for both material conditions are given in Table III. Graphical interpretation of creep strength of the base material and the weldments is shown in Figures 1 and 2, respectively. The creep rupture properties obtained from eq. (5) were used for calculation of the strength and time factors. These factors for chosen temperatures, times to rupture or stresses are given in Tables 4 and 5.

Table 3. Material parameters of eq. (5).

Parameter	Value	Parameter	Value
A_{11}	-4.781469E+00	A_{12}	-6.201512E+00
A_{21}	1.048977E-03	A_{22}	1.107287E-03
A_{31}	-3.900733E-08	A_{32}	-3.606272E-08
A_{41}	1.560199E+01	A_{42}	1.832711E+01

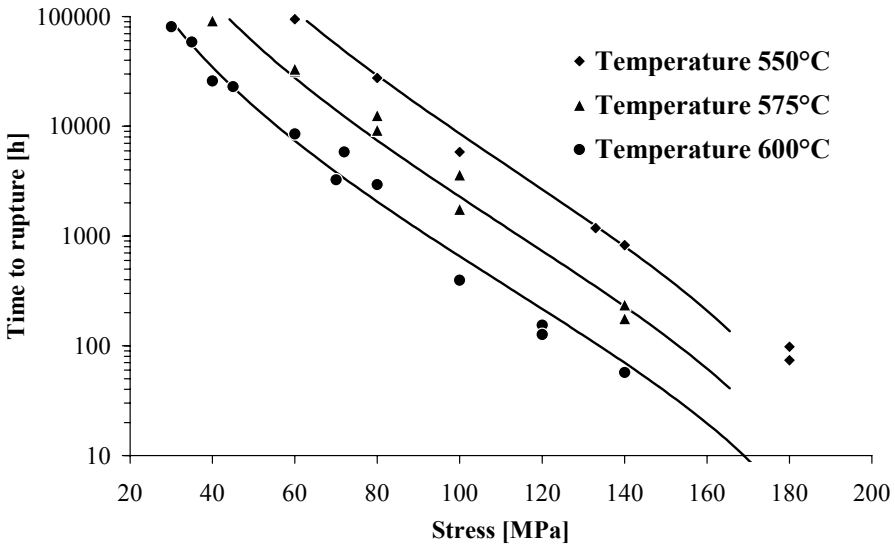

Figure 1. Creep strength of base material (steel 15 313.5).

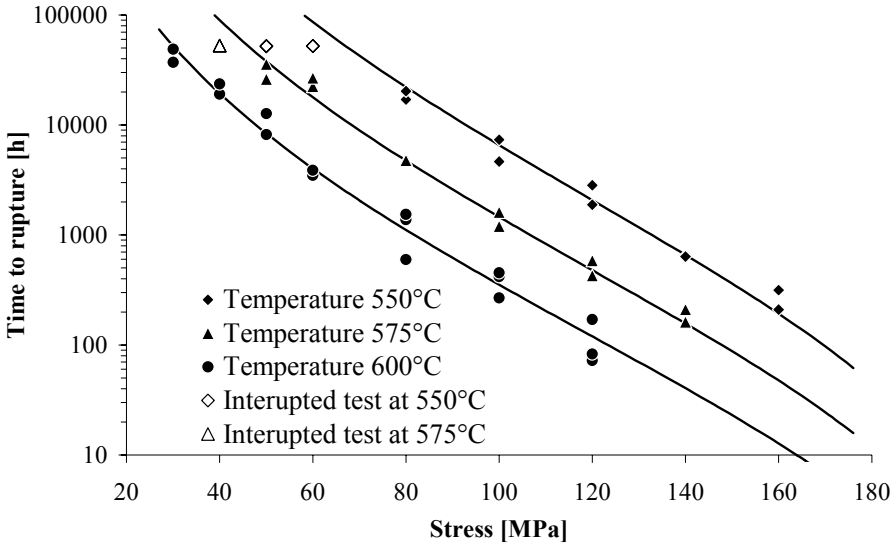

Figure 2. Creep strength of weldment (steel 15 313.5).

Table 4. Values of WSF and SRF of weldments of 15 313.5 steel for chosen levels of temperature and creep exposures time.

$\log(t_r)$ [h]	Temperature 525°C		Temperature 550°C		Temperature 575°C		Temperature 600°C	
	WSF	SRF	WSF	SRF	WSF	SRF	WSF	SRF
1	1	0	1	0	1	0	0.9700	0.0300
1.4	1	0	1	0	0.9904	0.0096	0.9492	0.0508
1.8	1	0	1	0	0.9732	0.0268	0.9304	0.0696
2.2	1	0	1	0	0.9578	0.0422	0.9135	0.0865
2.6	1	0	0.9839	0.0161	0.9440	0.0560	0.8984	0.1016
3	1	0	0.9733	0.0267	0.9320	0.0680	0.8850	0.1150
3.4	1	0	0.9642	0.0358	0.9215	0.0785	0.8732	0.1268
3.8	0.9943	0.0057	0.9566	0.0434	0.9125	0.0875	0.8631	0.1369
4.2	0.9896	0.0104	0.9505	0.0495	0.9051	0.0949	0.8544	0.1456
4.6	0.9863	0.0137	0.9458	0.0542	0.8991	0.1009	0.8473	0.1527
5	0.9844	0.0156	0.9426	0.0574	0.8946	0.1054	0.8416	0.1584

Table 5. Values of WTF and TRF of weldments of 15 313.5 steel for chosen levels of temperature and stress.

Stress [MPa]	Temperature 550°C		Temperature 575°C		Temperature 600°C	
	WTF	TRF	WTF	TRF	WTF	TRF
160	0.9221	0.0779	0.7683	0.2317	0.6468	0.3532
153.5	0.8763	0.1237	0.7312	0.2688	0.6164	0.3836
147	0.8444	0.1556	0.7053	0.2947	0.5953	0.4047
140.5	0.8213	0.1787	0.6866	0.3134	0.5799	0.4201
134	0.8041	0.1959	0.6726	0.3274	0.5684	0.4316
127.5	0.7912	0.2088	0.6621	0.3379	0.5598	0.4402
121	0.7814	0.2186	0.6542	0.3458	0.5533	0.4467
114.5	0.7741	0.2259	0.6482	0.3518	0.5484	0.4516
108	0.7687	0.2313	0.6439	0.3561	0.5448	0.4552
101.5	0.7650	0.2350	0.6409	0.3591	0.5424	0.4576
95	0.7628	0.2372	0.6391	0.3609	0.5409	0.4591
88.5	0.7618	0.2382	0.6382	0.3618	0.5402	0.4598

4.1 Regression model for the calculation of strength reduction factors

When formulating the model, the relationship existing between the strength factors WSF and SRF was taken into account:

$$\mathrm{WSF}(t/T) = 1 - \mathrm{SRF}(t/T) \tag{6}$$

After sufficient extent of data was obtained and analysed, the following model was formulated for the weld strength factor:

$$\mathrm{WSF} = 1 - S_1 \cdot \exp\left(-S_2 \cdot \ln(t_r + 1)^{-S_3}\right) \tag{7}$$
$$S_1 = s_{11} + s_{12} \cdot T + s_{13} \cdot T^2$$
$$\ln(S_2) = s_{21} \cdot \exp(s_{22} \cdot T)$$
$$S_3 = s_{31} \cdot \exp(s_{32} \cdot T)$$

where T is the temperature [K],
t_r is the time to rupture [h],
s_{11}, s_{12}, s_{13}, s_{21}, s_{22}, s_{31}, s_{32} are material constants.

Relationship (6) shows that model (7) can be used to describe also the dependence of the SRF factor (2) on temperature and creep exposure time. For the SRF factor, the following holds

$$SRF = S_1 \cdot \exp\left(-S_2 \cdot \ln\left(t_r + 1\right)^{-S_3}\right) \tag{8}$$
$$S_1 = s_{11} + s_{12} \cdot T + s_{13} \cdot T^2$$
$$\ln\left(S_2\right) = s_{21} \cdot \exp\left(s_{22} \cdot T\right)$$
$$S_3 = s_{31} \cdot \exp\left(s_{32} \cdot T\right)$$

where T is the temperature [K],
t_r is the time to rupture [h],
s_{11}, s_{12}, s_{13}, s_{21}, s_{22}, s_{31}, s_{32} are material constants.

The material constants s_{11}, s_{12}, s_{13}, s_{21}, s_{22}, s_{31}, s_{32} were estimated from WSF values obtained for the steel 15313.5. Figures 3 and 4 show good agreement of the calculated WSF and SRF values with the mean values. This circumstance is indicative of the suitability of the proposed model (7).

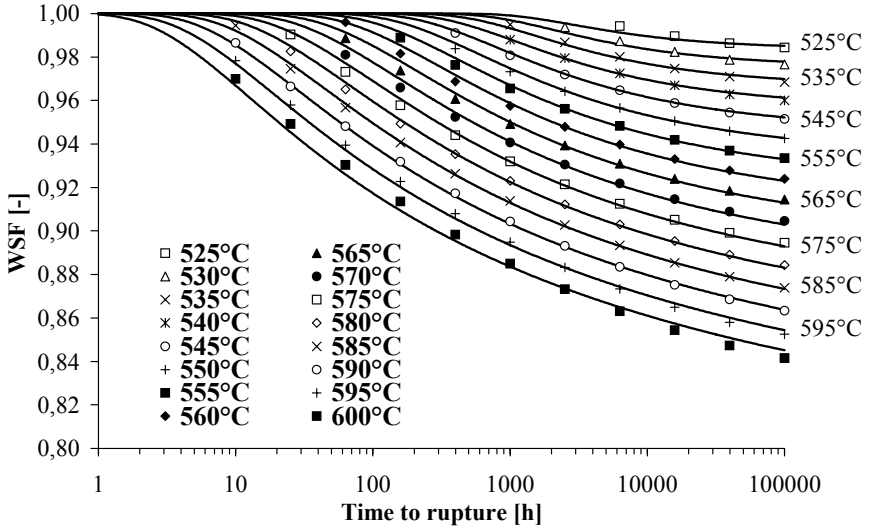

Figure. 3. WSF dependence on temperature and time of creep exposure.

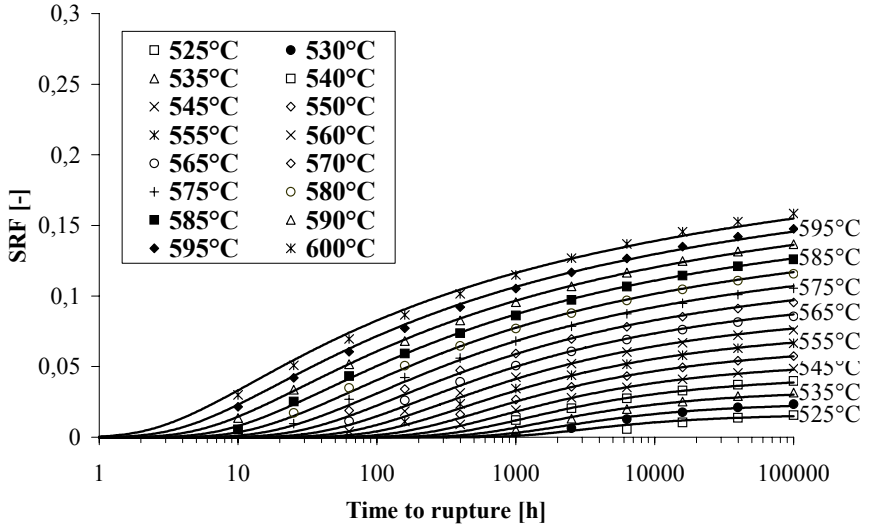

Figure 4. SRF dependence on temperature and time of creep exposure.

4.2 Regression model for the calculation of time reduction factors

Due to the similarity with the strength factors, identical basic model was used to evaluate the time factors. However, the dependence of material parameters S_1, S_2 and S_3 on temperature had to be modified to accommodate the non-linear relationship (5) of stress on time to rupture. The final model for the Weld Time Factor WTF was formulated as follows:

$$\begin{aligned} WTF &= 1 - L_1 \cdot \exp\left[- L_2 \cdot \ln(\sigma)^{-L_3} \right] \\ L_1 &= l_{11} + l_{12} \cdot T + l_{13} \cdot T^2 \\ \ln(1/L_2) &= l_{21} + l_{22} \cdot T + l_{23} \cdot T^2 \\ -L_3 &= l_{31} + l_{32} \cdot T + l_{33} \cdot T^2 \end{aligned} \tag{9}$$

where T is the temperature [K],
σ is the stress [MPa],
l_{11}, l_{12}, l_{13}, l_{21}, l_{22}, l_{23}, l_{31}, l_{32}, l_{33} are material constants.

Analogously, for the Weld Time Reduction Factor TRF the proposed model is

$$\begin{aligned} TRF &= L_1 \cdot \exp\left[- L_2 \cdot \ln(\sigma)^{-L_3} \right] \\ L_1 &= l_{11} + l_{12} \cdot T + l_{13} \cdot T^2 \\ \ln(1/L_2) &= l_{21} + l_{22} \cdot T + l_{23} \cdot T^2 \\ -L_3 &= l_{31} + l_{32} \cdot T + l_{33} \cdot T^2 \end{aligned} \tag{10}$$

where T is the temperature [K],
σ is the stress [MPa],
l_{11}, l_{12}, l_{13}, l_{21}, l_{22}, l_{23}, l_{31}, l_{32}, l_{33} are material constants.

Graphically are factors WTF and TRF for studied low-alloy steel shown in Figs. 5 and 6, while the relevant material constants are given in Table 6.

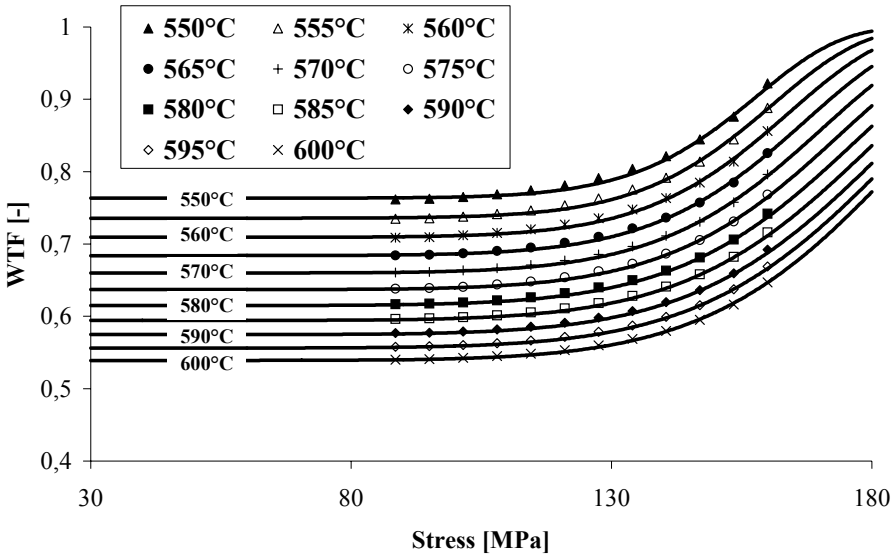

Figure 5. WTF dependence on temperature and stress.

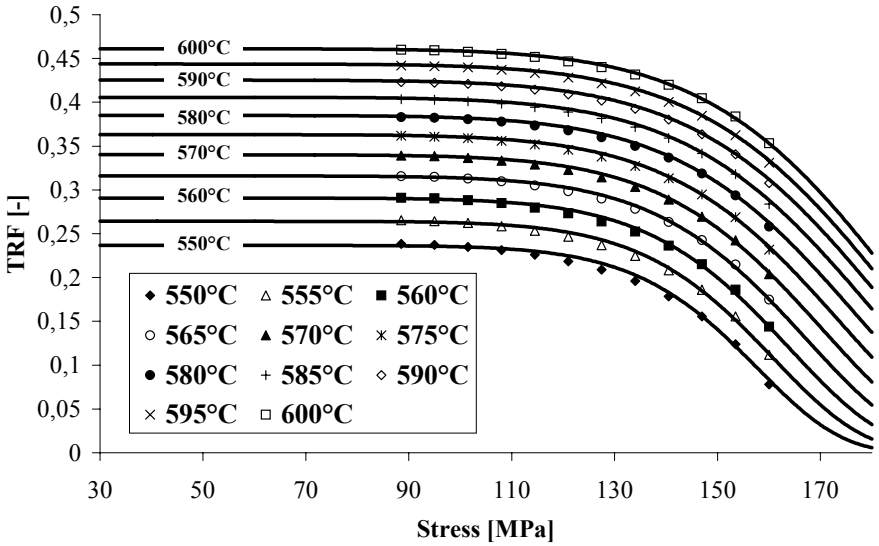

Figure 6. TRF dependence on temperature and stress.

Table 6. Values of material parameters of regression models (7) a (9).

Parameter	Value	Parameter	Value
s_{11}	1.181960E+01	l_{11}	-1.992464E+01
s_{12}	-3.114623E-02	l_{12}	4.335172E-02
s_{13}	2.049534E-05	l_{13}	-2.291067E-05
s_{21}	2.580170E+01	l_{21}	5.153313E+03
s_{22}	-2.908126E-02	l_{22}	-1.181944E+01
s_{31}	2.241991E+01	l_{23}	6.833867E-03
s_{32}	-2.577407E-02	l_{31}	1.063182E+03
		l_{32}	-2.436566E+00
		l_{33}	1.406846E-03

The suitability and usability of the proposed models can be documented by the following examples. Provided the strength and time factors can be calculated, the heat resistance properties of the weld can be calculated from those of the base material as follows:

a) For the design life of a welded structure of 10^5 hours at the service temperature of 580°C, the creep strength is
$R_{u(w)/t/T} = SRF(t/T) \cdot R_{u/t/T} = 0.8831 \cdot 40.28797 = 35.5 \cong 36\,[\mathrm{MPa}]$.
In our case, the weld heat resistance tests carried out can be used to verify this value, and it is $R_{u(w)/t/T} = 35.6 \cong 36\,[\mathrm{MPa}]$

b) The designed service life of welded structure 10^5h is achieved at 570°C a 42MPa. In this situation, the corresponding lifetime of base material is
$$t_{u/\sigma/T} = \frac{t_{u(w)/\sigma/T}}{WTF(\sigma/T)} = \frac{10^5}{0.6599} = 151\,538 \cong 150\,000\mathrm{h}$$
From extrapolated creep rupture data, the respective lifetime of base material is $t_{u(w)/\sigma/T} = 150\,442 \cong 150\,000\mathrm{h}$.

5. Discussion

The analysis of the dependence of the strength factors WSF and SRF on temperature and time (Figs. 3 and 4) has revealed significant effect of the creep exposure parameters for the reduction in the creep resistance of boiler tubes at the weld location. In particular the effect of temperature is a dominant one, since in terms of practical applications the area of times to rupture of 10^5 hours and longer must be considered of prime importance. In that time interval, the intercritical area of the heat affected zone is clearly the critical location of the weld joint suffering the most from creep damage, both under the service

conditions of boiler tube systems and during laboratory creep tests under uniaxial tensile loads. This is a general and characteristic feature of circumferential weld joints on boiler tubes made of low-alloy creep resistant steels [8–13]. It is apparent from that view-point that the magnitude of the reduction in the creep resistance at the weld location and hence also the WSF factor can be significantly affected by the welding technology, namely by the amount of heat introduced across the width of the joint critical location, the scope of deterioration of the microstructure in that location and some other effects. Our findings (Figs. 3 and 4) were shown to be in good conformity with the WSF values

- observed in the circumferential weld on super-heater tubes made of the 2.25Cr-1Mo steel made by the TIG orbital welding technology [9, 10]
- recommended according to ASME Code (CC N-47-32) [14] for weld joints made by any arc fusion welding technology with filler materials of the type 2.2-3%Cr-1%Mo (Table 7).

Table 7. Comparison of values of strength factor WSF of welded tubes made of 2.25Cr-1Mo steel, evaluated for creep life-time of 10^5 hrs.

Temperature °C	WSF/10^5		
	This paper	Preheater tube 38/4,5mm (TIG welded) [9]	ASME CODE N-47-32* [14]
550	0.94	0.93	0.94
575	0.89	0.90	0.89
600	0.84		0.89

Therefore, it appears that the findings presented in this paper can be generalized to common types of weld joints on heat exchanger and steam pipeline tubes, made by usual fusion welding technologies with heat input of up to roughly 2 kJ/mm.

6. Conclusions

On the basis of long term creep tests, the reduction in the creep resistance of welded joints of tubes made of the 2.25Cr-1Mo steel was calculated. This phenomenon was quantified using strength (1, 2) and time (3, 4) factors, and models (7, 8 and 9, 10) defining the dependence of these factors on temperature and time to rupture and stress were proposed. The diagrams of these relationships are shown in Figs. 3–6. The benefits of mathematical modelling of experimental data include the possibility to calculate the realistic estimate of creep resistance reduction under the effect of a weld for different service conditions.

7. Acknowledgement

This work was supported by the Ministry of Education, Youth and Sports of Czech Republic in frames of contract No. OC 522.10.

References

1. ECCC Recommendation 2001. Creep data validation and assessment procedures, ERA Technology Ltd., UK, 2001.

2. Czech Standard ČSN 41 5313. Valid since 1.3.1979.

3. Standard EN 10216. Seamless steel tubes for pressure purposes, Part 2 – Non-alloy and alloy steel tubes for pressure purposes, 2002.

4. pr ISO 9329-2. Seamless tubes for pressure purposes, Non-alloy and alloy steels with specified elevated temperature properties, 1992.

5. ASME Boiler and Pressure Code. Sec. IIA, 1995.

6. T. Vlasák, J. Hakl & J. Sobotka. Evaluation of creep strength reduction of low alloy steel weldments under long-time exploitation (in Czech), Research report No. 9 31 1104, SVUM, Prague, 2003.

7. Siefert, W. Warmfeste metallische Werkstoffe, Kamer der Technik, Zittau 1987.

8. Sobotka, J., Thiemel, K., Bobek & J, Zváranie-Svařování. 48, 1999, p. 173.

9. Sobotka, J., Thiemel, K., Bína, V., Hakl & J. Zváranie-Svařování. 48, 1999, p. 51.

10. Sobotka, J., Thiemel, K., Bína, V., Hakl, J. & Vlasák, T. Influence of vanadium on creep rupture strength reduction factor of boiler tubes made of low-alloy creep-resistant steels. In: Mathematical Modelling of Weld Phenomena 5, IOM Com., London 2001, p 479.

11. Smith, D.J., Walker, N.S. & Kimmins, S.T. Int. J. Pres.Ves. and Piping, 80, 2003, p. 617.

12. Parker, J.D. & Parsons, W.J. Int. J. Pres. Ves. and Piping, 63, 1995, p.45.

13. Fujibayshi, S. & Endo, T. ISIJ Intern., 42, 2002, p. 1309

14. ASME Boiler and Pressure Vessel Code. Class 1, Components in Elevated Temperature Service (Code Case N-47-32).

Prediction of creep strain and creep strength of ferritic steels for power plant applications

Stefan Holmström & Pertti Auerkari
VTT Industrial Systems
POB 1704, FIN-02044 VTT, Finland
stefan.holmstrom@vtt.fi

Abstract

Of the conventional time-temperature parameters (TTP's) for creep rupture, one of the most common is the Larson-Miller (LM) expression, which unfortunately predicts relatively inaccurate and optimistic values of extrapolated life. Some improvement can be expected by using better models such as the Manson-Haferd (MH) expression, which also can apply a low number of fitting constants, or other more complex standard models if there is sufficient data.

However, similarly accepted models have not been standardised for creep strain data. In an example of constant stress creep data of 2¼Cr-1Mo (10CrMo9-10) steel, acceptable fitting of the time to given strain was obtained using a simple and robust modified MH model. The model involves four free fitting parameters, and provides a relatively good fit and an easier fitting procedure than a the more complex strain hardening model tested on the same data. Comparison to the standard creep strength of the 2¼Cr-1Mo steel suggests that the predicted long term creep strength from short term data of the example material tends towards increasingly optimistic values with increasing time and temperature. This difference appears more pronounced for time to rupture than for time to 1% creep strain, and is probably at least partly because the standard values originate from constant load testing with a systematically shorter time to rupture than under constant stress. The example involves a single data set, but demonstrates the need to avoid excessive extrapolation beyond the range of data. The conventional rule of maximum extrapolation up to three times the longest testing time is usually accepted for creep rupture. A somewhat more extensive extrapolation could be tolerated for the time to a modest strain up to about 1%.

1. Time-temperature parameters for creep rupture data

Most practical work in predicting creep rupture behavior of ferritic steels beyond the range of the available test data is based on the classical time-temperature parameters (TTP's), which themselves are based on physical or phenomenological creep models. The relative value of TTP's can depend e.g. on

the likely error and (un)conservatism in extrapolation, simplicity in terms of degrees of freedom (number of parameters fitted), and the size of the data set. To accommodate such differences, advanced standards such as PD 6605 [1] and the European ECCC recommendations [2] require that the performance of several TTP's is compared using certain agreed criteria before selecting the preferred model. However, in some cases the user may be inclined to select a single simple TTP for applications such as life prediction, failure analysis or initial design assessment. For such purposes, the Larson-Miller parameter (LM) is often applied, but tends to systematically overpredict creep life and often shows inferior model accuracy statistics compared to other models available in the PD6605 (see *Table 1*).

Table 1. Creep rupture models of the PD6605 procedure supported by GLIM[2)] macros.

Soviet model 1 (SM1) $\log(t_r)=\beta_0+\beta_1\cdot\log[T]+\beta_2\cdot\log[\sigma_0]+\beta_3/T+\beta_4\cdot\sigma_0/T$	Soviet model 2 (SM2) $\log(t_r)=\beta_0+\beta_1\cdot\log[T]+\beta_2\cdot\log[\sigma_0]/T+\beta_3/T+\beta_4\cdot\sigma_0/T$
Minimum Commitment Method (MC) $\log(t_r)=\beta_0+\beta_1\cdot\log[\sigma_0]+\beta_2\cdot\sigma_0+\beta_3\cdot\sigma_0^2+\beta_4\cdot T+\beta_5/T$	Simplified Mendelson-Roberts-Manson(MRn)[1)] $\log(t_r)=\left\{\sum_{k=0}^{n}\beta_k\cdot(\log[\sigma_0])^k\right\}/(T-T_0)^r+\beta_5$
Larson-Miller (LMn)[1)] (or MRn with T_0=0) $\log(t_r)=\left\{\sum_{k=0}^{n}\beta_k\cdot(\log[\sigma_0])^k\right\}/T+\beta_5$	Manson-Haferd (MHn)[1)] $\log(t_r)=\left\{\sum_{k=0}^{n}\beta_k\cdot(\log[\sigma_0])^k\right\}\cdot(T-T_0)+\beta_5$
Manson-Haferd with T_0=0 (MH0n)[1)] $\log(t_r)=\left\{\sum_{k=0}^{n}\beta_k\cdot(\log[\sigma_0])^k\right\}\cdot T+\beta_5$	Orr-Sherby-Dorn (OSDn)[1)] $\log(t_r)=\left\{\sum_{k=0}^{n}\beta_k\cdot(\log[\sigma_0])^k\right\}+\beta_5/T$

1) for n=2,3,4
2) the standard PD6605 is supported by the creep rupture and post-assessment macros for the Generalized Linear Interactive Modeling (GLIM) software of NAG.

The model accuracy can be described by the root mean square (RMS) value calculated from the actual and predicted logarithmic time, or

$$RMS=\sqrt{\frac{\sum\left(\log(t_{actual})-\log(t_{predicted})\right)^2}{n}} \tag{1}$$

where n is the number of data points. The fitting efficiency is the better the smaller is the scatter factor Z, defined as

$$Z=10^{2.5\cdot RMS} \tag{2}$$

According to ECCC recommendations for effective fitting, the Z-value should not be higher than 4 (or RMS higher than 0.24), and values between 3 and 4 are considered as marginal. The fitting is acceptable when $Z < 3$, good when $Z \leq 2$, and for a perfect fit $Z = 1$ (RMS = 0).

Experience suggests that models such as Manson-Haferd (MH), Minimum Commitment (MC) or a "Soviet Model" (SM1) from the list of Table 1 will generally perform better than the LM model (Figure 1). For the data sets on steels in Fig. 1, a limit of $Z = 4$ would disqualify the LM in all but one case, while the Minimum Commitment Method (in its general form) would qualify for all cases. In particular, the MH model can be used with a low number of fitting constants similarly to LM, although with similar limitations from the polynomial stress functions. The MC and SM1 models exhibit more robust stress functions, but also require larger data sets than LM or MH models to converge in fitting.

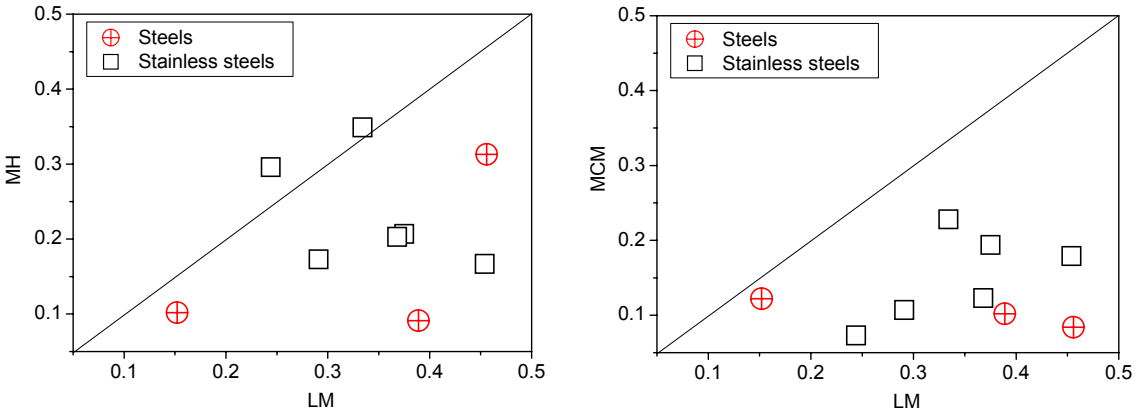

a) b)

Figure 1. Comparative RMS values reflecting model accuracy of a model in relation to the Larson-Miller of a) the Manson-Haferd model and b) the Minimum Commitment method (here in the general nonlinear form). Each point represents one data set assessed by Goldhoff [3]; points on the right side of the dividing line signify a better fit by the model on the ordinate axis.

Although the LM model is very popular for its simplicity, it is clearly not performing particularly well for steels. What is even more important, the LM model tends to induce this error by systematically overpredicting life in extrapolation [3, 4].

2. Predicting creep strain and rupture

No current materials or evaluation standards cover general creep strain prediction to a similar extent as is available for time to rupture, with some exceptions for fixed limit strains (such as 1%). However, for creep analysis of components, creep strain is needed in more detail for transfer from uniaxial materials testing data to multi-axial component behaviour. Also, extrapolation from shorter term data to longer term component lifetimes is of interest both for design and in-service evaluation. A common approach is to use directly some creep models, but also the TTP's can be extended to describe the time to given creep strain. In particular, application of an extended MH parameter is described here in a form modified for predicting creep strain.

As an example on the 2¼Cr-1Mo (10CrMo9-10) low alloy steel, a constant stress creep testing data set has been evaluated using different strain-based models. The data set of 30 constant stress creep curves, provided for the exercise by ECCC (WG1), includes five isotherms in the range of 510–600°C with rupture times ranging from 40 to 3000 h. The data is rather short term and one should avoid extrapolation to rupture times beyond 10 000 h. Nine data points were selected of each creep curve by log-log interpolation for the creep strain assessment. The selected data points were taken at engineering strain values of 0.1%, 0.2%, 0.5%, 1%, 2%, 5%, 10%, 15% and maximum strain (in total 30 x 9 = 270 points). The first applied strain model was taken from the Manson-Haferd expression modified with the arguments of Grounes [5], resulting in

$$\mathrm{MHG}(\sigma,\varepsilon) = [\log(t)-C]/T = a_0+a_1\cdot\log(\sigma)^2+a_2\cdot\log(\varepsilon)^2 \quad (3)$$

where a_0,a_1, a_2 and C are fitting constants. The second, more complex model was based on a classical strain hardening law and can be expressed as

$$t = \frac{1}{A(T)}\left(\frac{\sigma_{ref}}{\sigma_0}\right)^r \cdot \int_0^{\varepsilon} \frac{\varepsilon^s}{\exp(r\omega\varepsilon)}\, d\varepsilon \quad (4)$$

$$s = s_0 + s_1 \cdot T + s_2 \cdot \sigma \quad (5)$$

$$r = r_0 + r_1 \cdot T + r_2 \cdot \sigma \quad (6)$$

$$\omega = \omega_0 + \omega_1 \cdot T + \omega_2 \cdot \sigma \quad (7)$$

where s_n, r_n and ω_n are fitting constants. The temperature dependent rate factor A(T) is of the form

$$A(T) = \exp(-A_1 / T + A_0) \quad (8)$$

The fitting capabilities of the selected models are shown in Figs. 2 to 4.

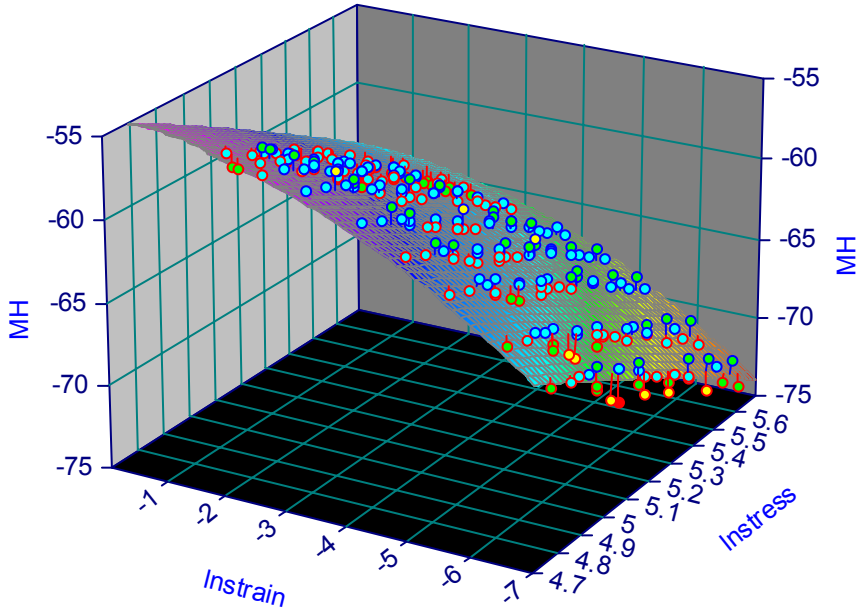

Figure. 2. Predicted and actual experimental strain values for 2¼Cr-1Mo steel, using the MHG expression of the equation (3) as a strain based TTP.

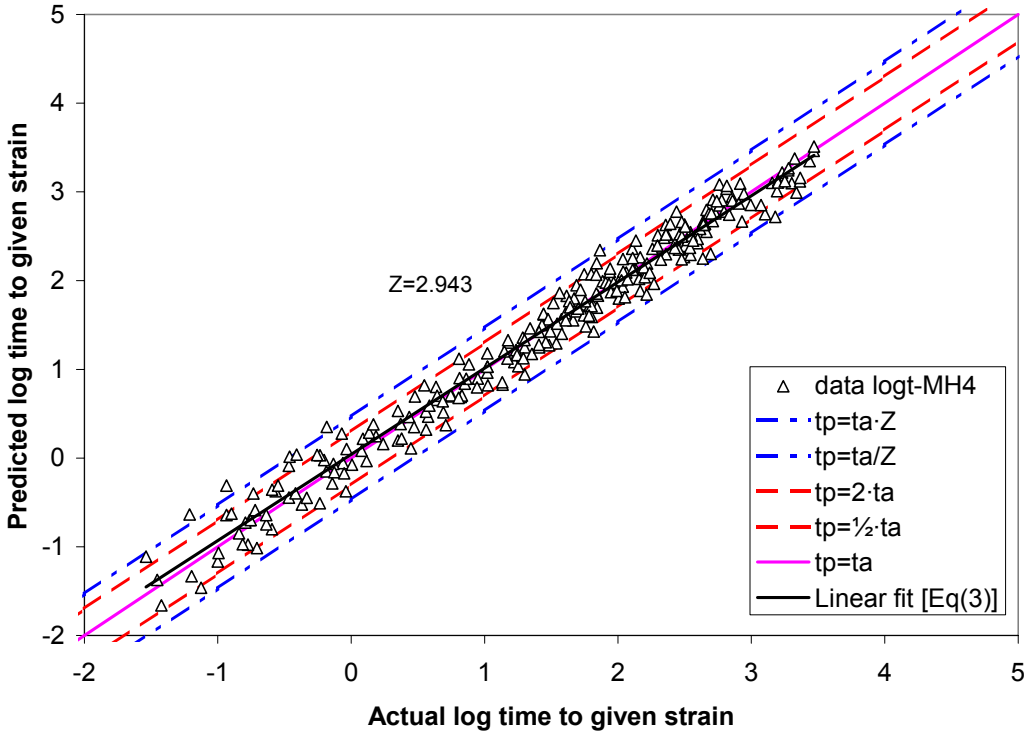

Figure 3. Comparison of predicted and actual time to strain of the data when using the MHG expression of the equation (3) for the 2¼Cr-1Mo steel. The Z value is calculated on all 270 data points. The corresponding Z value for equation (4) is 2.455.

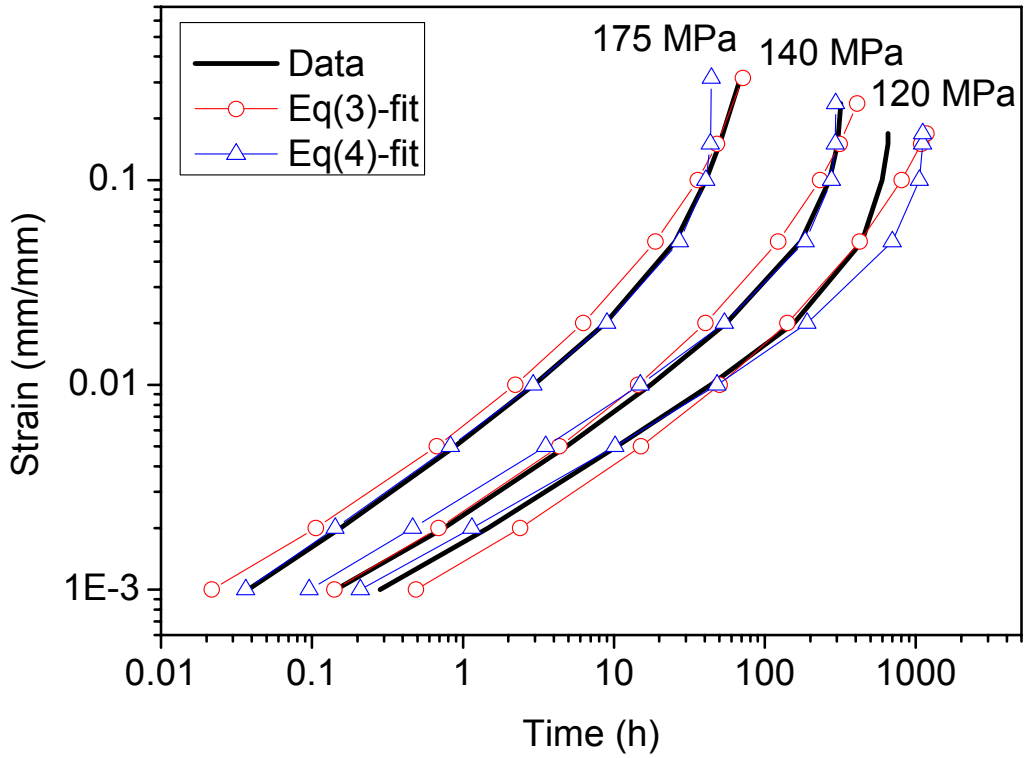

Figure 4. Comparison of predicted and actual example creep curves at 600°C using models of the equations (3) and (4).

3. Discussion and conclusive remarks

Somewhat unfortunately, the LM expression is by far the best known and most widely used TTP in engineering, probably partly because it is similar in form as the Hollomon-Jaffe parametric expression for thermally activated processes. This is unfortunate, because the LM model tends to predict less accurate and more optimistic extrapolated creep rupture life than the best alternative models. Even the number of fitting constants is no lower for LM than for the MH model, which usually shows a clearly reduced tendency to overpredict creep life for steels in comparison with predictions using the LM model. If the data set is relatively large, then other models like MC and SM1 are also often competitive with MH.

Even the best models are not good enough to allow safe extrapolation very far beyond the longest duration of the test data. This has been repeatedly demonstrated particularly for steels, when the standard creep rupture strength values have been later corrected and nearly always downwards.

Multiple TTP models need to be tested according to modern assessment standards such as PD6605 [1] and ECCC Guidelines [2]. The best model can depend on material and the data set, but the conventional approach is still limited to creep rupture data. The standard methods do not extend to creep strain data,

but an attempt is being made within ECCC to compare different approaches and models for this purpose. In the example of constant stress creep data of 2¼Cr-1Mo (10CrMo9-10) steel, a very reasonable fit was obtained with a simple and robust modified MH model for the time to given strain. This model involves only four free fitting parameters in the form of the equation (3), but results in an acceptable Z-value of less than 3 for the whole data set (270 points). The predicted 10 000h stress values at 500, 525 and 550°C of both equation (3) and equation (4) are compared with the standard 10 000 h stress levels for creep rupture and 1% creep strain as given by DIN 17175 for the same steel type. In addition for both rupture and 1% strain traditional Larson-Miller and a Manson-Haferd models were fitted with target data only (30 points). (Tables 2–3 and Fig. 6).

Table 2. Comparison of predicted stress to 1% creep strain of eq(3) and eq(4) at 10 000 h. Note that the stress for 1% strain involves a extrapolation by a time factor of about 30. For comparison purposes the Z value has been calculated for equation s(3) and (4) to incorporate 1% strain data only, i.e. 30 points.

Model	Z	500°C	525°C	550°C
Eq(3) [1)]	2.55	131	107	86
Eq(4) [1)]	2.06	155	122	97
MH04 [2)]	2.10	134	112	98
LM4 [2)]	2.07	146	120	103
DIN 17175	-	147	113 [3)]	83

1) whole creep curve modeled (270 points)
2) 1% data only, assessed as for creep rupture (30 points)
3) interpolated value

Table 3. Comparison of predicted stress to creep rupture (assumed at 30% strain for eq(3) and eq(4)) at 10 000 h. The stress for rupture involves extrapolation by a time factor of 3. For comparison purposes the Z value has been calculated for equations (3) and (4) to incorporate rupture data only, i.e. 30 points.

Model	Z value	500°C	525°C	550°C
Eq(3) [1)]	3.206	197	163	135
Eq(4) [1)]	2.415	197	163	135
MH04 [2)]	1.94	196	164	135
LM4 [2)]	1.95	199	167	138
DIN 17175	-	196	147 [3)]	108

1) whole creep curve modeled (270 points)
2) rupture data only (30 points)
3) interpolated value

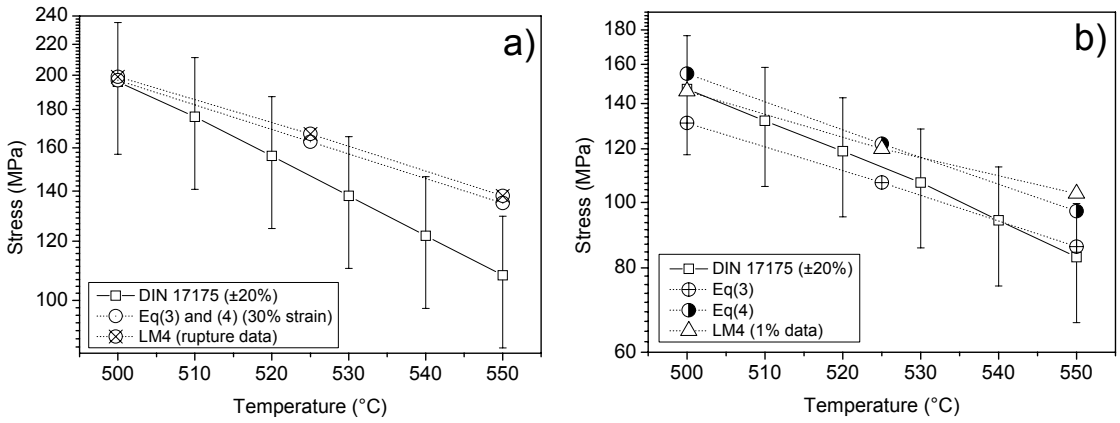

Figure 5. The standard mean (± 20%) stress values for a) creep rupture and b) 1% creep strain in 10 000 h in comparison with predicted corresponding stress values from the equations (3) and (4).

Comparison to the standard creep strength of the 2¼Cr-1Mo steel suggests that the predicted long term creep strength from short term data of the example material tends towards optimistic values with increasing time and temperature. This applies both for time to rupture and time to 1% creep strain, although the difference may be more pronounced for rupture. This is at least partially because the standard creep strength values have been obtained from constant load testing, which results in a systematically shorter time to rupture than in constant stress testing at same temperature and initial stress. The corresponding time to 1% creep strain should show less difference between constant load and constant stress, because at 1% strain the stresses are not very different between constant load and constant stress tests.

Nevertheless, although limited to a single data set, the results also demonstrate the need to avoid too extensive extrapolation beyond the data. The conventional rule of maximum extrapolation up to three times the longest data point is usually accepted for creep rupture. Using the above example data set and a similar rule for 1% creep strain, the allowable maximum extrapolated time would be an order of magnitude shorter (about 1000 h) than that for rupture (about 10 000 h). However, as less influence is likely from rupture-related damage processes at low strain than close to failure, a more extensive time extrapolation could be tolerated for modest 1% strain than for rupture. The models for the entire creep curves would probably support the predictions better than singular data points of the curves (like rupture data). This needs to be confirmed for data sets involving longer term creep testing and less ideal composition than in the example case. For example, real scale assessments would include multiple heats and much wider scatter for a nominally single steel grade.

4. Acknowledgement

The authors wish to acknowledge the helpful discussions with the members of the Working Group 1 of the European Creep Collaborative Committee (ECCC), managed under the EU Network Project "Advanced Creep".

References

[1] PD 6605, 1998. Guidance on methodology for assessment of stress rupture data. Part 1 and 2. BSI, London. 51 + 27p.

[2] ECCC recommendations, 2003. Volume 5 Part 1a [Issue 5], Generic recommendations and guidance for the assessment of full size creep rupture data sets. ECCC recommendations, 2003. Volume 5 Part 1b [Issue 2]. Recommendations and guidance for the assessment of creep strain and creep strength data.

[3] Goldhoff, R.M. Towards the Standardization of Time-Temperature Parameter Usage in Elevated Temperature Data Analysis. J. Test. Eval. 1974 2(5), p. 387.

[4] Auerkari, P. & Holmström, S. Models and methods for predicting creep life and creep strength of ferritic steels. NIMS Seminar, Tsukuba, 17 March, 2004.

[5] Grounes, M. A Reaction-Rate Treatment of the Extrapolation Methods in Creep testing. Journal of basic engineering, Series D, Trans. ASME 1969.

Validation of the small punch test as a method for assessing ageing of a V modified low alloy steel

F. Di Persio[1], G.C. Stratford[2] & R.C. Hurst[1]
[1] Institute for Energy/JRC of the EC – Petten – The Netherlands.
[2] University of Wales – Swansea – UK

Abstract

The industrial need for plant integrity and life extension assessment encourage methods and analyses based on realistic material mechanical properties for in service components in their current state of damage. The Small Punch (SP) miniaturised test technique is a promising candidate as effectively a non-destructive test method capable of providing direct values of the mechanical properties of materials of operating components. The method is of course not yet standardised but is currently under study in a number of laboratories and common Codes of Practice are under development. In the present work, the authors propose the SP test as a promising method for assessing the level of damage of material caused by ageing at elevated temperatures. The SP test results for aged low alloy steels indicate a clear reduction in creep life associated with enhancement of damage. In an effort to quantify this level of damage in terms of conventional creep behaviour, a stress-strain model is presented as a contribution towards a better comprehension of the SP technique, thereby facilitating its acceptance for implementation in applications where remanent life of components is under assessment.

1. Introduction

The life time assessment and potential for possible failure of in service components is a critical issue in the safety and reliability analysis of industrial plants since many operating power stations and petrochemical plants are approaching the end of their design lives. For thirty years or more since those plants were built, several degradation processes have potentially reduced the mechanical properties, in particular the creep resistance, of their structural components. At the time of construction the design life was based on relatively simplistic codes endorsed by practical experience, and finally corrected by an appropriate safety factor. Indeed, in light of the major advances in metallurgical knowledge and currently available analytical methodologies, today it would be possible to reduce the safety factor and to thus extend design lives. In addition,

the new policies for environmental protection and the safety regulations for industrial plants make it more practical and economically convenient to extend the lifetime of existing component beyond their original design life rather than to build new plants. However, major investment to modernise existing plants is only profitable if the plant under consideration has sufficient residual life. Hence, reducing the uncertainty in the estimation and monitoring of remaining life of plant components is of fundamental importance to industry.

Although damage can be assessed using surface replication techniques, this procedure does not give the full picture. The component integrity can be rarely evaluated with the traditional and well-standardised mechanical test techniques, such as the uniaxial creep test, because there is insufficient material to sample non-invasively from the component. Hence, the need for evaluating the residual mechanical properties of structural components by direct testing methods has led to innovative techniques based on miniaturised specimens. Among these, a technique called the Small Punch (SP) test has emerged as a promising candidate. Firstly introduced in the USA [1, 2] and Japan [3, 4], in recent years it has become known in Europe [5–7]. The SP testing can be considered as effectively a non-destructive technique because of the very limited amount of material to be sampled, with the specimens being discs 0.25–0.5 mm thick and 8–10 mm diameter. It is an efficient and cost-effective technique and has the potential to enable measurement of the realistic material properties for the specific component, identifying the present state of damage and focusing on the more critical (more stressed, more damaged) locations in the component. The method is not yet standardised and is currently under study in a number of laboratories and common Codes of Practice are under development [8, 9]. Not only is the test method not standardised but its promise for acceptance is undermined through an unclear relationship between the creep results obtained from the SP test compared to those obtained from conventional testing and applied in component design.

The objective of this paper is to demonstrate that a thorough understanding of the processes taking place during the SP test when incorporated within a novel analytical stress-strain model may contribute towards the acceptance of the Small Punch creep testing technique as a useful tool for evaluating creep properties for damaged material. A modern, low-alloy steel (2 ¼ Cr – 1 Mo, V modified) currently employed for high temperature plant applications, was deliberately aged at a temperature higher than its usual temperature of application to induce metallurgical damage, and subsequently tested in SP testing equipment under creep conditions. The viability of the SP technique in conjunction with the new analytical model for determining the degree of damage of the alloy induced by ageing has been assessed and validated by comparing the SP results with those from conventional uniaxial creep tests.

2. Experimental procedure

2.1 Material

The material selected was a low-alloy heat-resistant Chromium-Molybdenum steel: 2¼Cr – 1Mo, V modified with an isotropic bainitic (acicular ferrite) microstructure. This steel has come into quite common use, particularly in the petrochemical industry due both to its good hydrogen attack resistance and relatively low cost. In a parallel study the degradation through hydrogen exposure has also been evaluated using the SP test technique [10]. The material was tested in the as-received condition as well as aged in air for 3000h at a temperature of 600° C.

2.2 Small punch creep test

The SP specimen was a disc of 8 mm diameter and 0.5 mm thick which was clamped around its circumference so to avoid any sliding of the sample during the test. The load was applied to the sample by a hemispherical punch, with a radius of R = 1 mm, made of a creep resistant Nimonic alloy. A circular hole *a* = 4 mm in diameter is located in the die below the specimen, into which the sample bulged under the action of the punch at the specified load. The whole of the die/specimen/punch arrangement was enclosed in a cylindrical furnace which kept the sample temperature at the desired temperature to within ± 1°C. In order to prevent severe oxidation of the specimen, the tests were carried out in a protective argon gas atmosphere. The vertical deflection, *d,* of the specimen as it bulged was monitored by measuring the displacement of a quartz rod using a linear variable differential transducer (Figure 1 and Figure 2).

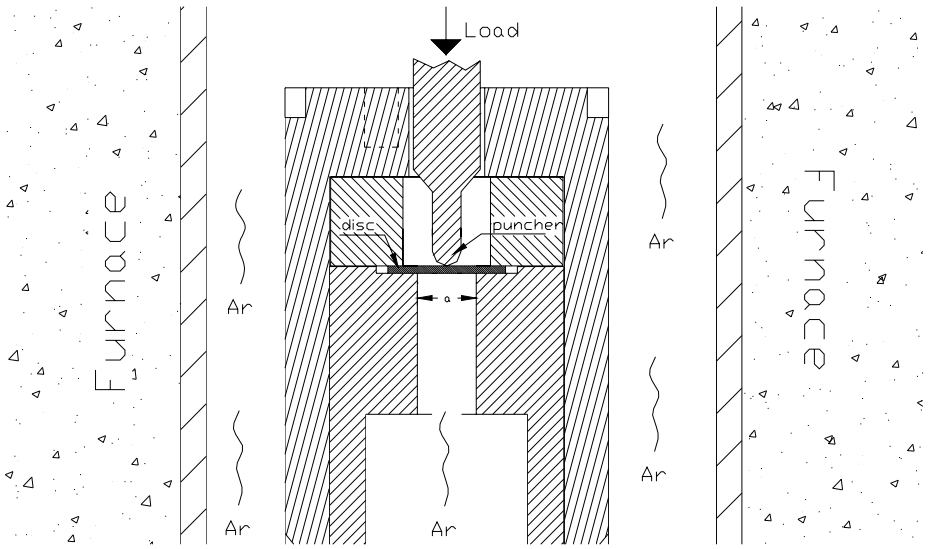

Figure 1. Schematic of the SP experimental set-up.

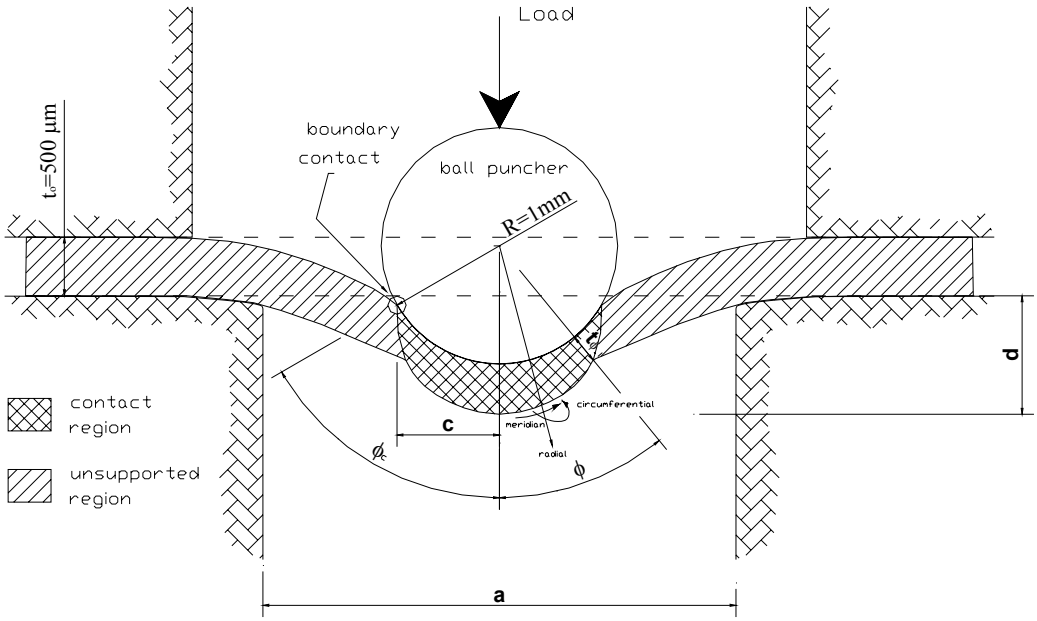

Figure 2. Sketch of a typical deformed SP creep specimen with definition of curvatures and main directions.

The SP creep tests were run at at load levels from 230 to 340 N at a temperature of 600°C, on both the as received material and the aged material. The results are presented in Table 1. The typical outcome of a SP test is the plot vertical deflection versus time, which is illustrated in Figure 3.

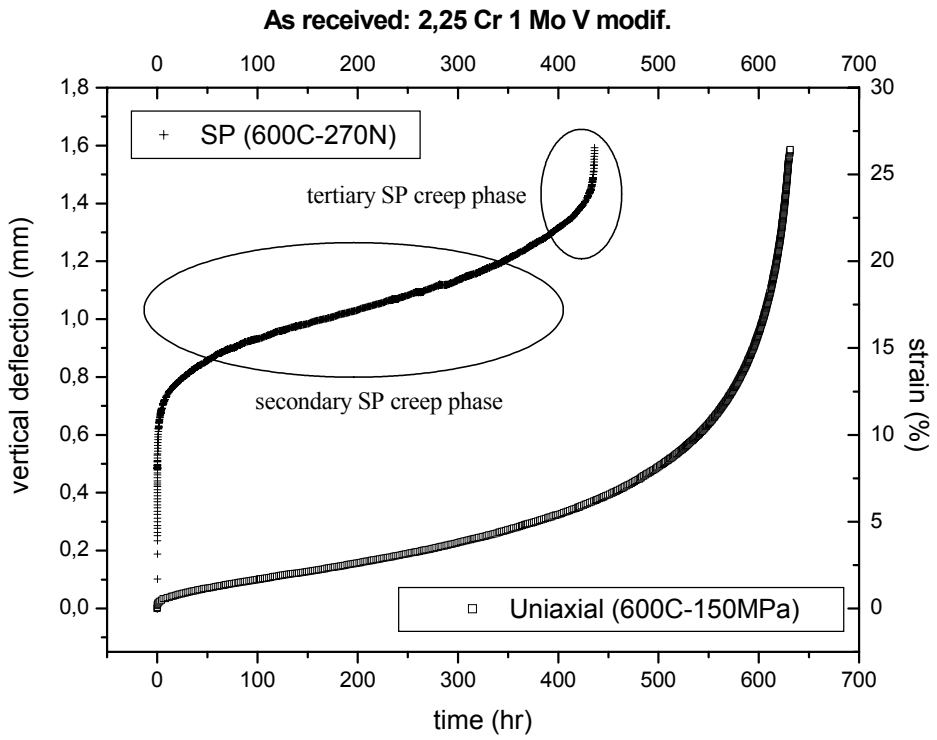

Figure 3. Typical SP creep curve compared with the uniaxial creep curve obtained on the same material at the same temperature and with similar rupture life.

The SP creep curve is compared with a uniaxial creep curve obtained on the same as received material, at the same temperature and with similar rupture life. As in the conventional uniaxial creep test, the SP creep test also exhibits clear primary, secondary and tertiary creep phases.

2.3 Conventional uniaxial creep test

The uniaxial creep tests used in this work were carried out in 20 kN constant load creep machines. The uniaxial specimen was a cylinder with an 8 mm diameter and a 50 mm parallel gauge length. The conventional creep tests were run at nominal stresses of 190, 150, 140 and 130 MPa at 600°C on as received material. The aged material was only tested at a single stress, 140 MPa at 600°C. Again the results of this test are to be found in Table 1:

Table 4. Creep rupture life results on both the uniaxial tests and SP tests.

Isothermal (uniaxial and SP) creep results					
test type	time fail hr	stress Mpa	Label	material	temp. °C
Uniaxial	1363	130	U-09	As received	600
Uniaxial	816	140	U-10	As received	600
Uniaxial	629	150	U-06	As received	600
Uniaxial	70	190	U-12	As received	600
Uniaxial	323	140	U-20	Aged 3000 hr	600
test type	time fail hr	Load N	label	material	temp. °C
SP	93	340	M1-03	As received	600
SP	56	340	M6-01	As received	600
SP	115	305	M1-07	As received	600
SP	436	270	M1-08	As received	600
SP	187	270	M6-10	As received	600
SP	1215	230	M1-06	As received	600
SP	8	340	AM7-03	Aged 3000 hr	600
SP	25	270	AM7-02	Aged 3000 hr	600
SP	596	210	AM7-01	Aged 3000 hr	600

3. Results and discussion

The SP test is a promising non-destructive technique for estimating the residual life of in-service industrial components. The technique would work if it were capable to accurately define the stresses that could lead to failure, at the critical

location of the component. Thus, the SP test at a given load, conducted on a specimen extracted from the component, would answer such a question only if the state of stress and strain were known during the whole test. The SP specimen during the test is clearly subject to a multiaxial state of stress, but at the same time the results reported in the literature [11, 12] and the results of this research show that the mechanism of creep and the rate determining the creep damage process (represented by the Norton-Arrenhius relationship [13]) are similar in both SP and uniaxial techniques. Therefore, testing the same material with both techniques at the same temperature, the SP load resulting in the same time of failure is expected to lead to values of stress comparable with the stress of the equivalent uniaxial test, although the evolution of the stress during the tests may differ considerably.

3.1 SP creep data

In order to follow the evolution of stress and strain within the SP creep specimen a series of SP tests were interrupted at different fractions, namely 50, 60 and 97% of the creep life, the highest value being of course quite difficult to estimate in the tertiary region close to failure. These specimens were sectioned and the geometrical features (Figure 2), such as the thickness t_ϕ at different angles ϕ and the contact angle ϕ_c, were measured and the state of stress for each of those samples was defined using a model developed by the authors.

The portion of sample in which the model describes the behaviour of the material is the annular area defined by the necking and where later the SP specimen will fail. This area, from the beginning of the secondary creep phase, is situated within the contact region, and is subject to a membrane stretching stress regime. In the contact region three main directions can be defined: the meridian, the circumferential and the radial. The outcome of the model showed that at the external side of the sample there was only a positive balanced biaxial state of stress active on both the meridian and the circumferential direction, which can be defined as:

$$\sigma = \frac{L \cdot \cos\phi \cdot \sin\phi}{2\pi \cdot R^2 \cdot (1 - \cos\phi_c) \cdot (1 + \sin\phi)} \cdot \left(\frac{R}{t_\phi} + f + 1 \right) \tag{1}$$

Where R is the punch radius, L is the load, t_ϕ the thickness at the angle ϕ, and ϕ_c the contact angle which defines the extension of the imprint left by the punch. Finally f is the supposed friction coefficient between the punch and the sample.

During the secondary creep phase, the calculated membrane stress at the critical area has the tendency to assume an approximately constant value. It seems in fact that during the SP secondary creep phase, the decrease of stress due to the growth

of the contact surface is balanced with the increase of stress due to the reduction in thickness. The experimental results are indicative of such behaviour. Applying equation 1, the calculated load/stress ratios (the friction coefficient has been fixed to 0.8) found at the external side of the thinnest section were found to be 1.64 (50%), 1.79 (60%) and 1.46 (97%).

Therefore, it seems that during the secondary and even tertiary SP creep phase, the membrane stress is kept approximately constant. The explanation is found in the combination of hardening and softening processes, which are developing at the same rate as expected in the steady state creep phase. In fact the expression [14] for the strain rate in the steady state is:

$$\frac{d\varepsilon}{dt} = \dot{\varepsilon}_s = -\frac{\partial\sigma/\partial t}{\partial\sigma/\partial\varepsilon} = \frac{r}{h} \tag{2}$$

Where *h* is the rate for the work hardening and *r* is the rate for the recovery.

When the strain is high enough to make the material contained in the thinnest section so damaged that is not capable any more of maintaining the balance between hardening and softening, then the tertiary creep phase commences and the sample will subsequently fail. The fracture will proceed along the more stressed area which is identified by the arc at the boundary between the contact region and the unsupported region (Figure 2).

3.2 Comparison with the conventional uniaxial creep data

Before starting to compare the results from the SP creep tests with the uniaxial creep data, it is worth considering the different way in which the stress evolves in the two techniques. First, the uniaxial creep data are coming from tests performed under constant load. Thus, the stresses are continuously increasing in a way strictly related with the material creep ductility. The nominal value of stress, which identifies the uniaxial creep test, is just representing the initial stress. In the uniaxial creep tests, for this material and in the range of the given stresses, the increase of the axial stress follows approximately the axial strain trend. Thus, for the as received material, at the end of the test, the stresses were estimated to increase up to 20–25% of the nominal value whatever level of stress was chosen. (see strain to failure in Figure 4)

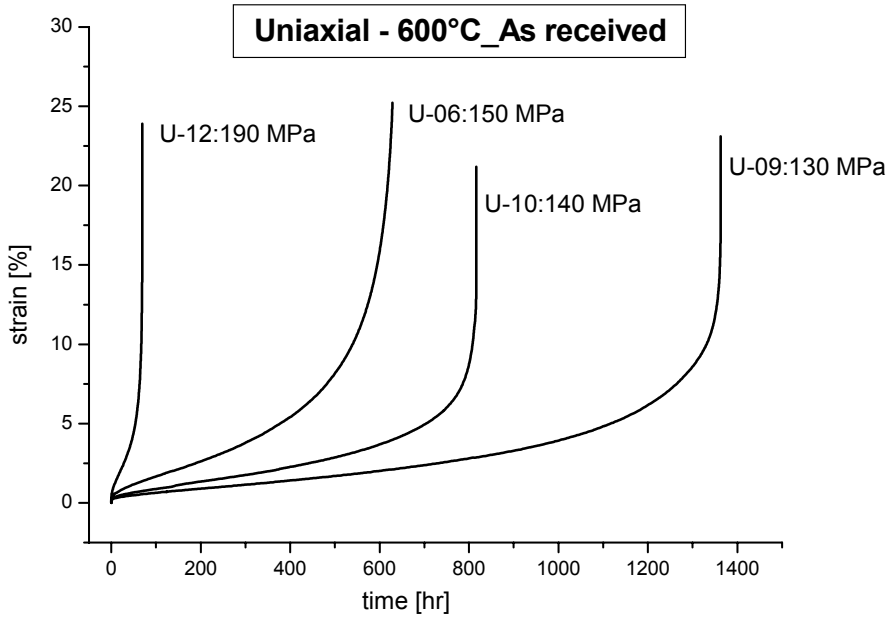

Figure 4. Isothermal uniaxial creep curves for the as received material.

Conversely, the stresses in the SP creep sample appear to be quite constant for most of the creep life (the extensive primary is mostly related to the bending deformation mode which can be considered a transition phase towards the more meaningful and crucial membrane stretching phase), with only a significant increase just during the tertiary creep phase close to the failure (Figure 3). This behaviour is reflected in the trend assumed by the load/stress ratio found for the interrupted tests made on the as received material (Figure 5).

On such a plot can be superimposed the trend of the uniaxial stress for the same material tested at a certain nominal stress, in this case 140 MPa, fixing the starting point as a load/stress ratio which fits well with the interrupted SP tests. For this purpose the starting point is giving a value estimated as 1.76. Consequently, this ratio can be employed for all the SP tests made on the as received material (Table 1) and the relative rupture lives can be represented on the stress rupture curve for a temperature of 600°C (Figure 6).

Even these few experimental observations, in particular from measurements on the interrupted tests, give robust support in favour of the stress-strain model that has been presented. In fact as expected, the stresses at the more critical location in the SP specimen follow approximately the same path as in the uniaxial conventional creep test, and the strain evolution is in agreement with such behaviour. More interrupted tests and sectional measurements would be expected to improve the accuracy in determining the appropriate load/stress ratio.

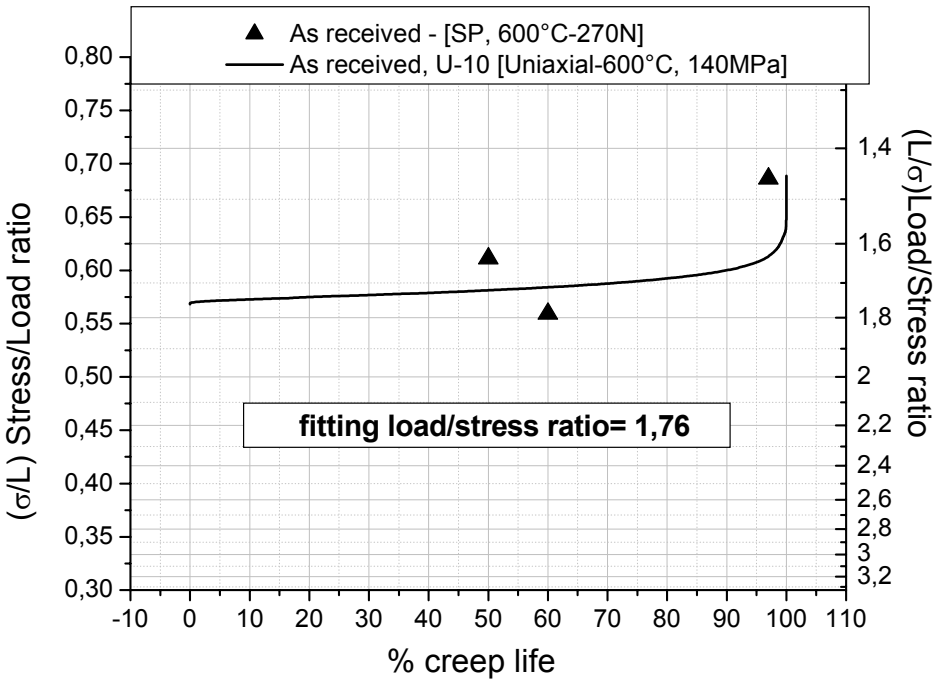

Figure 5. Evolution of SP stress compared with uniaxial stress trend in terms of load/stress ratio.

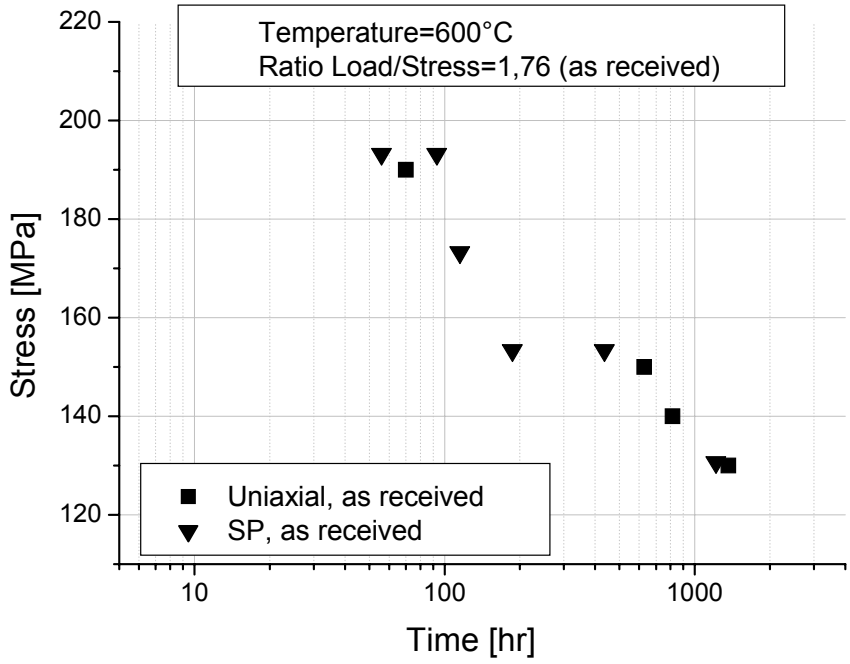

Figure 6. Isothermal rupture life plot for the as received material.

3.3 Change in the SP creep property for the aged material

The aged material is expected to experience a drop of its creep rupture life and a change of its creep ductility due to instability of strengthening carbides [15, 16, 17]. In order to analyze the differences in the way the stresses in the SP aged sample are evolving in comparison with the "as received" material, a single SP creep test on aged material was interrupted at a certain stage of its creep life and its geometrical features analyzed. Although this interrupted test was made at slightly lower temperature therevealed load/stress ratio of 1.7 at 50% of the creep life fits quite well with the ratios found for the as received material (1.76) and can be applied to deduce the equivalent stresses for the SP tests carried out at 210, 270 and 340 N (Figure 7).

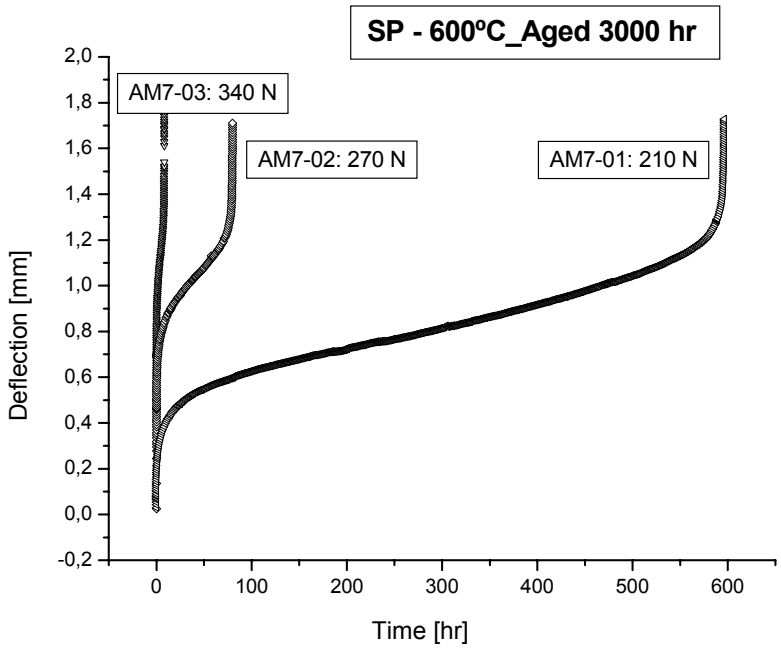

Figure 7. SP creep curves for aged material tested at 600°C.

The results are shown in Figure 8 and fit remarkably well with the single uniaxial test result on the aged material at 140 MPa at the same temperature.

Basing the success of the proposed methodology on so few results is of course premature. Much more validation testing is required and needs to be introduced into the test programmes which will need to be set up to move the SP test towards standardisation. Nevertheless, it is demonstrated through these results that the SP creep testing technique indeed shows potential for evaluating directly the degradation of creep properties for in-service aged components, and thus may play a major role in assessing their remaining life. For instance, from an in-service component working at high temperature, a sufficient number of SP

specimens (say 10) can be removed in a non-intrusive way. A few of these can be tested up to failure at different stresses at the operating temperature. A suitable test load is to be chosen to allow the other SP samples to be tested with interruptions at regular life fractions. Analyzing their geometrical features, and using the model cited in this paper, the evolution of stress could be defined and evaluated in terms of load/stress ratio. The stress rupture data can then be calculated from the load of the SP tests using the load/stress ratio, and used for remanent life estimation.

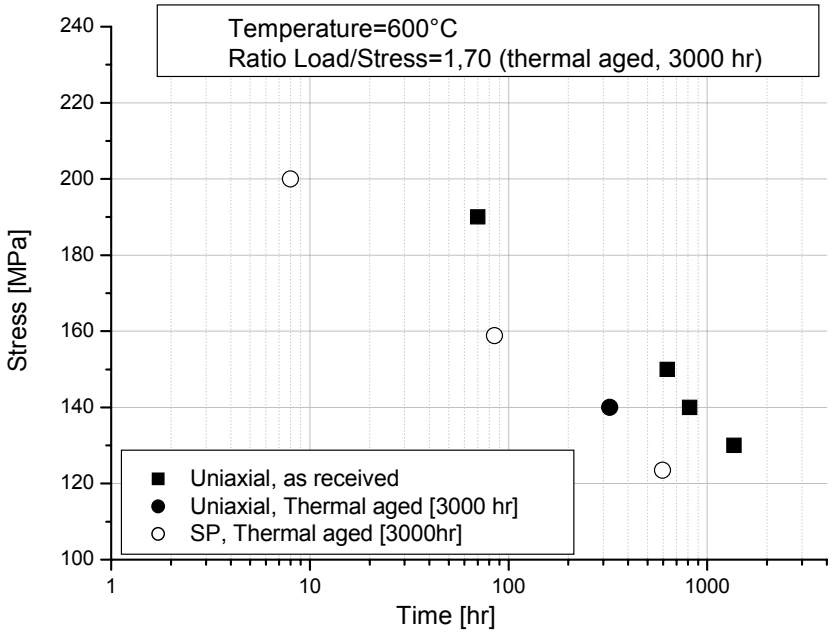

Figure 8. Isothermal SP rupture life plot for the thermally aged material exposed for 3000 h compared with the uniaxial rupture life data.

4. Conclusions

The SP testing technique has been applied to the low alloy - 2¼Cr 1Mo V modified ferritic steel typical of high temperature applications in power generation and petrochemical plants. This technique has been demonstrated for evaluating creep properties and material deterioration due to ageing, in comparison with conventional uniaxial creep methods. From the present investigation the following conclusions can be drawn:

1. The stress evolution during a SP test can be successfully evaluated by using the proposed stress model based on measurements taken from interrupted tests.

2. The relationship between the load applied in a SP test and the stress in a conventional uniaxial test can then be used in order to correlate SP and uniaxial test data.

3. Although based on a minimal number of tests, the material deterioration due to ageing leading to degradation of creep rupture strength was quite well reflected in the SP creep properties.

4. Given sufficient validation testing programmes, the SP creep testing technique has potential to be an appropriate tool for integrity assessment of in service plant components.

References

1. Manaham, M.P., Argon A.S. & Harling O.K. (1981). The Development of a Miniaturised Disc Bend Test for the Determination of Postirradiation Mechanical Property. Journal Nuclear Materials, 103 & 104, North Holland Publishing Company, pp. 1545–1550.

2. Baik J.M., Kameda J. & Buck O. (1987). Development of Small Punch Test for Ductile-Brittle Transition Temperature Measurement of Temper Embrittled Ni-Cr Steels. ASTM STP 888, ASTM Philadelphia PA. Pp. 92–111.

3. Mao, X. & Takahashi, H. (1987). Development of a Further-Miniaturised Specimen of 3 mm Diameter for TEM Disc (∅ 3 mm) Small Punch Tests. Journal of Nuclear Material, Vol. 150, pp. 42–52.

4. Komazay, S., Hashida, T., Shoij, T. & Suzuki, K. (2000). Development of Small Punch Tests for Creep Property Measurement of Tungsten-Alloyed 9% CR Ferritic Steels. J. of Testing and Evaluation, Vol. 28, No. 4, pp. 249–256.

5. Parker, J.D., Stratford, G.C., Shaw, N., Spik, G. & Tate, E. (1995). Deformation and Fracture Processes in Miniature Disc Tests of CrMoV Rotor Steel. Third International Charles Parsons Turbine Conference, Materials Engineering in Turbines and Compressors, Vol. 2, pp. 419–428.

6. Tettamenti, S. & Crudeli, R. (1998). Small Punch Creep Test: a Promising methodology for High Temperature Plant Components Life Evaluation. Proc. of Baltica IV Conf: Plant Maintenance for Managing Life & Performance. Vol. 2, BALTICA. VTT Symposium 185. Pp. 501–509.

7. Dobes, F. & Milicka, K. (2001). Small Punch Testing in Creep Conditions. Journal of Testing and Evaluation, Vol. 29, No. 1, pp. 31–35.

8. Maile, K. et al. (1998). COPERNICUS – SP Test Method Assessment for the Determination of the Residual Creep Life of Service Exposed Component. Final report, EU project ERB CIPA CT94 0103.

9. Bicego, V., Di Persio, F. & Rantala, H. (2003). Small Punch Creep Test Method: Results from a Round Robin Carried out within EPERC TTF5. EPERC technical report Nr. 2, European Commission, JRC, T.N. P.03.112.

10. Di Persio, F., Stratford, G. & Hurst, R.C. (2004). Small Punch test for assessing H_2 induced damage in steel for pressurized equipment. Proc. of "High Temperature Plant Integrity & Life Extension" Conference, Cambridge 14–16 April 2004.

11. Parker, J.D., Stratford, G.C., Shaw, N. & Metcalfe, H. (1998). The Application of Miniature Disc Testing for the Assessment of Creep Damage in CrMoV Rotor Steel. Conference Proceedings, BALTICA IV, Plant Maintenance for Managing Life & Performance, Vol. 2. Pp. 477–488.

12. Hayhurst, D.R. (1983). Continuum Damage Model in Creep State of Stress and Evolution of Damage. Engineering Approaches to High Temperature Design, Eds. Wilshire & Owen, Pineridge Press.

13. Dorn, J.E. (1954). Some Fundamental Experiments on High Temperature Creep. Journal of the Mechanics and Physics of Solids, Vol. 3, pp. 85–116.

14. Evans, R.W. & Wilshire, B. (1993). Introduction to Creep. Department of Materials Engineering, University of Wales, Swansea (UK)

15. Kuzuku, V., Aksoy, M. & Korkut, M.H. (1998). The effect of strong carbide-forming elements such as Mo, Ti, V and Nb on the microstructure of ferritic stainless steel. Journal of Materials Processing Technology, Vol. 82, pp. 165–171.

16. Výrostková, A., Kroupa, A., Janovec, J. & Svoboda, M. (1998). Carbide reactions and phase equilibria in low alloy Cr–Mo–V steels tempered at 773–993 K. Part I: Experimental measurements. Acta Materialia, Vol. 46, 1, pp. 31–38.

17. Yang, H. & Kim, S. (2001). A study on the mechanical strength change of 2.25Cr-1Mo steel by thermal aging. Mat. Sci. and Eng. A319–321, pp. 316–320.

High temperature oxidation and corrosion modelling using thermodynamic and experimental data

Liisa Heikinheimo[1], Karri Penttilä[2], Marko Hämäläinen[3], Ulrich Krupp[4], Vicente Trindade[4], Michael Spiegel[5], Andreas Ruh[5] & Klaus Hack[6]
1: VTT Industrial Systems, Espoo Finland
2: VTT Processes, Espoo Finland
3: HUT, Espoo Finland
4: University of Siegen, Siegen Germany
5: Max Planck Institute, Düsseldorf Germany
6: GTT Technologies, Aachen Germany

Abstract

The aim of EU-OPTICORR project is to develop a modelling tool for high temperature oxidation and corrosion specifically in boiler conditions with HCl and SO_2 containing combustion gases. The work necessitates thermodynamic data collection and processing. At present the tools are ChemSheet based programmes with a kinetic module and easy to use interface and a more sophisticated numerical finite-difference based diffusion calculation programme, InCorr, developed for prediction of internal corrosion. For the development and modelling knowledge about the corrosion mechanisms and exact data are needed. Therefore exposure tests and TG-tests (thermo gravimetry) are included in the project work for specific boiler tube steels.

1. Introduction

The development of a life-cycle approach (LCA) for the materials in energy production, particularly for the steels used in waste incinerators and co-fired boiler plants aiming at safe and cost effective energy production includes aims of:

- The control and optimisation of in-service performance of boiler materials,
- Understanding of HT corrosion and oxidation mechanisms under service conditions,
- Improvement of reliability to prevent the failure of components and plant accidents and
- Expanding the limits of boiler plant materials by corrosion simulations for flexible plant operation conditions (steel, fuel, temperature etc.).

The kinetics of high temperature oxidation and corrosion are determined from laboratory thermo gravimetric tests (TG) and multi-sample exposure tests. The materials studied are typical boiler tubes and fin-steels: ferritic alloys, austenitic steel T347 and Ni-based alloy Inconel 625. The exposure gases are dry air, air with 15 vol-% H_2O, and with 2000 ppm HCl and 200 ppm SO_2. The salt deposits used are based on KCl-$ZnCl_2$ and Ca, Na, K, Pb, Zn-sulfate. The test temperatures for exposures with deposits are 320 and 420°C, and for gas exposures 500, 550 and 600°C [1].

The development of modelling tools for oxidation and high temperature corrosion has been started with thermodynamic data collection for relevant systems and thermodynamic mappings. The second step is simulation model and tool development for salt-induced hot corrosion based on ChemSheet approach. The most detailed kinetic modelling tool will be developed for internal corrosion simulation using InCorr programme [2].

2. Thermodynamic data collection

Selection of the chemical systems - The first task of the project was to define the chemical system to be treated. The alloys under investigation contain many elements, the gas phase in a power plant/waste incinerator can contain a multitude of compounds, and the salt deposited on the heat exchangers may lead to dissolution of alloy components or even to solid-liquid equilibria among the salt phases. As a result the whole data package has been split into metal, salt, oxide and sulphide subsystems, Fig. 1.

Database development - In the metal (alloy) subsystem the components are being treated with respect to their Gibbs energies in the FCC_A1 and BCC_A2 states in order to treat austenite and ferrite bulk materials, but also superalloys. In the salt subsystem the combination Al, Ca, Fe(2+,3+), K, Mn, Na, Ni, Pb, Zn // Cl, SO_4, CrO_4, OH, MoO_4 has to be dealt with. The phases to be considered are the liquid solution and a large number of solid stoichiometric compounds. In the oxide subsystem the component oxides are all solid, mostly stoichiometric compounds but there are also solubility effects to be considered such as in wüstite $(Fe^{2+}, Fe^{3+}, V, Ni, Mn)O$, corundum $(Al, Cr, Fe)_2O_3$ or spinel $FeO\times(Al,Cr,Fe)_2O_3$. Tailor-made thermochemical data files of these components is now available. In the sulphide subsystem, the components are FeS, FeS_2, CrS, Cr_2S_3, MnS, NiS etc. Moreover, there may appear higher order stoichiometric sulphides such as $FeCr_2S_4$.

Phase diagrams for the systems - Systems Fe-Cr-O_2, Fe-Si-Cr-O_2 and Fe-Si-Cr-O_2-Mn etc have been calculated using FactSage [3] and the phase sequences correlate with the experimental results, in Figs. 2–3 [4–8]. Also for the salt

systems Fe-Na-K-Zn-Cl_2 stability diagrams (T vs. log ($p(Cl_2)$) have been calculated to evaluate the presence of molten phases in the system. In the Fe-Na-K-Cl_2 salt system there exists a large stability field with salt melt coexisting with solid $FeCl_2$. As log $p(Cl_2)$ increases to –2 there is a salt melt consisting of alkali chlorides and $FeCl_3$ which is important due to its high volatility, Fig. 4. The diagrams will form the basis of a phase diagram "atlas" within the project.

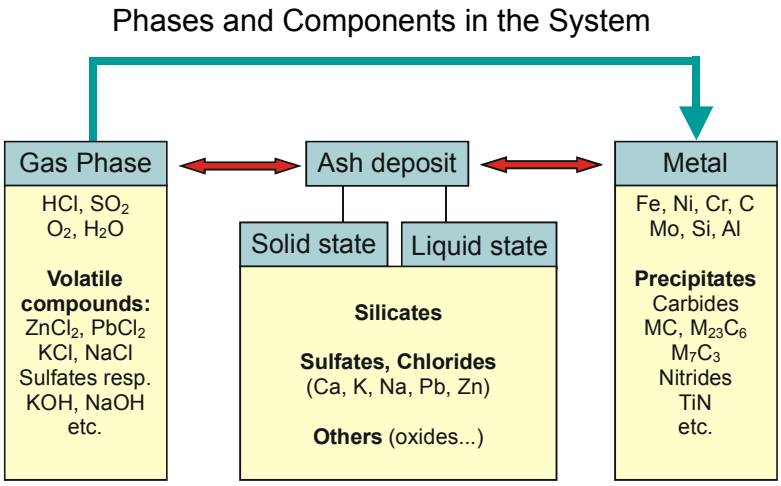

Figure 1. The thermodynamic data collection for modelling [1].

3. Corrosion and oxidation modelling

The development is split into two different approaches. First, modelling of general oxidation and corrosion using a tool implemented in Excel and separate Fortran-based libraries to calculate the thermodynamic equilibrium using ChemApp-library is carried out. This technique called Chemsheet is applied to model and simulate salt deposit-metal interaction for the KCl-$ZnCl_2$ /steel case. Second, modelling of inwards oxidation and internal corrosion with the InCorr tool based on ChemApp (local thermodynamic-equilibrium calculations) and finite – difference technique (FD model) has been developed for oxidation and internal corrosion. The tool enables simulations for prediction of internal corrosion depths and inwards corrosion of the metal. For both of these a self-consistent thermochemical database for high and low alloyed steels has been collected and corresponding comprehensive one- and two-dimensional equilibrium mappings to show the phase formation in corrosive systems have been created. The full modelling approach is presented in Table 1.

Table 1. Data and tools necessary for modelling high temperature corrosion of boiler tube materials in combustion environments.

Data and Tools	**Source**	**Processing > input** **Deliverables**
Material data	Material specifications Analyses	Elements for the thermodynamic system Corrosion model description
Service and process condition data	Plant data Testcorr/PREWIN data Specific analyses	Fuel & gas composition Temperature range Ash & deposit / type Exposure/service time temperature - time excursions
Integrated thermodynamic data bank system: FactSage	Data banks for alloys, oxides and salts specially made for the project based on known data SGTE and Fact	Phase and stability diagrams for selected material and process conditions
Kinetic data	Literature Experimental data Diffusion data - coefficients	Input for ChemSheet and InCorr models
Experimentation	Exposure tests TGA tests Metallography & analyses (EDS, XRD)	Model structures/corrosion products Data for the thermodynamic system Kinetic data and fitting of results Verification of models
Corrosion model description	Model for the corrosion mechanisms*	Boundary conditions and relations to describe the mechanisms for modelling Understanding of HT corrosion phenomena
Modelling Tools: - FactSage - Chemsheet: HTCM - InCorr: OXIDATION	 GTT & FACT VTT & GTT & MPIE UNISiegen	 Tailor made stability diagrams Modelling tool / modelling cases Modelling tool / modelling cases

* schematic pictures of layer sequences and types etc.

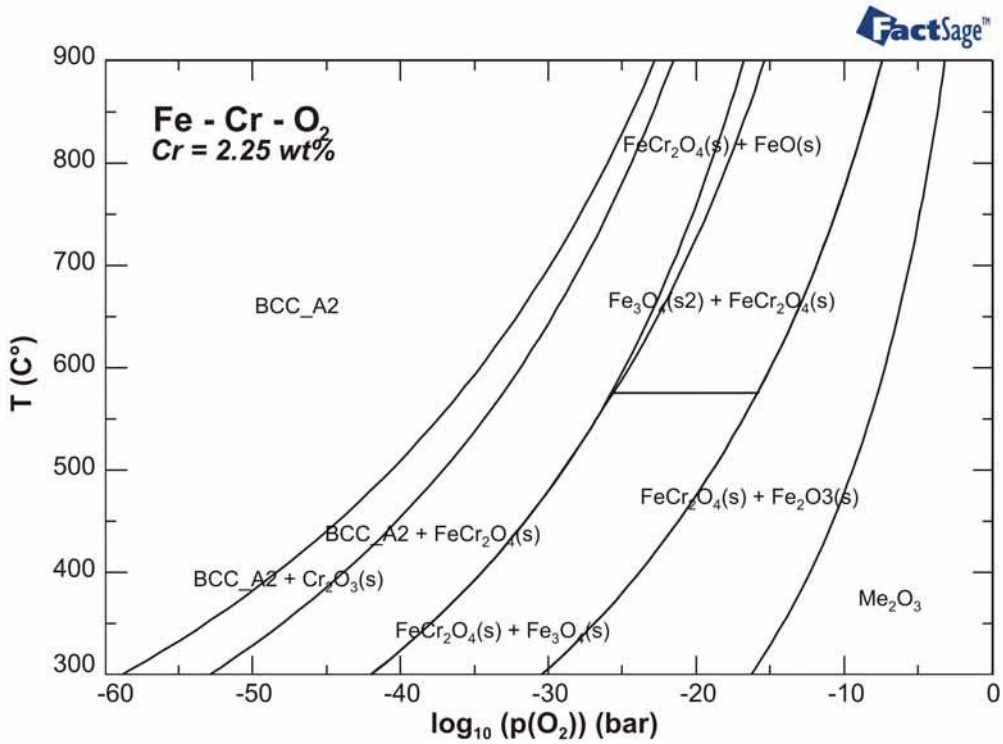

Figure 2. Fe-Cr-O stability diagram – $p(O_2)$ versus temperature – for 2.25% Cr alloy realised using FactSage. [1].

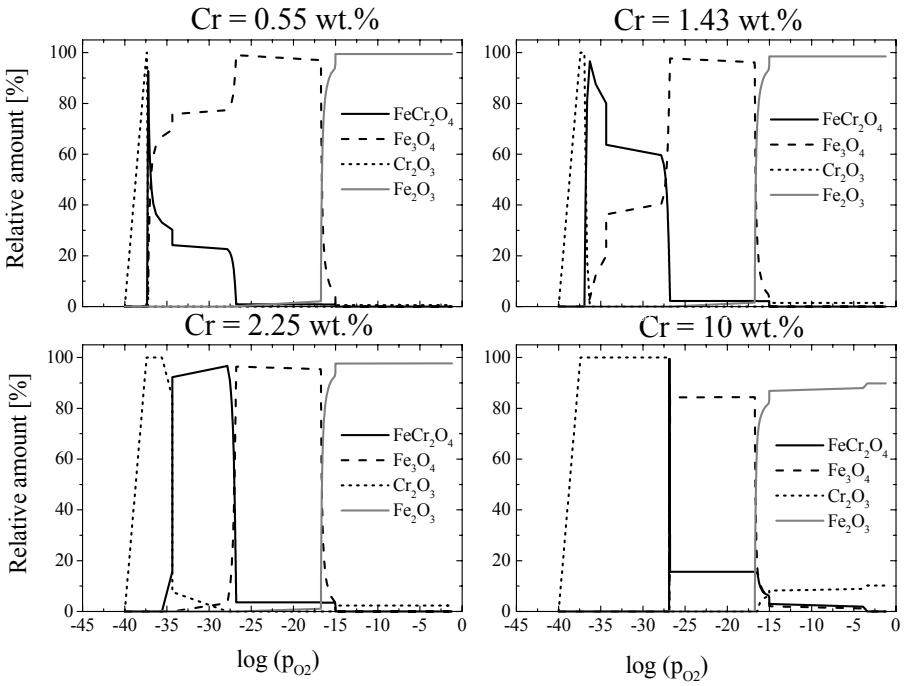

Figure 3. Steel scale composition as a function of oxygen partial pressure and chromium content at 550°C. This type of a presentation can be directly correlated to metallographic cross-sections of exposed corrosion samples. [1].

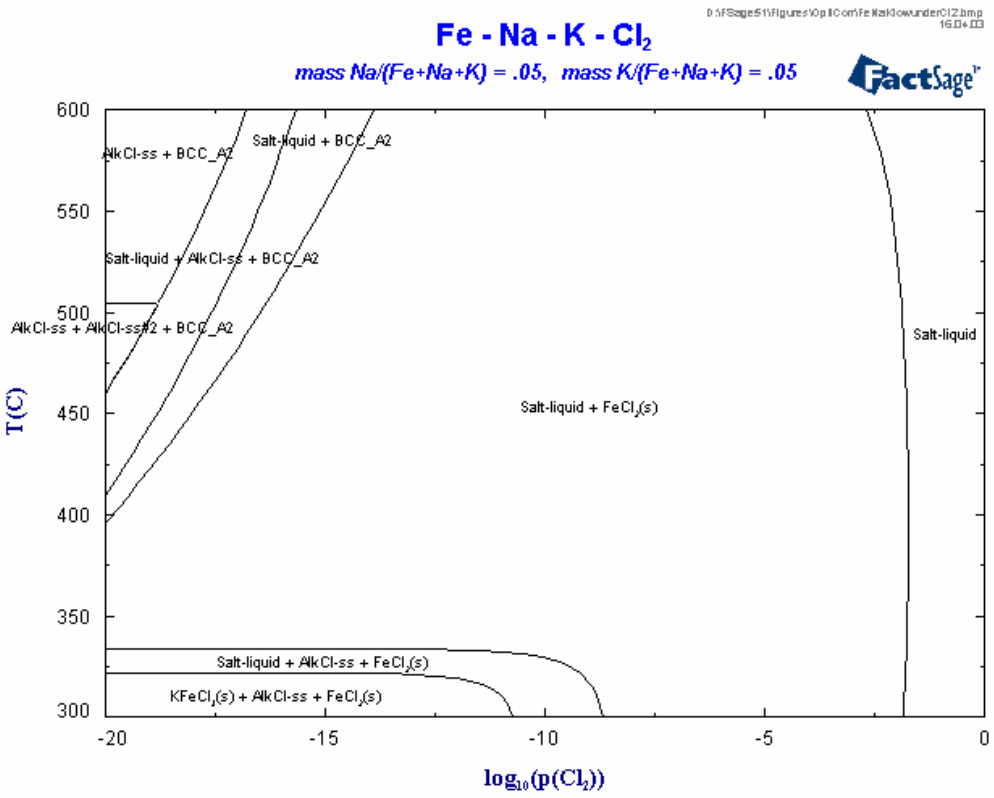

Figure 4. Phase diagram for the salt system Fe-Na-K-Cl_2. [9, 10].

3.1 ChemSheet based modelling tool for high temperature corrosion

The ChemSheet model developed at VTT and described in the text can be used to simulate any initially stationary liquid and/or solid medium that undergoes changes in its composition and volume due to diffusion and chemical reactions. The model assumes that temperature and pressure in the medium are constant.

The first part of ChemSheet-modelling consists of models for salt-induced high temperature corrosion system. The observations confirm the model initially described by Spiegel [9], Fig. 5. Therefore, the corrosion sequence can be subdivided into three different parts that correspond to the kinetic steps observed in the experiment:

- Dissolution of metal in the chloride melt at the melt scale interface
- Transport of dissolved chloride to the gas/melt interface
- Precipitation of oxide in contact with the gas phase
- Formation of a porous oxide scale.

Corresponding experimental results have been presented in [10]. A Cross section of the Fe - salt interface exposed to 320°C is presented in Fig. 6.

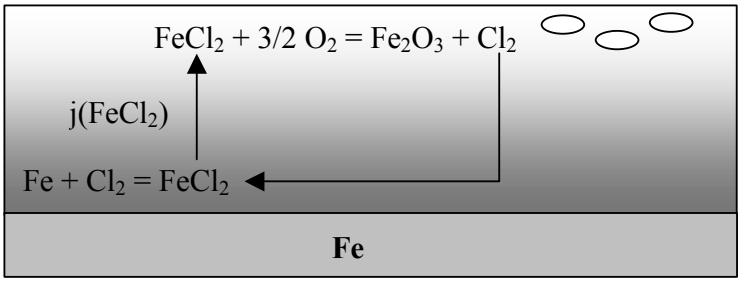

Figure 5. Model for salt melt induced corrosion [9], showing iron dissolution, transport of iron chloride and oxide precipitation.

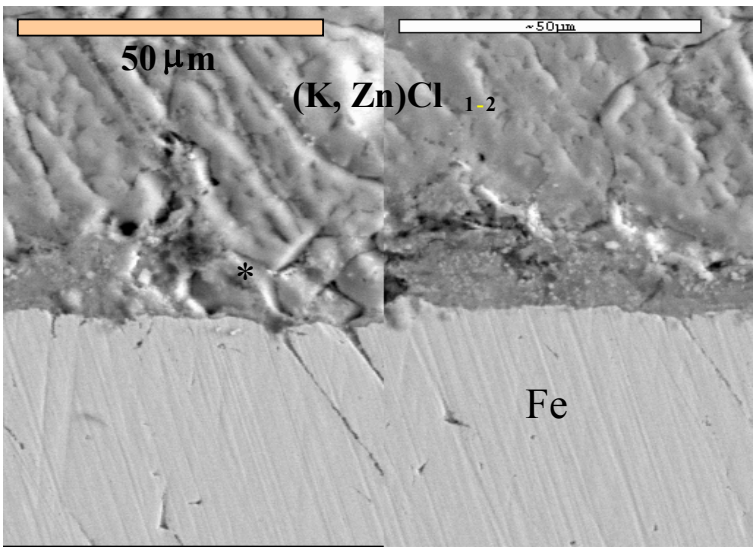

Figure 6. Thin layer of iron chloride (*), formed during the incubation time of corrosion (T = 320°C, Ar – 4 vol.% O_2, KCl-$ZnCl_2$ deposit).

In the Salt Melt Model the layer is formed on the metal alloy. The layer may be represented as one-dimensional slab with uniform or non-uniform mesh size. The boundary conditions for the slab are the interfaces between the gas flow and the salt (left side boundary in model coordinate system) and salt and the metal alloy (right side boundary in model coordinate system), Fig. 7.

For the gas/salt interface it is assumed that the diffusion in the salt is the limiting factor in the overall mass transport instead of the mass transfer from the gas to the interface. Then the concentrations of gas species at the gas/salt interface can be taken equal to their concentrations in the gas flow. Another method is to calculate the concentrations of gas species at the interface by using their solubilities to condensed species at the interface as follows

A simple one-dimensional (from gas interface to metal interface) diffusion model was made that takes both boundary interfaces into consideration. Model divides the salt layer into a number of control volumes and local equilibrium is

calculated in each volume after concentration of constituents in them is updated with a separate diffusion model (linear system of continuity equations).

A one-dimensional (from gas interface to metal interface) diffusion model was made that takes both boundary interfaces into consideration. Model divides the salt layer into a number of control volumes and local equilibrium is calculated in each volume after concentration of constituents in them is updated with a separate diffusion model (linear system of continuity equations).

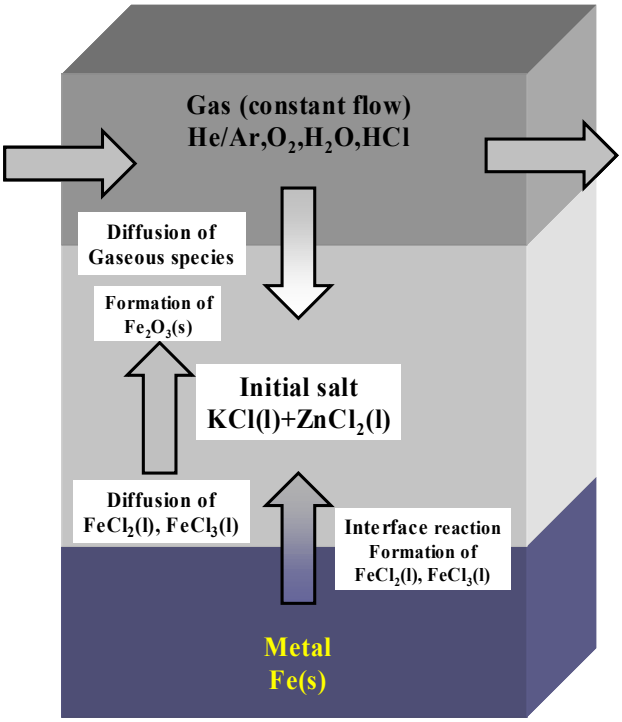

Figure 7. Representation of salt melt system.

The first data-file version is a system of seven components: Zn-K-Fe-He-O-Cl-H. It contains the gas phase, liquid salt phase, which is composed of four constituents: KCl, $ZnCl_2$, $FeCl_2$, $FeCl_3$, and several condensed phases (oxides, chlorides and etc.). As the interaction between the salt and the metal is very dependant on the interaction between the salt and the gas it seemed reasonable to make a model which could calculate the whole system. The first output is presented in Figs. 8 and 9. Fig. 9 shows only constituents between selected lower and upper limits. Here is shown the formation of Fe_2O_3, $FeCl_2$ and $FeCl_3$ in the liquid salt. The main components in the salt are KCl (initial value 50 mol-%) and $ZnCl_2$ (initial value 50 mol-%).

As the diffusion model combined with Gibbs energy minimization is quite slow to calculate a simple ChemSheet model was developed in which the gas/salt and salt/metal layers are combined into one control volume. Then measured mass gain data is used to control the rate of mass transfer from gas to control volume

as a function of time so that simulated values give good fit against the measurement, Fig. 10. The model development has been presented in conference papers describing the project [1, 7, 11].

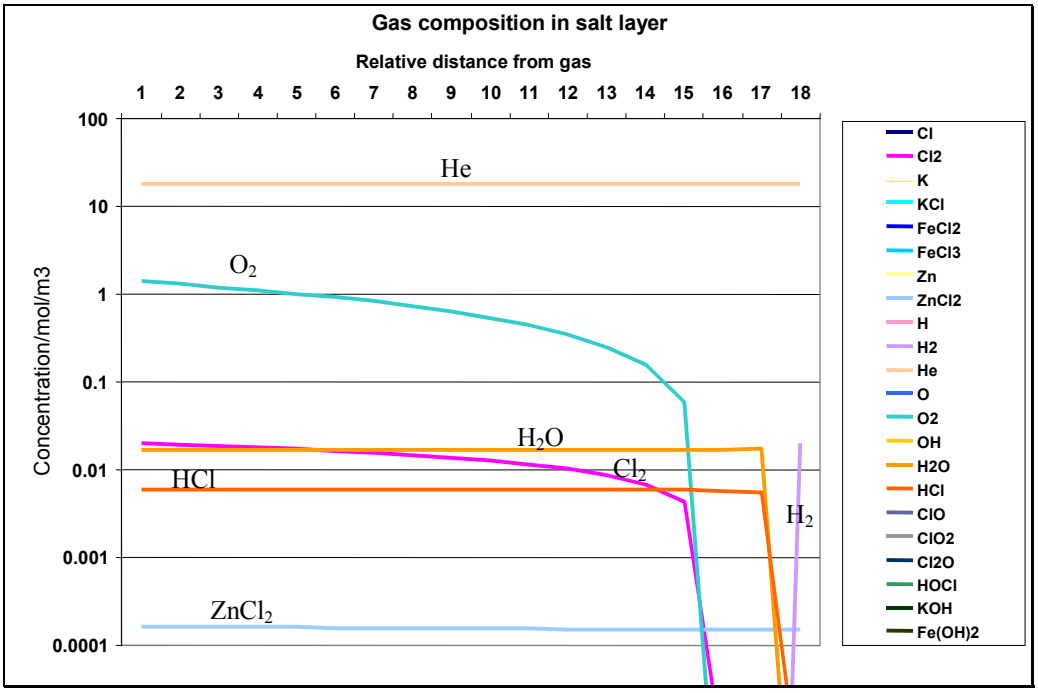

Figure 8. Gas composition in the salt layer at early stage of simulation, from the outer surface to metal interface.

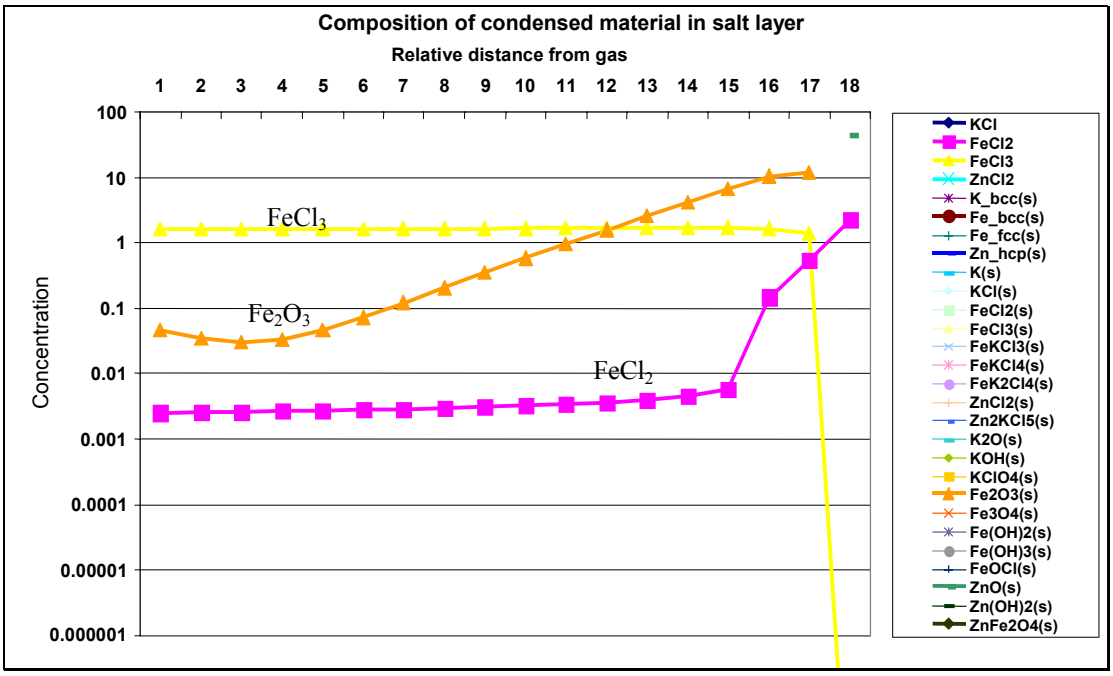

Figure 9. Formation iron oxide and iron chlorides in salt layer at early stage of simulation.

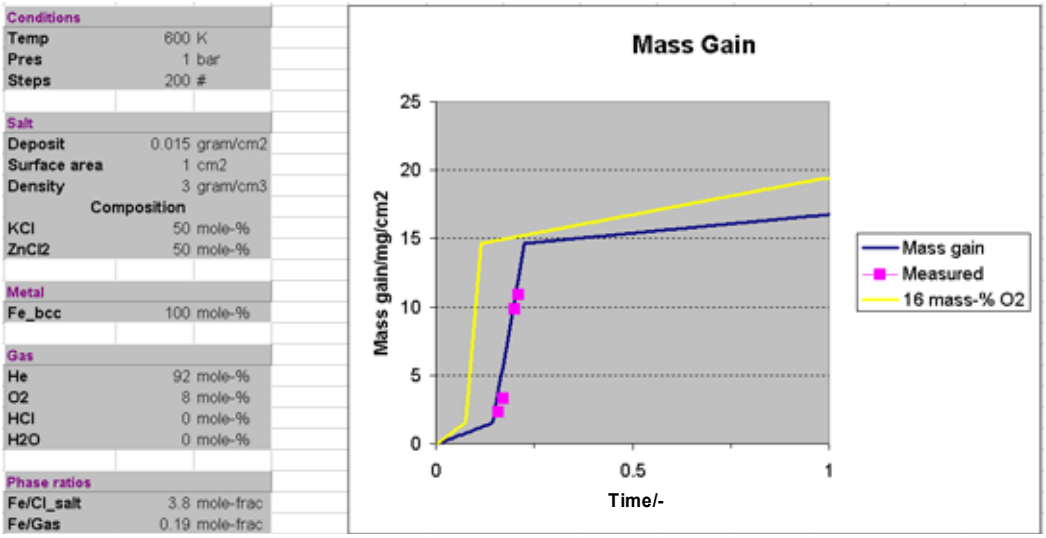

Figure 10. ChemSheet model for simulation of mass gain in salt layer using measured data.

3.2 InCorr tool development for modelling inward/internal oxidation

The overall simulation of high-temperature corrosion processes under near-service conditions requires both, a thermodynamic model to predict phase stabilities for given conditions and a mathematical description of the process kinetics, i.e., solid state diffusion. Such a simulation has been developed by integrating the thermodynamic program library ChemApp into a numerical finite-difference diffusion calculation InCorr to treat internal oxidation and nitridation of Ni-base alloys [2]. This simulation was intended to serve as a basis for an advanced computer model for internal oxidation and sulfidation of low-alloy boiler steels.

The original computer program to calculate concentration profiles during internal-corrosion was written in FORTRAN using the standard ChemApp interface to call the Gibb's energy minimiser routine. Since these calls are required after each step of the finite-difference lattice computation time for two-dimensional corrosion processes were unacceptable long.

Adaptation of the model to oxidation of low alloy steels –The model is capable to simulate multi-phase internal corrosion processes that are governed by solid-state diffusion in the bulk metal. The oxidation experiments in lab air and He-O_2-H_2O mixtures revealed that internal corrosion of low-alloy steels occurs along grain boundaries (GBs) as part of the inward oxide growth process. Since the low-alloy boiler steels contain small amounts of Cr the phase composition of the inner layer exhibits a gradual transition of the $(Fe,Cr)_3O_4$ phase to islands of the spinel phase $FeCr_2O_4$ and Cr_2O_3. To establish a suitable simulation procedure for

the inward oxide growth time-depending boundary conditions and a subdivision of the diffusion into GB and bulk diffusion in two coupled finite difference lattices had to be introduced.

Kinetics calculation – Fick`s second law (eq. 1) was solved by means of the numerical finite-difference technique using the implicit Crank-Nicolson scheme, which is schematically represented in Fig. 11. It was assumed that the diffusion coefficients in *x*- and *y*- direction, respectively, is independent of the local concentration and is only affected by temperature.

$$\frac{\partial \mathrm{C}}{\partial \mathrm{t}} = \mathrm{D_x}\frac{\partial^2 \mathrm{C}}{\partial \mathrm{x}^2} + \mathrm{D_y}\frac{\partial^2 \mathrm{C}}{\partial \mathrm{y}^2} \tag{1}$$

The basic idea of the finite differences method of solving partial differential equations is to replace spatial and time derivatives by suitable approximations, then to numerically solve the resulting difference equations. In other words, instead of solving for *C(x,t)* with *x* and *t* continuous, it is solved for $C_{i,j} \equiv C(x_i, t_j)$, where $x_i \equiv i\Delta x$ $t_j \equiv j\Delta t$. Thus the concentrations C_i^{j+1} of the diffusing species for the location step i and the time step j+1 are calculated from the neighbouring concentrations according to the implicit Crank-Nicholson solution for the diffusion differential equation [2]:

$$C_i^{j+1} = C_i^j + \frac{\Delta T}{2\Delta X^2}\left[\left(C_{i+1}^{j+1} + C_{i+1}^{j}\right) - 2\left(C_i^{j+1} + C_i^j\right) + \left(C_{i-1}^{j+1} + C_{i-1}^{j}\right)\right] \tag{2}$$

The resulting new concentrations for the following time step *j+1* are then corrected according to the thermodynamic equilibrium. The sequential calls for the ChemApp subroutines have been replaced by parallel computation, i.e. the Matlab main program (manager) operates the equilibrium calculation (thermodynamic worker) on several processors at the same time. This method allows a reduction of the computation time by a factor of 100 and more.

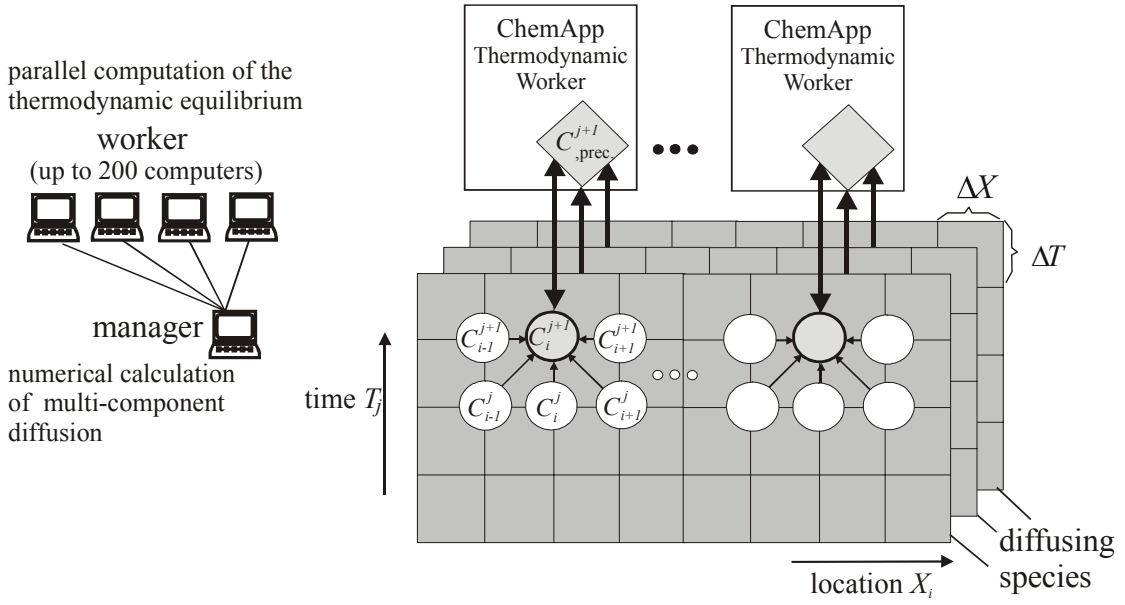

Figure 11. Scheme of the Crank-Nicholson algorithm to solve the diffusion differential equation in combination with the ChemApp programme.

In order to investigate the effect of grain size on the kinetics of oxidation, the finite difference technique was used to perform the diffusion calculation in such a way that it distinguishes between grain boundary diffusion and bulk diffusion, Fig. 12. The diffusion coefficient along grain boundaries was assumed to be 100 times higher than that in the bulk. Within the grains the diffusion coefficient was supposed to be isotropic. Thus, it was possible to simulate intergranular oxidation as it was experimentally observed in low-alloy steels. The amount of the species depends on the initial chromium content in the steel. The diffusion coefficient of oxygen in magnetite is available from the literature only for very high temperatures.

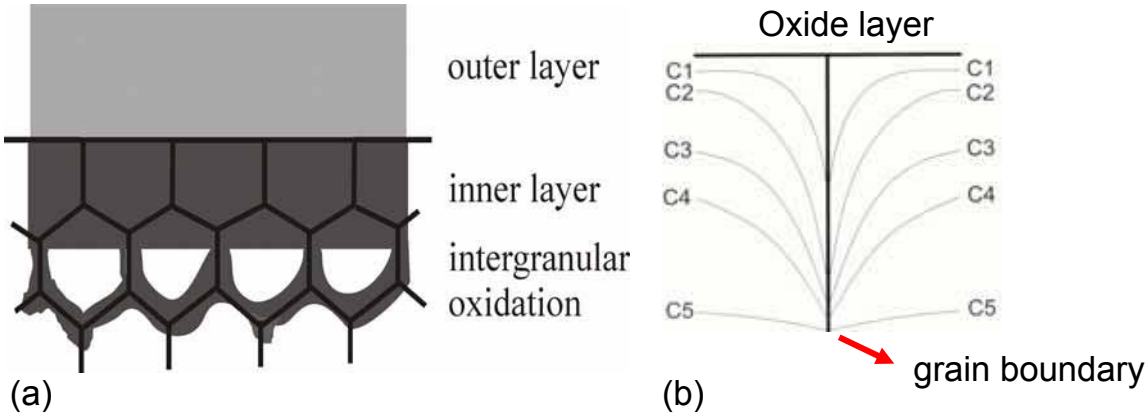

Figure 12. Diffusion mechanism for the simulation of intergranular corrosion; (a) model of the complete oxide scale with oxidized grain boundaries; (b) differentiation between bulk and grain boundary diffusion.

Fig. 13 shows a comparison of the experimental results obtained at 550°C after 72 h for a low alloyed steel at two different grain sizes with the results of the corresponding computer simulations (only the inner oxide layer is shown). For the simulation a mesh of 36 grains was used. There is a quantitative agreement between experiment and simulation. The increasing of the alloy grain size leads to decreasing inner oxide layer thickness, because the density of grain boundaries yields to an decrease in the supply of oxygen to the oxide / substrate interface.

Fig. 14 shows simulation results of the inwards oxidation of a low-alloy steel with 2.25 wt.% Cr as the alloying element at 550°C. The oxygen concentration at the outer / inner layer interface is determined by the thermodynamically stable appearance of the Cr containing spinel phase ($FeCr_2O_4$). The concentration profiles reflect the experimental results for the inward oxidation of this steel. The higher thermodynamics stability of Cr_2O_3 enables its easily formation even though the oxygen content is rather low, say with oxygen dissolved in Fe, therefore, its first appearance at the reaction front can be understandable. With the depletion of Cr, Fe will take part in the reaction process, when the oxygen concentration increased up to the necessary level, and combine with Cr_2O_3 to form spinel phase ($FeCr_2O_4$). As the oxygen potential increases part of $FeCr_2O_3$ will be further oxidized to form Fe_3O_4. And the depth of the Fe_3O_4 precipitation front is responsible for the thickness of the inner scale, it can be found, after 20 h exposure, the thickness of the inwards oxidation layer is about 8 µm, which is in a very good agreement with the experimental results [8].

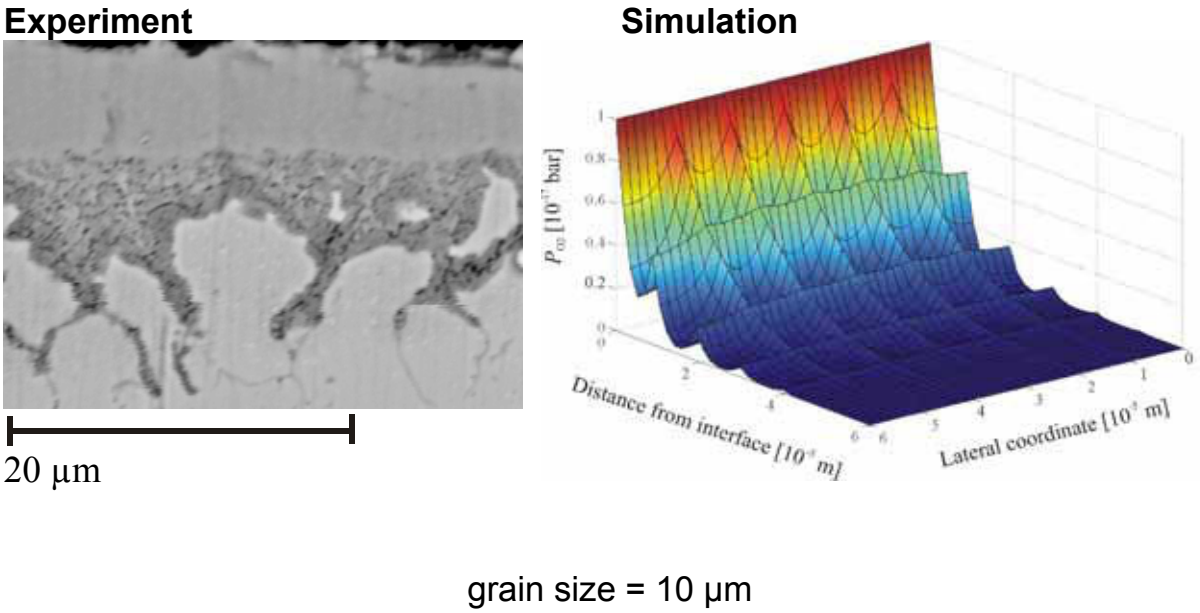

Figure 13. Comparison of experimental and simulated results for a low alloyed steel oxidized at 550°C for 72 h in laboratory air.

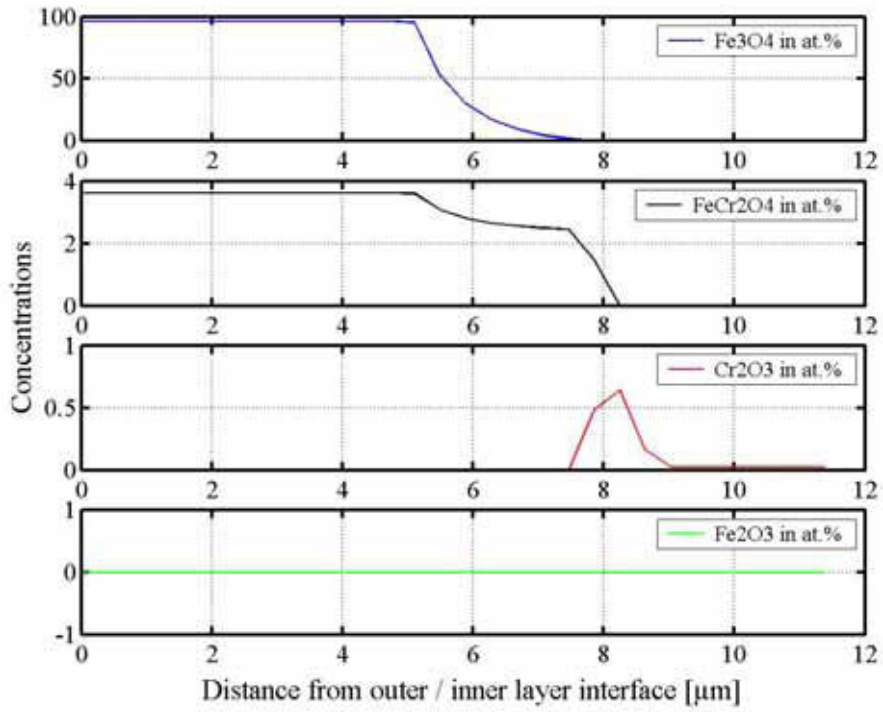

Figure 14. Simulation results of inwards oxidation of a low-alloy steel with Cr content of 2.25wt. % at 550°C after 20 h exposure; oxide phase profile (in at.%).

4. Summary

The paper presents a novel approach to model high temperature oxidation and corrosion for boiler components using thermodynamic and diffusion kinetic data and libraries.

The first step is to tailor stability diagrams for the given steel or deposit compositions at the ambient temperature range and for the atmospheric conditions. The second development presented is a modification of ChemSheet tool calculating thermochemical processes. The modification enables the use of the ChemSheet routines and interface templates for kinetic calculations combined to thermodynamic stability calculations. A salt induced corrosion case is presented as a case.

The third alternative presented is the development of InCorr tool for internal and inwards corrosion, based on finite element calculations. This method is based on thermodynamic stability calculations with solid state diffusion algorithms. The model examples describe high temperature oxidation kinetics for a 2.25Cr Steel.

References

1. L. Heikinheimo, K. Hack, D. Baxter, M. Spiegel, U. Krupp, M. Hämäläinen & M. Arponen. Optimisation of in-service performance of boiler steels by modelling high temperature corrosion – EU FP5 OPTICORR project. 6th International Symposium High Temperature Corrosion and Protection of Materials, 16–21 May 2004, Les Embiez France.

2. U. Krupp & H.-J. Christ. Ox. Met., Vol. 52 (1999), pp. 299.

3. C.W. Bale et al. CALPHAD 26(2) (2002), pp.189–228.

4. S. Tuurna, L. Heikinheimo, M. Arponen & M. Hämäläinen. EUROCORR (2003), 28.9.–2.10.2003 Budapest Hungary.

5. A. Ruh & M. Spiegel. Ibid.

6. M. Spiegel, A. Zahs & H.J. Grabke. Materials at high temperatures 20(2), pp. 153–159.

7. S. Sroda, S. Tuurna, K. Penttilä & L. Heikinheimo. 6th International Symposium High Temperature Corrosion and Protection of Materials, 16–21 May 2004, Les Embiez France.

8. U. Krupp, V.B. Trindade, B.Z. Hanjari, S. Yang, H.-J. Christ, U. Buschmann & W. Wiechert. Ibid.

9. M. Spiegel. Molten Salt Forum, Vol. 7, (2003), pp. 253–268.

10. A. Ruh & M. Spiegel. Kinetic investigations on salt melt induced high-temperature corrosion of pure metals. 6th International Symposium High Temperature Corrosion and Protection of Materials, 16–21 May 2004, Les Embiez France.

11. P. Koukkari, et. al. Y. Brechet (editor), Euromat 99 – Volume 3, Wiley-VCH Publishers, Weinheim, 2000, pp. 323–330.

The corrosion resistance of boiler steels in simulated combustion atmospheres with various CO_2 content

Szymon Środa[1] & Martti Mäkipää[2]
[1]European Commission Joint Research Centre, Institute for Energy, P.O. Box 2, NL-1755 ZG Petten, The Netherlands, szymon.sroda@jrc.nl
[2] VTT Processes, Espoo, Finland

Abstract

In the present study the common ferritic and austenitic steels (2.25Cr1Mo, X10, X20, TP347H, AC66, Sanicro28, Esshete 1250) usually used in biomass and waste combustion processes were investigated. The multi-sample exposure tests were carried out at isothermal temperature of 535°C in various simulated combustion atmospheres (22%H_2O+ 5%O_2 +xCO_2 + N_2) with different CO_2 content varying from 0 to 25 vol-% for the samples without deposit and with filter/cyclone ash deposition. Post experimental analyses have been made using SEM/EDS and XRD techniques. The presence of the deposit increases the corrosion rate of all studied materials, especially for the ferritic steels. The corrosion rate increases with increasing CO_2 content in the atmosphere. That behaviour was observed on no-deposited and deposited samples. The obtained result shows that for the ferritic steel the corrosion resistance increases with increasing Cr content in steel but only for non-deposited samples. The ferritic steels with deposits behave different. There is only a small difference on the corrosion rate of X10 (8.5 m-% Cr) and X20 (12.7 m-% Cr), even in some cases X10 exhibits better corrosion resistance. This effect could be especially observed in the atmospheres with high CO_2 content.

1. Introduction

The main limiting factor in the performance and reliability of waste incineration systems and biomass-waste co-combustion systems is the durability of materials used for boiler components; more specifically service life is limited by hot corrosion due to presence of fuels which contain very aggressive contaminants. Due to materials constraints steam temperatures in biofueled boilers are currently around 480^{o}C and even lower with waste fuels. These relatively low temperatures lead to low power generation efficiency. By increasing the understanding of corrosion mechanisms new superheater materials with higher corrosion resistance could be designed/selected in order to permit steam temperatures of up to 550^{o}C.

This would result in about a 10% increase in power generation efficiency. In addition, significant savings in maintenance costs could be achieved due to longer durability of superheaters.

The corrosion mechanisms in waste and especially in biomass combustion are not well understood due to the complex and variable ash behaviour and chemical nature of the fuel ashes. Numerous studies on failure cases and field exposure testes [1–6] lab-scale exposure tests [7–9] have provided valuable information on high temperature behaviour of plants used in waste and biomass-fired incinerator boilers. The main high temperature corrosion mechanisms causing severe metal wastage in incinerators are gaseous corrosion (oxidation, sulphidation and chloridation), hot corrosion and corrosion beneath deposit [10–18]. Despite the relatively low concentrations of HCl in the flue gas, it is believed that chloridation is one of the main reasons of severe corrosive degradation of the tubes in waste incinerators, although S-bearing species may also play role as well [6]. Beside the corrosion attack of HCl, O_2, SO_2 also H_2O (g) as one of the main constituent in combustion atmosphere can play an important rule in corrosion process [19, 20]. As it is reported in the literature, the direct attack of the other gas species like CO, CO_2 have the minor relevance on corrosion but the presence of those species affect the phase equilibrium of the slag formation process [21].

This study is the part of the FP5 Project entitled “Mitigation of Formation of Chlorine Rich Deposits Affecting on Superheater Corrosion under Co-Combustion Conditions“ (CORBI) which is aimed to improve the understanding of corrosion mechanisms in cases of biomass and waste combustion. The main aim of presented paper is to understand the effect deposition as well as the CO_2 content in combustion atmospheres on corrosion rate and mechanism of the boiler steels.

2. Experimental

2.1 Materials

In the present study several ferritic and austenitic materials usually used for the boiler applications were investigated. The chemical composition of all tested materials is shown in the Table 1. The samples for the tests were cut from the plates into rectangle shape coupons of 10 x 10 x 2–5 mm dimensions. Their surfaces were bright polished with SiC paper of 1000 grit, then degreased in an ultrasic bath with ethanol. The cyclone and filter ash samples are supplied by VTT. Chemical and SEM-analysis were conducted at MPI Dusseldorf. Figure 1(a,b) shows the SEM pictures of a filter ash (a) and a cyclone ash (b),

Table 1. The chemical compositions of studied materials [m-%].

Steel	Cr	Ni	Mo	V	C	Si	Mn	P	S	Nb	Other
2.25Cr1Mo	2.29	0.44	0.96	0.01	0.09	0.23	0.59	0.02	0.02	0.02	Cu 0.15 Al 0.01 Ti 0.003, Co 0.03
X20	10.3	0.72	0.87	0.26	0.18	0.23	0.62	0.02	0.01		
X10	8.7	0.26	0.97	0.23	0.10	0.38	0.48	0.01	0.01	0.07	Al 0.01
AC66	27.3	32.2			0.06	0.21	0.64	0.01	0.01	0.78	Al 0.01 Ce 0.055
TP347H	17.6	10.7			0.05	0.29	1.84	0.03	0.01	0.56	
Esshete 1250	15.0	9.65	0.94	0.22	0.08	0.58	6.25	0.02		0.86	B=0.004
Sanicro 28	26.7	30.6	3.32	--	0.02	0.42	1.73	0.02	0.01	--	Cu=0.87 Co=0.059 N=0.066

Table 2 shows the chemical analysis of the filter ash and cyclone ash samples. The particles of the filter ash are much finer than the particles of the cyclone ash. Chemical analysis indicated that $CaSO_4$ is the major component. The amount of chlorine is about 0.2 m-%, which will be mainly present as KCl and/or NaCl. This amount of chlorine is potentially enough to initiate corrosion of boiler tubes.

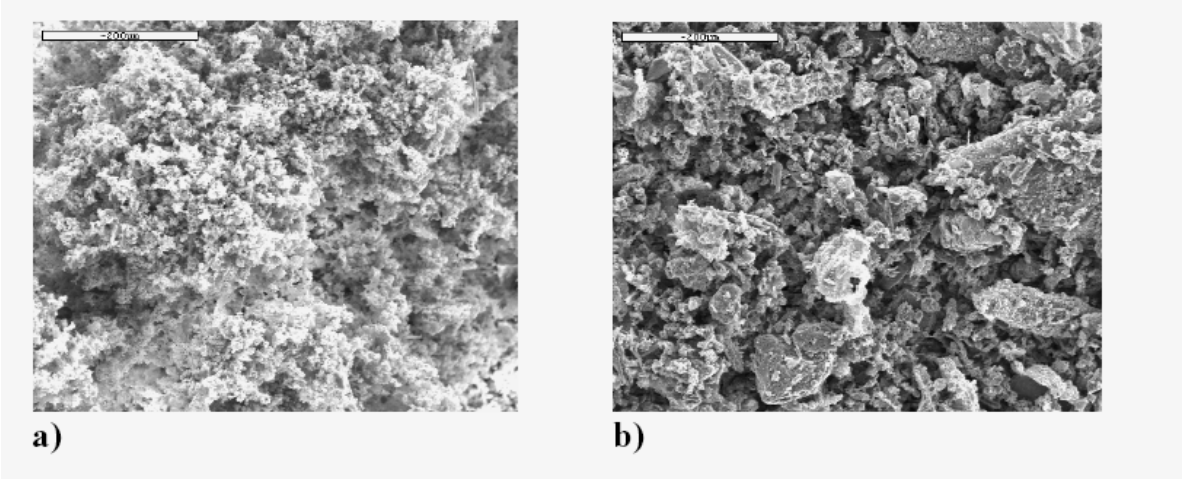

Figure 1. SEM-photograph of filter ash (a) and cyclone ash (b).

Table 2. Chemical composition of used ashes [m-%].

Ash type	Na	K	Ca	Fe	C	Si	Cl	S
Filter ash	0.2	0.8	5.7	2.4	6.2	0.6	0.2	3.1
Cyclone ash	0.3	1.1	13.1	2.5	1.7	1.3	0.2	3.1

2.2 Experimental procedure

The multi-sample exposure tests were carried out under isotermal conditions at temperature of 535°C in N_2-5% O_2-22% H_2O- x%CO_2 atmospheres with different CO_2 content varying from 0 to 25 vol-%. The exposure testes are made on the samples without and with cyclone/ fly ash deposition. Before the experiment, the ash was first mixed with the ethanol and deposited on the sample. After it was preheated at 70°C to obtain the adherent ash deposition about 50 mg/cm^2. The exposure tests were carried out in a vertical tube furnace, tube diameter 80 mm. The gas flow was 10 l/h. The gas before the furnace was passed through the humidifier at appropriate temperature to obtain 15% of the water vapour in the gas mixture. Mass change measurements combine with SEM/EDS and XRD analysis of the exposed samples were made.

3. Results

3.1 Mass change measurements

Figures 2, 3 and 4 present the mass changes per unit area for the samples without and with filter/cyclone ash deposition exposed in simulated combustion atmospheres for 360 h.

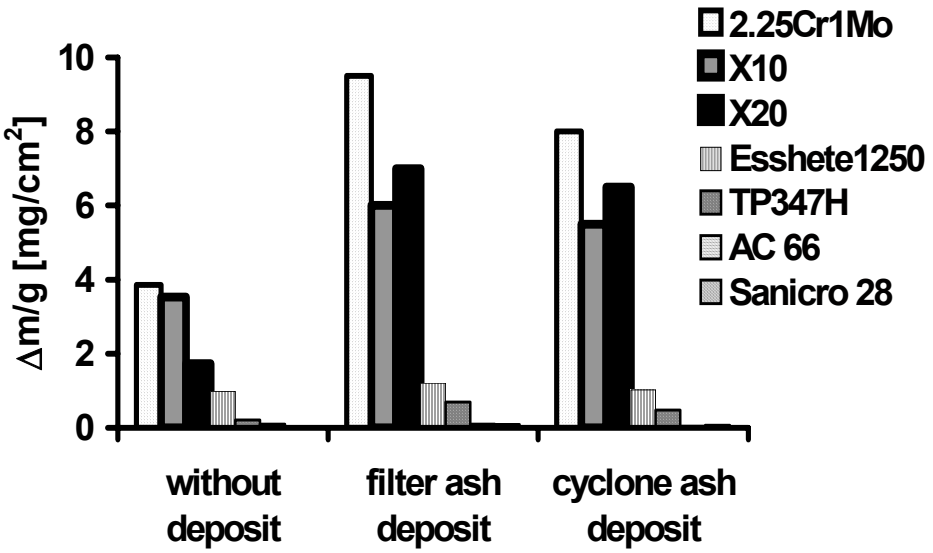

Figure 2. Mass changes per unit area for the samples exposed at 22%H2O + 5%O2 + N2 atmosphere without and with fly/cyclone ash deposition for 360 h.

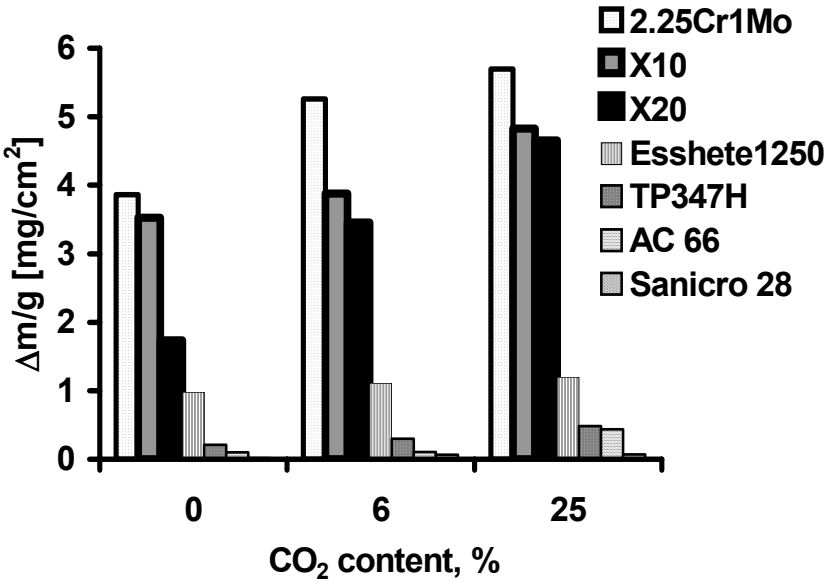

Figure 3. Mass changes per unit area for the non deposited samples exposed at 22%H_2O + 5%O_2 + x%CO_2 + N_2 atmosphere for 360 h.

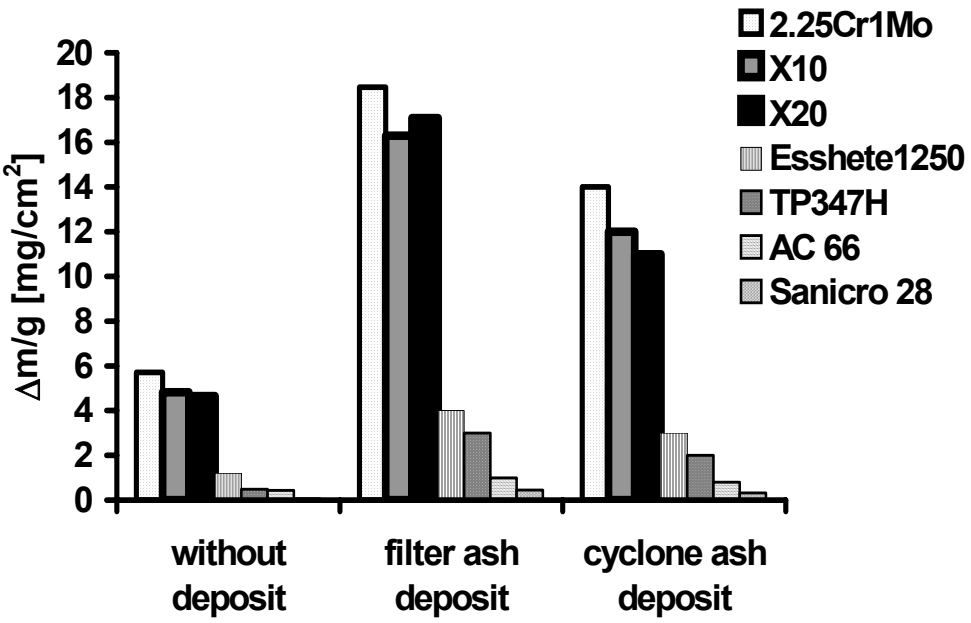

Figure 4. Mass changes per unit area for the samples exposed at 22%H_2O + 5%O_2 + 25%CO_2 + N_2 atmosphere without and with filter/cyclone ash deposition for 360 h.

3.2 Oxide scale composition and morphologies

Figure 5 presents the cross-sections of studied samples with fly ash deposit oxidized in N_2 –5%O_2-22%H_2O atmosphere at 535 °C for 360 h.

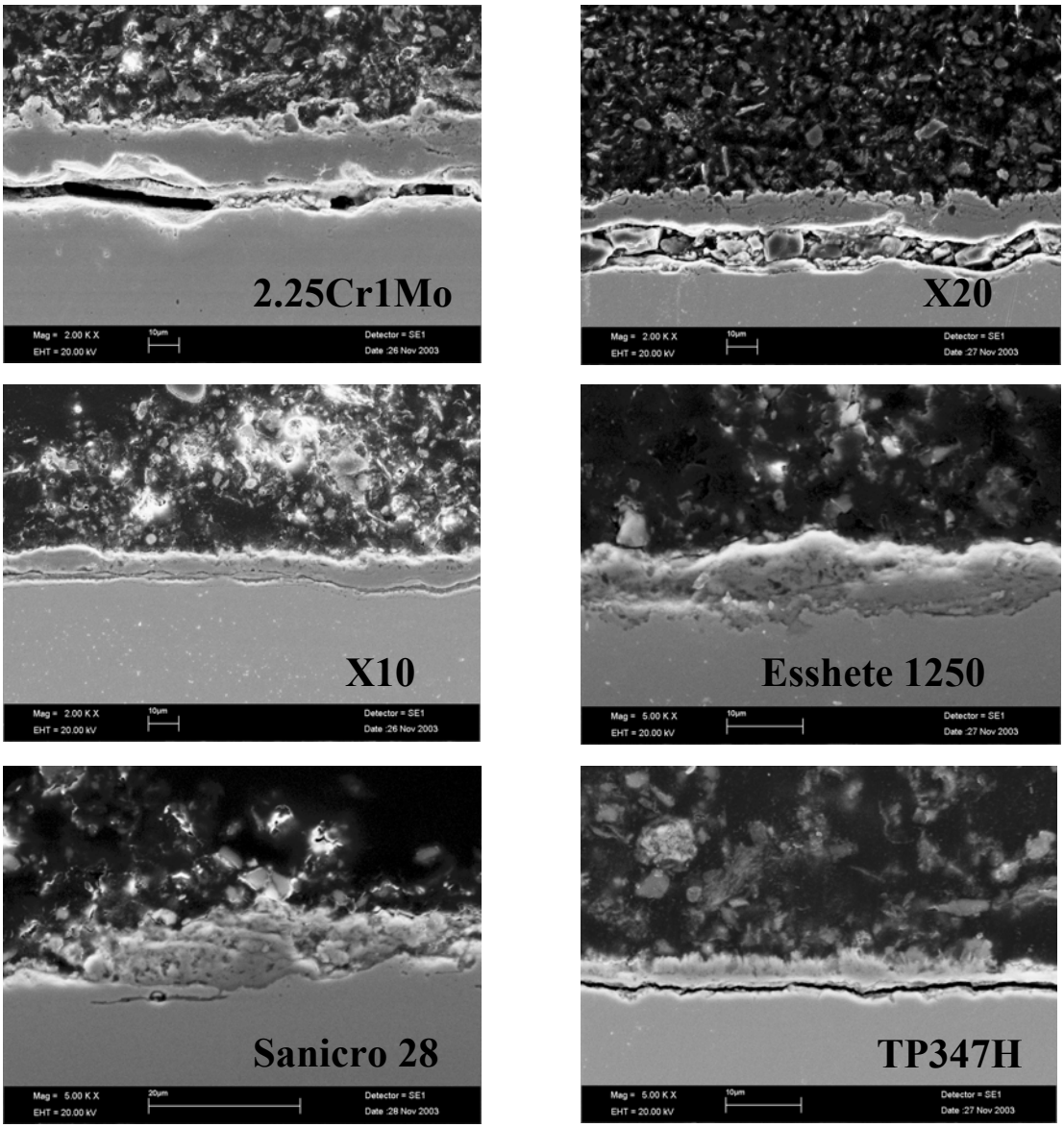

Figure 5. Cross sections of studied samples with fly ash deposit oxidized in N_2 – 5%O_2 -22%H_2O atmosphere at 535 ℃ for 360 h.

a)

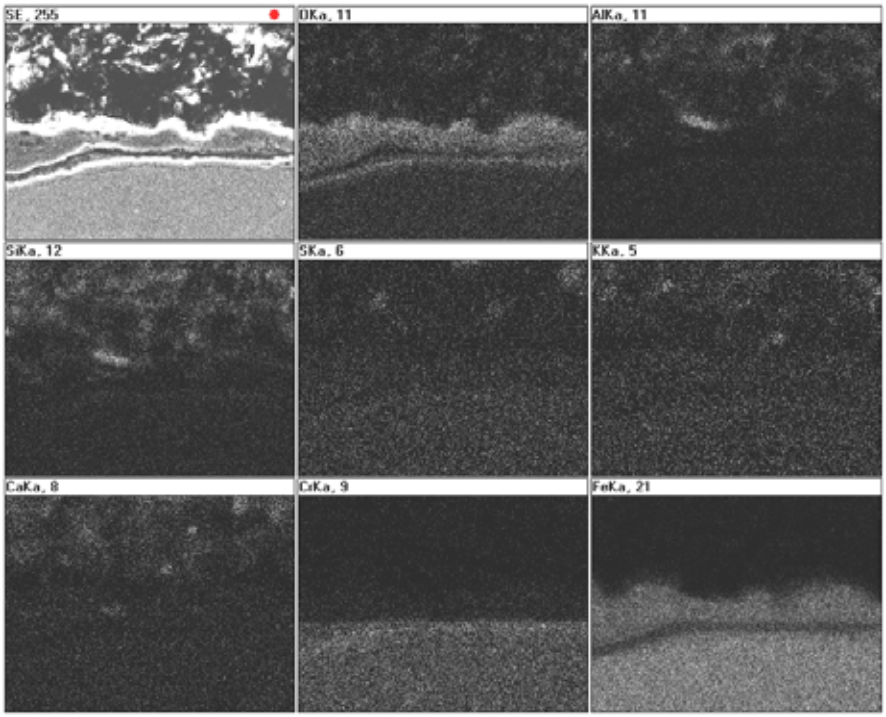

b)

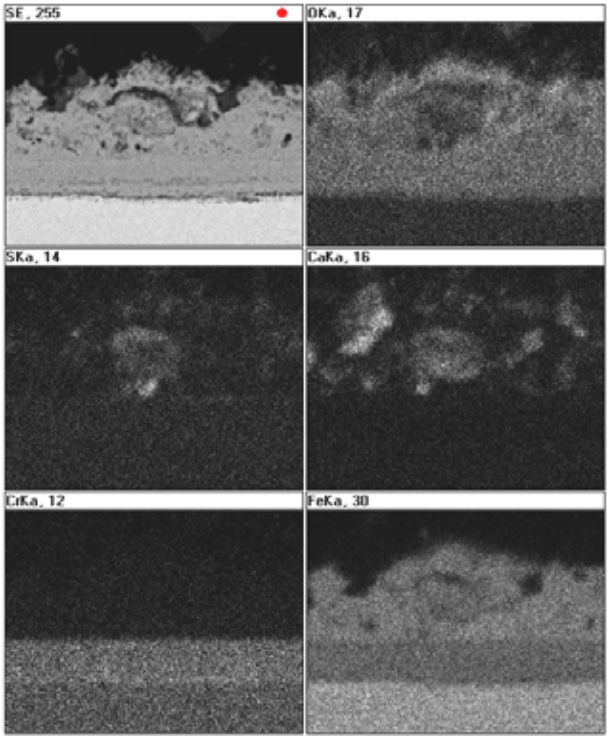

Figure 6. Cross sections X-ray maps of the X10 steel with fly ash deposit oxidized in a) N_2 – 5%O_2-22%H_2O and b) N_2 – 5%O_2-22%H_2O + 32%CO_2 atmosphere at 535°C for 360 h.

a)

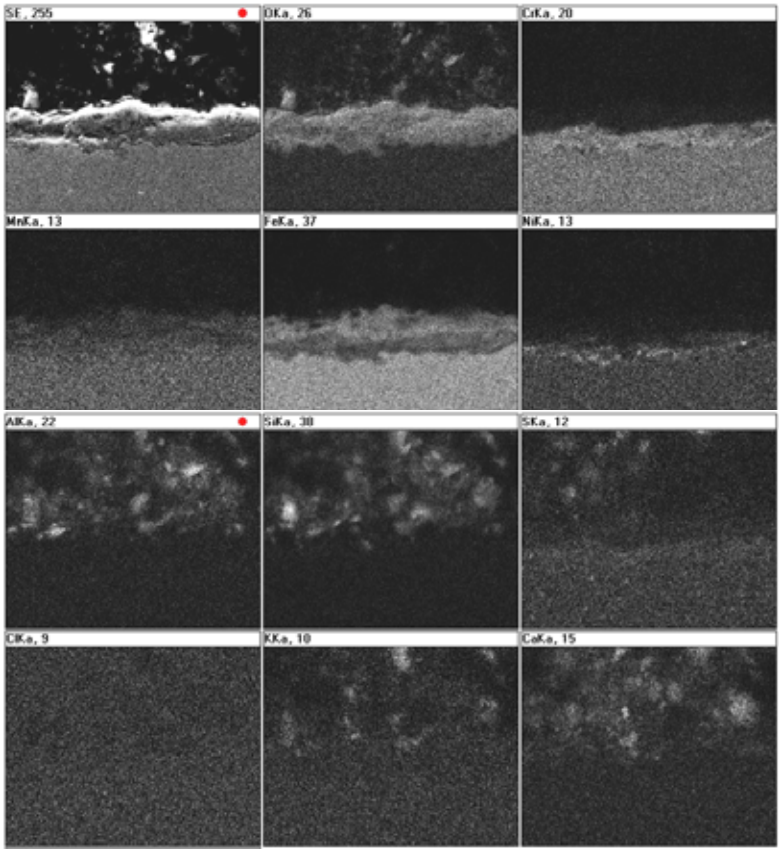

b)

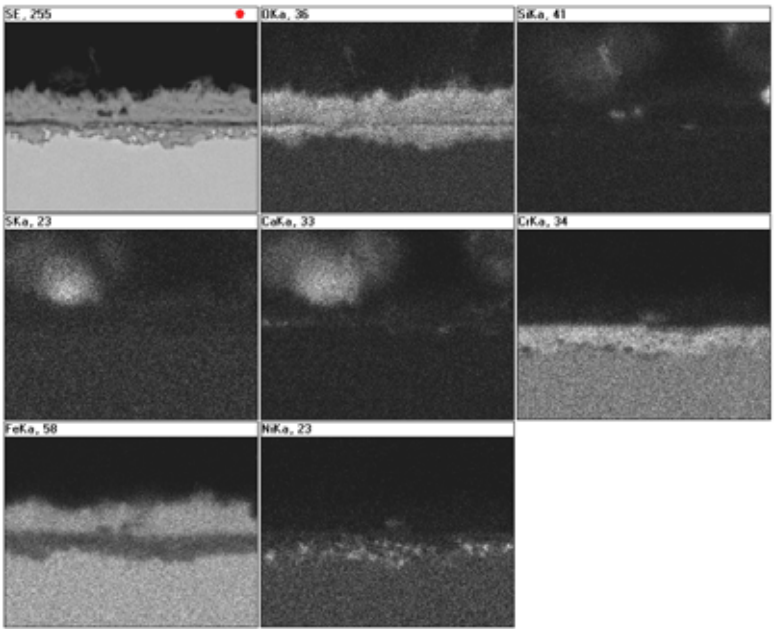

Figure 7. Cross sections X-ray maps of the Esshete 1250 steel with fly ash deposit oxidized in a) N_2 – 5%O_2-22%H_2O and b) N_2 – 5%O_2-22%H_2O + 32%CO_2 atmospheres at 535 °C for 360 h.

4. Discussion

4.1 Ferritic steels

The obtained mass changes on studied samples shows that the deposition of the samples by cyclone or ash deposit effects in acceleration of the corrosion rate. The corrosion resistance of ferritic materials increases with increasing Cr content but only for non-deposited samples (Figure 3). The ferritic steels with deposits behave differently. There is only a small difference on the corrosion rate of X10 (8.5 m-% Cr) and X20 (12.7 m-% Cr), even in some cases X10 exhibits better corrosion resistance (Figures 2, 4 and 5). The corrosion rate increases with increasing CO_2 content in the simulated combustion gas (Figure 3). The microstructure of the scales is similar to that found in oxygen containing water vapor [19, 20]. The scale consist of a thin outer layer Fe_2O_3, the middle layer (Fe_3O_4) and the inner layer ($(Cr,Fe)_3O_4$), Figure 8. On the 2.25Cr only two layers were found outer thin layer consist of Fe_2O_3 and the inner layer (Fe_3O_4).

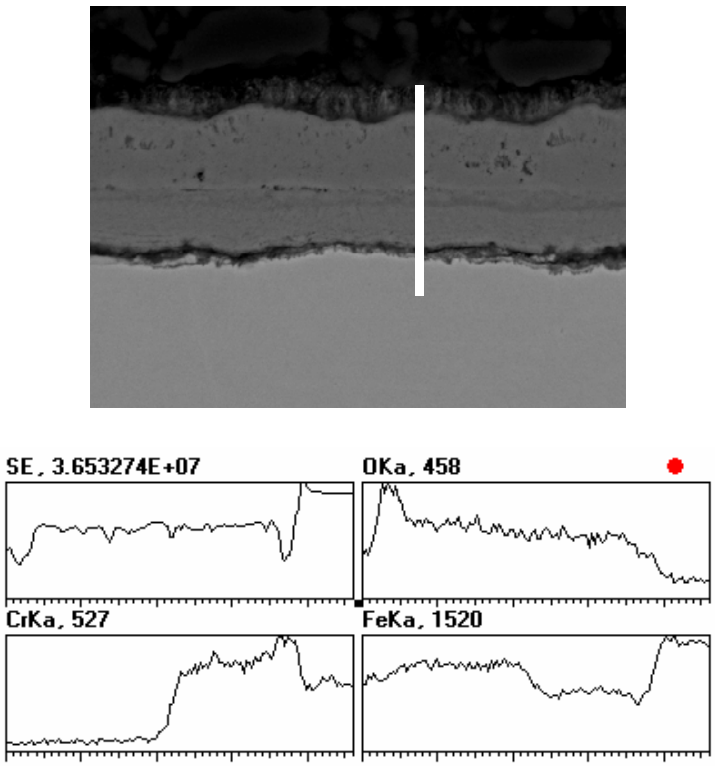

Figure 8. Cross section and linescan analysis of the X20 steel oxidized in N_2 – 5%O_2-22%H_2O + 6%CO_2 atmosphere at 535 ℃ for 360 h.

4.2 Austenitic steels

The austenitic steels exhibit rather good corrosion resistance in used conditions. The deposition of the samples as well as increase of CO_2 content in the atmosphere increase the corrosion rate of those steels, but not considerably.

The scale formed on those alloys is double-layered. The outer layer is the magnetite; the inner layer is the mixture of chromium and nickel oxide (Figure 9). The internal oxidation and localized corrosion attack were observed especially with high CO_2 concentrations in the atmosphere.

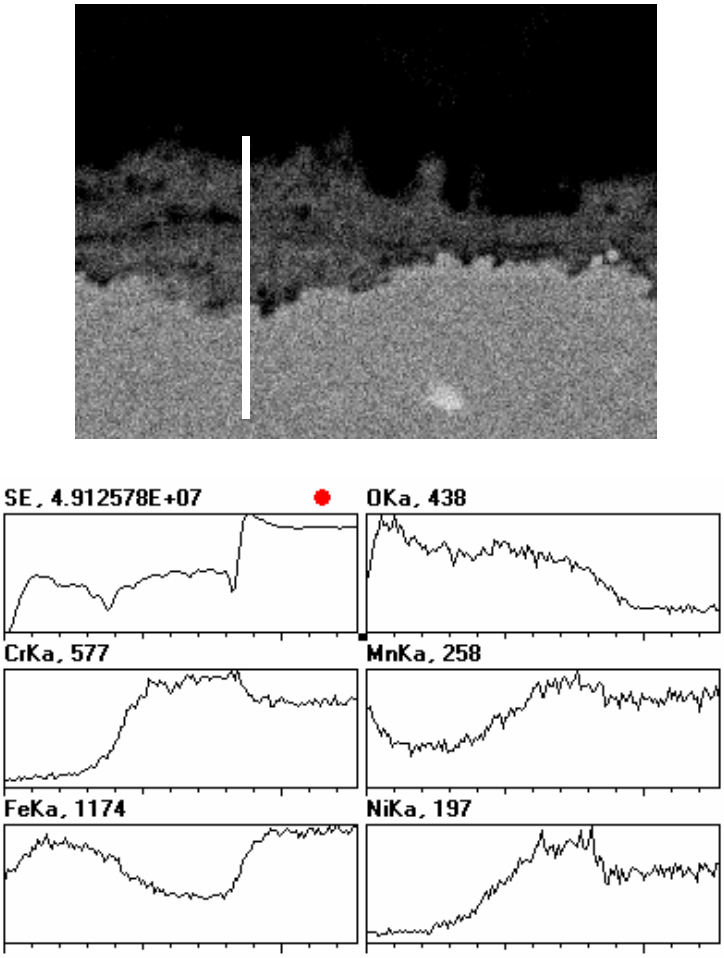

Figure 9. Line scan and X-ray maps of the TP347H steel with fly ash deposit oxidized in N_2 – 5%O_2-22%H_2O + 32%CO_2 atmosphere at 535 °C for 360 h.

4. 3 General discussion

The presence of deposit, which are used in present study, accelerates the corrosion process especially for the ferritic steels. The amount of Cl in the deposits is theoretically high enough to initiate the "active oxidation process" [13].

Solid salts like (K, Na)Cl could attack the oxide scale (i.e. composed of Fe_2O_3) in the presence of oxidant. In the presence of water vapor the reaction could take place due to (Eq. 1):

$$Fe_2O_3 + 4\,(K, Na)\,Cl\,(s) + 3/2\,O_2\,(g) + 2H_2O = 2(K, Na)_2FeO_4 + 4HCl(g) \quad (1)$$

Due to the simultaneous presence of $CaSO_4$ and $CO+CO_2$ relatively high SO_2 activities are established (Eq. 2)

$$CaSO_4 + CO = CaO + SO_2 + CO_2 \quad (2)$$

In the presence of HCl the sulfates could be also transfer to the chlorides [22] Eq. 3:

$$CaSO_4\,(s) + 2HCl(g) = CaCl_2 + SO_2(g) + H_2O(g) + ½\,O_2(g) \quad (3)$$

As a consequence, the corrosion process could involve simultaneous oxidation and /or sulphidation [19].

When CO_2 is present in the corrosion atmosphere the carbonates could form (Eq. 4)

$$Me + 2CO_2 = MeCO_3 + CO \quad (4)$$

In those conditions also solid carbon could be form due to the Boudouard reaction, but also, more preferably, by the oxidation reactions (Eq. 5 and 6):

$$2Me+CO_2 = 2MeO + C \quad (5)$$

$$Me+CO = MeO + C \quad (6)$$

And so the presence of solid carbon changes the thermodynamic conditions on the interfaces, which could result the carbides formation (e.g. $Cr_{23}C_6$, Cr_7C_3 and Cr_3C_2). Due to this process the concentration of Cr in metal became lower and resulting the lower corrosion resistance of the alloy. In those condition the internal oxidation zone appears due to direct oxidation of Cr and/ar the oxidation of chromium carbides.

5. Conclusions

The presence of the cyclone/filter ash deposit accelerates the corrosion rate of studied samples due to presence the solid salts: KCl, NaCl and $CaSO_4$. The presence of CO_2 in simulated combustion atmosphere accelerates the corrosion process. The corrosion rate increases with increasing CO_2 content in the atmosphere for no-deposited as well as for deposited samples. The obtained results show that for the ferritic steel the corrosion resistance increase with increasing Cr content in steel but only for non-deposited samples. In the atmospheres with high CO_2 content, the deposited samples of X10 steel have better corrosion resistance than steel X20 which has higher Cr concentration.

6. Acknowledgements

This study was made under FP5 Project entitled "Mitigation of Formation of Chlorine Rich Deposits Affecting on Superheater Corrosion under Co-Combustion Conditions" CORBI (ENK5-CT-2001-00532)

References

1. B. Wallen, A. Bergquist & J. Nardström. Mater. Perform. 34 (1995) 47.

2. J. I. Federer. Corrosion of Fluidized Bed Boiler Materials in Synthetic Flue Gas, ORNL/TM-8819, ORLN, Oak Ridge, TN (1983).

3. H.H. Krause. In: Incinerating municipal and industrial waste. ed. by R.W. Bryers (Hemisphere Publ. Corp., New York, Washington, Philadelphia, London, 1991).

4. H. Asteman, K. Segerdahl, J.-E. Svensson & L.-G Johansson. Materials Science Forum, Vol. 369–372, pp. 277–286, 2001.

5. H.H. Krause & I.G. Wright. Mater. Perform. 35 (1996) 46.

6. R.W. Bryers. Prog. Energy Combust. Sci. 22 (1996) 29.

7. M. Spiegel. In: *Corrosion 99, 25–30 Apr. 1999, San Antonio, TX* (NACE, Houston, TX, 1999), pp. 1–14, paper 337.

8. M. Spiegel. Mater. Corros. 50 (2000) 373.

9. M. Spiegel. Mater. Corros. 51 (2000) 303.

10. Y. Kawahara, K. Takahashi, Y. Nakagawa, T. Hososda & T. Mizuko. Corrosion 2000, Paper no. 265, NACE, Orlando, FL, 2000.

11. D.B. Meadowcroft. In: UK Corrosion'93, (Icorr, London, 1993).

12. F.H. Stott. In: *3rd NACE Latin American Region Corrosion Congress (Latincorrosion 98), 30 Aug. – 4 Sep. 1998*, Cancun (NACE, Huston, TX, 1998).

13. H.J. Grabke, E. Reese & M. Spiegel. Corros. Sci. 37 (1995) 1023.

14. K. Wickert. Warme, Band74, Heft 4 (1969) 103.

15. R. U. Hausemann. VGB-Kraftwerkstechnik, 72 (1992) H. 10, pp. 918–927

16. G. Sorell. Materials at High Temperatures 14 (3), pp. 207–220, 1997.

17. D. Bramhoff, H.J. Grabke, E. Reese & H.P. Schmidt. Werkst. Korros. 41 (1990)

18. D.B Meadowcroft. In: *Proc. Conf. Materials for Advanced Power Engineering 3–6 Oct. 1994, Liege*, ed. by Coutsouradis et al., Part II. Pp. 1413–1430

19. S. Sroda, S. Turna, K. Pentila & L. Heikinheimo. 6th International Symposium High Temperature Corrosion and Protection of Materials, 16–21 May 2004, Les Embiez France.

20. H. Nickel, Y. Wouters, M. Thiele, W.J. Quadakkers & J. Fresenius. Anal. Chem. (1998) 540–544.

21. K. Görner. Proc. Conf.: 13th IFRF Members' Conference: "Waste Incineration State-of-the-Art and New Developments", Noordwijkerhout, Netherlands, 2001.

22. M. Spiegel. Mater. High Temp. 14 (1997) 221.

The European project "CRETE": Development and harmonisation of Creep crack growth Testing for industrial specimens

V. Bicego[a], B. Dogan[b], H. Jaffal[c], K. Nikbin[d] & B. Petrovski[b]

[a] CESI, Milan, Italy
[b] GKSS Research Centre, Geesthacht, Germany
[c] CETIM, Senlis Cedex, France
[d] Imperial College, London, UK

Abstract

The integrity assessments of high temperature components containing flaws rely on the use of structural analysis, assessment methods and information of material behaviour and data. The aim of the "CRETE" project (2001–2004), partially funded by EC, is to develop harmonised techniques for measuring Creep Crack Growth (CCG) data, material characteristics by non-conventional specimen geometries, suitable to match the size, crack position, shape and the constraint of the actual component to be assessed, and convenient to be sampled from small sections and tubes. A state of the art review of CCG testing of non-standard test geometries, finite element studies, and integrated CCG tests on a number of alternative specimen types, will lead to the main deliverables. These are a testing Code of Practice and a specimen selection guideline document, which are presented in the present paper.

1. Introduction

The integrity and remaining life assessments of high temperature components in service rely on the application of structural analysis using fracture mechanics methods and material characteristics and data [1–3]. The defects have been detected or assumed to exist, defined by minimum allowable limits of detectable flaws using Non Destructive Testing (NDT) methods. Herewith the difficulty is faced in obtaining the information from experiments that needs to be validated and furthermore standardised.

The only existing CCG testing standard for metallic materials is the American Standard, ASTM E1457-00 [4], addressing particular geometry of Compact Tension, C(T), specimen. While C(T) specimen geometry is not a problem for

CCG testing and analysis for material development studies as ad hoc sized casts can be utilised, special difficulty has always existed in producing specimens machined out of components in power, petrochemical and chemical industry, e.g. of pipes, rotors and disks. For example, in recent years a number of laboratories have had to use specimens machined out of components from thin wall tubes of 6–7 mm wall thickness and pipes of 12–20 mm thickness, in order to study CCG failure in fossil power stations and petrochemical industry. This work was conducted on the only possible specimen types that can be machined from these components, namely circumferentially curved shapes, or flat specimens sampled with the major length along the pipe axis, or elongated rod specimens similar to impact testing specimens. A view of several non standardized geometries which were used in various CCG studies to date is provided in Fig. 1, with the standard C(T) geometry included.

A three year European project CRETE: Development and Harmonisation of Creep Crack Growth Testing for Industrial Specimens – a Route to a European Code of Practice [5] was started in 2001, in the frame of the EC Measurement & Testing programme. It aims at developing testing procedure and drafting a Code of Practice (CoP) for a number of non-conventional geometries. The seven partners in the CRETE project are: CESI (Italy), VTT Industrial Systems (Finland), British Energy Generation (UK), GKSS Research Centre (Germany), CETIM (France), Technical University of Darmstadt (Germany), and Imperial College (UK).

The specimen types considered in the project are C-shape tension (CS(T)), middle cracked tension (M(T)), single edge notch bend (SEN(B)), single edge notch tension (SEN(T)), double edge notch tension (DEN(T)), as well as the standard C(T) specimen for reference. The new specimen geometries bear a number of unknowns for a verifiable CCG data generation. Firstly, it has been shown that stress state and the level of constraint markedly affects the CCG rates which need to be addressed in the project. Secondly, compared to data from C(T) specimens, very little comprehensive verified CCG data exist for these geometries. On the other hand, advantages over the traditional C(T) specimen is potential matching of the size, crack position, shape and the constraint of the actual component. In particular when specimens have to be sampled from small sections of industrial components, for example in the power and petrochemical industries, it has been found that the so-called non-standard specimens are more relevant and convenient to machine and test for data generation.

2. The CRETE project work programme

The main objectives of the activities within CRETE are directed to provide two deliverables:

- a Code of Practice for creep crack growth testing of non-standard specimen geometries, essentially targeted to testing labs and suitable for eventual standardisation, and
- Specimen Selection Guidelines, namely a document providing guidance for the choice of best specimen geometry in terms of size, constraint, range of valid data generation, targeted to industrial end users of components at high temperature.

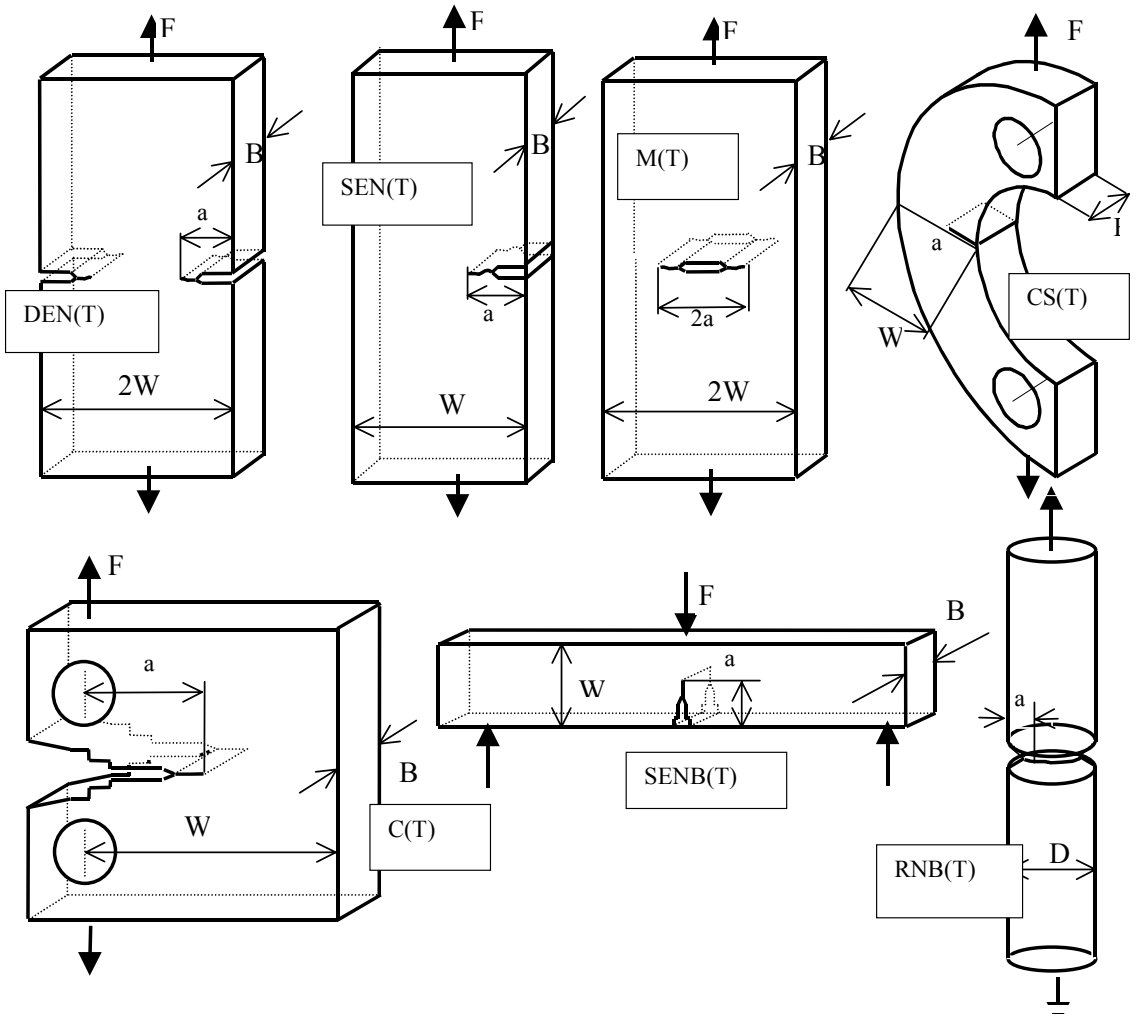

Figure 1. Shapes of specimens that can be considered for CCG testing: DEN(T) = double edge notched tension, SEN(T) = single edge notched tension, M(T) = middle cracked Tension, CS(T) = C-shaped (in) tension, C(T) = the standard compact tension, SEN(B) = single edge notched bend, and RNB(T) = round notch bar tension.

The two documents are to be built based upon the experience of previous CCG studies of experimental and FEM analyses with these nonstandard specimen geometries. The data will be obtained and the code will be verified with tests to be carried out within this project and supported by literature data.

Therefore, firstly a review was undertaken on the state of the art CCG activities using various specimen geometries and an inventory of available data was made. A number of features, such as initial crack size, use of side grooves, and thickness to length ratio were examined and defined. It was found that CS(T), SEN(B), M(T), DEN(T), and SEN(T) specimens emerged as the first priority (see Figure 1). They were chosen to be included in the draft Code of Practice which is to be produced as the main deliverable of this project [6]. In addition, there was also some support for the RNB(T) specimen to be considered in CRETE. However past experience on RNB(T) was less advanced, limited to a few attempts in UK, Italy and Japan. Therefore, the RNB(T) activity was left aside, to be re-examined possibly at end of this project. Finite Element Analyses (FEA) is undertaken to validate a number of formulae currently proposed for the analytical estimation of crack tip parameters, K and C*. The characteristic transition times of creep fields were estimated for the different geometries.

A Round Robin testing programme was designed to be carried out by six partners involved in CRETE using two steels, a carbon-manganese (C-Mn) steel and the 316H stainless steel, tested at 400 and 550°C, respectively. Starter cracks using fatigue precracking and electro-discharge machining (EDM) notches were compared to observe their effect on crack initiation behaviour. The results were then analysed using analysis programs including 'ZRATE'. Also the characteristic transition times of creep fields were estimated for the different geometries. The specimen geometries and dimensions are shown in Table 1, including crack size a, section width W, specimen thickness B, and net (i.e. total minus side grooving) specimen thickness B_n. The load is denoted F, in all cases and for the SEN(B) specimen this is defined as the central point load.

Table 1. The dimensions of the specimens considered in CRETE.

Specimen	B (mm)	B_n (mm)	W (mm)	a_0 (mm)	Load Line Offset (mm)	Pin Diameter (mm)	End Thickness (mm)
CS(T)	25	20	25	5	12.5	12.5	-
SEN(B)	12.5	10	25	7.5	100[@]	-	-
DEN(T)	12.5	10	12.5[#]	3.75[#]	-	12.5	25
SEN(T)	12.5	10	25	7.5	-	12.5	25
M(T)	12.5	10	12.5[#]	3.75[#]	-	12.5	25
C(T) (ref.)	25	20	50	25	-	12.5	-

[#] Semi-dimensions for DEN(T)
[@] Span for SEN(B)

It is intended that from the results of this study the CoP and the guideline document for optimum selection of test specimens will be covering a range of creep brittle to creep ductile material behaviour.

3. Achieved results

In the following part the progress made to date are briefly reported. It is pointed out the following:

- The project is due to be concluded in September 2004, therefore main conclusive analyses are still not achieved per BALTICA VI Conference drafting. Although the experimental work is almost concluded in terms of testing effort, the final overall data analysis is pending. Therefore, the CoP is fully drafted [7], however, requires verification with final inputs from CRETE tests.
- The CoP is only marginally presented/discussed here, as another specific CRETE paper in this Conference is intended to present CRETE CoP matters [7].

3.1 Finite Elements (FE) analyses

The C^* can be determined experimentally or using numerical and limit analysis methods. The experimental procedure is applicable to testing laboratory specimens as in of CRETE project for generation of CCG materials data. The other two methods are employed for calculation of C^* for components. In experimentally approach, C^* is calculated from the general relationship:

$$C^* = \frac{P\dot{\Delta}}{B_n(W-a)}\frac{n}{n+1}\eta \tag{1}$$

where

$$\eta = -\frac{1}{m}\frac{dm}{d(a/W)} \tag{2}$$

where $\dot{\Delta}_c$ is the load-line creep displacement rate, B_n is the net thickness of the specimen with side-grooves and W is the width, and n is the stress exponent in creep law and m is the yield load ratio. The η functions for each geometry allow solutions for C^* to be evaluated using experimental load-line displacement rate and crack length data. Therefore, the main objectives of FEM task within the CRETE project was to perform generic calculations in order to evaluate and validate analytical formulas for fracture mechanics analysis on new specimen geometries of DEN(T), SEN(T), SEN(B) and CS(T). The calculations performed in the project were:

- Elastic plane strain analyses to determine the stress intensity factors and the corresponding contour integrals for selected specimens;

- Elastic-perfectly plastic plane strain analyses to calculate the collapse loads and the reference stresses and η_p factors for selected specimens;
- Elastic-power law creep plane strain analyses for a range of n values (3, 7, 10, 20) and evaluation of C* normalised factors for selected specimens.

The range of dimensions for these specimen are those defined above section 2.

The ABAQUS software, version 6.3, was used to perform all the necessary finite element analyses. Plane strain hypothesis was made to carry out the calculations. Typical FE models are shown in Figures 2 and 3.

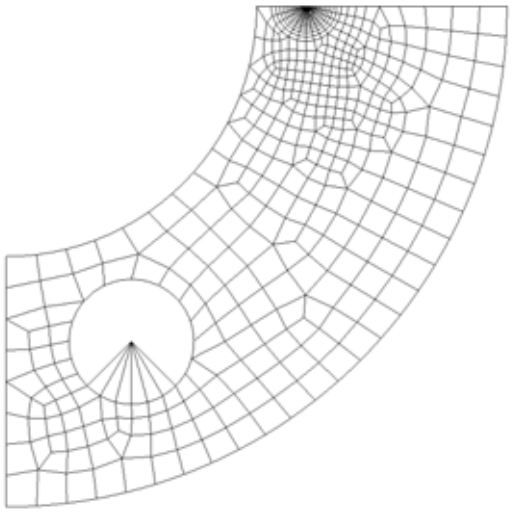

Figure 2. FE model for CS(T) specimen.

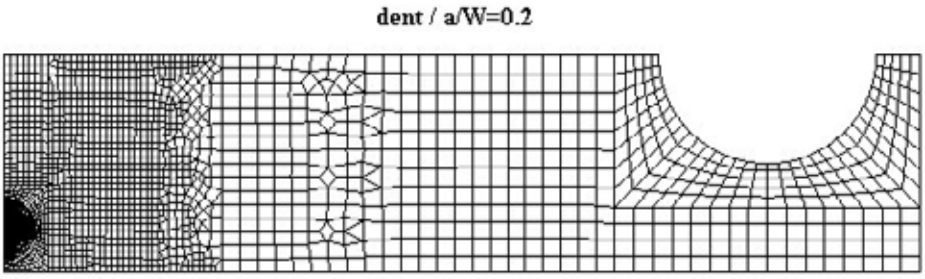

Figure 3. FE model for DEN(T) specimen.

3.1.1 Elastic parameters

For elastic behaviour, the stress intensity factor (K) and contour integral (J) were evaluated for the selected specimens. The same total concentrated load, F = 20 kN, was applied to all the specimens.

For comparison, analytical values for stress intensity factors [8] were compared with the FE solutions. Figure 4 shows this for SEN(B) and SEN(T) geometries. The maximum error obtained was less than 5% for all the geometries looked at.

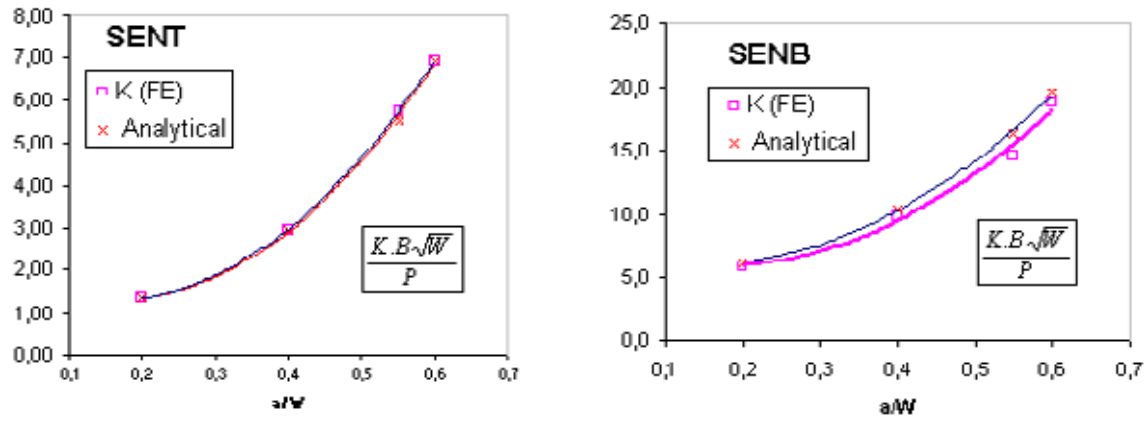

Figure 4. Comparison of FE and analytical K values for SEN(B) and SEN(T) specimens.

3.1.2 Evaluation of eta (η) factor

The predicted η-factors for load line displacement and crack mouth opening displacement (CMOD) had been evaluated as a function of a/W. The following graphs, Figures 5 and 6, show that FE calculation produced correct estimation of η-factors for all specimens compared to analytical values derived from collapse solutions using Equation 2.

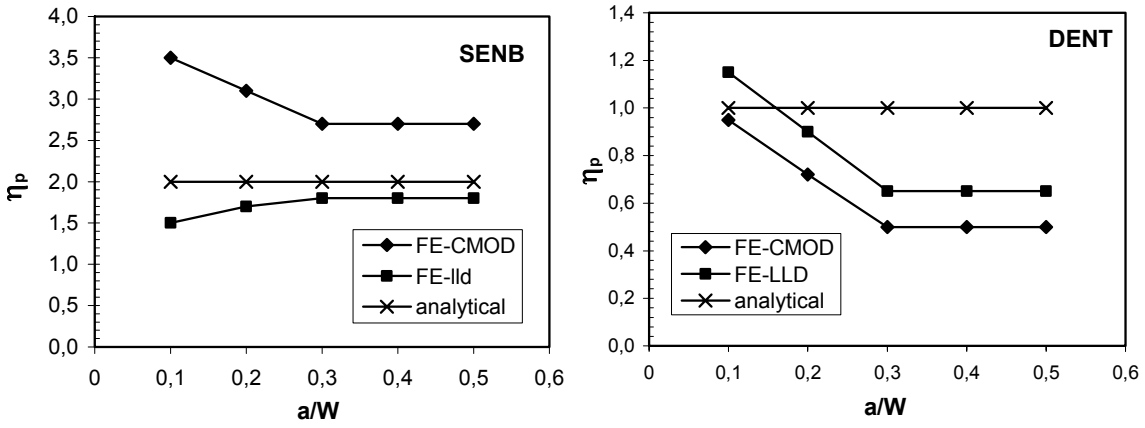

Figure 5. Comparison of η-factors for SEN(B) and SEN(T) derived from local CMOD and load-line displacement and the analytical values.

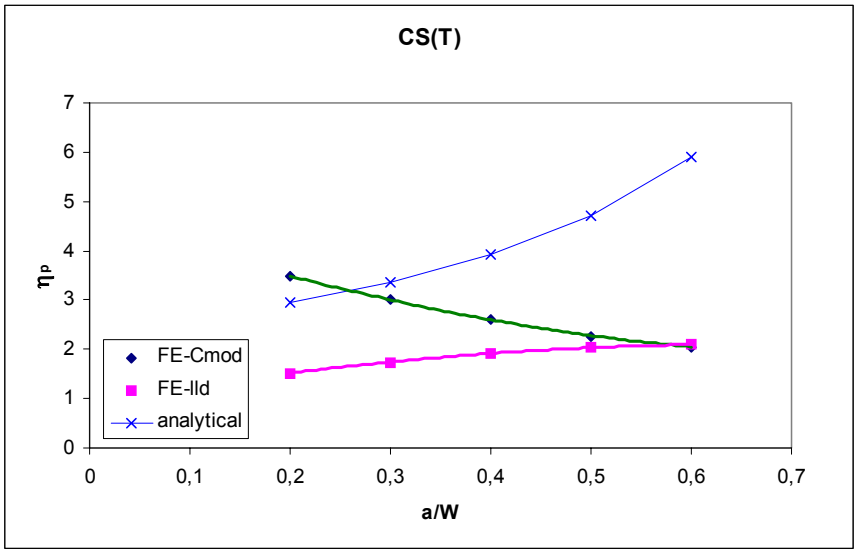

Figure 6. Comparison of η-factors for CS(T) derived from local CMOD and load-line displacement and the analytical values.

3.2 Creep crack growth tests

A systematic approach taken to determine the CCG properties of materials that involved a matrix for tests carried out by six laboratories of CRETE partners. The test specimen geometries and two steels selected for the test program is presented in Table 2, together with test conditions and progress st. Note that each test lab. possesses different equipment (loading frames, grips, extensometry etc.), testing and data analysis software, and follow test procedures. Therefore, the test matrix was decided after a careful consideration of

- optimising the coverage of test conditions (geometries, materials, notch preparation state),
- allowing significant comparisons,
- taking into account partners limitations, especially laboratories max. loading capacities.

Table 2. The current test matrix and progress made to date in the experimental CCG work programme of CRETE project.

Spec. Type	Steel	Test partner	T (°C)	a_o (mm)	Initial crack[a]	SG[b] (%)	Load (kN)	Test duration
SEN(T)	316H	CESI	550	7.5	PC	20	30	aborted at power black out
SEN(T)	316H	CESI	550	7.5	PC	20	30	≈ 400
SEN(T)	316H	CESI					28	not started
CS(T)	C-Mn	CESI	400	5	PC	20	22 or 24	not started
CS(T)	C-Mn	CESI	400	5	EDM	40	17 or 21?	not started
SEN(T)	C-Mn	CESI	400	7.5	EDM	40	30	>5000 ongoing
SEN(T)	C-Mn	CESI	400	7.5	PC	40	29	>5000 ongoing
DEN(T)	C-Mn	GKSS	400	3.75*	EDM	20	55	952
DEN(T)	C-Mn	GKSS	400	3.75*	PC	40	45	>3200 ongoing
M(T)	C-Mn	GKSS	400	3.75*	EDM	20	55	1520
DEN(T)	316H	IC	550	3.75*	PC	20		1710
DEN(T)	316H	IC	550	3.75*	PC	20		> 5000 ongoing
M(T)	316H	IC	550	3.75*	PC	20		> 5000 ongoing
SEN(B)	316H	BE	550	8.16	PC	20	12.2	500 ?
SEN(B)	316H	BE	550	8.32	PC	20	9.0	500 ?
SEN(B)	316H	BE	550	8	PC	20	7.6	>3500 ongoing
SEN(B)	C-Mn	BE	400	7.5	EDM	40		not started
SEN(B)	C-Mn	BE	400	7.5	PC	40		not started
SEN(T)	316H	TUD	550	7.5	PC	20	35	600
SEN(T)	316H	TUD	550	>7.5	PC	20	32	520
SEN(T)	C-Mn	TUD	*400*	7.5	EDM	40	35	1600
SEN(T)	C-Mn	TUD	*400*	7.5	EDM	40	32	> 1300 ongoing
SEN(T)	C-Mn	TUD	*400*	7.5	EDM	40	37	> 120 ongoing
CS(T)	316H	VTT	550	5	PC	20	20	275
CS(T)	316H	VTT	550	5	PC	20	18	1263
CS(T)	316H	VTT	550	5	PC	20	20	286
CS(T)	316H	VTT	550	5	PC	20	16.5	3800
CS(T)	C-Mn	VTT	400	5	EDM	40	17	not started
C(T)	C-Mn	VTT	400	25	EDM	40	26	completed
C(T)	C-Mn	VTT	400	25	PC	40	30	ongoing

Notes :

a PC = pre cracked by fatigue, EDM = electro-diuscharge (spark erosion) slit

b SG = side grooving

The CCG data is obtained from tests (Table 2) on different geometries (Figure 1) shown in the legend of the Figure 7. Two SEN(T) specimens tested at two partners labs. demonstrate the lab. to lab. variation of data, hence the need for harmonisation of CCG testing and assessment. Note that the data received from the partners is in as processed form without any further processing and reduction. The figure points out the encouraging low scatter of CCG data from different

specimen geometries that may be represented with a linear fit to data. The deviation is seen in DEN(T) and SEN(T) specimens. Lab-to-lab variation in SEN(T) data defined the upper and lower limits of the scatter band. This issue will further addressed when additional data from the planned test programme will be available, considering;

a) specimen geometry effect, including loading mode, leading to different crack tip constraint,

b) starter crack, EDM versus fatigue precrack,

c) test procedure, laboratory test equipment,

d) data reduction and analysis methods including used software.

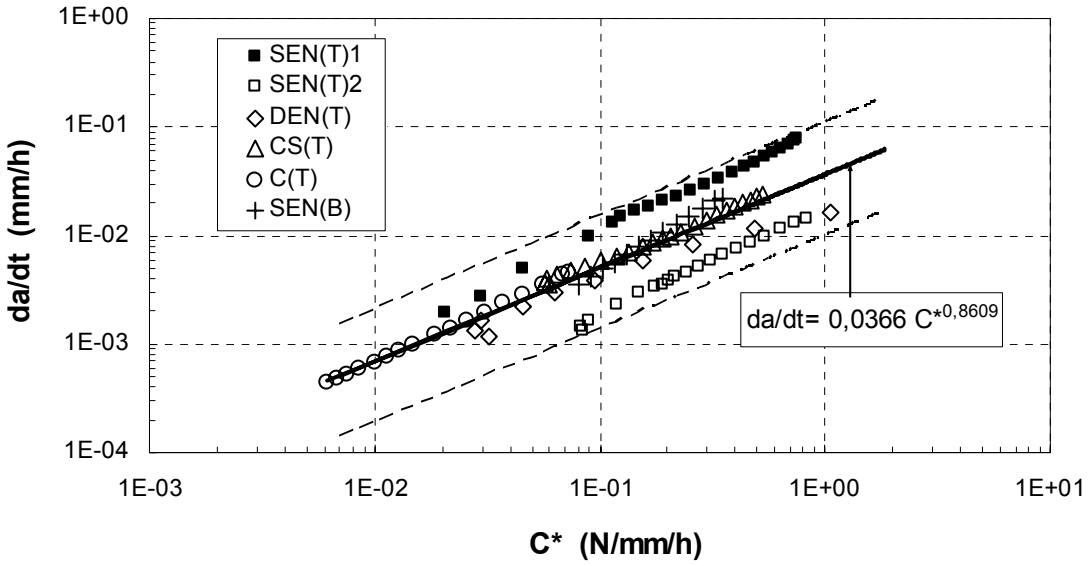

Figure 7. Correlation of CCG rate, da/dt with C for different specimen geometries of 316H steel at 550°C.*

3.3 Fracture and metallography

Metallographic investigations were undertaken, in order to study material behaviour with possible deviations in some tests from normal trends and from expected findings. Specimens were sectioned by spark erosion at mid thickness plane (i.e. in planes parallel to the loading and crack growth directions) then, a half specimen was fatigue fractured at room temperature in order to examine fracture mode and accurate final crack length measurements. The second half was used for microscopy work on the crack tip region of the sectioned side surface. The intention was here to clarify the extents and shapes of crack tip creep damaged zones, to be compared with triaxiality extents as predicted by FEM and by experience. Therefore, appropriate microstructural features suitable

to be indicative of creep damage phenomena in the C-Mn and in the 316H steels will be investigated.

Unfortunately, the most interesting specimens are those of the longest tests in the test programme, being the last to be concluded, so such results could not be provided for this paper. As with the other conclusive activities still ongoing at this time, the interested reader is invited to have a look at the CRETE dissemination activities, at http://www.eurocrete.org.

4. Summary

4.1 Fracture mechanisms

Certain conditions must be satisfied in choice of laboratory specimens for testing in order to apply creep crack incubation and growth rate data to structural assessments that necessitate correlations with C^*. In special circumstances, these conditions may be relaxed, but in general, laboratory tests should be conducted to guarantee that creep component be the dominant deformation mode. The crack tip region needs to be constrained to deform in plane strain, even though the bulk deformation may sometimes be more characteristic of plane stress.

It is commonly observed that creep rupture ductilities decrease with increasing test duration. Intergranular cavitation increasingly dominates the failure mechanism at longer times. In crack incubation and growth tests, the multi-axial stress state ahead of a crack promotes low displacement failures. For materials that cavitate readily such mechanisms may be reproduced by testing at higher stress levels. However, in materials where the low stress mechanism is replaced by matrix deformation dominated failure at higher stresses it may be necessary to accelerate tests by increasing temperatures rather than stresses. In either case, it is essential that the mechanisms operative in the test specimen lead to deformation resembling the service conditions.

4.2 Specimen geometry selection in CCG tests

Creep crack growth data are required for prediction of service behaviour of components using design and/or assessment procedures [1–3]. Therefore, it is important to be able to demonstrate that the creep crack growth data obtained are:

i) suitable to the geometry and loading being considered, or
ii) conservative for the geometry and loading being considered for the components.

In the former case, if service loads are exclusively tensile, the DENT(T) or M(T) specimens may be most appropriate. However, if conservative creep crack

growth data are required for a range of applications, it is more appropriate to test highly constrained geometries such as the C(T) or SEN(B). The specimen thickness should normally be chosen to be equal to, or exceed, the section thickness of the component being assessed.

Material availability considerations influence the choice of specimen geometry. In many cases, the volume and dimensions of available material are limited. This issue will be of particular concern when testing material obtained from components in both virgin and service exposed conditions. The shape of the material available can also influence the choice of specimen; for instance the CS(T) specimen is particularly suited for testing material from tubular components. The location and orientation of the crack in the specimen need to be consistent with the defect orientation in the component being assessed. The required specimen orientation, together with the volume and dimensions of available material, can significantly influence the choice of specimen geometry.
The machine capacity available for performing the creep crack growth tests will have a significant influence on the specimen geometry and dimensions which can be tested for a given material condition. The highly constrained C(T), SEN(B) and CS(T) specimens will require lower test loads for given ligament dimensions, B_n, (W-a), than the DENT(T) and M(T) geometries.

4.3 Specimen size and load level

ASTM E1457-00 [4] specifies that specimen size and load levels must be selected to ensure that the transition time to extensive creep is small in comparison with the anticipated test time. However, firmer recommendations are given below, although it should be checked that these are consistent with the requirement given above for the particular material being tested. The size requirements are based on analogy with ambient temperature fracture toughness testing requirements, an analogy which is currently subject to debate but provides reasonable guidance. It is recommended that specimens should be large enough to obtain sensibly straight crack fronts, using side grooves if necessary. In practice this usually means testing the largest practicable specimen which is not always the most practical case. In order to promote crack tip deformation in plane strain and lead to incubation times which are not overestimated in the laboratory specimens compared with the structure, the test specimen should meet the minimum requirements:

$$B_n, (\mathrm{W} - \mathrm{a}_0), \mathrm{a}_0 > 25\,\delta_i \qquad (3)$$

where B_n is the net specimen thickness, a_0 is the initial crack size, and the incubation COD, δ_i, is determined after 0.2 mm of crack extension.

To obtain crack growth rates measured in the laboratory specimens which do not

underestimate those in the structure, the data are only valid for times during propagation which meet the minimum requirements:

$$B_n, (\mathrm{W} - \mathrm{a}), \mathrm{a} > 25\,\delta \tag{4}$$

where a and δ are the instantaneous crack depth and COD, respectively. The numerical constant appearing in Equations (3) and (4) is approximate and is only relevant to the C(T) specimen geometry. The conclusive part of the CRETE programme is intended to review the test results, in order to define the corresponding factors for the other specimen geometries considered (Figure 1).

5. Conclusions

The experimental CCG testing programme carried out in this study was a good compromise between the need to cover, within the time schedule of this project, the several geometries of interest for the specimens, and comparison of CCG data from distinct laboratories. Therefore, it aimed at distinguishing geometry/loading configuration effects from other differences due to crack starter notches, material variability, used procedures, and equipment. The preliminary results show that the test to test variations in crack growth rates were contained within a range spanning more that an order of magnitude, for the same values of C*. This is not felt to be caused by material variability, intrinsic test scatter or test methods variabilities including software for data analysis. The major part of this effect is size and geometry related. Similar variations are, therefore, a real concern, for cracks in components too. In order to make reliable predictions of high temperature component integrity containing flaws a sound understanding of constraint effects on CCG rates is needed. This necessitates CCG data from tests in relevant loading mode constraint condition that is well representative of the component situation.

The final deliverables of CRETE project, namely the CCG Code of Practice and a guideline to selection of specimen geometries for testing, have been drafted. FE analyses were performed to validate and integrate existing methods of determination of the C* parameter for the non-conventional geometries considered, and an extensive testing programme was carried out by the project partners. These deliverables will be made available in the project website along with project information and partners´ contact details.

In this conclusive part of the project a significant effort is being made for a possible future standardisation of the developed CoP for CCG testing. As a satisfying strategy could not be identified for standardisation through the CEN system, main effort is now intended in the post-project phase to be focussed on CRETE CoP dissemination initiatives within the European Structural Integrity

Society (ESIS), whereas standardisation routes for the CRETE CoP will follow throught the International Institute of Welding (IIW), towards ISO.

6. Acknowledgements

The authors gratefully acknowledge the European Commission support, for partial funding the CRETE project in the Measurement & Testing Programme of the 5th Framework Programme. The contributions of other project partners to the activities reported in this paper are also acknowledged, in particular C. Rinaldi and A. Cammi of CESI, D. Dean of British Energy, F. Muller of Technical University of Darmstadt, U. Ceyhan of GKSS and P. Auerkari of VTT Industrial Systems.

References

[1] British Standard BS 7910. Guide on Methods for Assessing the Acceptability of Flaws in Metallic Structures. 2000.

[2] American Petroleum Institute. Fitness-for-Service API Recommended Practice 579, 1st Ed., Jan. 2000.

[3] R5 Procedure BEG Ltd. Assessment Procedure for the High Temperature Response of Structures, Issue 3, 2003.

[4] ASTM E1457-00. Standard test method for measurement of creep crack growth rates in metals. ASTM 03.01, Philadelphia: ASTM 2000, PA 19103, USA.

[5] CRETE: Development and Harmonisation of Creep Crack Growth Testing for Industrial Specimens – a Route to a European Code of Practice, EU project GRD1 - 2000–3002.

[6] B. Dogan, K. Nikbin & B. Petrovski. Development of European Creep Crack Growth Testing Code of Practice for Industrial Specimens. EPRI Int. Conf. Materials and Corrosion Experience for Fossil Power Plants, Nov. 18–21, 2003, Wild Dunes Resort, Isle of Palms, South Carolina, USA

[7] B. Dogan, K. Nikbin, B. Petrovski & D. Dean. Crete Code of Practice for European Creep Crack Growth Testing of Industrial Specimens. BALTICA VI Conf. Proceedings, VTT Industrial Systems, 2004.

[8] Tada, H. Stress Analysis of Cracks Handbook. Paris Productions Incorporated, 2nd edition, 1985.

CRETE code of practice for European creep crack growth testing of industrial specimens

B. Dogan[1], K. Nikbin[2], B. Petrovski[1] & D. Dean[3]
1. GKSS Research Centre, Geesthacht, Germany,
2. Imperial College, London, UK.
3. British Energy Generation Ltd, Gloucester, UK.

Abstract

A Code of Practice (CoP) drafted in the partially EC funded project CRETE is presented. The guidelines are followed in specimen selection for the experimental work. The CoP is prepared based on the authors and project partners long years of experience in the subject field of high temperature testing, deformation studies and creep crack growth on ferritic and austenitic materials including C-Mn, P22, P91 and 316 steels, in internal as well as various European and international projects. FE calculations and validation tests were carried out on industrially relevant specimen geometries. The CoP gives advice on testing, measurements and analysis of test data for a range of creep brittle to creep ductile materials. The code may be used for material selection criteria and inspection requirements for damage tolerant applications and life assessment of components.

1. Introduction

The industrial need for harmonized procedures for material testing and data analysis cover testing for materials development, design of components for engineering applications and defect assessment of in-service components for lifing. The available codes for high temperature crack growth testing and characterization of materials are limited in scope and international acceptance. The most widely used standard for creep crack growth testing of metallic materials [1] is mainly addressing compact tension, C(T), type specimens testing. Therefore, the outstanding need for characterization of industrial specimens is being worked on in a European project CRETE [2] that will serve for harmonization of testing and defect tolerance assessment of components. Recent reviews of high temperature defect assessment procedures [3] and significance of creep in defect assessment procedure for low to high temperature [4] emphasize the need for reliable crack growth data. The British Standard document BS 7910 [5] contains some specialized data for creep crack growth assessment, whereas, the R5 [6] procedure does not supply elevated temperature data, except where specifically used to validate the procedures.

Furthermore, the characterization of defect shapes and sizes is an essential part of the analysis for defects detected during in service inspection. The BS 7910 [5], R5 [6] and A16 [7] procedures describe methodologies for crack shape characterization. The minimum detectable crack size will affect the subsequent calculations and therefore improvements in detection techniques will assist in improved life estimation procedures. Within the context of Fast Breeder Reactor assessments, a 'long' crack is considered greater than 1 mm in depth. 'Short' cracks may initiate and, up to a certain critical depth, arrest, yet their average growth rate would still be greater than predicted by linear elastic fracture mechanics [8]. The guidelines are presented for experimental determination and analysis of Creep Crack Growth (CCG) rate data including an application example.

2. European CoP for CCG testing of industrial specimens

The reader is assumed to be familiar with materials behaviour, materials testing and data assessment together with basic knowledge of high temperature fracture mechanics.

2.1 Scope and use

The specific aim of the CoP document is to provide recommendations and guidance for a harmonized procedure for measuring and analyzing CCI and CCG characteristics using a wide range of industrial fracture mechanics specimen geometries. It will allow user laboratories with limited test material to carry out validated tests on different test geometries [9].

2.2 Specimens

The novel aspect of the presented CoP is the inclusion of component relevant industrial specimen geometries [9]. It covers testing and analysis of CCG in metallic materials at elevated temperature using six different cracked geometries [Fig. 1], that have been validated in [2].

The choice of specimen should reflect a number of factors as [10]; availability and the size of material for testing, material creep ductility and stress sensitivity, capacity of the test rig. The emphasis is put on:

- Type of loading under consideration (tension, bending, tension/bending),
- Compatibility with size and stress state of the specimen with the component under investigation.

It is likely that not all conditions can be satisfied at any one time. The appropriate decision will need expert advice in the relevant field or industry.

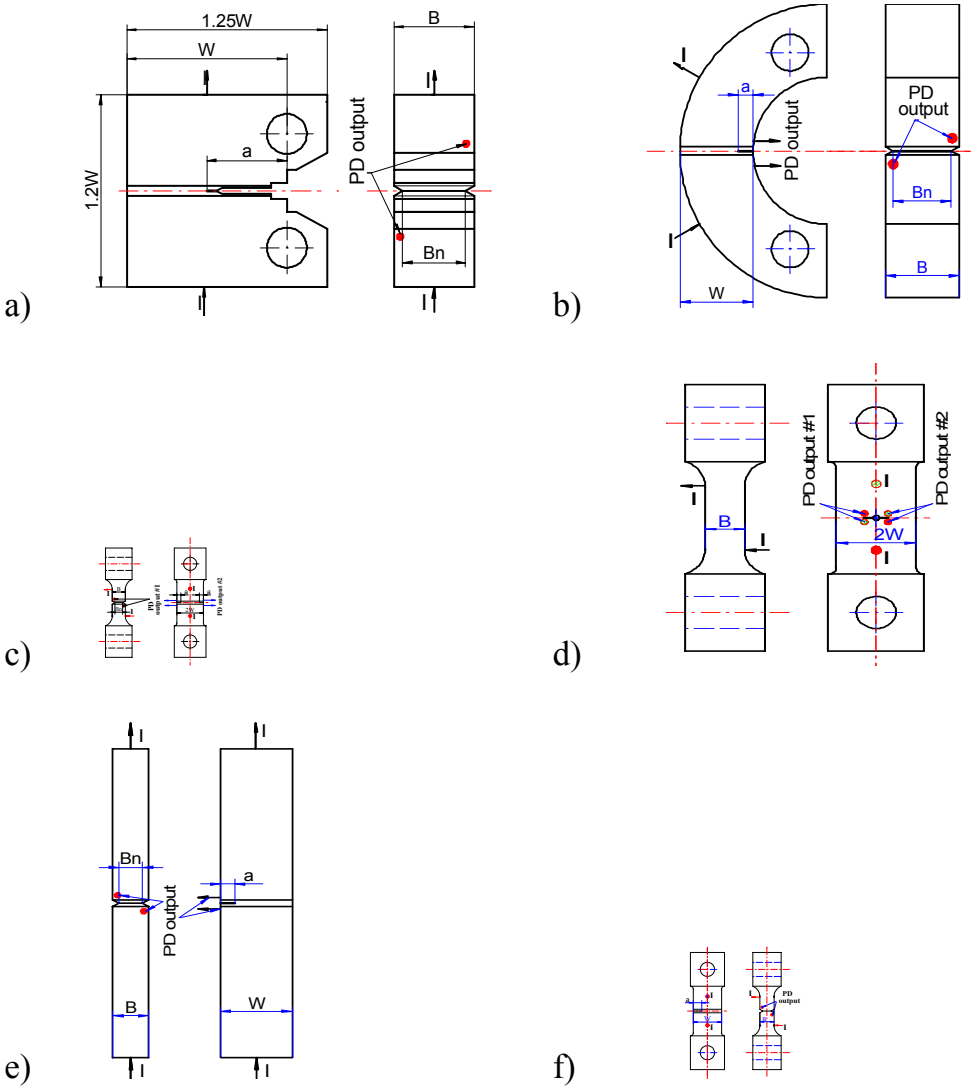

Figure 1. Specimen geometries a) Compact Tension, C(T); b) C-Shaped Tension, CS(T) c) Double Edge Notched Tension, DEN(T); d) Middle cracked Tension, M(T); e) Single Edge Notched Bend, SEN(B); f) Single Edge Notched Tension SEN(T).

2.2.1 Geometry, size, dimensions and machining of the specimens

The recommended specimen geometries have the size chosen suitable for the test capacity of the loading system, and heating furnace with sufficient room for attaching the necessary extensometers. It should provide sufficient ligament size for a stable crack growth. The dimensions of specimens shown in Fig. 1, for experimental and numerical validation are given in [11]. It is possible to use half or double size thickness specimens, or any intermediate ratios depending on

machine capacity and the need to consider size and constraint effects. The initial crack lengths shall be within a range of (0.2–0.4) a_o/W for tension specimens, (0.3–0.5) a_o/W for the other specimens.

Specimen abbreviations and loading arrangements are: Compact Tension C(T) in Pin loading, C-Shape Tension CS(T) in Pin loading, Double Edge Notched Tension DEN(T) in Pin loading/thread, Middle Crack Tension M(T) in Pin loading/thread, Single Edge Notched Bend SEN(B), Single Edge Notched Tension SEN(T) in Pin loading/thread.

Fatigue pre-cracked starter cracks have been used in cases where there is high creep ductility and where CCI information may be affected by the initial crack-tip conditions. The preferred method for deriving steady state CCG is to use an Electric Discharge Machining (EDM), especially for creep brittle conditions. Side grooving (SG) is needed to get straight crack front, i.e. 20% in total.

2.3 Tests

Test techniques together with accuracy limits for measuring test variables will provide correct and repeatable test data that help to reduce data scatter. Constant load or constant displacement rate tests may be used in CCI and CCG testing. In some cases where the material is very brittle (with uniaxial creep failure strain <10 per cent) or very stress sensitive with the creep index n >> 10, it is advisable to perform constant displacement tests rather than constant load tests.

Test methods cover isotropic polycrystalline metallic materials. Where material inhomogenity exists such as in testing single crystals, directionally solidified materials, welds (Cross-welds and Heat Affected Zone (HAZ)) the testing techniques are subject to verification [12]. However, caution should be exercised with the treatment of the data and its analysis since the correlation parameters have been validated only for homogenous materials.

2.3.1 Preparing the specimens

Prior to testing specimen preparation consists of spot welding of thermocouples and Potential Drop (PD) wires. For advice on positioning of the wires advice should be sought from the PD equipment manufacturer. Current input wires should be placed remote from the crack tip and the potential output wires should be placed on the opposite face of the specimen, aligned near the crack tip, as shown in the specimen Fig. 1.

2.4 Environment

Aggressive environments at high temperatures can significantly affect the CCI and CCG behaviour. Attention must, therefore, be given to the proper selection and control of temperature and environment in data generation. All relevant information should be fully logged for each test in order to identify diversions from the norm as specified in the CoP [9].

Tests are mostly carried out in laboratory air at test temperatures. Tests should be done in vacuum or aggressive atmosphere in order to simulate service conditions of the structural component to be assessed. Note that aggressive environment enhances damage and hence affects the crack initiation and growth processes.

2.5 Measurements during tests

The load, potential drop and displacement data should be logged all the way to full load starting from pre-load. This information is important both for the subsequent analysis of the data using C* and K. Any instantaneous deviation from the elastic loading condition prior to creep at or near zero time should be noted. In addition the load/displacement measured will give the specimen's elastic compliance for the initial crack length. The values of initial elastic displacement Δ_{ei} at full load and the final elastic displacement Δ_{ef} during the final unloading should be measured and logged in addition to the time increment Δ_t between the two readings. It is also possible to perform a partial unloading during the test if there was concern regarding a premature failure of the test piece. Partial unloading compliance may also be used for crack length estimation during the testing.

2.6 Test interruption and termination

Data logging and taking additional readings at the beginning of the test when rapid changes occur is important. Also when the test nears its final stage and CCG begins to accelerate additional readings should be taken. A decision must be made at some point to stop the test when CCG begins to accelerate towards rupture. It is ideal to stop the test just before failure or approximately when the specimen has reached 90–95% of life. Alternatively, the test should be stopped as soon as both the potential drop and the displacement measurements indicate that final failure of the specimen is imminent noted in crack growth rate acceleration. On-line crack length calculations using Johnson's formula as well as unloading compliance measurements may give guidance in making the test stopping decision.

2.7 Post-test measurements and metallographic examination

An accurate measure of the initial (a_o) and final (a_f) crack front and crack size should be made when the specimen is broken open outside the furnace after testing. The total crack extension, Δa_f, is derived by subtracting the initial crack size, a_o from the value of the final crack size, a_f. The final crack size shall be determined from fracture surface measurements where possible. The initial and final measured crack lengths are used to compute the incremental crack length from PD measurements obtained during the tests. Post-test measurements should be carried out on the specimen. Any dimensional changes, necking, crack front shape and observing the fractured surface should be recorded. Detailed metallography to observe damage ahead of the crack tip, especially when crack initiation is of interest should be performed. Crack tip damage development is examined on completion of the test, on the sectioned half of the specimen, normal to the crack plane, using EDM and the other half is broken open for the fractography.

2.8 Choice of appropriate correlating parameter: C*, Ct, J, K

The choice of the appropriate crack growth rate correlation parameter depends mainly on the material behaviour under service conditions, whether the material exhibits creep-ductile or creep-brittle behaviour [1, 13]. Steady-state creep crack growth rates in creep-ductile materials, exhibiting extensive creep, are correlated with C*. In the small-scale creep region the parameter C_t could also be used. However for most practical examples in laboratory test pieces, it can be assumed that $C_t \cong C^*$ [1, 13]. Therefore this procedure will adopt C* for use in the correlation of the data for extensive creep conditions.

Creep crack initiation (CCI) could constitute a major portion of the time to failure. The collected data for initiation times to a crack extension of 0.2 mm can be correlated with K, C* or K^c_{mat}. In most cases initiation times are inversely proportional to the parameters. Same condition regarding the validity of K or C* will apply as specified for CCG. The users are advised, in any event, to correlate CCI and CCG data with K and C* using the formulae given in [9], and report their findings.

The correlations of steady state crack growth rate with K and C* can be represented by straight lines of different slopes on log/log plots and expressed by power laws of the form

$$\dot{a} = A' K^{m'} \tag{1}$$

$$\dot{a} = D_o C^{*\phi} \tag{2}$$

where A', D_o, m', and ϕ are material constants. A steady state relationship between crack growth rate and the parameters in equations (1) and (2) physically imply a progressively accelerating creep crack growth rate.

In experimental data the two main components of the total displacement rate, $\dot{\Delta}$, are usually creep and elastic components, $\dot{\Delta}_c$ and $\dot{\Delta}_e$. The necessary condition for C* correlation is that $\dot{\Delta}_c / \dot{\Delta} \geq 0.5$. This can be tested by incrementally checking $\dot{\Delta}$ and calculating the $\dot{\Delta}_e$ component from either the compliance of the specimen or numerical calculation of $\dot{\Delta}_e$ and plotting $\dot{\Delta}_c / \dot{\Delta}$ versus test time. If this condition is established then C* can be determined using the total measured displacement rate, $\dot{\Delta}$, for the cases $\dot{\Delta}_c \cong \dot{\Delta}$.

In creep-brittle materials ($\varepsilon_f < 10\%$) which constitutes a minor portion of the observed component creep behaviour, C* will not be valid. Therefore, if $\dot{\Delta}_c / \dot{\Delta} \leq 0.25$ for which the data are classified as being creep-brittle K may be used for correlating the crack growth data. However, these are not verified for this CoP.

Steady-state creep conditions is said to have been achieved when a fully developed creep stress distribution has been produced at the crack tip.

Under small-scale creep conditions, C* is not path-independent and is related to the crack tip stress and strain fields only for paths local to the crack tip and well within the creep zone boundary. Under these circumstances, C_t is related uniquely to the rate of expansion of the creep zone size [13]. There is considerable experimental evidence that the C_t parameter correlates uniquely with creep crack growth rate in the entire regime ranging from small-scale to extensive creep regime and is equal to C* in the extensive creep regime. For CCI correlation the time to 0.2 mm crack growth, defined as crack initiation period, t_i, should be plotted as a function of C* or K.

2.8.1 Creep crack growth rate, da/dt

CCG rate is correlated with crack tip parameter K or C*. Background information on the rationale for employing the fracture mechanics approach in the analyses of creep crack growth data is presented in [9]. In order to correlate da/dt versus K or C*, the required material properties may be obtained from uniaxial and CCG tests. The test conditions in which the tests are performed and the data reduction method and fitting may have considerable affect on the test results. The da/dt values are determined from crack size data using secant or seven point polynomial fit of crack length data. The da/dt vs. time and da/dt vs. C* correlations may contain kinks due to high degree polynomial fit of crack length or load line deflection that may be misinterpreted as material phenomena

such as pop-in in crack growth. Therefore, low degree of polynomial fit of test data is recommended for data reduction.

The appropriate solutions for K and C* are presented for crack growth rate correlations in an annex of [9]. These are valid for the size and specification of the test geometries given in Fig. 1. For a side-grooved specimen the applied load will be acting over a shorter crack front, equal to the net section thickness B_n, and, therefore, the stress intensity will be higher by the following amount [9]:

$$K_{\mathrm{n}} = K\left(\frac{B}{B_{\mathrm{n}}}\right)^{0.5} \tag{3}$$

where B is the gross section thickness and

$$K = \sigma\sqrt{\pi a}\cdot Y(a/W) \tag{4}$$

where Y(a/W) is a function of geometry, crack length a and width W, as shown in Fig. 1. For specimens loaded under a tensile load P the membrane stress, σ_m, is given by

$$\sigma_{\mathrm{m}} = P/(BW) \tag{5}$$

(replace W with 2W for M(T) and DEN(T) specimens), and for specimens subjected to a constant bending moment M the nominal bending stress at the outer fibre (surface) is given by

$$\sigma_{\mathrm{b}} = 6M/(BW^2) \tag{6}$$

Where analytical expressions do not exist or where an alternative solution is sought, K can be calculated from the EPRI J integral:

$$K = \sqrt{EJ_{\mathrm{el}}} \tag{7}$$

where $J_{el}=J_{N=1}$ given by the following formula:

$$J = \sigma_{\mathrm{o}}\varepsilon_{\mathrm{o}}(W-a)h_1\left(\frac{P}{P_{\mathrm{o}}}\right)^{N+1} \tag{8}$$

with P_o is the limit load, N is the strain hardening exponent defined as $P/P_y=(\varepsilon/\varepsilon_y)^N$, and the h_1 functions are tabulated in Reference [9].

The crack growth initiation toughness under creep conditions may be denoted by K^c_{mat}, which is named in literature as creep toughness [14,15]. The values of K^c_{mat} may be derived from creep crack growth tests as a function of crack growth increment, Δa, using

$$K^c_{mat} = \sqrt{E' J_T} \tag{9}$$

or inserting J into eq. (9), alternative expression is

$$K^c_{mat} = \left[\frac{E' \eta U_T}{B_n (W - a_0)} \right]^{1/2} \tag{10}$$

based on the ESIS fracture toughness testing procedure [16] method for evaluating J_T where U_T is the total area under the load-displacement curve partitioned into elastic, plastic and creep components, denoted U_e, U_p, U_c, respectively.

Considering the elastic contribution to J based on K^2/E' are more robust than the ESIS approach based on U_e, the following expression for direct evaluation of creep toughness from experimental load-displacement information has been proposed [15] as

$$K^c_{mat} = \left[K^2 + \frac{E' \eta}{B_n (w - a_0)} \left(U_p + \frac{n}{n+1} U_c \right) \right]^{1/2} \tag{11}$$

where the factor n/(n+1) is required for consistency with standard creep crack growth testing procedures [1].

2.9 Number of tests

The da/dt values at a given value of C* can vary by a factor of two for creep-ductile materials if all other variables such as geometry, specimen size, crack size, loading method and temperature are kept constant. For creep-brittle materials, the scatter in da/dt versus K relationship can be up to a factor of 4. This scatter may be increased further by variables such as microstructural differences, loading precision, environmental control, and data processing techniques. Therefore, it is good practice to conduct repeat tests at the same conditions. When this is impractical, multiple specimens should be planned such that regions of overlapping da/dt versus C*, or K data are obtained. Confidence in the data will increase with the number of tests performed on any one batch of material.

The minimum number of specimens to be tested is dependent on a number of factors. It is suggested that a minimum of five tests at different loads should be performed. If the material exhibits such factors as irregular voids, large grains, weld (X-weld, HAZ) and other inhomogeneities the minimum number of tests should be increased [12]. Also, more tests should be performed if the material CCG behaviour exhibits increased scatter regardless of the reason for the variability. If there is insufficient material available or if there are other reasons which would restrict multiple testing then the results should be considered with increased caution.

The time for holding at temperature prior to start of test should be governed by the time necessary to ensure that the temperature can be maintained within ±2°C [12]. This time will not be less than one hour per 25 mm of specimen thickness. Report the time to attain test temperature and the time at temperature before loading.

If failure of the specimen occurs prior to the stoppage of the test then measurements of the final crack size on fractured surface may not be possible. In this case or when $\Delta a_f/a_i > 0.2$ an upper bound estimate of the final crack size should be made (i.e. < 0.75a/W). However, a repeat test may also be needed.

3. Application to experimental CCG data

The CCG data is obtained from tests [11] on different geometries as shown in the legend of the Figure 2. Two SEN(T) specimens tested at two partners labs. demonstrate the lab. to lab. variation of data, hence the need for harmonisation of CCG testing and assessment.

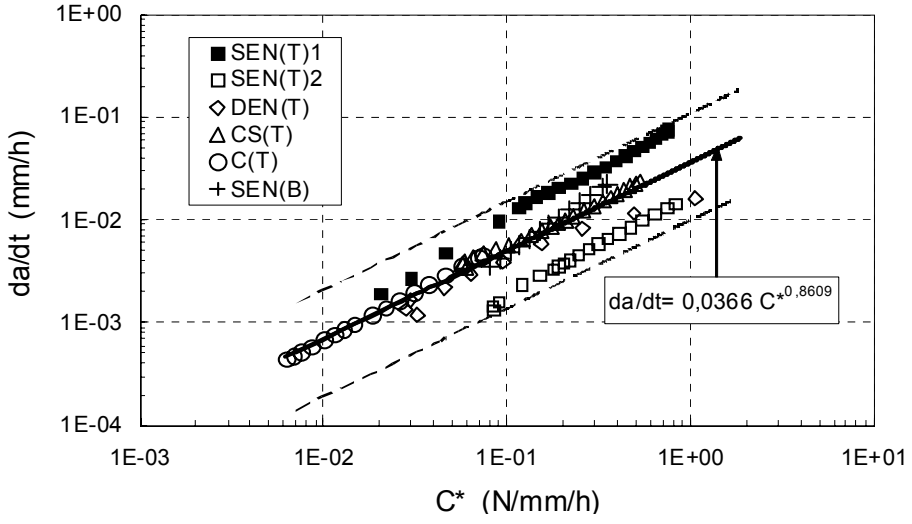

Figure 2. CCG rate data as a function of C for 316H stainless steel at 550°C. Upper and lower bands are given in dashed lines.*

Note that the data received from the partners is presented without any further processing and reduction. The figure points out the encouraging low scatter of CCG data from different specimen geometries that may be represented by a linear fit to data. The deviation is seen in DEN(T) and SEN(T) specimens. Lab. to lab. variation in SEN(T) data defined the upper and lower limits of the scatter band. C* may be calculated using Crack Mouth Opening Displacement (CMOD) or Load Line Displacement (LLD) as shown in Fig. 3**.** C* calculated by using CMOD gives lower values for both loading geometries of SEN(B) and SEN(T) than C* calculated by using the LLD, however , the difference is small.

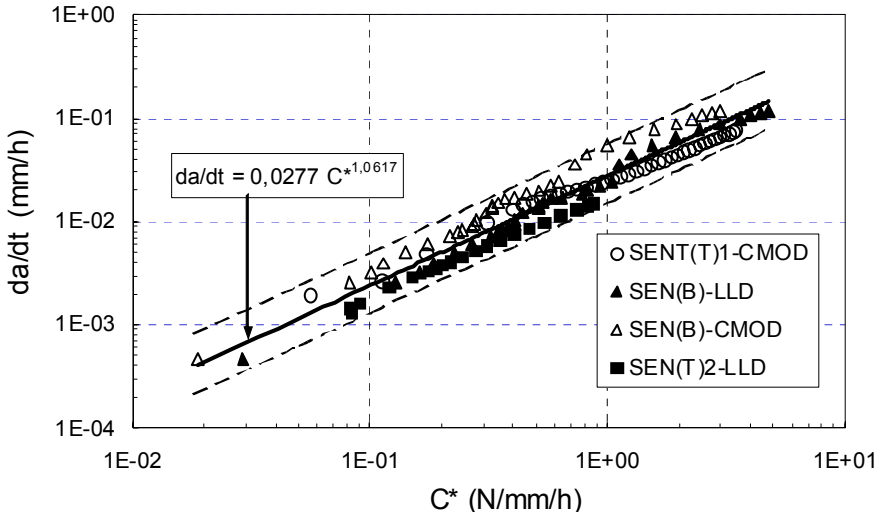

Figure 3. CCG rate as a function of C calculated using Crack Mouth Opening Displacement (CMOD) and Load Line Displacement (LLD) SEN(T) and SEN(B).*

4. Summary

Procedures for assessing the significance of flaws in components that operate in the low to high temperature range describe failure by net section rupture, crack growth or some combination of both processes. The comparison between the applied and the material side is made with relevant crack tip parameters such as the linear elastic stress intensity factor, K, the J integral, the reference stress, σ_{ref}, and C* that may be determined experimentally. The presented CoP gives guidelines for experimental determination of CCG rate data and correlation with crack tip parameters for a range of specimen geometries of industrial relevance.
For the final issue of the reported CoP a number of aspects will be addressed within the project [2] that include; constraint, material properties, eta factor, FE analysis, stress relaxation and stress-strain fields, residual stresses, partitioning displacement, analysis of elastic-creep, elastic compliance measurements.

5. Acknowledgements

The CoP has been prepared with EC financial support within the FP5 'CRETE' Project Contract N°: G6RD-CT-2001-00527, Project N°: GRD2-2000-30021 (2001–2004). Contributions in drafting the document from the 'CRETE' Partners CESI – Centro Elettrotecnico Sperimentale Italiano – IT, GKSS Geesthacht – DE, Imperial College London – UK, British Energy Generation Ltd – UK, TU Darmstadt – DE, Centre Technique des Industries Mecaniques – FR, VTT Industrial Systems – FI that is gratefully acknowledged. Thanks are due to U.Ceyhan of GKSS – DE for his technical assistance in drafting of the CoP.

References

1. ASTM E1457-00. Standard test method for measurement of creep crack growth rates in metals. ASTM 03.01, Philadelphia: ASTM 2000, PA 19103, USA.

2. EC Project CRETE: Development and Harmonisation of Creep Crack Growth Testing for Industrial Specimens – A Root to a European Code of Practice. EC Project No: GRD2-2000-30021.

3. B. Dogan. High temperature defect assessment procedures. Int. J. of Pressure Vessels and Piping, 80, 2003, p. 149.

4. B. Dogan & R. Ainsworth. Defect assessment procedure for low to high temperature. ASME Conf. PVP2003-2032, Vol. 463, 2003, p. 105.

5. British Standard BS7910. Guidance on methods for assessing the acceptability of flaws in metallic structures. British Standards Institution, 2000.

6. R5. Assessment procedure for the high temperature response of structures. Goodall I.W. (Ed.), British Energy, Issue 2, 1998.

7. A16. Guide for Leak Before Break Analysis and Defect Assessment. RCC-MR, Appendix A16, Edition 2002, AFCEN No: 94-2002.

8. A.M. Clayton, B. Tomkins, J. Wintle & E. Morland. A review of structural integrity in UK industry. HMSO, London, 1991, p. 1.

9. B. Dogan, K. Nikbin & B. Petrovski. Code of Practice for European Creep Crack Growth Testing of Industrial Specimens. 1st Draft, EC Project CRETE, Deliverable 6, 2003.

10. D. Dean. Selection of Specimens. EC Project CRETE, Deliverable 7, 2003.

11. V. Bicego, B. Dogan, H. Jaffal, K. Nikbin & B. Petrovski. The European project CRETE: Development and Harmonisation of Creep Crack Growth Testing for Industrial Specimens. Proc. Int. Conf. BALTICA VI, VTT-Helsinki, 8–10 June 2004.

12. B. Dogan. CoP for High Temperature Testing of Weldments. ESIS TC11, WG: on High Temperature Testing Weldments, 1st Draft 2003.

13. Engineering Fracture Mechanics, Special Issue on Crack Growth in Creep-brittle Materials, Vol. 62, No. 1, January 1999.

14. D.W. Dean & D.G. Hooton. A Review of Creep Toughness Data for Austenitic Type 316 Steels, BEGL Report E/REP/GEN/0024/00, 2003.

15. R.A. Ainsworth. Private communication. 2004.

16. European Structural Integrity Society. ESIS Procedure for Determining the Fracture Behaviour of Materials, ESIS P2-92, 1992.

Significance of creep crack initiation for defect assessment

B. Dogan, B. Petrovski & U. Ceyhan
GKSS Research Centre, Geesthacht, Germany,

Abstract

The integrity and residual life assessment of high temperature structures rely on the determined defects in components. The effort has been made to develop tools to detect flows in service-components and determine crack growth using metallography and fracture mechanical testing. However, less work is done on creep crack initiation and assessment.

The experimental determination of creep crack initiation on specimens of P91 steels and weldments and its significance in defect assessment of components are reported. An attempt is made to define creep crack initiation using both fracture mechanics test data. Test method, data analysis and defect assessment approach are addressed.

1. High temperature defect assessment

The manufacturer's recommendations and their past experience have been the basis for the design of vital engine components such as turbine blades, vanes, discs, gas steam pipes and pressure vessels containing weldments. Failure in engineering weld components leads to substantial portion of the direct costs of the plant in addition to danger to human lives and environment. The progress made in defect assessment and lifing procedures contribute substantially to safety and reliability of plants [1, 2].

Development of harmonized procedures for material testing and data analysis stems from the industrial need for material development, component design for engineering applications and in-service defect assessment for lifing. The most widely used standard for high temperature testing of metallic materials [3] involves only the creep crack growth in compact tension, C(T), type specimens of only homogeneous materials. The testing and analysis of weldments is being worked on in working group (WG) of European Structural Integrity Society (ESIS) TC11 [4].

Recent reviews of high temperature defect assessment procedures [5] and defect assessment at low to high temperature [6] emphasize the need for reliable data for design and in-service assessment. Design codes generally consider defect free structures, whereas assessment codes address flaws and their treatment. The British Standard document BS 7910 [7] contains some specialized data for creep crack growth assessment.

There is no provision made in the ASME N-47 Code [8]. For the assessment of short defects. The 'no initiation' criterion is based on factored laboratory endurance data where this constitutes failure of a specimen typically 8 mm in diameter. The problem of initiation and growth of defects from an assessment point of view has been presented step-by-step in 7 volumes in R5 [9]. The A16 procedure [10] for the initiation and growth of short cracks combines the RCC-MR concept of evaluating damage at a distance d from the crack tip which will lead to a finite size defect [11]. The approach considers the stress state at a distance d ahead of a notch-like defect, given by $\Delta K/(2\pi d)1/2$ [12]. Over the last two decades, the study of 'microstructurally' short crack growth has emerged [11] where defects proceed in fits and starts, becoming temporarily arrested at microstructural barriers such as grain boundaries.

1.1 Estimation of crack initiation time

The incubation period can be estimated from the equations where data are not available for the material used in the component. The incubation time is calculated using [13]

$$t_I = 0.0025\left[\frac{\sigma_{ref} t_{R(ref)}}{\left(K_a^p\right)^2}\right]^{0.85} \tag{1}$$

The incubation time for the component in secondary creep stage can be obtained from the following equations when incubation time data are available from test specimens.

$$\left(\frac{t_{lcomp}}{t_{lspec}}\right) = \left(\frac{C^*_{spec}}{C^*_{comp}}\right)^{n/n+1} \tag{2}$$

where subscripts comp. refers to the component and spec. refers to the specimen.

2. Creep crack initiation and growth tests

Constant load (CL) or constant displacement rate (CDR) tests were carried out for obtaining CCI and CCG data. The load, potential drop (PD) and load line displacement (LLD) data are logged all the way to full load starting from pre-load for the subsequent analysis of the data for crack size, C* and K determination. In addition the load/displacement measured will give the specimen's elastic compliance for the initial crack length.

2.1 Crack size determination

2.1.1 Partial-unloading compliance

The measurement of compliance from load-load line displacement (LLD) data requires loading and unloading of a specimen at time t=0. The below expression is used for time zero compliance,

$$C_o = \Delta LLD/\Delta F = tg\ \alpha_o. \quad (3)$$

The initial crack length is calculated from initial compliance at t=0, using the formula for a fatigue pre-cracked C(T) specimen [14];

$$a_o/W = 1{,}000196 - 4{,}06319\ U_{xo} + 11{,}242\ U_{xo}^2 - 106{,}043\ U_{xo}^3 + 464{,}335\ U_{xo}^4 - 650{,}677\ U_{xo}^5 \quad (4)$$

where $U_{xo} = \frac{1}{(B_e E' C_o) + 1}$, effective thickness $B_e = B - \frac{(B - B_n)}{B}$, and $E' = \frac{E}{(1 - \nu^2)}$

There is significant influence of elastic modulus, E, on crack length calculation accuracy. It is important to have proper E data obtained at the test temperature. For E range between 100 and 200 MPa the difference in Δa is depicted in Fig. 1.

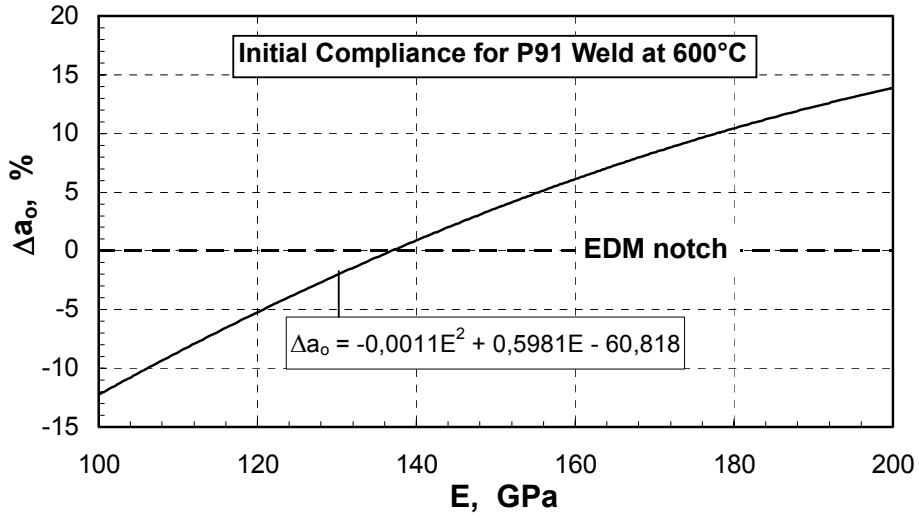

Figure 1. Variation of crack length Δa_0 determined by partial unloading compliance method with elastic modulus E of the material at test temperature, determined for P91 weld at 600°C.

2.1.2 Potential drop method

Direct current potential drop (DCPD) method is applied to monitor the crack initiation and growth during testing. The crack size is determined from PD data using Johnson's formula given for C(T) geometry [3]. Correct use of PD data is particularly important to determine the CCI due to possible variation of the PD-time records as seen in Figure 2.

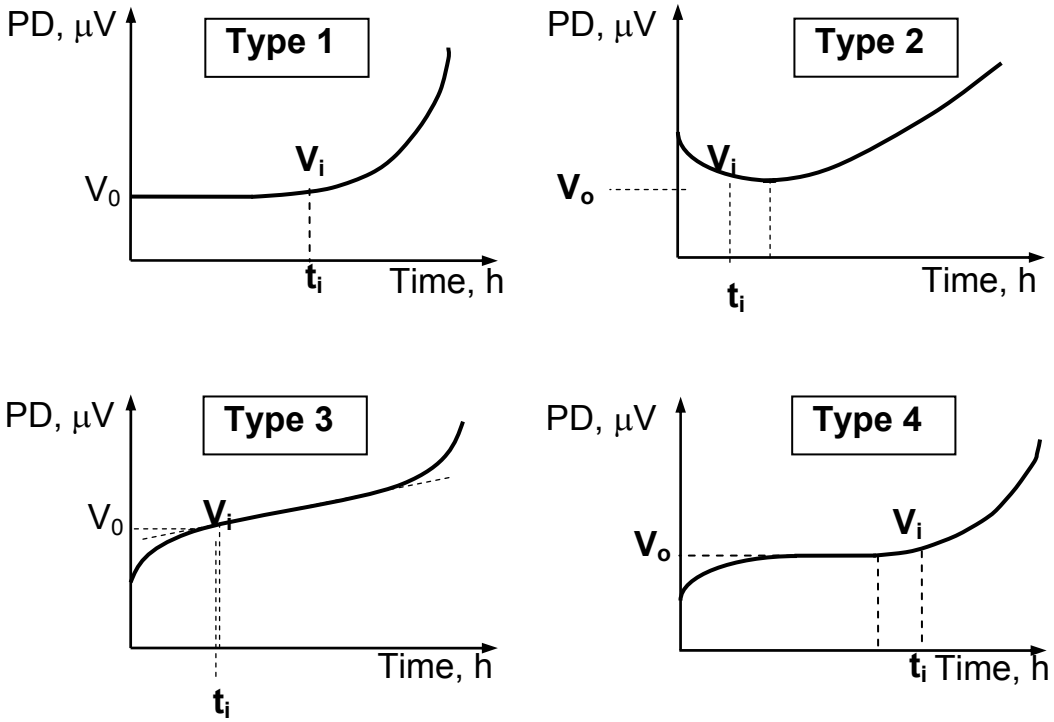

Figure 2. Types of potential drop (PD) vs. time records in creep crack growth tests.

The scatter in crack size using PD method is increased by the crack channelling with unbroken ligaments as observed on fracture surfaces. An accurate measure of the initial (a_o) and final (a_f) crack front and crack size were made when the specimen was broken open outside the furnace after testing.

3. The current CCI assessment methods

3.1 Time dependent failure assessment diagram (TDFAD)

Failure assessment diagram (FAD) methods, such as those in R6 [15], have been extensively developed to assess components containing defects. The FAD method have been extended to the creep regime, named as the time dependent failure assessment diagram (TDFAD) [16]. The advantage of using a TDFAD are: a) detailed calculations of crack tip parameters such as Cp are not needed, b) it is not necessary to establish the fracture regime in advance and c) the TDFAD can indicate whether failure is controlled by crack growth in the small-scale or widespread creep regime or by creep rupture.

In the TDFAD, the parameters K_r and L_r are defined as:

$K_r=K/K^c_{mat}$, and $L_r=\sigma_{ref}/\sigma^c_{0.2}$

where K is the stress intensity factor, K^c_{mat} is the material creep toughness corresponding to a given crack extension at a given time, $\sigma^c_{0.2}$ is the stress corresponding to 0.2% inelastic (creep and plastic) strain from an isochronous stress–strain curve at a particular time and temperature.

K^c_{mat}, which is the fundamental concept for TDFAD, at a particular time and crack extension. The details of the TDFAD assessment approach is given in [16].

3.2 Application of two criteria diagram (2CD)

For the description of crack initiation using 2CD approach there are three parameters, namely; the stress intensity factor K_I, the path independent integral C* and the nominal stress in the far field/ligament, σ_n [17]. Among these parameters, K_I is chosen to be used in 2CD, which is designated as K_{Iid}, which is the fictitious elastic K that describe the crack tip stress state. K_{Iid} parameter is being used to characterize crack tip geometry since K_I solutions are available for a wide range of geometries.

The component loading parameters are normalized by time and temperature dependent data, which indicates material resistance,

$R_\sigma = \sigma_{n0} / R_{mt}$ and $R_K = K_{Iid0} / K_{Ii}$

where R_σ is the far field stress ratio and R_K is the crack tip stress intensity ratio. R_{mt} is the creep rupture strength obtained from tensile specimens. K_{Iid0} is the fictitious elastic value at time zero at the crack tip of the component. K_{Ii} is the creep crack initiation value of the material, which is a material property.

4. Experimental data and discussion

4.1 Creep crack initiation

The behaviour of components under creep loading conditions is described by load line displacement – time diagrams. On application of steady (constant) load to a pre-cracked component the load point displacement increases with time. The creep zone ahead of the crack tip is defined as the region in which creep strain exceeds the elastic strain, the creep zone size increases with time according to,

$$r_c = K^2 (EBt)^{2/(n-1)} F_c(\theta) / 2\pi \tag{5}$$

where Fc(θ) is a shape function as defined in [18]. The microstructural damage occurs as a consequence of accumulation of creep strain. Initiation of creep crack requires attainment of critical local strain at the crack tip. The magnitude of time to initiate a creep crack, t_i, depends on the increment of crack extension, Δa_i, determined for the definition of crack initiation, x_c, [19]. Therefore, determination of Δa_i, by using either PD method or partial unloading compliance is of engineering importance as it directly affect the life of a structural component.

The time to generate critical displacement, therefore damage, to initiate a microcrack i.e. x_c=10 μm grain size, will be significantly less than a microcrack, i.e. x_c=0.2 or 0.5 mm as in engineering definition adopted in testing and assessment codes. In engineering terms, detection of a crack using non-destructive testing (NDT) is required in service components that correspond to the adopted engineering macro crack initiation size.

In component defect assessment, the data analysed to determine crack growth rate vs. crack tip parameter K or C* that gives an initial “tail” with a decreasing growth rate prior to steady-state growth rate. The tail represents the transition depends on material properties and loading conditions. However, the data prior to crack growth initiation that reflects the stress redistribution and development of damage need to be recorded and analysed as it may cover a large part of component life in service. Initial microcrack extension occurs at a relatively low

rate with small defect size where the magnitude of crack tip parameter, i.e. C*, may be negligible. The experimental data obtained on two P91 steel welds of butt weld (BW) and narrow size electron beam weld (EBW) are shown in Figures 3–6. The data correlation with K for crack initiation defined for initiation time at Δa=0.2 and 0.5 mm are depicted in Figures 3 and 4, respectively.

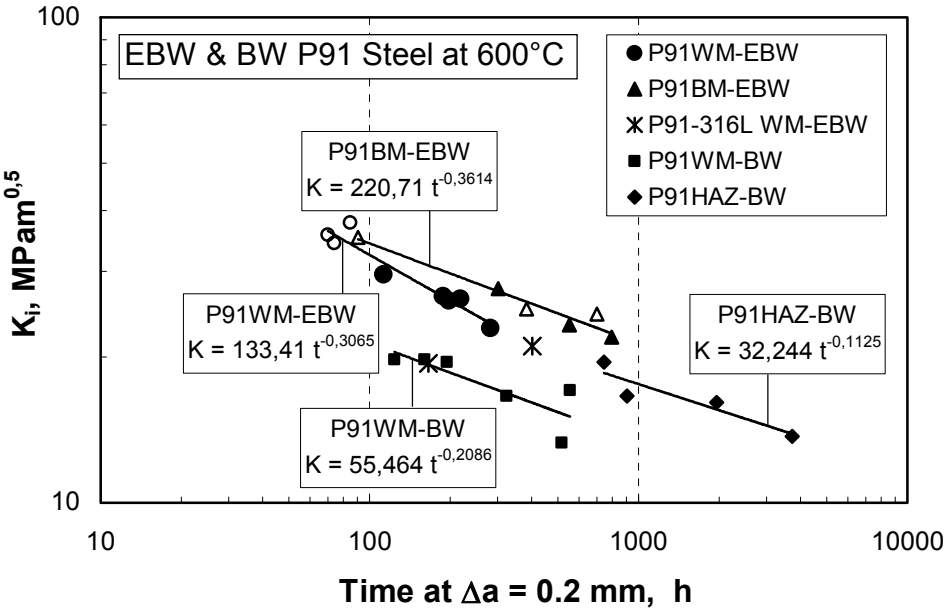

Figure 3. Variation of K at crack initiation at time, t_i, for Δa=0.2 mm .

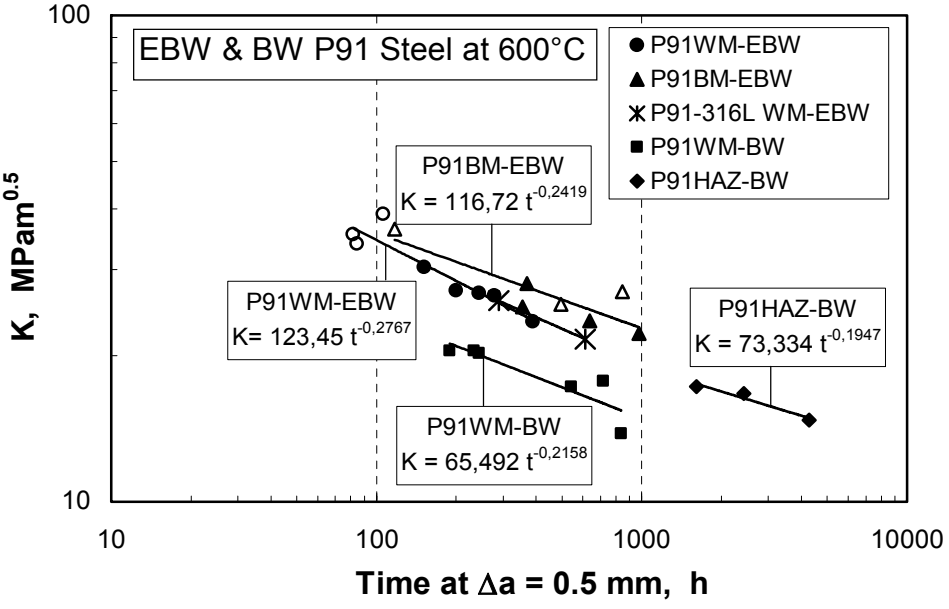

Figure 4. Variation of K at crack initiation at time, t_i, for Δa=0.5 mm .

The micromechanical approach taken by specialists [20] relies on C* to predict creep crack initiation time that involves the use of C* vs. time diagrams, established for a material at temperature and crack initiation criterion. A typical crack size for initiation is taken as 50 μm, based on direct experimental observation. This approach is also based on the argument that the use of C* to describe creep crack behaviour is only rigorously valid for stationary cracks hence, it is employed for only to correlate creep crack initiation times. Therefore, C* vs. crack initiation time data are presented in Figs. 5 and 6 in order to shed some light on the crack initiation defined in terms of micro and macro crack size.

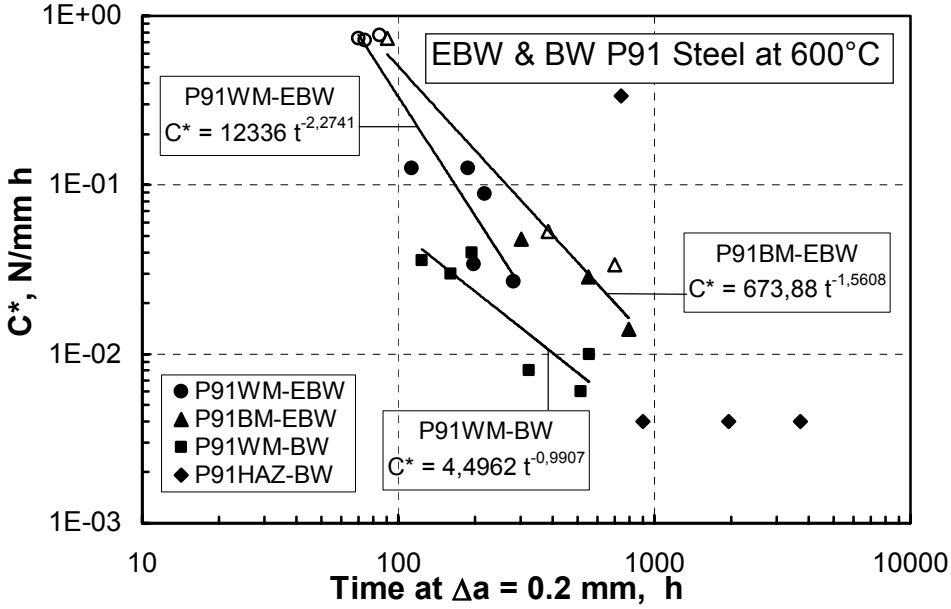

Figure 5. Variation of C at crack initiation at time, t_i, for Δa=0.2 mm.*

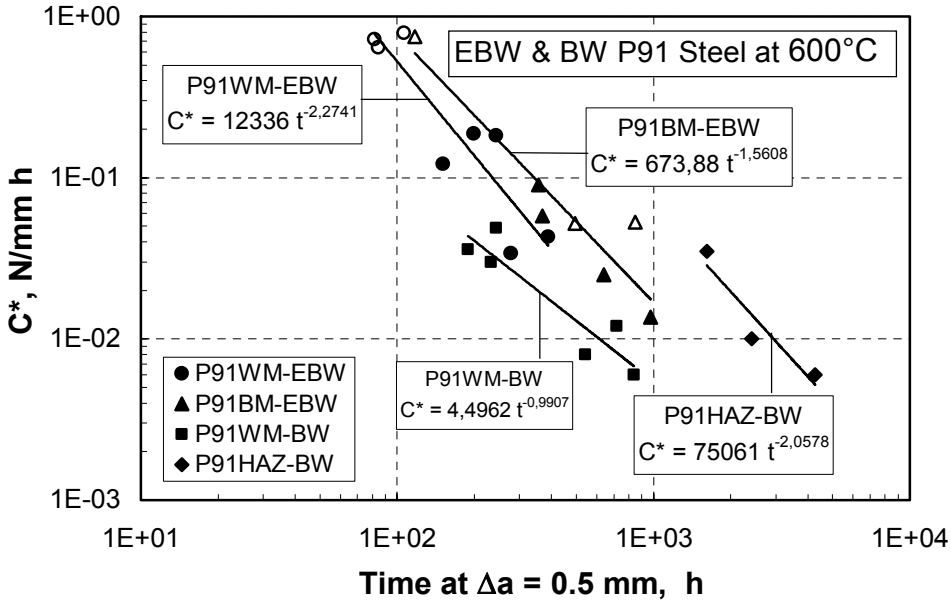

Figure 6. Variation of C at crack initiation at time, t_i, for Δa=0.5 mm .*

The scatter increases in the C* correlation that directs attention to the choice of crack tip parameter for crack initiation studies. Better correlation is seen at larger crack size times of Δa=0.5 mm as in engineering crack initiation definition. Constant displacement test data (hollow symbols), also agree well with constant load data (solid symbols), however, at higher load and shorter time end of the plots. This phenomenon reflects the crack behaviour under displacement rate control where load is increased steadily to grow crack instead of allowing the material at the crack tip under constant load to deform with time to lead to crack growth initiation.

4.2 Time dependent failure assessment diagram (TDFAD) approach

A central feature of the TDFAD approach is the definition of an appropriate creep crack initiation toughness, K^c_{mat}. When used in conjunction with the failure assessment diagram, it ensures that crack growth in the assessment period is less than a value Δa. Crack initiation toughness values may be estimated indirectly from conventional creep crack incubation and growth data or evaluated directly from experimental load versus displacement information [21].

The TDFAD method is applied to P91 similar weld data shown in Figure 7. Taken a crack initiation time of 900 h, TDFAD is constructed, and K_r and L_r are calculated for crack initiation times for Δa=0.2 mm and 0.5 mm. In calculating K^c_{mat} only the creep component of total strain energy is used. The results given in Figure 7, agree well with the P91 WM data. However, P91 HAZ data needs further assessment, the work is in progress.

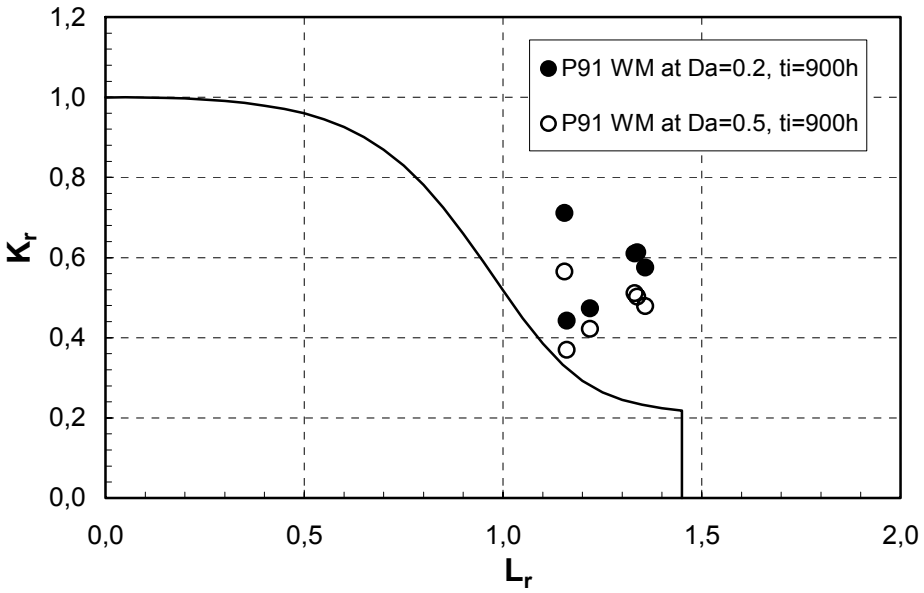

Figure 7. TDFAD Diagram for P91WM at 600°C, Δa=0.2 mm (solid symbols) and Δa=0.5 mm (hollow symbols) for crack initiation time of 900 h.

The TDFAD is used either to determine crack extension of Δa in a given time, or the time required for a limited crack extension too occur. Hence, approximate initiation times are obtained for defined crack length for crack growth initiation of 0.2 or 0.5 mm.

4.3 Two-criteria diagram (2CD) approach

The 2CD has been developed to assess creep crack initiation in ferritic steels [22]. Crack tip and ligament damage parameters, R_k and R_σ, respectively, are used in 2CD approach, which are similar to the TDFAD parameters K_r and L_r. The critical stress intensity factor, K_{Ii}, is used as a measure of crack initiation resistance rather than the creep crack initiation toughness, K^c_{mat}, that used in TDFAD approach. The experimental data from P91 similar BW zones of BM, HAZ and WM, are used for 2CD as depicted in Figure 8.

All data fall in the mixed mode damage zone as also confirmed metallographically on tested and fractured C(T) (W=25 mm, B=12.5 mm) type specimens. Note that the parameter K_{Ii} characterising the creep crack initiation of the material need to be determined from high constrained specimens with high K_{Iid}/σ_{npl}. For the specimens on which higher loads were applied higher nominal stress, σ_{no}, hence R_σ is increased leading to CCI with higher ligament damage.

A detailed comparison of TDFAD and 2CD is currently being worked on in a collaborative European action, EC TN Advanced Creep of ECCC. A recent publication sheds light on the state of the art of the mentioned group activity [23].

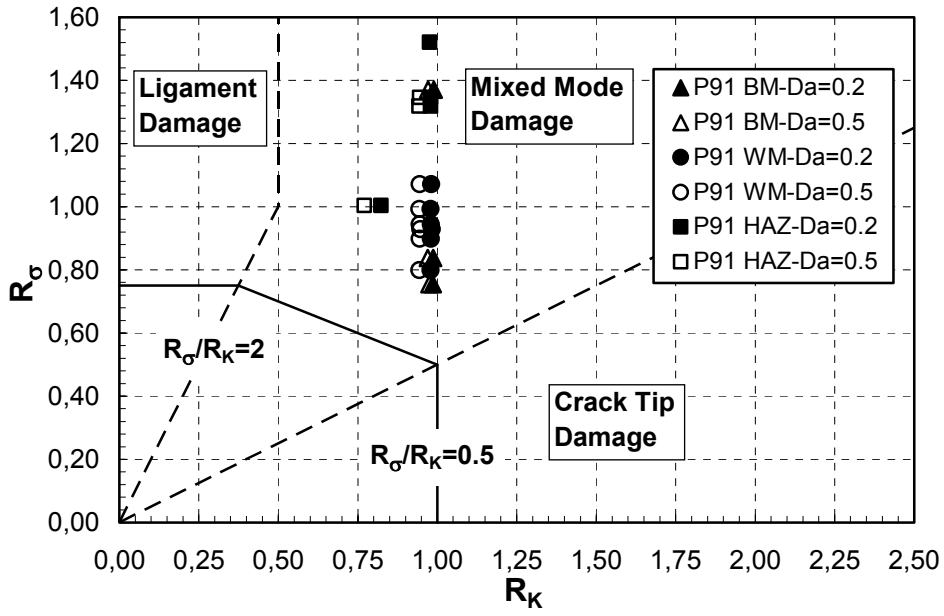

Figure 8. Two criteria diagram for P91 weld zones (BM, HAZ, WM) at 600°C for Δa=0.2 mm (solid symbols) and Δa=0.5 mm (hollow symbols).

5. Concluding remarks

Significance of crack initiation for defect assessment of components in high temperature service is addressed. The industrial relevance, therefore, importance of the CCI has been recognised and international European effort continues addressing the issue. Furthermore, assessment of weldments stands as a challenge for industry and academia alike due to its direct relevance to engineering structure where damage and CCI occurs predominantly in functionally graded materials of weldments.

The present paper only partly addresses this important issue which requires international collaborative effort. The reported work is considered as preliminary results of a planned long term study of different approaches for CCI of weldments. Particularly, the data presented for TDFAD and 2CD method application will be further assessed when further data on material as well as from different specimen sizes and geometries of industrial interest will be available. However, present study directs attention to the needs and contributes to

a) experimental aspects of CCI and CCG testing, including use of PD and unloading compliance methods for crack size monitoring,
b) choice of crack tip parameter,
c) definition of CCI, and
d) approaches for assessment of CCI of components for service assessment.

6. Acknowledgements

The authors would like to thank Drs. J. Ewald, and R.A. Ainsworth and D. Dean for providing material and fruitful discussions on 2CD and TDFAD methods.

References

1. W.M. Steen & G.J. Shannon. Proc. Int. Conf. Trends in Welding Research, Eds., J.M. Vitek et al. ASM International, 1998. P. 423.

2. K.M. Nikbin. Proc. Int. Conf. CREEP 7, JSME, No.01-201, Ed. Y. Asada, 2001. P. 123.

3. ASTM E1457-00. Standard test method for measurement of creep crack growth rates in metals. ASTM 03.01, Philadelphia: ASTM 2000, PA 19103, USA.

4. B. Dogan. CoP for High Temperature Testing of Weldments. ESIS TC11, WG: on High Temperature Testing Weldments, 1st Draft 2003.

5. B. Dogan. High temperature defect assessment procedures. Int. J. of Pressure Vessels and Piping, 80, 2003, p. 149.

6. B. Dogan & R. Ainsworth. Defect assessment procedure for low to high temperature. ASME Conf. PVP2003-2032, Vol. 463, 2003, p.105.

7. British Standard BS7910. Guidance on methods for assessing the acceptability of flaws in metallic structures. British Standards Institution, 2000.

8. ASME Section III. Rules for construction of nuclear power plant components. Division 1, Sub-section NH, Class 1 components in elevated temperature service, ASME, 1995.

9. R5. Assessment procedure for the high temperature response of structures. Goodall I.W. (Ed.), British Energy, Issue 2, 1998.

10. A16. Guide for Leak Before Break Analysis and Defect Assessment. RCC-MR, Appendix A16, Edition 2002, AFCEN No: 94-2002.

11. B. Drubay, D. Moulin, C. Faidy, C. Poette & S. Bhandari. Defect assessment procedure: a French approach. ASME PVP, Vol. 266, 1993, pp. 113–118.

12. C.E. Jaske. Materials data needs for fatigue design of pressure vessel systems. In: C. Amzallag et al. (Eds.), Low cycle Fatigue and Life Prediction, STP 770, ASTM, Philadelphia, 1982. Pp. 600–611.

13. R.A. Ainsworth & P.J. Budden. 1994. Design and assessment of components subjected to creep. J. Strain Anal., 29, pp. 201–208.

14. ASTM E 1737 – 96 Standard Test Method for J-Integral Characterization of Fracture Toughness.

15. R6. Assessment of integrity of structures containing defects. Procedure R6, Revision 3. Gloucester, UK: Nuclear Electric Ltd., 1997.

16. R.A. Ainsworth, D.G. Hooton & D. Green. Failure Assessment Diagrams for High Temperature Defect Assessment, 1999, 62, pp. 95–109.

17. J Ewald, S Sheng, A Klenk & G Schellenberg. Engineering guide to assessment of creep crack initiation on components by two criteria diagram. Int. J. of Pressure Vessels and Piping, 2001, 78, pp. 937–949.

18. H. Riedel & J.R. Rice, ASTKM STP 700, 1980, p. 112.

19. S.R. Holdsworth. Materials at High Temperatures. Vol. 10, No. 2, May 1992, p. 127–137.

20. R. Pique, P. Bensussan & A. Pineau. Proc. MECAMAT, Int. Seminar on High Temperature Fracture Mechanisms and Mechanics, Dourdan, France, 1987.

21. D.W. Dean & D.G. Hooton, A. Review of Creep Toughness Data for Austenitic Type 316 Steels, BEGL Report E/REP/GEN/0024/00, 2003.

22. J. Ewald & K.-H. Keienburg. A Two Criteria Diagram for Creep Crack Initiation. Int. Conf. on Creep, Tokyo, 14–18 April 1986. Pp. 173–178.

23. A. Klenk et al. ECCC Seminar, Advanced Creep Data, Prague, 2003.

Creep crack growth life estimation of a surface crack in pressure vessels

Kee Bong Yoon & Jin Sang Lee
Dept. of Mechanical Engineering, Chung Ang University, Seoul, Korea

Ashok Saxena
Mechanical Engineering Dept., University of Arkansas, USA

Abstract

Using the newly developed method, a procedure for assessing creep crack growth life was demonstrated for an elliptic axial surface crack located on the internal surface of a pressurized vessel at high temperature. C_t values at both the deepest point along the crack front and also at the crack tip on the surface were estimated. Then, the aspect ratios of the surface crack were updated for every time step of crack growth calculations and were reflected in determining C_t value of the next step. Changes of crack depth, crack size and C_t values at the deepest point and surface point of the crack tip are estimated and used to predict the residual life and the evolution of crack shape during creep crack growth.

1. Introduction

Remaining crack growth life prediction methodology based on time dependent fracture mechanics has been developed and applied successfully to many structural components in power generating industry [1]. The geometry of a crack uncovered during on-site inspection is generally a surface crack of finite size. Due to lack of accurate expressions for determining high temperature fracture parameters such as C^* and C_t for surface cracks, the crack geometry is usually simplified considerably and represented as infinitely long crack for which reliable C^* and C_t expressions are available. For example surface crack in the radial-axial plane in a pressurized thick wall cylinder for creep crack growth analysis is simplified as an infinitely long axial crack. This simplification results in considerable reduction in computational effort for determining crack growth life. However, the assumption leads to a conservative estimate of life. Recently the creep crack growth life prediction methodology was extended for the surface crack case and an analysis method is proposed that does not require simplifying assumptions on the crack geometry [2]. A procedure was proposed for estimating

C^* along the entire front of surface crack and this expression relies on the C^* equation derived for the case of surface crack in a flat plate under uniform tension. Equations were also given for calculating C_t at both the deepest point along the crack front and at the crack tip on the surface.

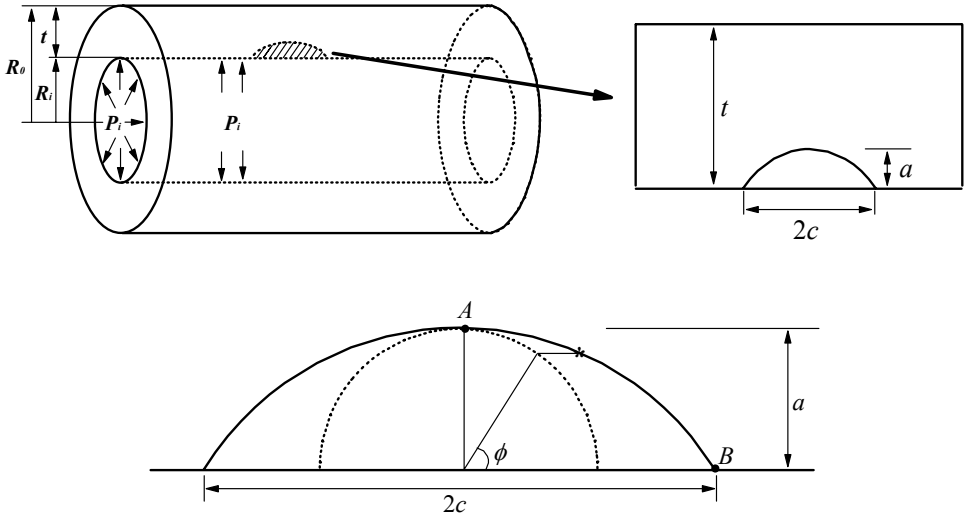

Figure 1. Geometry of an elliptic surface crack located in the radial-axial plane on the internal surface of a thick wall cylinder (R_i = inner radius, R_o = outer radius, t = thickness, a = crack depth, c = half crack length, P_i = internal pressure).

In this study, using these newly proposed equations for estimating C_t, creep crack growth analysis is conducted for an elliptic axial surface crack located on the internal surface of a 1.25Cr steel pressure vessel at high temperature. The aspect ratios of the surface crack were updated for every time step of crack growth calculations and were reflected in determining C_t value of the next step. Changes of crack depth, crack size and C_t values at the deepest point and surface point of the crack tip are shown. The same procedures can be applied for the cracks in 316LN, 9Cr and 12Cr steels if the *da/dt* vs. C_t data are available. Comprehensive data for these metals are gathered from the literature and demonstrated.

2. *K* and C^* for surface crack under internal pressure

An elliptic surface crack located in the radial-axial plane on the internal surface of a thick wall cylinder is shown in Fig. 1. The deepest point along the crack front is denoted as crack front location *A* and the crack tip location on the surface is denoted as location *B*.

2.1 Equations for *K*

Stress intensity factor equations for a wide range of surface cracks on the inside of a pressurized cylinder were derived by Newman and Raju [3]. The aspect ratio defined as the ratio of crack depth to half crack length on the surface ranged from 0.2 to 1. The ratio of crack depth to wall thickness ranged from 0.2 to 0.8. The stress intensity factor was written as follows. Stress intensity factor at the deepest crack front location, K_A, is obtained when $\phi = \pi/2$ and stress intensity factor at the crack tip on the surface, K_B, is obtained when $\phi = 0$.

$$K = \frac{P_i R_i}{t}\sqrt{\pi\frac{a}{Q}}\cdot F\left(\frac{a}{c},\frac{a}{t},\frac{R_i}{t},\phi\right) \tag{1}$$

$$Q = 1 + 1.464\left(\frac{a}{c}\right)^{1.65} \tag{2}$$

$$F = 0.97\left(m_1 + m_2\left(\frac{a}{t}\right)^2 + m_3\left(\frac{a}{t}\right)^4\right) f_\phi \cdot g \cdot f_c \tag{3}$$

$$m_1 = 1.13 - 0.09\left(\frac{a}{c}\right) \tag{4}$$

$$m_2 = -0.54 + \frac{0.89}{0.2 + \frac{a}{c}} \tag{5}$$

$$m_3 = 0.5 - \frac{1.0}{0.65 + \frac{a}{c}} + 14\left(1 - \frac{a}{c}\right)^{24} \tag{6}$$

$$f_\phi = \left(\left(\frac{a}{c}\right)^2 \cos^2\phi + \sin^2\phi\right)^{\frac{1}{4}} \tag{7}$$

$$g = 1 + \left(0.1 + 0.35\left(\frac{a}{t}\right)^2\right)(1 - \sin\phi)^2 \tag{8}$$

$$f_c = \left(\frac{R_o^2 + R_i^2}{R_o^2 - R_i^2} + 1 - 0.5\sqrt{\frac{a}{t}}\right)\frac{t}{R_i} \tag{9}$$

2.2 Estimation equation for C^*

Equations of C^* are derived from the plastic part of *J*-integral, J_p solutions. However, J_p solutions for overall crack front of surface cracks on the inside of a pressurized cylinder are not available as a function of the configuration parameters such as *a/c*, *a/t* and Norton's creep exponent, *n*. Hence comprehensive C^* solutions for the surface crack on the inside of a pressurized

cylinder cannot be derived from either of the known J_p solutions. For a surface crack in a plate under tension a comprehensive set of C^* solutions were derived by Yagawa et al. from three dimensional finite element analyses [4, 5]. In the Yagawa solution, C^* can be estimated at both the deepest point of the crack front and at the crack tip on the surface. However, the solutions are for a crack in a plate and not in a cylinder. The Yagawa solution was given for full ranges of ϕ values. At the deepest point on the crack front, *A,* it was shown that

$$C^* = A \cdot t\left(1-\frac{a}{t}\right)\sigma^{n+1} q_A\left(\frac{a}{t},\frac{a}{c},n\right) \tag{10}$$

$$q_A\left(\frac{a}{t},\frac{a}{c},n\right) = [\xi]\cdot[q]\cdot[n]^T \tag{11}$$

where, $[\xi]$ is a function of *a/t* and *a/c* and $[n]^T$ depends on *n* as follows :

$$[\xi] = \left[1,\left(\frac{a}{t}\right),\left(\frac{a}{c}\right),\left(\frac{a}{t}\right)^2,\left(\frac{a}{c}\right)\left(\frac{a}{t}\right),\left(\frac{a}{c}\right)^2,\left(\frac{a}{t}\right)^2\left(\frac{a}{c}\right),\left(\frac{a}{t}\right)\left(\frac{a}{c}\right)^2,\left(\frac{a}{t}\right)^2\left(\frac{a}{c}\right)^2\right] \tag{12}$$

$$[n] = \left[1, n, n^2, n^3\right] \tag{13}$$

And $[q]$ is coefficient which was determined for various crack front locations.

For extending the application of Eq. (13) to the case of cracks in a cylinder, the tensile stress term, σ, in the equation is replaced by the average net section stress over the uncracked ligament of a cross section given by

$$\sigma = \frac{P_i \cdot R_i}{t - \frac{\pi \cdot a}{4}} \tag{14}$$

It was shown that by employing Eqs (10) and (14), C^* can be conservatively evaluated at every location of a surface crack front for all ranges of aspect ratio, $0.2 \le a/c \le 1.0$, and crack depth ratio, $0.2 \le a/t \le 0.8$, for *n* values exceeding 5 [2]. This estimation scheme enables calculation of creep crack growth life from any initial surface crack whose geometry is in the above range without having to assume that the crack is infinitely long.

2.3 Equation for C_t

The estimation equation of C_t employed for the elastic-plastic-secondary creeping material is as follows [6],

$$C_t = \frac{4\alpha\beta\tilde{r}_c(\theta,n)}{E(n-1)}\frac{(1-\nu^2)K^4}{t}\frac{F'}{F}(EA)^{\frac{2}{n-1}}(t+t_{pl})^{-\frac{n-3}{n-1}} + C^* \tag{15}$$

where, F is K-calibration factor, $F'=dF/d(a/W)$, β is 1/3 determined by finite element calculation and $\tilde{r}_c(\theta,n)$ is a dimensionless function dependent on n. Detailed meanings of variables in Eq. (15) are also explained in other references [2]. A value of t_{pl}, $2.4\times10^{-2}hr$, reported for 1.25Cr-0.5Mo steel[7] is used in the current analysis. As described in the previous section C^* is determined using equations (10) and (14). F'/F functions are derived from Eq. (3) as Eq. (16) and Eq. (17) for the deepest crack surface location A and for the surface location B respectively.

$$\frac{F'}{F} = \frac{n_1 - \sqrt{\frac{a}{t}}}{2n_1\cdot\left(\frac{a}{t}\right) - \left(\frac{a}{t}\right)^{\frac{3}{2}}} + \frac{2m_2\cdot\left(\frac{a}{t}\right) + 4m_3\cdot\left(\frac{a}{t}\right)^3}{m_1 + m_2\cdot\left(\frac{a}{t}\right)^2 + m_3\cdot\left(\frac{a}{t}\right)^4} \tag{16}$$

$$\frac{F'}{F} = \frac{2m_2\cdot\left(\frac{a}{t}\right) + 4m_3\cdot\left(\frac{a}{t}\right)^3}{m_1 + m_2\cdot\left(\frac{a}{t}\right)^2 + m_3\cdot\left(\frac{a}{t}\right)^4} + \frac{\frac{n_1}{2}\cdot\left(\frac{a}{t}\right)^{-\frac{1}{2}} - \frac{1}{2}}{n_1\cdot\sqrt{\frac{a}{t}} - \frac{1}{2}\left(\frac{a}{t}\right)} + \frac{0.7\left(\frac{a}{t}\right)}{1.1 + 0.35\left(\frac{a}{t}\right)^2} \tag{17}$$

where, $n_1 = \dfrac{2R_o^{\,2}}{R_o^{\,2} - R_i^{\,2}}$ (18)

The creep crack growth rate is characterized by the following equation :

$$\frac{da}{dt} = H(C_t)^q \tag{19}$$

where, da/dt is the creep crack growth rate, H and q are material constants and C_t is a crack tip parameter that is valid from small-scale to extensive creep conditions [8]. Since under small-scale creep conditions the value of C_t is highly dependent on K whose values are quite accurate as shown in Eqs (1) to (9), and much less dependent on C^*, the highest discrepancy in predicted crack growth rate is likely to occur under extensive creep conditions when $C_t \fallingdotseq C^*$. The values of q in Eq. (19) range from 0.5 to 0.8 [8] for several Cr-Mo ferritic steels and extensive stainless steels. The discrepancy in predicted crack growth rate can then be between a factor of 2 to 3 in case the estimation equation of C^* given by Eq (10) is used. This discrepancy range may be reasonable for inspection interval determination.

3. Creep crack growth analysis

A pressurized cylinder with 355.6 *mm* outer radius(R_o) and 309.9 *mm* inner radius(R_i) is chosen for creep crack growth analysis. The thickness of the cylinder(t) is 45.7 *mm*. It is assumed that the internal pressure to be 6.89 *MPa*. The material properties are also assumed as follows: creep coefficient (A) is 4.49×10^{-20} MPa^{-n}, creep exponent (n) is 8.0, creep crack growth coefficient (H) is

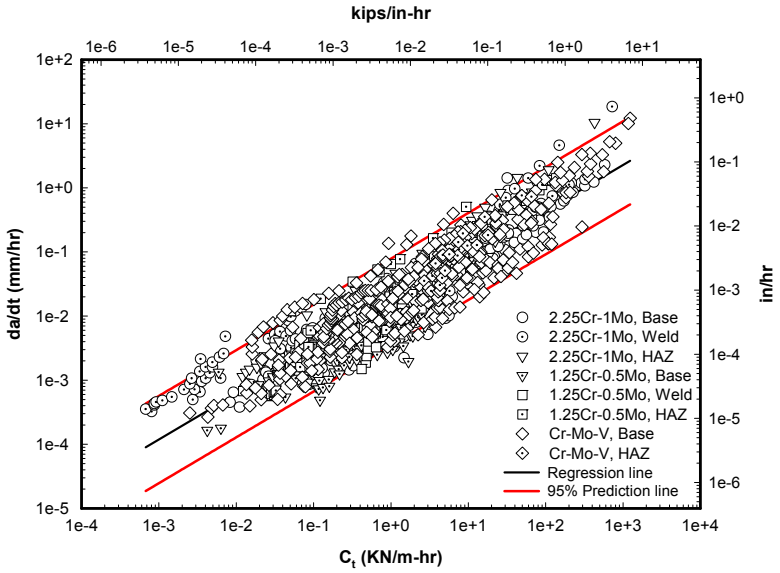

Figure 2. Creep crack growth data collected for low alloy steels [9].

1.643×10^{-2} (C_t in *KN/m-hr* and *da/dt* in *mm/hr*), creep crack growth exponent (q) is 0.714 and the time for crack tip creep zone development retardation due to crack tip plastic zone(t_{pl}) is 2.4×10^{-2} *hr*. It is assumed that the creep behavior follows Norton's creep law expressed as $\dot{\varepsilon} = A\sigma^n$. Primary creep is not considered. The creep crack growth model with C_t as a crack tip parameter characterizing the crack growth rate was described in Eq (15). Constants H and q were determined from the data collected for low alloy Cr-Mo steels in the previous work as shown in Fig. 2 [9]. The materials included were 2.25Cr-1Mo, 1.25Cr-0.5Mo and Cr-Mo-V steels. The constants shown above represent mean creep crack growth behavior. Similar creep crack growth data for 9Cr and 12Cr steel are shown in Figs. 3 and 4. For 316SS, 316LN and 316FR steel the similar data are summarized in Fig. 5 [10].

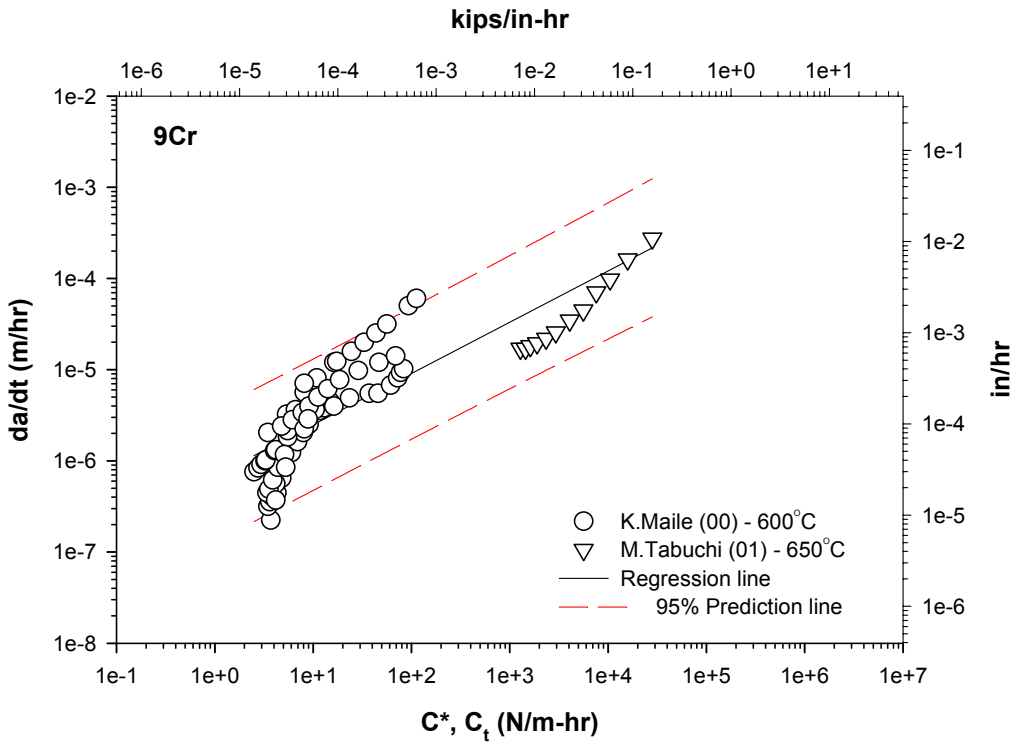

Figure 3. Creep crack growth data collected for 9Cr steel.

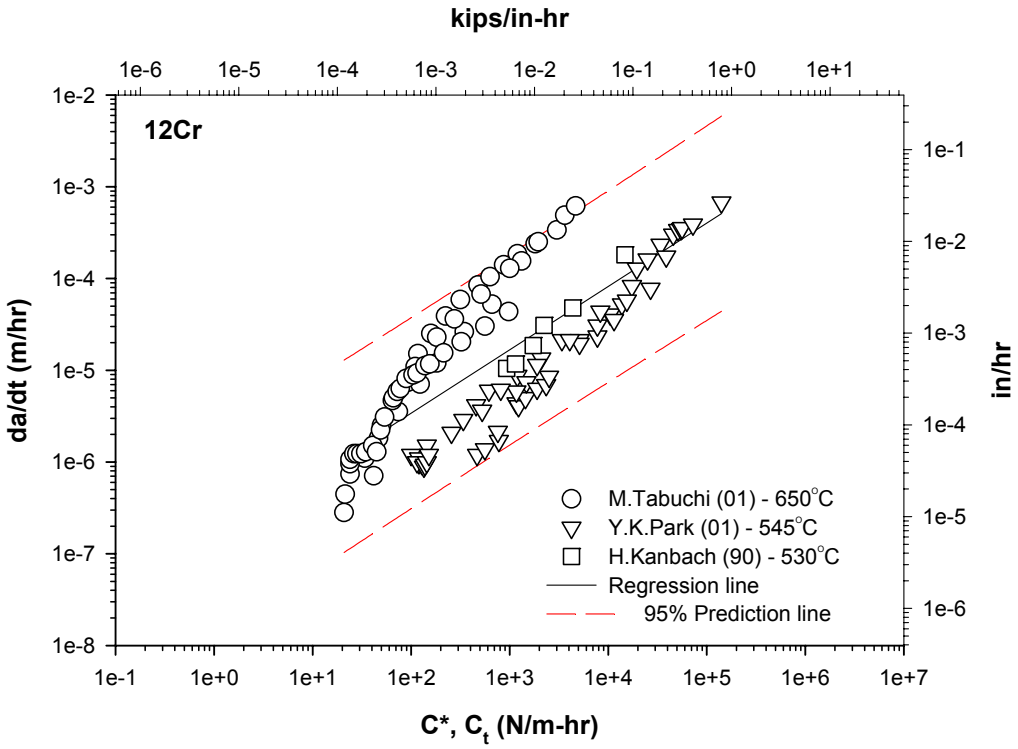

Figure 4. Creep crack growth data collected for 12Cr steel.

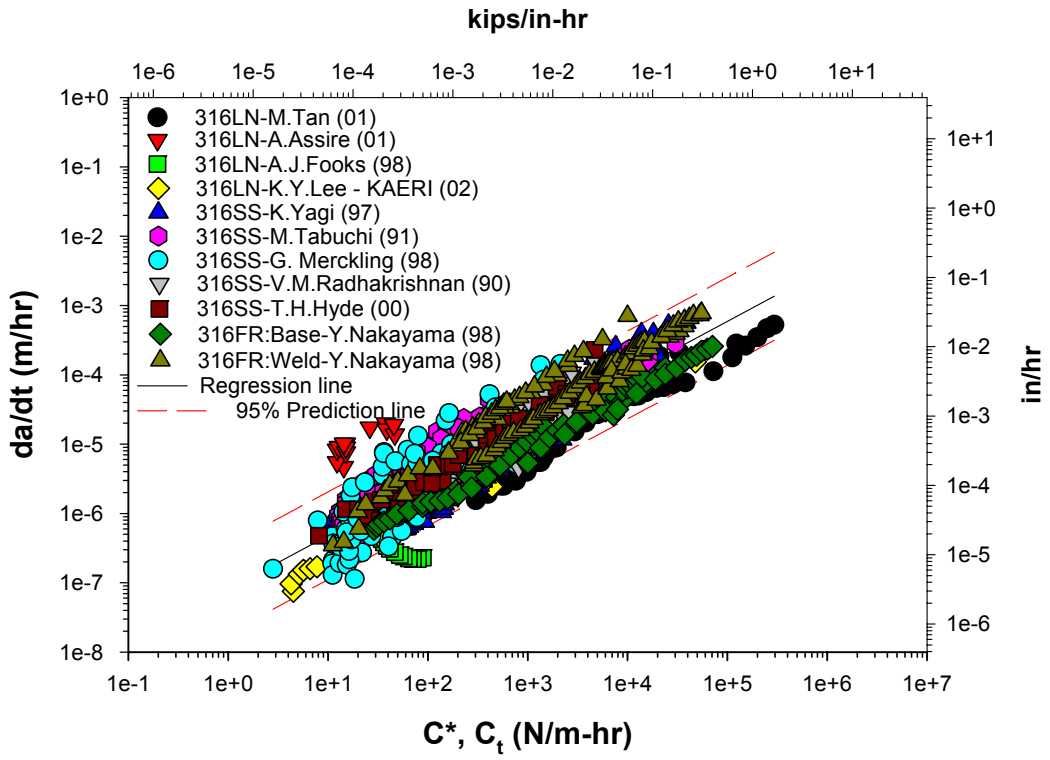

Figure 5. Creep crack growth data collected for 316SS, 316LN and 316FR steel.

A set of analysis were carried out for the initial crack geometry shown in Fig. 6. The initial half crack length, c, is fixed as 38.1 *mm* and the crack depth is varied as 11.43, 15.24, 19.05, 22.86 and 26.67 *mm* respectively. Thus, the ratios of a/c for these analyses become 0.3, 0.4, 0.5, 0.6 and 0.7.

Creep crack growth analyses were conducted and the analyses were terminated when the crack depth exceeds 30.48 *mm* which is 67% of the thickness. Figure 7(a) shows crack depth growth behavior as a function of the loading time and Fig. 7(b) shows surface crack length growth behavior. The crack growth rates of Figs. 7(a) and 7(b) were determined from the C_t values at each location of A and B of the surface crack using the creep crack growth model expressed as Eq. (19).

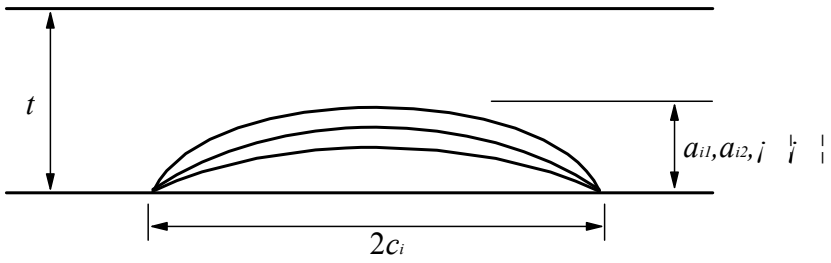

Figure 6. Initial crack geometries for two sets of creep crack growth analysis when surface crack size is fixed.

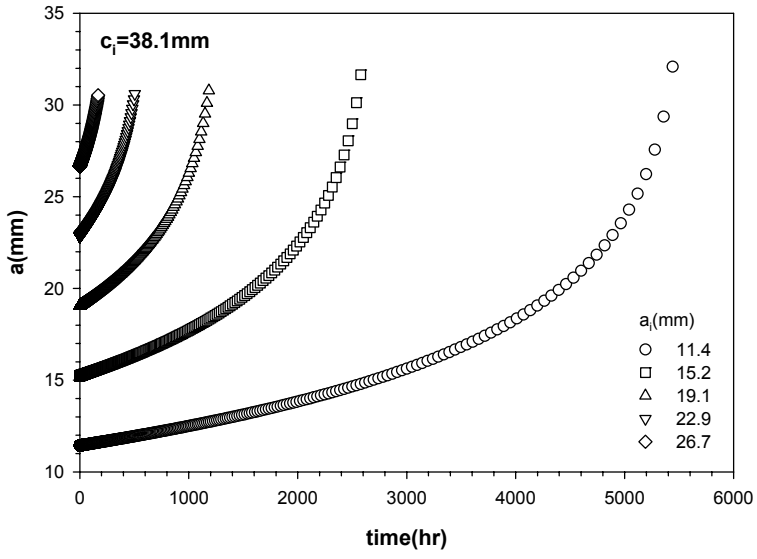

(a)

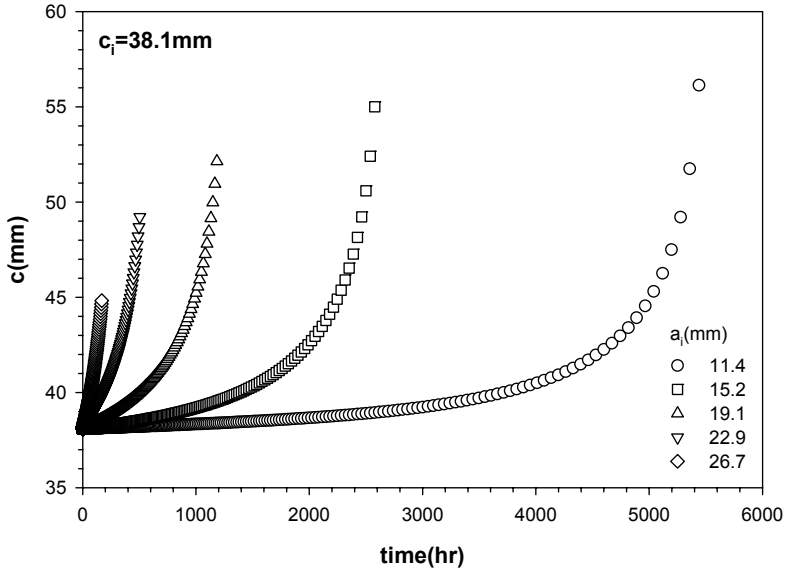

(b)

Figure 7. (a) Crack depth growth and (b) surface crack length growth behaviors as a function of time.

Variations of the C_t values with time are shown in Fig. 8(a) for the crack front location *A* and Fig. 8(b) for the location *B*. During the initial period after the internal pressure is applied, the contribution of the first term in Eq. (15) is significant since the small scale creep is dominant and the C_t value during this period is much higher than the value of C^*. As extensive creep condition is achieved C_t value approaches to C^* since the first term in Eq. (15) vanishes and the second C^* term becomes dominant. During the last stage of life, C_t value is increased because crack length increases substantially. Figure 9 shows change of aspect ratio for the surface crack over the creep crack growth life. It is shown that as the crack grows the aspect ratio is approaching to an asymptotic value whatever the initial aspect ratio would be.

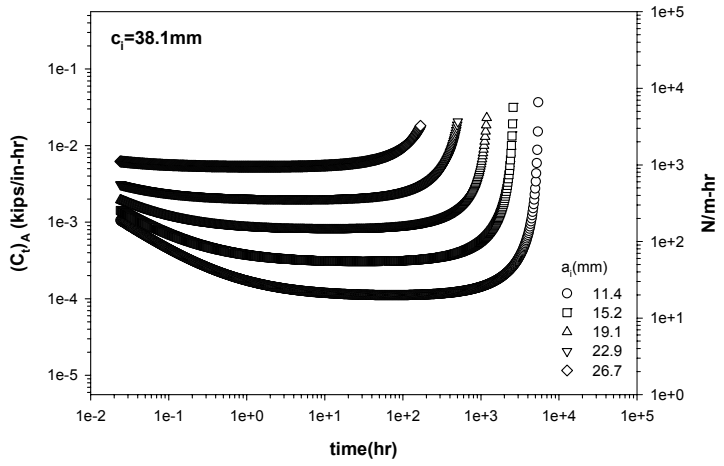

(a)

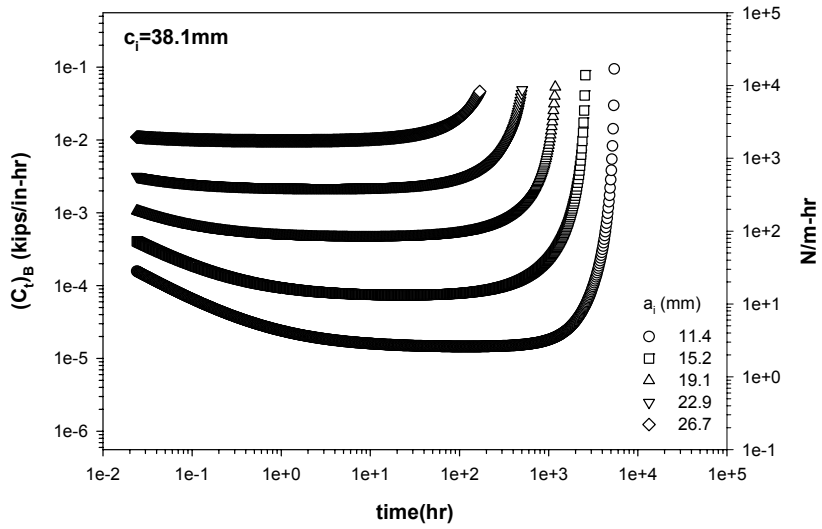

(b)

Figure 8. Variation of C_t during the crack growth at the crack fronts A and B.

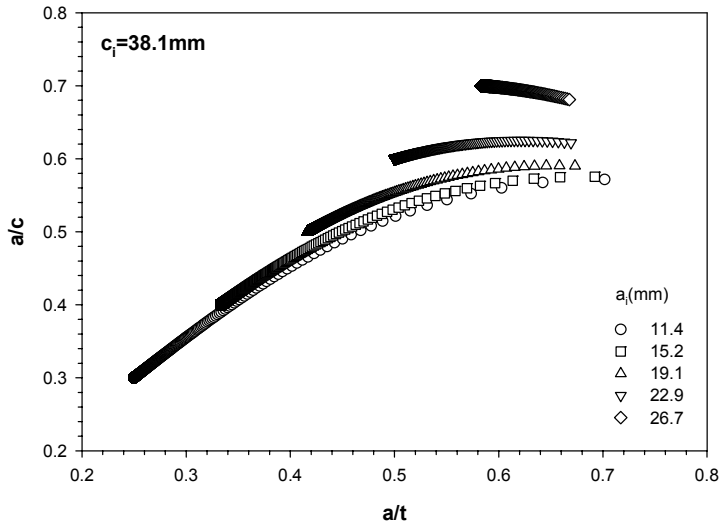

Figure 9. Change of aspect ratio of the surface cracks during creep crack.growth.

Finally residual life diagrams are obtained and are shown in Fig. 10. As the initial crack length is fixed the residual life is shown as a function of the initial crack depth, a. It can be argued that the residual life strongly depends on the crack depth. On the contrary to the trend shown in Fig. 10, if the initial crack depth is fixed and the residual life is shown as a function of initial crack length, the residual life is quite insensitive to crack length, indicating that the assumptions in the early analyses in which surface cracks were treated as through length axial cracks were in fact quite adequate. Creep crack growth life prediction methodology using C_t as a fracture parameter was shown to be valid by comparing the predicted life with the field failure data [11]. Since the method in the above studies is essentially the same as in this study, this approach can be considered to be valid and be expected to yield conservative residual life predictions. In the results presented in Fig. 7, the crack depth, a, increases steadily with time while the surface crack length, c, changes very little during the initial portion of the life. The value of c changes abruptly during the final stage. This implies that accurate measurement of crack depth during inspection is very critical for ensuring integrity of high temperature components.

There are some uncertainties that need to be addressed in future studies. *(i)* The same creep crack growth law expressed as Eq. (19) was applied for both locations A and B and the same constants of H and q were used. However, the constants in the crack growth law can be different between the locations A and B due to differences in constraint similar to stress encountered in the fracture toughness behavior. This needs to be explored further. *(ii)* The crack shape was assumed to be semi-elliptic at all times. The C_t values and crack growth rates were evaluated at locations A and B assuming the maximum C_t occurs at A or B. However, under certain conditions of loading and crack geometry, the maximum C_t can occur elsewhere leading to mushroom type of crack growth. This is not considered in the current approach.

Despite of the limitations mentioned above, the approach used in this study can be used reliably for practical purpose. Most of the creep crack growth life is consumed when a/t is less than 0.4. The discrepancy between the proposed C^* equation and the known accurate equation is minor. Also a mushroom type of crack growth is not probable until the last stage of crack growth when the crack depth is approaching the vessel thickness.

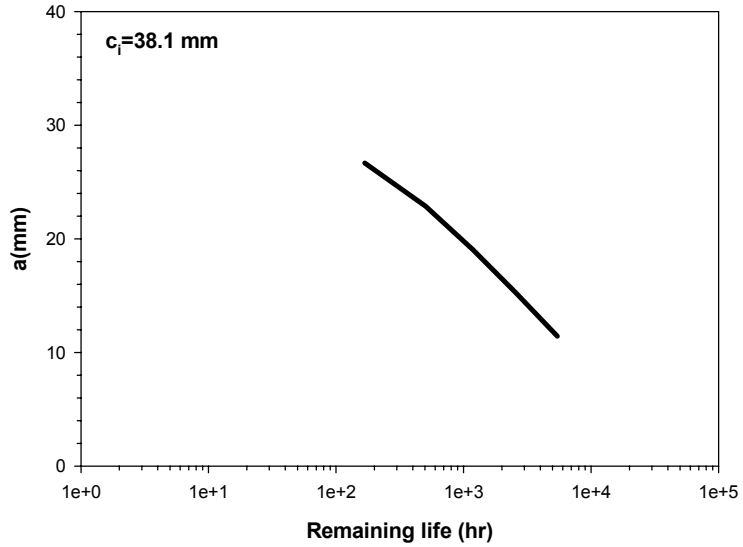

Figure 10. Residual life diagrams when initial c is fixed as 38.1 mm.

4. Conclusions

A creep crack growth life prediction procedure is demonstrated for the case of surface crack located in the radial-axial plane and on the internal surface of a pressurized cylinder. The method used does not require simplifying assumptions regarding the crack geometry used in earlier studies. Using the newly proposed equations for estimating C_t, creep crack growth analysis is conducted for 1.25Cr-0.5Mo steel and an internal surface crack of a pressure vessel at high temperature. The creep crack growth data for 9Cr, 12Cr and 316LN steels are summarized. The aspect ratios of the surface crack were updated for every time step of crack growth calculations and were reflected in determining the C_t value of the next step. Changes of crack depth, crack size and C_t values at the deepest point and surface point of the crack tip are presented. Finally, limitations of the current approach are discussed. It is argued that the approach developed in this study can be used reliably for practical purpose despite of these limitations.

5. Acknowledgement

The first author wishes to acknowledge the financial support of MOST to CAU through KAERI subcontract (*High Temperature Material Characterization and Advanced Materials Development*, *PI: Dr Woo Seok Ryu*).

References

1. Saxena, A. Nonlinear fracture mechanics for engineers. CRC Press, 1998.

2. Yoon, K.Bb, Park, T.K. & Saxena, A. Creep crack growth analysis of elliptic surface cracks in pressure vessels. Int. J. of Pres. Ves. and Piping 2003, 80, pp. 465–479.

3. Newman, .JC., Raju, I.S. Stress intensity factors for internal surface cracks in cylindrical pressure vessels. J. Pressure Vessel Technol. Trans. ASME 1980, 102, pp. 342–346.

4. Yagawa, G., Kitajima, Y. & Ueda, H. Three-dimensional fully plastic solutions for semi-elliptical surface cracks. Int. J. Pressures Vessel Piping 1993, 53, pp. 457–510.

5. Yagawa, G., Kitajima, Y. & Ueda, H. Erratum. Int. J. Pressures Vessel Piping 1997, 74, pp. 77–80.

6. Yoon, K.B., Saxena, A. & McDowell, D.L. Influence of crack-tip cyclic plasticity on creep fatigue crack growth. ASTM STP 1131 1992, pp. 267–392.

7. Yoon, K.B., Saxena, A. & Liaw, P.K. Characterization of creep-fatigue crack growth behavior under trapezoidal waveshape using C_t-parameter. Int. J. Fract. 1993, 59, pp. 95–114.

8. Saxena, A. Creep crack growth under nonsteady state conditions. ASTM STP 905 1986. Pp. 185–201.

9. Saxena, A. & Yoon, K.B. Assessment of defects in high temperature components: Part II-creep crack growth analysis of surface cracks in a pressurized cylinder. WRC Bulletin, 2003, 483, pp. 26–43.

10. Ryu, W.S. et al. Reactor Core Materials Research and Integrated Material Database Establishment, KAERI/RR-2224/2001, Final Report, 2001

11. Bloom, J.M. Validation of creep crack growth life estimation methodology /hot reheat steam pipes. J. Pressure Vessel Technol. Trans. ASME 1994, 116, pp. 331–335.

A future approach on life monitoring

I. Marcelles[(1)]; I. Báscones[(1)]; A. Sánchez-Biezma[(1)] & M. Soler[(2)]
(1) Tecnatom, s.a.; (2) Endesa Generación – Andorra FPP, Spain

Abstract

LifEtime Monitoring System (LEMS) is a new software tool developed to allow fossil power plant (FPP) operating and maintenance staff to analyze and control the main components lifetime consumption associated with new operational practice. This system has on-line and off-line capabilities to determine episodes of high lifetime consumption by thermal fatigue or creep in the FPP main components. The system detects these episodes and informs the operator for them to perform the most appropriate maneuvers to extend the life of affected components. Moreover the system could be used in an off-line way to analyze transients and normal operation.

1. Introduction

Some operational practices, used in fossil power plants (FPP) in the recent years, are introducing high stresses than transients and normal operation considered during the initial design:

- Frequency regulation, in order to be more competitive in the new European markets
- Reduced plant start-up/stop times and reduced overhaul times,
- Use of new fuels, including coal and waste mixtures, co-firing and co-combustion.

These new operational conditions are improving the plant economic results in the short term, but most of the mentioned conditions drive to reduce the lifetime of operating plant components. After some years of working under these new operational conditions, important maintenance problems are appearing.

LifEtime Monitoring System (LEMS) is a software developed to calculate the main components lifetime consumption, in order to improve the plant operational practices and reduce the maintenance problems as much as possible. LEMS system has on-line/off-line capabilities to determine episodes of high lifetime consumption by thermal fatigue or creep, in FPP main components. A prototype is now working in Teruel FPP (Spain), which was developed under the European project SICOBO [3].

2. LEMS system description

2.1 LEMS architecture

The LEMS system collects on-line data associated with a specific component (temperatures and pressures) to calculate the component lifetime consumption associated with two main phenomena of creep and thermal fatigue.

LEMS obtains the necessary on-line data from monitoring and control system (DCS system). In most cases, metal temperature of main plant components are monitored by several sensors placed along the component. An average value of temperature is taken for each instant. An array of metal temperature and working pressure is acquired for each component.

The architecture of the application is the following:

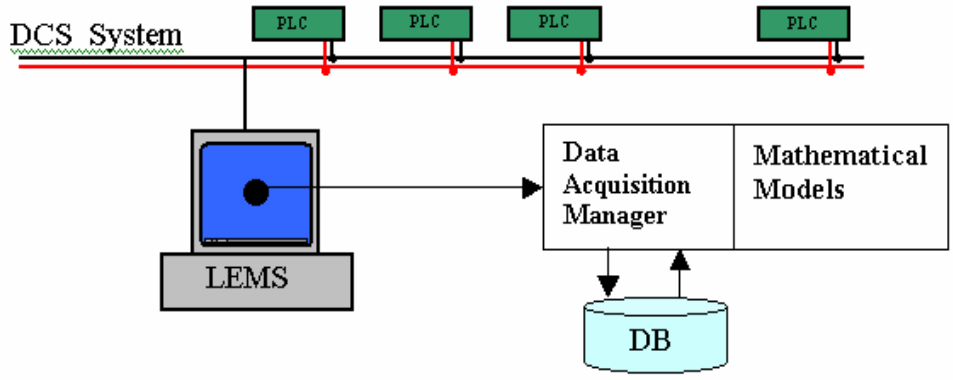

Figure 1. LEMS architecture.

The main components of LEMS are the following:

1. Data Acquisition Manager module is the main component of LEMS, controlling the program to carry out the following functions:
   - Collect data from the DCS, filtering significant values
   - Access to the information available within the database (DB): components for each FPP, sensors for each component, type of sensors and physical situation (use of virtual sensors is possible), materials characteristics, components geometry, etc.
   - Access to mathematical models (*Creep and Fatigue Models*).
   - Store results in database.

2. Database stores:
   - The entire configuration parameters:
     - Components associated to FPP
     - Sensors associated to component
     - Type of sensor, and physical situation (use of virtual sensors possibility)
     - Materials characteristics
     - Thermal properties
     - Component geometry
     - Tags name in DCS system, etc.

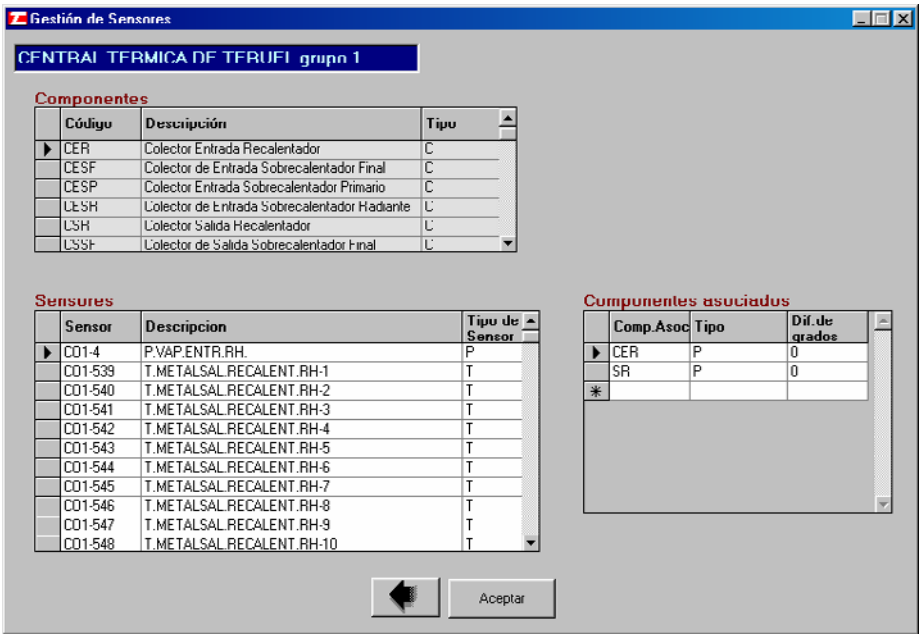

Figure 2. Sensor management screens.

   - Results:
     - Lifetime consumption by creep (snapshot and accumulated)
     - Lifetime consumption by thermal fatigue (snapshot and accumulated).

3. LEMS Mathematical Models, including two different types of models (*Creep and Fatigue Models*), based on standard Technical Rules for Steam Boilers (TRD) Series 301 (DDA) [1].

2.2 LEMS capabilities

LEMS system has both on-line and off-line capabilities whose objectives are different:

1. On-line Capability: The system continuously determines episodes of high lifetime consumption by thermal fatigue or creep in the FPP main components, informing the operator. This on-line information allows operators to perform the most appropriate maneuvers to reduce the consumption and extend the lifetime of affected components.

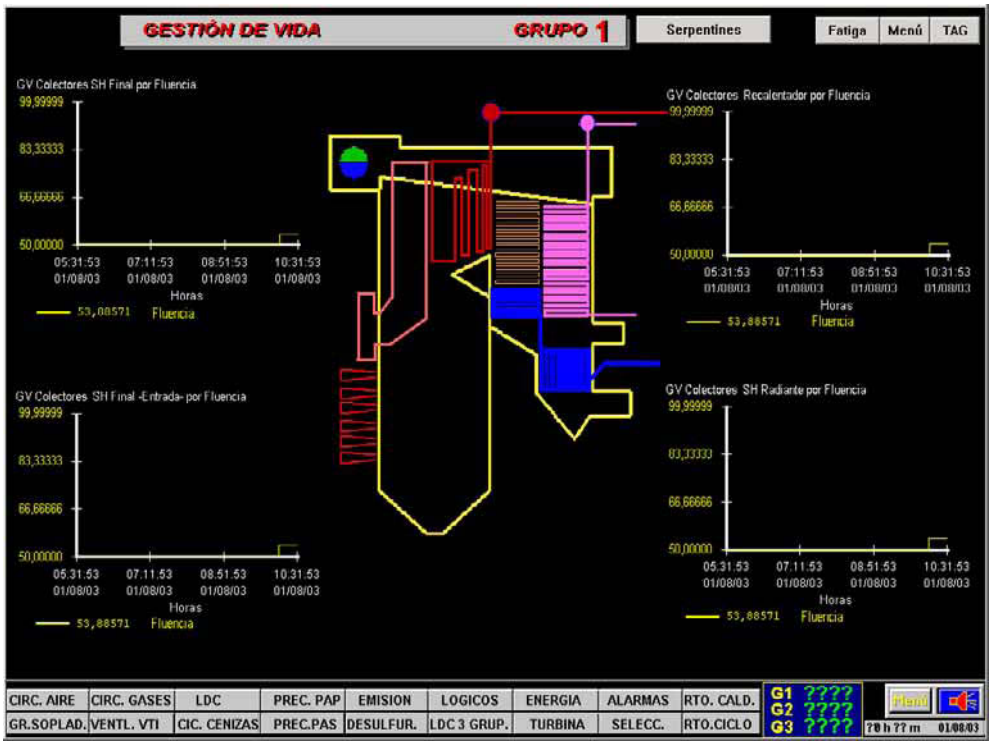

Figure 3. On-line capability: lifetime consumption by creep.

2. Off-line capability: The system can be used in an off-line way to analyze transients and normal operation to determine the lifetime consumption for particular components for specific periods. The information provided by the system will allow improving the plant operational practices and reducing the maintenance problems as much as possible.

Microsoft Excel - ListFatiga1

Archivo Edición Ver Insertar Formato Herramientas Datos Ventana ?

E17 157

FATIGA

CENTRAL TERMICA DE TERUEL grupo 1

Componente	Fecha	Temperatura Inferior (ºC)	Temperatura Superior (ºC)	Presión mínima (kg/cm^2)	Presión Máxima (kg/cm^2)	Factor Consumido	Factor Acumulado
Colector Entrada Recalentador	03/01/2003	435,8412	568,975	17,59995	38,09995	8,33366E-11	8,45918E-11
	04/01/2003	521	571,844	26,29995	39,99995	6,25844E-12	8,9593E-11
Colector Salida Recalentador	03/01/2003	407,8872	569,8647	17,29995	40,09995	2,77575E-11	2,77575E-11
Colector de Entrada Sobrecalentador Final	03/01/2003	507,2918	555,4573	157	168,0999	1,95025E-10	1,95025E-10
	04/01/2003	518,3115	564,7053	163,0999	166,8	2,26774E-11	2,17702E-10
Colector Entrada Sobrecalentador Primario	03/01/2003	401,2368667	453,88075	164,5	166,5	8,02935E-12	8,02935E-12
Colector de Entrada Sobrecalentador Radiante	03/01/2003	437,44195	487,3741	158,5	174,7	6,83981E-11	6,83981E-11
	04/01/2003	429,7587	479,3658	166,0999	171,8	3,27505E-11	1,01149E-10
Colector de Salida Sobrecalentador Final	03/01/2003	507,2918	555,4573	157	168,0999	1,95681E-10	1,95681E-10
	04/01/2003	518,3115	564,7053	163,0999	166,8	2,27999E-11	2,18481E-10
Colector Salida Sobrecalentador Primario	03/01/2003	407,5533833	441,466425	158,5	174,3	7,97108E-11	7,97108E-11
	04/01/2003	410,3099	442,6331	164,8	174,7	1,27847E-12	8,09893E-11
Colector de Salida Sobrecalentador Radiante	03/01/2003	409,8701	615,4999	157	168,0999	2,03823E-10	2,03823E-10
	04/01/2003	452,2743	470,2835	163,0999	166,8	3,30638E-11	2,36886E-10

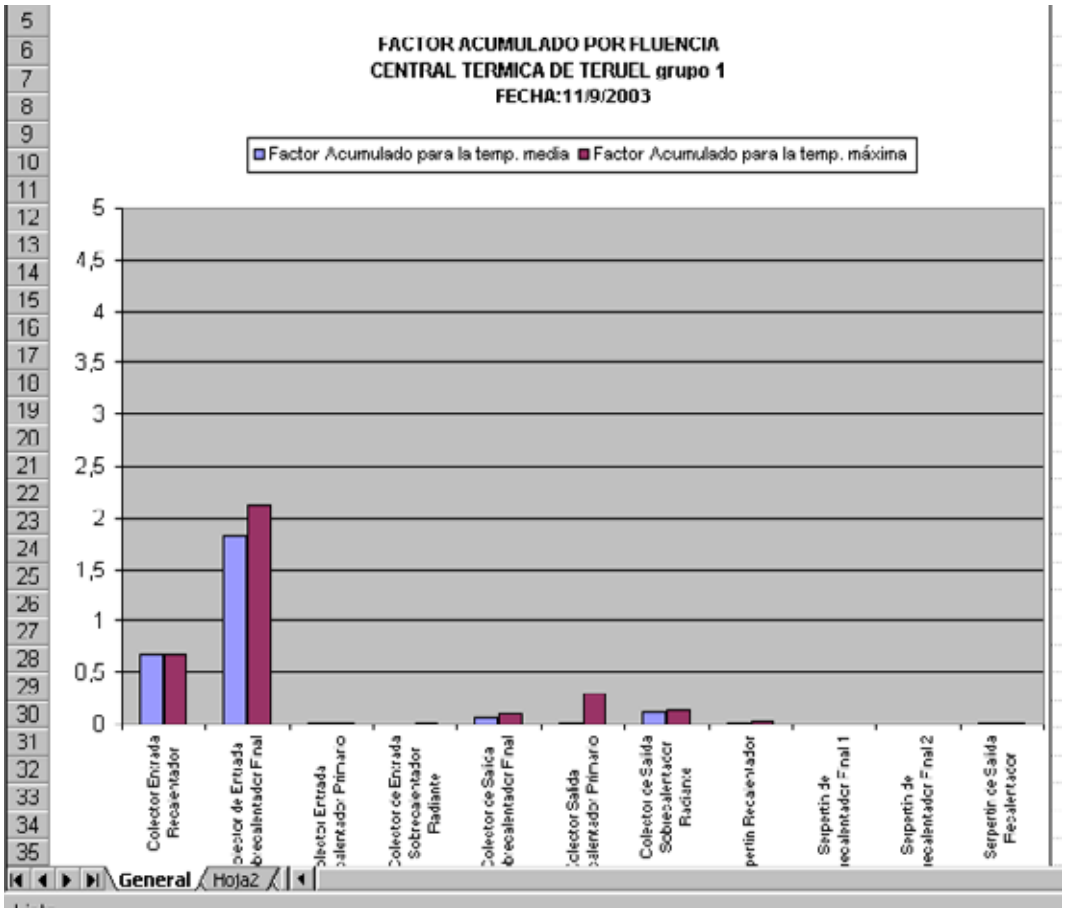

Figure 4. Off-line capability: thermal fatigue report and creep results.

3. Phenomena analyzed

As it is already mentioned, the LEMS system collects on-line data associated with a specific component (temperatures and pressures) to calculate the component lifetime consumption associated with two main phenomena:

- *creep, and*
- *thermal fatigue.*

Creep is a process produced under a continuous load, producing inelastic deformation increase in time. Main agents affecting creep are:

- Temperature
- Load
- Application time.

A specific material has creep degradation over a specific activation temperature. This activation temperature depends on material:

Material	**Activation T^a (°C)**
Aluminum alloys	205
Titanium alloys	315
Carbon steel	370
Austenitic steel	540
Nickel alloys	650

In FPP, creep affects components in high temperatures (over 360ºC for steel low-alloys, and over 430ºC for austenitic steel) and high stress conditions.

Thermal fatigue is a process produced under cyclic loads, producing crack increasing in components. At low loads (below elastic limit), this degradation process can appear. A component is affected by a summing-up of mechanical and thermal stresses.

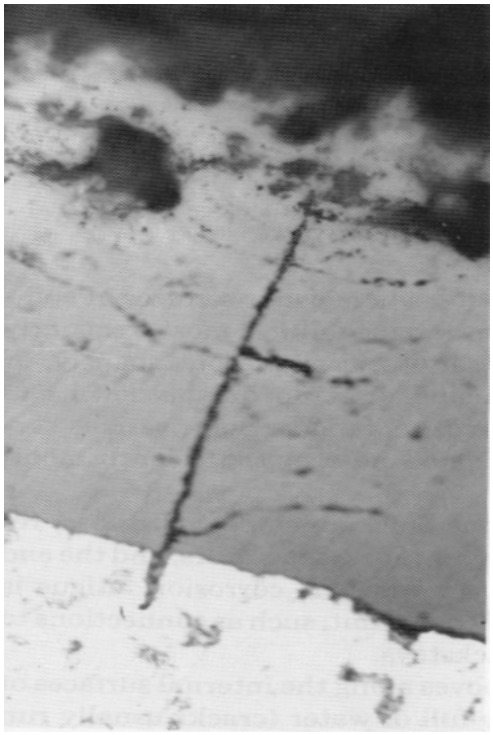

Figure 5. Crack produced by fatigue.

3.1 Creep

Lifetime consumption is calculated considering operation time of the component, in specific pressure and temperature conditions.

The creep factor is calculated as follows:

$$L_{cr} = \sum_{P_i\theta_i} \left(\frac{t}{T} \right)_{P_i\theta_i} \times 100 \qquad (1)$$

Where:

L_{cr} :	creep factor (%).
Pi:	internal pressure under condition i (kg/cm^2).
θi:	temperature under condition i (ºC).
t:	performance time under condition i (h).
T:	lifetime (h) under condition i, for the component material.

For determining lifetime of a component, the application uses standard materials properties and measured operating conditions. The estimation requires to calculate internal stress and compare it with stress rupture curves, which could be parametrized or interpolated from tables.

3.2 Thermal fatigue

This model calculates fatigue cycles produced in the component, in real time, by the rainflow method (Standard ASTM E1049 [2]).

In the rainflow method a cycle is counted when this sequence is detected: peak-valley-peak or valley-peak-valley (X-Y-Z) when the second range ΔYZ is bigger than first one ΔXY.

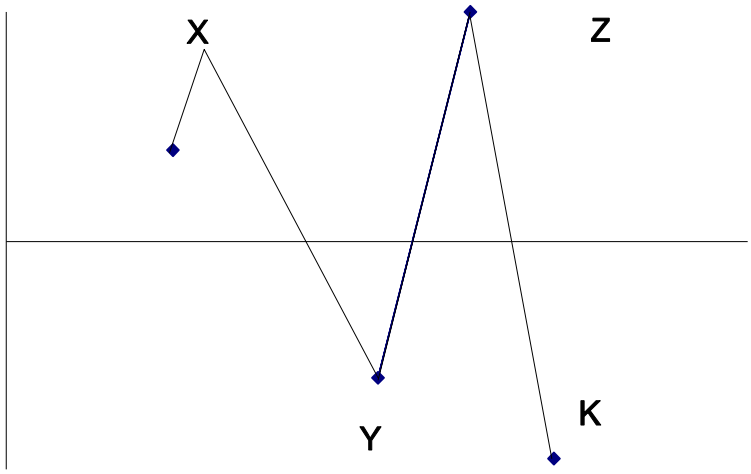

Figure 6. Rainflow cycle counting method.

The lifetime consumption calculation is made for each closed fatigue cycle. The life assessment is done based on:

- geometrical data, such as diameters, thickness,
- operational parameters, including pressures and temperatures
- materials parameters, such as elastics limits, thermal characteristics, etc.

The material parameters depend on temperature. The temperature taken for these parameters is the dominant temperature in the cycle, which is calculated by the system considering maximum and minimum temperatures during the cycle.

3.2.1 Mechanical stress determination

The general expression to determine mechanical stress, considering a simplified scenario with only elastic stresses, is the following:

$$\sigma_P = \alpha_m P \frac{d_m}{2s} \tag{2}$$

where

σ_P	stress due to internal pressure
P	governing internal pressure
d_m	component average diameter
α_m	stress concentration factor, computed by the system using the TRD 301, Annex 1 [1].

Maximum and minimal mechanical stress will be:

$$\sigma_{p_{min}} = \alpha_m P_{min} \frac{d_m}{2s} \qquad \sigma_{p_{max}} = \alpha_m P_{max} \frac{d_m}{2s} \tag{3}$$

3.2.2 Thermal stress determination

Thermal stress could be calculated in a simple way assuming a symmetrical temperature distribution and elastic stresses. In this way, the simplified formula provided by TRD 301 Annex 1 [1] is valid:

$$\sigma_\theta = \alpha_\theta \frac{\beta E}{1-\upsilon}\left(\vartheta_m - \vartheta_i\right) \tag{4}$$

where

υ	Poisson's ratio
θ_m	average wall temperature
θ_i	internal wall temperature
β	differential thermal expansion coefficient
α_υ	stress concentration factor
E	elastic modulus.

3.2.3 Total stress

If there is neither external forces nor momentum, but internal pressure, total stress can be determined as follows:

$$\sigma_i = \sigma_{iP} + \sigma_{i\vartheta} \tag{5}$$

3.2.4 Allowable number of load cycles

The existing alternating stress range:

$$\Delta\sigma = \hat{\sigma} - \check{\sigma} \tag{6}$$

$$\hat{\sigma} = \sigma_{P_{max}} + \sigma_{\vartheta -} \qquad \check{\sigma} = \sigma_{P_{min}} + \sigma_{\vartheta +} \tag{7}$$

where load cycle stress limits are used as follows:

Depending on the $\Delta\sigma$ value the codes distinguish the super-elastic case : $\Delta\sigma > 2\sigma_{ela}$ and the elastic one: $\Delta\sigma \leq 2\sigma_{ela}$, and provide different equations for each case.

3.2.5 Cycle number determination

Starting from a calculated value of $2\sigma_a$, and the mathematically expressed fatigue curves provided by codes ASME or TRD 301 Annex 1 [1], number of cycles to crack initiation is easily determined.

$$\hat{n} = func(\sigma_a) \qquad \text{Para } 2\,\sigma_a > A \tag{8}$$

$$\hat{n} \longrightarrow \infty \qquad \text{Para } A \geq 2\,\sigma_a \tag{9}$$

3.2.6 Lifetime consumption by thermal fatigue

For each closed stress cycle, % lifetime consumption by thermal fatigue will be:

$$L_f = \frac{1}{\hat{n}} \times 100 \tag{10}$$

4. Conclusions

The changes in operational practices, introduced in fossil power plants (FPP) during the recent years, are producing much higher stresses on plant components than transients and normal operation considered during the initial design. That is why the FPP are demanding new tools to support operating and maintenance personnel to manage the plant with these new operational conditions.

New software tool as LEMS system, allows to analyze transients and normal operation, determining lifetime consumption of the FPP main components by creep and thermal fatigue. This analysis will facilitate operating, engineering and maintenance staff to modify or improve operational and maintenance practices to limit life consumption in normal operation, and during transients (start-ups, heating, cooling, etc.). LEMS will help to select the plant optimal operation, when is the most economical moment for changing or repairing a component, or if it is possible to operate during a determined number of years with specific operational conditions.

References

1. Technical Rules for Steam Boilers (TRD) Series 300 (DDA).
2. Standard practices for Cycle Counting in Fatigue Analysis. ASTM International. E1049.
3. CECA 7220-PR-075 “On-line Management System for the Advanced Control of Utility Boiler Efficiency” (SICOBO).
4. R. Viswanathan. Damage mechanisms and life assessment of high temperature components. ASTM International. ISBN: 0-87170-358-0
5. Informe final Proyecto PIE 131.106-01. Metodología de análisis de vida residual de CCTT (MAVRe). Asinel, TECNATOM y TGI.
6. G.A. Lamping & R.M. Arrowwood. Manual for Investigation and Correction of Boiler Tube Failures”. EPRI Report CS-3945.
7. Proceedings: Fossil Plant Life Extension Conference and Workshop. EPRI CS-4207s.

Development of on-line displacement monitoring system for high temperature steam pipe of fossil power plant

Song Gee Wook, Hyun Jung Seob & Cho Sun Young
Korea Electric Power Research Institute / Korea Laboratory Engineering System
Daejeon, Korea / Suwon, Korea

Abstract

Most domestic fossil power plants have exceeded 100,000 hours of operation with severe operating conditions. Among the critical components of fossil power plant, high temperature steam pipe systems have had many problems and damage from unstable displacement behavior because of frequent start ups and shut downs. In order to prevent serious damage and failure of the critical pipe system in fossil power plants, 3-dimensional displacement measurement system was developed for on-line monitoring. The displacement measurement system was developed with a use of a LVDT type sensor and a rotary encoder type sensor. This system was successfully installed and operated on a real power plant.

1. Introduction

The rapid change of environment in the domestic power industry is aggravating operating conditions of fossil power plants. As a result, pipes, boilers, and turbines are damaged by frequent start-ups, shut downs, and load changes. According to the results of precise life evaluation on power equipment that are 20 years old or more, many cases of damage are being found and the number is increasing [1–2]. For example, high temperature steam pipes, with more than 400°C, such as main steam pipes and hot reheat pipes have often failed to provide adequate pipe thermal expansion due to the undesirable operation of support and restraints. Consequently, structures adjacent to the support were interfering and the pipes suffered ruptures due to the restraints. Currently, a vertical hanger is installed in the support equipment to endure weight of the pipe itself and thermal expansion load and to indicate vertical displacement. However, the displacement is measured in the vertical direction only. Furthermore, the hanger cannot properly support when it generates excessive displacement in the direction of the pipe or sideways. Then there may be serious damage that generates shut downs, including fissures in the pipe due to the interference or

restraint with the structures. In response to this problem, on-line displacement or strain monitoring system is urgently needed [3]. The system is expected to prevent damage in pipes by checking high temperature pipes' excessive displacement that deviates from the designed displacement.

This study aims at developing an on-line displacement monitoring system that can be used during the operation of high temperature steam pipes in fossil power plants. We developed a displacement measurement device, which measures 3-dimensional displacement of the pipe. Also, the study is to develop a data measurement and monitor system that transmits data obtained from the measurement device to the central control unit of the power plant. In effect, the system was installed in the high temperature steam pipe in the "P" fossil power plant. The research analyzed results of a long-operated pipe test, then measured the changes of steam temperature during the operation, and compared the outcome with the results previously analyzed using a commercial pipe analysis program. In this method, the study will establish the applicable form of the piping displacement monitoring system.

2. Development of piping displacement measurement device

2.1 Background information based on a theory

To measure 3-dimensional displacement during the operation of high steam pipes, 3-dimensional spherical coordinates should be used as Fig. 1 shows. The distance and angle from one fixed point to another moved point can be measured and transformed into rectangular coordinates.

As a result, a point of space from two angles and distances can be designated. One LVDT measures the distance 'r', and two Encoders measure the angles 'θ' and 'ϕ'.

LVDT is attached to the pipe and measures the distance by transforming changes in the internal magnetic field into electric signals according to the displacement of attached part. Encoder detects the angles in a way that a sensor reads the inscribed calibrations that are made by rotation in the internal disc.

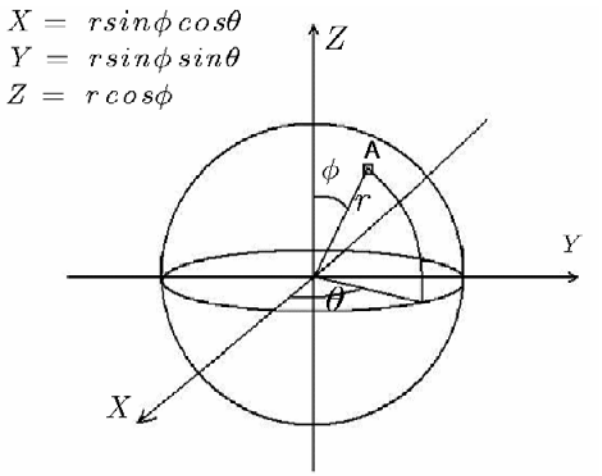

Figure 1. 3-Dimensional spherical coordinates.

2.2 Making of piping displacement measurement device

Main devices such as LVDT and Encoder were used to measure 3-dimensional displacement during the operation of high temperature pipe. Fig. 2. explains how the 3-dimensional measurement device is designed. The device is composed of Fixtures that are fixed to the structure to maintain strength of the measuring device. Those are: LDVT rod for gauging the distance with the attached part of the pipe; LVDT body that generates magnetic force with the move of the rod; bearing that provides friction by rotation and a point of angles; two Encoders that measure two rotation angles within 360°C from a fixed point; and I-Beam. The device was made of aluminum alloy to reduce weight. To measure the 3-dimensional displacement that occurs by thermal expansion, universal joint was attached at the end part of the device, which is connected to the piping displacement measurement part. The attached part is in a moment free state by the universal joint. When, the attached part moves to a point in the 3-dimensional space, the 3-dimensional displacement can be calculated with the application of the spherical coordinates.

To confirm the precision of the device, it was temporarily fixed and imposed 4 points in the universal joint and the data was obtained. From a direct measure of the displacement through Vernier Calipers, the study confirmed the device was quite precise when the error limits turned out to be -0.09~+0.15%.

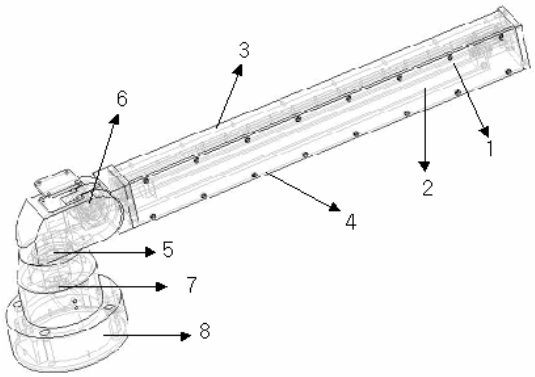

No.	Part
1	LVDT rod
2	LVDT guide
3	LVDT body
4	Guide support
5	Bearing
6	Encoder 1
7	Encoder 2
8	Fixture

Figure 2. 3-dimensional displacement measuring device.

3. Development of displacement data monitoring system

The piping displacement data measurement system transmits 3-dimensional displacement data, obtained from the 3-dimensional piping displacement measurement device, to central control unit in the power plant. This system was designed to transform analogue signals from the device into digital signals and be able to transmit them through communications cables without any loss of data. Furthermore, the system was developed for operator's convenience in monitoring [4–5].

3.1 The method of transmitting data

Analogue signals are obtained from the 3-dimensional piping displacement measurement sensor. Digital Output (20 bit) and Analog Output 1CH(0~10V) come out of two Encoders and LDVT respectively. These analogue signals should be transmitted to the local server in the central control unit. The methods of transmission are various. They can be TCP/IP, RS232&RS485, or high-frequency radio transmission. However, radio transmission cannot be applied to undesirable operating environment. Furthermore, its durability and reliance deteriorates when it comes to a long operation. Therefore, it makes little difference to use TCP/IP or RS232&RS485 since both of them require cables. However, we would recommend optic cables for long distance in the

transmission of data. The data should be connected to and amplified through AD converter and terminal in the device to prevent data loss or noise. Thus, RS-485 serial communications method was used in the transmission of data between displacement measurement devices or displacement measurement device and control PC.

3.2 Displacement monitoring program

The movement of the main steam pipe was measured during the operation of the power plant and the program for the monitoring was developed as shown in Fig. 3 and 4. The research used LabVIEW, which was developed by NI, as a Program tool. The program is divided into a control part and a monitor part. The upper one in the control part shows on-line displacements of x, y, z coordinates in a graph from the system 1, 2, 3 that are installed in the pipe. In the lower one, operators can input initial position value and limit position value of each direction into the program. Then, it shows an alarm that turns from green into red when measured displacement deviates from the designed displacement.

Moreover, measured data can be stored with the interval of hours or seconds on-line. The program is set to start measuring immediately after a push of start button when the initial setting is done. The monitor part of the program indicates cold state and hot state of the high temperature pipe from boiler to turbine, positions of installed displacement measurement device, and the sum of vectors of x, y, z displacements from each position during the operation.

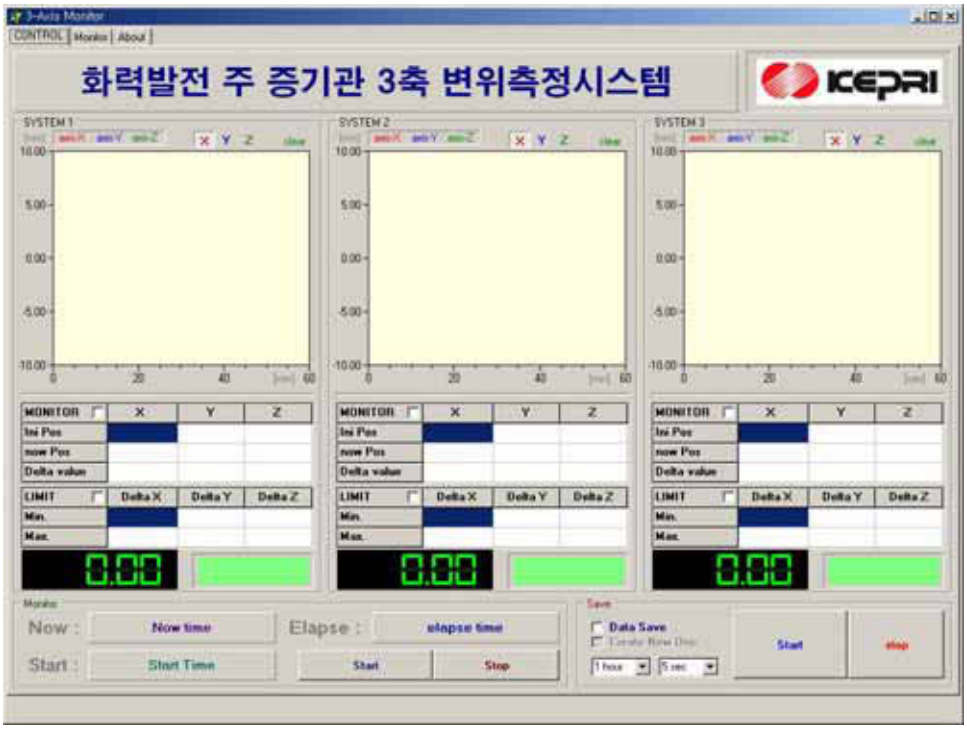

Figure 3. Displacement monitoring program (control part).

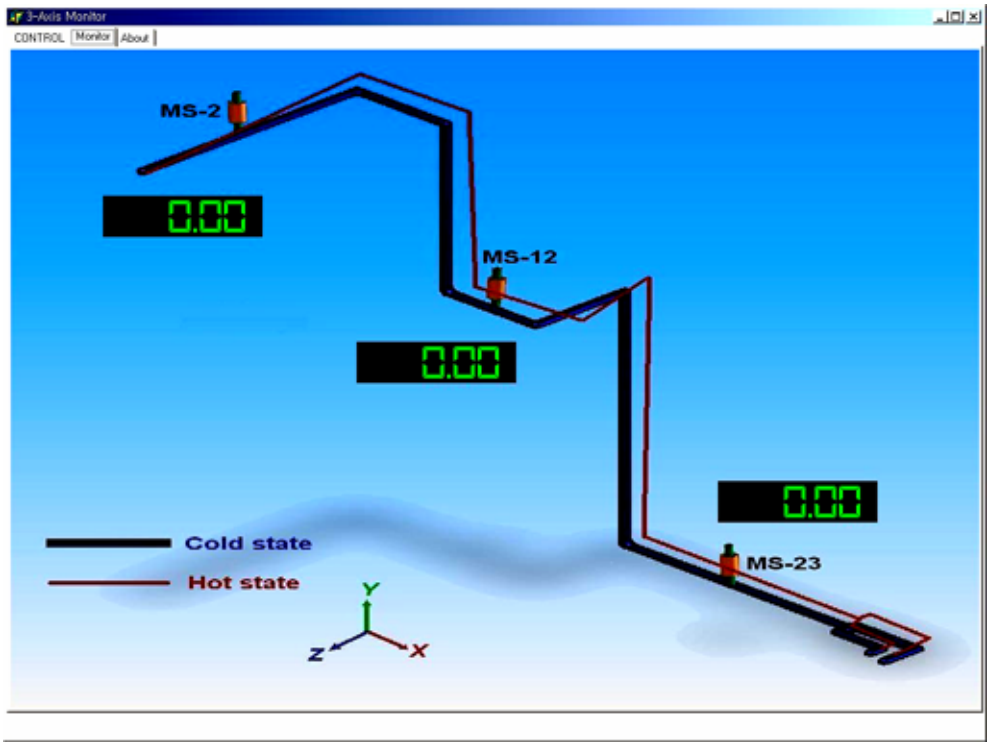

Figure 4. Displacement monitoring program (monitor part).

4. Installation of piping displacement measurement device

4.1 Appointing the installing place of the device

The piping displacement measurement device was placed in 3 hangers; the upper part of the boiler (MS-2), the middle part (MS-12), and the mouth of the turbine (MS-23). Attaching the device directly to the pipe surfaces on those parts may cause damage on the welded part and have negative influence on the parent material of the pipe during a long operation. Thus, the device was installed in the piping support that connects hangers as shown in Fig. 5.

Then the piping support connecting hangers with the pipe, was completely fixed with the pipe so that thermal expansion displacement in the pipe would be the same in the support as well. Finally, piping displacement measurement device was connected to the center of the support that is I-beam shaped, by using a high temperature grip.

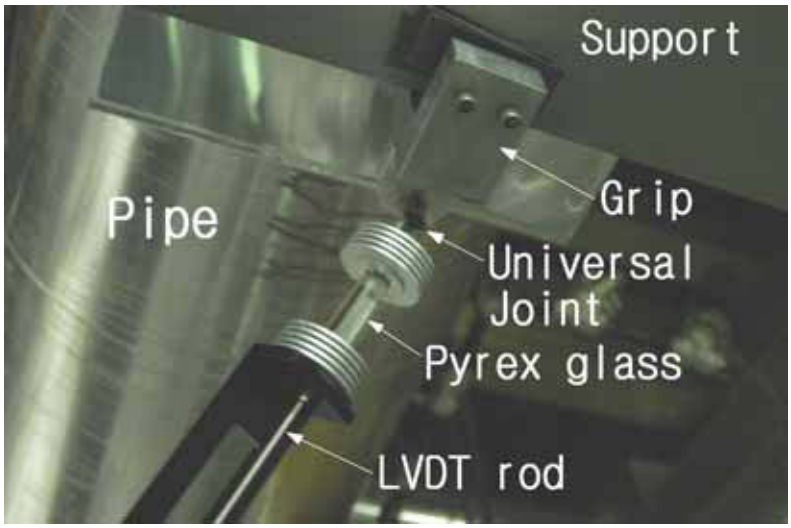

Figure 5. Universal joint type grip.

4. 2 Installation of the measurement device

Three components are in need to connect the measurement device with the piping support. Given the fact that the internal temperature in the high temperature steam pipe is about 550°C, components for the connection between the two should meet the conditions of heat-resistance, strength, and corrosion-resistance. Therefore, the components can be a combination of high temperature grip, heatproof kit, and universal joint. The grip fixes the measurement device to the support, heatproof kit blocks heat transmission to the device from the pipe, and universal joint makes it easier for the ending part of the device to rotate in the space smoothly.

High temperature grip was Cr plated and heat treated. Heatproof kit was made of an aluminum heat-resistant plate and a rod of pyrex glass so that it could cool down enough to minimize heat transmission to the device. The universal joint was made by using high temperature housing and bearing so that it would not generate moment towards the 3 axles when rotating in the space. Fig. 6 demonstrates the completed installation of piping displacement measurement device on the MS-23 support in the mouth of the turbine.

5. Application of piping displacement monitoring system

5.1 Selecting the standard mode of the steam pipe

The two major operation modes of fossil power plants are cold start-up, which operates after overhaul for maintaining and repairing the installations, and warm start-up, which operates after temporary shut down during weekends in response

to the power demand. Fig. 6 shows steam temperature and pressure curve per each operating hour in "P" domestic fossil power plant with 500 MW. The steam temperature per hour generates thermal expansion displacement in the pipe as the steam goes through the pipe.

5.2 Analysis of 3-axial displacement at the measured point

Three dimensional modeling of the piping system was carried out, using Pipeplus [6], an analysis program for piping, to evaluate reliance of piping displacement monitoring system in the three measuring parts. The analysis is demonstrated in the Figs. 7 and 8. The piping modeling was based on the design of piping and support device [7]. Piping shape (OD635×90.6t) and material data (SA335 P22) are input for the design.

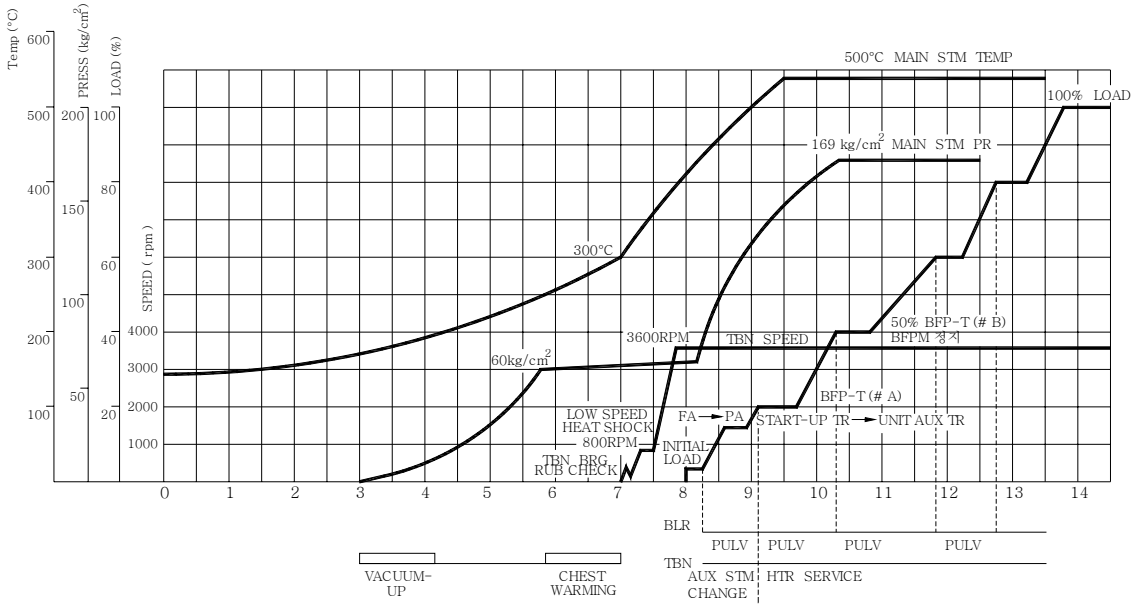

Figure 6. Cold start-up schedule of operation.

Conditions of limits had to be imposed from the starting point of piping, the outlet header of the boiler, to the ending point of the piping, the inlet of the turbine. In addition, steam temperature and pressure inside of the pipe were also given. A total of 32 hangers are used to support the weight of the pipe and thermal expansion load. Designed weights were put in each hanger.

The results of the analysis are explained in Table 1, in which each displacement from each measuring device is calculated under the condition of 100% load, 538 and 169 kg/cm^2 by using the standard mode of cold start-up.

5.3 The result of analysis of 3-axial displacement

As Fig. 7 is showing, the piping displacement monitoring system was installed in three steam pipes – MS-2, MS-12, and MS-23 - during the overhaul when the first machine in "P" fossil power plant was temporarily shut down. Fig. 9 indicates chronological displacement at the measured point from 3 axis and the sum of vectors of them, from the start of the installation to the maximum output. In the state of shut down, there was a minor generation of displacement because of releasing locking of hangers and preheating after setting the initial value. There was almost no displacement in the MS-12 part, which is in the middle. With the start up of the boiler, the steam inside the pipe did not directly flow into the turbine but bypassed. The turbine was preheating for the start up. As the turbine started to operate, the displacement skyrocketed to the maximum output. Fig. 10 demonstrates the monitoring part of the displacement program in the central control unit in the power place at the moment of maximum output.

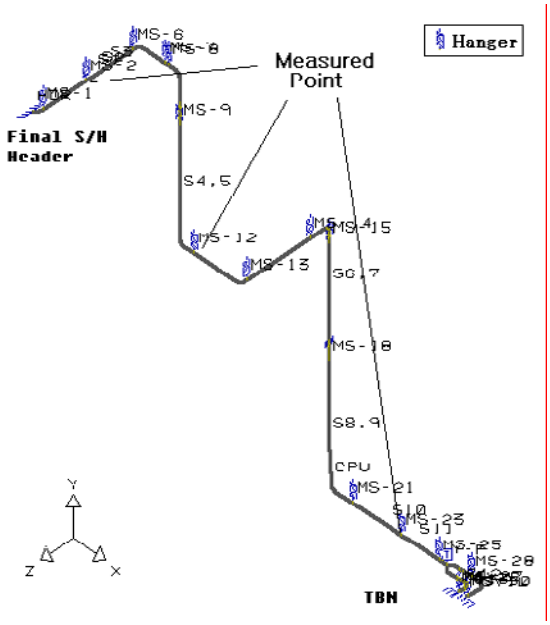

Figure 7. Model of piping system.

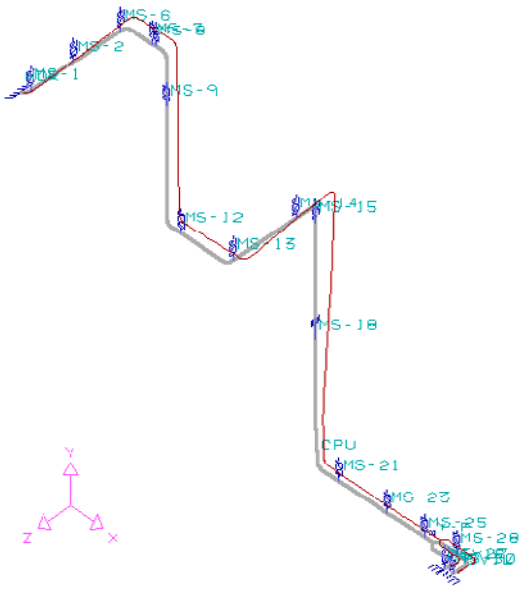

Figure 8. Displacement analysis result.

5.4 Comparison of measured outcome with the result of analysis

To evaluate reliance of the on-line measured data from three high temperature piping parts, the data of Fig. 9 was analyzed during the maximum output and compared in Table 1. Table 1 shows that measured and analyzed values are the same in all directions in the positive and negative direction. As a result, the current start up of the pipe generates similar thermal expansion displacement to the one in the designed piping direction. Even though the directions are the same, the values of the vector are slightly different. There are two possible causes to this phenomenon. One is that precise designed displacement might have not been

produced due to various reasons such as wrong thermal expansion from the outlet header of the boiler to the inlet of the turbine. The other one is that there could have been differences between the piping design and actual lengths, shapes and curvatures. Or, thermal expansion coefficient might have been wrong.

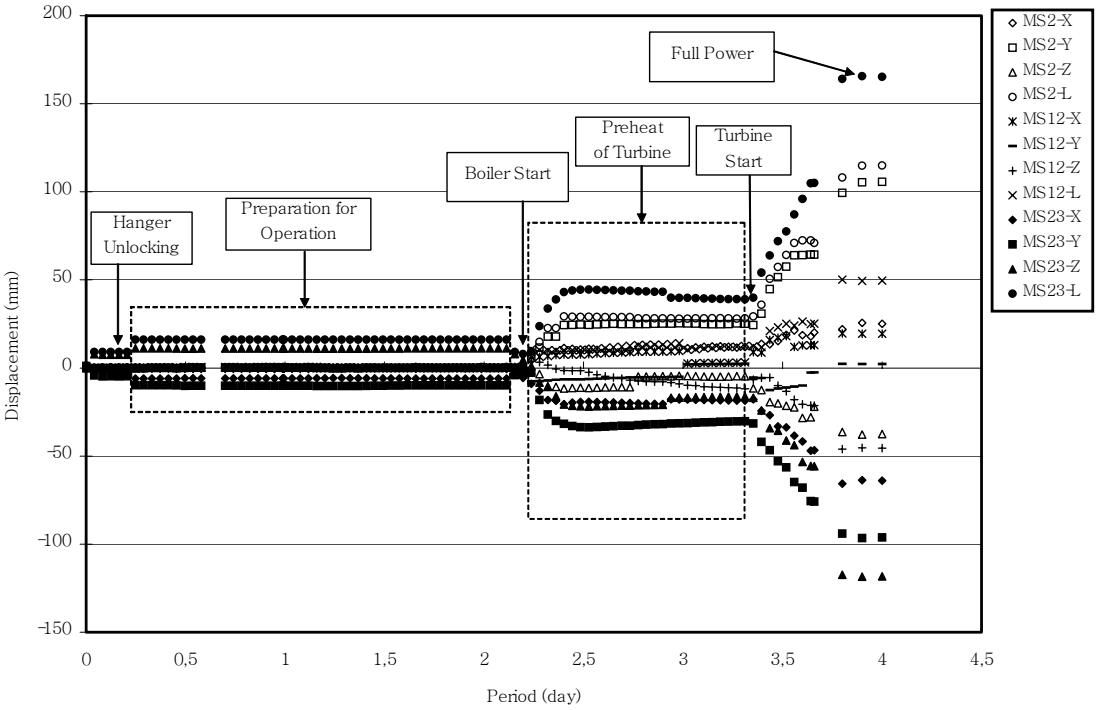

Figure 9. 3-dimensional piping displacement measurement.

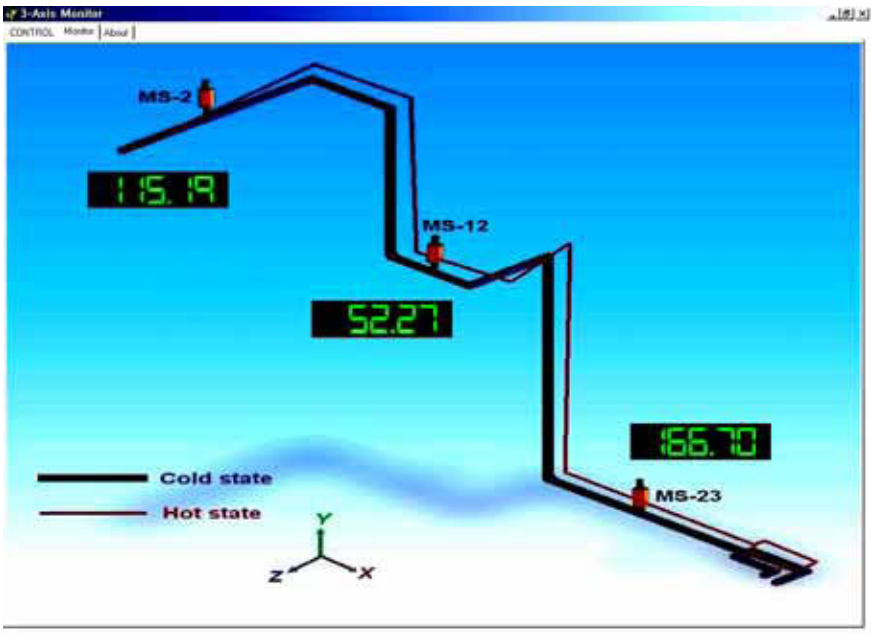

Figure 10. Real-time pipe movement monitoring at full power.

Table 1. Comparison of measuring and analyzing data (Unit: mm).

Location	Data	X	Y	Z	L
MS-2	Measurement	22.6	106.8	-36.6	115.2
	Analysis	34.9	100.6	-57.2	120.8
MS-12	Measurement	13.3	2.8	-50.4	52.2
	Analysis	38.9	22.8	-128.4	136.1
MS-23	Measurement	-62.3	-98.3	-119.2	166.6
	Analysis	-51.3	-65.4	-150.1	171.5

6. Conclusions

The main steam pipe in a fossil power plant has 3-dimensional and geometrical shape in terms of its structure, and operates under the condition of high temperature and high pressure. Consequently, it generates 3-axis. If there is an error in the design during the initial construction, the pipe suffers much damage due to excessive displacement when operating for a long period of time. Therefore, the research developed a system to measure 3-dimensional displacement of the high-temperature and high-pressure pipe and to monitor them on-line. The key results are as following.

(1) A measurement device was successfully developed to measure 3-dimensional thermal expansion displacement of the pipe, using LVDT to gauge the distance and Encoders to gauge the angles, and in universal joint.

(2) A measuring and monitoring program was developed to check data obtained from the measurement device on line, by using RS-485 serial communications method.

(3) Piping displacement analysis was performed with a use of a piping analysis program to verify the reliance of the 3-dimensional data, obtained from the displacement measurement device.

(4) The research is expected to connect domestic power plants as a national network in the future. The developed system will greatly contribute to safe operation of power plants if applied to high-temperature and high-pressure piping, and can be further applied in the heat absorption and in the oil and chemical industry.

References

1. A Study on the Life Extension Technology in the Fossil Power Plants. Technical Report, TR.97GS06.S2001.046, Korea Electric Power Research Institute, 2000.

2. J.P. King. Current Experience in Typical Problems and Failures with Boiler Piping Components and Supports. PVP-Vol. 376, Component Analysis and Evaluation, Aging and Maintenance, and Pipe Supports, ASME, 1998. Pp. 161–168.

3. M.T. Flaman & B.E. Mills. Development of a Strain Gauge Based On-line Structural Integrity Monitoring System for Fossil-Fuelled G.S. CEA Project No. 726 G 627, Ontario Hydro Research Division, USA, 1992.

4. B. Hahn et al. In-service Condition Monitoring of Piping Systems in Power Plants Requirements and Advanced Techniques. OMMI, 2002, Vol. 1, Issue 1, pp. 1–13.

5. Y. Takahashi et al. Trend of Operating Data Monitoring and Fatigue Evaluation System for BWR in Japan, SMIRT-12K. Kussmaul, North-Holland, 1993. Pp. 265–270.

6. Algor[R] PipePak, PipePlus Version 7.02, 2000.

7. ASME Code for Power Piping, B31.1, 1998.

Lifetime monitoring of high temperature components using innovative X-ray diffraction method (Xpection)

I. Marcelles[1], J. Azcue[1], V. Kolarik[2], L. Rol[2], H. Fietzek[2], G. Calderon[3], J.M. Armesto[3], A. Giménez[3], J.M. Jiménez[4], V. Mentl[5], F. Hnilica[6], J. Fiala[7] & T. Abbas[8]

[1]Tecnatom, s.a., [2]Fraunhofer-ICT, [3]Endesa, s.a., [4]Repsol-YPF, [5]Skoda Research, [6]UJP-Praha, [7]West-Bohemian University, [8]CINAR Ltd.

Abstract

Advanced on site inspection methods, modern monitoring of inspection data and user friendly while highly reliable assessment systems are needed for a safe operation of high temperature plants. It is one of the purposes of the Xpection project to strengthen the market position of the European industry.

The analysis of material structure using replicas can be used only in accessible areas and for limited number of materials. Destructive techniques require material withdraval, test specimens manufacturing, repair welding and other problematic actions. Usually, these techniques cannot be considered for in-service materials, because they may affect the structural integrity of the component, reduce plant availability and are expensive.

The X-ray diffraction based material degradation monitoring will modify the situation in a following way:

- The new technique can be used in field, without material removal
- It is a non-destructive technique without damage to the component
- Localitions that cannot be inspected by replicas are accessible with this technique
- The technique has been demonstrated to be very promising for austenitic steels.

1. Introduction

In most industrial applications materials are subjected to high temperatures and/or to high mechanical loading like high pressure in various plant components. Such components are, for example, boilers and turbines in the electric power generation or reactor vessels in the chemical industry, both taking part in the Xpection project. Material degradation due to corrosion, overheating,

creep, and fatigue occurs during service and the economic losses are high, especially when failure is the consequence.

The electric power generation as well as the petrochemical industries are introducing novel technologies for minimizing the emission of pollutants like CO_2, NO_x, SO_x and possible dioxin formation. Such technologies are re-burning, co-firing and low-NO_x burners. In order to save the fossil natural resources, especially in the electric power generation industry, biomass and waste blends are fired. The consequences on the ageing behaviour of the materials and thus on the lifetime of the plant components however, are not yet completely evaluated and understood. Advanced on-site inspection methods, modern monitoring of inspection data and user friendly while highly reliable assessment systems are needed for safe operation of high temperature plants responding to the dynamic of new technical developments and increasing the competitiveness in a global market.

To analyse component degradation, in addition to conventional non-destructive testing, NDT, it is usual to perform destructive metallographic analyses. During revision outage, metallographic replicas are used as an alternative NDT method to determine component status in industrial plants components. The components are locally polished, etched and studied or material samples are cut from the structure component and analysed metallographically by optical or electron microscopy. The assessment of the components uses the fact that mechanical properties of most materials depend strongly on grain size and orientation, which are crucial parameters for the determination of the ageing state and the prediction of residual lifetime of the components.

In many cases, however, the chemical attack visualises macroscopic grains only, but does not show the crystallites. These techniques yield a structure characterisation in morphological terms (e.g., grain size, grain form, etc). Deformation processes, however, often change the crystallite morphology in such way that the real crystallographic structure is masked (pseudo morphology). A mismatch between observed failure and assessment from previous inspection may be the consequence. For instance, grains look like lengthened on micrographs after rolling. But in fact, these grains are no more single crystals. The original crystalline grains can decay into a number of fragments as a consequence of mechanical or thermal loads or phase transitions. Frequently this fragmentation is not apparent by a microscope, though it may happen that the material behaves like consisting of small grains, while the micrograph shows coarse grains.

X-ray diffraction however, detects the real structure as it characterises the crystallographic structure of the particles and not the optical appearance. Recrystallisation effects for instance are recognised by X-ray diffraction often

before they are visible in miscroscopy [1–3]. Therefore, X-ray diffraction is a powerful tool to perform an ageing state characterization in order to deliver a database for a lifetime forecast software system.

2. Technical and industrial objectives

The Xpection project has the following main objectives:

- To develop a prototype of an integrated monitoring and assessment system for residual lifetimes of high temperature plant components in fossil power generation and chemical industry.
- To design and complete a transportable X-ray diffraction system for real structure analysis on-site.
- To develop algorithms and the corresponding software for residual lifetime assessment using information from the real structure analysis and conventional methods and to set-up a database for assessment.
- To simulate ageing and degradation processes as well as to forecast the stability of a real structure.
- To develop an information system for monitoring and assessment of the ageing state of the plant component material and software for a reliable residual lifetime prediction.
- To integrate the developed Xpection method into the infrastructure of inspection and maintenance, thus providing an additional innovative tool for a highly reliable assessment.
- To reduce the maintenance cost by enhanced reliability of the residual lifetime assessment allowing longer replacement intervals of components based on a non-destructive inspection.
- To contribute to increase in the safety of fossil power plants as well as chemical and petrochemical plants.

3. Main innovative aspects

X-ray diffraction is a powerful method to identify crystalline compounds and to study their structures. In X-ray diffraction (XRD), counts per second are detected as a function of the Bragg angle 2θ. Equipped with a two-dimensional detector yielding besides the conventional 2θ – axis the azimuthal axis χ of each detected diffraction peak additional information on grain size, texture and orientation is obtained. During service at high temperature grain coarsening due to recrystallisation occurs and leads to changes of the mechanical properties and

thus to degradation. The two-dimensional X-ray diffraction pattern reveals such structure changes directly from the crystallographic information. Correlating the mechanical properties from a created data base for a selected material at defined stages of degradation with the measured χ–profile for a selected diffraction angle 2θ the ageing state of the material is determined. Knowing the structure at a stage, when the material properties are not anymore in accordance with the required component performance (lifetime end) the residual lifetime can be estimated.

The main innovative aspects are

- the use of two-dimensional X-ray diffraction (2D-XRD) as a non-destructive method gathering crystallographic information about the material structure,
- relatively high penetration depth in comparison to the conventional metallographic replica,
- performance of the 2D-XRD on site,
- systematic correlation of the 2D-XRD patterns to the materials degradation process from a created data base,
- residual lifetime forecast based on 2D-XRD information (Xpection),
- integration of the Xpection into the infrastructure of inspection and maintenance.

4. Experimental and methodological approach

The scientific and technological objectives of the Xpection project are to develop a prototype of an integrated measuring and monitoring system for residual lifetime assessment of high temperature plant components in fossil power generation and chemical industry. This is in particular the development of an innovative inspection methodology using real structure analysis by on-site X-ray diffraction and of its integration into the infrastructure of inspection and maintenance.

For achieving an assessment of the material properties from the two-dimensional X-ray diffraction patterns an evaluation procedure has been developed taking into account particular features like the statistic and crystallographic underground separation as well as the isolation of the coarse grain figures in the measured patterns. The needed evaluation procedure is not available in the frame of commercial software and is therefore being worked out especially for the Xpection purposes.

The components for the on site application of the two-dimensional X-ray diffraction analysis were selected, purchased and tested in the laboratory. The key components are an air-cooled microfocus X-ray source from IfG Berlin (Fig.

1) and a global area detector for two-dimensional X-ray diffraction patterns from Bruker AXS (Fig. 2). A final on-site testing in a real fossil power plant boiler is planned for April 2004 and February 2005 and shall demonstrate the feasibility and benefits of the Xpection technique.

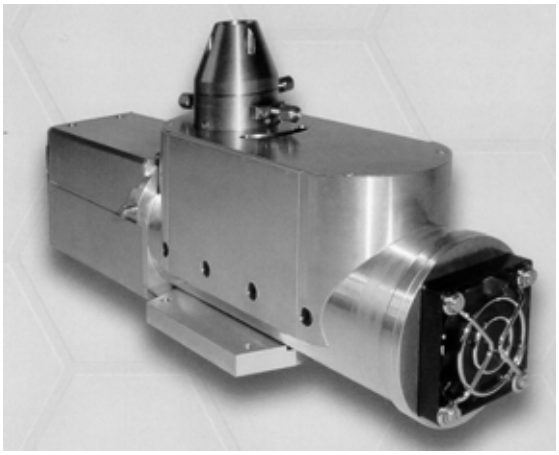

Figure 1. Air-cooled microfocus X-ray source.

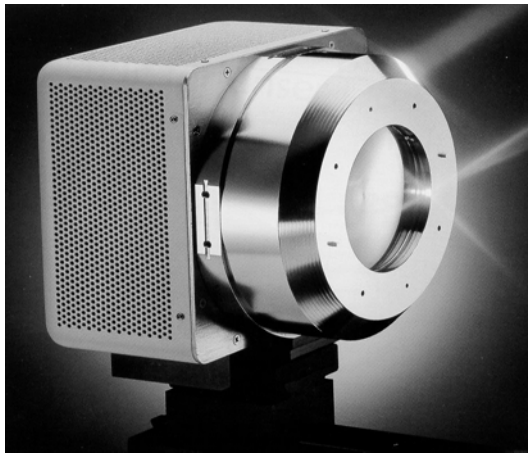

Figure 2. Global area detector.

In case of crystallites greater than 10 μm, the whole diffraction line in its two-dimensional shape, the so called azimuthal profile ξ, has to be considered. Diffracted X-ray beams, which fulfil Bragg´s law are no single "lines", but cones with two-dimensional information (Debye cones). When a polycrystalline sample with random orientation of the crystallites is placed into the X-ray beam, the Debye cones are detected, and any linear scan through that cone will give an accurate powder pattern. When the sample consist of few coarse crystallites, not all orientations are represented and the diffracted beams are focused on single spots allocated on the Debye cone. Cut by a film or a two-dimensional detector, circles are measured in their whole shape or partially. In this way, each X-ray diffraction angle has characteristic 2θ–position that allows the substance identification and a characteristic azimuthal profile (Fig. 3). The latter is used for the real structure analysis [4].

In the case of fine crystallites the diffraction lines are continuous with homogeneous azimuthal intensity distribution like in Fig. 3. In the case of coarse crystallites greater than 10 μm however, the diffraction lines become spotty and the information on the size, shape, orientation and various structural defects of crystallites can be derived from the distribution of diffraction intensity throughout the corresponding spots (azimuthal or lateral diffraction line profile) by the so called grain-by-grain (GBG) method (Fig. 4). And even in case of fine-grained material, narrow and parallel beam makes the diffraction line spotty and enables the application of GBG method [5–8].

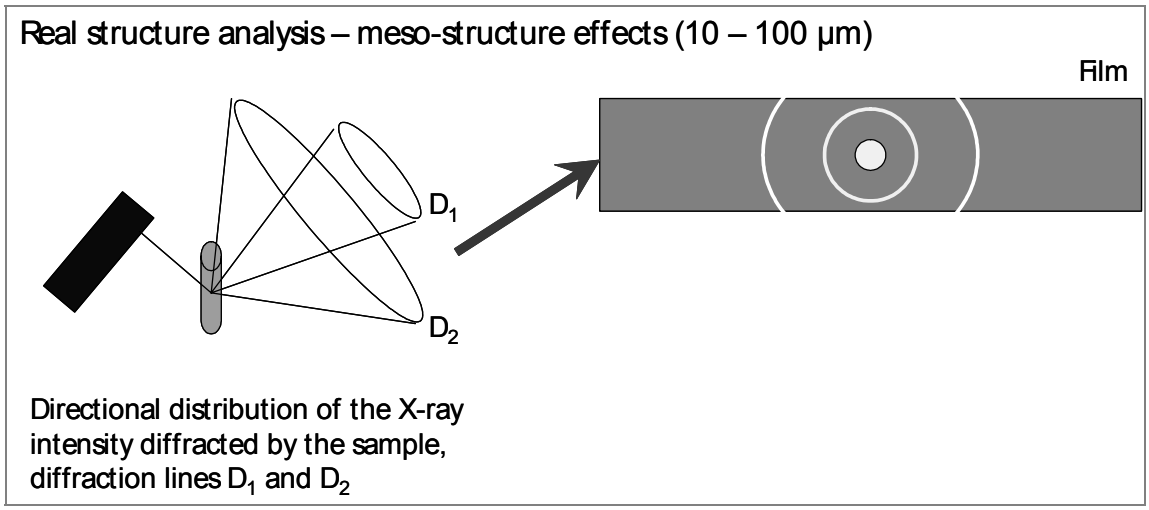

Figure 3. Scheme of the directional distribution of X-ray diffraction lines of polycrystalline materials and of their two-dimensional shape.

However, real structure investigation by GBG method requires special detection techniques. While conventional powder diffraction uses zero or one dimensional detectors, measuring the azimuthal diffraction line profile requires two dimensional detectors (global area detectors). Such detectors record X-ray diffraction patterns efficiently with exposure times in the range of ten seconds. This opens the door for the field or on-site XRD for real structure investigation of critical components using modern digital technologies.

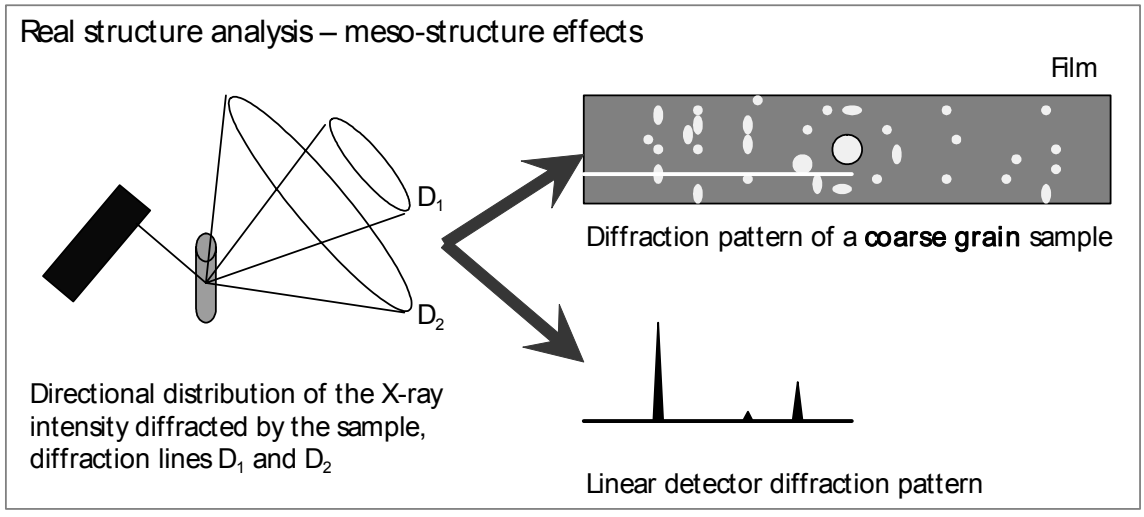

Figure 4. Scheme of the directional distribution of X-ray diffraction lines of polycrystalline materials and the spotty profiles in the case of coarse crystallites.

5. Remaining lifetime assessment

The structure changes during ageing and the influence of grain size and texture on mechanical properties of selected high temperature materials, is investigated with laboratory equipment.

The adaptation of the grain-by-grain method for the grain size and real structure analysis by X-ray diffraction needed for the purposes of material ageing state evaluation as well as the corresponding software development, requires expertise in X-ray diffraction, data processing, measuring techniques and information technology as well as in materials science.

As results of this work researchers will achieve the following results:

- To develop an assessment algorithm from the grain by grain results
- To acquire knowledge for prediction of further ageing behaviour
- To integrate the ageing assessment from the grain-by-grain method into the conventional methodology.

The database on material ageing of selected materials provides the information about the ageing progress correlated with the observed real time structure and the expected residual lifetime.

At present, the Consortium has investigated two typical materials as reference and two others are used for comparison. Selected materials are available in a wide number of industrial plants over the EU and NAS countries and include ferritic steels P11 and P22, a stainless steel type 304 and an advanced HP40 modified alloy.

Scope of material research is dependent on material availability, including both new and naturally aged materials. As conclusions, for materials which basic research has been finished, real structure, grain size, destructive testing results and other characteristics has been correlated with X-ray diffraction results.

The two-dimensional XRD pattern contains the information about the portions of fine grains as well as coarse grains (> 10 μm). When the azimuthal profiles are homogeneous, showing a constant intensity, then the material consists of fine crystallites with random orientation. If however, the azimuthal profiles show single spots, then coarse grains are present. Figs. 5, 6 and 7 show the two-dimensional X-ray diffraction patterns for P22 samples exposed during 500 h, 2500 h, and after service respectively. The horizontal axis is the diffraction angle 2θ and the vertical axis the Debye cone angle χ, or the so called azimuthal or χ-

profile. There are two lines showing higher intensity, the left one corresponds to the crystallographic plane (200) and the right one to (110).

For an appropriate interpretation and understanding of the azimuthal χ–profiles the physical meaning of their structure has to be analysed. In Figs. 8, 9, and 10 the peaks in the χ–profiles reflect the portion of coarse crystallites – which is represented by the area within these peaks. If Fig. 8 is compared with Fig. 10, the area within the ξ–peaks (i.e. inside the peaks) is larger in the ξ–profile of the ex-service state, where each peak corresponds to a spot along the diffraction line selected. In the case of small grains with random orientation or bended crystallites with continuous boundaries, the χ–profile has a high background and low single peaks and usually the material presents good conditions (Fig. 8). On the other hand, if the χ–profile shows a low background and high single peaks, this is due to the coarse crystallites, where orientation is no longer random or paracrystallite distortion with sharp boundaries exists, and the material is generally more fragile. With time, the amount of large crystallites will increase while the proportion of small crystallites will decrease. After 2500 h at 650°C the portion of coarse grains is higher than after 500 h, but not so high as in the ex-service sample (Fig. 9).

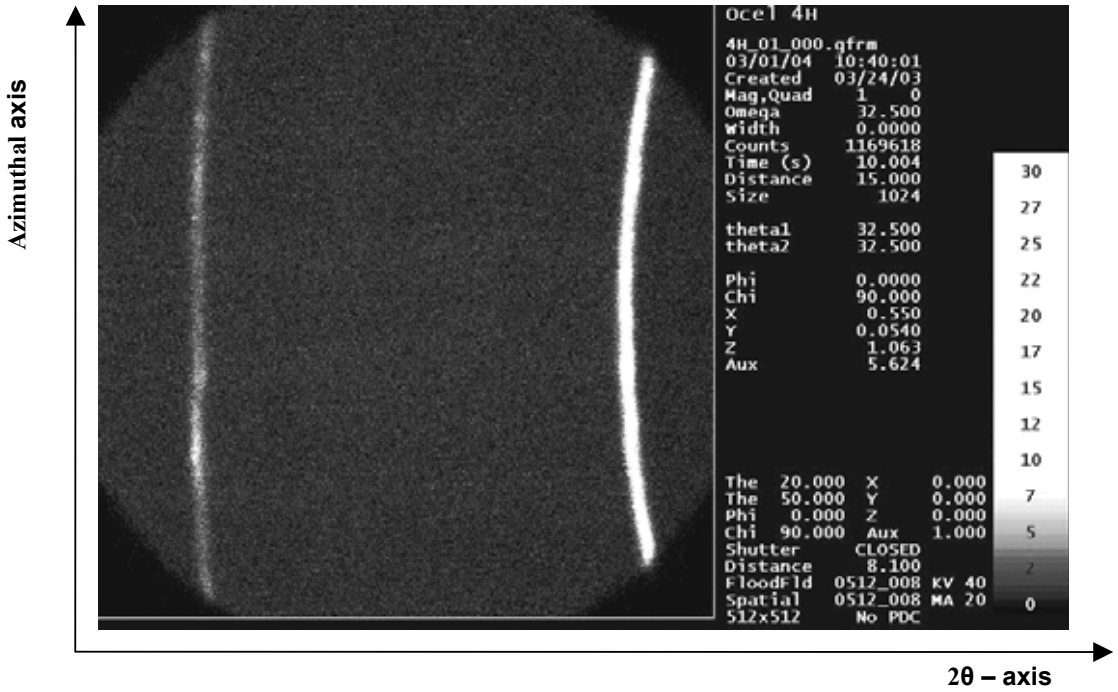

Figure 5. Two-dimensional XRD pattern of SA-335-P22 after furnace exposure at 650°C during 500 h.

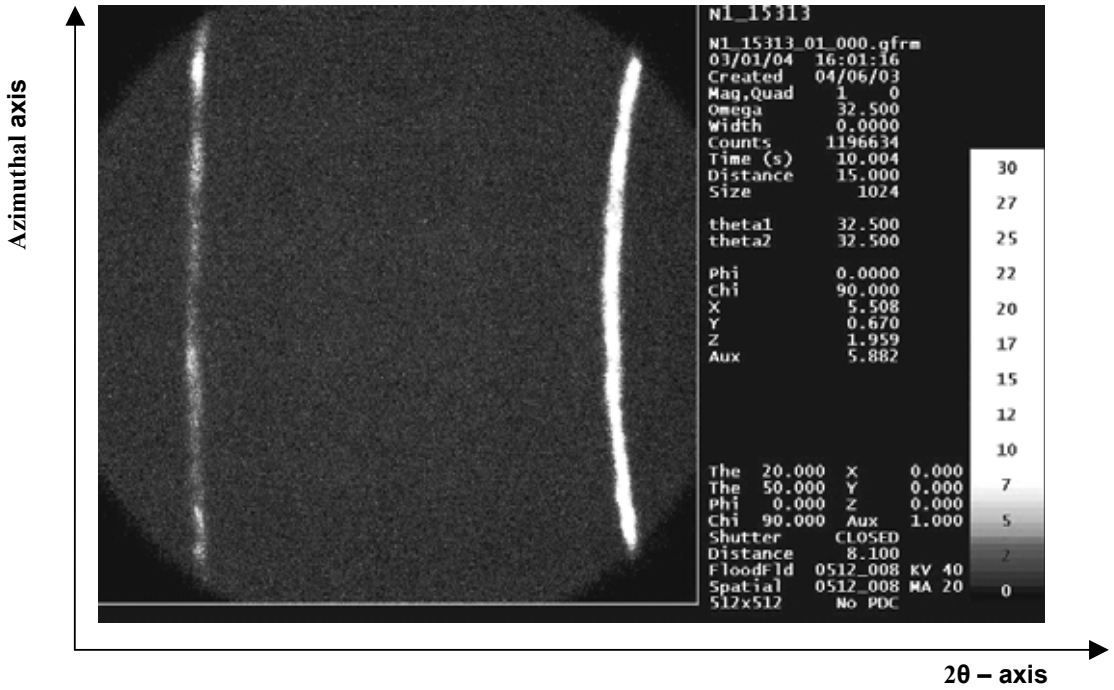

Figure 6. Two-dimensional XRD pattern of SA-335-P22 subjected to thermal ageing by furnace exposure at 650°C during 2500 h.

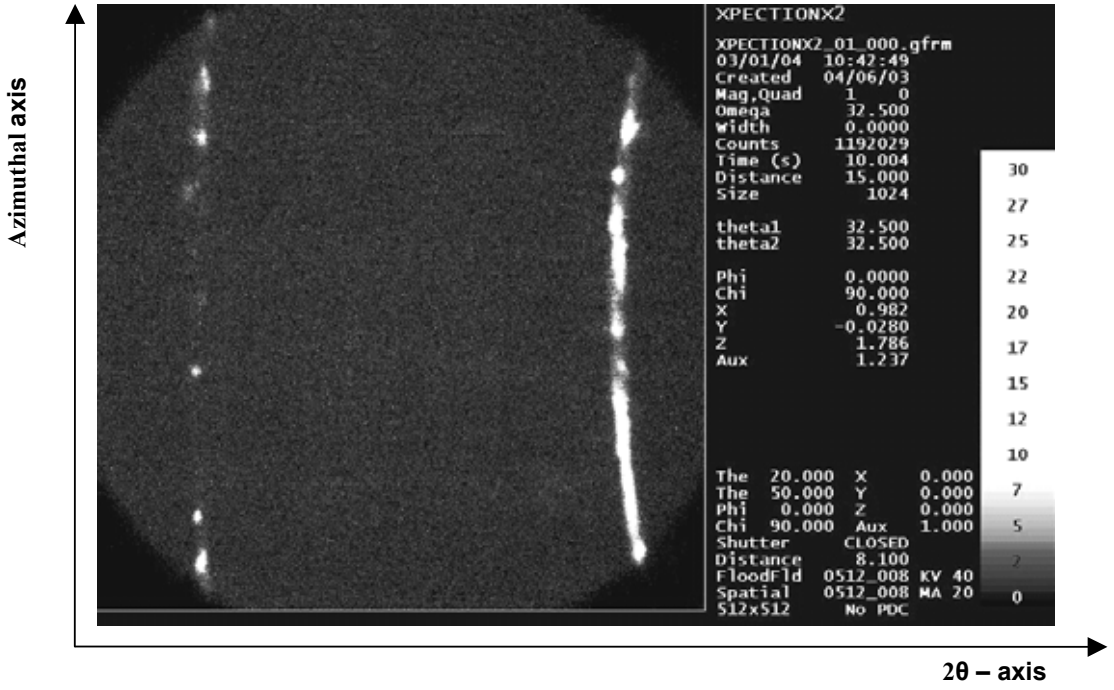

Figure 7. Two-dimensional XRD pattern of SA-335-P22 after service in the boiler.

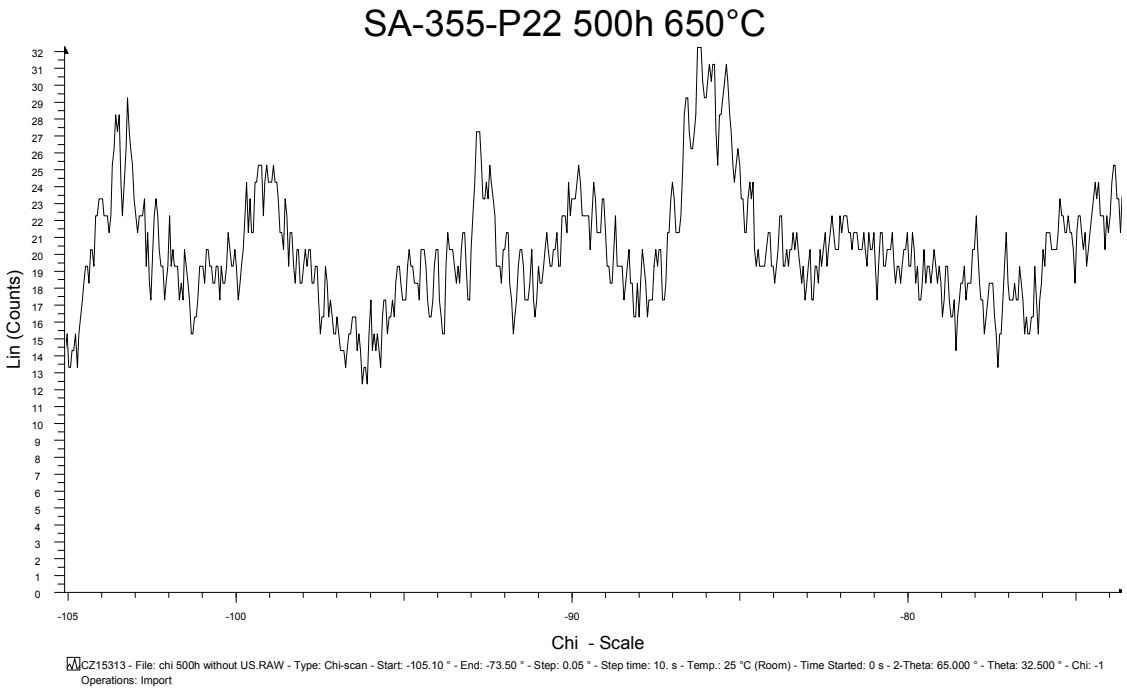

Figure 8. Azimuthal χ–profile for SA-335-P22, after 500 h at 650°C. The y-axis shows the intensity in arbitrary units, while the x-axis represents the azimuthal angle χ.

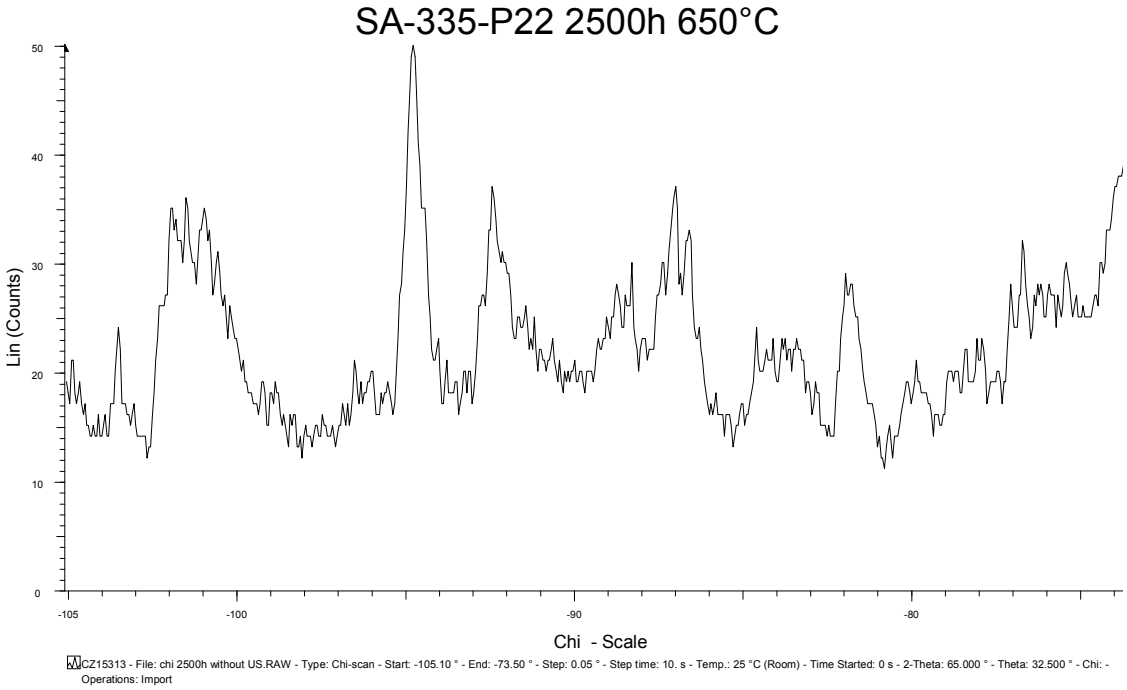

Figure 9. Azimuthal χ–profile for SA-335-P22 after 2500 h at 650°C. The y-axis shows the intensity in arbitrary units, while the x-axis represents the azimuthal angle χ.

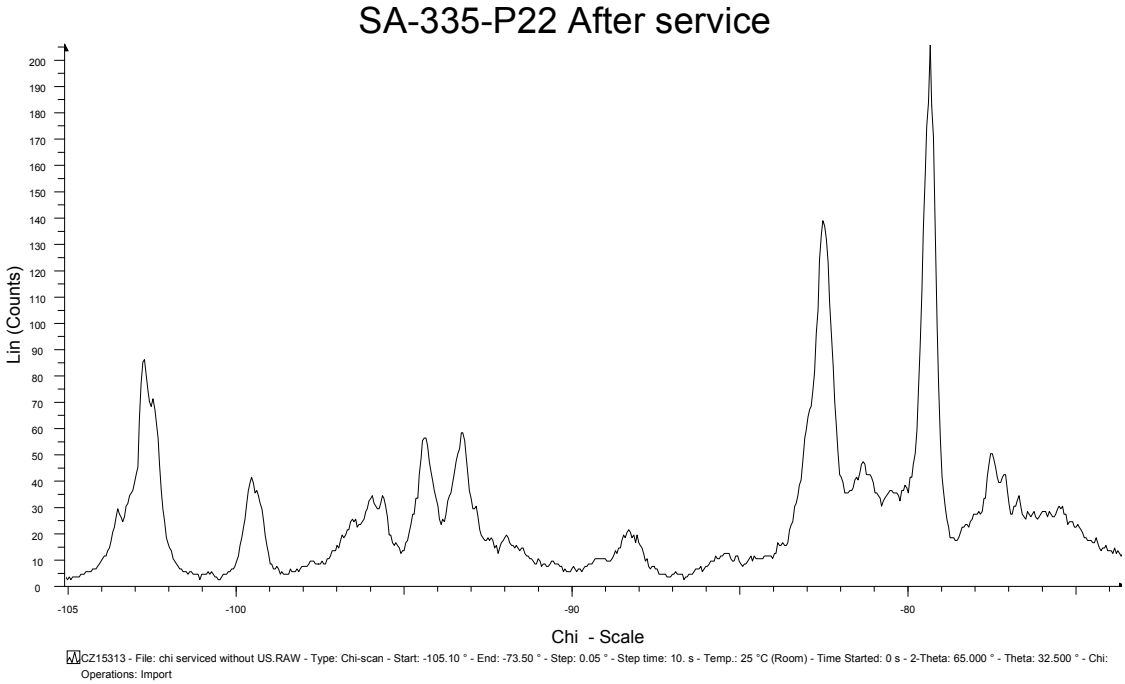

Figure 10. Azimuthal χ–profile for SA-335-P22 after service. The y-axis shows the intensity in arbitrary units, while the x-axis represents the azimuthal angle χ.

The examples show that exposing the SA-355-P22 to a temperature of 650°C, which is higher than in real service, produces a slight grain coarsening after 2500 h, but no significant degradation. After service however, the ξ–profiles indicate coarse grains with small portions of fine grains only, a degradation effect usually leading to a more fragile material.

Within the project, cases similar to the above examples are under analysis for comparison with other techniques, such as metallographic, impact, tensile and other destructive testing, etc.

6. Project status

The Xpection project started in May 2002. At the time of writing this paper, the system is in the final phase of the design. Laboratory research and testing as well as other activities are finalised as described in the paper. Future tasks to complete the work are also commented in different sections of the paper. In addition, validation in field of the system will be done in both pilot plants. The project will finish in April 2005.

Near future tasks will include installation and putting in operation of the components for on site X-ray diffraction and validate it on real plant components and on selected samples with defined exposure parameters.

Present status can be obtained in the public web page of the project:

http://projects.tecnatom.es/xpection

References

1. Fiala, J. & Nemecek. S. XRD analysis of coarse crystalline materials. J. Applied Crystallography, Proc. XVII. Conf (2000). Pp. 233–238.

2. Fiala, J. & Nemecek. S. X-Ray diffraction as a tool of mesostructure analysis, Advances in X-Ray Analysis 44 (2001), pp. 24–31.

3. Rol, L., Kolarik, V., Juez-Lorenzo, M., Fietzek, H. & Eisenreich, N. In situ-investigation of the oxide scale formation and recrystallization of a FeCrAl foil, Accepted for publication in Proc. Int. Symp. High Temperature Corrosion and Protection of Materials, 16–21 May 2004 in Lez Embiez, France.

4. Klug, H.P. & Alexander, L.E. X-Ray Diffraction Procedures. A Wiley-Interscience Publication, ISBN 0-471-49369-4

5. Black, D.R., Burdette, H.E., Kuriyama, M. & Spal, R.D. Journal of Materials Research 6 (1991), pp. 1469–1476.

6. Weissmann, S. & Lee, L.H. Progress in Crystal Growth and Characterization 18 (1989), pp. 205–226.

7. Weissmann, S. Advances in X-ray Analysis 35 (1992), pp. 221–237.

8. Snyder, R.L., Fiala, J. & Bunge, H.J. Defect and Microstructure Analysis by Diffraction, Oxford University Press: Oxford, 1999. Pp. 1–15.

9. Fiala, J. Real structure study by diffraction, Microstructural investigation and analysis. Euromat-99, Vol. 4.

10. Innovative residual service time assessment of industrial plant components using real structure analysis by on site X-ray diffraction. Xpection (Project G1RD-CT-2002-00696). 6th month project report. (Confidential).

Manufacturing and quality evaluation of component integrated fibre optical sensors for condition monitoring

Stefan Sandlin & Harri Jeskanen
Technical Research Centre of Finland, VTT, Espoo, Finland

Xiaochun Li
Assistant Professor, University of Wisconsin, Department of Mechanical Engineering, Wisconsin, Madison, USA

Alf Björklöf
Reliability Manager, Tellabs, Espoo, Finland

Abstract

Metal embedding of fibre optical sensors provides new possibilities in structural monitoring. The embedded sensors can either be used for validating of prototype design or for condition monitoring of functional components in service. In this paper two different methods for embedding of optical fibres in high melting point metallic alloys are presented. One method is based on a shape deposition manufacturing process consisting of a combination of electroplating and laser cladding. The other method is based on vacuum brazing. The base materials used are Inconel 600 and stainless steel 304 and 316L. The embedded fibres are equipped with in-fibre Bragg gratings (FBGs) in both cases. First results for temperature and strain measurement using the embedded FBGs are demonstrated. A long term (over five months) elevated temperature test up to 550ºC was also performed as well as a thermal cycling test up to 600ºC lasting a few days. The high temperature capabilities of metal embedded FBGs is thus well demonstrated. Temperature and strain cycling tests are of great importance in final evaluation of the performance of the embedded FBGs. However, during development of the embedding techniques, non-destructive methods for finding pores, cavities or cracks near the fibre are also useful because these defects may have a catastrophic effect on the sensing function and light guiding properties of the embedded fibres. The potential of two non-destructive methods was therefore investigated and found useful. These methods are scanning acoustic microscopy (SAM) and microfocus X-ray tomography.

1. Introduction

Embedding of fibre optical sensors in high melting point metallic alloys is a new and emerging field of research. Fibre optical sensors provide unique possibilities of collecting large amounts of measurement data both spatially and temporally. Furthermore, embedding of the sensors enable measurement from otherwise inaccessible places and also provides a firm protection for the fibre. The ultimate goal of this kind of research is to build fully integrated sensing networks into components for condition monitoring in service, for monitoring of the manufacturing process or for validation of prototype design. The embedding techniques presented can of course also be used for manufacturing discrete sensors. In-fibre Bragg gratings (FBG) have been used in this work. One reason for this is that many kinds of sensors can be built using FBGs. Another reason is that monitoring of the light reflected from the embedded FBGs during strain or temperature cycling gives a direct observation of the quality of the embedding as any fibre slipping will be readily observed as a sudden wavelength change of the reflected light peak. Monitoring of the reflected light form the embedded FBGs during cyclic tests is thus of great importance in final evaluation of the embedding quality. Other methods used in developing the embedding techniques are:

- Microscopic investigations of cross-sections
- Scanning electron microscopy (SEM) analysis of cross-sections
- Microfocus X-ray tomography of embedded fibres
- Scanning acoustic microscopy (SAM) of embedded fibres.

The last two methods are helpful in deciding where it is worth making cross-sections of samples with embedded fibres.

One of the presented embedding techniques is based on “Layered Manufacturing” or “Solid Free-form Fabrication” using a combination of electroplating and laser cladding, while the other method is based on vacuum brazing.

Embedded sensors can be used to gain data for validating or improving designs during the prototype stage or to obtain information on the performance and structural integrity of functional components in service. The capability to obtain such information from embedded sensors is important to many industries. Examples include the manufacturing industry (molds, dies, drilling bits, etc.), the aerospace industry (components of jet engines), the oil industry (drilling equipment), the power industry (vessels and pipes), the automotive industry (components of motors), and the construction industry (structural components in buildings). FBGs have been considered suitable for measuring static and dynamic fields, such as temperature, strain, and pressure [1]. Betz et al. [2] have considered the problem of acousto-ultrasonic sensing using FBGs by demonstrating detection of ultrasonic Lamb waves. Furthermore, Frenandez

Fernandez et al. [3] have presented promising results in temperature monitoring of a nuclear reactor core using fibre Bragg sensors.

1.1 The principle of fibre Bragg grating sensors

Hill and co-workers first observed fibre photosensitivity in germanium-doped silica fibre in 1978 [4, 5]. Since then an entire class of in-fibre components, called the Fibre Bragg Grating (FBG), has been introduced. Basically, a FBG consists of a periodic modulation of the index of refraction along the fibre core, as shown in Fig. 1.

Ultraviolet (UV) laser light can be used to write the periodic modulation directly into photosensitive fibres. An FBG functions like a filter when broad-band light is transmitted into the fibre core, reflecting light at a single wavelength (i.e. a narrow peak), called the Bragg wavelength. Thus, a single wavelength is filtered out in the transmitted light spectrum. When an FBG is expanded or compressed, its grating spectral response is changed. This is the basis of FBG-sensors. The temperature and axial strain sensitivities of bare Bragg gratings are about 0.0125 nm/ºC and 0.001254 nm/με at a wave length of 1550 nm. At the wavelength of 1300 nm the corresponding sensitivities are 0.0105 nm/ºC respective 0.001051 nm/με.

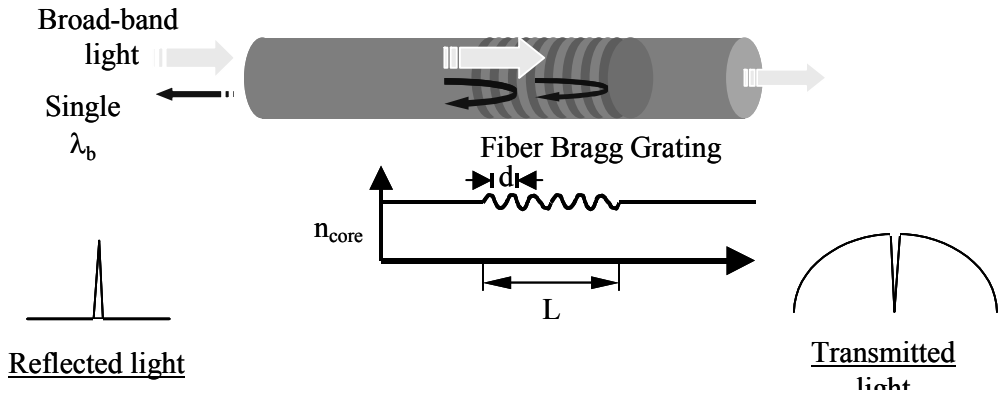

Figure 1. A schematic representation of a fibre Bragg grating in the core of a fibre. The grating reflects a narrow peak (central wavelength λ_b) of the incident broadband light. The corresponding wavelength is missing in the transmitted light spectrum. Here n_{core} is the refractive index of the core, L is the length of the grating and d is the Bragg grating period.

1.2 State-of-the-art and trends

Embedding sensors in structural non-metallic composites has been a topic of research in the last two decades. In this arena, fibre optic sensors have emerged as the dominant technology [6–12], so-called fibre optic smart structures. They allow critical parameters of materials and structures to be sensed while offering

light weight, immunity to electromagnetic interference, non-obtrusive embeddability, resistance to hostile environments, and extremely high bandwidth capability. However, the open literature give practically no information on embedding of optical fibres in high melting point metallic alloys, the topic of this paper.

The embedding of fibre optic sensors in various materials has been investigated as already stated. However, only a few papers demonstrate techniques for embedding these sensors in metal parts [13–15]. Taylor et al. and Lee et al. embedded a fibre Fabry-Perot Interferometer into aluminium, whose melting point is 660°C, by casting it in a graphite mold [13, 14]. Baldini et al. used gold coating on optical fibres before placing these fibres into titanium matrix composites produced by arc spraying [15]. However, none of these embedding techniques are successful enough to be useful for the embedding of fibre optic sensors during the production of 3-D fully dense metallic structures in Layered Manufacturing.

Embedding optical fibres is challenging because the fibres need to be embedded in a metal structure that has a high melting temperature. Clearly, the optical fibre needs protection during the high-temperature deposition steps. In particular, a protective layer may be necessary to overcome the temperature and stress induced by the embedding process. A metallic coating serving as the protective layer may mitigate the problem. Clearly, the soft polymer coating on the optical fibre must be replaced by a metallic coating. In this work both nickel and copper coated fibres are used. In the following we briefly describe the embedding methods used and the quality evaluation of the embedded fibres. Metal embedding of FBGs increases their temperature sensitivity by almost 160% as compared with bare gratings. Further, embedded FBGs can also measure compressive axial strains. The integration of optical sensors into components made of high melting point alloys is expected to open up completely new possibilities in condition monitoring, especially in hash environments.

2. The embedding methods and test results

In this chapter two different methods for metal embedding of optical fibres are discussed. One method is based on a combination of electroplating and laser deposition (a layered manufacturing process). This method was developed in USA. The other method is based on vacuum brazing and this method was developed in Finland. Both methods utilise metal coated fibres with FBGs. Strain and temperature behaviour of the embedded FBGs are evaluated for both methods.

2.1 Embedding of FBGs using a layered manufacturing process

Fig. 2 illustrates the layered manufacturing process for embedding optical fibres. Nickel was electrolytically deposited on a stainless steel substrate, then optical fibers were placed on the substrate and topped with electroplated nickel. The final deposition step was a laser deposited layer of stainless steel. The laser deposited layer of SS316L was created using 20 mm/s velocity, 2000 W laser power and 20 g/min deposition rate. In Fig. 3 we see cross-sections of fibres embedded using this technique.

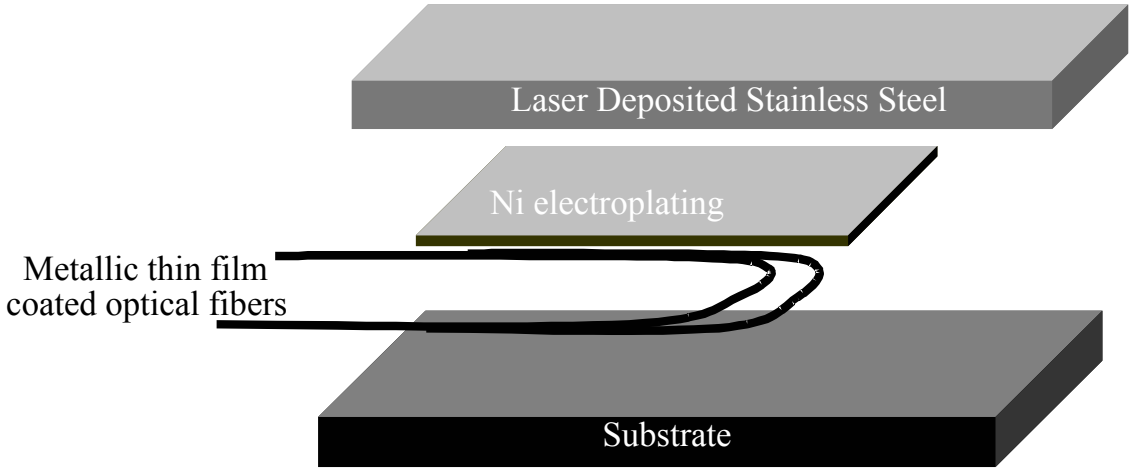

Figure 2. Explosive view of the embedding sequence. The metal coated optical fibres are placed on a stainless substrate. Then the fibres are covered with a layer of electroplated nickel and finally a layer of stainless steel is laser deposited on the nickel layer.

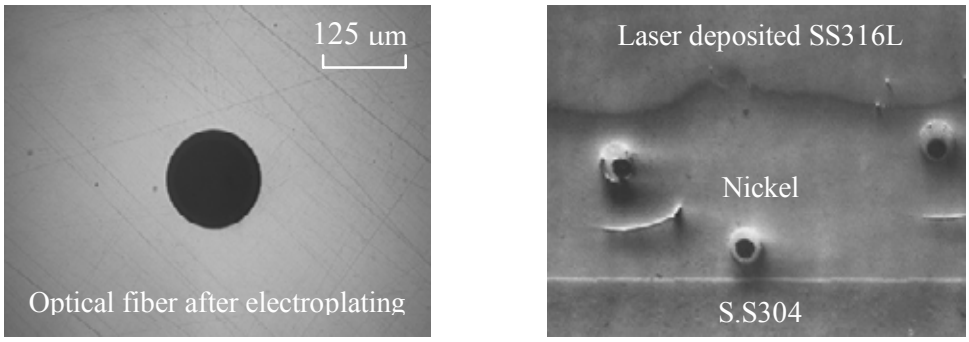

(a) (b)

Figure 3. Cross-sections of embedded fibre, a) an optical fibre in electroplated nickel. In b) the stainless steel substrate (SS304) and the laser deposited stainless steel (SS316L) can also be seen.

2.1.1 Characterisation of the embedded FBGs

To characterize the behaviour of embedded FBGs, we made a four-point bending test (4PBT), using a stainless steel beam with an embedded FBG with a Bragg wavelength of 1543.785 nm. After the laser deposition, the Bragg wavelength shifted almost 1.2 nm, perhaps due to the residual stress. Fig. 4 shows the setup for the 4PBT and the dimensions, in units of mm, of the cross section of the beam. A commercially available strain gauge was placed on top of the beam. This setup allows an exact comparison of FBGs with the calibrated commercial gauge. The nominal Young's modulus and yield strength for the stainless steel are 193 GPa and 170 MPa, respectively, at room temperature.

The commercial gauge, which has a resistance of 120 Ω, was connected to a specialized strain indicator box (Model P-3500 from Measurements Group) that has the ability to provide both a digital readout of the strain as measured by the gauge and an output signal to be processed by external Data Acquisition Systems (DAQS). The embedded FBG was connected to a 2x2 optical coupler that was in turn connected to a broad-band light source and an Optical Spectrum Analyzer. The testing equipment is manufactured by MTS and was equipped with a 2240N-load cell. The accompanying control electronics were used to operate the system in displacement-control mode. The beam was mounted on a 4PBT rig in such a way that, when load was applied, the sensors would be in compression.

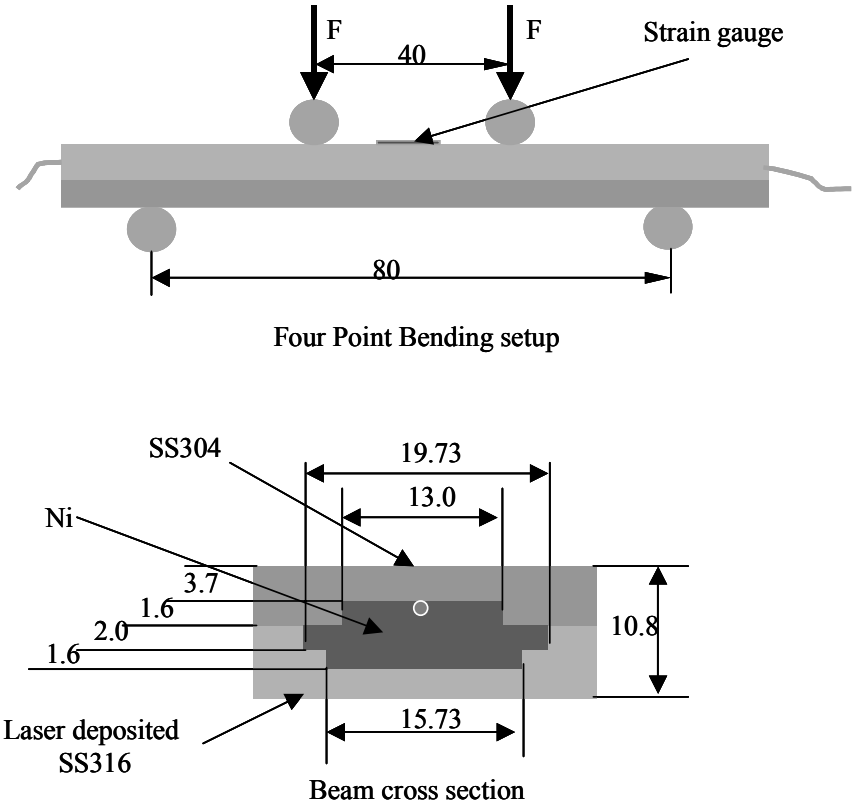

Figure 4. A setup for a four-point bending test and a cross-section of the beam. The small circle is the embedded fibre with a Bragg grating.

Fig. 5 shows the results of a four point bending test of the beam. The wavelength shifts of the FBG are plotted against the strain from the strain gauge. The higher strain readings, up to 5700 με, show that the beam was in plastic deformation. The wave length shifts are linear to the strains through all elastic and plastic regimes. Because the FBG is closer to the neutral axis than the surface mounted strain gauge, the value 0,0004 nm/μm (from the equation in Fig. 5) should be multiplied by 3.1765, which is the ratio of distances of the strain gauge and the FBG from the neutral axis. This operation gives the value 0.001270 nm/μm for the strain sensitivity.

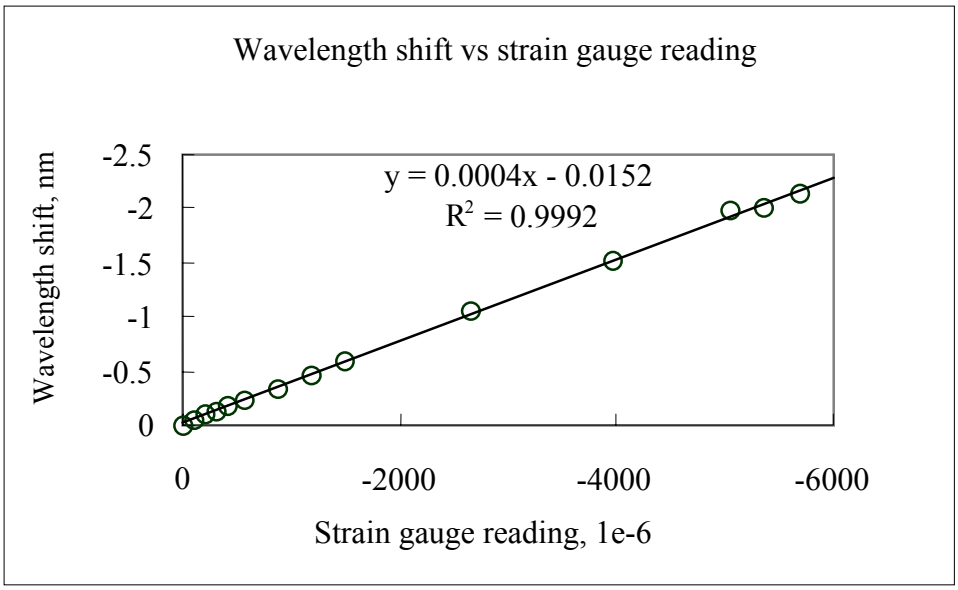

Figure 5. The response of an embedded FBG to the four point bending test shown in Fig. 4. At the higher strains the beam was in plastic deformation. Both the FBG and the strain gauge measure compressive strain. This test gave a strain sensitivity of 0.001270 nm/μm.

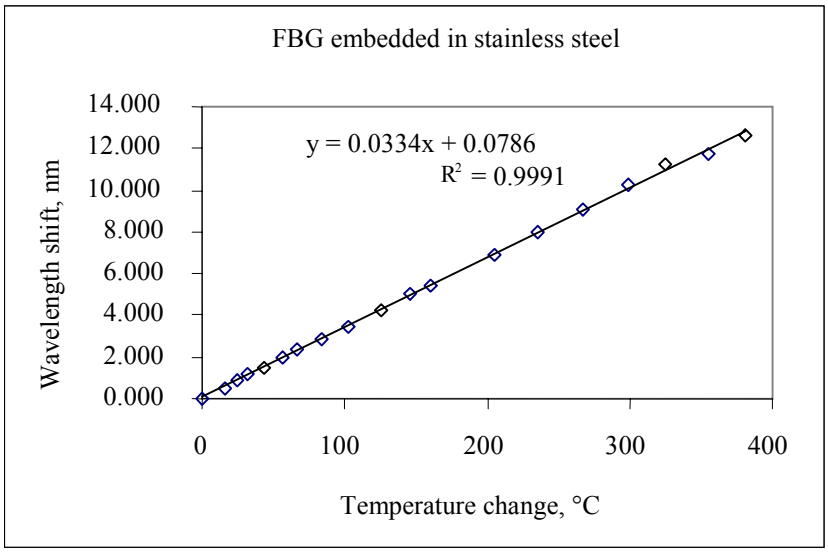

Figure 6. Thermal response of an embedded FBG. In this case the temperature sensitivity is 0.0334 nm/ºC.

Thermal response of the embedded FBG was also tested. Fig. 6 presents the results. The beam was placed in an oven and temperature was controlled. It is interesting to note that the thermal sensitivity of the stainless steel embedded FBG, 0.0334 nm/°C, is higher than that of the Ni-coated FBG, 0.0257 nm/°C. One explanation may be the CTE of stainless steel is higher, 17 με/°C, than that of nickel, 12 με/°C.

2.2 FBGs embedded using vacuum brazing

The tested specimens was manufactured by machining a small groove (about 0.4×0.4 mm) into a metallic substrate, Inconel 600 in the cases presented. Inconel 600 has the main composition of 72% Ni, 16% Cr, 8% Fe and 2% Si and is a refractory alloy. The metal coated optical fibre is placed in the groove and covered by brazing material in the form of a paste or foils. Finally another piece of Inconel or a thin foil of Hastelloy was placed over the substrate. Fig. 7 show a Inconel specimen used in developing at brazing technology. This specimen was a strain and temperature transducer prototype. Deflecting the feet outwards puts the strain grating in compression. Another grating on the cantilever to the left was used for temperature measurement.

Two kind of brazing alloys were used. One was Cusin-1 ABA, a paste manufactured by Wesgo Metals with nominal composition of 63% Ag, 34.25% Cu, 1.75% Ti and 1.0% Sn. The other brazing alloy was MBF-35, which was in form of foils with nominal composition of 90.5% Ni, 7.3% Si and 2.2% B. This alloy was manufactured by Honeywell International. The temperature and strain measurement demonstrations are made using specimens brazed with the alloy Cusin-1 ABA. During the vacuum brazing process the specimens were held at the

maximum temperature of 900ºC for 15 minutes. A couple of microscopic cross-sections of fibres embedded using this alloy has been presented elsewhere [16].

In using the other brazing alloy, MBF-35, a maximum temperature of 1050ºC is needed and the hold time at this temperature is about 20 minutes. The temperature cycling tests on gratings embedded using this alloy remains to be done. Some cross-sections of fibres embedded using this alloy will be presented. The alloy MBF-35 is interesting because it is expected to have better corrosion- and creep properties and therefore to allow even higher service temperatures for the embedded fibres.

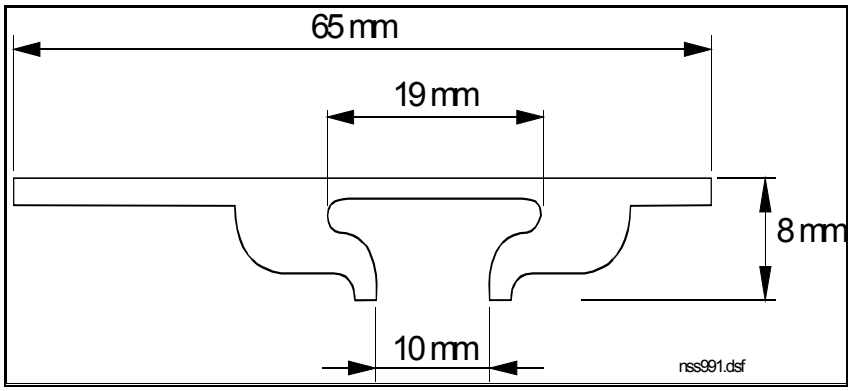

Figure 7. A specimen used in developing the brazing technology. This transducer prototype was used to study temperature and strain measurement using metal embedded FBGs. Two 10 mm long FBGs were embedded in a small groove on top of the specimen. One FBG was in the middle of the 19 mm broad area and the other one on the cantilever to the left. The thickness of the specimen is 2 mm.

It is worth noting that for both alloys the nickel coating on the fibres (thickness about 20 μm) will dissolve into the brazing alloy. This is considered important because it causes a "reversed stress state" where the interfacial stress between the fibre and the embedding metal alloy is high at low temperatures but low at the elevated sensor service temperature. This behaviour can be verified by measuring the grating wavelengths (at room temperature) before and after the brazing process.

In Fig. 8 a cross-section of an embedded fibre is shown. The groove in which the metal coated fibre was placed can also be seen. This specimen was used only for methodology development. In this case the metal coated fibre was placed in a small nickel tube with inner diameter of 0.35 mm and a wall thickness of 0.025 mm. The nickel tube protects the fibre during handling and it also seems to help to keep the fibre in position during the brazing process. As can be seen both the tube and the fibre coating have dissolved into the brazing alloy MBF-35.

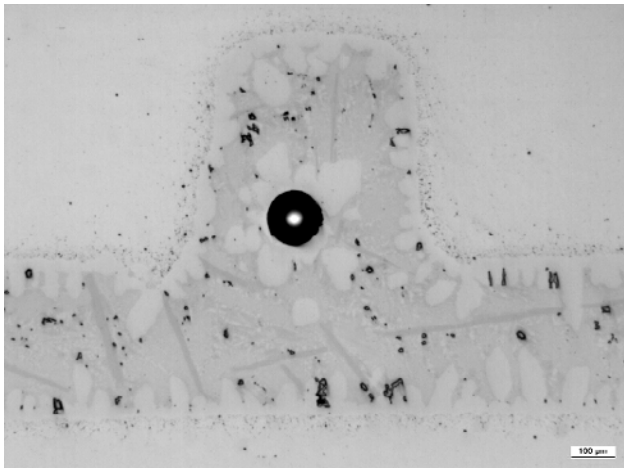

Figure 8. Cross-section of a specimen used in developing the brazing process. The fibre was placed in a groove between two pieces of Inconel. In this case the fibre was placed in a small nickel tube with inner diameter of 0.35 mm and a wall thickness of 0.025 mm. The tube and the fibre coating have dissolved into the brazing alloy MBF-35.

2.2.1 Characterisation of brazed FBGs

Fig. 9 shows the temperature sequences and hold times used in a thermal cycling test of two embedded FBGs. The metal embedded gratings was taken to 600ºC three times and the longest hold time at this temperature was 2.8 days. Fig. 10 show the wavelength response of these FBGs due to the thermal expansion of the surrounding metal alloy. The measured Bragg wavelengths fall well on the curves. This would not be expected if the fibres were slipping inside the embedding. The curves are slightly curved upwards due to, among other things, the increase of the coefficient of thermal expansion of the embedding alloy with temperature. The special FBGs used in the following tests were manufactured by Acreo AB in Sweden [17].

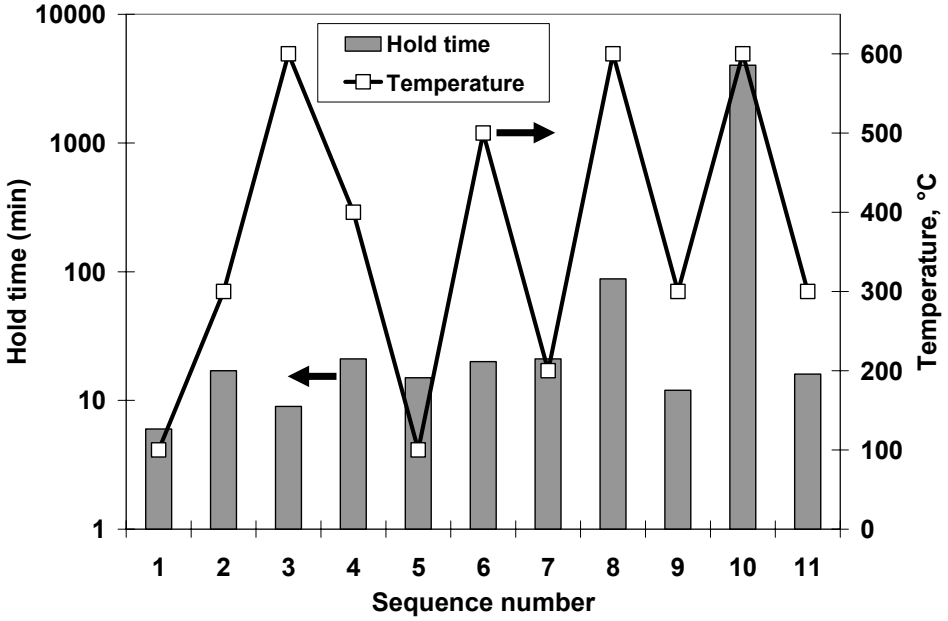

Figure 9. Temperatures and hold times used in testing of two metal embedded FBGs. The specimen was taken to 600ºC three times and the longest hold time at this temperature was 2.8 days.

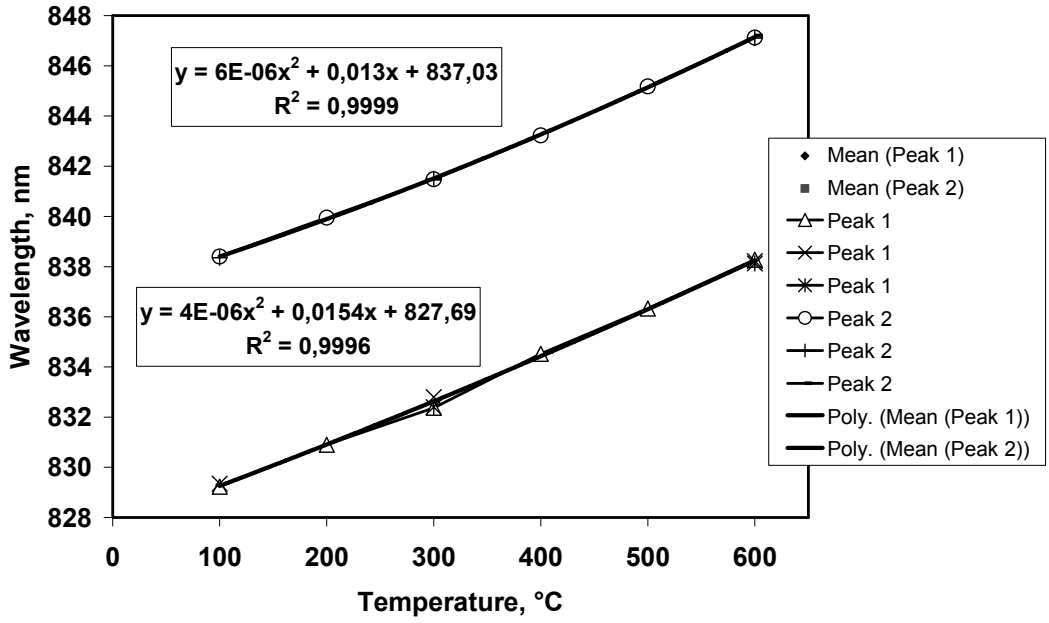

Figure 10. Wavelength response of two metal embedded FBGs due to the temperature sequences shown in Fig. 9. The FBG wavelengths are well situated on the curves indicating that there is no serious fibre slipping inside the embedding metal alloy.

In Fig. 11 we see four spectra (series1 to series4) of two metal embedded FBGs taken within 23 minutes at a temperature of 600ºC. The form of the FBG peaks is

quite good. A bad embedding may cause an uneven stress distribution around the FBG and thus cause serious distortion in the form of the FBG peak or split it into two peaks. The results shown in Figs. 10–11 were obtained using an optical spectrum analyser (Ando, AQ – 6315A).

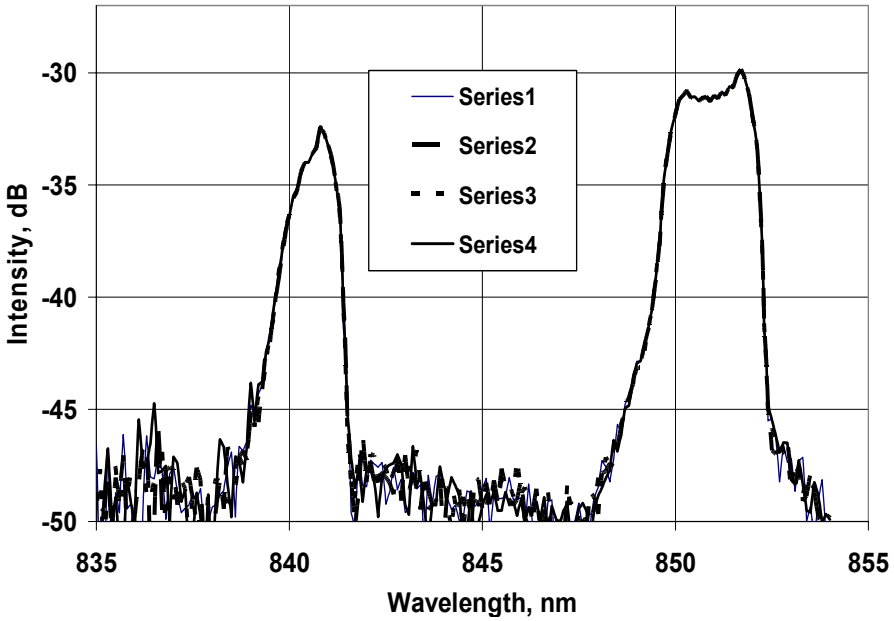

Figure 11. Four spectra of two metal embedded FBGs at 600ºC taken within 23 minutes. The peak spectra overlap. These are different FBGs from those measured in Fig. 10.

Next the results of a about five months long elevated temperature test of two metal embedded FBGs are presented. The embedded gratings were thermally cycled between 502ºC, 527ºC and 552ºC. In Fig. 12 the wavelength shifts have been plotted against the temperature in the test furnace. The temperature was measured by a thermocouple. In these measurements an instrument built around an Ocean Optics S2000 spectrometer was used and the peak wavelengths were automatically calculated and stored using a LabView software. The instrument measured every fifth minute and stored data about three times per hour. The use of this instrument is the reason to why the FBGs have wavelengths in the 850 nm area. The instrument contained a reference grating whose wavelength was subtracted from the wavelengths of the tested embedded gratings. During the long term test 8302 sets of time, test furnace temperature and wavelength readings were collected. In Fig.12 we have further subtracted 10.25 nm from the longer wavelength grating to more clearly be able to plot the wavelength shifts of both gratings in the same figure. From the equations in Fig. 12 we get the following temperature sensitivities:

21.01 pm/ºC for the shorter wavelength grating (GRT1)
19.63 pm/ºC for the longer wavelength grating (GRT2)

The temperature sensitivity is lower than obtained in Fig. 6 mainly because the FBGs used for obtaining the data in Fig. 12 have a shorter wavelength.

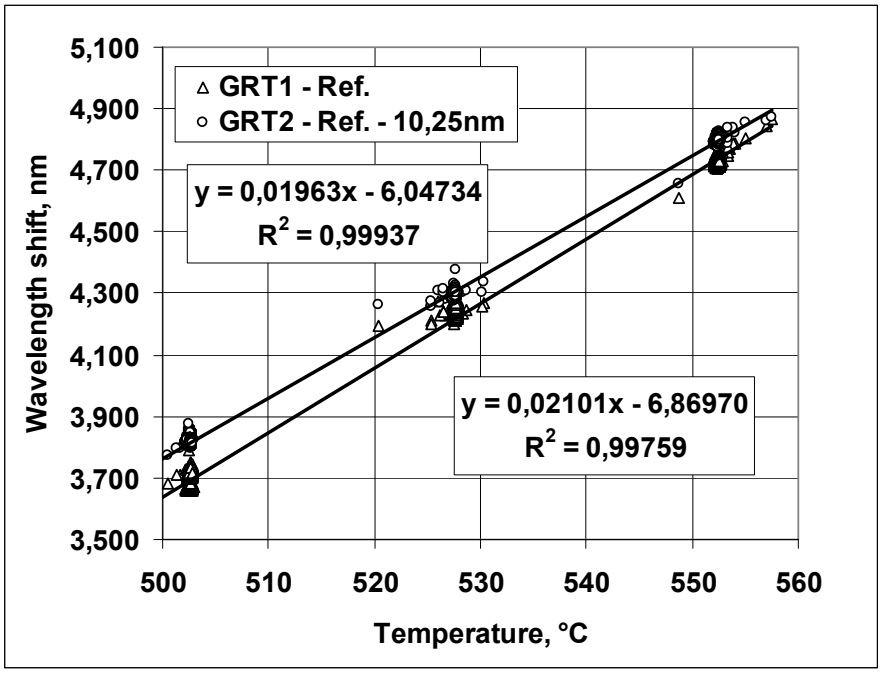

Figure 12. The wavelength shifts of two metal embedded FBGs plotted against the temperature in the test furnace as measured using a thermocouple.

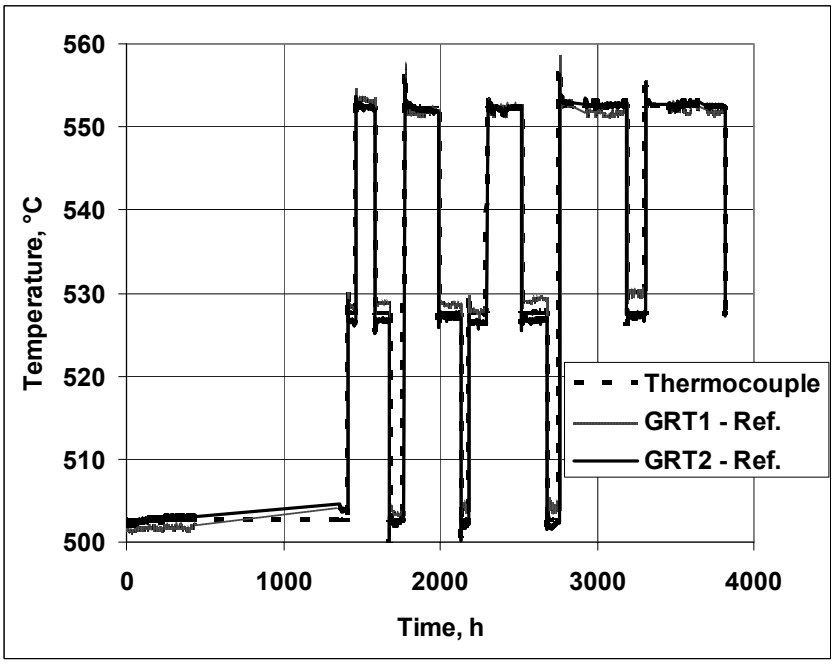

Figure 13. Temperature measurements using two metal embedded FBGs (GRT1 and GRT2) compared to temperature measurements using a thermocouple. The total testing time is over five months.

Using the equations obtained in Fig. 12 the measured wavelength shifts can be converted to temperature. This has been done in Fig. 13 where the temperature measured using the two FBGs and the thermocouple has been plotted as function of time in the same figure. During the whole testing period of about five months the difference between temperature measured by the two FBGs and the thermocouple is usually less than 2.5ºC.

Finally strain measurements using a prototype transducer like the one in Fig. 7 are presented in Fig. 14. When the feet of the transducer are deflected outward the embedded FBG goes into compression as shown in Fig. 14. In this care the strain grating measures a compression strain of about 395 μm/m.

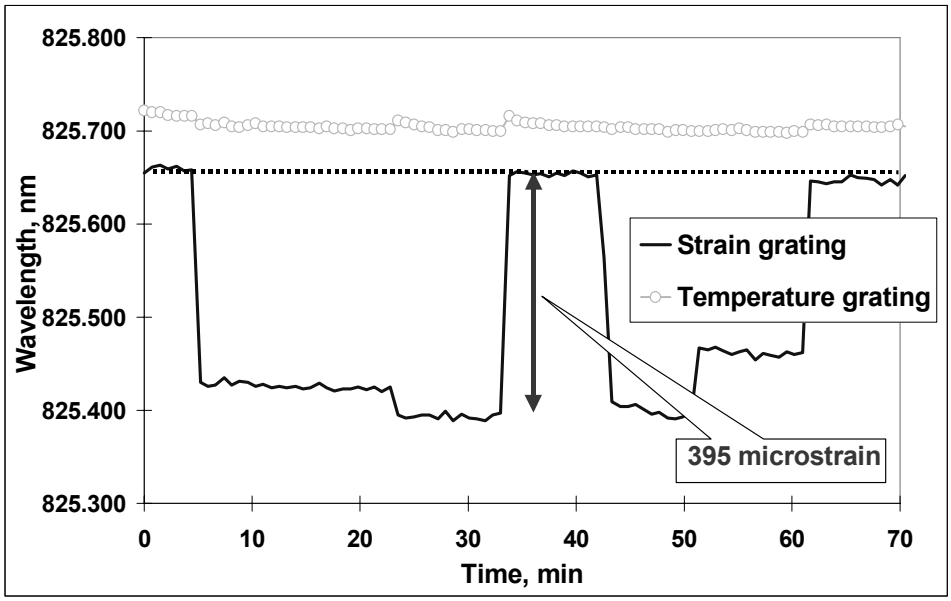

Figure 14. Demonstration of strain and temperature measurement using the transducer prototype shown in Fig. 7. The outward deflection of the transducer feet gave a compression strain of about 395 μm/m in the strain grating. The dotted line indicate zero compressive strain. The uppermost signal is the wavelength from the temperature grating.

3. Investigation of the distribution of metal around the fibre

As mentioned earlier there should be an even distribution of metal around the embedded fibre. Stress variations, pores, cracks etc may cause unacceptable large attenuation, distort the form of the Bragg peak or in other ways disturb the sensing function. In the following two methods, micro focus X-ray tomography and scanning acoustic microscopy, for investigating the distribution of metal around the fibre. Microscopic and scanning electron microscopy (SEM) investigations of cross-sections are of course effective methods, but the

preparation of the cross-sections is time consuming and there is still no guarantee that the embedding is sound a bit apart from the cross-section. In Fig. 15 two SEM pictures of a good embedding can be seen. The right part of the picture shows a zoom-in of the metal fibre boundary. Fig. 16 shows an optical micrograph of an embedded (originally) copper coated fibre. Some pores can be seen in the brazed joint together with remains of the copper coating. Micro focus X-ray tomography measurements and scanning acoustic microscopy measurements were performed in order to find out if these kinds of defects can be observed. Inconel is considered to be a difficult material for both X-ray and ultrasonic measurements due to high attenuation. The specimen used in these measurements had a width of 4 mm, a length of 100 mm and a thickness of about 2.7 mm. This specimen was a part of an originally 300 mm long part in which the embedded fibre shoved a high attenuation.

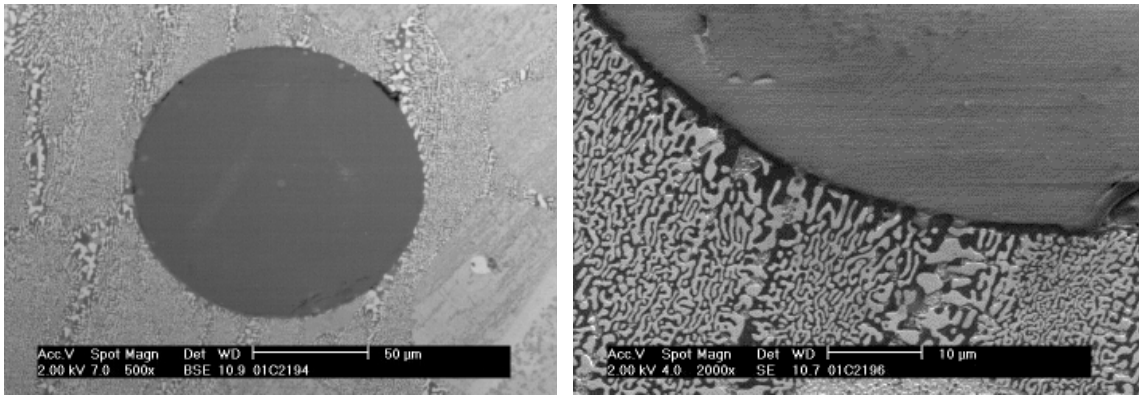

Figure 15. SEM pictures of a well embedded single mode fibre. To the right a zoom-in of the metal fibre boundary is shown.

Figure 16. A cross-section of a (originally) copper coated multimode fibre. Some remains of the copper coating can be seen as well as some pores. This is considered to be a bad embedding result.

3.1 Microfocus X-ray tomography

In Fig. 17 a Planar Computer Tomography (PCT) image of an embedded fibre is shown. The embedded fibre can be seen as a brighter horizontal band in the middle. The vertical dimension of the specimen is 4 mm. From this knowledge and from the measured width of the brighter band it can be estimated that the band originate from a structure having a diameter of 0.1 mm in the vertical direction. This is in good agreement with the diameter of the fibre which is 0.125 mm. The bright spots to the right are considered to be cavities in the brazed joint between two pieces of Inconel. Fig. 18 shows a 3D reconstruction (Algebraic Reconstruction Technique, ART) of a similar cavity. These cavities are large but details seen in the figure indicate that much smaller defects can be seen. Although the interpretation of these pictures may need some further work it seems clear that the embedded fibre can be observed together with eventual cavities with a diameter of at least 0.1 mm. Also the straightness of the embedded fibre can be estimated. However, we are close to the resolution limit of this X-ray method in this material.

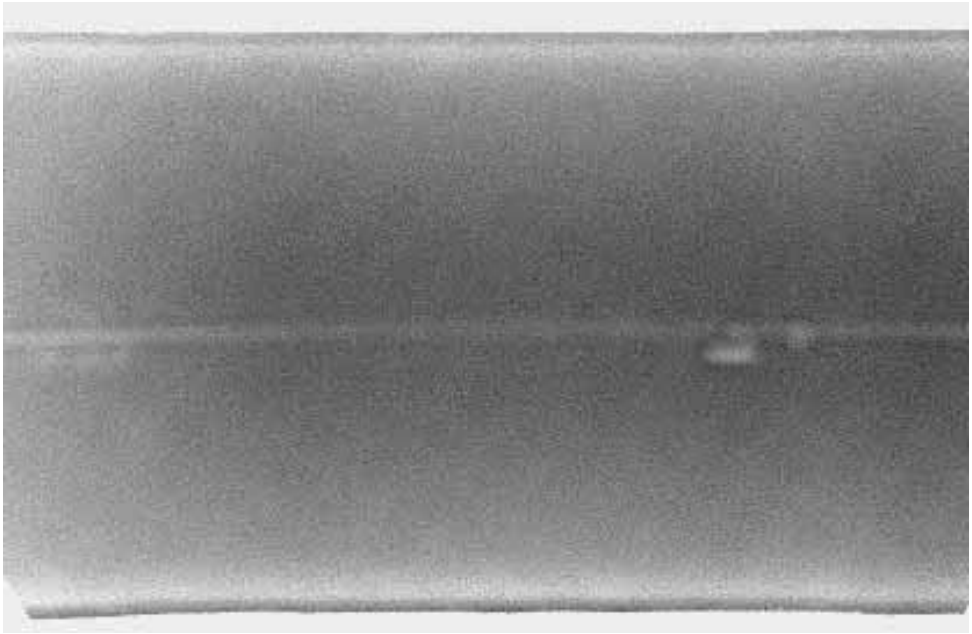

Figure 17. Planar Computer Tomography (PCT) of an embedded fibre. The fibre can be observed as a brighter horizontal band in the middle. The bright spots are cavities in the joint between two pieces of Inconel. The vertical dimension of the specimen is 4 mm end the thickness about 2.7 mm.

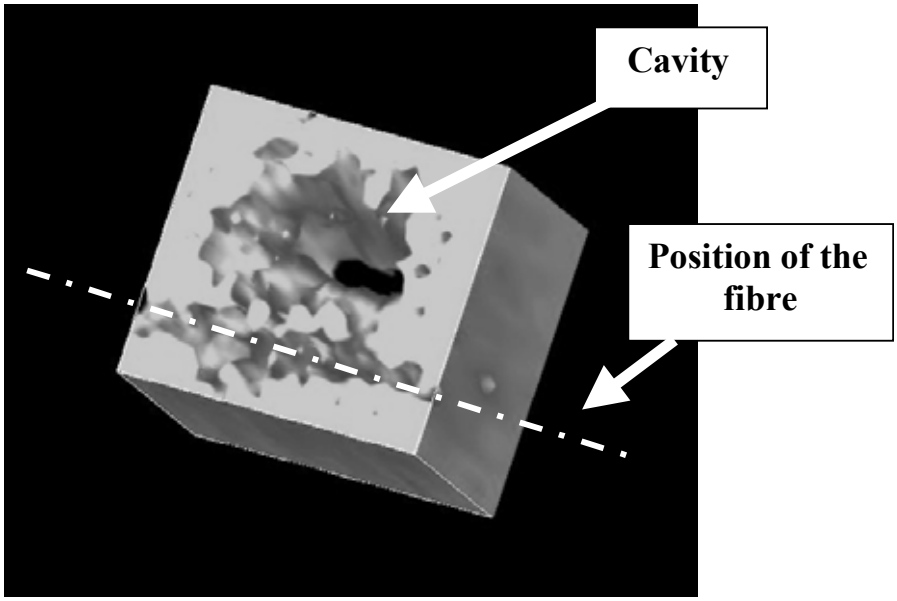

Figure 18. Algebraic Reconstruction Technique (ART) used to construct a 3D view of a cavity near an embedded fibre.

3.2 Scanning acoustic microscopy

Scanning acoustic microscopy (SAM) was also used to investigate the quality of embedding. As in the case of X-ray tomography Inconel can also be considered to be a difficult material for SAM-examinations. The scanning acoustic microscopy is high frequency ultrasonic testing and imaging method using immersion technique and focused transducers. In this work a 30 MHz transducer was used. In Fig. 19 so called C- and B-pictures are shown. The C-picture is a projection of the received echoes on the upper surface of the specimen i.e. the axis of the transducer is perpendicular to this surface. The B-picture on the other hand is a projection of the same echoes on a surface in the length direction of the specimen and perpendicular to the upper surface. In Fig. 19 the uppermost picture is the C-picture, the middle one is the B-picture and the lowest picture represent the amplitude scale (unfortunately these colour pictures does not reproduce well in greyscale). The echoes from the embedded fibre can be observed in both C- and B-pictures. In the B-picture the fibre signal is seen in the upper part while the weaker signal at a dept of about 2.5 mm is the bottom echo from the specimen. To the left in the C- and B-pictures a high amplitude area is observed. These signals are believed to originate from the same defect as seen to the right in Fig. 17. From the picture one might get the impression that the fibre is winding. The ultrasonic interaction between the fibre and its surrounding is however complex and variations in acoustic impedance influence the result. For example uneven dissolution of the copper coating may influence the result. However, also this technique can also be useful in evaluating the quality of embedding because great variations in acoustic impedance near the fibre probably also indicate large variations in the stress distribution.

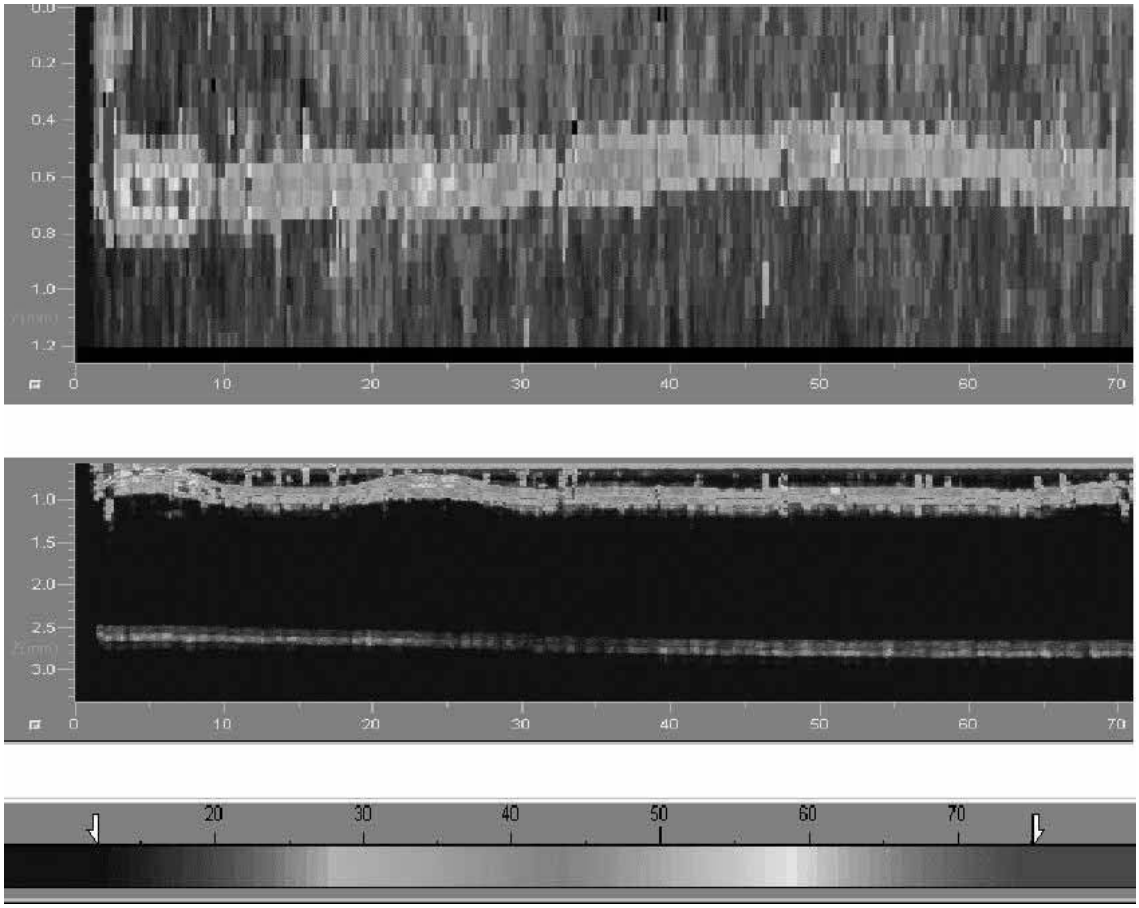

Figure 19. Scanning acoustic microscopy of an optical fibre embedded in Inconel. From above C-picture, B-picture and the amplitude scale. The C-picture is a top view of the echo distribution while the B-picture shows through thickness distribution of the echoes in a plan through the length direction of the fibre.

4. Conclusions

Two different methods for embedding of optical sensing fibres in high melting point metallic alloys (stainless steel and Inconel 600) have been developed and tested independently by two laboratories, one in USA and one in Finland. The embedded fibres were equipped with in-fibre Bragg gratings (FBGs) in both cases. The functionality of the embedded FBGs was demonstrated by strain measurements and elevated temperature cycling tests. The most remarkable tests results were:

- Demonstration of the stability of two metal embedded FBGs at temperatures between 500ºC and 550ºC for more than five months
- Demonstration of the stability of two metal embedded FBGs during thermal cycling between 100ºC and 600ºC for a few days.

- Metal embedded FBGs have a temperature sensitivity of up to 160% higher than bare FBGs.
- Demonstration of (compressive) strain measurements using metal embedded FBGs.
- A decoupling technique was developed to separate temperature and strain effects in embedded FBGs.

During the long term elevated test it was demonstrated that temperature measured using two metal embedded FBSs usually differed less than 2.5ºC from temperature measured by a thermocouple. The authors have not yet found any similar results in the open literature.

This work also considers the use of micro focus X-ray tomography and scanning acoustic microscopy for evaluating the quality of embedding. Both were found useful.

It is believed that the methods for embedding sensing fibres in high melting point metallic alloys can be further exploited development of new methods for condition monitoring in harsh industrial and power plant environments. Potential applications for metal embedded FBGs are numerous. Further, if at least tens of meters of fibres can be embedded on for example high temperature tubes and vessels new temperature monitoring possibilities would be provided by the fibre optical distributed temperature sensing technique (DTS). Investigation of the possibility of reliably applying the DTS-technique together with metal embedded fibres is therefore suggested.

5. Acknowledgements

The authors are grateful for financial support from the National Science Foundation (Dr. D. Durham, Program Director) and the Office of Naval Research. Financial support from the Academy of Finland (decision 72327) and from The Technical Research Centre of Finland (VTT) is also gratefully acknowledged. Our sincere thanks are due to Dr Anatol Rabinkin at Honeywell International for providing the brazing alloy MBF-35. Further thanks are due to Ari Hokkanen at VTT for assistance in setting up the optical measurement systems.

References

1. A.D. Kersey, M.A. Davis, H.J. Patrick, M. LeBlanc, K. P. Koo, C.G. Askins, M.A. Putnam & E.J. Friebele. Fiber grating sensors. Journal of Light Wave Technology, vol. 15, 1997, pp. 1442–1463.

2. D.C. Betz, G. Thursby, B. Culshaw & W.J. Staszewski. Acousto-ultrasonic sensing using fiber Bragg gratings. Smart Materials and Structures. 12. February 2003, pp. 122–128.

3. A. Fernadez Fernandez, A.I. Gusarov, B. Brichard, S. Bodart, K. Lammens, F. Berghmans, M. Decréton. P. Mégret, M. Blondel & A. Delchambre. Temperature monitoring of nuclear reactor cores with multiplexed fiber Bragg grating sensors. Opt. Eng. 41, June 2002, pp. 1246–1254.

4. K.O. Hill, Y. Fujii, D.C. Johnson & B.S. Kawasaki. Photosensitivity in Optical Fiber Waveguides: Application to Reflection Filter Fabrication. Applied Physics Letters, Vol. 32, 1978, pp. 647–649.

5. B.S. Kawasaki, K.O. Hill, D.C. Johnson & Y. Fuji. Narrow-band Bragg Reflections in Optical Fibers. Optics Letters, Vol. 3, 1978, pp. 66–68.

6. E. Udd. Fiber Optic Smart Structures. Wiley (Interscience), New York, 1995.

7. C.M. Lawrence. Embedded Fiber Optic Strain Sensors for Process Monitoring of Composites. Ph.D thesis, Stanford University, 1997.

8. R. Foedinger, D. Rea, J. Sirkis, R. Wagreich, J. Troll, R. Grande, C. Davis & T.L. Vandiver. Structural Health Monitoring of Filament Wound Composite Pressure Vessels with Embedded Optical Fiber Sensors. International SAMPE Symposium and Exhibition-Proceedings, Vol.43, no. 1, 1998, pp. 444–457.

9. K. Kim, M. Breslauer & G.S. Springer. Effect of Embedded Sensors on the Strength of Composite Laminates. Journal of Reinforced Plastics and Composites, Vol. 11, no. 8, Aug. 1992, pp. 949–958.

10. X.D. Jin, J.S. Sirkis, J.K. Chung & V.S. Venkat. Embedded In-line Fiber etalon/Bragg Grating Hybrid Sensor to Measure Strain and Temperature in a Composite Beam. Journal of Intelligent Material Systems and Structures, Vol. 9, no. 3, March 1998, pp. 171–181.

11. V.M. Murukeshan, P.Y. Chan, L.S. Ong & L.K. Seah. Cure Monitoring of Smart Composites Using Fiber Bragg Grating Based Embedded Sensors. Sensors and Actuators, A: Physical, Vol. 79, no. 2, 2000, pp. 153–161.

12. V.M. Murukeshan, P.Y. Chan & L.S. Ong. Intracore Fiber Bragg Gratings for Strain Measurement in Embedded Composite Structures. Applied Optics, Vol. 40, no. 1, Jan. 2001, pp. 145–149.

13. H.F. Taylor & C.E. Lee. Sensing Applications of Fiber Fabry-Perot Interferometers Embedded in Composites and in Metals. Experiments in Smart Materials and Structures, ASME, AMD-Vol. 181, 1993, pp. 47.

14. C.E. Lee, J.J. Alcoz, W. Gibler, R.A. Atkins & H.F. Taylor. Method for Embedding Optical Fibers and Optical Fiber Sensors in Metal Parts and Structures. Fiber Optic Smart Structures and Skins IV, SPIE, Vol. 1588, 1991, pp. 110.

15. S.E. Baldini, D.J. Tubbs & W.A. Stange. Embedding Fiber Optic Sensors in Titanium Matrix Composites. Fiber Optic Smart Structures and Skins III SPIE, Vol. 1370, 1990, pp. 162.

16. S. Sandlin & L. Heikinheimo. Evaluation of a new method for metal embedding of optical fibres for high temperature sensing purposes. Baltica V Conference. Condition and Life Management of Power Plants, Vol. 2, 2001. VTT Symposium 212. Pp. 547–557.

17. M. Fokine. Photosensitivity, chemical composition gratings, and optical fiber based components. Ph.D. dissertation, Royal Institute of Technology, Stockholm, 2002.

Ultrasonic assessment of material degradation by thermal fatigue

Jorma Pitkänen, Pentti Kauppinen & Harri Jeskanen
VTT Industrial Systems
P.O. Box 1704, FI-02044 VTT, Finland

Abstract

Near surface areas can contain many types of defects, material changes and degradation. Materials subjected to thermal fatigue or annealing have been evaluated with a special ultrasonic probe optimised for surface measurements, and with a 0° longitudinal wave probe. Combining measured data from a large area and calculating depths of interest in the sound path (RF-signal) information provides improved estimation of degradation levels. The technique is using a combination of three factors: (1) back-scattered ultrasonic signals and induced leaky Rayleigh wave information), and (2) simple statistical data analysis in combination with (3) an optimised ultrasonic transducer. The back-scattered ultrasonic signal is a measure of the effect of geometrical reflectors such as micro-pores, inclusions, precipitates, segregation, micro-cracks and cracks as well as of back-scattering from phase boundaries during fatigue damaging and increase of degradation inside the material. The leaky Rayleigh wave component is sensitive to surface properties, and especially to cracks. Deep cracks will totally cancel the leaky Rayleigh wave signal.

1. Introduction

The ageing of conventional as well as nuclear power plants gives motivation to non-destructive detection of degradation of materials. Many NDE techniques have potential for detection of degradation. These methods offer the possibility of studying these effects on-site reliably. The information gained using this type of techniques gives background for evaluation of the lifetime of a component. This helps power plant operators to plan more accurately their in-service tasks and to reduce costs.

This study focuses on the ultrasonic response evaluation. Many techniques like eddy current or other electromagnetic NDE techniques give similar tools as this type ultrasonic solution. This effect has been reported for instance by Goebbels [2, 3], but this topic has not been fully studied [1]. The chosen ultrasonic technique and the evaluation scheme will be presented.

Thermal loading causes materials degradation that consists of various microstructural changes like phase changes, pore initiations, increased grain size, sensitisation of austenitic material [4] etc. Austenitic steel specimens (AISI 321 and AISI 304) were tested in this study.

2. The techniques and equipment used

2.1 The techniques

For the study two techniques were chosen: the leaky Rayleigh wave and the 0° longitudinal wave technique. Figure 1 shows signals produced by the leaky Rayleigh wave probe [5, 6]. Figure 1a shows selected area, where the back-scattered signals are analysed. Figure 1b shows same selected area box for back-scattered signals and visualises also frequency content of the back scattered signals. The principle of the leaky Rayleigh wave probe is shown in Figures 1c and 1d. Back scattered signals from the 0° longitudinal wave probe are simple chosen from the depth area of interest.

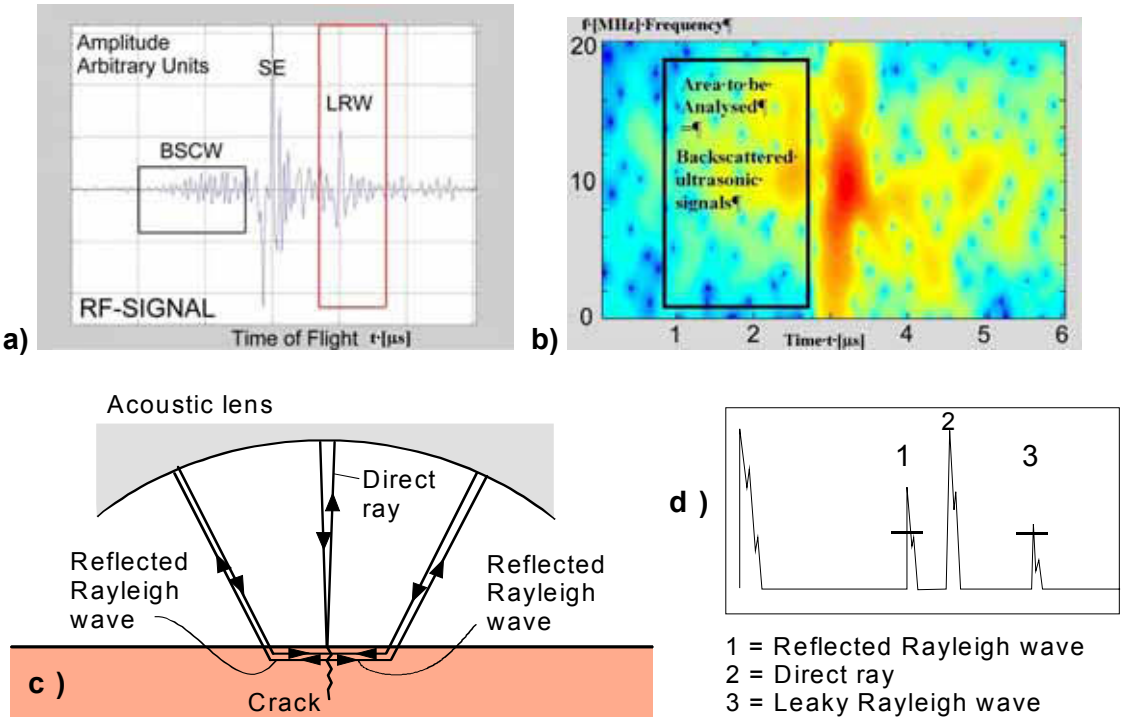

Figure 1. a) RF-signal from the leaky Rayleigh wave probe; BSCW = back-scattered waves; SE = surface echo, LRW = leaky Rayleigh wave; b) time and frequency domain visualisation from signals produced by leaky Rayleigh wave probe; c) principle of leaky Rayleigh wave probe with a crack under the probe; d) an A-scan showing the arrival times of reflected and leaky waves.

2.2 The equipment

For measurement and data acquisition, an ultrasonic immersion system MIDAS was used, see Figure 2. A focussed 25 MHz-probe and a 15 MHz leaky-Rayleigh wave probe having a broad frequency band were used. MIDAS and VTT Ultratone software were used in the analysis.

Figure 2. Arrangement for measurement (left) MIDAS ultrasonic immersion testing equipment (right).

2.3 Measured data

Amplitude data were calculated from raw data and compared with different loading factors. As a comparison, a reference material was used with either zero loading or exactly known reference loading. The calculated amplitude values are obtained from the following equation:

$$V = 20\log(f(A_i, \Delta A_i) / f(\sum_{i=1}^{i_{max}} A_{0i} / i, \sum_{i=1}^{i_{max}} \Delta A_{0i} / i))$$

where A_i is the computed statistical amplitude value from specimen i,
ΔA_i is the computed statistical amplitude variation from specimen i,
A_{0i} is the computed statistical amplitude from the reference specimen i with reference loading,
ΔA_{0i} is the computed statistical amplitude variation from the reference specimen i with reference loading.

3. Measurements and results

Austenitic steel specimens (AISI 321) were loaded with low cycle thermal fatigue. The specimens were measured after loading with leaky Rayleigh wave technique, measuring only the back-scattered area shown earlier. The statistical amplitude values (rms) were calculated for each measurement point. The number of measurement points for each specimen was about 10000. The computed rms-values are shown in a C-scan form in Figure 3. The rms-value increases with increasing thermal low cycle fatigue. Figure 3 shows results from measured

specimen of 5 different loads with increasing degradation from left to right. The lower row shows the specimen with highest degradation. From these specimens the effect of degradation is clearly seen. The amplitude increase was in best cases about 10–14 dB and the reference material was material, which was not subjected to low cycle fatigue. In the degraded material micro-cracks and even macro-cracks were already seen in some specimens.

This back-scattered noise technique was also applied also to measure grain boundary precipitation. Specimens of overlay welded austenitic steel (AISI 304) were studied for the effects of welding and ageing (sensitisation and grain growth). Thermal ageing for low temperature sensitisation (LTS) was conducted at 400°C for 69 days (specimen A) and for 650 days (specimen B). Ageing treatment caused increase in the degree of sensitisation (DOS) due to growth of carbides ($M_{23}C_6$) during the weld cycle at LWR operation temperature within the heat affected zone (HAZ), see Figure 4 [4].

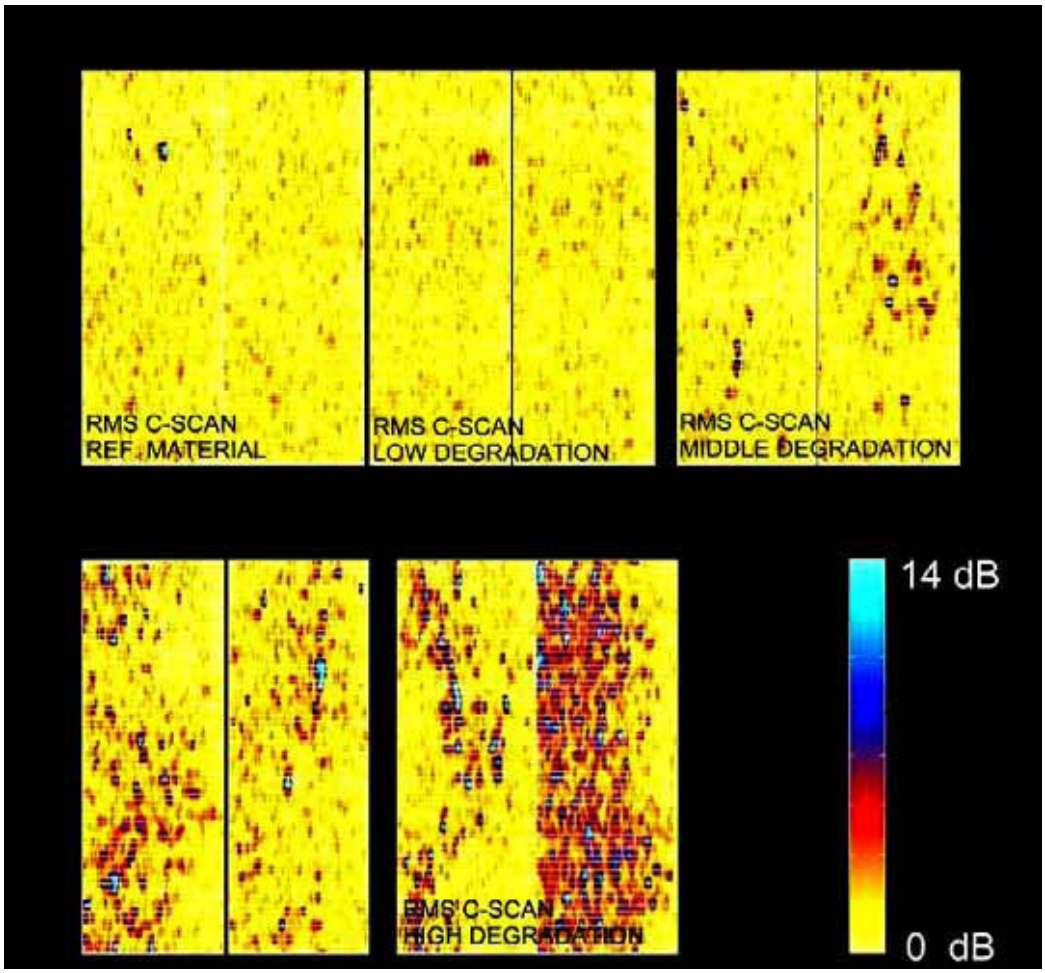

Figure 3. C-scan from computed rms-values for back-scattered ultrasonic signals showing degradation caused by low cycle fatigue.

The measured C-scans of computed rms-values are shown in Figure 5, as well the rms-frequency distribution from the studied volume. Rms-amplitude of the frequency distribution is increasing with increasing heat treatment time. Table 1 shows the determined amplitude values from the two specimens. Unlike specimen A, the specimen B with a longer ageing treatment showed a detectable increase in the rms-amplitude from RF-signal (Rms_A) and from power spectrum amplitude (Rms_F) of back-scattered ultrasonic signals.

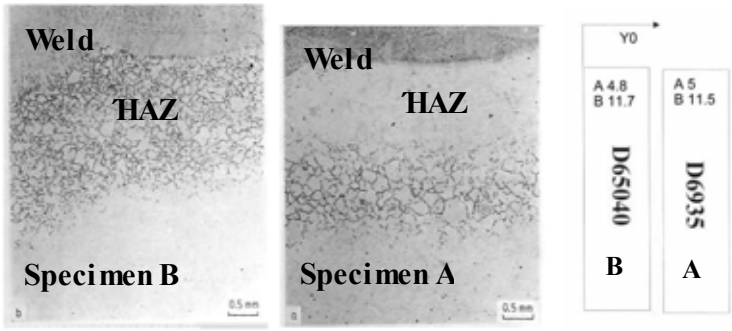

Figure 4. Micrographs [4] from two austenitic steel specimens showing different carbide grain sizes in the heat affected zone.

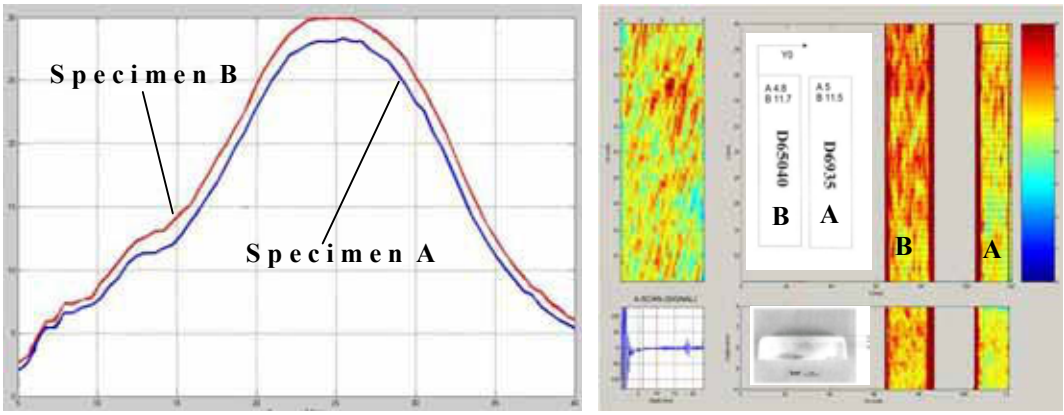

Figure 5. Rms-frequency distribution from the studied volume on the left and the measured C-scans of computed amplitude rms-values on the right (A = Rms C-scan from specimen A; B = Rms C-scan from specimen B).

Table 1. Statistical characteristics from measurements of two heat treated austenitic steel specimens.

Material	RMS_A	RMS_F	RMS_t	X (mm)	Y (mm)	Z (mm)	f (MHz)
B	5.61 ± 0.72	4.68 ± 0.72	2.54 ± 0.36	70–82	0.5–38.5	6–10	2–14
A	5.01 ± 0.63	4.15 ± 0.62	2.62 ± 0.36	107–119	0.5–38.5	6–10	2–14

4. Discussion and conclusions

The following conclusions have been drawn from the inspections of different materials. The surface condition has an effect on the results and this has to be considered in the evaluation of data. Ultrasonic back scattering showed correlation with degradation of studied austenitic materials. Effects of heat treatment on $M_{23}C_6$ carbides in the heat-affected zone was detectable as increasing noise in the back-scattered ultrasonic signals. The analysis of rms-values of a large measurement area can be a useful method for determining degradation in austenitic materials. Calibration standards are needed for analysis. Frequency analysis of the measured data gives supplementary information for degradation analysis. Noise measurement based on the back scattering of ultrasonic waves shows potential to determine material characteristics and its changes.

References

1. Thompson, R.B. Use of elastodynamic theories in the stochastic description of the effects microstructure on ultrasonic flaw and noise signals. Wave motion 36 (2002), pp. 47–365.

2. Vary, A. Ultrasonic measurement of materials properties by scattered ultrasonic radiation. In: Research Technique in Nondestructive Testing, Volume IV. Ed. R. S. Sharpe. London: Academic Press, 1980. Pp. 159–204.

3. Goebbels, K. Structure analysis by scattered ultrasonic radiation. In: Research Technique in Nondestructive Testing, Volume IV. Ed. R.S. Sharpe. London: Academic Press, 1980. Pp. 87–157.

4. Kekkonen, T. Sensitation of austenitic stainless steel weld in low temperatures. Master of Science Thesis, Helsinki University of Technology, Espoo, Finland, 1983. 85 p.

5. Jeskanen, H., Pitkänen, J. & Kauppinen, P. Applications of materials property ultrasonic probe. ECNDT, Barcelona, Spain, 17–21 June, 2002. 7 p.

6. Kauppinen, P. The evaluation of integrity and elasticity of thermally sprayed coatings by ultrasonics. Dissertation Thesis. Helsinki University of Technology, Espoo, Finland, 1997. 130 p.

7. Pitkänen, J., Kauppinen, P. & Jeskanen, H. Materials degradation and altering influence on ultrasonic scattering by light statistical approach in austenitic thermal loaded materials. Review of progress in quantitative nondestructive evaluation, Vol. 23. D.O. Thompson; D. E. Chimenti, 2004. 5 p.

Applicable methods for NDT of tubes

Jorma Pitkänen, Aarne Lipponen & Pentti Kauppinen
VTT Industrial Systems Espoo, Finland

Abstract

For inside inspection of tubes, eddy current testing (ET) and internal rotating ultrasonic inspection (IRIS) are mainly used at the moment. Special eddy current method, remote field technique (RFEC) is being used to some extent, but normally only for ferritic tubes. This paper presents a review of techniques that can be used for internal inspections of tubes in boilers, heat exchangers and steam generators. Material affects the choice of the method, considering given defect type and detectability with the selected technique. In general ET methods are used for inspection of non-ferromagnetic tubes and IRIS and RFEC methods for inspection of ferromagnetic tubes. New techniques have been introduced, to determine the tube condition accurately. One of the developed techniques is for instance inspection of the internal surface by combination of dye penetrant and optical laser inspection. New applications of ultrasonic techniques include defect detection and characterisation by tip diffraction echoes, defect analysis by echo dynamics and the TOFD-technique for defect sizing. Ultrasonic guided waves have a great potential to increase inspection speed for defect detection, although sizing is still under development. For inspection of ferromagnetic tubes, a method based on magnetic flux leakage has been used. In addition to the basic techniques visualisation of the measured data is one of the key factors for improved exploitation of the inspection results.

1. Introduction

Eddy current testing (ET) is the most common technique for inspections. One important factor when choosing the inspection method is the magnetic property of the material – ferromagnetic or not. In the ferromagnetic materials magnetic permeability can vary locally very strongly, and this sets limitations to the application of ET. Even though there are techniques to suppress this effect, ET is often replaced by other techniques. In some cases ET has been reported to show problems in detecting or sizing OD-cracking caused by crevice corrosion in nickel base alloys (Kenefick et al. 1999, Lahdenperä 2002).

This review describes alternative techniques that especially can be used for steam generator tube inspection. The information given can help decision making for life time management of the tubes.

This presentation reviews the NDT methods that have been developed or are under development to meet new requirements. Improvements have taken place e.g., in sensor technology and in software for eddy current and ultrasonic techniques, and in magnetic flux leakage testing as well as in dye penetrant technique combined with a laser detection system. The NDT-measurements need also a concept to visualise measured data to make rapid evaluation of defect concentration in tube areas as well as in length locations possible. This type of visualisation software has been developed by VTT (Lipponen et al. 2002).

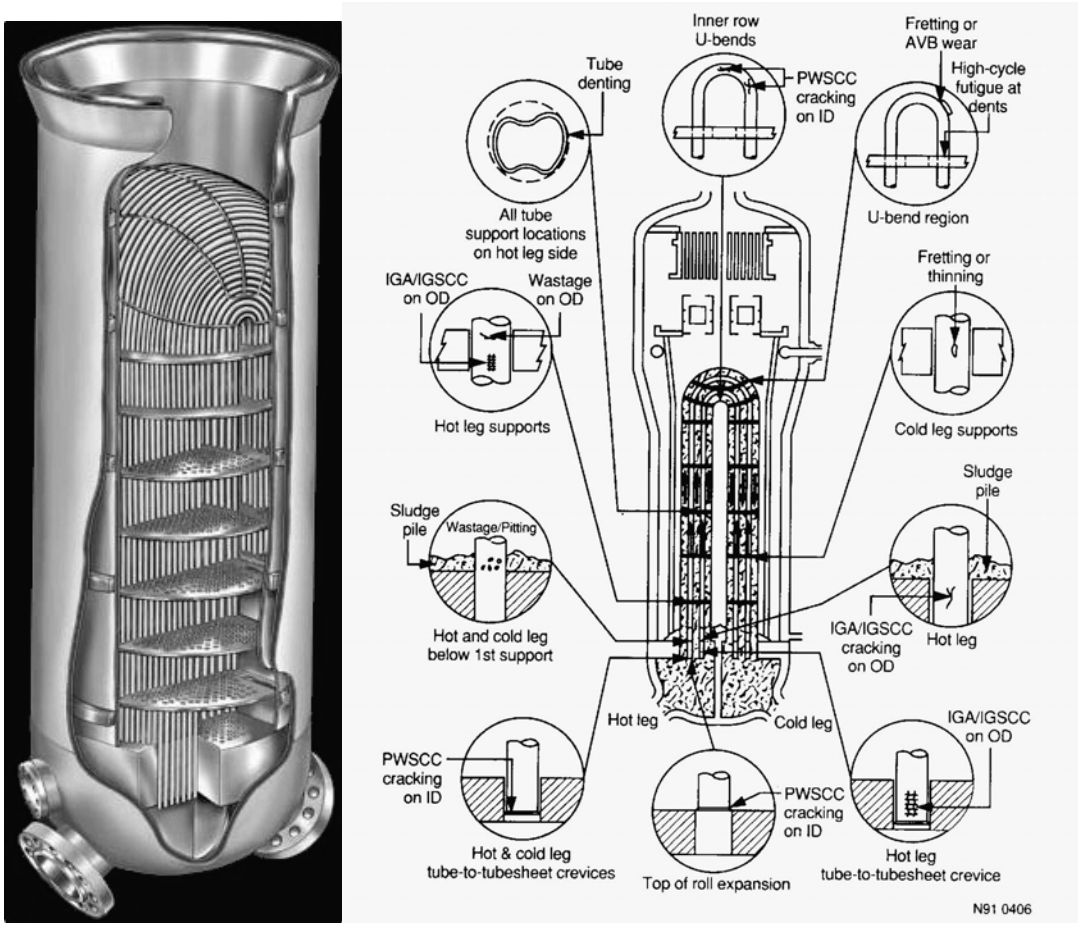

Figure 1. Structure of a steam generator (left, Nuson 2003) and defect types located in regions where they have been detected (right, Shah et al. 1993).

The basic choice for inspection technique depends on the defect types in components like heat exchangers, boilers and steam generators. In Figure 1 has been shown the structure of a steam generator and possible defect types in a steam generator caused by different reasons. It is obvious that these various defects types have caused this need for development in non destructive testing methods.

Accurate NDT methods can offer savings in life prediction. If it has been shown that no defects are growing in the tubes savings will come in prolonging in-

service inspection intervals. In the future there will be much effort to improve NDT to meet all these requirements, not to forget the total efficiency and speed of inspection that are important to save in inspection and downtime cost.

2. Techniques used to inspect tubes

This review does not cover all techniques, but describes techniques that the authors consider as potential ones.

2.1 Eddy current techniques

Eddy current techniques have here been divided into four categories according to the coil type used:

- bobbing coil
- rotating coil
- array coil
- remote field coil.

In addition, it should be noted that interpretation of the eddy current signal is a complex task where the results depend on the inspected component, inspector and the equipment and software of the ET system.

2.1.1 Bobbing coil

The conventional bobbing coil is still the most important coil type in eddy current testing. The bobbing coil can be an absolute or a differential coil. The inspection with the bobbing coil system is fast and relatively reliable. Defect detectability in support plate and in head plate areas of exchangers can be improved by using multi-frequency technique during data acquisition. Bobbing coils are designed to detect mainly corrosion and axial cracks of tubes. Circumferential cracks cannot be detected properly with bobbing coils. Bobbing coil is measuring an integral of the whole circumference volume where eddy currents are induced.

2.1.2 Rotating coil

Normal pancake or plus point coils are used in the rotating probes. The rotating probe surface coil is mechanically rotated in circumferential direction of the tubes. These coils have been until recently the main tool for clarifying suspicious indications measured with bobbing coils. Plus point coil is an improved version from the pancake coil. In plus point coils detection of cracks both in axial and circumferential directions is improved. The advantage using rotating coils compared to bobbing coil is improved defect detection. The circumference resolution is better but the rotating probe inspection is clearly slower compared to bobbing coils.

2.1.3 Array coil

The structure of an array coil is shown in Figure 2. The array consists of several rows of coils arranged around the circumference of the sensor. Each separate coil can be used as a probe. It is also possible to scan digitally each coil very fast. This array structure allows for detection of defects in both axial and circumference direction. An array probe is about 40–80 times faster than rotating probe (almost as fast as a bobbing coil), but has an equal resolution in circumferential direction. An array probe provides a possibility to analyse the detected indications in several ways. The amount of the stored data is larger compared to data stored by the bobbing coil (Isnan 1998, Siegel 1999). Visualisation of an array coil measurement is shown in Figure 3.

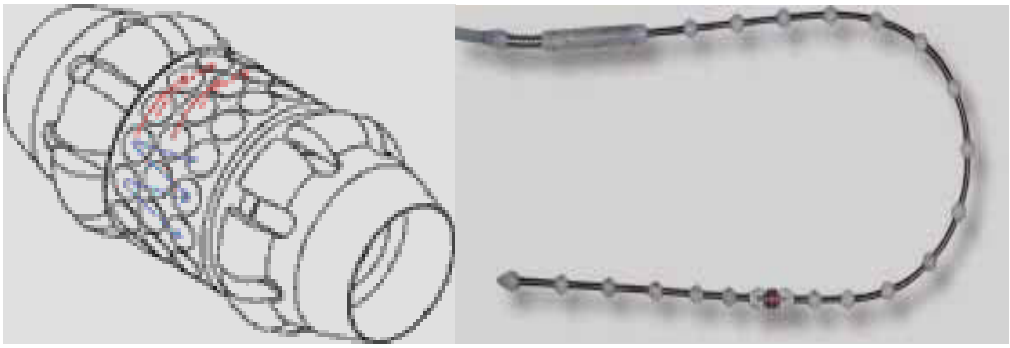

Figure 2. The principle of X-probe (array coil) developed by RD Tech (left) and X-probe used for inspection of bend areas of steam generators (right).

2.1.4 Remote field coil

Remote field eddy current technique (RFEC) uses low frequency AC, normally about 20-30 kHz for magnetic materials. The sensitivity of this technique is approximately similar for detection of outer and inner defects. The transmitting coil is a large bobbing coil type. The receiver is either a single coil or an array coil, which is located near the inner diameter at a distance of 2 × outer diameter from the transmitter coil. RFEC was originally designed for ferritic tube inspection already in 1950s. FE-modelling has been carried for improved design of this method for the inspection of steam generator tubes.

In the eddy current inspection two different kinds of fields are available: indirect field and direct field. In conventional eddy current inspection the direct field is used but in RFEC the indirect field is measured. In direct coupling the field is propagating on the inner surface at the same side with the probe. This field attenuates strongly when the circumference eddy currents will be induced on the inner surface of the tube. The indirect coupling originates from the transmitter coil and propagates through the wall to the inner surface. The indirect field is attenuating slowly and is dominant in the remote field region, where the direct field is already attenuated (Schmidt 1984).

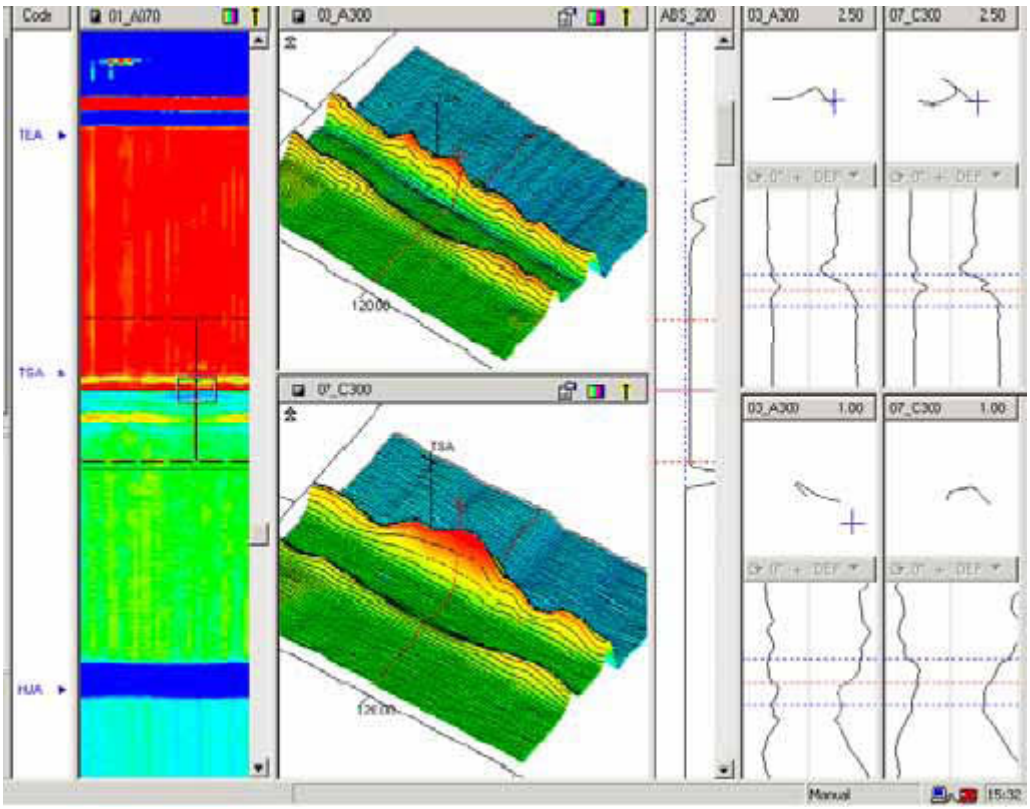

Figure 3. 3D presentation of ET signal amplitude from a NRC steam generator mock up. The axis of the tube is from lower left to upper right (Kupperman et al. 2002).

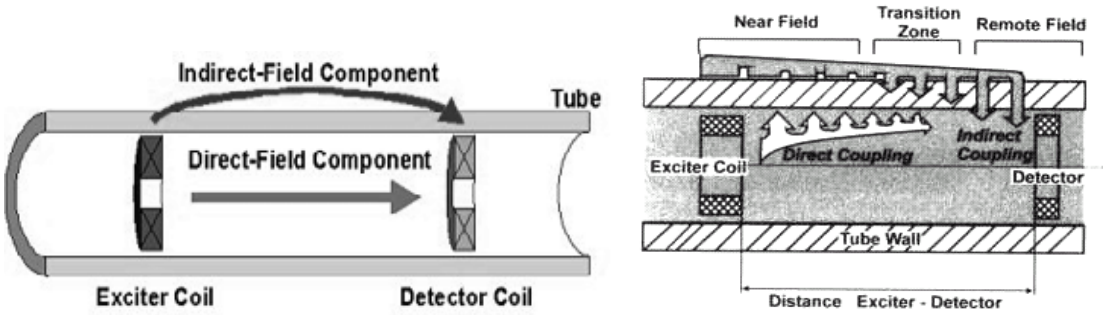

Figure 4. The principle of RFEC. The transmitter generates direct field and indirect field components, of which the indirect field is measured (right, Ostermeyer et al. 1999).

The defects in the tubes affect the received amplitude and phase that can be used for detection of defects. In eddy current testing the surface effect limits detectability simultaneously for OD and ID defects when using the same frequency in the probe. In the remote field inspection the sensitivity is similar for OD as well ID defects without changing the frequency of the RFEC-probe. Remote field inspection is sensitive to calibration notches. There has been interest to use this method for detection of SCC-cracks in steam generator tubes.

The material in steam generator tubes is usually an Inconel type of a nickel base alloy. Sullivan et al. (1989) tested and analysed RFEC for non-magnetic steam generator tube inspection but the used frequencies were quite low compared to values estimated by Shin et al. (2001). Based on modelling results, they proposed that for RFEC the optimal frequency should be about 300 kHz. A suitable distance between transmitter and receiver should be 1.5 × OD, which is a half of the corresponding value for ferromagnetic tubes.

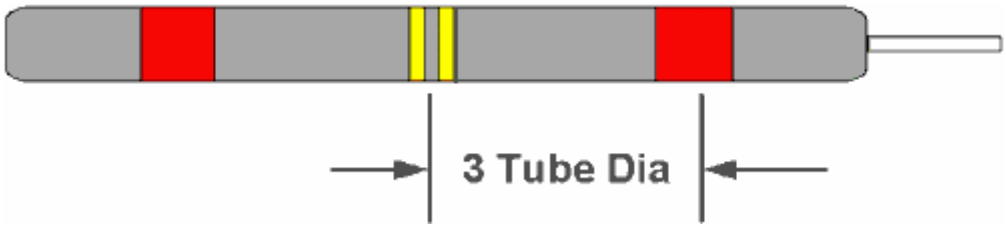

Figure 5. Twin-transmitter-RFEC-coil designed for ferromagnetic material inspection with a differential receiver coil (Krzywosz et al. 1997).

A conventional remote field probe includes only one transmitter and one differential receiver. In the RFEC-probe shown in Figure 5, there are two transmitters in the probe which are driven using low frequency AC in opposite phase. The defect sizing capability is increased especially in support plate regions. It is possible to separate ID/OD-defects using the phase change of the indication. The indications of the defects traverse clockwise and artefacts from the support plates in the opposite direction.

2.2 Ultrasonic inspection techniques

Ultrasonic techniques offer many possibilities in tube inspection for improved condition monitoring and defect sizing. The simplest ultrasonic inspection is thickness measurement, which reveals the local and large area thinning in tubes. However, several ultrasonic techniques can be used for example to inspect steam generators:

IRIS (wall thickness measurement)

- Pattern recognition
- Echodynamics
- Crack tip detection
- TOFD-technique
- Guided waves
- EMAT
- Phased array
- Creeping waves
- Leaky Rayleigh waves.

Of the many techniques the most promising ones must be found for each application.

Ultrasonic probes for these applications have to be constructed to meet the needs in the tubing as shown as an example in Figure 6.

Figure 6. Centering the ultrasonic probe for relatively larger diameter tubes (left, Nuson 2003) and ultrasonic probe for bend region (right, Broere 2001).

2.2.1 IRIS

Tube wall thickness measurement using ultrasonic testing is a basic method for inspection of tubes. In this measurement the ultrasonic probe sends a signal at a frequency that can vary from 5 to 25 MHz. The inner surface echo is the 1st echo and the 2nd echo originates from the outer surface. From these echoes the wall thickness can be determined. Figure 7 shows the principle of the IRIS-method. Thickness measurement allows follow-up of corrosion and possible deflection of tubes.

The measured results can be shown in two B-scans (side views) and C-scans (top view). This gives 3D information of the tube condition (Figure 8). With the help of the 3D-visualisation, the defects can be mapped as shown in Figure 9. This gives also possibility to estimate the nature of the defect in different regions of the inspected component.

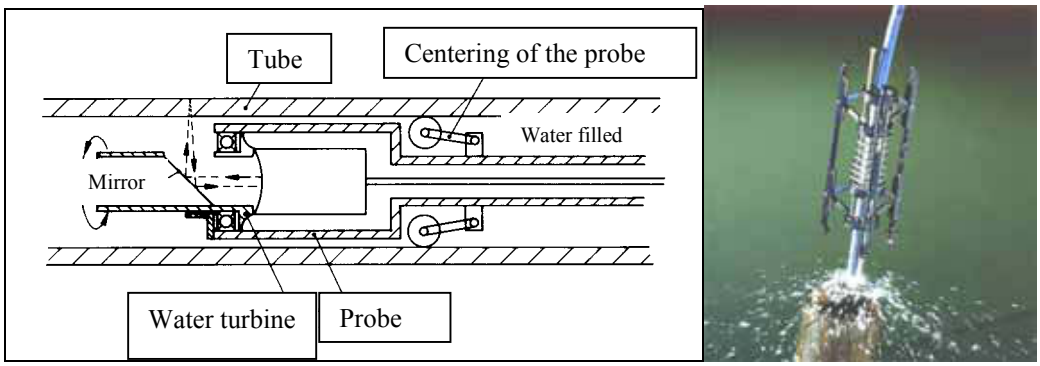

Figure 7. Principle of the IRIS-measurement and the corresponding probe.

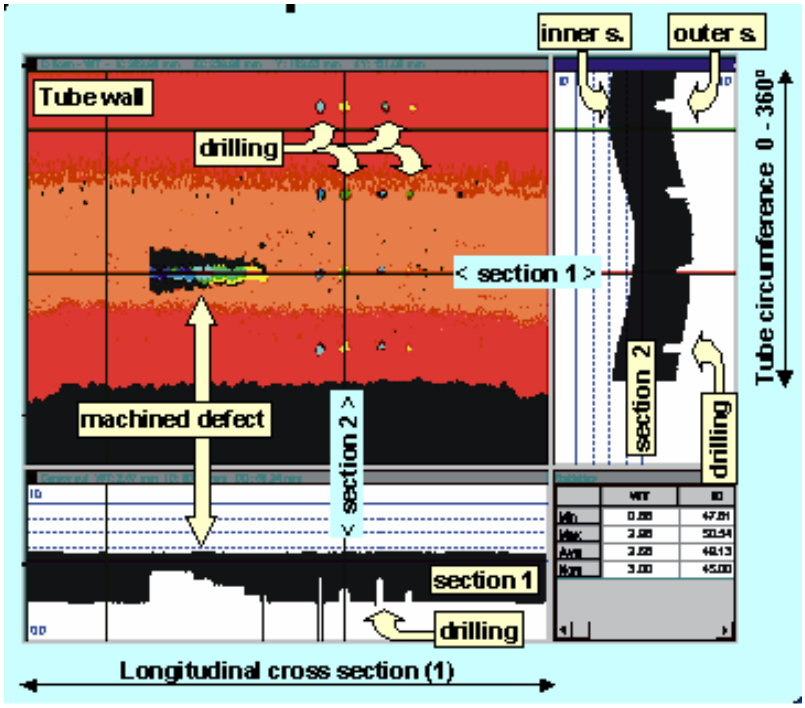

Figure 8. Visualisation during thickness measurement from a reference block with an IRIS-system.

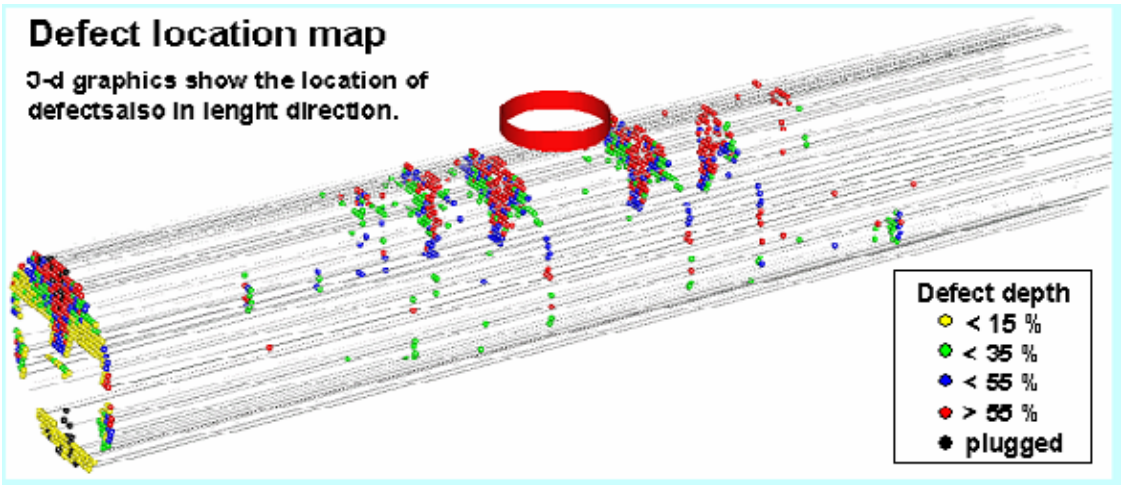

Figure 9. Location map of detected defects in 3D. Visualisation shows defect locations also in tube length positions (Lipponen et al. 2000).

2.2.2 Diffraction echoes for defect characterization

Figure 10 presents an indication caused by outer diameter cracking. The measurement uses a multi-element-probe which includes 2 elements for defect detection and sizing in axial direction and 2 elements in circumferential direction (Fig. 11), and an additional 5th element, a 0-degree probe for profile and thickness measurement. The crack indications are analysed with help of A-, B-

and C-scan data. During the analysis defect length and size can be extracted very fast from data. After detection the cracks are analysed sequentially following separate B-scans. According to Kenefick (1999, 2001) the method is based on the time of flight difference between corner and tip diffraction echoes (Fig. 12).

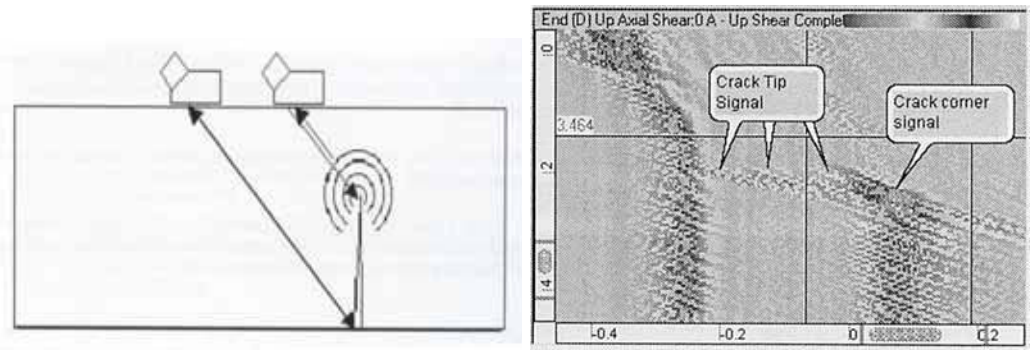

Figure 10. The ultrasonic inspection and analysis principle of the EPRI-method (left). The data is analysed from the dynamic A-, B- (right) and C-scans and defect size can be estimated. In the Figure left is presented one B-scan showing signals from crack tip and corner (Kenefick et al. 2001).

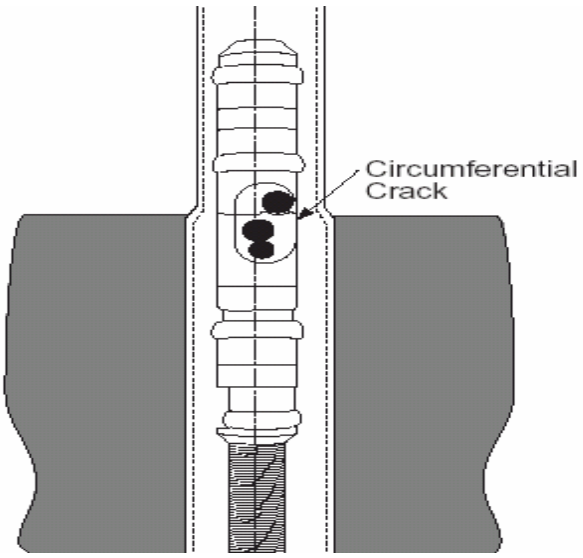

Figure 11. The principle of ultrasonic probe using tip diffraction echo (Kenefick et al. 1999).

Table 1. Comparison of UT and metallographic results (Kenefick et al. 1999); ODSCC = outer diameter stress corrosion crack.

	Ultrasonic	**Metallography**
ODSCC area	0.0171 square-in	0.0166 square-in
ODSCC length	80 degrees	84 degrees
Maximum depth	91% through wall	96% through wall

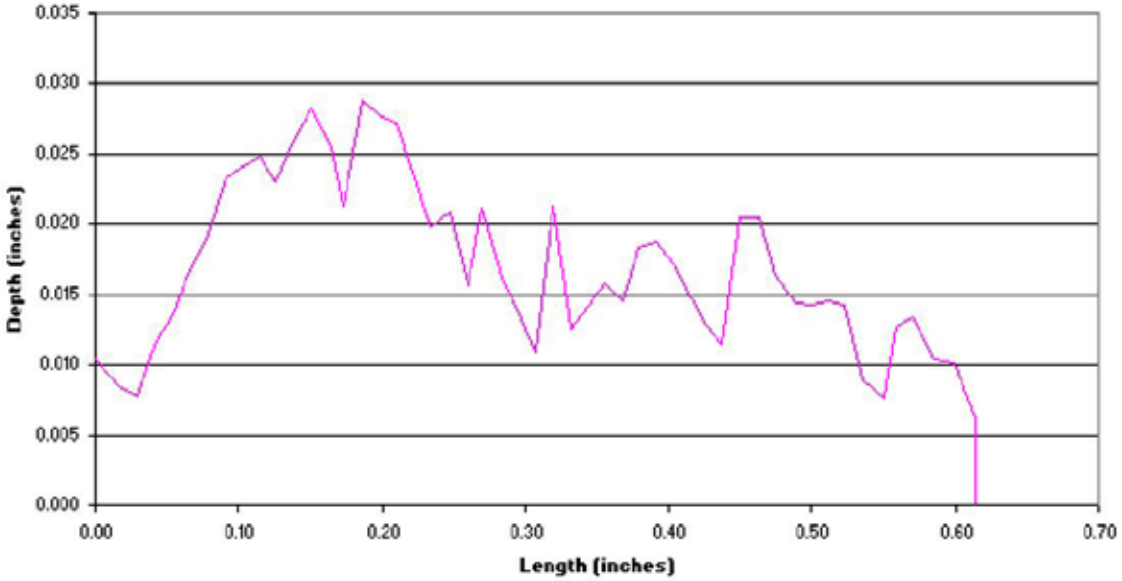

Figure 12. Flaw profile forms as a result the fracture surface of the crack and crack tip behaviour. Crack tip can be clearly resolved from the corner reflection and the defect size can be determined with good accuracy (Kenefick 2002).

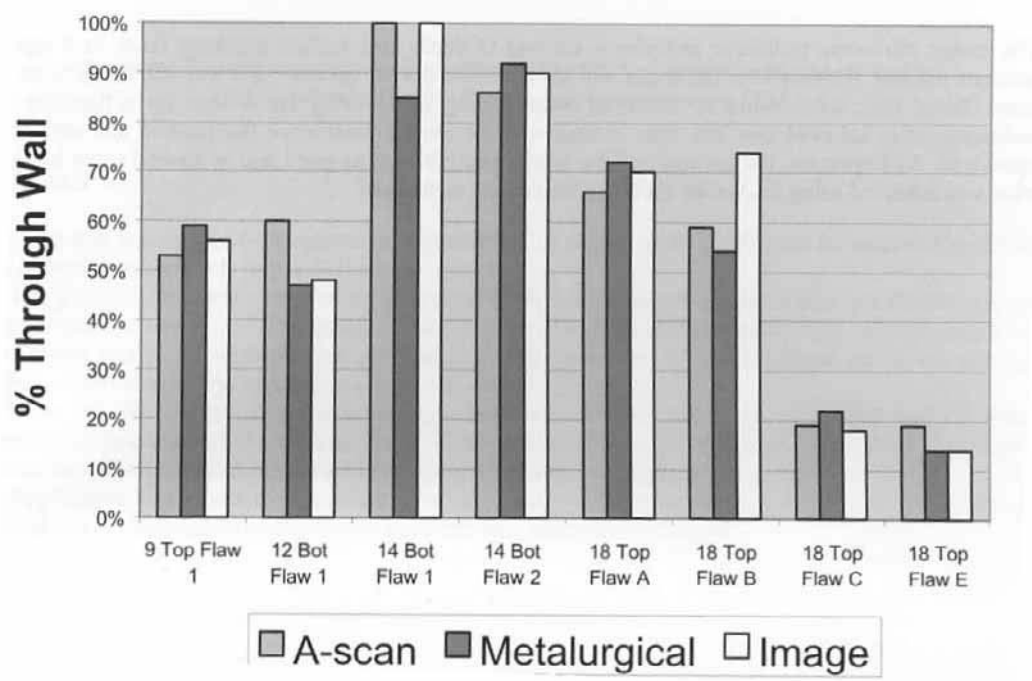

Figure 13. Comparison of crack sizing by metallographic examination, A-scan results and analysis results from EPRI-method (Kenefick et al. 1999).

2.2.3 TOFD for defect detection

The TOFD technique was developed to apply a time-of-flight measurement of tip diffracted signals (Silk 1982). Signals are originating from both ends of the

defects and originally the method was used for quick inspection of ferritic welds. Inspection of thin walled tubing has been very rarely carried out using TOFD. The principle of the TOFD technique is shown in Figure 14, where two longitudinal wave probes in a pitch-catch arrangement are used the measurement. The applied angle of incidence varies between 56°–70°. The opening angle of the TOFD probe is large. Following signals can be received from an internal crack: lateral wave, backwall echo, and tip diffraction echoes from the crack. For calibration both lateral wave (sound velocity checking) and backwall echo (sound path calibration) are used. The measured signals can be shown in A-, B-, C- or D-scans. The size of a crack is determined by help of the sound paths of diffracted signals from the upper and lower tips of the crack. The maximum sensitivity of measured signals from fixed depth depends on the distance between the probes. The TOFD technique is faster than normal ultrasonic inspection. The frequency range of the probes varies normally from 5 to 15 MHz. The advantages of the TOFD technique are precise and simple sizing, rare false calls, the calibration curves are not normally necessary and inspection can be carried out also for a complicated geometry.

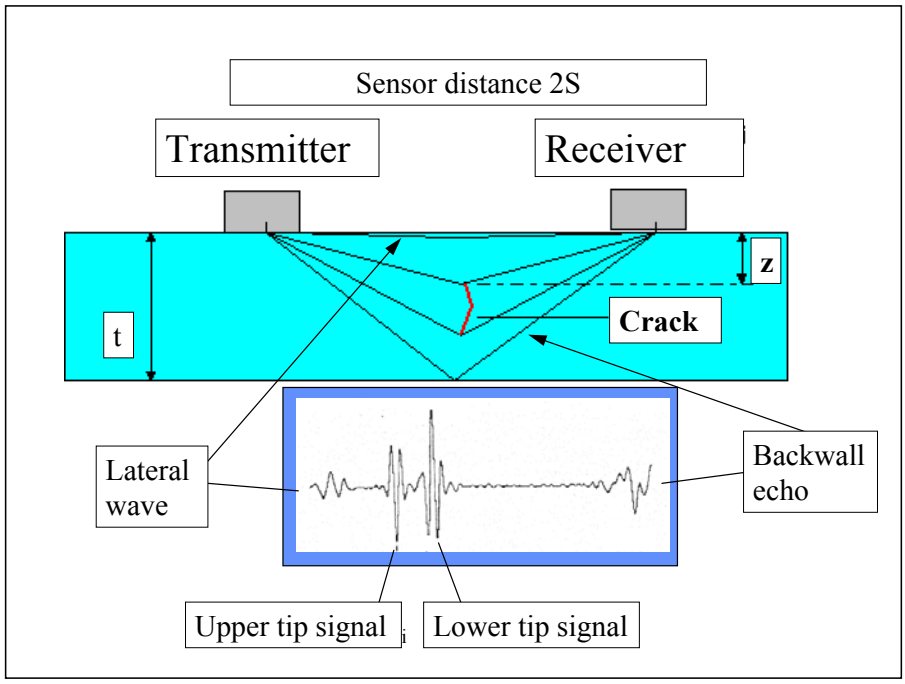

Figure 14. The principle of the TOFD-technique in the case of an internal crack.

Detection of small ID-cracks is rather complicated with TOFD. In thin walled tubing the death zone of the TOFD-probe, with a frequency of 10 MHz is about 3 mm. By increasing frequency of the probe the death zone is decreased (Krutzen et al. 1998). Crack tip signals are normally 20 dB less than the backwall echo and by averaging and signal processing the tip signal amplitude can be increased compared to noise. Often the crack tip signals are not detected because of

tightness of the crack. In case of small OD-cracks, pulse-echo is recommended (Krutzen et al. 1998).

2.2.4 Echodynamics for defect detection

In the echodynamic technique the probe is moved either in the axial or circumferential direction. The echodynamics from the crack is measured simultaneously. The defect size is determined according to the echodynamic curve extension. Corner echoes of surface breaking cracks are giving the maximum amplitude (Figure 15). By using this technique the opening of the sound beam (S) has to be corrected by a compensation factor (E). The compensation factor depends on the dimensions of the tube, tube material and defect type. For inspection sensitivity the setting of calibration defects are used and this can be corrected and optimised by using destructive results from the measured tubes. The depth of the defect (D) as a percentage of the wall thickness (W) can be calculated from (Krutzen et al. 1998).

$$D = (L \text{x} S)/(E x W) x 100\% \quad (1)$$

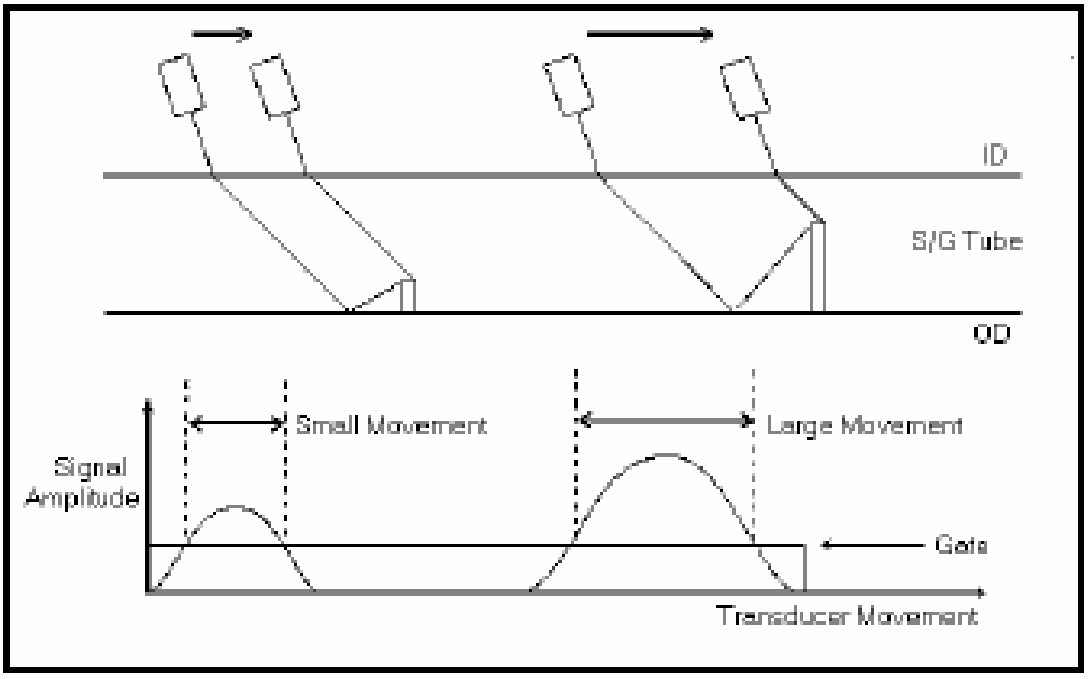

Figure 15. The principle of echodynamics inspection of steam generator tubing (Krutzen et al. 1998).

During measurement of the echodynamic curve the probe is moved by a probe displacement distance, L (Fig. 15). The probes for steam generator tubing inspection have frequencies from 10 to 20 MHz, and the angle of incidence is 45° for a shear wave probe. The advantage of the method is straightforwardness,

defect detection capability, simple signal processing and automated defect sizing procedure. Additionally the defect can be sized manually by the help of a cursor from either B- or C-scans.

2.2.5 Phased array technique

A circular phased array technique (Fleury et al. 1998) has been used to inspect the Superphoenix steam generator tubing. This phased array probe rotates the ultrasonic beam digitally 360° (see Fig. 16). The technique combines fast scanning with good detection capability. In this case the ultrasonic probe is built from 80 elements. Several elements can be used to generate ultrasonic waves simultaneously. These probes are made of composite materials, which offer excellent coupling in water. The phased array technique can detect both axial and circumferential defects. With a phased array probe a 0.26 mm deep crack (10% of the wall thickness) was detected, with a length of 1.5 mm and a depth sizing error of 0.1 mm. The inspection speed was 50 mm/s. The tube U-bend parts can be also inspected with the phased array technique.

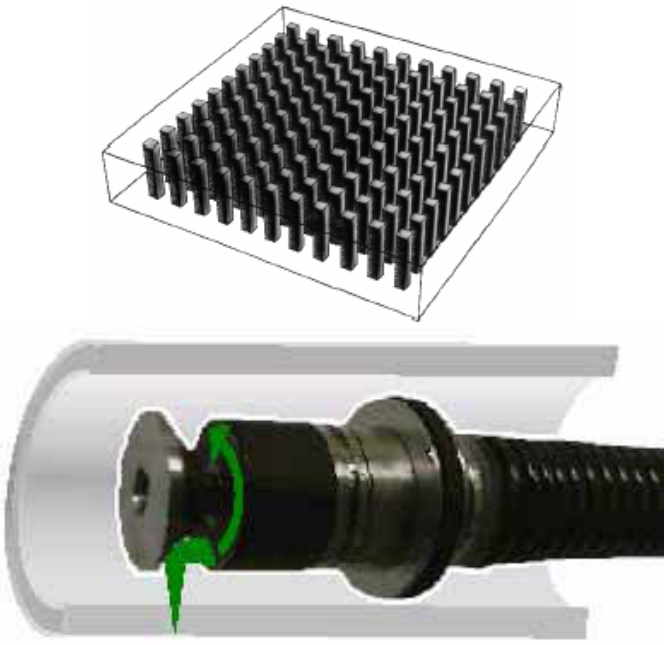

Figure 16. Composite phased array probe for steam generator tubing inspection: the principle of the structure (left) and technique (right) of inspection

2.2.6 Guided wave technique

Guided waves can be generated in tubes so that the waves propagate on both surfaces simultaneously filling the whole tube volume. The waves generated in a fixed position can be made to propagate distances of several meters. Multiple reflections take place during propagation, and a plate wave type guided wave is generated during constructive interference of the waves. The generation of

guided wave mode depends on the frequency, tube wall thickness, generation method (magnetostriction, acoustical waves, thermal waves) and material properties. In a tube several wave modes can exist with different properties. For example, each mode has a certain phase and group velocity. One of the most important factors is to choose the right wave mode to measure the desired defect type. Normally axisymmetric longitudinal wave mode is used to detect defects in steam generator tubing. Adjustment of the guided wave frequency is carried out using a higher frequency transmitter and the echo is measured using different frequencies in the receiver. If the defect is larger than the wavelength, several factors affect the reflection and defect sizing is complicated.

Figure 18 shows a probe consisting of several parts. The guided wave probe is inserted into the tube. The sender and receiver coils are positioned on a steady rod. When the rod is inserted into the tube, generating pulse is merged through the sending coil to generate elastic waves that propagate in two directions. The distance of the probe compared to the end of the tube must be set manually to receive maximum constructive interference from point C of the tube (Figure 18). By changing the frequency of signal, also the optimum distance L from the tube end changes. The amplitude difference between signals A and D is 14 dB, even though the distance to the notch D is larger (Figure 17). The indications are notches with a same depth but different length in the circumferential direction. By changing the inspection frequency the amplitude of the indication can be considerably changed. For the case in Fig. 17, the frequency varied from 18 to 48 kHz.

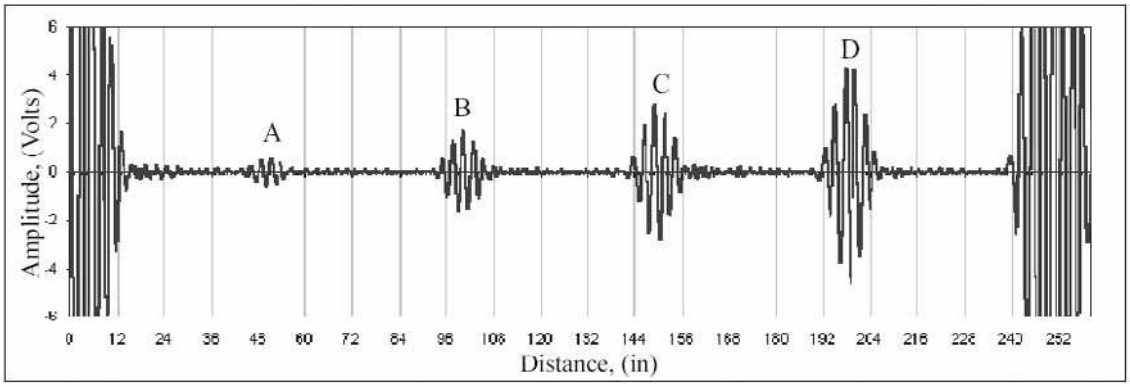

Groove	A	B	C	D
Depth, (in)	0.02	0.02	0.02	0.02
Axial extent, (in)	0.125	0.375	0.75	1.5

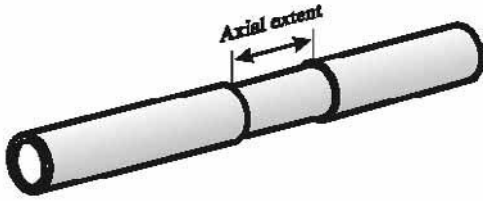

Figure 17. Indications from different axial distances in the probe when using guided waves for tube inspection. The reference reflectors have same depth but the length varies (Vinogradov et al. 2002a).

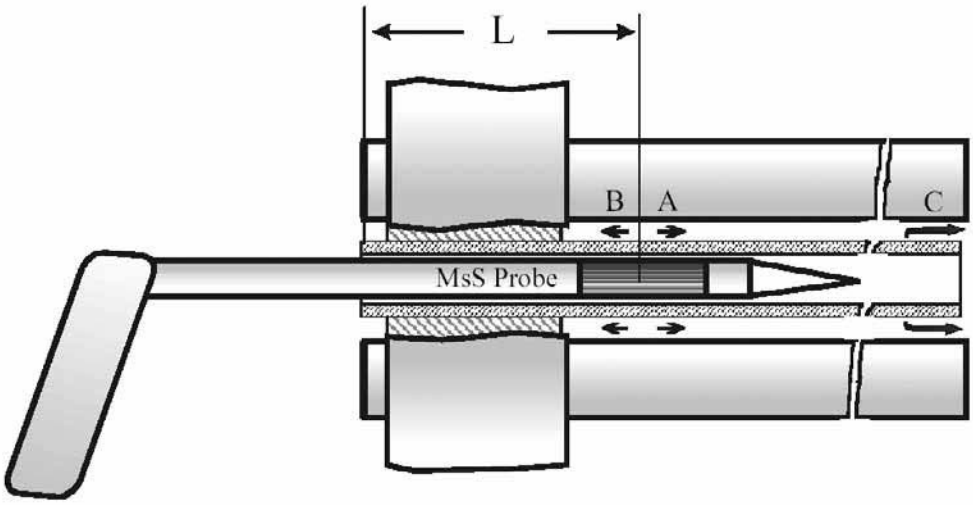

Figure 18. Probe for guided waves in thin tubes (Vinogradov et al. 2002a).

The guided waves can be used to classify defects, but sizing is extremely difficult (Vinogradov et al. 2002a, b). The advantages of the technique are that the inspection can be carried out from one point, and support plates do not affect much the guided waves. The sensitivity of the method is similar to detect the ID- and OD-defects, but to distinguish these from each other is difficult.

2.2.7 Electromagnetic acoustic transducers (EMAT)

An EMAT-probe can generate different types of waves including guided waves, surface waves and horizontally polarised shear waves (SH-waves). One of the first applications of the EMAT-probe was detection of circumferential cracks under the support plates in long tubing. To generate SH-waves the EMAT-probe is divided into two parts: permanent magnet and coil. The permanent magnet is constructed sequentially and located behind the coil. This probe generates torsional shear waves in circumferential direction, and these waves propagate in the axial direction. Circumferential cracks in the support plate area cause a strong reflection. The support plate causes hardly any reflection and additionally the wave can propagate in bent areas too. This technique is capable of detecting all defects in the support plate areas with one measurement (Alers 2003).

For inspection of Zr-Nb-tubing an EMAT-probe has been developed for measuring the hydride concentration. The hydrides are associated with very small cracks in the tube wall. EMAT-probes have been constructed with focussing only to ¼ of the circumference. By moving the probe it is possible to measure the part of the circumference outside the focus area. The Lamb waves are sensitive to hydride concentration and also to physical stage of the tube. The generated Lamb waves are insensitive for ID-cracks (Alers 2003).

2.3 Magnetic flux leakage technique

The magnetic flux leakage technique is only applied for ferromagnetic materials. The method is based on magnetisation of the material so that when a magnet is inserted in a tube to be inspected, the magnetic field is modified by defects located between the poles. Corresponding magnetic flux leakage lines emerge from the material, and this flux leakage can be detected with an inductive pick up coil or Hall-probe (Nestleroth et al. 1999, Figure 19).

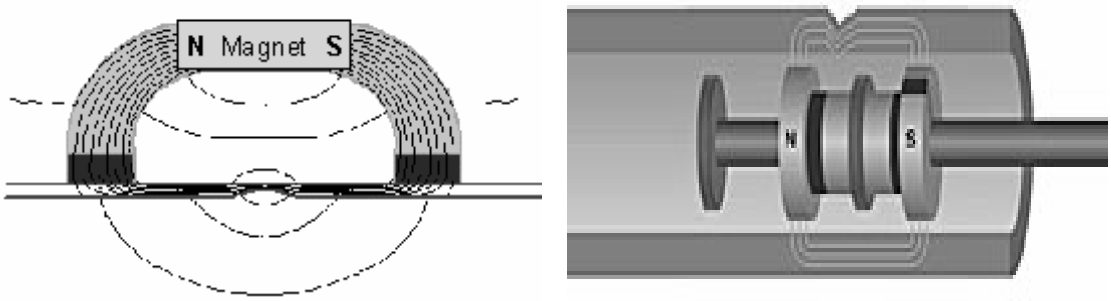

Figure 19. The principle of the magnetic flux leakage technique for tube inspection.

The accuracy of the technique is affected by many factors like magnetisation, coupling between magnet and material to be inspected, discontinuance and visualisation of the flux leakage amplitude. One of the main factors is permeability, which decreases with increasing magnetic field strength. Sufficient level of magnetic field strength is needed to indicate local corrosion (Nestleroth et al. 1999, Figure 20).

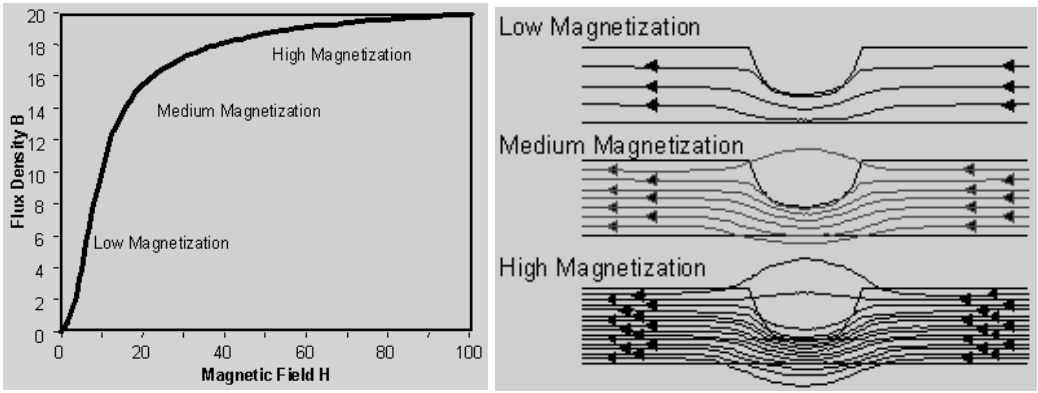

Figure 20. The magnetization strength affects the strength of magnetic flux leakage amplitude outside the inspected material.

The magnetic flux leakage emerges from the ID- and OD-surfaces. The flux density also depends on the defect geometry, so that a high flux density outside the tube is observed if the defect is sharp like a crack. The magnetic flux leakage can also give the amount of corrosion loss of the wall thickness (Figure 21, Nestleroth et al. 1999). The defect size, length, stress stage, elongation and other present defects can affect the magnetic flux leakage.

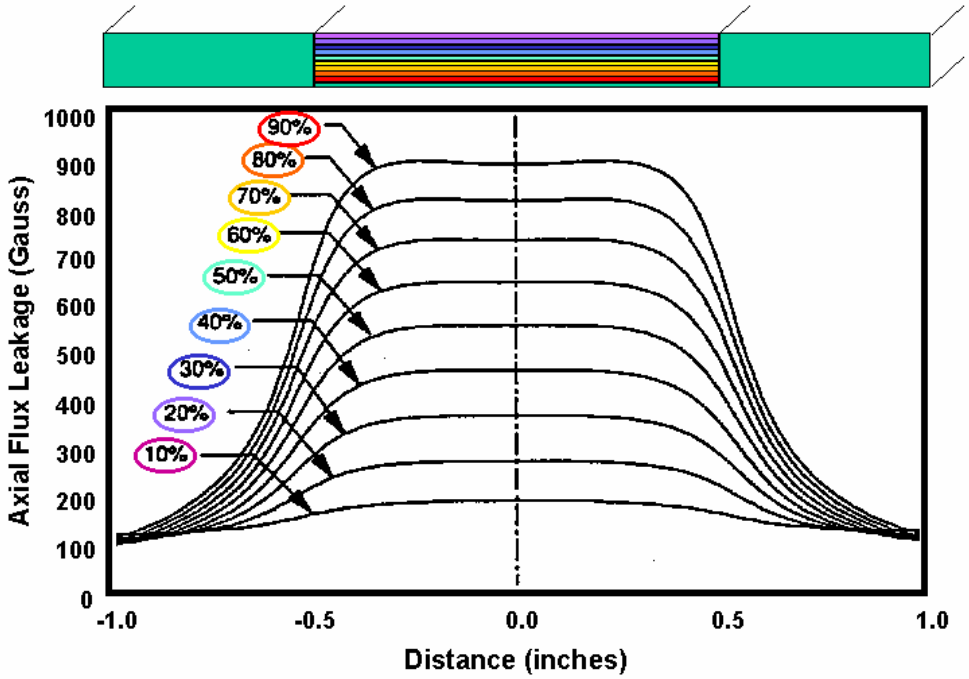

Figure 21. The wall thickness effect to the magnetic flux leakage amplitude.

2.4 Dye penetrant testing of internal surface

A dye penetrant inspection (PT) technique with a laser system (LSPI) to record images has been developed for indications on the inner surface of tubes (Figure 22). This method can be used for inspecting boiler, heat exchanger or steam generator tubing. Reliable detection and recording of internal surface cracks is claimed, with one tube inspection taking a few minutes. Similar resolution as for (macroscopic) surface replication is quoted, although the required surface condition is not reported (LTC, 2004).

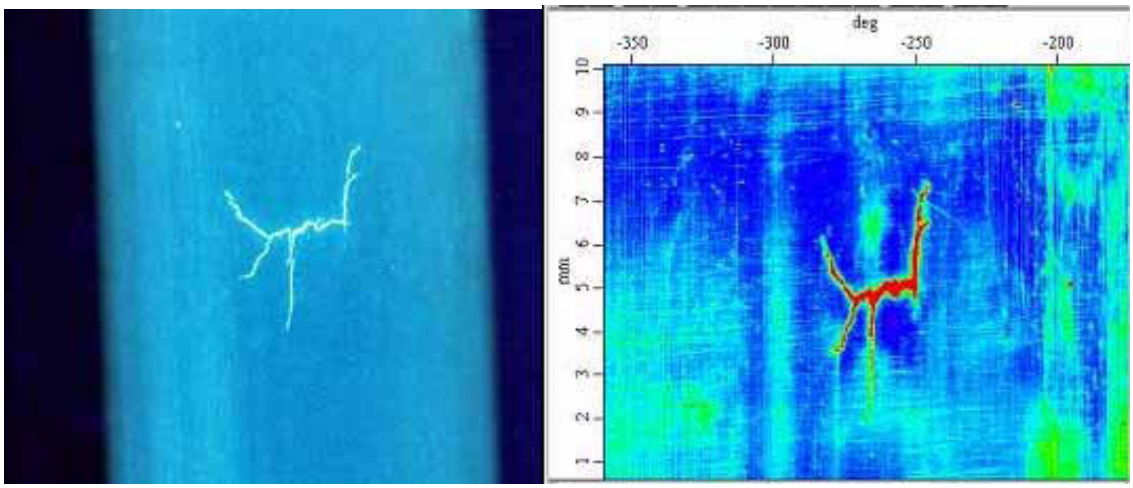

Figure 22. Comparison of a laser scanned image (right) and direct dye penetrant appearance (left) for the same 4–5 mm defect on the internal surface of a ∅ 17 mm tube.

The advantage of the technique is a recorded quantitative inspection result for the inner surface of the tubes. About the defect depth this technique gives practically no information. The equipment is working with remote control and the results are in real time.

3. Comparison of tube inspection techniques

Eddy current techniques are market leaders in tube inspection, but also show some limitations in defect detection and sizing. This may lead to unnecessary shortening of inspection intervals or unnecessary plugging of tubes and related extra cost, if sufficiently accurate tube life cannot be estimated from the inspection results. In such cases other and slower but more accurate inspection techniques may well be economically justified. For alternative options in tube inspection, one comparison has been previously made by Birring (1999). An extended comparison between different techniques is shown in Table 2.

Table 2 . Comparison of different methods for tube inspection.

Technique	Materials	Defect type	Detection	Sizing	Speed
ET-bobbing coil	conductors	all	partly limited	partly limited	very fast
ET-rotating coil	conductors	all	good	partly limited	fast
ET-array coil	conductors	all	good	partly limited	very fast
ET-magnetising coil	conductors	all	limited	limited	very fast
ET-remote field	conductors	all	partly limited	partly limited	fast
UT-pattern recogn.	all	all	partly limited	poor	slow
UT-IRIS	all	corrosion	partly limited	poor	slow
UT-echodynamics	all	all	partly limited	partly limited	slow
UT-tip diffraction	all	cracks	good	good	very slow
UT-TOFD	all	cracks	good	good	very slow
UT-phased array	all	all	good	good	satisfactory
UT-guided waves	all	all	partly limited	limited	fast
UT-EMAT	conductors	all	partly limited	limited	fast
UT-creeping waves	all	cracks	good	partly limited	slow
UT-leaky Rayleigh	all	cracks	good	partly limited	slow
MFL	conductors	corrosion, cracks	partly limited	partly limited	satisfactory
PT/VT-laser	all	surface cracks	surface cracks	poor	slow

4. Summary and conclusions

Tube inspection techniques have shown much development during the last five years. Particular improvements have been introduced to remove or decrease some of the major disadvantages of various techniques.

In case of eddy current techniques (ET), detection of small defects has been difficult. Array coil techniques offer improved defect detection probability without losing much in the speed of the traditional eddy current inspection. The

remote field inspection (RFEC) provides opportunities for defect sizing both in ferromagnetic and other materials. Although the method is slower than conventional eddy current testing, it is faster for non-ferromagnetic than for ferromagnetic tubes, because higher inspection frequencies can be applied for non-ferromagnetic tubes. For all ET, proper visualisation of the inspection results is important.

Ultrasonic inspection techniques (UT) can provide particular improvements in defect characterisation and sizing. This can be important in the common cases where the accuracy of the inspection results limits the precision of estimated tube life. Promising or already established ultrasonic techniques for this purpose include for example the phased array technique using small probe elements, diffraction techniques, guided waves and EMAT-probes that can help in various special cases.

The magnetic flux leakage technique offers in many cases a sufficient inspection method for tubes with rough surfaces and ferromagnetic materials. Not only surface cracking but also corrosion pits can be detected with a suitably optimised flux leakage technique. Visualisation of the results is an important factor for convenient application of the flux leakage method.

Laser scan imaging can be combined with dye penetrant testing (PT) for internal surface testing of tubes. This technique is reported to offer a resolution almost comparable to surface replica inspection. However, like PT in general, the approach is applicable for surface cracking only.

All inspections are based of course on assumption that the largest defects are detected. In reality the tubes also contain defects that the applied methods do not detect. Qualification is a tool to manage the probability of detection and probability of false calls, both non-zero in all cases.

Inspection of tubes has to meet requirements of detection of real degradation in an optimised and cost saving way. This may well require a combination of several techniques depending on the case, degradation mechanisms, materials and defect types as well as the variation in the defects and tubing geometry.

References

Alers, G.A. 2003. Personal information, application of EMATs to problems in industry. 5 p.

Birring, A.S. 1999. Selection of NDT techniques for inspection of heat exchanger tubing. ASNT International Conf. on Petroleum Industry Inspection, June, Houston, Texas. 14 p.

Broere, C., Krutzen, R. & de Boer, F. 2001. Ultrasonic testing for IDSCC in small radius U-bends of steam generator tubes. Proceedings of the 3rd International Conference on NDE in Relation to Structural Integrity for Nuclear and Pressurised Components. Seville, Spain, 14–16 October, 2001. Pp. 896–900.

EPRI 2000. Steam Generator Progress Report 1000805, Revision 15. Final Report, Nov. 2000. 423 p.

Fleury, G., Poguet, J., Burat, O. & Moreau G. 1998. Circular phased array probes for inspection of superphoenix steam generator tubes. 9 p.

Fukutomi, H., Takagi, T. & Nishikawa, M. 2001. Remote field eddy current technique applied to non-magnetic steam generator tubes, Vol. 34, No. 1, pp. 17–34.

Guill, R. & Henry, G. 2000. X-probe: Eddy current Array probe as a high-Speed alternative to rotating probes. EPRI Center lines No. 11, Vol. 10, Summer 2000, EPRI NDE Center, Charlotte, pp. 1–3.

Henry, G. & Muthu, N. 2000. PWSCC flaw sizing performed for Ontario power generation. EPRI Center lines No. 1, Vol. 10, Spring 2000, EPRI NDE Center, Charlotte, p. 6.

Isnan, M. 1998. Entwickung und Optimierung eines Wirbelstrom-Sonden-Arrays mit umlaufender Abtastung für die Rohrinnen-prüfung unter Einbeziehung von numerischen Filtern zur Steigerung der Fehlernachweisempfindlichkeit und def Verbesserung der Fehlercharakterisierung, Dissertation Saarland Universität. D Nr. 307. 68 p.

Kenefick S. & Henry G. 1999. UT-Transducer used for steam generator inspection. EPRI Center lines No. 1, Vol. 9, Spring 1999, EPRI NDE Center Charlotte, pp. 1–5.

Kenefick, S. & Henry, G. 2001. Ultrasonic imaging technique for characterizing surface breaking flaws. Proc. of the 3rd International Conference on NDE in Relation to Structural Integrity for Nuclear and Pressurised Components. Seville, Spain, 14–16 October 2001. Pp. 552–562.

Kenefick, S. 2002. Ultrasonic examination of steam generator tubes, 12th Annual NDE issues meeting, Kingston Plantation, Myrtle Beach, 10th July. 79 p.

Krutzen, R. Cummings Bodenschatz, H. & Broere, C. 1998. Evaluation of currently applied ultrasonic sizing techniques for stress corrosion cracks in steam generator tubes. 17th EPRI Steam generator NDE Workshop, August 17–19, Breckenridge, Colorado, USA. 10 p.

Krzywosz, K. & Ammirato, F. 1997. Performance baser remote-field. Eddy current examination of high-pressure feedwater heaters. Proc. of the 3rd International Workshop on ENDE, Reggio Calabria, Italy, September. 5 p.

Kupperman, D.S., Muscara, J., Bakhtiari S., Park, J.Y. & Shack, W.J. 2002. Eddy current analysis round robin using the NRC steam generator mock up. 11 p.

Lahdenperä, K. 2002. Steam generator eddy current inspection techniques. Espoo: Technical Research Centre of Finland, Industrial Systems. VTT Research Report BTUO77-021067. 29 p.

Lipponen, A., Pitkänen, J., Kauppinen, P. Vuorio, L., Brusin. J. & Lintunen, A. 2002. The use of exact determination of defect location in heat exchanger tubes for total view of the process. 8th European Conference on Non-destructive Testing, ECNDT, Barcelona, Spain 17–21 June. Asociacion Espanola de Ensayos No Destructivos. 5 p.

LTC, 2004. Brochure in internet: http://www.laser-ndt.com/penetranttube.html

Mayes, D. 2002. Revision 6, PWR SG Examination Guidelines; Significant changes and issues. EPRI 21st SG NDE Workshop, July 15–17. 28 p.

NEI 97-06 (Revision 1), January 2001.

Nestleroth, J.B., Bubenik, T.A. & Haines, H. 1999. Magnetic flux leakage (MFL) technology for natural gas pipeline inspection. Battelle, 187 p.

Nuson, 2003. Internet: http:\\www.Nuson.nl\index.html.

Ostermeyer, H. & Stegeman, D. 1999. New aspects for remote field eddy current probe development. NDT.net, August, Vol. 4, No. 8. 6 p.

Shah, V. & MacDonald, P. 1993. Aging and life extension of major light water reactor components. Elsevier. 943 p.

Schmidt, T.R. 1984. The remote field eddy current inspection technique. Materials Evaluation, Vol. 42, February, pp. 225–230.

Shin, Y.-K., Chung, T.-E. & Lord, W. 2001. Remote field eddy current technique applied to the inspection of nonmagnetic steam. Review of progress in quantitative nondestructive evaluation, Vol. 20. Ed. by D.O.Thompson & D.E. Chimenti, April 30. Pp. 392–399.

Siegel, J.D. 1999. Array coil versus single rotating coil probes for the inspection of steam generator tubes. Insight, Vol. 41, No. 9, pp. 592–595.

Silk, M.G. 1979. Defect sizing using ultrasonic diffraction. British Journal of NDT, Vol. 21, No. 1, pp. 12–15.

Sullivan, S. & Atherton, D.L. 1989. Analysis of the remote field eddy current effect in non-magnetic tubes. Materials Evaluation, Vol. 47, No. 1. pp. 80–86.

Vinogradov, S., Jacobs, B. & Godwin, J. 2002a. Application of guided waves ti sizing corrosion/erosion defects in pipes. 6th EPRI Piping and Bolting Inspection Conference, July 30 – August 1, 2002 Point Clear, Alabama. 8 p.

Vinogradov, S., Jacobs, B. & Godwin, J. 2002b. Experimental and theoretical investigation for the use of guided waves to detect and size, corrosion/erosion defects in heat exchanger tubes. 7th EPRI Balance of Plant Heat Exchanger NDE Symposium, 17–19 June 2002, Santa Ana Pueblo, New Mexico. 9 p.

Published by

Series title, number and report code of publication

VTT Symposium 234
VTT–SYMP–234

Author(s)
Veivo, Juha & Auerkari, Pertti (eds.)

Title

BALTICA VI
Life Management and Maintenance for Power Plants. Vol. 2

Abstract

BALTICA VI International Conference on Life Management and Maintenance for Power Plants, held on June 8–10, 2004 in Helsinki – Stockholm – Helsinki

This is one of the two volumes of the proceedings of the BALTICA VI Conference, which provides a forum for the transfer of technology from applied research to practice. The Conference focuses on reviewing new technology, recent experience and improvements in applied life management and maintenance for successful and economical operation of power plants.

Keywords
power plant, maintenance, boiler, machinery, equipment, inspection, monitoring, condition, life, performance, risk, reliability

Activity unit
VTT Industrial Systems, Kemistintie 3, P.O.Box 1704, FIN–02044 VTT, Finland

ISBN			Project number
951–38–6293–3 (soft back ed.) 951–38–6294–1 (URL: http://www.vtt.fi/inf/pdf/)			
Date May 2004	Language English	Pages 354 p.	Price H
Name of project BALTICA VI		Commissioned by	
Series title and ISSN VTT Symposium 0357–9387 (soft back ed.) 1455–0873 (URL: http://www.vtt.fi/inf/pdf/)		Sold by VTT Information Service P.O.Box 2000, FIN–02044 VTT, Finland Phone internat. +358 9 456 4404 Fax +358 9 456 4374	

BALTICA VI International Conference on Life Management and Maintenance for Power Plants, June 8–10, 2004 in Helsinki–Stockholm–Helsinki

This is one of the two volumes of the proceedings of the BALTICA VI Conference. The Conference focuses on reviewing new technology, recent experience and improvements in applied life management and maintenance for supporting successful and economical operation of power plants.

The BALTICA events:

BALTICA I. Materials Aspects in Life Extension of Power Plants, Helsinki–Stockholm–Helsinki, September 19–22, 1988

BALTICA II. International Conference on Plant Life Management & Extension, Helsinki–Stockholm–Helsinki, October 5–6, together with the International Symposium on Life and Performance of High Temperature Materials and Structures, Tallinn, Estonia, October 7–8, 1992

BALTICA III. International Conference on Plant Condition & Life Management, Helsinki-Stockholm-Helsinki, June 6–8, 1995

BALTICA IV. Plant Maintenance for Managing Life & Performance, Helsinki–Stockholm–Helsinki, September 7–9, 1998

BALTICA V. International Conference on Condition and Life Management for Power Plants, Hotel Haikko Manor, Porvoo, Finland, June 6–8, 2001

BALTICA VI. International Conference on Life Management and Maintenance for Power Plants, Helsinki–Stockholm–Helsinki, June 8–10, 2004

Tätä julkaisua myy	Denna publikation säljs av	This publication is available from
VTT TIETOPALVELU PL 2000 02044 VTT Puh. (09) 456 4404 Faksi (09) 456 4374	VTT INFORMATIONSTJÄNST PB 2000 02044 VTT Tel. (09) 456 4404 Fax (09) 456 4374	VTT INFORMATION SERVICE P.O.Box 2000 FIN–02044 VTT, Finland Phone internat. +358 9 456 4404 Fax +358 9 456 4374

ISBN 951–38–6293–3 (soft back ed.)
ISSN 0357–9387 (soft back ed.)

ISBN 951–38–6294–1 (URL: http://www.vtt.fi/inf/pdf/)
ISSN 1455–0873 (URL: http://www.vtt.fi/inf/pdf/)

VTT SYMPOSIUM 234 BALTICA VI. Life Management and Maintenance for Power Plants. Vol. 2